NanoScience and Technology

Hideo Aoki
Mildred S. Dresselhaus *Editors*

Physics of Graphene

Springer

NanoScience and Technology

Series Editors

For further volumes:
www.springer.com/series/3705

The series NanoScience and Technology is focused on the fascinating nano-world, mesoscopic physics, analysis with atomic resolution, nano and quantum-effect devices, nanomechanics and atomic-scale processes. All the basic aspects and technology-oriented developments in this emerging discipline are covered by comprehensive and timely books. The series constitutes a survey of the relevant special topics, which are presented by leading experts in the field. These books will appeal to researchers, engineers, and advanced students.

Hideo Aoki • Mildred S. Dresselhaus
Editors

Physics of Graphene

Springer

Editors
Hideo Aoki
Faculty of Science, Department of Physics
University of Tokyo
Tokyo, Japan

Mildred S. Dresselhaus
Physics and Electrical Eng. Department
Massachusetts Institute of Technology
Cambridge, MA, USA

ISSN 1434-4904
ISSN 2197-7127 (electronic)
NanoScience and Technology
ISBN 978-3-319-02632-9
ISBN 978-3-319-02633-6 (eBook)
DOI 10.1007/978-3-319-02633-6
Springer Cham Heidelberg New York Dordrecht London

Library of Congress Control Number: 2013957703

Printed on acid-free paper

Springer is part of Springer Science+Business Media (www.springer.com)

Preface

Fascination with graphene has been growing very rapidly in recent years and the physics of graphene is now becoming one of the most interesting as well as the most fast-moving topics in condensed-matter physics. Needless to say, the Nobel prize in physics awarded to Andre Geim and Konstantin Novoselov in 2010 has given a tremendous impetus to this topic. Several years have passed since Andre Geim and his group put forward their method for the fabrication of graphene, as a result of which an anomalous quantum Hall effect was observed. This, however, is only one of the hallmarks of the unusual properties of the graphene system. The horizon of the physics of graphene is ever becoming wider, where physical concepts go hand in hand with advances in experimental techniques. Thus we are now expanding our interests to not only transport but also optical and other properties for layered systems that include multilayers as well as monolayer graphene.

Thus it should be very timely to publish a book that overviews the physics of graphene, which is exactly why we have edited the present volume, where general and fundamental aspects in the physics of graphene are overviewed by outstanding authorities. The book comprises five experimental and five theoretical chapters. A birds' eye view of the chapter contents is given in the figure overleaf.

We have endeavored to have reasonable levels of accessibility to students as well, with some heuristic introductions in each chapter. Given the unusually rapid progress in the field of graphene, we have found it impossible to cover all the frontiers, while parts of the chapters do extend to advanced levels. For instance, we have not covered much on graphene applications, which would require another volume. We hope the state-of-the-art articles presented here on graphene physics, which start from the "massless Dirac particle" and proceed with further unique aspects of graphene, will benefit a wide audience, and encourage them to go even further and to explore new avenues in this fascinating topic.

Tokyo, Japan — Hideo Aoki
Cambridge, MA, USA — Mildred S. Dresselhaus

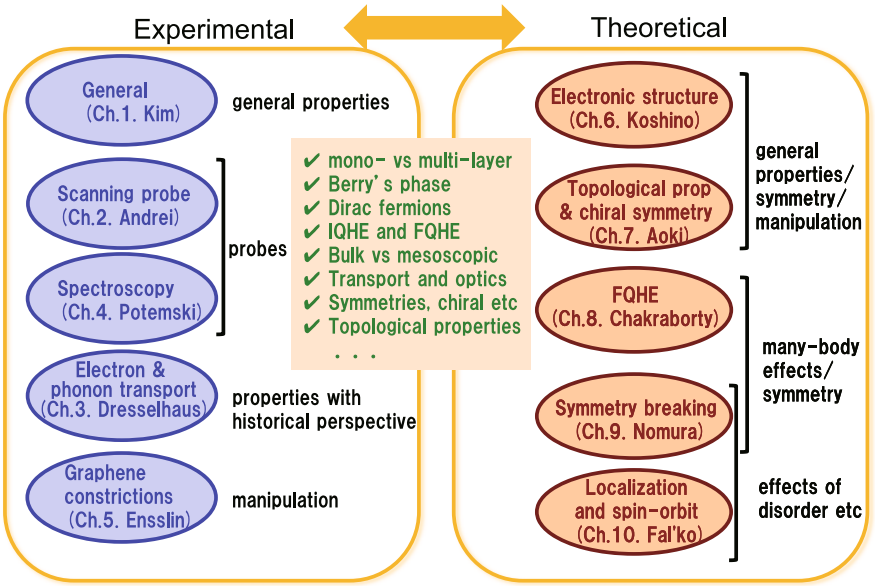

Fig. 1 Plan of the book

Contents

Part I
Experimental

Chapter 1
Experimental Manifestation of Berry Phase in Graphene

Andrea F. Young, Yuanbo Zhang, and Philip Kim

Abstract The honeycomb lattice structure of graphene requires an additional degree of freedom, termed as pseudo spin, to describe the orbital wave functions sitting in two different sublattices of the honeycomb lattice. In the low energy spectrum of graphene near the charge neutrality point, where the linear carrier dispersion mimics the quasi-relativistic dispersion relation, pseudo spin replaces the role of real spin in the usual Dirac Fermion spectrum. The exotic quantum transport behavior discovered in graphene, such as the unusual half-integer quantum Hall effect and Klein tunneling effect, are a direct consequence of the pseudo spin rotation. In this chapter we will discuss the non-trivial Berry phase arising from the pseudo spin rotation in monolayer graphene under a magnetic field and its experimental consequences.

1.1 Introduction

Many of the interesting physical phenomena appearing in graphene are governed by the unique chiral nature of the charge carriers in graphene owing to their quasi relativistic quasiparticle dynamics described by the effective massless Dirac equation. This interesting theoretical description can be dated back to Wallace's early work of the electronic band structure calculation of graphite in 1947 where he used the simplest tight binding model and correctly captured the essence of the electronic band structure of graphene, the basic constituent of graphite [1]. Since then the chiral nature of the graphene band structure has been rediscovered several times in different contexts [2–5]. Independent to these theoretical works, experimental efforts to obtain graphene dated back to Böhm et al.'s early work of transmission elec-

A.F. Young
Department of Physics, MIT, Cambridge, MA, USA

Y. Zhang
Department of Physics, Fudan University, Shanghai, China

P. Kim (✉)
Department of Physics, Columbia University, New York, NY 10027, USA
e-mail: pkim@phys.columbia.edu

H. Aoki, M.S. Dresselhaus (eds.), *Physics of Graphene*, NanoScience and Technology,
DOI 10.1007/978-3-319-02633-6_1,

tron microscopy [6] and the early chemical deposition growth of graphene on metal surfaces developed in the 1990s [7].

In the past decade, renewed efforts to obtain the atomically thin graphite have been pursued through several different routes. In retrospect, these various methods fall into two categories: the bottom-up approach and the top-down approach. In the former, one started with carbon atoms and one tries to assemble graphene sheets by chemical pathways [8, 9]. This is best exemplified by work of the W.A. de Heer group at the Georgia Institute of Technology. In Ref. [9], they demonstrated that thin graphite films can be grown by thermal decomposition on the (0001) surface of 6H-SiC. This method opens the way to large scale integration of nanoelectronics based on graphene. Recent progress through this chemical approach to graphene synthesis has had dazzling successes by diverse routes, including epitaxial graphene growth [10], chemical vapor deposition [11, 12], and solution processing [13].

On the other hand, the top-down approach starts with bulk graphite, which essentially involves graphene sheets stacked together, and tries to extract graphene sheets from the bulk by mechanical exfoliation. The mechanical extraction of layered material dates back to the 1970s. In his seminal experiment [14], Frindt showed that few layers of superconducting $NbSe_2$ can be mechanically cleaved from a bulk crystal fixed on an insulating surface using epoxy. While it is known for decades that people routinely cleave graphite using scotch tape when preparing sample surfaces for Scanning Tunneling Microscopy (STM) study and all optics related studies, the first experiment explicitly involving the mechanical cleavage of graphite using scotch tape was carried out by Ohashi et al. [15]. The thinnest graphite film obtained in this experiment was about 10 nm, corresponding to $\sim$30 layers.

Experimental work to synthesize very thin graphitic layers directly on top of a substrate [16] or to extract graphene layers using chemical [17] or mechanical [18–20] exfoliation was demonstrated to produce graphitic samples with thicknesses ranging from 1 to 100 nm. Systematic transport measurements have been carried out on mesoscopic graphitic disks [21] and cleaved bulk crystals [15] with sample thicknesses approaching $\sim$20 nm, exhibiting mostly bulk graphite properties at these length scales. More controllability was attempted when Ruoff et al. worked out a patterning method for bulk graphite into a mesoscopic scale structure to cleave off thin graphite crystallites using atomic force microscopy [20].

A sudden burst of experimental and theoretical work on graphene followed the first demonstration of single- and multi-layered graphene samples made by a simple mechanical extraction method [22], while several other groups were trying various different routes concurrently [9, 23, 24]. The method that Novoselov et al. used was pretty general, and soon after, it was demonstrated to be applicable to other layered materials [25]. This simple extraction technique is now known as the mechanical exfoliation method. It also has a nick name, 'scotch tape' method, since the experimental procedure employs adhesive tapes to cleave off the host crystals before the thin mesocoscopic samples are transferred to a target substrate, often a silicon wafer coated with a thin oxide layer. A carefully tuned oxide thickness is the key to identify single layer graphene samples among the debris of cleaved and transferred mesoscopic graphite samples using the enhanced optical contrast effect due to Fabry-Perot interference [26].

Since this first demonstration of experimental production of an isolated single atomic layer of graphene sample, numerous unique electrical, chemical, and mechanical properties of graphene have been investigated. In particular, an unusual half-integer quantum Hall effect (QHE) and a non-zero Berry's phase [27, 28] were discovered in graphene, providing unambiguous evidence for the existence of Dirac fermions in graphene and distinguishing graphene from conventional 2D electronic systems with a finite carrier mass. In this review, we will focus on the chiral nature of the electron dynamics in monolayer graphene where the electron wave function's pseudo-spin plays an important role. We will present two experimental examples: the half-integer QHE [27, 28] and the Klein tunneling effect in graphene [29]. The quasi relativistic quantum dynamics of graphene has provided a compact and precise description for these unique experimental observations and further providing a playground for implementing tests of quantum electrodynamics (QED) in a simple experimental situation [30], where electron Fabry-Perrot oscillations were recently observed [29].

1.2 Pseudospin Chirality in Graphene

Carbon atoms in graphene are arranged in a honeycomb lattice. This hexagonal arrangement of carbon atoms can be decomposed into two interpenetrating triangular sublattices related to each other by inversion symmetry. Taking two atomic orbitals on each sublattice site as a basis, the tight binding Hamiltonian can be simplified near two inequivalent Brillouin zone corners $\mathbf{K}$ and $\mathbf{K}'$ as

$$\hat{H} = \pm\hbar v_F \boldsymbol{\sigma} \cdot (-i\hbar\nabla) \tag{1.1}$$

where $\boldsymbol{\sigma} = (\sigma_x, \sigma_y)$ are the Pauli matrices, $v_F \approx 10^6$ m/s is the Fermi velocity in graphene and the $+$ $(-)$ sign corresponds to taking the approximation that the wave vector $\mathbf{k}$ is near the $\mathbf{K}$ ($\mathbf{K}'$) point (see Fig. 1.1).

The structure of this 'Dirac' equation is interesting for several reasons. First, the resulting energy dispersion near the zone corners is linear in momentum, $E(\boldsymbol{\kappa}) = \pm\hbar v_F|\boldsymbol{\kappa}|$, where the wave vector $\boldsymbol{\kappa}$ is defined relative to $\mathbf{K}$ (or $\mathbf{K}'$), i.e., $\boldsymbol{\kappa} = \mathbf{k} - \mathbf{K}$ (or $\mathbf{K}'$). Consequently, the electrons near these two Dirac points always move at a constant speed, given by the Fermi velocity $v_F \approx c/300$ (rather than the real speed of light c). The electron dynamics in graphene are thus effectively 'relativistic', where the speed of light is substituted by the electron Fermi velocity v_F. In a perfect graphene crystal, the Dirac points ($\mathbf{K}$ and $\mathbf{K}'$) are coincident with the overall charge neutrality point (CNP), since there are two carbon atoms in the unit cell of graphene and each carbon atom contributes one electron to the two bands, resulting in the Fermi energy E_F of neutral graphene lying precisely at the half-filled band.

For the Bloch wave function near $\mathbf{K}'$, the 'Dirac' equation in (1.1) can be rewritten as

$$\hat{H} = \pm\hbar v_F \boldsymbol{\sigma} \cdot \boldsymbol{\kappa} \tag{1.2}$$

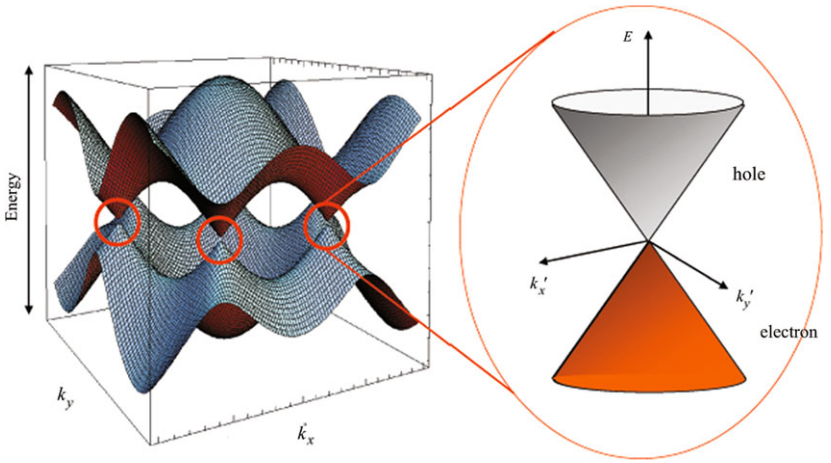

Fig. 1.1 Energy band structure of graphene. The valence band (*lower band*) and conduction band (*upper band*) touch at six points, where the Fermi level is located. In the vicinity of these points, the energy dispersion relation is linear. Reproduced from Ref. [31]

The solution of this massless Dirac fermion Hamiltonian is studied by [5, 32, 33]:

$$|\boldsymbol{\kappa}\rangle = \frac{1}{\sqrt{2}} e^{i\boldsymbol{\kappa}\cdot\mathbf{r}} \begin{pmatrix} -ise^{-i\theta_\kappa/2} \\ e^{i\theta_\kappa/2} \end{pmatrix} \tag{1.3}$$

where θ_κ is the angle between $\boldsymbol{\kappa} = (\kappa_x, \kappa_y)$ and the y-axis, and $s = +1$ and -1 denote the states above and below $\mathbf{K}$, respectively. The corresponding energy for these states is given by

$$E_s(\boldsymbol{\kappa}) = s\hbar v_F |\boldsymbol{\kappa}| \tag{1.4}$$

where $s = +1/-1$ is an index for the positive/negative energy band, respectively. The two components of the state vector give the amplitudes of the electronic wave functions on the atoms of the two sublattices, so the angle θ_κ determines the character of the underlying atomic orbital mixing.

The two-component vector in formula in (1.3) can be viewed as a result of a spinor-rotation of θ_κ around $\hat{z}$ axis with the spin-1/2 rotation operator

$$R(\theta) = \exp\left(-i\frac{\theta}{2}\sigma_z\right) = \begin{pmatrix} e^{-i\theta/2} & 0 \\ 0 & e^{+i\theta/2} \end{pmatrix} \tag{1.5}$$

More explicitly, the vectorial part of the Bloch state, $|\boldsymbol{s}_p\rangle = e^{-i\boldsymbol{\kappa}\cdot\mathbf{r}}|\boldsymbol{\kappa}\rangle$ can be obtained from the initial state along the y-axis

$$|\mathbf{s}_p^0\rangle = \frac{1}{\sqrt{2}} \begin{pmatrix} -is \\ 1 \end{pmatrix} \tag{1.6}$$

by the rotation operation, $|\mathbf{s}_p\rangle = R(\theta_\kappa)|\mathbf{s}_p^0\rangle$. Note that this rotation operation clearly resembles that of a two-component spinor describing the electron spin, but arising from the symmetry of the underlying honeycomb graphene lattice. In this regard,

$|\mathbf{s}_p\rangle$ is often called 'pseudo spin' in contrast to the real spin of electrons in graphene. The above operation also implies that the orientation of the pseudospin is tied to the $\boldsymbol{\kappa}$ vector. This is completely analogous to the real spin of massless fermions which always points along the direction of propagation. For $s = +1$, i.e., corresponding to the upper cone at $\mathbf{K}$ in Fig. 1.1, the states have pseudospin parallel to $\boldsymbol{\kappa}$, and thus correspond to the right-handed Dirac fermions. For $s = -1$, i.e. for the antiparticles in the lower cone, the situation is reversed, resulting in the left-handed Dirac antifermions.

So far our analysis is focused on the $\mathbf{K}$ point. It would be interesting to see what happens at the $\mathbf{K}'$ point. We apply a similar analysis at $\mathbf{K}'$, and the only difference is that now we expand the Hamiltonian around the $\mathbf{K}'$ point: $\mathbf{k} = \boldsymbol{\kappa} + \mathbf{K}'$. Then we obtain a new equation for $\mathbf{K}'$ from (1.1),

$$H = \hbar v_F \boldsymbol{\kappa} \cdot \bar{\boldsymbol{\sigma}} \tag{1.7}$$

where $\bar{\boldsymbol{\sigma}}$ are the complex conjugate of the Pauli matrices $\boldsymbol{\sigma}$. This Hamiltonian is known to describe left-handed massless neutrinos. Therefore at $\mathbf{K}'$ the electron dynamics is again characterized by massless Dirac fermions, but with opposite helicity.

The chirality of the electrons in graphene has important implications on the electronic transport in graphene. In particular, a non-trivial Berry phase is associated with the rotation of the $1/2$-pseudo spinor which plays a critical role to understand the unique charge transport in graphene and nanotubes, as first discussed in Ando et al.'s [5] theoretical work. For example, let us consider a scattering process $\boldsymbol{\kappa} \to \boldsymbol{\kappa}'$ due to a potential $V(\mathbf{r})$ with a range larger than the lattice constant in graphene, so that it does not induce an inter valley scattering between $\mathbf{K}$ and $\mathbf{K}'$ points. The resulting matrix element between these two states is given by [5, 33]

$$\left|\langle \boldsymbol{\kappa}' | V(\mathbf{r}) | \boldsymbol{\kappa} \rangle\right|^2 = \left|V\left(\boldsymbol{\kappa} - \boldsymbol{\kappa}'\right)\right|^2 \cos^2(\theta_{\kappa,\kappa'}/2) \tag{1.8}$$

where $\theta_{\kappa,\kappa'}$ is the angle between $\boldsymbol{\kappa}$ and $\boldsymbol{\kappa}'$, and the cosine term comes from the overlap of the initial and final spinors. A backscattering process corresponds to $\boldsymbol{\kappa} = -\boldsymbol{\kappa}'$. In this case, $\theta_{\kappa,\kappa'} = \pi$ and the matrix element vanishes. Therefore such backward scattering is completely suppressed. In terms of the pseudo spin argument, this back scattering process can be described by rotating $|\boldsymbol{\kappa}\rangle$ by the rotating operation $R(\pi)$. For an atomically smooth potential the matrix element in (1.8) can be expressed

$$\langle \boldsymbol{\kappa}' | V(\mathbf{r}) | \boldsymbol{\kappa} \rangle \approx V\left(\boldsymbol{\kappa} - \boldsymbol{\kappa}'\right) \langle \boldsymbol{\kappa} | R(\pi) | \boldsymbol{\kappa} \rangle \tag{1.9}$$

Note that a π rotation of the $1/2$ spinor always produces an orthogonal spinor to the original one, which makes this matrix element vanish.

The experimental significance of the Berry's phase of π was demonstrated by McEuen et al. [33] in single-wall carbon nanotubes (SWCNTs), which are essentially graphene rolled up into cylinders. The suppression of backscattering in metallic SWCNTs leads to a remarkably long electron mean free path on the order of a micron at room temperature [34].

The suppression of backward scattering can also be understood in terms of the Berry's phase induced by the pseudo spin rotation. In particular, for complete backscattering, (1.5) yields $R(2\pi) = e^{i\pi}$, indicating that rotation in $\boldsymbol{\kappa}$ by 2π leads to

a change of the phase of the wave function $|\boldsymbol{\kappa}\rangle$ by π. This non-trivial Berry's phase may lead to non-trivial quantum corrections to the conductivity in graphene, where the quantum correction enhances the classical conductivity [35]. This phenomena is called 'anti-localization' in contrast to such quantum corrections in a conventional 2-dimensional (2D) system which lead to the suppression of conductivity in a weak localization. This can simply be explained by considering each scattering process with its corresponding complementary time-reversal scattering process. In a conventional 2D electron system such as in GaAs heterojunctions, the scattering amplitude and associated phase of each scattering process and its complementary time-reversal process are equal. This constructive interference in conventional 2D system leads to the enhancement of the backward scattering amplitude and thus results in the localization of the electron states. This mechanism is known as weak localization [36]. In graphene, however, each scattering process and its time reversal pair have a phase difference by π between them due to the non-trivial Berry phase, stemming from 2π rotation of the pseudospin between the scattering processes of the two time reversal pairs. This results in a destructive interference between the time reversal pair to suppress the overall backward scattering amplitude, leading to a positive quantum correction in conductivity. These anti-weak localization phenomena in graphene have been observed experimentally [37].

While the existence of a non-trivial Berry's phase in graphene can be inferred indirectly from the aforementioned experiments, it can be directly observed in the quantum oscillations induced by a uniform external magnetic field [27, 28]. In a semi-classical picture, the electrons orbit along a circle in $\mathbf{k}$ space when subjected to a magnetic field. The Berry's phase of π produced by the 2π rotation of the wave vector manifests itself as a phase shift of the quantum oscillations, which will be the focus of the discussion of the next section.

1.3 Berry Phase in Magneto-Oscillations

We now turn to the massless Dirac fermion described by Hamiltonian in (1.1). In a magnetic field, the Schrödinger equation is given by

$$\pm v_F(\mathbf{P} + e\mathbf{A}) \cdot \boldsymbol{\sigma}\, \psi(\mathbf{r}) = E\psi(\mathbf{r}) \tag{1.10}$$

where $\mathbf{P} = -i\hbar\bigtriangledown$, $\mathbf{A}$ is the magnetic vector potential, and $\psi(\mathbf{r})$ is a two-component vector

$$\psi(\mathbf{r}) = \begin{pmatrix} \psi_1(\mathbf{r}) \\ \psi_2(\mathbf{r}) \end{pmatrix} \tag{1.11}$$

Here we use the Landau gauge $\mathbf{A}$: $\mathbf{A} = -By\widehat{x}$ for a constant magnetic field $\mathbf{B}$ perpendicular to the x–y plane. Then, taking only the $+$ sign in (1.10), this equation relates $\psi_1(\mathbf{r})$ and $\psi_2(\mathbf{r})$:

$$v_F(P_x - iP_y - eBy)\psi_2(\mathbf{r}) = E\psi_1(\mathbf{r}) \tag{1.12}$$

$$v_F(P_x + iP_y - eBy)\psi_1(\mathbf{r}) = E\psi_2(\mathbf{r}) \tag{1.13}$$

Substituting the first to the second equations above, we obtain the equation for $\psi_2(\mathbf{r})$ only

$$v_F^2\left(P^2 - 2eByP_x + e^2B^2y^2 - \hbar eB\right)\psi_2(\mathbf{r}) = E^2\psi_2(\mathbf{r}) \tag{1.14}$$

The eigenenergies of (1.14) can be found by comparing this equation with a massive carrier Landau system:

$$E_n^2 = 2n\hbar eBv_F^2 \tag{1.15}$$

where $n = 1, 2, 3, \ldots$. The constant $-\hbar eB$ shifts the LL's by half of the equal spacing between the adjacent LLs, and it also guarantees that there is a LL at $E = 0$, which has the same degeneracy as the other LLs. Putting these expressions together, the eigenenergy for a general LL can be written as [4, 38]

$$E_n = \mathrm{sgn}(n)\sqrt{2e\hbar v_F^2|n|B} \tag{1.16}$$

where $n > 0$ corresponds to electron-like LLs and $n < 0$ corresponds to hole-like LLs. There is a single LL sitting exactly at $E = 0$, corresponding to $n = 0$, as a result of the chiral symmetry and the particle-hole symmetry.

The square root dependence of the Landau level energy on n, $E_n \propto \sqrt{n}$, can be understood if we consider the DOS for the relativistic electrons. The linear energy spectrum of 2D massless Dirac fermions implies a linear DOS given by

$$N(E) = \frac{E}{2\pi\hbar^2 v_F^2} \tag{1.17}$$

In a magnetic field, the linear DOS collapses into LLs, each of which has the same number of states $2eB/h$. As the energy is increased, there are more states available, so that a smaller spacing between the LLs is needed in order to have the same number of state for each LL. A linear DOS directly results in a square root distribution of the LLs, as shown in Fig. 1.2(c).

A wealth of information can be obtained by measuring the response of the 2D electron system in the presence of a magnetic field. One such measurement is done by passing current through the system and measuring the longitudinal resistivity ρ_{xx}. As we vary the magnetic field, the energies of the LLs change. In particular ρ_{xx} goes through one cycle of oscillations as the Fermi level moves from one LL DOS peak to the next as shown in Fig. 1.2(c). These are the so called Shubinikov de-Haas (SdH) oscillations. As we note in (1.15), the levels in a 2D massless Dirac fermion system, such as graphene, are shifted by a half-integer relative to the conventional 2D systems, which means that the SdH oscillations will have a phase shift of π, compared with the conventional 2D system.

The phase shift of π is a direct consequence of the Berry's phase associated with the massless Dirac fermion in graphene. To further elucidate how the chiral nature of an electron in graphene affects its motion, we resort to a semi-classical model where familiar concepts, such as the electron trajectory, provide us a more intuitive physical picture.

We consider an electron trajectory moving in a plane in a perpendicular magnetic field $\mathbf{B}$. The basic equation for the semi-classical approach is

$$\hbar\dot{\mathbf{k}} = -e(\mathbf{v} \times \mathbf{B}) \tag{1.18}$$

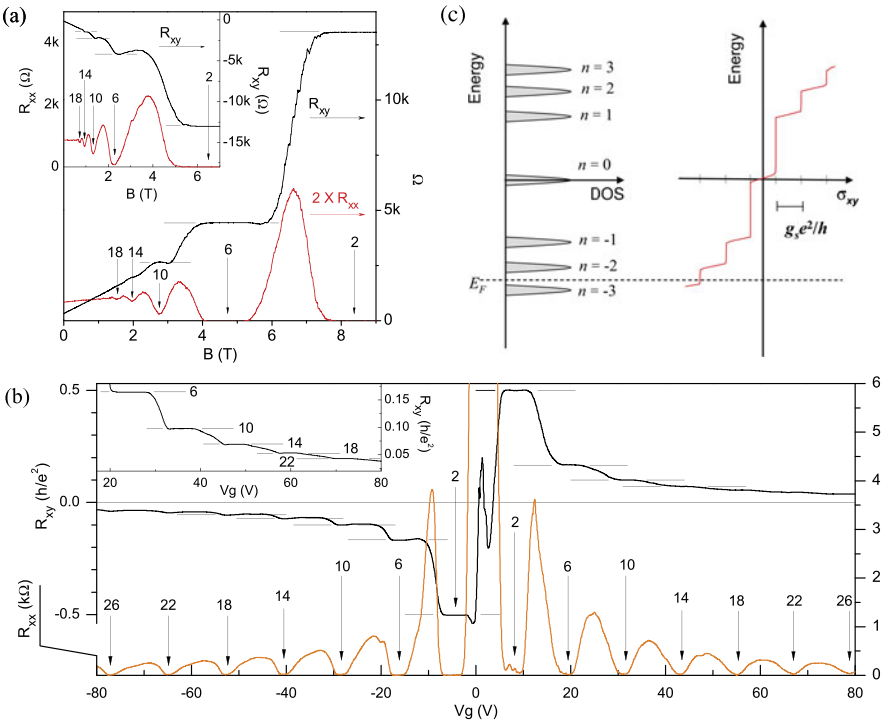

Fig. 1.2 Quantized magnetoresistance and Hall resistance of a graphene device. (**a**) Hall resistance (*black*) and magnetoresistance (*red*) measured in a monolayer graphene device at $T = 30$ mK and $V_g = 15$ V. The *vertical arrows* and the numbers on them indicate the values of B and the corresponding filling factor ν of the quantum Hall states. The *horizontal lines* correspond to $h/\nu e^2$ values. The QHE in the electron gas is demonstrated by at least two quantized plateaus in R_{xy} with vanishing R_{xx} in the corresponding magnetic field regime. The *inset* shows the QHE for a hole gas at $V_g = -4$ V, measured at 1.6 K. The quantized plateau for filling factor $\nu = 2$ is well-defined and the second and the third plateaus with $\nu = 6$ and 10 are also resolved. (**b**) The Hall resistance (*black*) and magnetoresistance (*orange*) as a function of gate voltage at fixed magnetic field $B = 9$ T, measured at 1.6 K. The same convention as in (**a**) is used here. The *upper inset* shows a detailed view of high filling factor R_{xy} plateaus measured at 30 mK. (**c**) A schematic diagram of the Landau level density of states (DOS) and corresponding quantum Hall conductance (σ_{xy}) as a function of energy. Note that in the quantum Hall states, $\sigma_{xy} = -R_{xy}^{-1}$. The LL index n is shown next to the DOS peak. In our experiment, the Fermi energy E_F can be adjusted by the gate voltage, and R_{xy}^{-1} changes by an amount of $g_s e^2/h$ as E_F crosses a LL. Reproduced from Ref. [28]

which simply says that the rate of change of momentum is equal to the Lorentz force. The velocity $\mathbf{v}$ is given by

$$\mathbf{v} = \frac{1}{\hbar} \nabla_{\mathbf{k}} \epsilon \tag{1.19}$$

where ϵ is the energy of the electron. Since the Lorentz force is normal to $\mathbf{v}$, no work is done to the electron and ϵ is a constant of the motion. It immediately follows

that electrons move along the orbits given by the intersections of constant energy surfaces with planes perpendicular to the magnetic fields.

Integration of (1.18) with respect to time yields

$$\mathbf{k}(t) - \mathbf{k}(0) = \frac{-eB}{\hbar}\big(\mathbf{R}(t) - \mathbf{R}(0)\big) \times \widehat{\mathbf{B}} \tag{1.20}$$

where $\mathbf{R}$ is the position of the electron in real space, and $\widehat{\mathbf{B}}$ is the unit vector along the direction of the magnetic field $\mathbf{B}$. Since the cross product between $\mathbf{R}$ and $\widehat{\mathbf{B}}$ simply rotates $\mathbf{R}$ by 90° inside the plane of motion, (1.20) means that the electron trajectory in real space is just its k-space orbit, rotated by 90° about $\mathbf{B}$ and scaled by $\hbar/eB$.

It can be further shown that the angular frequency at which the electron moves around the intersection of the constant energy surface is given by

$$\omega_c = \frac{2\pi eB}{\hbar^2}\left(\frac{\partial a_k}{\partial \epsilon}\right)^{-1} \tag{1.21}$$

where a_k is the area of the intersection in the k-space. For electrons having an effective mass m^*, we have $\epsilon = \hbar^2 k^2/2m^*$ and a_k is given by $\pi k^2 = 2\pi m^* \epsilon/\hbar^2$, while (1.21) reduces to $\omega_c = eB/m^*$. Comparing this equation with (1.21), we find

$$m^* = \frac{\hbar^2}{2\pi}\left(\frac{\partial a_k}{\partial \epsilon}\right) \tag{1.22}$$

which is actually the definition of the effective mass for an arbitrary orbit.

The quantization of the electron motion will restrict the available states and will give rise to quantum oscillations such as SdH oscillations. The Bohr-Sommerfeld quantization rule for a periodic motion is

$$\oint \mathbf{p} \cdot d\mathbf{q} = (n + \gamma)2\pi\hbar \tag{1.23}$$

where $\mathbf{p}$ and $\mathbf{q}$ are canonically conjugate variables, n is an integer and the integration in (1.23) is for a complete orbit. The quantity γ will be discussed below.

For an electron in a magnetic field,

$$\mathbf{p} = \hbar\mathbf{k} - e\mathbf{A} \qquad \mathbf{q} = \mathbf{R} \tag{1.24}$$

so (1.23) becomes

$$\oint (\hbar\mathbf{k} - e\mathbf{A}) \cdot d\mathbf{R} = (n + \gamma)2\pi\hbar \tag{1.25}$$

Substituting this equation into (1.20) and using Stokes' theorem, one finds

$$\mathbf{B} \cdot \oint \mathbf{R} \times d\mathbf{R} - \int_S \mathbf{B} \cdot d\mathbf{S} = (n + \gamma)\Phi_0 \tag{1.26}$$

where $\Phi_0 = 2\pi\hbar/e$ is the magnetic flux quanta. S is any surface in real space which has the electron orbit as the projection on the plane. Therefore the second term on the left hand side of (1.26) is just the magnetic flux $-\Phi$ penetrating the electron

orbit. A closer inspection of the first term on the left hand side of (1.26) finds that it is 2Φ [39]. Putting them together, (1.26) reduces to

$$\Phi = (n+\gamma)\Phi_0 \tag{1.27}$$

which simply means that the quantization rule dictates that the magnetic flux through the electron orbit has to be quantized.

Remember that the electron trajectory in real space is just a rotated version of its trajectory in k-space, scaled by $\hbar/eB$ (1.20). Let $a_k(\epsilon)$ be the area of the electron orbit at constant energy ϵ in k-space; then (1.20) becomes

$$a_k(\epsilon_n) = (n+\gamma)2\pi eB/\hbar \tag{1.28}$$

which is the famous Onsager relation. This relation implicitly specifies the permitted energy levels ϵ_n (Landau Levels), which in general depend on the band structure dispersion relation $\epsilon(k)$.

The dimensionless parameter $0 \leq \gamma < 1$ is determined by the shape of the energy band structure. For a parabolic band, $\epsilon = \hbar^2k^2/2m^*$, the nth LL has the energy $\epsilon_n = (n+1/2)\hbar\omega_c$. Each LL orbit for an isotropic m^* in the plane perpendicular to the magnetic field B is a circle in k-space with a radius $k_n = \sqrt{2eB(n+1/2)/\hbar}$. The corresponding area of an orbital in k-space for the nth LL is therefore

$$a_k(\epsilon_n) = \pi k_n^2 = \left(n+\frac{1}{2}\right)2\pi eB/\hbar \tag{1.29}$$

A comparison of this formula with (1.28) immediately yields

$$\gamma = \frac{1}{2} \tag{1.30}$$

For a massless Dirac fermion in graphene which obeys a linear dispersion relation $\epsilon = \hbar v_F k$, the nth LL corresponds to a circular orbit with radius $k_n = \epsilon_n/\hbar v_F = \sqrt{2e|n|B/\hbar}$. The corresponding area is therefore

$$a_k(\epsilon_n) = \pi k_n^2 = |n|2\pi eB/\hbar \tag{1.31}$$

This gives, for a semiclassical Shubnikov de Haas (SdH) phase,

$$\gamma = 0 \tag{1.32}$$

which differs from the γ for the conventional massive fermion by $\frac{1}{2}$ [40].

The difference of $\frac{1}{2}$ in γ is a consequence of the chiral nature of the massless Dirac fermions in graphene. An electron in graphene always has the pseudospin $|\mathbf{s}_p\rangle$ tied to its wave vector $\mathbf{k}$. The electron goes through the orbit for one cycle, $\mathbf{k}$, as well as the pseudospin attached to the electrons. Both go through a rotation of 2π at the same time. Much like a physical spin, a 2π adiabatic rotation of pesudospin gives a Berry's phase of π [5]. This is exactly where the $\frac{1}{2}$ difference in γ comes from.

The above analysis can be generalized to systems with an arbitrary band structure. The work of Roth [41] and Mikitik [42] show that the quantity γ is purely a property of the topology of the electronic energy band structure. In general, γ can be expressed in terms of the Berry's phase, ϕ_B, for the electron orbit:

$$\gamma - \frac{1}{2} = -\frac{1}{2\pi}\phi_B \tag{1.33}$$

For any electron orbits which surround a disconnected electronic energy band, as is the case for a parabolic band, this phase is zero, and we arrive at (1.30). A non-trivial Berry's phase of π results if the orbit surrounds a contact between the bands, and the energies of the bands separate linearly in $\mathbf{k}$ in the vicinity of the band contact. In monolayer graphene, these requirements are fulfilled because the valence band and conduction band are connected by $\mathbf{K}$ and $\mathbf{K}'$, and the energy dispersion is linear around these points. This special situation again leads to a $\gamma = 0$ in graphene (in fact, $\gamma = 0$ and $\gamma = \pm 1$ are equivalent). Note that this non-trivial γ is only for monolayer graphene; in contrast for bilayer graphene, whose band contact points at the charge neutrality point have a quadratic dispersion relation, a conventional $\gamma = 1/2$ is obtained [43].

γ can be probed experimentally by measuring the quantum oscillation of the 2D system in the presence of a magnetic field, where γ is identified as the phase of such oscillations. This becomes evident when we explicitly write the oscillatory part of the quantum oscillations, e.g., as for the SdH oscillation of the electrical resistivity, $\Delta\rho_{xx}$ [28, 44, 45]

$$\Delta\rho_{xx} = R(B,T)\cos\left[2\pi\left(\frac{B_F}{B} - \gamma\right)\right] \tag{1.34}$$

Here we only take account of the first harmonic, in which $R(B,T)$ is the amplitude of the SdH oscillations and B_F is the frequency in units of $1/B$, which can be related to the 2D charge carrier density n_s by

$$B_F = \frac{n_s h}{g_s e} \tag{1.35}$$

where $g_s = 4$ accounts for the spin and valley degeneracies of the LLs. The relation $\gamma = 1/2$ (for a parabolic band) and $\gamma = 0$ (for graphene) produces a phase difference of π between the SdH oscillation in the two types of 2D systems. In the extreme quantum limit, the SdH oscillations evolve into the quantum Hall effect, a remarkable macroscopic quantum phenomenon characterized by a precisely quantized Hall resistance and zeros in the longitudinal magneto-resistance. The additional Berry's phase of π manifests itself as a half-integer shift in the quantization condition, and leads to an unconventional quantum Hall effect. In the quantum Hall regime, graphene thus exhibits a so-called 'half-integer' shifted quantum Hall effect, where the filling fraction is given by $\nu = g_s(n + 1/2)$ for integer n. Thus, at this filling fraction $\rho_{xx} = 0$, while the Hall resistivity exhibits quantized plateaus at

$$\rho_{xy}^{-1} = \frac{e^2}{h} g_s\left(n + \frac{1}{2}\right). \tag{1.36}$$

The experimental observation of the quantum Hall effect and Berry's phase in graphene were first reported in Novoselov et al. [27] and Zhang et al. [28]. Figure 1.2a shows R_{xy} and R_{xx} of a single layer graphene sample as a function of magnetic field B at a fixed gate voltage $V_g > V_{Dirac}$. The overall positive R_{xy} indicates that the contribution to R_{xy} is mainly from electrons. At high magnetic field, $R_{xy}(B)$ exhibits plateaus and R_{xx} is vanishing, which is the hallmark of the QHE. At least two well-defined plateaus with values $(2e^2/h)^{-1}$ and $(6e^2/h)^{-1}$, followed by

a developing $(10e^2/h)^{-1}$ plateau, are observed before the QHE features are transformed into Shubnikov de Haas (SdH) oscillations at lower magnetic field. The quantization of R_{xy} for these first two plateaus is better than 1 part in 10^4, with a precision within the instrumental uncertainty. In recent experiments [46], this limit is now at the accuracy of the 10^{-9} level. We observe the equivalent QHE features for holes ($V_g < V_{Dirac}$) with negative R_{xy} values (Fig. 1.2a, inset). Alternatively, we can probe the QHE in both electrons and holes by fixing the magnetic field and by changing V_g across the Dirac point. In this case, as V_g increases, first holes ($V_g < V_{Dirac}$) and later electrons ($V_g > V_{Dirac}$) are filling successive Landau levels and thereby exhibit thus the QHE. This yields an antisymmetric (symmetric) pattern of R_{xy} (R_{xx}) in Fig. 1.2b, with R_{xy} quantization accordance to

$$R_{xy}^{-1} = \pm g_s \left(n + \frac{1}{2} \right) e^2/h \tag{1.37}$$

where n is a non-negative integer, and $\pm$ stands for electrons and holes, respectively. This quantization condition can be translated to the quantized filling factor, ν, in the usual QHE language. Here in the case of graphene, $g_s = 4$, accounting for 2 by the spin degeneracy and 2 by the sub-lattice degeneracy, equivalent to the **K** and **K**′ valley degeneracy under a magnetic field.

The observed QHE in graphene is distinctively different from the 'conventional' QHEs because of the additional half-integer in the quantization condition (1.37). This unusual quantization condition is a result of the topologically exceptional electronic structure of graphene [44, 45]. The sequence of half-integer multiples of quantum Hall plateaus has been predicted by several theories which combine 'relativistic' Landau levels with the particle-hole symmetry of graphene [47–49]. This can be easily understood from the calculated LL spectrum (1.16) as shown in Fig. 1.2(c). Here we plot the density of states (DOS) of the g_s-fold degenerate (spin and sublattice) LLs and the corresponding Hall conductance ($\sigma_{xy} = -R_{xy}^{-1}$, for $R_{xx} \to 0$) in the quantum Hall regime as a function of energy. Here σ_{xy} exhibits QHE plateaus when E_F (tuned by V_g) falls between LLs, and jumps by an amount of $g_s e^2/h$ when E_F crosses a LL. Time reversal invariance guarantees particle-hole symmetry and thus σ_{xy} is an odd function in energy across the Dirac point [4]. However, in graphene, the $n = 0$ LL is robust, i.e., $E_0 = 0$ regardless of the magnetic field, provided that the sublattice symmetry is preserved [4]. Thus the first plateaus of R_{xy}^{-1} for electrons ($n = 1$) and holes ($n = -1$) are situated exactly at $g_s e^2/2h$. As E_F crosses the next electron (hole) LL, R_{xy}^{-1} increases (decreases) by an amount of $g_s e^2/h$, which yields the quantization condition in (1.37).

A consequence of the combination of time reversal symmetry with the novel Dirac point structure can be viewed in terms of Berry's phase arising from the band degeneracy point [42, 50]. A direct implication of Berry's phase in graphene is discussed in the context of the quantum phase of a spin-1/2 pseudo-spinor that describes the sublattice symmetry [5, 44]. This phase is already implicit in the half-integer shifted quantization rules of the QHE. It can further be probed in the magnetic field regime where a semi-classical magneto-oscillation description holds

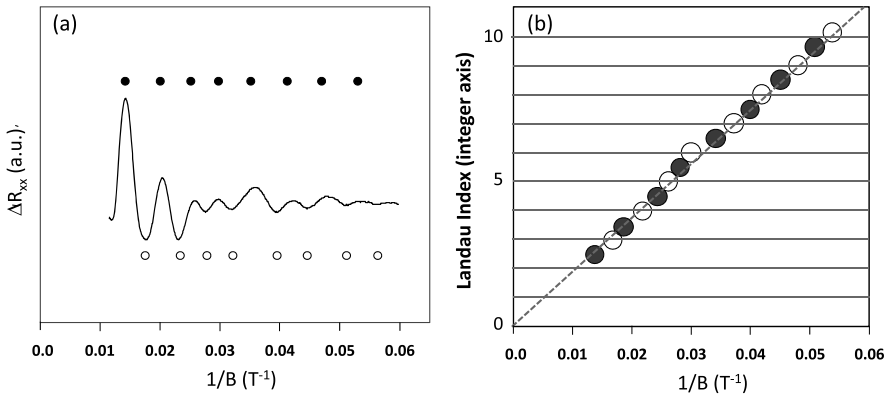

Fig. 1.3 An example of the SdH fan diagram for a few layer graphite. (**a**) The oscillatory part of the longitudinal resistance, ΔR_{xx}, plotted as a function of $1/B$. The peaks and valleys are indicated by solid and open circles, respectively. (**b**) The Landau index n of each oscillation plotted against its location in terms of $1/B$ in (**a**). The slope of the linear fit (*broken line*) yields the oscillation frequency, B_F, and the y-axis intercept yields the Berry's phase, β, in units of π. The linear fit results in $\beta = 0$ for this data set, indicating a trivial Berry phase for this few layer graphite sample. Reproduced from Ref. [52]

[45, 51]. Reproducing (1.34), the first harmonic of the SdH oscillations can be written as

$$\Delta\rho_{xx} = R(B,T)\cos\left[2\pi\left(\frac{B_F}{B} + \frac{1}{2} + \beta\right)\right]. \tag{1.38}$$

Here $R(B,T)$ is the SdH oscillation amplitude, B_F is the frequency of the SdH oscillation in $1/B$, and $\beta = \frac{1}{2} - \gamma$ is the associated Berry's phase (divided by 2π) of a value $-1/2 < \beta \leq 1/2$. Berry's phase $\beta = 0$ corresponds to the trivial case. A deviation from this value is indicative of interesting new physics with $\beta = 1/2$ (or equivalently $\beta = -1/2$ implying the existence of Dirac particles [42]).

Experimentally, this phase shift in the semi-classical regime can be obtained from an analysis of the SdH fan diagram. An example of the SdH fan diagram is given in Fig. 1.3. We first locate the peaks and valleys of the SdH oscillations in terms of $1/B$, and then plot them against their Landau index n. The slope of a linear fit to the data points gives the SdH oscillation frequency, B_F, which is related to the sheet carrier density n_s (1.35). The intercept of the linear fit with the n-index axis yields Berry's phase, β, in units of π, modulo an integer.

Figure 1.4 shows SdH fan diagram for graphene at different gate voltages, V_g. Remarkably, the resulting β is very close to 0.5 (upper inset to Fig. 1.4) for all the gate voltages, providing further evidence for the existence of a non-zero Berry's phase in graphene and the presence of Dirac particles. Such a non-zero Berry's phase was not observed in the early few layer graphite specimens [22, 51, 52], although there have been claims of hints of a phase shift in earlier measurements on bulk graphite [45]. Experimental data for graphene provide indisputable evidence for such an effect in a solid state system.

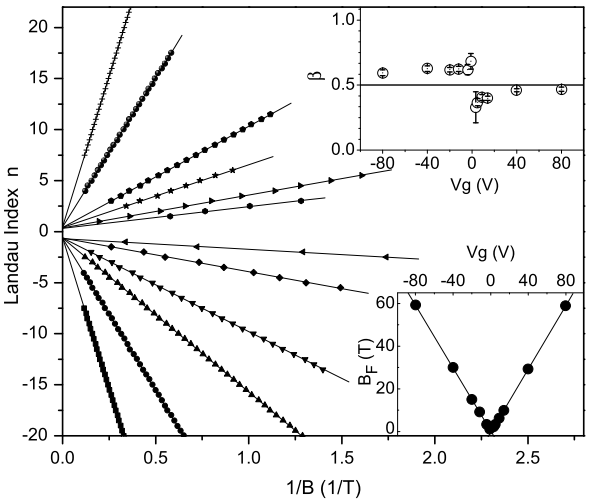

Fig. 1.4 Measurement of Berry's Phase in Graphene. Landau fan diagrams are shown for SdH oscillations at different gate voltages. The location of $1/B$ for the nth minimum of R_{xx} counting from $B = B_F$ is plotted against n. The lines correspond to a linear fit, where the slope (*lower inset*) indicates B_F values and the n-axis intercept (*upper inset*) provides a direct probe of Berry's phase in the magneto-oscillation in graphene. Reproduced from Ref. [28]

The linear energy dispersion relation also leads to a linearly vanishing 2D density of states near the charge neutrality point (CNP) at $E = 0$, $\rho_{2D} \propto |\epsilon_F|$. This differs from that for conventional parabolic 2D systems in which the density of states, at least in the single particle picture, is constant, leading to a decrease in the ability of charge neutral graphene to screen electric fields. Finally, the sublattice symmetry endows the quasiparticles with a conserved quantum number and chirality, corresponding to the projection of the pseudospin on the direction of motion [30]. In the absence of scattering which mixes the electrons in the graphene valleys, pseudospin conservation forbids backscattering in graphene [5], momentum reversal being equivalent to the violation of pseudospin conservation. This absence of backscattering has been advanced as an explanation for the experimentally observed unusually long mean free path of carriers in metallic as compared with semiconducting nanotubes [33].

1.4 Pseudospin and Klein Tunneling in Graphene

The observation of electron and hole puddles in charge neutral, substrate supported graphene [53] confirmed theoretical expectations [54] that transport at charge neutrality is dominated by charged impurity-induced inhomogeneities [55–57]. The picture of transport at the Dirac point is as a result of conducting puddles separated by a network of p-n junctions. Understanding the properties of graphene p-n junctions is thus crucial to quantitative understanding of the minimal conductivity, a problem that has intrigued experimentalists and theorists alike [27, 54, 57–62]. Describing transport in the inhomogeneous potential landscape of the CNP requires introduction of an additional spatially varying electrical potential into (1.1) in the previous section; transport across a p-n junction corresponds to this varying potential crossing zero. Because graphene carriers have no mass, graphene p-n junctions

provide a condensed matter analogue of the so called 'Klein tunneling' problem in quantum electro-dynamics (QED). The first part of this section will be devoted to the theoretical understanding of ballistic and diffusive transport across such as barrier.

In recent years, substantial effort has been devoted to improving graphene sample quality by eliminating unintentional inhomogeneity. Some progress in this direction has been made by both suspending graphene samples [63, 64] as well as by transferring graphene samples to single crystal hexagonal boron nitride substrates [65]. These techniques have succeeded in lowering the residual charge density present at charge neutrality, but even the cleanest samples are not ballistic on length scales comparable to the sample size (typically $\gtrsim$1 μm). An alliterative approach is to try to restrict the region of interest being studied by the use of local gates.

Graphene's gapless spectrum allows the fabrication of adjacent regions of positive and negative doping through the use of local electrostatic gates. Such heterojunctions offer a simple arena in which to study the peculiar properties of graphene's massless Dirac charge carriers, including chirality [30, 66] and emergent Lorentz invariance [67–69]. Technologically, graphene p-n junctions are relevant for various electronic devices, including applications in conventional analog and digital circuits [70, 71] as well as novel electronic devices based on electronic lensing [72–75]. In the latter part of this review, we will discuss current experimental progress towards such gate-engineered coherent quantum graphene devices.

The approach outlined in the previous section requires only small modifications to apply the approach to the case of carrier transport across graphene heterojunctions. While the direct calculation for the case of graphene was done by Katsnelson et al. [30], a similar approach taking into account the chiral nature of carriers was already discussed a decade ago in the context of electrical conduction in metallic carbon nanotubes [5]. In low dimensional graphitic systems, the free particle states described by (1.1) are chiral, meaning that their pseudospin is parallel (antiparallel) to their momentum for electrons (holes). This causes a suppression of backscattering in the absence of pseudospin-flip nonconserving processes, leading to the higher conductances of metallic over semiconducting carbon nanotubes [33]. To understand the interplay between this effect and Klein tunneling in graphene, we introduce external potentials $\mathbf{A}(\mathbf{r})$ and $U(\mathbf{r})$ in the Dirac Hamiltonian,

$$\hat{H} = v_F \boldsymbol{\sigma} \cdot \left(-i\hbar\nabla - e\mathbf{A}(\mathbf{r})\right) + U(\mathbf{r}). \tag{1.39}$$

In the case of a 1-dimensional (1D) barrier, $U(\mathbf{r}) = U(x)$, at zero magnetic field, and the momentum component parallel to the barrier, p_y, is conserved. As a result, electrons normally incident on a graphene p-n junction are forbidden from scattering obliquely by the symmetry of the potential, while chirality forbids them from scattering directly backwards: the result is perfect transmission as holes [30], and this is what is meant by Klein tunneling in graphene (see Fig. 1.5(a)). The rest of this review is concerned with gate induced p-n junctions in graphene; however, the necessarily transmissive nature of graphene p-n junctions is crucial for understanding

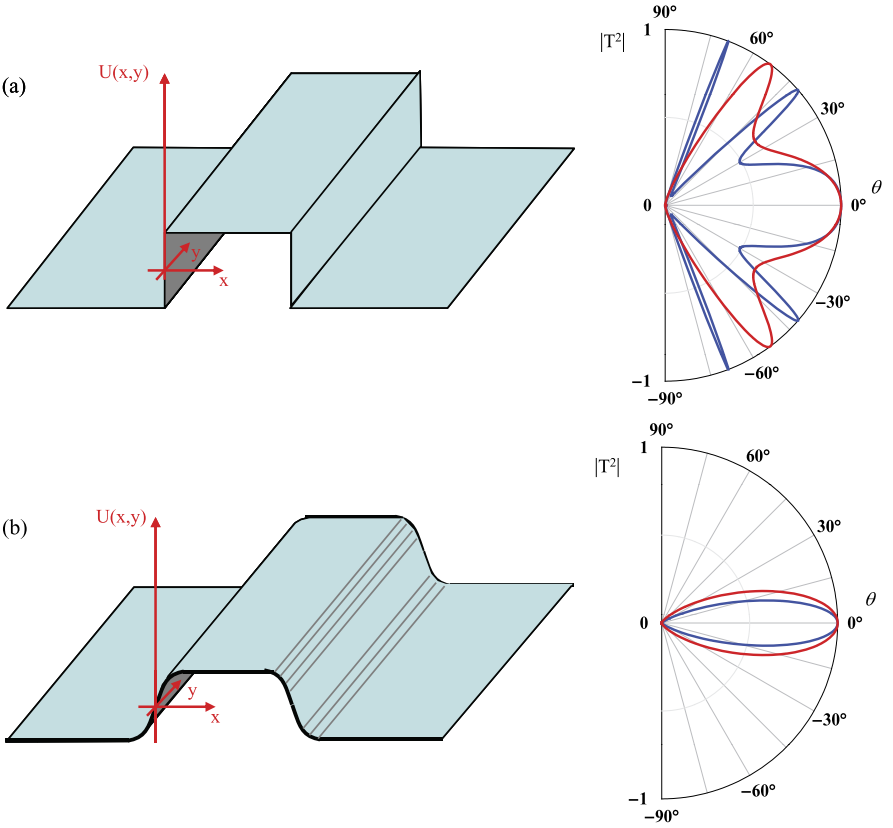

Fig. 1.5 Potential landscape and angular dependence of quasiparticle transmission through (**a**) an atomically sharp pnp barrier and (**b**) an electrostatically generated smooth pnp barrier in graphene, with their respective angle-dependent transmission probabilities $|T|^2$. *Red* and *blue lines* correspond to different densities in the locally gated region. Reproduced from Ref. [89]

the minimal conductivity [62] and supercritical Coulomb impurity [76–79] problems in graphene, as well as playing a role in efforts to confine graphene quantum particles [80, 81]. Moreover, p-n junctions appear in the normal process of contacting [82–86] and locally gating [70, 87] graphene, both of which are indispensable for electronics applications.

Even in graphene, an atomically sharp potential cannot be created in a realistic sample. Usually, the distance to the local gate, which is isolated from the graphene by a thin dielectric layer determines the length scale on which the potential varies. The resulting transmission problem over a Sauter-like potential step in graphene was solved by Cheianov and Fal'ko [66]. Substituting the Fermi energy for the potential energy difference $\varepsilon - U(x) = \hbar v_f k_f(x)$ and taking into account the conservation

of the momentum component $p_y = \hbar k_F \sin\theta$ parallel to the barrier, they obtained a result, valid for $\theta \ll \pi/2$, that is nearly identical to that of Sauter [88]:

$$k_F(x) = \begin{cases} -k_F/2 & x < 0 \\ Fx & 0 \le x \le L \\ k_F/2 & x > L \end{cases} \qquad |T|^2 \sim e^{-2\pi^2 \frac{hv_F}{F\lambda_F^2} \sin^2\theta}. \tag{1.40}$$

As in the massive relativistic problem in one-dimension, the transmission is determined by evanescent transport in classically forbidden regions where $k_x(x)^2 = k_F(x)^2 - p_y^2 < 0$ (Fig. 1.5). The only differences between the graphene case and the one dimensional, massive relativistic case are the replacement of the speed of light by the graphene Fermi velocity, the replacement of the Compton wavelength by the Fermi wavelength, and the scaling of the mass appearing in the transmission by the sine of the incident angle. By considering different angles of transmission in the barrier problem in two dimensional graphene, then, one can access both the Klein and Sauter regimes of $T \sim 1$ and $T \ll 1$.

The current state of the experimental art in graphene does not allow for injection of electrons with definite p_y [29, 90–95]. Instead, electrons impinging on a p-n junction have a random distribution of incident angles due to scattering in the diffusive graphene leads. Equation (1.40) implies that in realistically sharp p-n junctions, these randomly incident electrons emerge from the p-n junction as a collimated beam, with most off-normally incident carriers being scattered; transmission through multiple p-n junctions leads to further collimation [96]. Importantly, even in clean graphene, taking into account the finite slope of the barrier yields qualitatively different results for the transmission: just as in the original Klein problem, the sharp potential step [30, 97–102] introduces pathologies—in the case of graphene, high transmission at $\theta \neq 0$—which disappear in the more realistic treatment [66, 96, 103].

Transport measurements across single p-n junctions, or a pnp junction in which transport is not coherent, can at best provide only indirect evidence for Klein tunneling by comparison of the measured resistance of the p-n junction. Moreover, because such experiments probe only incident-angle averaged transmission, they cannot experimentally probe the structure $T(\theta)$. Thus, although references [83] and [94] demonstrated that the resistance of nearly ballistic p-n junctions are in agreement with the ballistic theory, to show that angular collimation occurs, or that there is perfect transmission at normal incidence, requires a different experiment. In particular, there is no way to distinguish perfect transmission at $\theta = 0$ from large transmission at all angles, begging the question of whether "Klein tunneling" has any observable consequences outside the context of an angle resolved measurement or its contribution to bulk properties such as the minimal conductivity. In fact, as was pointed out by Shytov et al. [104], an experimental signature of this phenomenon should manifest itself as a sudden phase shift at finite magnetic field in the transmission resonances in a ballistic, phase coherent, graphene pnp device.

Although graphene p-n junctions are transmissive when compared with p-n junctions in gapfull materials (or gapless materials in which backscattering is allowed,

such as bilayer graphene), graphene p-n junctions are sufficiently reflective, particularly for obliquely incident carriers, to cause transmission resonances due to Fabry-Perot interference. However, in contrast to the canonical example from optics, or to one dimensional electronic analogues [105], the relative phase of interfering paths in a ballistic, phase coherent pnp (or npn) graphene heterojunction can be tuned by applying a magnetic field. For the case where the junction width is only somewhat shorter than the mean free path in the local gate region (LGR), $L \lesssim \ell_{LGR}$, the Landauer formula for the oscillating part of the conductance trace can be derived from the ray tracing diagrams in Fig. 1.6(d),

$$G_{osc} = e^{-2L/l_{LGR}} \frac{4e^2}{h} \sum_{k_y} 2|T_+|^2|T_-|^2 R_+ R_- \cos(\theta_{WKB}), \tag{1.41}$$

in which $T_\pm$ and $R_\pm$ are the transmission and reflection amplitudes at $x = \pm L/2$, θ_{WKB} is the semiclassical phase difference accumulated between the junctions by interfering trajectories, and ℓ_{LGR} is a fitting parameter which controls the amplitude of the oscillations.

At zero magnetic field, particles are incident at the same angle on both junctions, and the Landauer sum in (1.41) is dominated by the modes for which both transmission and reflection are nonnegligible, so neither normal nor highly oblique modes contribute. Instead, the sum is dominated by modes with finite k_y, peaked about $k_y = \pm\sqrt{F/(\ln(3/2)\pi\hbar v_F)}$, where F is the electric force in the pn junction region. As the magnetic field increases, cyclotron bending favors the contribution of modes with $k_y = 0$, which are incident on the junctions at angles with the same magnitude but opposite sign (Fig. 1.6(c)). If perfect transmission at zero angle exists, then analyticity of the scattering amplitudes demands that the reflection amplitude changes sign as the sign of the incident angle changes [104], thereby causing a π shift in the reflection phase. This effect can also be described in terms of the Berry phase: the closed momentum space trajectories of the modes dominating the sum at low field and high k_y do not enclose the origin, while those at intermediate magnetic fields and $k_y \sim 0$ do. As a consequence, the quantization condition leading to transmission resonances is different due to the inclusion of the Berry phase when the trajectories surround the topological singularity at the origin, leading to a phase shift in the observed conductance oscillations as the phase shift containing trajectories begin to dominate the Landauer sum in (1.41).

Experimental realization of the coherent electron transport in pnp (as well as npn) graphene heterojunctions was reported by Young and Kim [29]. The key experimental innovations were to use an extremely narrow ($\lesssim$20 nm wide) top gate, creating a Fabry Perot cavity between p-n junctions smaller than the mean free path, which was $\sim$ 100 nm in the samples studied. Figure 1.6(a) shows the layout of a graphene heterojunction device controlled by both top gate voltage (V_{TG}) and back gate voltage (V_{BG}). The conductance map shows clear periodic features in the presence of p-n junctions; these features appear as oscillatory features in the conductance as a function of V_{TG} at fixed V_{BG} (Fig. 1.6(b)). For the electrostatics of the devices presented in this device, the magnetic field at which this π phase shift, due to the Berry

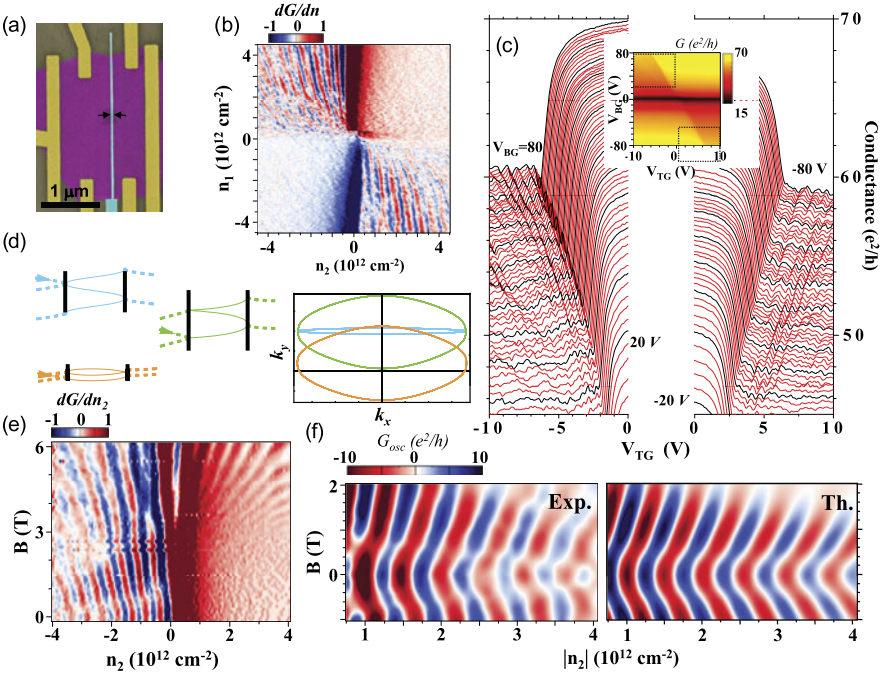

Fig. 1.6 (**a**) Scanning electron microscope image of a typical graphene heterojunction device. Electrodes, graphene and top gates are represented by yellow, purple and cyan, respectively. (**b**) A differential transconductance map of the device as a function of densities n_2 and n_1, corresponding to the locally gated region (LGR) and out side the LGR, i.e. graphene lead (GL) region, respectively. Interference fringes appear in the presence of pn junctions, which define the Fabry-Perot cavity. (**c**) *Inset*: Conductance map of the device in the back gate and top gate voltages (V_{BG}–V_{TG}) plane. The main panels show cuts through this color map in the regions indicated by the *dotted lines* in the *inset*, showing the conductance as a function of V_{TG} at fixed V_{BG}. Traces are separated by a step in V_{BG} of 1 V, starting from 80 V with traces taken at integer multiples of 5 V in black. (**d**) Schematic diagram of trajectories contributing to quantum oscillations in real and momentum space. With increasing B, the dominant modes at low magnetic field (*blue*) give way to phase-shifted modes with negative reflection amplitude due to the inclusion of the non-trivial Berry phase (*orange*), near $k_y = 0$. The original finite k_y modes are not yet phase shifted at the critical magnetic field B_c, above which the non-trivial Berry phase shift π (*green*) appears. But owing to collimation, these finite k_y modes no longer contribute to the oscillatory conductance. (**e**) Magnetic-field and density dependence of the transconductance dG/dn_2 for $n_1 > 0$ is fixed. Note that the low field oscillatory features from FP resonance only appear for $n_2 < 0$ where there is pnp junction forms. (**f**) Oscillating part of the conductance at $V_{BG} = 50$ V for low fields. G_{osc} as extracted from the experimental data over a wide range of densities and magnetic fields (*left*) matches the behavior predicted by a theory containing the phase shift due to Klein tunneling [104] (*right*). Reproduced from [29]

phase at the critical magnetic field discussed above, is expected to occur in the range $B^* = 2\hbar k_y/eL \sim 250$–$500$ mT, in agreement with experimental data which show an abrupt phase shift in the oscillations at a few hundred mT (Fig. 1.6(f)). Experiments can be matched quantitatively to the theory by calculation of (1.41) for the appro-

priate potential profile, providing confirmation of the Klein tunneling phenomenon in graphene. As the magnetic field increases further, the ballistic theory predicts the disappearance of the Fabry-Perot conductance oscillations as the cyclotron radius shrinks below the distance between p-n junctions, $R_c \lesssim L$, or $B \sim 2$ T for our devices (Fig. 1.6(e)).

There is an apparent continuation of the low magnetic field Fabry-Perot (FP) oscillations to Shubnikov-de Haas (SdH) oscillations at high magnetic fields. Generally, the FP oscillations tend to be suppressed at high magnetic fields as the cyclotron orbits get smaller than the junction size. On the other hand, disorder mediated SdH oscillations become stronger at high magnetic field owing to the large separation between Landau levels. The observed smooth continuation between these two oscillations does not occur by chance. FP oscillations at magnetic fields higher than the phase shift are dominated by trajectories with $k_y = 0$; similarly, SdH oscillations, which can be envisioned as cyclotron orbits beginning and ending on the same impurity, must also be dominated by $k_y = 0$ trajectories [106]. The result is a seamless crossover from FP to SdH oscillations. This is strongly dependent on the disorder concentration: for zero disorder, SdH oscillations do not occur, while for very strong disorder SdH oscillations happen only at high fields and FP oscillations do not occur due to scattering between the p-n junctions. For low values of disorder, such that SdH oscillations appear at fields much smaller than the phase shift magnetic field, B_c, the two types of coherent oscillations could in principle coexist with different phases. The role of disorder in the FP-SdH crossover has only begun to be addressed experimentally [29] and theoretically [68].

Similar experiments on at least partially phase coherent graphene heterojunctions were carried out by several other groups [93, 94], although they did not observe the phase shift that is the signature of Klein tunneling. Further theoretical considerations of quantum transport across pnp junctions in the presence of disorder were discussed by Rossi et al. [107], who calculated the resistance and the Fano factor in the presence of weak disorder: both resistance and Fano factor show broad resonance peaks due to the presence of quasi-bound-states. As expected from the phenomenological model described in (1.41), these features are washed out when the mean free path becomes of the order of the distance between the two p-n interfaces.

Expanding the number of p-n junction boundaries can be achieved simply by installing an array of top gates on graphene, producing a superlattice electrostatic potential. While this has not been demonstrated experimentally due to constraints on sample quality, there exist multiple theoretical studies of graphene p-n junction arrays [96–99, 102, 108–113]. In the simple case of one dimensionally periodic Dirac delta function barriers with the dimensionless barrier strength P whose potential is given by $V(x, y) = \hbar v_F P \delta(x)$, Barbier et al. [112] showed that the dispersion relation of this Kronig-Penney (KP) model of a superlattice is a periodic function of P and causes collimation of an incident electron beam for $P = 2\pi n$ where n is an integer. For a KP superlattice with an alternating sign for the height of the barriers, the Dirac point in the 2D dispersion becomes a Dirac line for $P = \pi(n + 1/2)$. The modification of the graphene spectrum remains an interesting direction to pursue experimentally.

Superlattices can also have a 'supercollimating' effect on ballistically propagating carriers, creating an electron beam with almost no spatial spreading or diffraction. The unit transmission of normally incident carriers means that, in a sample with minimal scattering, a highly collimated electron beam can be created without a waveguide or external magnetic fields [96]. Such a perfect collimation stems from the creation of a chiral quasi-one-dimensional metallic state originating from the collapse of the intrinsic helical nature of the charge carriers in the superlattice potential.

In realistic graphene devices, however, disorder dominates, and any experimental superlattice will need to be analyzed with this in mind. The conductance of disordered graphene superlattices with short-range structural correlations was studied theoretically [109, 111]. Ignoring intervalley scattering, these studies demonstrated that the transport and spectral properties of such structures are strongly anisotropic even in the presence of disorder. In the direction perpendicular to the barriers, the eigenstates in a disordered sample are delocalized for all energies and provide a robust minimum nonzero conductivity. However, along with extended states, there exist discrete sets of angles and energies with exponentially localized eigenfunctions, producing disorder-induced resonances. It is particularly interesting that the disorder not only suppresses the transmission of carriers across the barriers but, counter intuitively, can enhance transmission.

1.5 Conclusions

In this chapter, we discuss the role of pseudospin in electronic transport in graphene. We demonstrate a variety of new phenomena which stem from the effectively relativistic nature of the electron dynamics in graphene, where the pseudospin is aligned with two-dimensional momentum. Our main focus were two major topics: (i) the non-conventional, half-integer shifted filling factors for the quantum Hall effect (QHE) and the peculiar magneto-oscillation where one can directly probe the existence of a non-trivial Berry's phase, and (ii) Klein tunneling of chiral Dirac fermions in a graphene lateral heterojunction.

Employing unusual filling factors in QHE in single layer graphene samples as an example, we demonstrated that the observed quantization condition in graphene is described by half integer rather than integer values, indicating the contribution of the non-trivial Berry's phase. The half-integer quantization, as well as the measured phase shift in the observed magneto-oscillations, can be attributed to the peculiar topology of the graphene band structure with a linear dispersion relation and a vanishing mass near the Dirac point, which is described in terms of effectively 'relativistic' carriers as shown in (1.1). The unique behavior of electrons in this newly discovered $(2+1)$-dimensional quantum electrodynamics system not only opens up many interesting questions in mesoscopic transport in electronic systems with nonzero Berry's phase but may also provide the basis for novel carbon based electronics applications.

The development and current status of electron transport in graphene heterojunction structures were also reviewed. In these lateral heterojunction devices, the unique linear energy dispersion relation and concomitant pseudospin symmetry are probed via the use of local electrostatic gates. Mimicking relativistic quantum particle dynamics, electron waves passing between two regions of graphene with different carrier densities will undergo strong refraction at the interface, producing an experimental realization of the century-old Klein tunneling problem of relativistic quantum mechanics. Many theoretical and experimental discussions were presented here, including the peculiar graphene p-n and *pnp* junction conduction in the diffusive and ballistic regimes. Since electrons are charged, a magnetic field can couple to them and magnetic field effects can be studied. In particular, in a coherent system, the electron waves can also interfere, producing quantum oscillations in the electrical conductance, which can be controlled through the application of both electric and magnetic fields. A clear indication of a phase shift of π in the magnetoconductance clearly indicates again the existence of a non-trivial Berry's phase associated with the pseudo-spin rotation during the Klein tunneling process.

References

1. P.R. Wallace, Phys. Rev. **71**, 622 (1947)
2. D.P. DiVincenzo, E.J. Mele, Phys. Rev. B **29**, 1685 (1984)
3. G.W. Semenoff, Phys. Rev. Lett. **53**, 2449 (1984)
4. F.D.M. Haldane, Phys. Rev. Lett. **61**, 2015 (1988)
5. T. Ando, T. Nakanishi, R. Saito, J. Phys. Soc. Jpn. **67**, 2857 (1998)
6. H.P. Boehm, A. Clauss, G.O. Fischer, U. Hofmann, Z. Anorg. Allg. Chem. **316**, 119 (1962)
7. T.A. Land, T. Michely, R.J. Behm, J.C. Hemminger, G. Comsa, Surf. Sci. **264**, 261–270 (1992)
8. A. Krishnan, E. Dujardin, M.M.J. Treacy, J. Hugdahl, S. Lynum, T.W. Ebbesen, Nature **388**, 451 (1997)
9. C. Berger, Z.M. Song, T.B. Li, X.B. Li, A.Y. Ogbazghi, R. Feng, Z.T. Dai, A.N. Marchenkov, E.H. Conrad, P.N. First, W.A. de Heer, J. Phys. Chem. B **108**, 19912 (2004)
10. W.A. de Heer, C. Berger, M. Ruan, M. Sprinkle, X. Li, Y. Hu, B. Zhang, J. Hankinson, E.H. Conrad, Proc. Natl. Acad. Sci. USA **108**(41), 16900 (2011)
11. S. Bae et al., Nat. Nanotechnol. **5**, 574 (2010)
12. M. Yamamoto, S. Obata, K. Saiki, Surf. Interface Anal. **42**, 1637 (2010)
13. L. Zhang et al., Nano Lett. **12**, 1806 (2012)
14. R.F. Frindt, Phys. Rev. Lett. **28**, 299 (1972)
15. Y. Ohashi, T. Hironaka, T. Kubo, K. Shiiki, Tanso **1997**, 235 (1997)
16. H. Itoh, T. Ichinose, C. Oshima, T. Ichinokawa, Surf. Sci. Lett. **254**, L437 (1991)
17. L.M. Viculis, J.J. Jack, R.B. Kaner, Science **299**, 1361 (2003)
18. W. Ebbensen, H. Hiura, Adv. Mater. **7**, 582 (1995)
19. X. Lu, H. Huang, N. Nemchuk, R. Ruoff, Appl. Phys. Lett. **75**, 193 (1999)
20. X. Lu, M. Yu, H. Huang, R. Ruoff, Nanotechnology **10**, 269 (1999)
21. E. Dujardin, T. Thio, H. Lezec, T.W. Ebbesen, Appl. Phys. Lett. **79**, 2474 (2001)
22. K.S. Novoselov, A.K. Geim, S.V. Morozov, D. Jiang, Y. Zhang, S.V. Dubonos, I.V. Grigorieva, A.A. Firsov, Science **306**, 666 (2004)
23. Y. Zhang, J.P. Small, W.V. Pontius, P. Kim, Appl. Phys. Lett. **86**, 073104 (2005)
24. J.S. Bunch, Y. Yaish, M. Brink, K. Bolotin, P.L. McEuen, Nano Lett. **5**, 287 (2005)

25. K.S. Novoselov, D. Jiang, F. Schedin, T.J. Booth, V.V. Khotkevich, S.V. Morozov, A.K. Geim, Proc. Natl. Acad. Sci. USA **102**, 10451 (2005)
26. P. Blake, E.W. Hill, A.H. Castro Neto, K.S. Novoselov, D. Jiang, R. Yang, T.J. Booth, A.K. Geim, Appl. Phys. Lett. **91**, 063124 (2007)
27. K.S. Novoselov, A.K. Geim, S.V. Morozov, D. Jiang, M.I. Katsnelson, I.V. Grigorieva, S.V. Dubonos, A.A. Firsov, Nature **438**, 197 (2005)
28. Y. Zhang, Y.-W. Tan, H.L. Stormer, P. Kim, Nature **438**, 201 (2005)
29. A.F. Young, P. Kim, Nat. Phys. **5**, 222 (2009)
30. M.I. Katsnelson, K.S. Novoselov, A.K. Geim, Nat. Phys. **2**, 620 (2006)
31. M. Wilson, Phys. Today **1**, 21 (2006)
32. J.C. Slonczewski, P.R. Weiss, Phys. Rev. **109**, 272 (1958)
33. P.L. McEuen, M. Bockrath, D.H. Cobden, Y.-G. Yoon, S.G. Louie, Phys. Rev. Lett. **83**, 5098 (1999)
34. M.S. Purewal, B.H. Hong, A. Ravi, B. Chandra, J. Hone, P. Kim, Phys. Rev. Lett. **98**, 196808 (2006)
35. H. Suzuura, T. Ando, Phys. Rev. Lett. **89**, 266603 (2002)
36. B.L. Altshuler, D. Khmel'nitzkii, A.I. Larkin, P.A. Lee, Phys. Rev. B **22**, 5142 (1980)
37. F.V. Tikhonenko, D.W. Horsell, R.V. Gorbachev, A.K. Savchenko, Phys. Rev. Lett. **100**, 056802 (2008)
38. J.W. McClure, Phys. Rev. **104**, 666 (1956)
39. N.W. Ashcroft, N.D. Mermin, *Solid State Physics* (Holt, Rinehart and Winston, New York, 1976). ISBN 0-03-083993-9
40. R. Rammal, J. Phys. (Fr.) **46**, 1345 (1985)
41. L.M. Roth, Phys. Rev. **145**, 434 (1966)
42. G.P. Mikitik, Y.V. Sharlai, Phys. Rev. Lett. **82**, 2147 (1999)
43. E. McCann, V.I. Fal'ko, Phys. Rev. Lett. **96**, 086805 (2006)
44. S.G. Sharapov, V.P. Gusynin, H. Beck, Phys. Rev. B **69**, 075104 (2004)
45. I.A. Luk'yanchuk, Y. Kopelevich, Phys. Rev. Lett. **93**, 166402 (2004)
46. A. Tzalenchuk, S. Lara-Avila, A. Kalaboukhov, S. Paolillo, M. Syvajarvi, R. Yakimova, O. Kazakova, T.J.B.M. Janssen, V. Fal'ko, S. Kubatkin, Nat. Nanotechnol. **5**, 186 (2010)
47. Y.S. Zheng, T. Ando, Phys. Rev. B **65**, 245420 (2002)
48. V.P. Gusynin, S.G. Sharapov, Phys. Rev. Lett. **95**, 146801 (2005)
49. N.M.R. Peres, F. Guinea, A.H.C. Neto, Phys. Rev. B **73**, 125411 (2006)
50. Z. Fang, N. Nagaosa, K.S. Takahashi, A. Asamitsu, R. Mathieu, T. Ogasawara, H. Yamada, M. Kawasaki, Y. Tokura, K. Terakura, Science **302**, 92 (2003)
51. S.V. Morozov, K.S. Novoselov, F. Schedin, D. Jiang, A.A. Firsov, A.K. Geim, Phys. Rev. B **72**, 201401(R) (2005)
52. Y. Zhang, J.P. Small, M.E.S. Amori, P. Kim, Phys. Rev. Lett. **94**, 176803 (2005)
53. J. Martin, N. Akerman, G. Ulbricht, T. Lohmann, K. von Klitzing, J.H. Smet, A. Yacoby, Nat. Phys. **4**, 144 (2008)
54. E.H. Hwang, S. Adam, S. Das Sarma, Phys. Rev. Lett. **98**, 186806 (2007)
55. Y. Zhang, V.W. Brar, C. Girit, A. Zettl, M.F. Crommie, Nat. Phys. **5**, 722 (2009)
56. J.-H. Chen, C. Jang, S. Adam, M.S. Fuhrer, E.D. Williams, M. Ishigami, Nat. Phys. **4**, 377 (2008)
57. S. Adam, E.H. Hwang, V. Galitski, S.D. Sarma, Proc. Natl. Acad. Sci. USA **104**, 18392 (2007)
58. E. Fradkin, Phys. Rev. B **33**, 3257 (1986)
59. A.W.W. Ludwig, M.P.A. Fisher, R. Shankar, G. Grinstein, Phys. Rev. B **50**, 7526 (1994)
60. K. Ziegler, Phys. Rev. B **75**, 233407 (2007)
61. Y.W. Tan, Y. Zhang, K. Bolotin, Y. Zhao, S. Adam, E.H. Hwang, S. Das Sarma, H.L. Stormer, P. Kim, Phys. Rev. Lett. **99**, 246803 (2007)
62. V.V. Cheianov, V.I. Falko, B.L. Altshuler, I.L. Aleiner, Phys. Rev. Lett. **99**, 176801 (2007)
63. K.I. Bolotin, K.J. Sikes, Z. Jiang, G. Fundenberg, J. Hone, P. Kim, H.L. Stormer, Solid State Commun. **146**, 351 (2008)

64. X. Du, I. Skachko, A. Barker, E.Y. Andrei, Nat. Nanotechnol. **3**, 491 (2008)
65. C.R. Dean, A.F. Young, I. Meric, C. Lee, L. Wang, S. Sorgenfrei, K. Watanabe, T. Taniguchi, P. Kim, K.L. Shepard, J. Hone, Nat. Nanotechnol. **5**, 722 (2010)
66. V.V. Cheianov, V.I. Fal'ko, Phys. Rev. B **74**, 041403 (2006)
67. V. Lukose, R. Shankar, G. Baskaran, Phys. Rev. Lett. **98**, 116802 (2007)
68. N.G.M.K.A. Shytov, M. Rudner, L. Levitov, Solid State Commun. **149**, 1087 (2008)
69. N. Gu, M. Rudner, A. Young, P. Kim, L. Levitov, Phys. Rev. Lett. **106**, 066601 (2011)
70. I. Meric, M.Y. Han, A.F. Young, B. Oezyilmaz, P. Kim, K. Shepard, Nat. Nanotechnol. **3**, 654 (2008)
71. F. Schwierz, Nat. Nanotechnol. **5**, 487 (2010)
72. V.G. Veselago, Sov. Phys. Usp. **10**, 509 (1968)
73. V.V. Cheianov, V. Fal'ko, B.L. Altshuler, Science **315**, 1252 (2007)
74. J. Cserti, A. Palyi, C. Peterfalvi, Phys. Rev. Lett. **99**, 246801 (2007)
75. C. Peterfalvi, A. Palyi, J. Cserti, Phys. Rev. B **80**, 075416 (2009)
76. A.V. Shytov, M.I. Katsnelson, L.S. Levitov, Phys. Rev. Lett. **99**, 246802 (2007)
77. V.M. Pereira, J. Nilsson, A.H. Castro Neto, Phys. Rev. Lett. **99**, 166802 (2007)
78. V.M. Pereira, V.N. Kotov, A.H. Castro Neto, Phys. Rev. B **78**, 085101 (2008)
79. P.A. Maksym, H. Aoki, arXiv:1211.5552
80. P.G. Silvestrov, K.B. Efetov, Phys. Rev. B **77**, 155436 (2008)
81. G. Giavaras, P.A. Maksym, M. Roy, J. Phys. Condens. Matter **21**, 102201 (2009)
82. S. Barraza-Lopez, M. Vanevi, M. Kindermann, M.Y. Chou, Phys. Rev. Lett. **104**, 076807 (2010)
83. B. Huard, N. Stander, J.A. Sulpizio, D. Goldhaber-Gordon, Phys. Rev. B **78**, 121402 (2008)
84. J. Cayssol, Phys. Rev. Lett. **100**, 147001 (2008)
85. J. Cayssol, B. Huard, D. Goldhaber-Gordon, Phys. Rev. B **79**, 075428 (2009)
86. T. Mueller, F. Xia, M. Freitag, J. Tsang, Ph. Avouris, Phys. Rev. B **79**, 245430 (2009)
87. Y.-M. Lin, C. Dimitrakopoulos, K.A. Jenkins, D.B. Farmer, H.-Y. Chiu, A. Grill, Ph. Avouris, Science **327**, 662 (2010)
88. F. Sauter, Z. Phys. A, Hadrons Nucl. **69**, 742 (1931)
89. A.F. Young, P. Kim, Annu. Rev. Condens. Matter Phys. **2**, 101 (2011)
90. B. Huard, J.A. Sulpizio, N. Stander, K. Todd, B. Yang, D. Goldhaber-Gordon, Phys. Rev. Lett. **98**, 236803 (2007)
91. J.R. Williams, L. DiCarlo, C.M. Marcus, Science **317**, 638 (2007)
92. B. Özyilmaz, P. Jarillo-Herrero, D. Efetov, D. Abanin, L.S. Levitov, P. Kim, Phys. Rev. Lett. **99**, 166804 (2007)
93. G. Liu, J. Jairo Velasco, W. Bao, C.N. Lau, Appl. Phys. Lett. **92**, 203103 (2008)
94. R.V. Gorbachev, A.S. Mayorov, A.K. Savchenko, D.W. Horsell, F. Guinea, Nano Lett. **8**, 1995 (2008)
95. N. Stander, B. Huard, D. Goldhaber-Gordon, Phys. Rev. Lett. **102**, 026807 (2009)
96. C.-H. Park, Y.-W. Son, L. Yang, M.L. Cohen, S.G. Louie, Nano Lett. **8**, 2920 (2008)
97. J. Milton Pereira, V. Mlinar, F.M. Peeters, P. Vasilopoulos, Phys. Rev. B **74**, 045424 (2006)
98. C. Bai, X. Zhang, Phys. Rev. B **76**, 075430 (2007)
99. J. Milton Pereira Jr., P. Vasilopoulos, F.M. Peeters, Appl. Phys. Lett. **90**, 132122 (2007)
100. C. Bai, Y. Yang, X. Zhang, Phys. Rev. B **80**, 235423 (2009)
101. C. Bai, Y. Yang, X. Zhang, Physica E **42**, 1431 (2010)
102. J. Milton Pereira, F.M. Peeters, A. Chaves, G.A. Farias, Semicond. Sci. Technol. **25**, 033002 (2010)
103. E.B. Sonin, Phys. Rev. B **79**, 195438 (2009)
104. A.V. Shytov, M.S. Rudner, L.S. Levitov, Phys. Rev. Lett. **101**, 156804 (2008)
105. W. Liang, M. Bockrath, D. Bozovic, J.H. Hafner, M. Tinkham, H. Park, Nature **411**, 665 (2001)
106. M.G. Vavilov, I.L. Aleiner, Phys. Rev. B **69**, 035303 (2004)
107. E. Rossi, J.H. Bardarson, P.W. Brouwer, S. Das Sarma, Phys. Rev. B **81**, 121408 (2010)
108. C.-H. Park, L. Yang, Y.-W. Son, M.L. Cohen, S.G. Louie, Nat. Phys. **4**, 213 (2008)

109. Y.P. Bliokh, V. Freilikher, S. Savelev, F. Nori, Phys. Rev. B **79**, 075123 (2009)
110. C.-H. Park, Y.-W. Son, L. Yang, M.L. Cohen, S.G. Louie, Phys. Rev. Lett. **103**, 046808 (2009)
111. N. Abedpour, A. Esmailpour, R. Asgari, M.R.R. Tabar, Phys. Rev. B **79**, 165412 (2009)
112. M. Barbier, F.M. Peeters, P. Vasilopoulos, J.M. Pereira, Phys. Rev. B **77**, 115446 (2008)
113. J.J. Milton Pereira, P. Vasilopoulos, F.M. Peeters, Appl. Phys. Lett. **90**, 132122 (2007)

Chapter 2
Probing Dirac Fermions in Graphene by Scanning Tunneling Microscopy and Spectroscopy

Adina Luican-Mayer and Eva Y. Andrei

Abstract Graphene is a two dimensional system which can be studied using surface probe techniques such as scanning tunneling microscopy and spectroscopy. Combining the two, one can learn about the surface morphology as well as about its electronic properties. In this chapter we present a brief review of experimental results obtained on graphene supported on substrates with varying degrees of disorder. In the first part we focus on the electronic properties of single layer graphene without a magnetic field as well as in the presence of a perpendicular magnetic field. The second part focuses on twisted graphene stacks and the effects of rotating away from the equilibrium Bernal stacking on the electronic properties.

2.1 Scanning Tunneling Microscopy and Spectroscopy

Scanning tunneling microscopy (STM) is a powerful technique used to study the surface morphology of materials as well as to learn about their electronic properties. The idea behind the operation of an STM, for which Gerd Binnig and Heinrich Rohrer were awarded the Nobel prize in 1986 [1], is conceptually simple. By bringing a sharp metallic tip atomically close ($\approx$1 nm) to a conducting sample surface one can create a tunneling junction and when a bias voltage is applied between the two, a tunneling current will start flowing. Such a tunneling junction is depicted in Fig. 2.1. In this situation the electrons below the Fermi level of the sample will be tunneling into the tip, and therefore probe the filled electronic states. In the reverse situation when the Fermi level of the tip is above that of the sample, the electrons are flowing out of the tip into the sample probing the empty states of the sample. The current between the sample and the tip I_t can be calculated from a Fermi Golden rule expression which, assuming low temperatures, can be simplified to [2, 3]:

$$I \propto \frac{4\pi e}{\hbar} \int_0^{eV_{Bias}} \rho_{sample}(\epsilon)\rho_{tip}(eV_{Bias} - \epsilon)|M|^2 d\epsilon \tag{2.1}$$

A. Luican-Mayer · E.Y. Andrei (✉)
Department of Physics and Astronomy, Rutgers University, Piscataway, NJ 08854, USA
e-mail: eandrei@physics.rutgers.edu

H. Aoki, M.S. Dresselhaus (eds.), *Physics of Graphene*, NanoScience and Technology,
DOI 10.1007/978-3-319-02633-6_2,

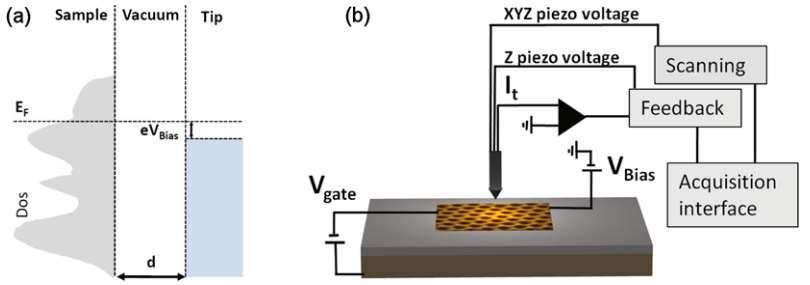

Fig. 2.1 (**a**) Sketch of the tunneling junction between the tip and the sample in an STM experiment. The important quantities are indicated: the tip-sample separation d, the Fermi level E_F, the bias voltage V_{Bias}. The indicated DOS for the sample has an arbitrary shape and for the tip it is assumed constant. (**b**) Sketch of the STM set-up in which a graphene flake is placed on a Si/SiO_2 substrate. The main parts of an STM experiment are indicated: the scanning head, the feedback system, the data acquisition interface, the bias voltage and tunneling current. In addition, a gate voltage is applied between the graphene and the gate electrode (typically Si)

The matrix element, assumed to be constant for the energy interval of integration, $|M|^2 \propto e^{\frac{-2d}{\hbar}\sqrt{2m\Phi}}$, yields:

$$I \propto e^{\frac{-2s}{\hbar}\sqrt{2m\Phi}} \int_0^{eV_{Bias}} \rho_{sample}(\epsilon)\rho_{tip}(eV_{Bias} - \epsilon)d\epsilon \tag{2.2}$$

Here ρ_{sample} and ρ_{tip} are the density of electronic states for the sample and tip, d is the separation between the tip and sample, m, e are the electron mass, charge, and Φ is the barrier height.

Topography Using the STM to measure the topography of a sample is based on the condition that I_t is very sensitive to the tip-sample separation:

$$I \propto e^{\frac{-2d}{\hbar}\sqrt{2m\Phi}} \tag{2.3}$$

A common measurement mode of STM is the constant current mode in which the tip moves across the sample and it is raised or lowered by a feedback loop in order to keep the tunneling current constant. Tracing the contour made by the tip will give information about the sample topography.

Spectroscopy If we assume that the tip density of states (DOS) is flat in the energy range of choice, by taking the derivative of I_t with respect to the V_{Bias}, we obtain:

$$\frac{dI_t}{dV_{Bias}} \propto \rho_{sample}(eV) \tag{2.4}$$

Therefore, the STM can be used to learn about the density of states of the sample in the scanning tunneling spectroscopy (STS) mode. For this, first the junction is set, then the feedback loop is disabled and the tunneling current is recorded while

varying the bias voltage. Typically this differential conductance is measured with a lock-in technique by applying a small ac. modulation to the bias voltage. By repeating such a measurement on a grid of points across a chosen region one obtains dI_t/dV_{Bias} maps which reflect the local density of states as a function of spatial coordinates.

In a realistic situation the measurement temperature imposes a lower bound on the resolution which cannot be better than the thermal broadening: $E \approx kT$. For measurements at 4 K the minimum resolution is thus ≈0.35 meV. At the same time the ac. bias modulation should be comparable to this value for optimal resolution. Furthermore, common materials used for the tip such as Pt/Ir, W, Au typically satisfy the condition of a flat DOS for small enough voltages. For a reliable STS measurement one needs to check that the experiment is done in the vacuum tunneling regime when the dependence of the tunneling current on tip-sample distance is exponential [4]. Reliable spectra are checked to be reproducible as a function of time and they do not depend on the tip-sample distance.

In the following sections we will discuss the results obtained by investigating graphene samples using scanning tunneling microscopy and spectroscopy.

2.2 From Disordered Graphene to Ideal Graphene

Graphene on SiO_2 Graphene was initially isolated by mechanical exfoliation from graphite (Highly Oriented Pyrolitic Graphite (HOPG) or natural graphite) onto Si wafers capped with SiO_2 [5]. In order to fabricate devices from these flakes, metallic contacts are added using standard e-beam lithography. This sample configuration allows using the highly doped Si as a back gate so that by applying a voltage between the flake and the back gate one can tune the carrier density in graphene. Much of the experimental work and in particular transport experiments have used this type of sample, but they are far from ideal.

Firstly, the nanofabrication procedure can result in disorder that can reside either between the graphene and the SiO_2 or on the surface of graphene. Secondly, graphene will conform to the surface of SiO_2 and it will therefore be rippled. An illustration of this situation is presented in Fig. 2.2. As a consequence of the disorder, the Fermi level of neutral graphene will not coincide with the Dirac point, meaning graphene is doped [6, 7]. The doping varies on the surface of graphene creating puddles of different carrier density (electron-hole puddles) [6, 7].

One of the main sources of the electron-hole puddles in graphene is the random potential induced by the substrate. For the standard SiO_2 substrates which are routinely used in graphene devices this is particularly problematic due to the presence of trapped charges and dangling bonds [8]. Recent experiments demonstrated that the use of dry-chlorinated SiO_2 substrates leads to a significant reduction in the random potential. The use of these substrates gave access to the intrinsic properties of graphene allowing the observation of Landau levels as detailed in a later section [9] (Sect. 2.2.4).

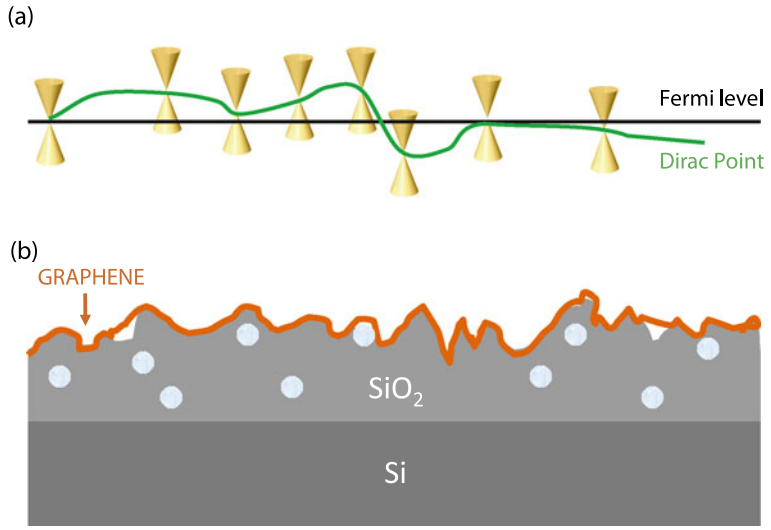

Fig. 2.2 (**a**) Illustration of the varying carrier concentration across a graphene sample due to the random potential underneath. The Fermi level and the Dirac point are shown by the *black* and *green lines*, respectively. (**b**) Sketch of how graphene (the *orange line*) deposited on the surface of SiO_2 will have a roughness comparable to the substrate [13]. The *light gray dots* schematically illustrate trapped charges

Graphene on Hexagonal Boron Nitride (BN), Mica etc. More recently, experimental methods were developed to manipulate other 2D materials from layered structures (e.g. BN) [5, 10]. In order to minimize the disorder due to the underlying substrate while still preserving the possibility of gating, graphene was placed on thin flakes of BN which in turn, were previously exfoliated on Si/SiO_2. The quality improvement by using BN as a substrate was significant; the mobilities for devices were above 100000 cm^2/Vs which is an order of magnitude higher than typical graphene devices on SiO_2 [10]. In very high magnetic fields the fractional quantum Hall effect was also observed in such samples [11]. Another substrate demonstrated to be suitable for obtaining flat graphene is mica [12].

Graphene Flakes on Graphite After cleavage of a graphite crystal, one often finds graphene flakes on the surface which are decoupled from the bulk graphite underneath. These flakes provide the most favorable conditions for accessing the intrinsic electronic properties of graphene as detailed in the following sections [13–15].

Epitaxial Graphene, Graphene Obtained by Chemical Vapor Deposition etc. Other avenues of producing graphene are epitaxial growth on SiC crystals [16–18] and chemical vapor deposition (CVD) [19–21]. In the epitaxial growth one starts with a SiC crystal terminated in Si or C and annealing to temperatures above 1500 °C leads to the formation of graphene layers at the surface. Often the layers

are misoriented with respect to each other thereby forming Moiré patterns. For the CVD growth, a metallic substrate that plays the role of a catalyst is placed in a hot furnace in a flow of gaseous carbon source. As a result, carbon is absorbed into the metal surfaces at high temperatures and precipitated out to form graphene during cool down to room temperature [22]. Other metallic substrates used for growing graphene films include Ru [23, 24], Ir [25, 26] and Pt [27].

2.2.1 Surface Topography of Graphene

The discussion about the morphology of a graphene surface is important because the stability of a 2D membrane in a 3D world is closely related to the tendency toward crumpling or rippling [28, 29]. The degree of rippling also influences the quality of the electronic properties [30]. The morphology of the graphene surface depends strongly on the type of substrate (or lack of substrate) underneath.

Transmission Electron Microscope (TEM) experiments performed on graphene films placed on TEM grids show that there is an intrinsic rippling of the suspended graphene membrane with deformations of up to 1 nm [31]. However, when deposited on a flat surface such as mica [12], BN [32, 33], or HOPG [34] the height corrugations become as small as 20–30 pm. On the surface of SiO_2 the Van der Waals forces will make graphene conform to the rough surface and typical values reported for the corrugations are 0.5 nm in height and a few nm in the lateral dimension [7, 9, 13, 35, 36].

The first STM experiments on graphene deposited on SiO_2 showed that the lattice is indeed hexagonal with almost no defects [37]. Moreover, they also showed the importance of sample cleaning in order to access the pristine graphene surface [38]. A more extensive analysis of the correlation between the substrate roughness and intrinsic graphene roughness [13] suggested that in areas where the graphene does not conform to the oxide surface and it is suspended over the high points, one can find an additional intrinsic corrugation on smaller length scales consistent with TEM studies [31].

A comparison between typical STM data for graphene on SiO_2 and decoupled graphene flakes on HOPG is presented in Fig. 2.3. In Fig. 2.3(a) the topography of a graphene area on SiO_2 shows a rippled surface. In contrast, graphene on HOPG is much flatter as seen in the topography map in Fig. 2.3(b). The corresponding atomic resolution data demonstrates that despite the corrugation of the surface of graphene, the honeycomb lattice is continuous across the hills and valleys (Fig. 2.3(c), (d)). Remarkably, in both cases the graphene lattice is defect-free over areas as large as hundreds of nanometers.

When deposited on BN, graphene is significantly flatter than on SiO_2 as shown in Fig. 2.4. A comparison between the surface morphology for areas of graphene on SiO_2 and on BN is presented in Fig. 2.4(a) and (b). Two line cuts arbitrarily shifted in the z direction in Fig. 2.4(c) show that, when placed on BN, graphene is one order of magnitude smoother than on SiO_2. On such samples STM/STS experiments report Moiré patterns that arise because of the lattice mismatch and rotation between

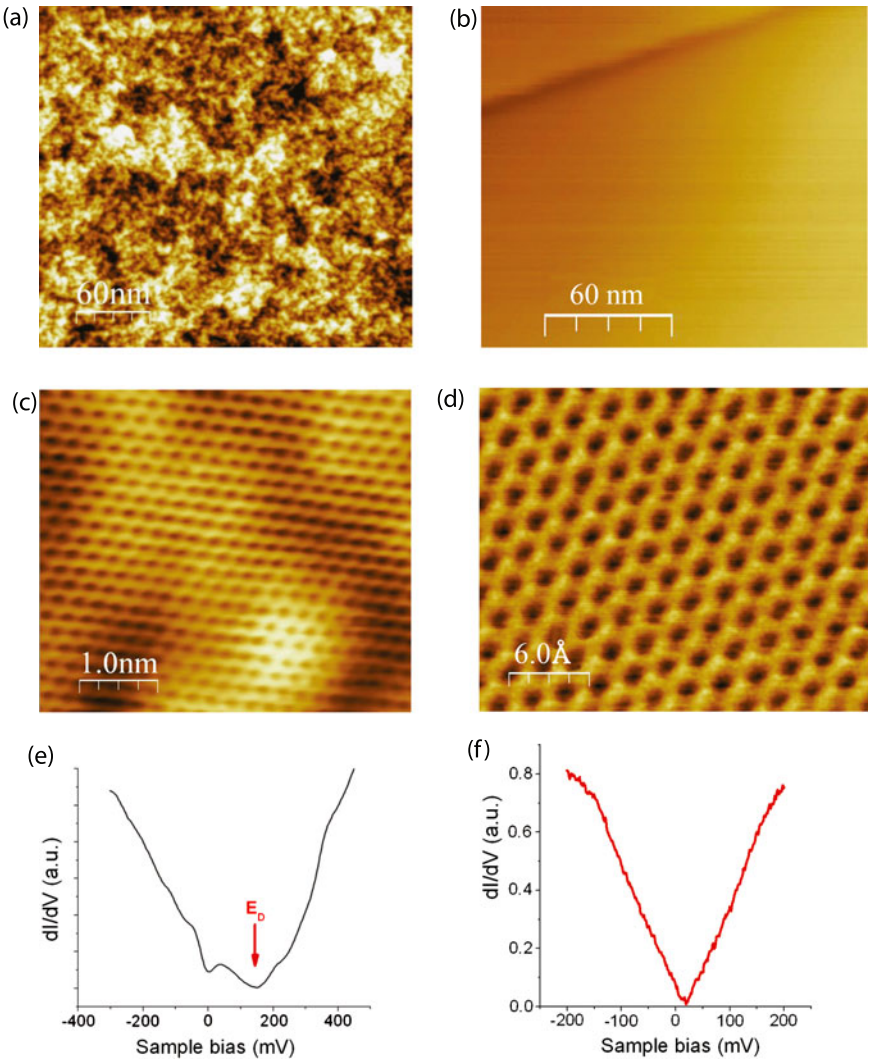

Fig. 2.3 (a) Scanning Tunneling Microscopy image of 300 nm × 300 nm graphene on a SiO_2 surface ($V_{bias} = 300$ mV, $I_t = 20$ pA). (**b**) Scanning Tunneling Microscopy image of 300 nm × 300 nm graphene on graphite surface ($V_{bias} = 300$ mV, $I_t = 20$ pA). (**c**), (**d**) Smaller size image showing atomic resolution on graphene in area (**a**) and (**b**), respectively. (**e**), (**f**) Scanning Tunneling Spectroscopy data obtained on the corresponding graphene samples in (**c**) and (**d**), respectively [9, 34]

graphene and the BN [32, 33]. Furthermore, the random potential fluctuation measured by scanning tunneling spectroscopy appears much smaller than on graphene samples exfoliated on SiO_2 [32, 33].

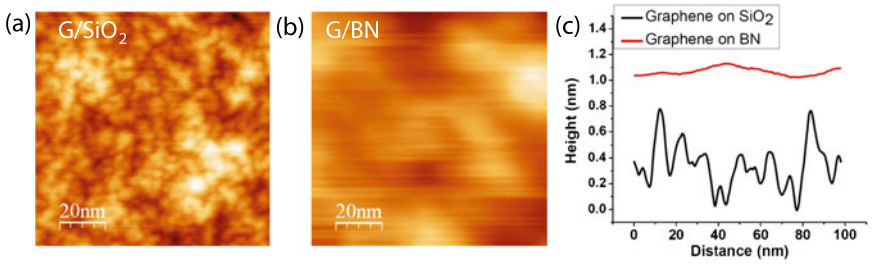

Fig. 2.4 Comparison between the topography of two areas 100 nm × 100 nm of (**a**) graphene on SiO_2 and (**b**) graphene on BN. (**c**) Comparison between two line cuts across (**a**), (**b**)

2.2.2 Tunneling Spectroscopy of Graphene

One of the reasons why graphene has attracted so much interest is its unique electronic band structure. In the low energy regime the charge carriers obey a Dirac-Weyl Hamiltonian and have a conical dispersion. To the first approximation, it is possible to obtain a closed analytical form for the density of states at low energy [39]:

$$\rho(E) = \frac{2A_c}{\pi}\frac{|E|}{v_F^2} \tag{2.5}$$

where, A_c is the unit cell area of graphene lattice.

The DOS in graphene differs qualitatively from that in non-relativistic 2D electron systems leading to important experimental consequences. It is linear in energy, electron-hole symmetric and vanishes at the Dirac point (DP)—as opposed to a constant value in the non-relativistic case. This makes it easy to dope graphene with an externally applied gate voltage. At zero doping, the lower half of the band is filled exactly up to the Dirac points. Applying a voltage to the graphene relative to the gate electrode (when graphene is on Si/SiO_2, the highly doped Si is the back gate) induces a nonzero charge. This is equivalent to injecting, depending on the sign of the voltage, electrons in the upper half of Dirac cones or holes in the lower half. Due to electron-hole symmetry the gating is ambipolar [40].

For graphene on graphite the measured density of states is linear and vanishes at the Dirac point (Fig. 2.3(f)) as expected from theory. For the data shown in Fig. 2.3(f), the Fermi level is slightly shifted away from the Dirac point (≈16 meV) corresponding to hole doping with a surface density $n = 2 \times 10^{10}$ cm^{-2}.

However, when disorder introduces a random potential, as is the case for the graphene on SiO_2, the spectrum deviates from the ideal V-shape [35, 36, 41–43]. Some of the measured features in the spectra were attributed to strain and ripples [43], others to local doping due to impurities. A typical spectrum is presented in Fig. 2.3(e) [9]. In this case, the Dirac point is shifted from the Fermi energy by ≈200 meV corresponding to a carrier concentration $n = 2 \times 10^{12}$ cm^{-2}.

Some STM experiments on graphene exfoliated on SiO_2 reported a gap at the Fermi level which was attributed to inelastic tunneling into graphene (via phonon

scattering) [42]. In other experiments though, the gap is seen only above certain tunneling currents [41]. In most cases a dip at the Fermi level is observed in the tunneling spectra of graphene on SiO_2 [9, 36] which can be attributed to a zero bias anomaly.

2.2.3 Doping and Electron Hole Puddles

Theoretically, in neutral graphene the Fermi level should coincide with the Dirac point. However, it is observed that graphene is often doped such that there is an energy difference between the Dirac point energy (E_D) and the Fermi energy (E_F). To find the dopant concentration, the carrier density can be calculated as follows:

$$n = \frac{N}{A} = 4\frac{\pi k_F^2}{(2\pi)^2} = \frac{k_F^2}{\pi} = \frac{1}{\pi}\frac{E_F^2}{\hbar^2 v_F^2} \tag{2.6}$$

Here the Fermi velocity is $v_F = 10^6$ m/s and taking $E_F = 1$ meV we get $n \approx 10^8/\text{cm}^2$.

The origin of this doping is not yet well understood. However, the most likely causes are trapped charges and absorbed species at edges/defects etc. Recent STM experiments using graphene films doped on purpose with nitrogen (N) were aimed at characterizing at atomic scales the electronic structure modifications due to individual dopants [44]. It was found that N, which bonds with the carbon in the lattice, can contribute to the total number of mobile carriers in graphene resulting in a shift of the Dirac point. Moreover, the electronic properties of graphene are modified around an individual N dopant on length scales of only a few atomic spacings [44].

The existence of electron-hole puddles was first pointed out by single electron transistor studies with a spatial resolution of a hundred nm [6]. Higher resolution studies of the spatial fluctuations of the carrier distribution using STM showed even finer density fluctuations on nm scales [7]. The typical variation in the Dirac point of graphene deposited on SiO_2 was found to be 30–50 meV corresponding to carrier densities of $(2 \times 10^{11}–4 \times 10^{11})$ cm^{-2} [6, 7, 9].

In the presence of scattering centers, the electronic wave functions can interfere to form standing wave patterns which can be observed by measuring the spatial dependence of dI/dV at a fixed sample bias voltage. By using these interference patterns, it was possible to discern individual scattering centers in the dI_t/dV_{Bias} maps obtained at energies far from the Dirac point when the electron wave length is small. No correlations were found between the corrugations and the scattering centers, suggesting that the latter play a more important role in the scattering process. When the sample bias voltage is close to the Dirac point, the electron wave length is so large that it covers many scattering centers. Thus, the dI_t/dV_{Bias} maps show coarse structures arising from the electron-hole puddles. The Fourier transform of the interference pattern provides information about the energy and momentum distribution of quasiparticle scattering, which can be used to infer band structure in-

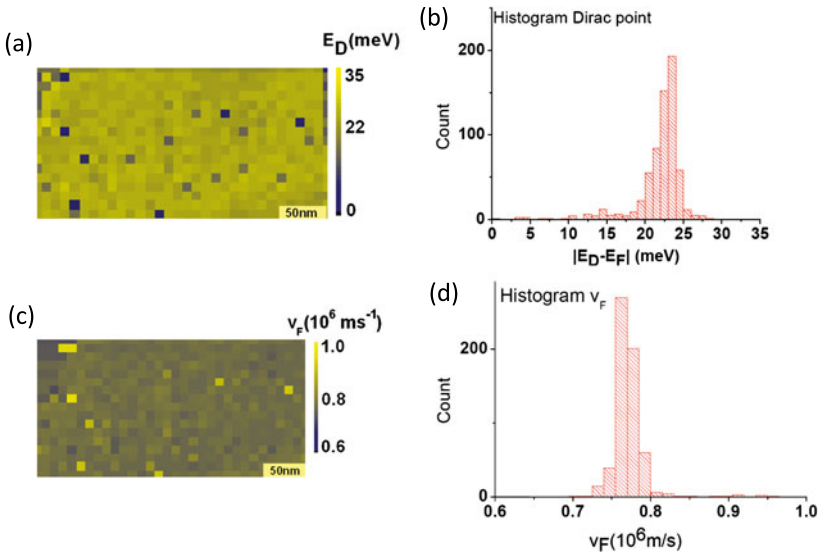

Fig. 2.5 (**a**) Map of the Dirac point on graphene on graphite [14]. (**b**) Histogram of the values of Dirac point in (**a**). (**c**) Map of the Fermi velocity on graphene on a graphite substrate [14]. (**d**) Histogram of the velocities in (**c**)

formation [45]. For unperturbed single layer graphene, interference patterns are expected to be absent or very weak [46]. However, due to the strong scattering centers, clear interference patterns are observed for graphene on SiO_2 [7], where the main scattering centers are believed to be trapped charges.

In contrast to graphene on SiO_2, graphene on graphite shows very little variation of the Dirac point (≈5 meV) across hundreds of nm [14, 34] (Fig. 2.5(b)). This is illustrated in the spatial map of the distance between the Dirac point and the Fermi level shown in Fig. 2.5(a). The value of the Dirac point was extracted by fitting the Landau level sequence, as discussed in the next section. Further demonstration of the homogeneity of the graphene flakes on graphite is given by the Fermi velocity which is found to vary by less than 5 % across the same area as shown in Fig. 2.5(c), (d). For the histogram is Fig. 2.5(d) the mean value of the velocity is $v_F = 0.78 \times 10^6$ m s^{-1}. Similarly, the fluctuations of the local charge density in graphene on h-BN were recently found to be much smaller than on SiO_2 [32, 33].

2.2.4 Landau Levels

In the presence of a magnetic field, B, normal to the plane, the energy spectrum of 2D electron systems breaks up into a sequence of discrete Landau levels (LL). For the non-relativistic case realized for example in the 2D electron system on helium [47] or in semiconductor heterostructures [48], the Landau level sequence consists

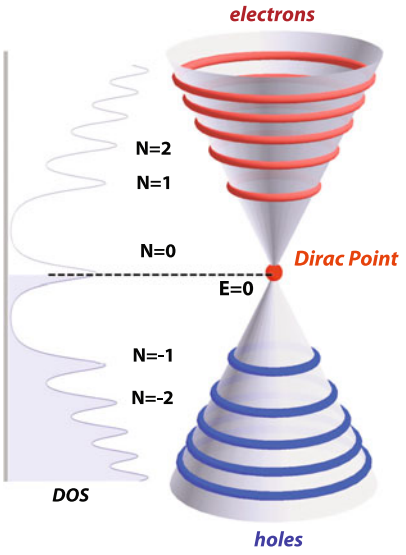

Fig. 2.6 Illustration of quantized energy levels in graphene and their signature in the density of states. *Right side*: Dirac cone which in a magnetic field no longer has a continuum energy, but discrete levels: *red rings* for electrons, *blue rings* for holes. *Left side*: the *vertical axis* is energy; the *horizontal axis* is the density of states. For each Landau level there is a peak in the density of states which is broadened by electron-electron interactions in ideal systems. In the presence of disorder, the LL are further broadened. The indexes of the LLs are $N = 0$ for the one at the Dirac point and $N = +1, +2, +3, \ldots$ for the electron side and $N = -1, -2, -3, \ldots$ for the hole side

of a series of equally spaced levels similar to that of a harmonic oscillator: $E = \hbar\omega_c(N + 1/2)$ with the cyclotron frequency $\omega_c = eB/m^*$, a finite energy offset of $1/2\hbar\omega_c$, and an effective mass m^*. In graphene, as a result of the linear dispersion and Berry phase of π, the Landau level spectrum is different [49]:

$$E_n = \pm\hbar\omega_G\sqrt{|N|}, \quad \omega_G = \frac{\sqrt{2}v_F}{l_B} \tag{2.7}$$

Here, $N = \ldots, -2, -1, 0, +1, +2, \ldots$ is the index of the Landau level, ω_G is the cyclotron energy for graphene and $l_B = \sqrt{\frac{\hbar}{eB}}$ is the magnetic length.

Compared to the non-relativistic case the energy levels are no longer equally spaced, the field dependence is no longer linear and the sequence contains a level exactly at zero energy, $N = 0$, which is a direct manifestation of the Berry phase in graphene [50–52]. We note that the LLs are highly degenerate, the degeneracy per unit area being equal to $4B/\phi_0$. Here B/ϕ_0 is the orbital degeneracy with $\phi_0 = h/e$ the flux quantum and $4 = g_s \cdot g_v$, where g_s and g_v ($g_s = g_v = 2$) are the spin and valley degeneracy, respectively.

In Fig. 2.6 an illustration of the quantized LL is presented. The conical dispersion of graphene in the absence of a magnetic field is transformed into a sequence of Landau levels corresponding to electron carriers above the Dirac point (DP) and holes below it. In the density of states, represented on the left side, a LL corresponds

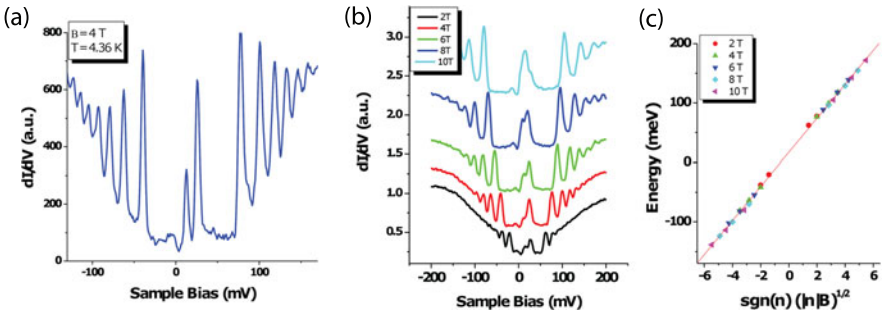

Fig. 2.7 (**a**) STS spectrum of graphene on graphite showing the presence of Landau levels. (**b**) The evolution of the LLs with magnetic field. (**c**) The energy dependence of the LLs on the reduced parameter $\mathrm{sgn}(N)\sqrt{|N|B}$ [34], where sgn refers to $\pm$ signs

to a peak in the DOS. The indexes of the LLs are indicated as $N < 0$ for holes and $N > 0$ for electrons. Assuming that the Fermi level is exactly at the DP (the case of neutral graphene), the gray area in Fig. 2.6 represents electronic states that are already filled.

Experimentally, a direct way to study the quantized Landau levels is through STS as was demonstrated in early studies on HOPG [53, 54] and adsorbate-induced two dimensional electron gases (2DEGs) formed by depositing Cs atoms on an n-InSb(110)surface [55].

2.2.4.1 Landau Levels in Almost Ideal Graphene

STM studies of graphene flakes on graphite in a magnetic field by Li et al. [34] gave direct access to the LL sequence and its evolution with magnetic field. The main results are presented in Fig. 2.7. In Fig. 2.7(a) the high resolution spectrum at 4 T shows sharp LL peaks in the tunneling conductivity dI_t/dV_{Bias}. The field dependence of the STS spectra, shown in Fig. 2.7(b), exhibits an unevenly spaced sequence of peaks flanking symmetrically, in the electron and hole sectors, a peak at the Dirac point. All peaks, except the one at the Dirac point, which is identified as $N = 0$, fan out to higher energies with increasing field. The peak heights increase with field, consistent with the increasing degeneracy of the LL. To verify that this sequence of peaks does indeed correspond to massless Dirac fermions, the field and level-index dependence of the peak energies in the sequence was measured. It was then compared to the expected values (2.7) measured relative to the Fermi energy (the convention in STS) as shown in Fig. 2.7(c). This scaling procedure collapses all the data onto a straight line. Comparing to (2.7), the slope of the line gives a direct measure of the Fermi velocity, $v_F = 0.79 \cdot 10^6$ m/s. This value is 20 % less than expected from single particle calculations and, as discussed later, the reduction can be attributed to electron-phonon interactions. The presence of a $N = 0$ field-independent state at the Dirac point together with the square-root dependence of

the LL sequence on both field and level index, are the hallmarks of massless Dirac fermions.

The technique described above, Landau level spectroscopy, can be used to obtain the Fermi velocity of Dirac fermions, the quasiparticle lifetime, the electron phonon coupling, and the degree of coupling to the substrate [14, 56]. LL spectroscopy gives access to the electronic properties of Dirac fermions when they define the surface electronic properties. This technique was adopted and successfully implemented to probe massless Dirac fermions in other systems including graphene on SiO_2 [9], epitaxial graphene on SiC [57], graphene on Pt [58] and topological insulators [59, 60].

An alternative, though less direct, method of accessing the LLs is to probe the allowed optical transitions between the LLs by using cyclotron resonance measurements. This was done on exfoliated graphene on SiO_2 [61, 62], epitaxial graphene [63] and graphite [15]. Other indirect methods include scanning electron transistor or similar capacitive techniques [64, 65].

Electron-Phonon Interaction and Velocity Renormalization The basic physics of graphene is captured in a tight-binding model. However, many-body effects are often not negligible. *Ab initio* density functional calculations show that the electron-phonon (e-ph) interactions introduce additional features in the electron self-energy, leading to a renormalized velocity at the Fermi energy [66]. Away from the Fermi energy, two dips are predicted in the velocity renormalization factor, $(v_F - v_{F0})/v_F$, at energies $E \pm \hbar\omega_{ph}$ where ω_{ph} is the characteristic phonon energy. At the energies of the phonons involved, such dips give rise to shoulders in the zero field density of states which can be measured in STS experiments.

Figure 2.8(a) plots the tunneling spectra measured on a decoupled graphene flake on graphite. Two shoulder features on both sides of the Fermi energy are seen around 150 meV. These features are independent of tip-sample distance for tunneling junction resistances in the range 3.8–50 GΩ. In Fig. 2.8(b) the corresponding two dips in the renormalized velocity are visible. This suggests that the optical breathing phonon, A_1' with energy $E \approx 150$ meV plays an important role in the velocity renormalization observed in graphene [66]. The line width of the A_1' phonon decreases significantly for bilayer graphene and decreases even more for graphite [67, 68]. Therefore the electron-phonon coupling through the A_1' phonon is suppressed by interlayer coupling and the induced velocity renormalization is only observed in single layer graphene decoupled from the substrate.

Landau Level Linewidth and Electron-Electron Interactions The lineshapes of the LLs for the case of graphene on graphite were found to be Lorentzian rather than Gaussian [34], suggesting that the linewidth reflects the intrinsic lifetime rather than disorder broadening. Furthermore, looking closer at the linewidth of the LLs in Fig. 2.8(c), it is found that the width increases linearly with energy. This dependence is consistent with the theoretical predictions that graphene displays a marginal Fermi liquid behavior: $\tau \propto E^{-1} \approx 9$ ps [69].

Another interesting feature is the presence of an energy gap with $E_{gap} \approx 10$ meV in the $B = 0$ T spectrum as shown in Fig. 2.8(d) which may have the same origin

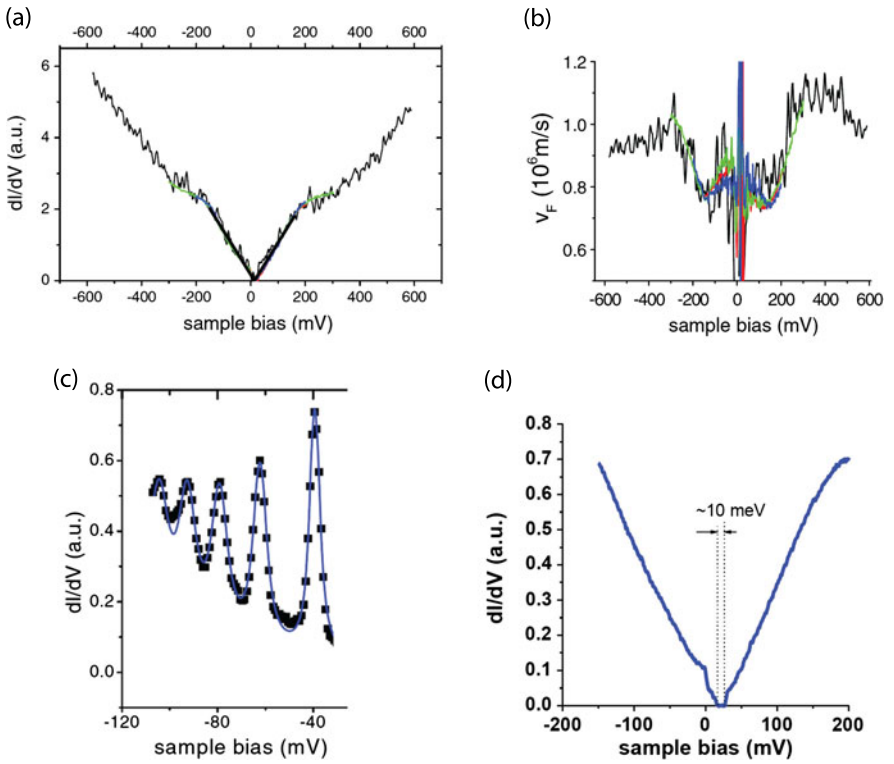

Fig. 2.8 (**a**) STS data for graphene flakes on HOPG showing how the Fermi velocity is renormalized below a certain energy (≈150 meV). (**b**) The calculated renormalization of the Fermi velocity versus sample bias from the data in (**a**). (**c**) Fit of the LL lineshape with Lorentzians. (**d**) Tunneling spectra taken with higher resolution revealing a 10 meV gap at the Dirac point [34]

as the splitting of the $N = 0$ level in finite field. One possible explanation for the presence of this gap is the broken A-B symmetry due to the Bernal stacking of the graphene layer with respect to the graphite substrate, but more work is needed to elucidate its origin.

Lifting of the LL degeneracy was observed in quantum Hall effect measurements on the highest quality suspended graphene devices [70, 71] and in STM experiments on epitaxial graphene on SiC [72].

2.2.4.2 Effects of Interlayer Coupling

For graphene flakes on graphite one can also address the effect of interlayer coupling in regions where the graphene flakes are weakly coupled to the substrate. It was found that the LL spectrum of graphene which is weakly coupled to a graphite substrate strongly depends on the degree of coupling.

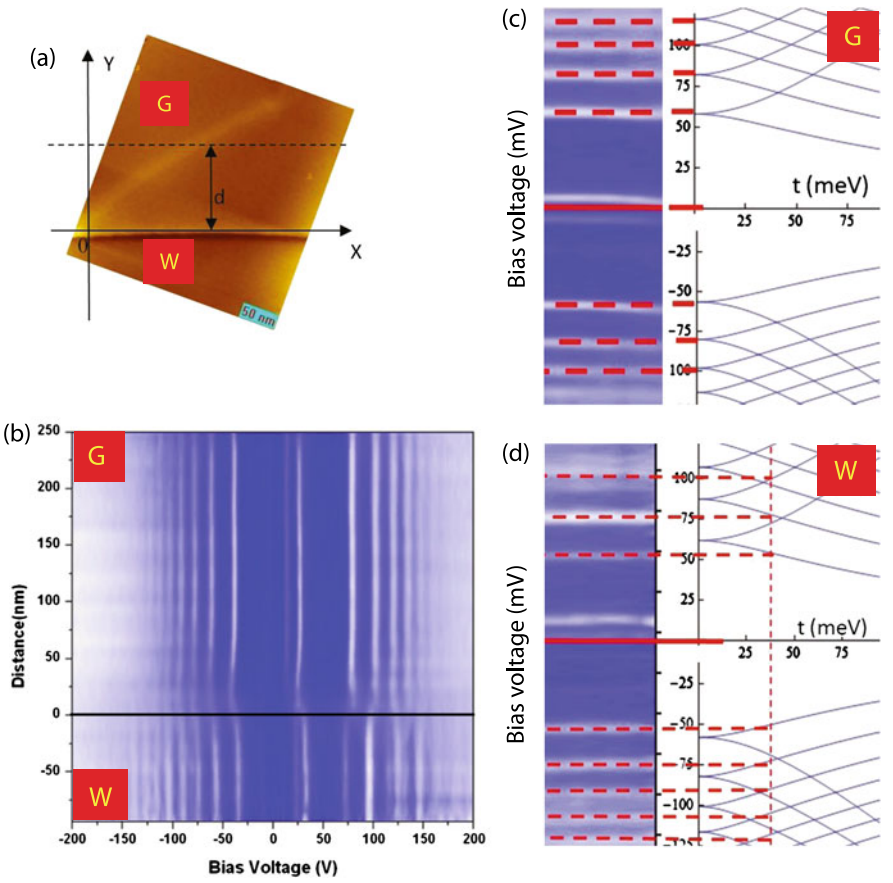

Fig. 2.9 (**a**) STM image showing two distinct regions: G—where the graphene flake is decoupled from graphite; W—where the graphene flake is weakly coupled to the graphite substrate. (**b**) The evolution of the Landau levels from region G to region W. The *vertical axis* is the position where the spectrum is measured indicated by *d* in (**a**); the *horizontal axis* is the sample bias. (**c**), (**d**) Fits of the LLs in (**b**) to the theoretical model [56], in which t is the coupling parameter between the layers, for no coupling (**c**) and weak coupling (**d**) [14]

In Fig. 2.9(a) the topography image shows two regions: G, where the top layer is decoupled and displays signatures of a single layer graphene and below it, a different region, W, where there is weak coupling to the underlying graphite substrate. In the presence of weak coupling the LL spectrum changes into a complex sequence resulting from splittings of the levels due to lifted level degeneracy. This is illustrated by the spatial dependence of the LLs in Fig. 2.9(b) where the LL sequence changes after crossing the boundary between G and W [14]. By fitting the LL sequence in W to the theoretical model described in [56], the coupling was found to be a tenth of the one in a regular Bernal stacked bilayer [14].

2.2.4.3 Landau Levels in Disordered Graphene

For graphene device applications which require gating and the ability to do transport measurements, it is necessary to use insulating substrates. Therefore, although the quality of graphene on graphite is far superior to that on an insulating substrates, graphite substrates cannot be used in practical applications.

Initially, the disorder potential found on standard SiO_2 substrates, was too large to allow observation of LLs by STS even in the highest magnetic fields [41] so further improvement of the substrate was needed. One procedure that was demonstrated to dramatically improve sample quality is to remove the SiO_2 substrate under the graphene which becomes suspended [70, 71, 73, 74]. However, such samples are fragile and small, so studying them is challenging.

Therefore, exploring ways to improve the substrate is of interest. In the semiconductor industry it is known that the quality of SiO_2 can be greatly improved using dry oxidation in the presence of chlorine. This process reduces the number of trapped charges in the oxide, improving the uniformity and quality of the insulator [75–78]. When using such substrates treated by chlorination, the STM and STS measurements show that it is possible to see well defined quantized levels for high enough magnetic fields [9]. The broadening of the LLs, however, together with the deviation from a V-shaped zero-field density of states, indicate that such samples are not ideal.

STS in zero field was used to give an estimate of the average length scale of the disorder, the electron-hole puddle size, $d \approx 20$ nm [9]. In order to observe well defined levels, the magnetic length should be at most $(d/2) \approx 10$ nm, corresponding to a magnetic field $B = 6$ T. In Fig. 2.10(a) the STS data taken for graphene on chlorinated SiO_2 shows how indeed, for smaller fields, below 6 T, the levels are not well defined, while above 6 T in Figs. 2.10(a), (b) they become clearly defined.

In such samples it is expected that the levels are broadened by disorder [79–81]. The measured width of the levels is typically $\gamma \approx 20$–30 meV, much larger than on HOPG and corresponds to a carrier lifetime of $\tau \approx 22$–32 fs consistent with values obtained by different techniques [61, 64, 65].

The Fermi velocity obtained by LL spectroscopy is $v_F = (1.07 \pm 0.02) \cdot 10^6$ m/s (Fig. 2.10(d)) and varies by 5–10 % depending on the position on the sample. To further illustrate the effect of disorder on the LLs, Fig. 2.10(c) shows how the sequence of levels changes along a 60 nm long line across the sample. The variation in brightness indicates spatial dependence of the LLs width and height due to disorder.

2.2.4.4 Gate Dependence of Landau Levels

Due to its band structure, in particular the electron-hole symmetry, graphene shows an ambipolar electric field effect. STS of gateable graphene on an insulating substrate can be used to study the evolution of the electronic wave function and density of states as the Fermi energy is moved through the LLs. The ability of STS to access both electron and hole states makes this a particularly powerful technique. In an

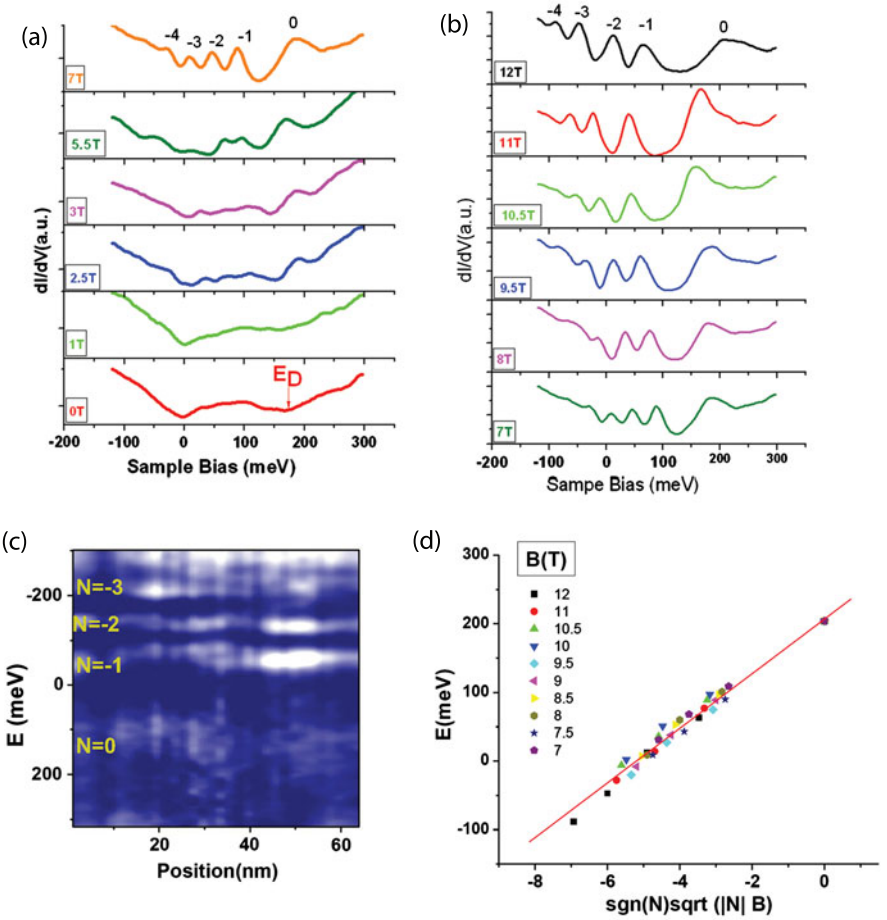

Fig. 2.10 (**a**) STS data for graphene on SiO_2 for magnetic fields up to 7 T. (**b**) STS data on graphene on SiO_2 for magnetic fields between 7 T and 12 T. (**c**) Example of typical evolution of the LL across a line of 60 nm for the graphene on SiO_2 sample in $B = 10$ T. (**d**) Fermi velocity extracted from the LL sequence in (**a**) and (**b**) [9]. The energies of the LLs were shifted so that the Dirac point is the same for all fields. The spread in the LLs for different fields reflects slight variations of the Fermi velocity due to the fact that the spectra for the different fields were not taken at the exact same location on the sample

STS experiment E_F is usually situated at zero bias and therefore it is convenient to define the E_F as the origin of the energy axis and to measure the Dirac point energy with respect to it.

Figure 2.11(a) shows a set of data taken at $B = 12$ T in which the spectrum was recorded for different gate voltages. Each vertical line is a spectrum at a particular gate voltage V_G. The intensity of the plot represents the value of the dI/dV, the lighter color corresponding to the peaks in the spectrum. The vertical axis

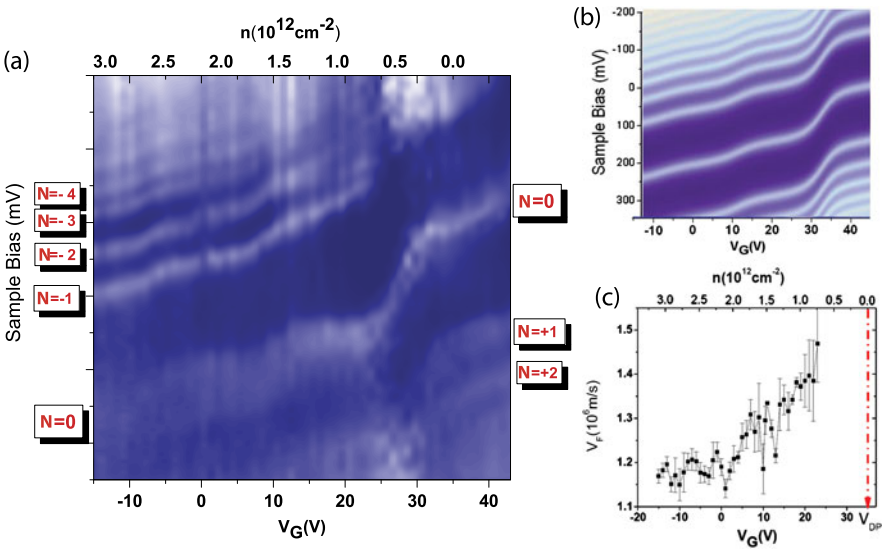

Fig. 2.11 (**a**) Map of the dependence of the LL in graphene on SiO_2 on charge carrier density for $B = 12$ T. The *vertical axis* is the sample bias, the *bottom horizontal axis* is the gate voltage and the *upper horizontal axis* is the corresponding charge carrier density. The LL indexes are marked $N = \ldots \pm 3, \pm 2, \pm 1, 0$. (**b**) Simulation of the evolution of the LL spectrum in (**a**). (**c**) Gate voltage dependence of the Fermi velocity. The Dirac point, at $V_G = 35$ V, is marked

is the sample bias and the horizontal axis is the gate voltage. The gate voltage was varied in the range $-15\ \text{V} < V_G < +43\ \text{V}$ corresponding to carrier densities: $3 \times 10^{12}\ \text{cm}^{-2} > n_c > -0.5 \times 10^{12}\ \text{cm}^{-2}$. In the spectrum taken at $V_G = -15$ V a very faint $N = 0$ level is seen at ≈240 meV. Because the sample was hole doped at neutral gate voltage already, in the energy range that we probe, we only measure the Landau levels corresponding to hole states: $N = -1, -2, -3, \ldots$. At higher gate voltages though, for $V_G > 40$ V the levels corresponding to electron states $N = +1, +2, +3, \ldots$ also become visible.

Qualitatively, one can understand the overall step-like features in Fig. 2.11 (plateaus followed by abrupt changes in slope) as follows: the LL spectrum contains peaks, corresponding to high DOS, separated by regions of low DOS (Fig. 2.11(a)). It takes a large change in the charge carrier density to fill the higher DOS regions—therefore plateaus appear; at this point the Fermi level is pinned to the particular Landau level being filled. On the other hand, filling the regions of low DOS in between the LLs does not require much change in carrier density—therefore an abrupt change in slope appears. For broad Landau levels the DOS in between the peaks is larger, thus smearing the step-like pattern.

A simulation considering the LL broadening and using $v_F = (1.16 \pm 0.02) \times 10^6$ m/s is plotted in Fig. 2.11(b) and shows good agreement with the measured data in Fig. 2.11(a).

Similar experiments on graphene exfoliated on SiO_2, probing areas of different disorder across the sample, where reported by Jung et al. [36].

In the two-dimensional electron system (2DES) of very high mobility GaAs samples, this pinning of the Fermi level to the LL was observed by time domain capacitance spectroscopy [82].

In contrast to electrical transport measurements that typically probe states near the Fermi surface, STS can access both filled and empty states. Therefore, in a magnetic field, through LL spectroscopy one can probe the full shape of the Dirac cone in the measured energy range. The shape of the cone was investigated as a function of carrier concentration by measuring the Fermi velocity from the LL sequence as a function of doping. Within the investigated range of charge carrier density (3×10^{12} cm$^{-2} > n_c > -0.5 \times 10^{12}$ cm^{-2}), it was found that closer to the Dirac point, the velocity increases by $\approx$25 % as seen in Fig. 2.11(c).

At low carrier density the effects of electron-electron interactions and reduced screening on the quasiparticle spectrum are expected to become important. The observed increase in the Fermi velocity is consistent with a renormalization of the Dirac cone close to the neutrality point due to electron-electron interactions [69, 83]. If the random potential is further reduced such that LLs can be observed already in small fields, the fact that the spacing between the levels is smaller will make it possible to probe the reshaping of the cone with higher accuracy.

A similar result was obtained by Elias et al. on suspended graphene samples by measuring the amplitude of the Shubnikov de Haas oscillations as a function of temperature [84].

2.2.4.5 Disorder Effects: Extended and Localized States

Impurities and the resulting random potential strongly affect the electronic wave function in graphene. By measuring STS in the presence of a perpendicular magnetic field, one can visualize the wavefunctions corresponding to the LLs in real space.

To this end, STS spectra are acquired on a fine grid of points across a chosen area. At a particular energy one can plot an intensity map having the x, y spatial coordinates and as z-coordinate the value of the dI/dV ($\propto$ DOS) at that energy. This map will illustrate the density of states variation in real space.

Such a procedure is shown in Fig. 2.12. Figure 2.12(a) represents the average over spectra taken in $B = 12$ T over a grid of points across the area of the sample shown by the STM image in the inset. The LLs with indexes $N = 0, +1, +2, \ldots$ are resolved at this field value. Figure 2.12(b) and (c) are the dI_t/dV_{bias} maps at energies marked in (a) as E and L where I_t is the tunneling current and V_{bias} is the bias voltage. At $E \approx 0$ eV corresponding to the peak of the $N = 0$ LL, Fig. 2.12(b) shows bright regions of high DOS forming an extended percolating state. At $E \approx$ 55 meV in between $N = 0$ and $N = +1$, Fig. 2.12(c) shows the complementary localized states around impurities [85].

The presence of extended and localized states on the peaks and valleys of the LL spectrum is often used to qualitatively understand the integer quantum Hall effect (IQHE). A typical IQHE measurement in a Hall bar configuration [86] measures the

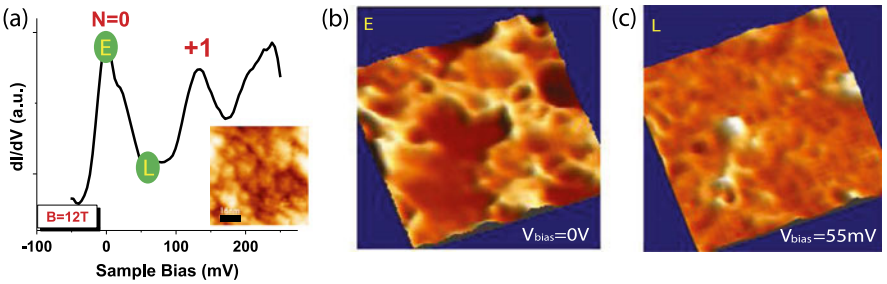

Fig. 2.12 (**a**) Averaged tunneling spectra across the area in the inset showing LLs with index $N = 0, +1, \ldots$. The letters E and L indicate the energies where the STS maps in (**b**) and (**c**) are taken. The scale bar of the inset is 16 nm. (**b**) STS map across the area in the inset of (**a**) at $V_{bias} = 0V$. (**c**) STS map across the area in the inset of (**a**) at $V_{bias} = 55$ mV [85]

Hall (transverse) resistivity ρ_{xy} and the longitudinal resistivity ρ_{xx} while varying the filling factor $\nu = (n_s h)/(eB)$ with n_s the carrier density, B the magnetic field, h the Planck constant and e the electron charge.

When the filling is such that the Fermi level lies in between two LLs the electrons are trapped in the localized states around the impurities and they do not play any role in the conduction. At this point $\rho_{xx} = 0$ and ρ_{xy} is quantized. When the Fermi level is at a peak of a Landau level, the electrons occupy the percolating state across the sample so ρ_{xx} is finite and ρ_{xy} increases making the transition between the quantized plateaus.

STM/STS experiments probing the extended and localized quantum Hall states were reported on the adsorbate-induced two dimensional electron gas on n-InSb(110) [55] and on epitaxial graphene on SiC [87].

2.2.5 *Measuring Small Graphene Devices with Scanning Probes*

The discovery of graphene opened exciting opportunities to study a 2D system by surface probes. However the fact that the cleanest samples obtained by exfoliation are only a few microns in size poses technical challenges. Some room temperature experimental set-ups containing optical microscopes can overcome this problem. Even low temperature experiments which are equipped with long range optical microscopes or scanning electron microscopes can find small samples, but most low temperature and magnetic field setups are lacking such tools. For this reason, a capacitive method was developed in order to guide the STM tip towards micron size samples as detailed in [88].

To measure STS one usually applies a small ac modulation to the sample bias voltage, $\tilde{V}_s$, so that there is an ac current, $\tilde{I}$, flowing through the STM tip: $\tilde{I} = G_t \cdot \tilde{V}_s + i\omega C \tilde{V}_s$, where G_t is the tunneling conductance and C is the tip-sample capacitance. The contributions to the ac current are from tunneling (first term) and from capacitive pickup (second term). The pick-up signal can be used to resolve

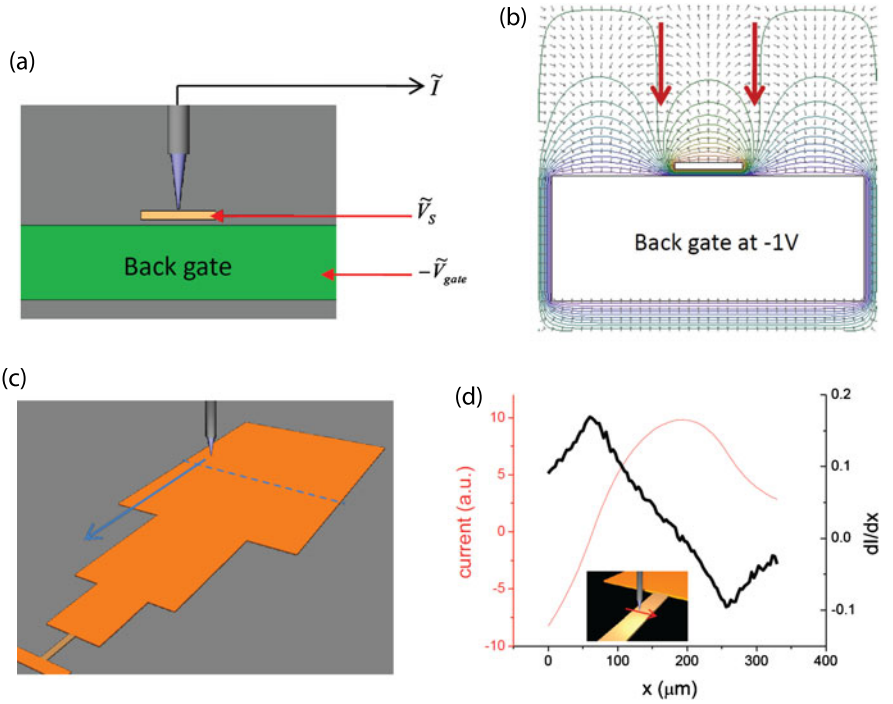

Fig. 2.13 (**a**) General set-up of the sample separated by a SiO_2 layer from the back gate and the quantities of interest: pick-up current $\tilde{I}$, the ac voltage applied to the sample $\tilde{V}_s$, and the gate voltage $\tilde{V}_{gate}$. (**b**) Electric field lines above the sample when the tip is not taken into account, but only the sample at $V = +1$ V and the back gate at $V = -1$ V. The *arrows* point to the edges of the sample. (**c**) Sketch of the metallic lead connected to the sample. The tip will travel across the largest pad on the indicated *dashed line* and after that towards the smaller pad as pointed by the *arrow*. (**d**) The typical measured current versus position for the tip moving across one of the pads as well as its derivative

small structures when the tip is far from the surface and it is not in the tunneling regime.

The schematic set up for this method is shown in Fig. 2.13(a). The output voltage from the reference channel of a lock-in amplifier is split into two with 180° phase shift between them. One of the signals (+) is applied to the sample directly as $\tilde{V}_s$, the other (−) is applied to the gate $-\tilde{V}_{gate}$ through a pot resistor to adjust the amplitude. The capacitive pickup current measured from the tip is $\tilde{I}$. One key aspect of the procedure is tuning the voltage applied to the back gate in order to minimize the background pick-up current as detailed in [88].

To qualitatively illustrate the sensitivity of this method in detecting sample edges, Fig. 2.13(b) shows the electric field lines around the sample, when $V_s = 1$ V and $V_{gate} = -1$ V, highlighting the presence of steep potential lines at the edges of the sample.

Another novel component is the design of the metallic lead connected to the sample. This lead is made of connected pads which are becoming smaller in size closer to the sample, as shown in a sketch of the typical design in Fig. 2.13(c). This contact pad geometry makes it possible to locate small (micron size) samples on large (mm size) substrates with an STM tip alone, without the aid of complicated optical microscopy setups.

The measured pick-up current across one of the pads is shown in Fig. 2.13(d). The vertical left axis is the measured current and the horizontal axis is the position on the pad. The signal is higher when the tip is above the pad and smaller when it is off the pad, riding on top of an overall background signal. In the derivative of this current with respect to position, the edges of the pad can be identified as seen in the Fig. 2.13(d)—right vertical axis.

Such a signal is dependent on the tip-pad distance, so after the edges of a large pad have been identified, one can approach the tip to the conductive surface in the STM mode and retract a smaller number of steps in order to resolve the edges of the next smaller pad. The fact that the tip is far from the surface while moving across the large pads prevents it from crashing.

This procedure is repeated until the smallest pad and the sample are found. The sensitivity of this method is sufficient for finding samples of a few microns in size as demonstrated by Luican et al. [9].

2.2.6 Graphene Edges

The two high symmetry crystallographic directions in graphene, zig-zag and armchair are described in Fig. 2.14(a). A graphene flake can terminate in one of the two or it can have an edge that is irregular and contains a mixture of zig-zag and armchair. The type of edge is predicted to have a significant impact on its electronic properties [90, 91].

One of the highest resolution imaging experiments of a graphene edge was done using Transmission Electron Microscopy [92]. However, to simultaneously characterize the atomic structure and probe the electronic properties of the graphene edges, STM/STS are the techniques needed.

Theoretically, the zig-zag edge is predicted to have a localized state [93], i.e. a peak in the DOS at the Fermi level. Experimentally this was observed on HOPG by STM experiments [94]. To determine the structure of the edges with STM, one compares the direction of the edge with the one of the graphite lattice which can be measured inside the sample. Once the type of edge was inferred from topography, Niimi et al. [94] found that when the spectrum is measured on a zig-zag edge, it shows a peak close to the Fermi level which is absent in the armchair case as expected from the theoretical calculations.

STM/STS experiments of graphene nanoribbons created by unzipping carbon nanotubes are able in principle to detect the presence of edge states and correlate them to the ribbon chirality [95].

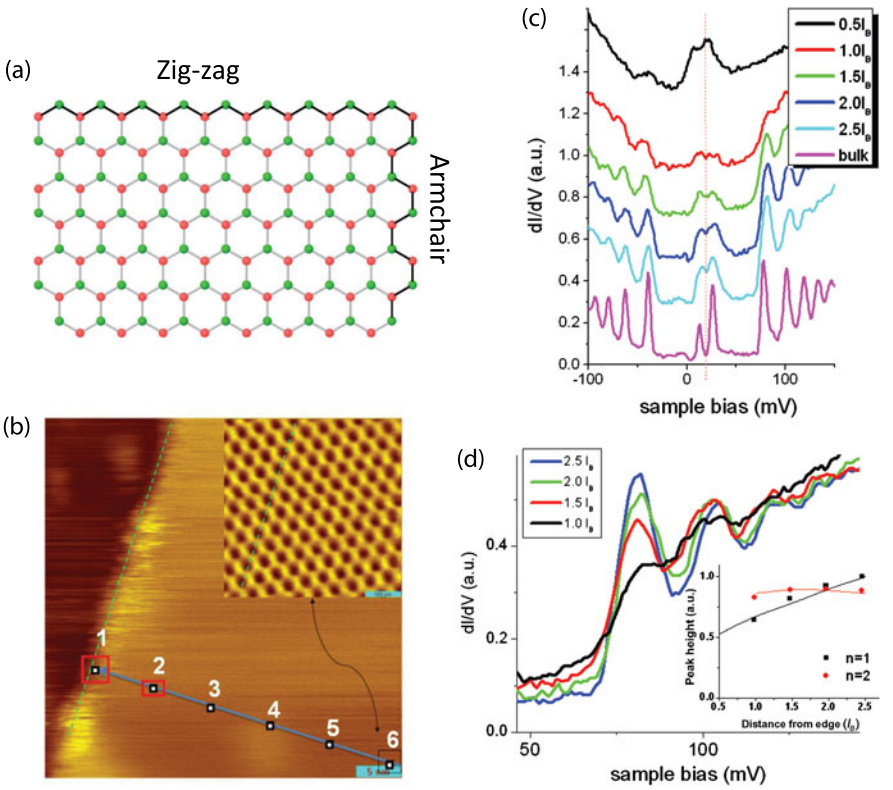

Fig. 2.14 (**a**) Sketch of the two crystallographic directions: zig-zag and armchair edges. (**b**) Topography image of a decoupled graphene flake on graphite, its edge and the positions where the tunneling spectra were taken. The *inset* is the atomic resolution image obtained on the flake as indicated. (**c**) STS traces at various distances from the edge of the flake in (**b**) towards the bulk. (**d**) Evolution of the LL intensities moving towards the edge. *Inset*: Data points are heights of the peaks for $N = 1, 2$ and the curves are theoretical calculations [89]

However, to make a connection between the atomic structure of edges in graphene and the magneto-transport experiments showing integer quantum Hall effect or evidence of many-body physics, it is important to study graphene edges in a magnetic field. This was possible on graphene flakes on graphite. The topographic image in Fig. 2.14(b) indicates the zig-zag edge as well as the positions where the spectra in Fig. 2.14(c) were taken. The inset is the honeycomb lattice measured on the decoupled flake. Figure 2.14(c) shows the spectra obtained, in a perpendicular magnetic field $B = 4$ T, at distances from 0.5 l_B (top curve) to bulk (bottom curve). One feature that is unique to the zig-zag edge is the fact that while the higher index LLs get smeared closer to the edge, the $N = 0$ is robust. The decay of the LL intensity upon approaching the edge is in good agreement with the theoretical prediction [96–98] as shown in the inset of Fig. 2.14(d).

2.2.7 Strain and Electronic Properties

Controlling strain in graphene is expected to provide new ways to tailor its electronic properties [99, 100]. Interestingly, as a result of strain in the lattice, the electrons in graphene can behave as if an external magnetic field is applied. The origin of this pseudo magnetic field is the fact that strain will introduce a gauge field in the Hamiltonian which mimics the presence of a magnetic field. In order to create a uniform field, however, the strain needs to be designed in particular configurations such as stretching graphene along three coplanar symmetric crystallographic directions [100].

Experimentally the effect of strain on the graphene spectrum was addressed by STM/STS measurements of graphene nanobubbles grown on a Platinum (111) surface [58]. On such samples, the peaks in the tunneling spectroscopy reported in [58] are interpreted as Landau levels originating from the pseudo magnetic field.

2.2.8 Bilayer Graphene

Graphene layers stack to form graphite in the so-called Bernal stacking arrangement. If we name the two inequivalent atomic sites in the graphene lattice A and B, the top layer will have B atoms sitting directly on top of A atoms of the bottom layer and A atoms of the top layer sit above the centers of the hexagons of the graphene underneath. A system consisting of two layers of graphene in Bernal stacking, bilayer graphene, is characterized by a hyperbolic energy dispersion of its massive chiral fermions.

In the presence of a magnetic field the LL sequence for an ideal Bernal-stacked graphene sample is given by: $E_n = (\frac{e\hbar B}{m^*})\sqrt{N(N-1)}$ where m^* is the effective mass of the carriers, B is the magnetic field, e is the electron charge, $\hbar$ is Planck's constant divided by 2π and $N = 0, 1, 2, 3, \ldots$. The eight fold degeneracy occurring for $N = 0$, $N = 1$ can be broken either by an applied electric field or by electron-electron interactions [101–103]. Experimentally, magneto-transport measurements of high quality suspended bilayer samples have revealed the presence of interaction-induced broken symmetry states [104–106].

In order to directly probe massive chiral fermions in bilayer graphene, STM/STS were performed on mechanically exfoliated graphene placed on insulating SiO_2 [107, 108]. It was found that the measured LL spectrum was dominated by effects of the disorder potential due to the substrate. The random potential creates an electric field between the two layers which results in locally breaking the LL degeneracy and a LL spectrum that is spatially nonuniform [108]. Therefore, in order to access the intrinsic properties of bilayer graphene, an improvement of samples that can be measured by STM/STS is necessary.

2.3 Electronic Properties of Twisted Graphene Layers

An infinitesimally small rotation away from Bernal stacking will completely change the electronic properties of the graphene bilayer system, suggesting the possibility of an extra knob to tune the electronic properties.

These rotational stacking faults are common and have been observed on graphite surfaces already in early STM studies [109–112]. It was not until the discovery of graphene that the electronic properties have been investigated both theoretically and experimentally. With the new methods of preparing graphene by chemical vapor deposition it became even more important to address questions regarding the properties of rotated layers since the growth mechanism seems to favor the formation of twisted layers [21].

The consequence of superposing and rotating two identical periodic lattices with respect to each other is the formation of Moiré patterns. Considering two hexagonal lattices, the Moiré pattern emerging for an arbitrary rotation angle is illustrated in Fig. 2.15(a). A commensurate pattern is obtained for discrete families of angles that can be mathematically derived [113–118]. One such family of angles is: $\cos(\theta_i) = (3i^2+3i+1/2)/(3i^2+3i+1)$ with $i = 0, 1, 2, \ldots$. The relation between the period of the superlattice L and the rotation angle θ is:

$$L = \frac{a}{2\sin(\frac{\theta}{2})} \tag{2.8}$$

where $a \approx 0.246$ nm is the lattice constant of graphene.

STM can reveal areas where a Moiré pattern resulting from the twist of graphene layers is formed, as shown in Fig. 2.15(b). In this case, the top graphene layer is misoriented with respect to the underlying graphite and has a Moiré pattern just until its boundary. Different angles will result in the formation of different patterns, as described by (2.8). Experimentally this is demonstrated by STM images showing superpatterns of different periodicity in samples with different twist angles. For example, at rotation angle $\theta = 1.79°$ the superperiod is $L = 7.7$ nm. The sequence of four topographic maps in Fig. 2.15(c), (d), (e), (f) have approximately the same field of view and they correspond to rotation angles of 1.16°, 1.79°, 3.5°, 21°. The inset in Fig. 2.15(d) (for $\theta = 1.79°$) highlights the fact that the period of the atomic lattice of the graphene layer is much smaller than the Moiré pattern and can be visible on top of it. Typically the height observed in topography for the Moiré patterns is ≈0.1–0.3 nm.

2.3.1 Van Hove Singularities

In momentum space, the consequence of the twist between layers is the rotation of the corresponding Dirac cones with respect to each other as sketched in Fig. 2.16(a).

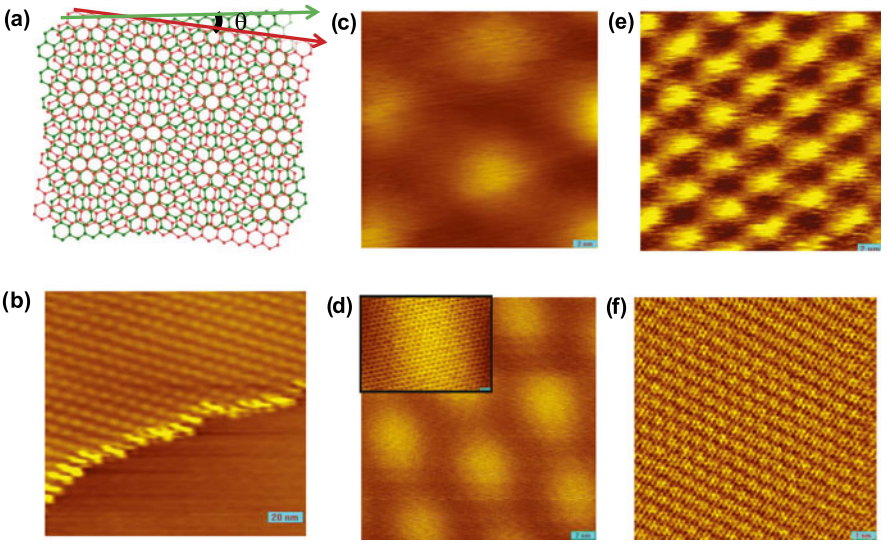

Fig. 2.15 (**a**) Illustration of an emerging Moiré pattern from the rotation of two graphene layers. (**b**) STM topography image showing a Moiré pattern and its border in HOPG. (**c**)–(**f**) STM images for Moiré patterns corresponding to angles 1.16°, 1.79°, 3.5°, 21°, respectively [53, 119]. Scale bar in (**c**)–(**e**) 2 nm, (**f**) 1 nm

The distance between the cones is given by:

$$\Delta K = \frac{4\pi}{3a} 2 \sin\left(\frac{\theta}{2}\right) \tag{2.9}$$

At the intersections of the two Dirac cones their bands will hybridize, resulting in the key feature of the band structure, the two saddle points in both the electron and hole sides [53, 113]. The theoretical calculation of the dispersion in the case of rotation angle $\theta = 1.79°$ is presented in Fig. 2.16(b).

In two dimensions, the saddle points in the electronic band structure lead to diverging density of states, also known as Van Hove singularities (VHS) [120]. It is important to note that in the absence of interlayer coupling, the Van Hove singularities will not appear. Corresponding to the saddle points in the dispersion shown in Fig. 2.16(b), the VHS in the DOS are presented in Fig. 2.16(c). The distance between the cones and implicitly between the saddle points is controlled by the rotation angle such that the distance in energy between the VHS depends monotonically on the angle θ. For the small angle regime, $2° < \theta < 5°$ the energy separation is: $\Delta E = \hbar v_F \Delta K - 2t^\theta$, where t^θ is the interlayer coupling. The rotation-induced VHSs are not restricted to the bilayer case. Qualitatively, if one layer is rotated with respect to a stack of layers underneath, the VHSs are still preserved.

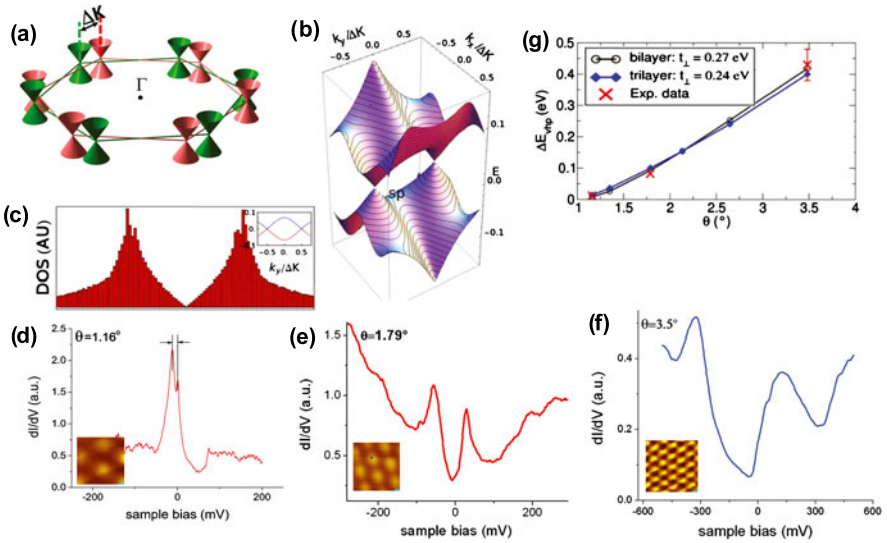

Fig. 2.16 (**a**) The relative rotation in momentum space of the Dirac cones corresponding to two twisted graphene layers. (**b**) The calculated energy dispersion for two graphene layers rotated by $\theta = 1.79°$. (**c**) The DOS corresponding to (**b**). The inset represents a cut through (**b**) along a line joining the two Dirac points. (**d**), (**e**), (**f**) STS for Moiré patterns corresponding to different angles, 1.16°, 1.79°, 3.5°. The *insets* are the corresponding real space superpatterns. (**g**) Theoretical curves and experimental data obtained for the separation of VHSs as a function of rotation angle [53, 119]

To explore the angle dependence of VHSs, Li et al. [53] studied graphene layers prepared by chemical vapor deposition [21] as well as rotated graphene layers on graphite. The experimental data obtained from STS for different angles, 1.16°, 1.79°, 3.5°, is presented in Fig. 2.16(d), (e), (f). The corresponding Moiré patterns are shown as insets. In each case, the measured spectra show two peaks, which are signatures of the VHS. The measured energy separation between the VHSs together with the theoretical curves are shown in Fig. 2.16(g) indicating a monotonic increase with rotation angle.

An interesting situation arises in the limit of small angles [53]. Figure 2.17(a) shows the measured topography of the Moiré pattern corresponding to $\theta = 1.16°$. The spectrum in this case is presented in Fig. 2.17(c) showing the two VHSs separated by a small energy $\Delta E \approx 12$ meV. It is known that when the Fermi energy is close to the VHS, interactions, however weak, are magnified by the enhanced density of states, resulting in instabilities, which can give rise to new phases of matter [121–123]. This is consistent with the observation that the STS maps in Fig. 2.17(b), taken at the energy of the singularity, suggest the formation of an ordered state such as charge a density wave. Such localization by Moiré patterns is also predicted by theoretical calculations [114].

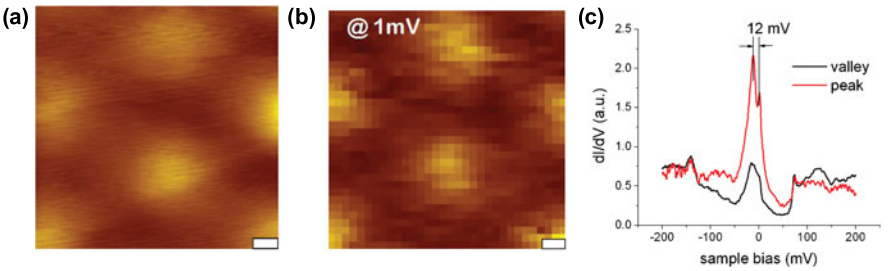

Fig. 2.17 (**a**) Topography of a Moiré pattern corresponding to a small rotation angle: $\theta = 1.16°$. The scale bar is 2 nm. (**b**) dI_t/dV_{Bias} map taken at the area in (**a**) at energy $E = 1$ meV. The scale bar is 2 nm. (**c**) STS on the peaks and valleys of the Moiré pattern in (**a**) [53]

2.3.2 *Renormalization of the Fermi Velocity*

While for sufficiently separated cones, the low energy electronic bands still describe Dirac fermions, the slope of the Dirac cone is influenced by the Van Hove singularities, leading to a renormalized Fermi velocity.

Theoretically the equation describing the velocity renormalization was derived to be [113]

$$\frac{v_F(\theta)}{v_F^0} = 1 - 9\left(\frac{t_\perp^\theta}{\hbar v_F^0 \Delta K}\right)^2 \tag{2.10}$$

where v_F^0 is the bare velocity, $v_F(\theta)$ is the renormalized value at an angle θ; the interlayer coupling is $t_\perp^\theta \approx 0.4 t_\perp$ and $t_\perp$ is the interlayer coupling in the Bernal stacked bilayer.

The curve corresponding to this relationship is plotted in Fig. 2.18(g). For large angles $\theta > 15°$ the renormalization effect is small, but the velocity is strongly suppressed for smaller angles.

In order to probe v_F, Luican et al. [119] measured the quantized LLs in a magnetic field and from their field and index dependence the velocity was extracted. For the large angle shown in Fig. 2.18(a) the measured LL spectrum is presented in Fig. 2.18(d). In this case of large angles, the low energy electronic properties are indistinguishable from those in a single layer and the measured $v_F = (1.10 \pm 0.01)10^6$ m/s.

In Fig. 2.18(b) the topography image shows two adjacent regions B and C. In region B, a Moiré pattern with period of 4.0 nm is resolved, while in region C, the pattern is not resolved, indicating an unrotated layer (or a much smaller period not resolved within the experimental resolution). In both regions STS in a magnetic field (Fig. 2.18(e)) shows LL sequences specific to massless Dirac fermions with different Fermi velocities: 0.87×10^6 m/s and 1.10×10^6 m/s for regions B and C, respectively.

At very small angles, $\theta < 2°$ such as the area in Fig. 2.18(c), the VHSs become so dominant that massless Dirac fermions no longer describe the electronic states (Fig. 2.18(f)). This regime is marked by a question mark in Fig. 2.18(g).

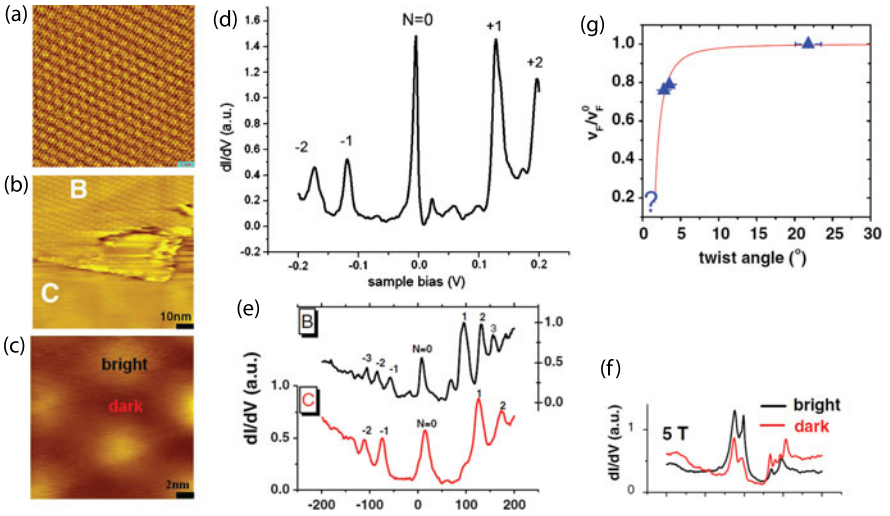

Fig. 2.18 (**a**) STM of a Moiré pattern due to rotation $\theta = 21°$. (**b**) STM of an area with two distinct regions: region B which has a Moiré pattern corresponding to rotation angle $\theta = 3.5°$ and region C where there is no superpattern. (**c**) STM for a Moiré pattern with $\theta = 1.16°$. (**d**) STS in a magnetic field showing the LL sequence measured in the area in (**a**). (**e**) STS in a magnetic field showing the spectrum for the area in (**b**) for regions B and C. (**f**) STS of the area in (**c**) for the dark and bright regions. (**g**) Plot of the theoretically predicted renormalization of the Fermi velocity together with the experimental values obtained from areas with different Moiré patterns [53, 119]

It is important to note that the mechanism for renormalization of the Fermi velocity due to the presence of VHS is different from the case of graphene flakes on graphite discussed previously. In the twisted layers the renormalization is a sensitive function of the misorientation angle. In contrast, the velocity renormalization observed in the case of graphene on graphite is due to electron-phonon interaction [34].

The results obtained on Moiré patterns on CVD graphene and graphite differ from the ones on epitaxially grown graphene on SiC [57, 124] which report a single layer graphene spectrum regardless of the twist angle. One clue towards understanding these results can be found in the unusual presence of a continuous atomic honeycomb structure across the entire Moiré superstructure in the case of epitaxial graphene. This is in contrast to Moiré patterns generated by two rotated layers where one sees a correlation between the Moiré pattern and the atomic structure which changes from triangular, to honeycomb, or in between the two, depending on the local stacking within the superpattern [53, 112].

If in addition to the twist of the top most layer, a Moiré pattern is present under the first layer (layer 2 rotated with respect to layer 3), it is expected that a complex superstructure involving several Moiré patterns will appear. This is the case in some of the experiments reported on epitaxially grown graphene on SiC [125]. In the case of the CVD graphene samples or graphite such multiple Moiré patterns were not observed. Therefore, the previously discussed features (VHS, reduction in Fermi

velocity) are consequences of twisting only the top most layer with respect to the underlying single layer graphene or Bernal-stacked multilayer graphene.

2.4 Conclusions

In this chapter we presented a brief review of experimental results obtained by scanning tunneling microscopy and spectroscopy of graphene systems with various degree of disorder.

When the charge carriers are minimally affected by potential fluctuations in the substrate, as is the case for graphene flakes on the surface of graphite, one can access the intrinsic properties of the massless Dirac fermions in graphene. STS measurements show that the charge carriers in such flakes exhibit the hallmarks of massless Dirac fermions: the density of states is V-shaped and vanishes at the Dirac point and in the presence of a magnetic field the LL sequence contains a level at zero energy and follows the predicted square root dependence on field and level index. The quality of such samples allows access to physics beyond the single particle picture and signatures of electron-phonon and electron-electron interactions can be studied.

Tuning the charge carrier concentration in graphene requires placing it on an insulating substrate such as SiO_2. In this case, graphene conforms to the rough surface of the oxide and the electrons are affected by the random potential introduced by the substrate. For this system, in the presence of a magnetic field, the Landau levels are broadened by disorder. The charge carrier density dependence of the LL spectrum shows pinning of the Fermi level at the respective LL which is filled. In such measurements that can probe the shape of the Dirac cone while tuning the carrier concentration, the velocity is found to increase upon reaching the Dirac point suggesting the onset of many body interactions.

Twisting graphene layers away from the equilibrium Bernal stacking leads to novel electronic properties. In the topographical images one can identify twisted graphene layers by the appearance of Moiré patterns dependent on the rotation angle. The twist gives rise to two Van Hove singularities which flank the Dirac point symmetrically on the electron and hole sides and are centered at an energy that increases with the angle of rotation. The Fermi velocity of the charge carriers in the twisted layers is indistinguishable from single layer graphene for angles close to 30°, but v_F is dramatically reduced at very small angles.

Acknowledgements We thank G. Li, I. Skachko and A.M.B. Goncalves for help with data and figures. Funding was provided by NSF-DMR-090671, DOE DE-FG02-99ER45742, and the Alcatel-Lucent Foundation.

References

1. G. Binnig, H. Rohrer, C. Gerber, E. Weibel, Surface studies by scanning tunneling microscopy. Phys. Rev. Lett. **49**(1), 57–61 (1982)

2. J. Tersoff, D.R. Hamann, Theory of the scanning tunneling microscope. Phys. Rev. B **31**(2), 805–813 (1985)
3. J. Bardeen, Tunnelling from a many-particle point of view. Phys. Rev. Lett. **6**(2), 57–59 (1961)
4. G. Li, A. Luican, E.Y. Andrei, Electronic states on the surface of graphite. Physica B, Condens. Matter **404**(18), 2673–2677 (2009)
5. K.S. Novoselov, D. Jiang, F. Schedin, T.J. Booth, V.V. Khotkevich, S.V. Morozov, A.K. Geim, Two-dimensional atomic crystals. Proc. Natl. Acad. Sci. USA **102**(30), 10451 (2005)
6. J. Martin, N. Akerman, G. Ulbricht, T. Lohmann, J.H. Smet, K. Von Klitzing, A. Yacoby, Observation of electron–hole puddles in graphene using a scanning single-electron transistor. Nat. Phys. **4**(2), 144–148 (2007)
7. Y. Zhang, V.W. Brar, C. Girit, A. Zettl, M.F. Crommie, Origin of spatial charge inhomogeneity in graphene. Nat. Phys. **5**(10), 722–726 (2009)
8. J.H. Chen, C. Jang, S. Adam, M.S. Fuhrer, E.D. Williams, M. Ishigami, Charged impurity scattering in graphene. Nat. Phys. **4**(5), 377–381 (2008)
9. A. Luican, G. Li, E.Y. Andrei, Quantized Landau level spectrum and its density dependence in graphene. Phys. Rev. B **83**, 041405 (2011)
10. C.R. Dean, A.F. Young, I. Meric, C. Lee, L. Wang, S. Sorgenfrei, K. Watanabe, T. Taniguchi, P. Kim, K.L. Shepard, J. Hone, Boron nitride substrates for high-quality graphene electronics. Nat. Nanotechnol. **5**(10), 722–726 (2010)
11. C.R. Dean, A.F. Young, P. Cadden-Zimansky, L. Wang, H. Ren, K. Watanabe, T. Taniguchi, P. Kim, J. Hone, K.L. Shepard, Multicomponent fractional quantum Hall effect in graphene. Nat. Phys. **7**(9), 693–696 (2011)
12. C.H. Lui, L. Liu, K.F. Mak, G.W. Flynn, T.F. Heinz, Ultraflat graphene. Nature **462**(7271), 339–341 (2009)
13. V. Geringer, M. Liebmann, T. Echtermeyer, S. Runte, M. Schmidt, R. Rückamp, M.C. Lemme, M. Morgenstern, Intrinsic and extrinsic corrugation of monolayer graphene deposited on SiO_2. Phys. Rev. Lett. **102**(7), 076102 (2009)
14. A. Luican, G. Li, E.Y. Andrei, Scanning tunneling microscopy and spectroscopy of graphene layers on graphite. Solid State Commun. **149**(27–28), 1151–1156 (2009)
15. P. Neugebauer, M. Orlita, C. Faugeras, A.L. Barra, M. Potemski, How perfect can graphene be? Phys. Rev. Lett. **103**(13), 136403 (2009)
16. C. Berger, Z. Song, T. Li, X. Li, A.Y. Ogbazghi, R. Feng, Z. Dai, A.N. Marchenkov, E.H. Conrad, N. Phillip, et al., Ultrathin epitaxial graphite: 2D electron gas properties and a route toward graphene-based nanoelectronics. J. Phys. Chem. B **108**(52), 19912–19916 (2004)
17. A.J. Van Bommel, J.E. Crombeen, A. Van Tooren, LEED and Auger electron observations of the SiC(0001) surface. Surf. Sci. **48**(2), 463–472 (1975)
18. I. Forbeaux, J.-M. Themlin, J.-M. Debever, Heteroepitaxial graphite on 6h-SiC(0001): interface formation through conduction-band electronic structure. Phys. Rev. B **58**, 16396–16406 (1998)
19. K.S. Kim, Y. Zhao, H. Jang, S.Y. Lee, J.M. Kim, K.S. Kim, J.H. Ahn, P. Kim, J.Y. Choi, B.H. Hong, Large-scale pattern growth of graphene films for stretchable transparent electrodes. Nature **457**(7230), 706–710 (2009)
20. X. Li, W. Cai, J. An, S. Kim, J. Nah, D. Yang, R. Piner, A. Velamakanni, I. Jung, E. Tutuc, S.K. Banerjee, L. Colombo, R.S. Ruoff, Large-area synthesis of high-quality and uniform graphene films on copper foils. Science **324**(5932), 1312–1314 (2009)
21. A. Reina, X. Jia, J. Ho, D. Nezich, H. Son, V. Bulovic, M.S. Dresselhaus, J. Kong, Large area, few-layer graphene films on arbitrary substrates by chemical vapor deposition. Nano Lett. **9**(1), 30–35 (2008)
22. Q. Yu, L.A. Jauregui, W. Wu, R. Colby, J. Tian, Z. Su, H. Cao, Z. Liu, D. Pandey, D. Wei, et al., Control and characterization of individual grains and grain boundaries in graphene grown by chemical vapour deposition. Nat. Mater. **10**(6), 443–449 (2011)
23. S. Marchini, S. Günther, J. Wintterlin, Scanning tunneling microscopy of graphene on Ru(0001). Phys. Rev. B **76**, 075429 (2007)

24. P.W. Sutter, J.I. Flege, E.A. Sutter, Epitaxial graphene on ruthenium. Nat. Mater. **7**(5), 406–411 (2008)
25. A.T. N'Diaye, S. Bleikamp, P.J. Feibelman, T. Michely, Two-dimensional Ir cluster lattice on a graphene Moiré on Ir(111). Phys. Rev. Lett. **97**, 215501 (2006)
26. E. Loginova, S. Nie, K. Thürmer, N.C. Bartelt, K.F. McCarty, Defects of graphene on Ir(111): rotational domains and ridges. Phys. Rev. B **80**, 085430 (2009)
27. P. Sutter, J.T. Sadowski, E. Sutter, Graphene on Pt(111): growth and substrate interaction. Phys. Rev. B **80**, 245411 (2009)
28. A. Fasolino, J.H. Los, M.I. Katsnelson, Intrinsic ripples in graphene. Nat. Mater. **6**(11), 858–861 (2007)
29. N.D. Mermin, H. Wagner, Absence of ferromagnetism or antiferromagnetism in one-or two-dimensional isotropic Heisenberg models. Phys. Rev. Lett. **17**(22), 1133–1136 (1966)
30. M.I. Katsnelson, A.K. Geim, Electron scattering on microscopic corrugations in graphene. Philos. Trans. R. Soc. A, Math. Phys. Eng. Sci. **366**(1863), 195 (2008)
31. J.C. Meyer, A.K. Geim, M.I. Katsnelson, K.S. Novoselov, T.J. Booth, S. Roth, The structure of suspended graphene sheets. Nature **446**(7131), 60–63 (2007)
32. J. Xue, J. Sanchez-Yamagishi, D. Bulmash, P. Jacquod, A. Deshpande, K. Watanabe, T. Taniguchi, P. Jarillo-Herrero, B.J. LeRoy, Scanning tunnelling microscopy and spectroscopy of ultra-flat graphene on hexagonal boron nitride. Nat. Mater. **10**(4), 282–285 (2011)
33. R. Decker, Y. Wang, V.W. Brar, W. Regan, H.Z. Tsai, Q. Wu, W. Gannett, A. Zettl, M.F. Crommie, Local electronic properties of graphene on a bn substrate via scanning tunneling microscopy. Nano Lett. **11**(6), 2291–2295 (2011)
34. G. Li, A. Luican, E.Y. Andrei, Scanning tunneling spectroscopy of graphene on graphite. Phys. Rev. Lett. **102**(17), 176804 (2009)
35. A. Deshpande, W. Bao, F. Miao, C.N. Lau, B.J. LeRoy, Spatially resolved spectroscopy of monolayer graphene on SiO_2. Phys. Rev. B **79**(20), 205411 (2009)
36. S. Jung, G.M. Rutter, N.N. Klimov, D.B. Newell, I. Calizo, A.R. Hight-Walker, N.B. Zhitenev, J.A. Stroscio, Evolution of microscopic localization in graphene in a magnetic field from scattering resonances to quantum dots. Nat. Phys. **7**(3), 245–251 (2011)
37. E. Stolyarova, K.T. Rim, S. Ryu, J. Maultzsch, P. Kim, L.E. Brus, T.F. Heinz, M.S. Hybertsen, G.W. Flynn, High-resolution scanning tunneling microscopy imaging of mesoscopic graphene sheets on an insulating surface. Proc. Natl. Acad. Sci. USA **104**(22), 9209 (2007)
38. M. Ishigami, J.H. Chen, W.G. Cullen, M.S. Fuhrer, E.D. Williams, Atomic structure of graphene on SiO_2. Nano Lett. **7**(6), 1643–1648 (2007)
39. A.H. Castro Neto, F. Guinea, N.M.R. Peres, K.S. Novoselov, A.K. Geim, The electronic properties of graphene. Rev. Mod. Phys. **81**(1), 109–162 (2009)
40. K.S. Novoselov, A.K. Geim, S.V. Morozov, D. Jiang, Y. Zhang, S.V. Dubonos, I.V. Grigorieva, A.A. Firsov, Electric field effect in atomically thin carbon films. Science **306**(5696), 666–669 (2004)
41. V. Geringer, D. Subramaniam, A.K. Michel, B. Szafranek, D. Schall, A. Georgi, T. Mashoff, D. Neumaier, M. Liebmann, M. Morgenstern, Electrical transport and low-temperature scanning tunneling microscopy of microsoldered graphene. Appl. Phys. Lett. **96**, 082114 (2010)
42. Y. Zhang, V.W. Brar, F. Wang, C. Girit, Y. Yayon, M. Panlasigui, A. Zettl, M.F. Crommie, Giant phonon-induced conductance in scanning tunnelling spectroscopy of gate-tunable graphene. Nat. Phys. **4**(8), 627–630 (2008)
43. M.L. Teague, A.P. Lai, J. Velasco, C.R. Hughes, A.D. Beyer, M.W. Bockrath, C.N. Lau, N.C. Yeh, Evidence for strain-induced local conductance modulations in single-layer graphene on SiO_2. Nano Lett. **9**(7), 2542–2546 (2009)
44. L. Zhao, R. He, K.T. Rim, T. Schiros, K.S. Kim, H. Zhou, C. Gutiérrez, S.P. Chockalingam, C.J. Arguello, L. Palova, D. Nordlund, M.S. Hybertsen, D.R. Reichman, T.F. Heinz, P. Kim, A. Pinczuk, G.W. Flynn, A.N. Pasupathy, Visualizing individual nitrogen dopants in monolayer graphene. Science **333**(6045), 999–1003 (2011)
45. G.M. Rutter, J.N. Crain, N.P. Guisinger, T. Li, P.N. First, J.A. Stroscio, Scattering and interference in epitaxial graphene. Science **317**(5835), 219–222 (2007)

46. I. Brihuega, P. Mallet, C. Bena, S. Bose, C. Michaelis, L. Vitali, F. Varchon, L. Magaud, K. Kern, J.Y. Veuillen, Quasiparticle chirality in epitaxial graphene probed at the nanometer scale. Phys. Rev. Lett. **101**(20), 206802 (2008)
47. E.Y. Andrei, *Two-Dimensional Electron Systems on Helium and Other Cryogenic Substrates*, vol. 19 (Kluwer Academic, Dordrecht, 1997)
48. J.H. Davies, *The Physics of Low-Dimensional Semiconductors: An Introduction* (Cambridge Univ. Press, Cambridge, 1998)
49. J.C. Slonczewski, P.R. Weiss, Band structure of graphite. Phys. Rev. **109**, 272–279 (1958)
50. G.W. Semenoff, Condensed-matter simulation of a three-dimensional anomaly. Phys. Rev. Lett. **53**(26), 2449–2452 (1984)
51. R. Rammal, Landau level spectrum of Bloch electrons in a honeycomb lattice. J. Phys. **46**(8), 1345–1354 (1985)
52. I. Rabi, Das freie Elektron im homogenen Magnetfeld nach der Diracschen Theorie. Z. Phys. A, Hadrons Nucl. **49**(7), 507–511 (1928)
53. G. Li, E.Y. Andrei, Observation of Landau levels of Dirac fermions in graphite. Nat. Phys. **3**(9), 623–627 (2007)
54. T. Matsui, H. Kambara, Y. Niimi, K. Tagami, M. Tsukada, H. Fukuyama, STS observations of Landau levels at graphite surfaces. Phys. Rev. Lett. **94**, 226403 (2005)
55. K. Hashimoto, C. Sohrmann, J. Wiebe, T. Inaoka, F. Meier, Y. Hirayama, R.A. Römer, R. Wiesendanger, M. Morgenstern, Quantum Hall transition in real space: from localized to extended states. Phys. Rev. Lett. **101**, 256802 (2008)
56. J.M. Pereira Jr, F.M. Peeters, P. Vasilopoulos, Landau levels and oscillator strength in a biased bilayer of graphene. Phys. Rev. B **76**(11), 115419 (2007)
57. D.L. Miller, K.D. Kubista, G.M. Rutter, M. Ruan, W.A. De Heer, et al., Observing the quantization of zero mass carriers in graphene. Science **324**(5929), 924 (2009)
58. N. Levy, S.A. Burke, K.L. Meaker, M. Panlasigui, A. Zettl, F. Guinea, A.H.C. Neto, M.F. Crommie, Strain-induced pseudomagnetic fields greater than 300 tesla in graphene nanobubbles. Science **329**(5991), 544–547 (2010)
59. P. Cheng, C. Song, T. Zhang, Y. Zhang, Y. Wang, J.F. Jia, J. Wang, Y. Wang, B.F. Zhu, X. Chen, et al., Landau quantization of topological surface states in Bi_2Se_3. Phys. Rev. Lett. **105**(7), 76801 (2010)
60. T. Hanaguri, K. Igarashi, M. Kawamura, H. Takagi, T. Sasagawa, Momentum-resolved Landau-level spectroscopy of Dirac surface state in Bi_2Se_3. Phys. Rev. B **82**, 081305 (2010)
61. Z. Jiang, E.A. Henriksen, L.C. Tung, Y.J. Wang, M.E. Schwartz, M.Y. Han, P. Kim, H.L. Stormer, Infrared spectroscopy of Landau levels of graphene. Phys. Rev. Lett. **98**(19), 197403 (2007)
62. R.S. Deacon, K.-C. Chuang, R.J. Nicholas, K.S. Novoselov, A.K. Geim, Cyclotron resonance study of the electron and hole velocity in graphene monolayers. Phys. Rev. B **76**, 081406 (2007)
63. M. Sadowski, G. Martinez, M. Potemski, C. Berger, W. De Heer, Landau level spectroscopy of ultrathin graphite layers. Phys. Rev. Lett. **97**(26), 266405 (2006)
64. J. Martin, N. Akerman, G. Ulbricht, T. Lohmann, K. Von Klitzing, J. Smet, A. Yacoby, The nature of localization in graphene under quantum Hall conditions. Nat. Phys. **5**(9), 669–674 (2009)
65. L.A. Ponomarenko, R. Yang, R.V. Gorbachev, P. Blake, A.S. Mayorov, K.S. Novoselov, M.I. Katsnelson, A.K. Geim, Density of states and zero Landau level probed through capacitance of graphene. Phys. Rev. Lett. **105**(13), 136801 (2010)
66. C.-H. Park, F. Giustino, M.L. Cohen, S.G. Louie, Velocity renormalization and carrier lifetime in graphene from the electron-phonon interaction. Phys. Rev. Lett. **99**, 086804 (2007)
67. C.H. Park, F. Giustino, M.L. Cohen, S.G. Louie, Electron-phonon interactions in graphene, bilayer graphene, and graphite. Nano Lett. **8**(12), 4229–4233 (2008)
68. J.-A. Yan, W.Y. Ruan, M.Y. Chou, Electron-phonon interactions for optical-phonon modes in few-layer graphene: first-principles calculations. Phys. Rev. B **79**, 115443 (2009)

69. J. Gonzalez, F. Guinea, M. Vozmediano, Marginal-Fermi-liquid behavior from two-dimensional Coulomb interaction. Phys. Rev. B **59**(4), 2474–2477 (1999)
70. X. Du, I. Skachko, F. Duerr, A. Luican, E.Y. Andrei, Fractional quantum Hall effect and insulating phase of Dirac electrons in graphene. Nature **462**(7270), 192–195 (2009)
71. K.I. Bolotin, F. Ghahari, M.D. Shulman, H.L. Stormer, P. Kim, Observation of the fractional quantum Hall effect in graphene. Nature **462**(7270), 196–199 (2009)
72. Y.J. Song, A.F. Otte, Y. Kuk, Y. Hu, D.B. Torrance, et al., High-resolution tunnelling spectroscopy of a graphene quartet. Nature **467**(7312), 185–189 (2010)
73. X. Du, I. Skachko, A. Barker, E.Y. Andrei, Approaching ballistic transport in suspended graphene. Nat. Nanotechnol. **3**(8), 491–495 (2008)
74. K.I. Bolotin, K.J. Sikes, Z. Jiang, M. Klima, G. Fudenberg, J. Hone, P. Kim, H.L. Stormer, Ultrahigh electron mobility in suspended graphene. Solid State Commun. **146**(9–10), 351–355 (2008)
75. P. Balk, The Si-SiO_2 system, in *Materials Science Monographs*, vol. 32 (1988)
76. Y.B. Park, S.W. Rhee, Microstructure and interfacial states of silicon dioxide film grown by low temperature remote plasma enhanced chemical vapor deposition. J. Appl. Phys. **86**, 1346 (1999)
77. Y.B. Park, S.W. Rhee, Effects of chlorine addition on the silicon dioxide properties deposited with remote plasma enhanced chemical vapor deposition at low temperatures. Appl. Phys. Lett. **66**, 3477 (1995)
78. J.C. Alonso, A. Ortiz, C. Falcony, Low temperature SiO_2 films deposited by plasma enhanced techniques. Vacuum **43**(8), 843–847 (1992)
79. T. Ando, Y. Uemura, Theory of quantum transport in a two-dimensional electron system under magnetic fields. I. Characteristics of level broadening and transport under strong fields. J. Phys. Soc. Jpn. **36**, 959 (1974)
80. N.M.R. Peres, F. Guinea, A.H. Castro Neto, Electronic properties of disordered two-dimensional carbon. Phys. Rev. B **73**, 125411 (2006)
81. W. Zhu, Q.W. Shi, X.R. Wang, J. Chen, J.L. Yang, J.G. Hou, Shape of disorder-broadened Landau subbands in graphene. Phys. Rev. Lett. **102**, 056803 (2009)
82. O.E. Dial, R.C. Ashoori, L.N. Pfeiffer, K.W. West, High-resolution spectroscopy of two-dimensional electron systems. Nature **448**(7150), 176–179 (2007)
83. M. Polini, R. Asgari, Y. Barlas, T. Pereg-Barnea, A.H. MacDonald, Graphene: a pseudochiral Fermi liquid. Solid State Commun. **143**(1–2), 58–62 (2007)
84. D.C. Elias, R.V. Gorbachev, A.S. Mayorov, S.V. Morozov, A.A. Zukov, P. Blake, L.A. Ponomarenko, I.V. Grigorieva, K.S. Novolselov, A.K. Geim, F. Guinea, Dirac cones reshaped by interaction effects in suspended graphene. Nat. Phys. **7**, 701–704 (2011)
85. A. Luican, G. Li, E.Y. Andrei et al., Visualizing the effect of isolated Coulomb impurities in the quantum Hall regime in graphene. arXiv:1311.0064
86. K. von Klitzing, G. Dorda, M. Pepper, New method for high-accuracy determination of the fine-structure constant based on quantized Hall resistance. Phys. Rev. Lett. **45**, 494–497 (1980)
87. D.L. Miller, K.D. Kubista, G.M. Rutter, M. Ruan, W.A. de Heer, M. Kindermann et al., Real-space mapping of magnetically quantized graphene states. Nat. Phys. **6**(10), 811–817 (2010)
88. G. Li, A. Luican, E.Y. Andrei, Self-navigation of a scanning tunneling microscope tip toward a micron-sized graphene sample. Rev. Sci. Instrum. **82**, 073701 (2011)
89. G. Li, A. Luican-Mayer, D. Abanin, L. Levitov, E.Y. Andrei, Evolution of Landau levels into edge states in graphene. Nat. Commun. **4** (2013)
90. L. Yang, C.-H. Park, Y.-W. Son, M.L. Cohen, S.G. Louie, Quasiparticle energies and band gaps in graphene nanoribbons. Phys. Rev. Lett. **99**, 186801 (2007)
91. Y.W. Son, M.L. Cohen, S.G. Louie, Energy gaps in graphene nanoribbons. Phys. Rev. Lett. **97**(21), 216803 (2006)
92. Ç.Ö. Girit, J.C. Meyer, R. Erni, M.D. Rossell, C. Kisielowski, L. Yang, C.H. Park, M.F. Crommie, M.L. Cohen, S.G. Louie et al., Graphene at the edge: stability and dynamics.

Science **323**(5922), 1705 (2009)
93. M. Fujita, K. Wakabayashi, K. Nakada, K. Kusakabe, Peculiar localized state at zigzag graphite edge. J. Phys. Soc. Jpn. **65**(7), 1920–1923 (1996)
94. Y. Niimi, T. Matsui, H. Kambara, K. Tagami, M. Tsukada, H. Fukuyama, Scanning tunneling microscopy and spectroscopy of the electronic local density of states of graphite surfaces near monoatomic step edges. Phys. Rev. B **73**(8), 085421 (2006)
95. C. Tao, L. Jiao, O.V. Yazyev, Y.C. Chen, J. Feng, X. Zhang, R.B. Capaz, J.M. Tour, A. Zettl, S.G. Louie et al., Spatially resolving edge states of chiral graphene nanoribbons. Nat. Phys. **7**, 616–620 (2011)
96. D.A. Abanin, P.A. Lee, L.S. Levitov, Charge and spin transport at the quantum Hall edge of graphene. Solid State Commun. **143**(1–2), 77–85 (2007)
97. D.A. Abanin, P.A. Lee, L.S. Levitov, Spin-filtered edge states and quantum Hall effect in graphene. Phys. Rev. Lett. **96**(17), 176803 (2006)
98. M. Arikawa, Y. Hatsugai, H. Aoki, Edge states in graphene in magnetic fields: a specialty of the edge mode embedded in the $n = 0$ Landau band. Phys. Rev. B **78**, 205401 (2008)
99. V.M. Pereira, A.H. Castro Neto, Strain engineering of graphene electronic structure. Phys. Rev. Lett. **103**(4), 46801 (2009)
100. F. Guinea, M.I. Katsnelson, A.K. Geim, Energy gaps and a zero-field quantum Hall effect in graphene by strain engineering. Nat. Phys. **6**(1), 30–33 (2009)
101. E. McCann, Asymmetry gap in the electronic band structure of bilayer graphene. Phys. Rev. B **74**, 161403 (2006)
102. F. Guinea, A.H. Castro Neto, N.M.R. Peres, Electronic states and Landau levels in graphene stacks. Phys. Rev. B **73**, 245426 (2006)
103. Y. Zhang, T.T. Tang, C. Girit, Z. Hao, M.C. Martin, A. Zettl, M.F. Crommie, Y.R. Shen, F. Wang, Direct observation of a widely tunable bandgap in bilayer graphene. Nature **459**(7248), 820–823 (2009)
104. R.T. Weitz, M.T. Allen, B.E. Feldman, J. Martin, A. Yacoby, Broken-symmetry states in doubly gated suspended bilayer graphene. Science **330**(6005), 812–816 (2010)
105. A.S. Mayorov, D.C. Elias, M. Mucha-Kruczynski, R.V. Gorbachev, T. Tudorovskiy, A. Zhukov, S.V. Morozov, M.I. Katsnelson, V.I. Falko, A.K. Geim, K.S. Novoselov, Interaction-driven spectrum reconstruction in bilayer graphene. Science **333**(6044), 860–863 (2011)
106. B.E. Feldman, J. Martin, A. Yacoby, Broken-symmetry states and divergent resistance in suspended bilayer graphene. Nat. Phys. **5**(12), 889–893 (2009)
107. A. Deshpande, W. Bao, Z. Zhao, C.N. Lau, B. LeRoy, Mapping the Dirac point in gated bilayer graphene. Appl. Phys. Lett. **95**, 243502 (2009)
108. G.M. Rutter, S. Jung, N.N. Klimov, D.B. Newell, N.B. Zhitenev, J.A. Stroscio, Microscopic polarization in bilayer graphene. Nat. Phys. **7**, 649–655 (2011)
109. Z.Y. Rong, P. Kuiper, Electronic effects in scanning tunneling microscopy: Moiré pattern on a graphite surface. Phys. Rev. B **48**, 17427–17431 (1993)
110. J. Xhie, K. Sattler, M. Ge, N. Venkateswaran, Giant and supergiant lattices on graphite. Phys. Rev. B **47**, 15835–15841 (1993)
111. K. Kobayashi, Moiré pattern in scanning tunneling microscopy of monolayer graphite. Phys. Rev. B **50**, 4749–4755 (1994)
112. W.T. Pong, C. Durkan, A review and outlook for an anomaly of scanning tunnelling microscopy (STM): superlattices on graphite. J. Phys. D, Appl. Phys. **38**, R329 (2005)
113. J.M.B. Lopes dos Santos, N.M.R. Peres, A.H. Castro Neto, Graphene bilayer with a twist: electronic structure. Phys. Rev. Lett. **99**, 256802 (2007)
114. G. Trambly de Laissardie‘re, D. Mayou, L. Magaud, Localization of Dirac electrons in rotated graphene bilayers. Nano Lett. **10**(3), 804–808 (2010)
115. E.J. Mele, Commensuration and interlayer coherence in twisted bilayer graphene. Phys. Rev. B **81**, 161405 (2010)
116. R. Bistritzer, A.H. MacDonald, Moiré bands in twisted double-layer graphene. Proc. Natl. Acad. Sci. USA **108**(30), 12233–12237 (2011)

117. S. Shallcross, S. Sharma, E. Kandelaki, O.A. Pankratov, Electronic structure of turbostratic graphene. Phys. Rev. B **81**, 165105 (2010)
118. S. Shallcross, S. Sharma, O.A. Pankratov, Quantum interference at the twist boundary in graphene. Phys. Rev. Lett. **101**, 056803 (2008)
119. A. Luican, G. Li, A. Reina, J. Kong, R.R. Nair, K.S. Novoselov, A.K. Geim, E.Y. Andrei, Single-layer behavior and its breakdown in twisted graphene layers. Phys. Rev. Lett. **106**, 126802 (2011)
120. L. Van Hove, The occurrence of singularities in the elastic frequency distribution of a crystal. Phys. Rev. **89**(6), 1189 (1953)
121. M. Fleck, A.M. Oleś, L. Hedin, Magnetic phases near the Van Hove singularity in s- and d-band Hubbard models. Phys. Rev. B **56**, 3159–3166 (1997)
122. J. González, Kohn-Luttinger superconductivity in graphene. Phys. Rev. B **78**, 205431 (2008)
123. T.M. Rice, G.K. Scott, New mechanism for a charge-density-wave instability. Phys. Rev. Lett. **35**, 120–123 (1975)
124. J. Hicks, M. Sprinkle, K. Shepperd, F. Wang, A. Tejeda, A. Taleb-Ibrahimi, F. Bertran, P. Le Fèvre, W.A. de Heer, C. Berger, E.H. Conrad, Symmetry breaking in commensurate graphene rotational stacking: comparison of theory and experiment. Phys. Rev. B **83**, 205403 (2011)
125. D.L. Miller, K.D. Kubista, G.M. Rutter, M. Ruan, W.A. de Heer, P.N. First, J.A. Stroscio, Structural analysis of multilayer graphene via atomic Moiré interferometry. Phys. Rev. B **81**, 125427 (2010)

Chapter 3
Electron and Phonon Transport in Graphene in and out of the Bulk

Jean-Paul Issi, Paulo T. Araujo, and Mildred S. Dresselhaus

Abstract Carbon atoms have the unique capability of associating with each other in different ways at the macro- and nanoscopic scales to form various architectures, some of them being unique. Following the discovery of fullerenes, these last twenty-five years witnessed the discovery of some new forms of carbon atom associations leading to a large diversity of nanocarbons with fascinating properties. As regards bulk carbons, the decade preceding the discovery of fullerenes paved the way for finding some physical properties which were found later to be displayed in these new nano entities. This mainly concerns the semiclassical and, more particularly, the quantum aspects of two-dimensional (2D) electronic transport and the behavior of phonons in low-dimensional materials. These effects are discussed here in relation to the electrical and thermal conductivities of various nano-carbon based materials. This chapter also reflects the obvious similarities and differences observed in the transport properties of an isolated single layer graphene out of the bulk (SLG), or a few layers of graphene out of the bulk (FLG), supported or suspended, and those of a single (stage-1) or more (stage-n, where $n = 2, 3, \ldots$) of these carbon layer planes sandwiched between planes formed by other chemical species, as is the case for macroscopic graphite intercalation compounds (GICs), and more particularly quasi

J.-P. Issi
CERMIN, Université Catholique de Louvain, 1348 Louvain-la-Neuve, Belgium
e-mail: jean-paul.issi@uclouvain.be

P.T. Araujo · M.S. Dresselhaus
Department of Electrical Engineering and Computer Sciences, Massachusetts Institute of Technology, Cambridge, MA 02139-4307, USA

P.T. Araujo
Department of Physics and Astronomy, University of Alabama, Tuscaloosa, AL 35487-0324, USA
e-mail: paulo.t.araujo@ua.edu

M.S. Dresselhaus (✉)
Department of Physics, Massachusetts Institute of Technology, Cambridge, MA 02139-4307, USA
e-mail: millie@mgm.mit.edu

H. Aoki, M.S. Dresselhaus (eds.), *Physics of Graphene*, NanoScience and Technology,
DOI 10.1007/978-3-319-02633-6_3,

2D acceptor compounds (GACs), or even, in some cases, pristine highly oriented pyrolytic graphite (HOPG).

3.1 General Introduction

Should one be asked to synthesize bulk graphite, one might start to pile up graphene sheets and, should he be infinitely patient, he would eventually end up with the required graphite material. This bottom up approach could be envisaged now that graphene sheets have been successfully isolated as either single layer graphene (SLG) or as few layers graphene (FLG) [1]. We know that a related synthetic sp^2 carbon material already exists in a bulk form,[1] and is known as highly oriented pyrolytic graphite (HOPG), and some properties of the isolated graphene sheets are already observable in this form of carbon and such properties are even more pronounced in its graphite intercalation compounds (GICs). As stated above, we shall hereafter call these isolated sheets, whether supported or suspended, the graphenes out of the bulk. They may occur as SLG or FLG according to the number of sheets, to differentiate them from the more traditional forms of graphene layers existing in a bulk material, which we shall identify as graphene in the bulk[2] [2], including HOPG or GICs.

3.1.1 Graphenes

Graphene is an infinite 2-D layer which consists of sp^2 hybridized carbon atoms, arranged in a hexagonal lattice. Each carbon atom in the layer is connected to three others, making an angle of 120 degrees with each other and a bond length of 1.42 Å.

Graphite is a highly anisotropic 3D crystal consisting of stacked graphene layers. Depending on the stacking of the graphene layers, these crystals could either have hexagonal (ABABAB…) or rhombohedral (ABCABC…) stacking. Graphite crystals can be either found naturally or they can be artificially synthesized at high pressure and temperature in the form of highly oriented pyrolytic graphite (HOPG) [3].

Graphite intercalation compounds (GICs) result from the insertion of atomic or molecular layers of a different chemical species, the intercalate, between layers of a graphite host material. The intercalation compounds are highly anisotropic 3D layered structures where, as is the case for the host graphite, the intraplanar binding forces are much stronger than the interplanar forces. Graphite intercalation compounds are identified by a stage index n denoting the number of graphene layers

[1] Note that HOPG is not a single crystal but instead could be considered as a 2D polycrystalline material with a crystallite size of about 10 micrometers when heat treated above 3,000 °C.

[2] One should note that the term "graphene" was already used in 1987 by Mouras et al. (Ref. [2]) to describe the single graphite sheets, which together with the intercalate species, constitute the graphite intercalation compounds (GICs).

between adjacent intercalate layers. The difference between the classical works discussed in the 1970 to 1985 timeframe and the work produced presently is that current interest is focused now on the intercalation of FLG and not bulk graphite. There are two important differences in the behavior of graphene in and out of the bulk:

(1) Pristine graphites cannot be considered as 2D materials, but rather as highly anisotropic 3D systems, though in many cases they might roughly be considered as almost 2D for some semi-quantitative analyses relative to a given property in a given temperature range. Besides, up to now, the highest quality HOPG samples available have limited in-plane coherence lengths, less than 15 μm (Fig. 3.1), and contain a significant density of point defects, and
(2) graphite acceptor compounds (GACs) are quasi-2D systems [4] with massless Dirac Fermions for stage-1 GACs, and the results of electronic transport measurements have for many years been interpreted coherently along these lines [5]. However, the presence of large-scale defects in GICs, which are inherent to the intercalation process—the so-called Daumas-Hérold domains [6]—as well as additional point defects, did not allow the observation of phenomena, such as ballistic transport, which is found in SLG and FLG [7, 8] but not in GICs.

In order to illustrate the limitations encountered in studying the transport properties of bulk pristine graphite, we present in Fig. 3.1 the room temperature resistivity of experimental graphitized carbon fibers of different structural perfection versus the in-plane coherence length, L_a, as determined by X-ray diffraction [9]. It may be seen that the electrical resistivity decreases with increasing structural perfection. Since L_a corresponds to the size of the 2D crystallites, we observe that below about a 1 μm size sample, the room temperature electrical resistivity of the graphene planes is size-dependent.

Indeed, the transport properties of bulk carbons depend dramatically on the in-plane coherence length, which in turn mainly depends on the heat treatment or annealing temperature. The data presented in Fig. 3.1 are also corroborated by the result of thermal conductivity measurements [10], where it was found that the phonon mean free path for boundary scattering is almost equal to the in-plane coherence length L_a as determined by X-ray diffraction. The fact that we are comparing results obtained on different carbon precursors (HOPG, vapor grown carbon fibers, mesophase carbons, . . .) in Fig. 3.1 is justified since the results refer to well identified and well characterized graphene planes in the bulk.

These observations also clearly show the advantages of SLG and FLG over graphene in the bulk as regards study of the electron (and phonon) mean free paths. These are limited to around 10 μm for the highest quality HOPGs. These observations also explain also why carbon materials, which are not treated at sufficiently high temperatures (≈2000 °C), have temperature-insensitive mobilities. In that case the temperature dependence of the resistivity should be ascribed to that of the carrier density.

When thinking about bulk carbons one should always bear in mind that, except for the case of diamond, we seldom deal with 3D electronic carbon systems. While bulk materials, such as HOPG and its intercalation compounds, have a 3D

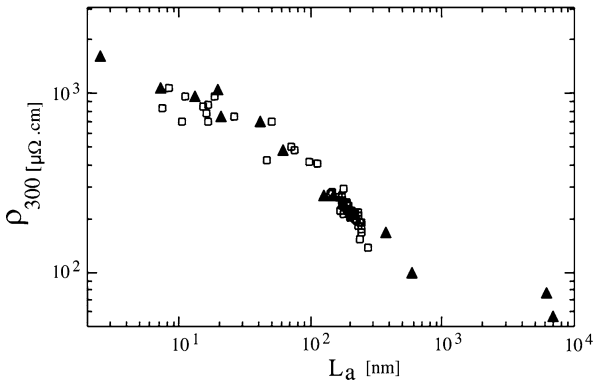

Fig. 3.1 Room temperature resistivity of experimental carbon fibers versus in-plane coherence length, L_a. The two lower resistivity values (higher L_a) are relative to data taken on vapor grown carbon fibers heat treated above 3,000 °C, while all other data pertain to pitch-based fibers graphitized at various different temperatures. It may be seen that the electrical resistivity decreases with increasing L_a, i.e. with increasing structural perfection. Note that the two lower values for vapor grown carbon fibers are close to those observed in HOPG (35 μΩcm) heat treated above 3,000 °C [9]

aspect (i.e., they occupy 3D space), the in-plane bonding is orders of magnitude stronger than the out-of-plane bonding, so that their physical properties are strongly anisotropic or quasi-2D. Some of them, such as acceptor graphite intercalation compounds (GACs), are definitely recognized as typical 2D (stage-1) or quasi-2D (stages higher than 1) hole gases, according to the stage of the intercalation compound. At the other end of the scale, a donor compound, such as a first stage potassium intercalation compound, KC_8, is permeated by a 3D anisotropic electron gas with a carrier density some orders of magnitude greater than that of HOPG. The 2D graphene layer has an electronic structure with a linear dispersion relation close to the Fermi level [11]. This 2D structure and linear electronic dispersion $E(k)$ proposed by Wallace [11] in 1947, was later adapted by Blinowski and Rigaux [4] in the late 1970s to the case of GACs and was used by them and by others to describe with some success the electronic and optical properties of GACs [12]. It was obvious to them that a linear dispersion leads to a zero effective mass and a Fermi velocity independent of energy in the 2D limit approximation.

Although this linear expression was used by researchers in the field to interpret electronic phenomena in GACs, some important physical consequences were only revealed recently when single graphene sheets were synthesized and investigated [1]. Also, bilayer- and few layer-graphene were found in the last decade to exhibit properties at variance with those of SLG, on one hand, and with graphite, on the other hand. A similar variance was found more than twenty years ago when multistage GACS were compared to stage-1 GACs [5].

3.1.2 Transport

Transport in general solids is concerned with the internal motion within a quasi particle electronic system, which has a momentum distribution in k-space that is initially isotropic but becomes directed in a preferred orientation under the action of external forces and fields. The charge carriers may be either electrons or holes or both, and these quasi particles may either carry electrical current (electrical conductivity) or heat energy (electronic thermal conductivity) [13]. The quasi-particles associated with the lattice vibrations, the phonons, are responsible for the lattice thermal conductivity. In all cases, collisions tend to bring each of these particle systems back into equilibrium and the relaxation time—or the mean free path—is generally the essential parameter that is used to describe the scattering process in the Boltzmann approximation [13].

Until the end of the 1980s, bulk carbons were described by semiclassical phenomenological transport theory. At that time, non relativistic quantum effects were observed in the electrical resistivity of "bulk" graphites and GACs [5]. Indeed, weak localization (WL) effects were reported and were consistently interpreted in terms of a 2D hole gas [5].

The emergence of nanotubes justified the use of non-relativistic quantum mechanics (NRQM) and the Boltzmann equation to describe many of the nanotube electronic and vibrational properties, while the era of graphene introduced a new concept to condensed matter physics involving relativistic quantum mechanics (RQM) or quantum electrodynamics (QED). Many properties of nanotubes and graphene can be extrapolated from our knowledge of bulk graphites. But new exciting features recently discovered in these nanostructured materials have shown up and have brought new physical concepts to our attention.

For in-plane thermal conduction, pristine HOPG together with diamond are known to be the best bulk heat conductors around room temperature [14]. Intercalation reduces the thermal conductivity, while carbon nanotubes and graphene were found to confirm their predicted exceptionally high thermal conductivity (see Fig. 3.13 and Tables 3.1 and 3.2 for more details).

3.1.3 Inelastic Scattering of Light

As stated above, phonons must be taken into account to properly explain many properties observed in carbon-based systems. Namely, electron-phonon and phonon-phonon scattering mechanisms are fundamental to understanding relaxation processes governing electrical and thermal properties.

In this context, mostly due to the linear electronic dispersion for carriers observed in carbon structures, the inelastic scattering of light (well known as Raman scattering), was found to be a particularly useful technique for understanding the electronic and vibrational properties of carbons and nanocarbons. Namely, resonant Raman scattering (RRS) is a fast, non-invasive and non-destructive technique

which, by means of first and second order scattering processes, allows us to study, for example, doping, disorder, thermal conductance, phonon dispersion and phonon self-energy renormalizations in carbon systems.

3.1.4 General References and Historical Background

In the following sections we discuss some of the most prominent features of conduction in bulk—pristine and intercalated—and nano-forms of carbons, mainly graphene. For more details on earlier works by pioneers in the field and for an historical outlook, the review papers on bulk carbons of the Ubbelohde group [3, 15], Mrozowski [16, 17], Pacault [18], Kelly [14] and Spain [19] should be consulted, as well as the research papers of Delhaes and Marchand [20, 21]. More recently, Delhaes published a book (three volumes) on the subject [22].

The work on intercalation compounds was first reviewed in 1981 [23]. Note that the review of Dresselhaus and Dresselhaus published in 2002, which is often cited by researchers on graphene, is dated 1981. Since this 2002 version was reprinted without modifications of the 1981 paper, it reflects the state of the art at the time of first publication (1981). It is important to emphasize that most of the papers on transport in GICs were performed after this date [5].

As regards graphene, since the time of the seminal work of Novoselov and co-workers [1], many review papers were published on the subject [24–29]. It is worth noting that a monolayer of graphene was already synthesized by Boehm in 1962 [30], though further detailed studies developed slowly before 2004.

3.1.5 Objectives

The present chapter: (1) shows how studies on bulk carbons in the 1970s and the 1980s paved the way for some of the physical properties observed in nanocarbons, more particularly in graphene, (2) stresses the similarities and differences observed in SLG and FLG and those observed in one or more graphene planes sandwiched between electrically insulating planes, as in graphite acceptor intercalation compounds (GACs), (3) shows how a 2D model for the band structure with massless fermions was already applied successfully in the 1980s to interpret the properties of GACs, (4) shows that despite the similarity between the dispersion relations in stage-1 GACs and graphene, there are some properties which could not be observed in GACs, and for such detailed studies, SLG or FLG host materials are needed, (5) shows that some of the very high mobilities reported up to now in graphene are by no means unique and that higher values have been observed and reported in other semimetals and in 2D electron gases in semiconducting superlattices, (6) addresses mainly semiclassical and quantum (non-relativistic) aspects of transport, as were used in these earlier

works that are often ignored by recent entrants to the nanocarbon field, (7) discusses briefly some important aspects of the inelastic scattering of light (Raman scattering) present in sp^2 carbon-based materials, including graphene and nanotubes.

3.1.6 Topics Addressed

In the 1980s the properties observed on bulk GICs were mainly compared with those obtained on pristine HOPG or vapor grown carbon fibers (VGCF). In the present overview we shall mainly concentrate on extracting the information available about the graphene layers in the GICs and compare this information to that recently obtained on SLG and FLG. From this knowledge of some properties of bulk carbons, we will show that one could have anticipated some of the properties of graphene at a much earlier time than occurred historically. In the same way, what has been observed recently in graphene should help our understanding of the properties of bulk carbons, some of which have found significant commercial use.

In the following sections, we shall first discuss electronic transport. After briefly introducing the electronic band structure, we will compare the scattering mechanisms and the effects of disorder in graphene in and out of the bulk. We will then compare the thermal conductivities. The comparison will concern bulk pristine and intercalated (GACs) and nanostructured carbons, mainly graphene. Concerning the bulk, we will be mainly interested in GACs, since in donor intercalation compounds, the anisotropy is less pronounced and it is less appropriate to consider the electron gas as quasi two-dimensional. Finally, we discuss the differences and similarities among the several carbon-based materials regarding their electronic and vibrational properties as they manifest themselves in Raman scattering experiments.

3.2 Electrical Conductivity

3.2.1 Introduction

The announcement three decades ago that an electrical conductivity comparable to that of copper has been observed at room temperature in an AsF_5 intercalation compound [31] was the starting point for the hype and the intensive research in the 1980s on GICs. This experimental result [31] was neither reproduced on AsF_5 since then, nor observed on any other compound and it was later on demonstrated [32, 33][3] that, within the state of our knowledge, resistivities below about 5×10^{-6} $\mu\Omega\,\mathrm{cm}$ could never be attained in acceptor GICs at 300 K, insofar as this value represents

[3] See also Ref. [5].

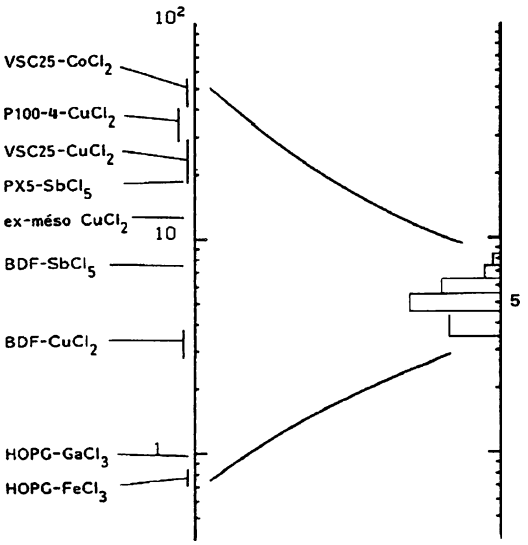

Fig. 3.2 Residual (left-hand scale) and ideal (right-hand scale) room temperature resistivities of acceptor GICs based on various host graphites. Resistivity values are in $10^{-6}\ \Omega\,\mathrm{cm}$ [33]

the intrinsic value of the resistivity (ideal resistivity) for the electron-phonon interaction at this temperature (Fig. 3.2). Nevertheless, this misleading announcement had beneficial effects, since it served to strongly promote a new exciting field of research. Intercalated carbon fibers have not replaced copper in cables for power transmission, but advances in lithium batteries, which are of commercial interest, have instead benefited much from the basic work performed in the past on donor intercalation compounds.

In metals and semimetals the charge carrier distributions are described by their Fermi surfaces. Around and above room temperature, electrons and holes are mainly inelastically scattered by phonons, while at low temperatures elastic scattering by point defects and crystal boundaries dominate the scene. Also, at low and ultralow temperatures, specific effects show up, revealing quantum effects at the macroscopic scale. These are the weak localization effects [34, 35], Coulomb interaction effects and the universal conductance fluctuations in a quasi-ballistic regime, which were observed in carbon nanotubes [36].

The physics of electronic conduction in bulk pristine carbons is dominated by: (1) the semimetallic behavior due to the presence of a small density of charged particles, electrons and holes, which has a drastic effect on the band structure and on the scattering mechanisms (cf. Sect. 3.2.3), (2) the effects of a very high anisotropy in both structures and properties, (3) the effects of disorder, even when relatively weak, in relation to quantum aspects of conduction, (4) the possibility of intercalation and its effects. And for intercalation compounds, one should consider also: (1) their metallic behavior, (2) the effects of reduced dimensionality, (3) the additional disorder introduced by the intercalation process itself.

The effect of reduced dimensionality will allow comparison with SLG and FLG, while the additional disorder introduced by intercalation will limit the scattering length of the charge carriers and mask some of the effects which were recently ob-

served in SLGs and FLGs. The other side of the coin is that intercalation compounds have allowed the observation of 2D weak localization effects in GACs, which have not been studied in as much detail in graphene. The impact of a small Fermi surface on the scattering mechanisms, which was already identified in the group V semimetals in the early 1950s [37], has been discussed later on for the case of graphites [38]. With regard to quantum aspects, they were mostly observed in the 1980s on carbons and graphites [34, 35], and more recently (in the 1990s) on carbon nanotubes [36].

In bulk graphites, including carbon fibers, we shall only be interested here in conduction in the graphene planes. Bulk HOPG presents the advantage that the anisotropy in resistivity can be investigated since the resistivity can be measured both in-plane and in the *c*-axis direction, while carbon fibers offer the advantage that high resolution resistivity measurements can be performed. Indeed, the fact that various geometries are available: bulk, fibers, particles, nanotubes is also a remarkable feature of sp^2 carbon materials.

Two dominant characteristics of the electrical conductivity of graphite intercalation compounds are their high in-plane conductivity and the anisotropy of the in-plane to *c*-axis conductivity. This anisotropy, which in stages 1 donor compounds may vary from 10 to 60, is much higher in all acceptor compounds, whatever the stage, where this anisotropy may reach 10^6 at 300 K [23]. These experimental observations confirm what could be inferred from the band structure calculations described in the section (Sect. 3.2.2).

3.2.2 Electronic Structure

In order to discuss the transport properties we first need to know about: (1) the electronic distribution of the quasi-particle system considered. In graphites, this means that we must have a model for the Fermi surface and for the phonon spectrum. (2) Some characteristic lengths, one of them being the mean free path, but for the case of charge carriers, some other characteristic lengths should also be considered, especially at low temperatures.

So, before discussing electronic transport, we will briefly describe how the charge carriers are distributed in energy and momentum, e.g., the dispersion relations for these carriers.

3.2.2.1 Pristine Graphite

Starting with the work of Wallace in 1947 [11], theorists have addressed graphene following a bottom-up approach, while experimentalists have had to comply with the materials and techniques at hand and, *faute de mieux*, have adopted a top-down approach. On physical grounds, the common feature of graphene sheets in FLG and in bulk pristine graphite is the strong intralayer covalent bonding and the relatively

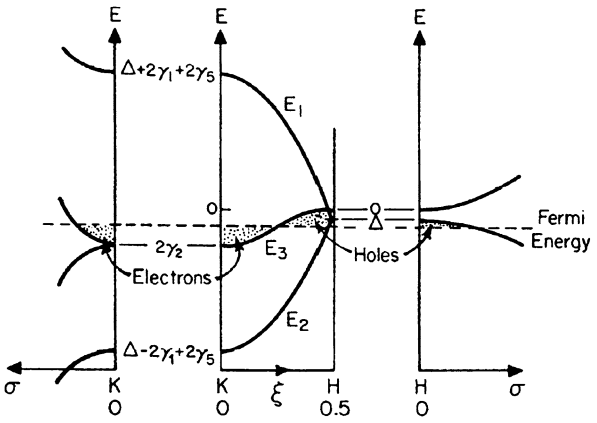

Fig. 3.3 Electronic energy bands near the HK axis in three-dimensional graphite as obtained from the SWMcC band model [39–41]

weak interlayer graphene-graphene Van der Waals type bonding. This is the dominant aspect which determines the physical properties of these materials.

The large anisotropy of the graphite crystal structure, suggested as a first approximation the use of a two-dimensional electronic structure [11]. However, a 2D model generates a zero gap semiconductor for graphite, which is contrary to experimental evidence. The interlayer interaction, though much weaker than the intralayer coupling, has a profound effect on some physical properties, mainly wherever charge carriers are concerned, since the interlayer interaction gives rise to a small band overlap between the valence and conduction bands. This band overlap is responsible for the semimetallic properties of graphite which governs most of its low-temperature electronic properties. However, since the band overlap is on the order of $k_B T$, this difference will not have dramatic effects on the room temperature transport properties.

So, a more realistic three-dimensional model, considering the AB Bernal stacking of the graphene layers, giving rise to four carbon atoms per unit cell, was developed a decade later by Slonczewski and Weiss [39] and by McClure [40, 41]. This model, known as the Slonczewski-Weiss-McClure (SWMcC) band model (Fig. 3.3), was found to explain most of the observed physical properties dependent on the electronic structure near the Fermi level, including transport, quantum oscillatory behavior, optical and magneto-optical properties.[4]

3.2.2.2 Quasi 2D Graphene

Just as for pristine graphite and FLG, in GACs the dominant feature of the electronic structure is the strong intralayer bonding in graphene and the relatively weak interlayer bonding. However, for the case of GACs, the strong binding also applies to the intercalate layers in-plane, while the graphene-intercalate layer interaction in

[4] See, for example Refs. [12, 19] and [23].

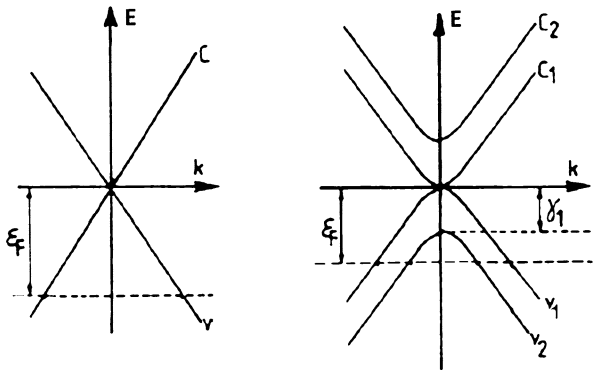

Fig. 3.4 Model developed by Blinowski et al. [4] for the $E(k)$ relation of graphite acceptor compounds for stages $n = 1$ (*left*) and $n = 2$ (*right*). For the stage 1 acceptors, the transport properties follow a linear dispersion relation, which is typical of two-dimensional models for pristine graphite for the energy bands near the zone edge, as seen in Fig. 3.3. Note the similarity between the electronic structure of stage-1 and stage-2 GACs and that of monolayer and bilayer graphene, respectively, shown in Fig. 3.5

the intercalation compounds modifies the graphene layer more than the intercalated layer.

The electronic structure of graphite intercalation compounds is expected to bear some similarity with that of the graphite host material. In the dilute limit (higher stages) one should expect an electronic structure closely related to that of pristine graphite [11]. This explains why, in the 1980s, a first model for the band structure for GICs was developed for dilute intercalation compounds [42].

This being stated, for comparison with SLG and FLG, we will consider here instead the lowest stage compounds, stages 1 and 2, and concentrate on the case of acceptor compounds, where graphene behaves most like a quasi 2D electronic system. In contrast to 3D graphite, charge carriers in these two systems are strictly confined in the graphene planes and can be considered as quasi free carriers for motion along these planes. Moreover, both SLG and stage-1 GACs may be ideally considered as typical massless 2D electron (hole) gases.

Along the lines of the SWMcC model, Blinowski et al. [4] developed a model for the electronic band structures of stage 1 and 2 graphite acceptor compounds in order to interpret their optical properties. For stage-1 acceptors, a two-dimensional version of the SWMcC model was used. This model was obtained by neglecting all interactions other than the nearest-neighbor in-plane overlap energy, γ_0:

$$-\varepsilon_v(k) = \varepsilon_c(k) = \frac{3}{2}\gamma_0 ak \tag{3.1}$$

where $a = 1.42$ Å is the in-plane nearest neighbor C–C distance.

This linear wave vector dependence of the energy in (3.1) is typical of two-dimensional models for graphene for the energy bands near the zone edge, and the dispersion relation for these systems are presented in Fig. 3.4 (left). The dispersion relations for the stage-2 compounds are shown in Fig. 3.4 (right). In addition

to measurements of the optical properties, these models were confirmed by quantum oscillatory measurements [23]. Also, when the dispersion relations were used for the interpretation of transport measurements they were found to lead to results consistent with each other [5].

Soon after the transport properties of individual graphene layers were successfully obtained [1], it was experimentally confirmed that the charge carriers in SLGs were 2D systems with linear dispersion relations (Fig. 3.5(a)) akin to the stage-1 GACs. Similarly, bilayer graphene presents the same dispersion relations as stage-2 GACs (compare Figs. 3.4 and 3.5). However, as will be seen later, the synthesis of almost defect-free suspended graphene layers with very high carrier mobilities allowed the observation of effects which could not be observed in the bulk.

Note the similarity between the dispersion relations presented in Fig. 3.4 for GACs and Fig. 3.5 for graphenes. Owing to the linear energy-momentum relation for monolayer graphene, electrons and holes in graphene at the Dirac point have zero-effective masses and have been called massless Dirac fermions. The corresponding density of states, which is also linear in energy should vanish at the Dirac point where the conduction and valence bands touch.

As is the case for GACs, electrons and holes in graphene and FLG are confined in the planes and behave as a 2D or as a quasi-2D electron (hole) gas, respectively. Transport studies have been performed in graphene and FLG and the nature and values of the effective masses of the charge carriers have been determined. GACs were found to behave as semimetallic systems with coexisting electrons and holes. One of the great advantages of the FLG systems over their bulk equivalents is that the carrier population can be easily and reversibly modified by applying a transverse electric field (gate voltage). One can switch from electron to hole transport by varying the Fermi level (or the gate voltage which determines the Fermi level). Also, in recent work a couple of additional parameters have been added to the Slonczewski-Weiss picture [43–45].

In Fig. 3.6 we present a summary of the models developed for the band structure of graphene in and out of the bulk.

3.2.3 Charge Carrier Densities and Scattering

In its simplest form, the semi-classical conductivity of an isotropic solid is a scalar which depends on two variable parameters: N, the carrier density and μ the carrier mobility, which are related by,

$$\sigma = qN\mu \tag{3.2}$$

This same relation applies for 3D and 2D solids. For the 3D case the carrier density is expressed in cm^{-3} and the conductivity in $\Omega^{-1}\,\mathrm{cm}^{-1}$, while in 2D the units are cm^{-2} and Ω^{-1}, respectively. In order to examine to what extent high conductivities can be observed in solids, or possibly can be achieved, we shall next examine the two parameters N and μ in (3.2).

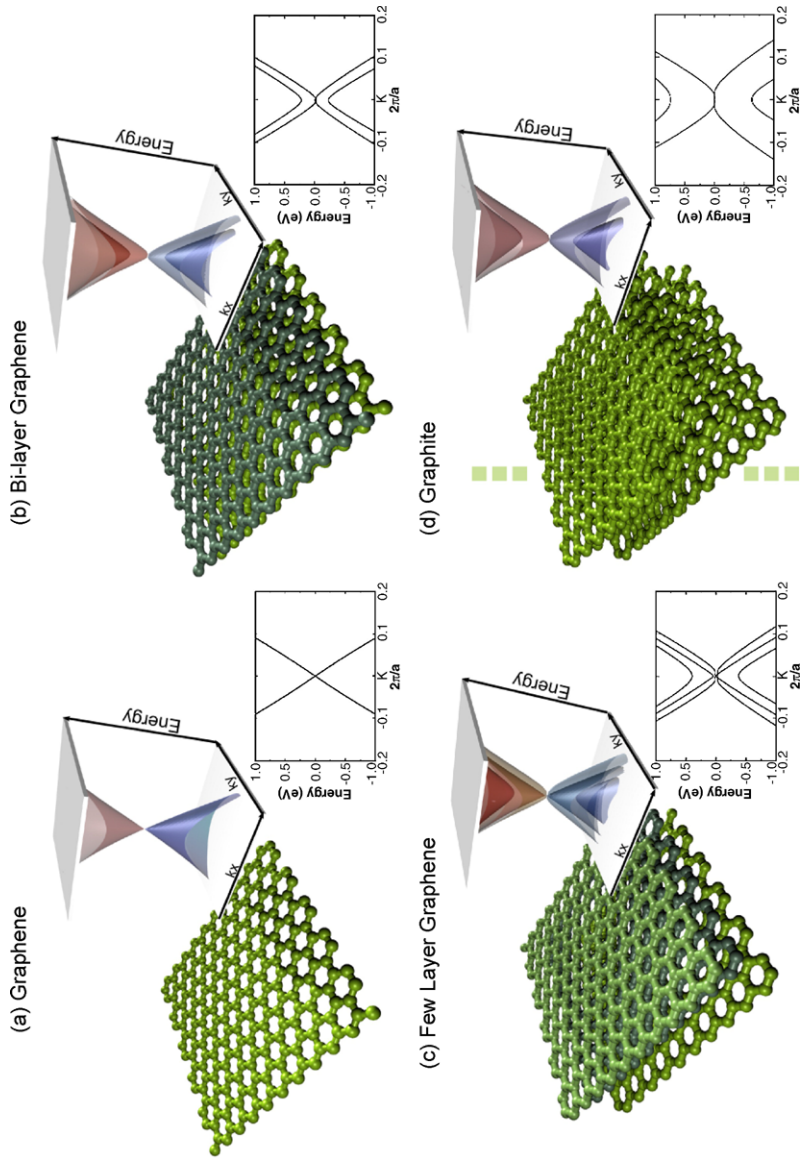

Fig. 3.5 Model for the electronic structure of monolayer graphene (**a**), bilayer graphene (**b**), trilayer graphene (**c**) and graphite (**d**) [27]

Year	Author (s)	Form of Carbon	Dimensionality
1947	Wallace (1)	Virtual graphene	2D
1957, 1960	SWMC (2)	HOPG	3D
1980	Blinowski-Rigaux (3)	GACs	2D
2004- …		Monolayer graphene	2D

Fig. 3.6 Summary of models developed for the band structure of graphene in and out the bulk. Here Wallace refers to [11], SWMC to [39–41], and Blinowski-Rigaux to [4]. For graphene, one should refer to the review papers in [24–29]

3.2.3.1 Intrinsic Carriers and Charge Transfer

Among the various types of solids, 3D metals have the highest carrier density, on the order of the atomic density, i.e., 10^{23} cm^{-3}. This density is temperature and impurity insensitive and thus its 0 K value cannot be modified. In contrast, semiconductors have no free carriers at 0 K, but electrons and/or holes may be thermally excited and the carrier densities in semiconductors increase strongly with temperature, though the carrier densities of semiconductors are typically several orders of magnitude lower than in metals. Semimetals share with metals the fact that they have carriers at 0 K and, as for semiconductors, the carriers in semimetals are small in number[5] and are temperature sensitive. Both semiconductors and semimetals are able to have their intrinsic carrier density readily modified through doping.

Doping[6] consists of introducing a small number of foreign atoms in a 3D solid, either by substitution or by insertion, while intercalation introduces in lamellar materials entire layers of foreign species and the whole layer can denote electron and hole carriers. The common feature between intercalation and doping is that both processes modify the intrinsic charge carrier densities of the host material.

While pristine HOPG is a semimetal with a small band overlap of nearly 0.040 eV (cf. Fig. 3.3), which is responsible for the presence of a small but equal number of electrons and holes at 0 K—around 2.3 and 13.5×10^{-18} cm^{-3} at 4.2 K and 300 K, respectively. In contrast, a graphene layer is a zero gap semiconduc-

[5] Actually the density of carriers at 0 K varies from one semimetal to another. If we consider the group V semimetals, the density at 0 K is very small in bismuth and is comparable to that of pristine graphite, it is larger in antimony and much larger in arsenic, where the electron gas is still degenerate at room temperature.

[6] The word "doping" commonly attributed to intercalation—as it is for conducting polymers—is not correct in this context. Solid state physicists introduced this concept initially to define the introduction of a small amount of foreign atoms which increases the charge carrier density without modifying the band structure which is considered according to the rigid band model. This is far from being the case in GICs or in electroactive polymers.

tor, or a zero band overlap semimetal. In GICs, through charge transfer, the density of electrons or holes increases dramatically and for lower stage intercalation compounds the charge density can be as large as that of a metallic conductor with a Fermi energy on the order of one eV. Once the intercalation process is achieved, the stage and carrier density are determined and cannot be modified, e.g., by applying a transverse electric field. Also, this field-induced charge density is practically temperature insensitive as in 3D metals. Although a finite transverse electric field could, in principle, be maintained in GACs because of the large out-of-plane resistivity, its effect could not be detected macroscopically along the planes, since the total density of charge carriers is too large.

In undoped graphene there are no charge carriers at 0 K, but these could be excited by means of a transverse electric field [1]. Also, when the temperature increases, charge carriers are excited, just as for the case of semimetals and semiconductors.

3.2.3.2 Scattering

For diffusive motion, the relaxation time, τ, is the parameter commonly used to characterize collision processes using the Boltzmann equation approximation. But the mobility,[7] which is defined in terms of the drift velocity, v_d, of the charge carriers per unit electric field, E:

$$\mu = v_d / E \tag{3.3}$$

can be imagined as the ease with which the carriers move in the crystal lattice. The parameter μ is usually used for sample characterization, since it may be derived from analysis of the measured transport coefficients. There is a direct relation between the mobility μ and the relaxation time τ:

$$\mu = q\tau / m^* \tag{3.4}$$

where m^* is the carrier effective mass. The relaxation time τ is the time elapsed between two collisions, and its inverse $1/\tau$ reflects the probability for a carrier to experience a scattering event. The mean free path (mfp), ζ, which is the mean distance between two scattering centers, is expressed as:

$$\zeta = v_F \tau \tag{3.5}$$

where v_F is the Fermi velocity. The conductivity then becomes:

$$\sigma = \frac{q^2 N \tau}{m^*} \tag{3.6}$$

or:

$$\sigma = \frac{q^2 N \zeta}{m^* v_F}. \tag{3.7}$$

[7] The mobility concept holds for a diffusive regime.

These expressions were derived for a single type of charge carrier. If there are more than one type of carrier, i.e., electrons and holes, as in pristine graphite or graphene, or there are several bands for electrons or holes as in GACs for stages higher than 1, the contribution of each type of carrier should be taken into account. In that case, the total electrical conductivity is given by the sum of the partial conductivities, σ_j of each group of charge carrier, j:

$$\sigma = \sum \sigma_j . \tag{3.8}$$

When there are more than one scattering mechanism, s, experienced by charge carriers and when the relaxation times describing these scattering events, τ_s, are of the same order of magnitude, then the total relaxation time τ is a combination of these τ_s parameters and is commonly given by Matthiessen's rule, which in that case may be expressed as:

$$\frac{1}{\tau} = \sum_s \frac{1}{\tau_s} \tag{3.9}$$

which effectively sums the scattering probability for each scattering process. In order that this rule applies, the various types of scattering processes that are considered must be independent of one another and the relaxation time must be isotropic. These assumptions are only partly true in many physical systems including sp^2 carbons.

Thus, the main contributions to the electrical resistivity of conductors, ρ, consist of an intrinsic temperature-sensitive ideal term, ρ_i, which is mainly due to electron-phonon interactions and an extrinsic temperature independent residual resistivity term, ρ_r, which is due to static lattice defects:

$$\rho = \rho_r + \rho_i \tag{3.10}$$

In graphites the residual resistivity is determined by the defect structure of the graphitic layers, which may vary widely according to the heat treatment temperature and, to a lesser extent, to the type of carbon and the quality of the precursor. In Fig. 3.7 we present the temperature dependence of the resistivity for pristine and intercalated benzene-derived graphite fibers (BDF) as a typical illustration of the validity of Matthiessen's rule for graphite intercalation compounds [46]. These results represent the lowest resistivity values and the highest residual resistance ratios (on the order of $\times 10^{-5}$) achieved to date in pristine and air-stable intercalated graphite fibers.

Equation (3.8) shows that the contributions to the conductivity from different carrier groups add, while (3.9) and (3.10) show that it is the resistivities due to various scattering mechanisms that add. Matthiessen's rule (3.9) should thus be applied independently for each type of carrier.

Through charge transfer, intercalation of chemical species between the graphene planes leads to an increase in the charge carrier density—electrons for donors and holes for acceptors—which is accompanied by a decrease in the electronic mobility. The net result of intercalation is thus generally an increase in the in-plane electrical conductivity as is shown in Fig. 3.7.

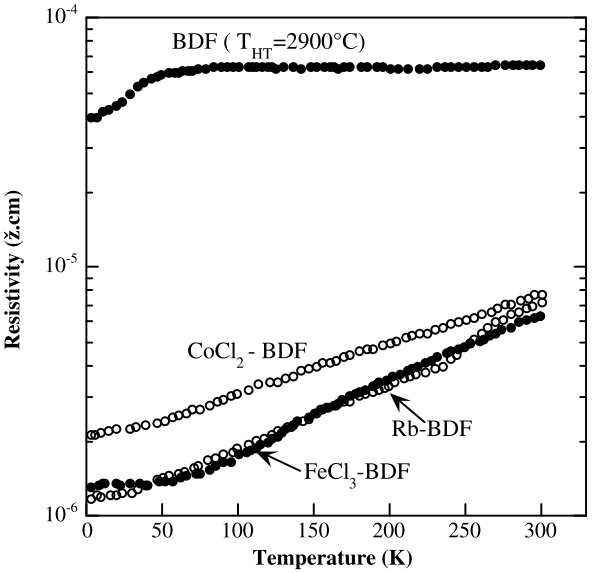

Fig. 3.7 Temperature dependence of the resistivity for benzene-derived graphite fibers (BDF), heat treated to 2900 °C, of a pristine fiber (*top curve*) and a Rb- and $FeCl_3$-intercalated fiber (curves labeled Rb-BDF and $FeCl_3$-BDF, respectively) [46]

It is commonly stated that the decrease in mobility is due to the defects generated by the intercalation process. This is true, but defects are not the only mechanism responsible for the loss of mobility. There is an additional effect, which is due to the increase of the carrier density, or in other words an increase in the magnitude of the Fermi energy. The relaxation time, τ, of the charge carriers is thus energy, ε, dependent, and this dependence is usually written as:

$$\tau = \tau_0 \varepsilon^p, \tag{3.11}$$

where p is the scattering parameter which takes the value of -1 when electron-phonon scattering is dominant for two-dimensional GACs [47]. This means that the relaxation time, and thus the conductivity, decreases with increasing Fermi energy in this case. This is well justified on physical grounds by the following argument: because of energy and momentum conservation requirements, with increasing energies, electrons interact with higher energy phonons which are more numerous. However, it is generally observed that the increase of the carrier density with respect to the pristine material due to charge transfer largely compensates the loss in mobility and that the net effect is an increase in conductivity. This means also that, even if ideally one could avoid the generation of defects during the intercalation process, the mobility would in any case remain lower than in pristine HOPG because of the increased intrinsic scattering.

Oddly enough, it was shown that for stage-1 acceptor compounds, because of the linear dispersion relation, the intrinsic conductivity would not be increased with additional charge transfer. This is due to the fact that the increase of the charge carrier density is exactly compensated by the decrease in relaxation time due to the enhancement of the Fermi level [5].

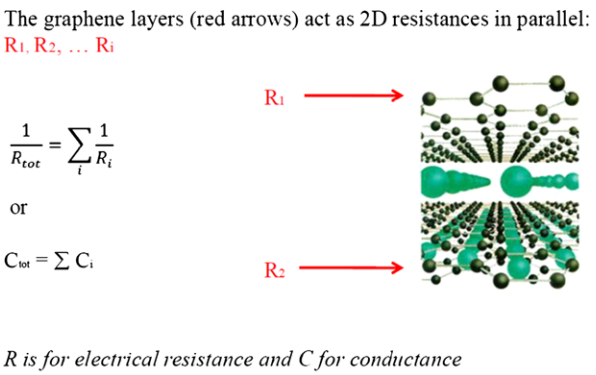

Fig. 3.8 Schematic representation of the graphene electrically conducting planes (*small black spheres*) and the intercalate electrically insulating layers (*large green spheres*). The graphene planes are considered as electrical conductors in parallel, as shown (*left*) for the calculation of their 2D resistivity

At room temperature, the intrinsic part of the mobility due to electron-phonon interactions generally dominates. Room temperature mobilities are relatively low in metals—generally below 100 $cm^2/(V\,s)$ (32 $cm^2/(V\,s)$ for copper)—and in intercalation compounds, with high mobilities occurring in semimetals, including graphite. We would therefore expect the mobilities to be the highest in a defect-free suspended SLG of large in-plane size.

In Fig. 3.8 we illustrate schematically how the graphene layers between the nearest intercalate layers in two-dimensional GACs may be considered as conductors acting in parallel. This allows us to calculate the conductivity of the graphene layers in the GAC from the results of measurements on the bulk.

3.2.3.3 Experimental Observations

For pristine HOPG, mobilities of 12,000 $cm^2/V\,s$ were early reported [19] at 300 K in-plane [18], which is comparable to the first values obtained in some FLGs. Indeed, in their first paper, Novoselov et al. [1] reported temperature independent mobilities larger than 10,000 cm^2/V in FLG at 300 K and around 60,000 $cm^2/(V\,s)$ at 4 K. Later on, Du et al. [48] reported mobilities of suspended graphene at different temperatures. They claimed low temperature mobilities as high as 200,000 $cm^2/(V\,s)$ for carrier densities below 5×10^9 cm^{-2}. This result is not surprising and, from measurements on other systems (cf. Fig. 3.9) and considering the particular electron-phonon interaction in 2D semimetallic systems, one should even expect higher values for large, free-defect samples.

At low temperatures charge carriers freeze out in semiconductors and thus, without external excitation, no carrier mobility can be observed. In semimetals instead, electrons and holes coexist naturally even at 0 K. In another highly anisotropic semimetal, bismuth, where the dispersion relation for electrons deviates appreciably from a parabolic energy-wavevector dependence, the effective mass components for electrons are as low as $0.001 m_0$ for certain wavevector directions [49, 50].

Zitter [51] and Hartmann [52] measured the galvanomagnetic properties of high purity bismuth single crystals at 4.2 K and deduced their carrier mobilities. One

Material	Remarks	Carrier mobility ($cm^2/V.s$)		
		~ 4.2K	~ 77K	300K
Copper			~ 200	32
Si (bulk)	For electrons (holes = 450)			1,450
GaAs	Heterostructure -2DEG	36.10^6	3.10^5	5.10^3
Bismuth	Single crystal, large size, high purity	43.10^6	$6.4\ 10^5$	$3.2\ 10^4$
HOPG	Heat treated above 3,000 C		$6.7\ 10^4$	$1.2\ 10^4$
Graphene	Highest values claimed*	$2.\ 10^5$-10^6		5.10^4

Fig. 3.9 Values of the mobilities at three temperatures for various electrical conductors compared to that of HOPG and graphene out of the bulk. For graphene, the different results obtained are not comparable since, in the diffusive regime, there are different definitions of mobility according to the experimental method used to measure it. Besides, the very high so-called mobilities are probably measured under ballistic conditions. It does not make sense then to speak about mobilities in that case, since the mobility concept applies only for the diffusive regime (cf. Sect. 3.2.3.2)

of the components of the mobility tensor (μ_1 in the trigonal plane, i.e., the plane perpendicular to the trigonal axis) for this semimetal was found to exhibit a value as high as 4.3×10^7 $cm^2/(V\,s)$. The same component of the mobility tensor was measured at higher temperatures [53] and was found to still exhibit very high values, 6.4×10^5 $cm^2/(V\,s)$ for a carrier density of 4.5×10^{17} cm^{-3} at 77 K and 3.2×10^4 $cm^2/(V\,s)$ for a carrier density of 24.5×10^{17} cm^{-3} at 300 K (cf. Fig. 3.9).

The very high mobility values observed in bismuth are to be ascribed in part to the small effective masses, but even more dramatically to the ineffectiveness of electron-phonon interactions in semimetals. Indeed, as was pointed out by Sondheimer long ago [37], because of energy and momentum conservation requirements, charge carriers in semimetals with small Fermi wave vectors can only interact with low energy phonons, even at high temperatures where they are less numerous than the thermal ones, which dominate the scene. This situation also holds for pristine HOPG [38], but should be analyzed differently in GACs [5], since the Fermi wave vector is much larger than in the pristine material. In 2D graphenes, this effect should be even more pronounced because of the limitation of the phonon spectrum for lower energy phonons, due to the limited size of the samples, and to restrictions imposed by the selection rules that are more stringent than for a 3D solid. Carbon nanotubes also exhibit very high mobilities, but this is generally attributed to the suppression of scattering in the 1D case [54].

MATERIAL	HIGH TEMPERATURE	LOW TEMPERATURE
METALS (high carrier densities)	large-angle scattering with large number of high energy interacting phonons. LOW MOBILTY	small-angle scattering with small number of interacting low-energy phonons. HIGH MOBILITY
SEMIMETALS (for small charge carrier densities)	large-angle scattering with small number of interacting low-energy phonons. HIGH MOBILITY	large or small-angle scattering with small number of interacting low-energy phonons. VERY HIGH MOBILITY
SEMICONDUCTORS (for small charge carrier densities)	large-angle scattering with small number of interacting low-energy phonons. HIGH MOBILITY	large or small-angle scattering with small number of interacting low-energy phonons. VERY HIGH MOBILITY

Fig. 3.10 Qualitative comparison of the intrinsic mobilities for electron-phonon interactions in electrical conductors (metals and semimetals) and semiconductors

Note that in Fig. 3.9, where we compare values of the mobilities at three temperatures for various electrical conductors, we must be cautious when considering graphene out of the plane. For graphene, the different results reported in the literature are not directly comparable. First, in the diffusive regime, there are different definitions in the literature for the mobility according to the experimental method used to measure the mobility. Second, the highest so-called mobilities are probably measured under ballistic conditions. It does not make sense then to speak about mobilities in the case of ballistic transport, since the mobility concept applies only for the diffusive regime (cf. Sect. 3.2.3.2). In Fig. 3.10 we compare the situation of intrinsic mobilities for electron-phonon interactions in electrical conductors, metals and semimetals, and semiconductors.

3.2.4 Quantum Effects

In the presence of weak disorder, which is always present in real graphites and in their intercalation compounds, one should consider a quantum correction to the residual resistivity (Fig. 3.11) due to weak localization resulting from quantum interference effects and/or that due to Coulomb interaction effects [55, 56]. These quantum effects, though they do not generally significantly affect the magnitude of the resistivity, introduce new features into our understanding of low temperature transport effects [55, 56]. So, in addition to the semiclassical ideal and residual resistivities of carbons discussed above, we must take into account the contributions due to weak localization and many body interaction effects. In the weak disorder limit, which, i.e., when $k_F\zeta \gg 1$, where k_F is the Fermi wave vector and ζ is the

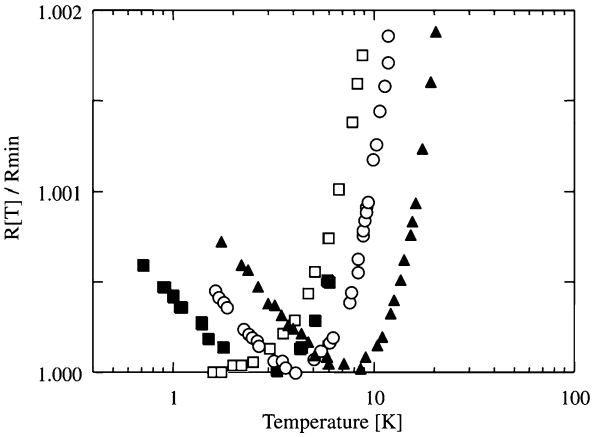

Fig. 3.11 Low temperature dependence of the resistance for low-stage fibrous acceptor GICs, with various hosts and intercalates, showing the logarithmic increase in resistivity with decreasing temperature, characteristic of localization and electron-electron interaction effects. All data are normalized to the minimum value of the resistance and temperature is plotted on a log scale [34, 60]

mean free path of the carriers,[8] a correction term, $\delta\sigma_{2D}$, should be added to the classical (Boltzmann) electrical conductivity, $\sigma_{2D,Boltz}$:

$$\sigma_{2D} = \sigma_{2D,Boltz} + \delta\sigma_{2D} \tag{3.12}$$

where

$$\delta\sigma_{2D} = -\frac{q^2}{2\pi^2\hbar}\ln\left(\frac{\tau_{in}}{\tau_r}\right) \tag{3.13}$$

in which $\delta\sigma_{2D}$ is the conductivity associated with weak localization effects, τ_{in} is the relaxation time due to inelastic collisions, mainly phonon scattering, and τ_r is the relaxation time due to elastic collisions mainly due to static defects.

These localization effects [34, 35, 57] were found to confirm the 2D character of conduction in acceptor GICs [34, 35] and in turbostratic carbons [57]. In the same way, in carbon nanotubes, experiments performed at the mesoscopic scale revealed quantum oscillations of the electrical conductance as a function of magnetic field, the so-called universal conductance fluctuations [36].

Two distinct mechanisms may be responsible for a quantum correction to the low temperature classical electrical conductivity, which shows up as a logarithmic increase in the resistivity. First, a single-carrier weak localization effect due to the constructive quantum interference appears between elastically back-scattered partial-carrier-waves.

For macroscopic samples, at high enough temperatures, inelastic collisions are dominant, mainly through electron-phonon interactions, where the phase memory of electrons is lost together with their momentum. At sufficiently high temperature, we are in the situation of diffusive motion described above (Sect. 3.2.3.2), and in this regime the charge transport is ohmic. When the temperature is lowered, the inelastic mean free path increases and, eventually, becomes much larger than the elastic mean

[8] Note that $k_F\zeta \gg 1$ is also the condition for transport in the Boltzmann approximation.

free path. Through elastic collisions, electrons lose momentum but not their phase memory. Interferences may then show up in the electronic system generating weak localization effects.

At low temperatures and in a metal sample of very small dimensions, the phase-coherence length may become larger than the dimensions of the sample. In that case, for an ideally perfect crystal, the electrons will propagate ballistically from one end of the sample to the sample boundary. We then enter into a ballistic regime where the laws of conductivity discussed above (Sect. 3.2.3.2) no longer apply. The propagation of an electron is then directly related to the quantum probability of transmission across the global potential of the sample. In a real crystal, static defects will scatter electrons elastically so that the electrons do not lose memory of the phase contained in their wave function and in this regime, the electrons propagate through the sample in a coherent way. This may happen in defect-free graphene. The second effect is the charge carrier many-body Coulomb interactions due to the screening by other charge carriers [58, 59]. These two effects are enhanced in the presence of weak disorder, i.e., by static defect scattering. A weak applied magnetic field suppresses the phase coherence of the backscattered waves, but does not influence the Coulomb interaction phenomenon. Thus magnetoresistance measurements allow separation of the two effects.

Weak electron localization and electron-electron Coulomb interactions were observed in GACs at low temperatures (Fig. 3.11) [5]. This anomalous resistivity behavior is accompanied by a negative magnetoresistance. The physical origin of this decrease in resistance with the applied magnetic field is different from that of the classical (positive) magnetoresistance, which is due to the deviation of the charge carriers from their original longitudinal path across the sample due to the Lorentz force.

GACs, and especially stage-1 compounds which have circular Fermi surfaces, are natural 2D electronic systems since this 2D characteristic is inherent in their electronic band structure. The 2D behavior results from the confinement of the charge carriers in the graphene planes and these carriers are otherwise quasi free, though weakly localized- for motion parallel to the planes. This is in contrast to metallic films where the quasi 2D behavior results from the anisotropic scattering of electrons at the surfaces. Indeed, in metallic films, where localization effects were first observed, the 2D character is associated with the anisotropy of the mean free path, the latter becoming very small in the direction perpendicular to the film, thus confining the motion of the carriers to the plane of the film. The differences between the 2D electronic structure of acceptor GICs and that of other quasi 2D electronic systems originate from differences in the energy dependence of the density of states, which is linear in stage-1 acceptor GICs (Sect. 3.2.2.2).

On the other hand, the possibility of varying the defect structure of the host material over wide ranges in GICs allows extensive investigations of the phenomena of weak localization. One may vary the host material through selection and control of the microstructure by choice of the precursor and control of the heat treatment temperature and other processing conditions. In addition, though to a lesser extent,

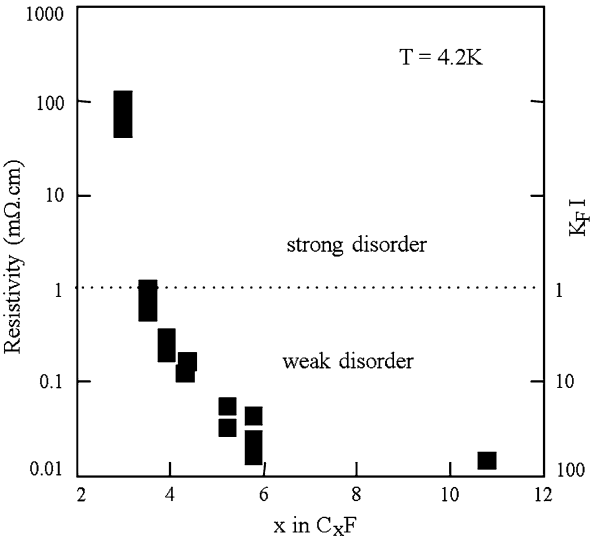

Fig. 3.12 Electrical resistivity at 4.2 K for various fluorine GICs showing the effect of the transition from weak to strong disorder by varying the fluorine content in the intercalation compound. It is worth mentioning that k_F is the Fermi wave number and I the mean free path. The product $k_F I$ sets the limit from weak to strong disorder. When it is larger than unity, we are in the weak disorder region [33]

the Fermi level may be modified by varying the nature of the intercalate and the stage of the compound. Acceptor GICs are thus among the best candidates to investigate 2D localization and interaction effects, since it is possible in this case to control the disorder over wide ranges and, to a lesser extent, to control the de Broglie wavelength.

With regard to the control of the Fermi level, it is worth noting that in graphene out of the bulk (SLG and FLG), one may use transverse electric fields and vary the carrier density at will, within certain limits, and thus investigate weak localization effects as a function of a single variable. In addition, one may shift from holes to electrons. However, in order to realize the conditions where localization effects show up, one needs a sample with a certain amount of static defects, such as point defects which scatter the charge carriers elastically.

Of particular interest is the transition from weak to strong localization which is observed in fluorine intercalated compounds by varying the fluorine content [60, 61]. Also, we find that by varying the fluorine content, one may, for a given pressure and temperature, transform a semimetal to a metal, to a poor electrical conductor, and finally to an insulator (Fig. 3.12). The degree of disorder is also increased with increasing fluorine content. During this profound concomitant change in geometric structure, electronic structure and consequent scattering modifications, the degree of localization is also modified from weak to strong. This combination is an unique situation in solid state physics. Recent measurements performed on graphene out of the bulk indicate also that profound structural and electronic modifications occur in fluorinated samples [62–65].

3.2.5 Summary

In this section we compare the electronic conduction properties of graphene in and out of the bulk. As in the case for GACs, electrons (holes) in SLG and FLG are confined in the graphene planes and behave as 2D or quasi-2D electron gases, respectively. The same dispersion relations are applicable to SLG and stage-1 GACs as well as to bilayer graphene (BLG) and stage-2 GACs, respectively. Stage-1 GACs and SLGs are both massless Dirac fermion systems.

The very high intrinsic mobility values observed in bulk semimetals are to be ascribed in part to the charge carrier small effective masses, and even more importantly to the ineffectiveness of electron-phonon interactions due to their small Fermi surfaces. However, in pristine HOPG, the mobilities are limited by boundary scattering at the limits (boundaries) of the crystallites and this effect is more pronounced in GACs, where the in-plane coherence length decreases after intercalation. The additional disorder introduced by intercalation limits the scattering length of the charge carriers and masks some of the effects which were recently observed in SLGs and FLGs. This disorder, however, allows the observation of 2D weak localization effects in GACs, where it is possible to control the disorder over wide ranges and, to a lesser extent, to control the de Broglie wavelength or Fermi Level. By contrast, in graphene out of the bulk (SLG and FLG) the use of transverse electric fields allows us to control the Fermi level and thus allows us to investigate weak localization effects as a function of a single variable. In this sense GACs and a combination of SLG and FLG provide complementary tools for the exploration of certain physical phenomena associates with transport in low-dimensional systems.

In Sect. 3.2 we have also shown that there exists other materials with mobilities comparable to those reported up to now for SLG and FLG. However, since in graphene out of the bulk, ballistic conditions could be realized, there is still room for improving charge carrier transmission across the graphene layers.

3.3 Thermal Conductivity of Graphene in and out of the Bulk

3.3.1 Preliminary Remarks

As stated in the general introduction, we will focus on the properties of the graphene layers in the pristine and intercalated bulk forms of HOPG and in this section we compare their thermal conductivities to those observed on a one layer graphene (SLG) or a few layer graphene (FLG) sample supported or suspended. We would like first to make three general remarks:

(1) The knowledge of the room temperature value of the thermal conductivity of a solid is important, especially when thermal management applications are envisaged. However, as is the case for other transport properties, the analysis of the

temperature dependence over a wide temperature range is important for gaining physical insights into the basic materials properties, especially regarding phonon transport when the thermal conductivity is concerned.

(2) When decreasing the size of a bulk material, the thermal conductivity decreases at low temperatures because of boundary scattering. Thus, the thermal conductivity of nanopowders and nanocrystalline bulk materials may be significantly lower than that of the bulk single crystal material, since phonons are scattered by the boundaries in all directions and their mean free path is thereby reduced. This does not happen in nanotubes or graphene. Owing to the reduced dimensionality, it is only the length which determines phonon boundary scattering for otherwise defect-free samples. Thus, long nanotube or graphene samples maintain, and often surpass, the thermal conductivity of bulk carbon.

(3) Thermal conductivity is usually one of the easiest transport properties to predict and analyze—especially in bulk carbons—and at the same time is one of the most delicate properties to measure correctly. This is particularly true for the case of nanoscopic systems. It is mainly due to the fact that heat flows are difficult to control and one has to make sure that the heat losses in the measuring system are not comparable, or even greater than the thermal conductance measurement of a nano sample. Thus, one must be very critical when examining the data in the literature and a reader must question the technique used in the experimental measurement. As a corollary, whenever possible, it is highly desirable to analyze the experimental data obtained on the same material with different measuring techniques and to compare the results thereby obtained. It is also helpful to check whether the magnitude of the thermal conductivity is consistent with the location of its so-called dielectric maximum (cf. Sect. 3.3.3.3).

3.3.2 Introduction

Recent experimental data on the room temperature thermal conductivity of suspended SLG and FLG graphene [66] have confirmed the exceptionally high thermal conductivity of an individual graphene layer that was previously predicted by Klemens [67, 68] before single layer graphene research started seriously. In his seminal work, Klemens calculations showed that isolated graphene sheets out of the bulk should have a thermal conductivity much higher than that of bulk graphite in-plane.

Recently, Nika and co-workers [69] proposed a model for the lattice thermal conductivity of graphene along the lines developed by Klemens. More recently, Ghosh et al. have measured the room-temperature thermal conductivity of suspended graphene layers [66] and found that it decreases from $\sim$ 2,800 to $\sim$1,300 W m^{-1} K^{-1} as the number of graphene sheets increases from 2 to 4.

In light of these results, we have revisited old results for κ pertaining to pristine HOPG and GACs [70] and have examined to what extent the data relative to the graphene sheets in the bulk are consistent with those obtained on monolayer and

few layer graphene (SLG and FLG). We show the observation of the thermal conductivity of supported graphene being relatively high, twice that of copper,[9] is not surprising at all if we consider the data obtained decades ago on bulk graphites and their intercalation compounds [5]. One might have expected from these old results that κ would indeed have such high values and perhaps even larger values.

After a short introduction to the mechanisms governing the thermal conductivity of solids, we then discuss in Sect. 3.3.3.4 the main results obtained in the past on bulk graphites and their intercalation compounds, and we compare them in Sect. 3.3.3.5 to those recently measured on SLG and FLG. We will also briefly discuss in Sect. 3.3.3.7 the thermal conductivity of carbon nanotubes.

3.3.3 Comparing the Thermal Conductivity of Graphene in and out the Bulk

3.3.3.1 Electronic and Lattice Conductivities

There are essentially two contributions to the transport of heat in solids [13, 71]: the electronic thermal conductivity, κ_E, which is due to the charge carriers, and the lattice thermal conductivity, κ_L, which is due to the phonons. In electrical insulators, heat is exclusively carried by phonons, while in pure metals it is the charge carriers that predominantly carry heat. Some values for the thermal conductivity of some selected materials at room temperature are given in Fig. 3.13.

As in the case of some heavily doped semiconductors, metallic alloys and group V semimetals, the lattice thermal conductivity of GICs may be comparable to the electronic contribution in GICs in certain temperature ranges. In general, the total thermal conductivity can be written as a sum of the electronic and lattice contributions (κ_E and κ_L):

$$\kappa = \kappa_E + \kappa_L \tag{3.14}$$

In principle, a high magnetic field, which decreases κ_E, may reduce κ_E to become insignificant with respect to κ_L, thereby allowing the separation of the two contributions.

[9]The common reference to copper, which is justified when we speak about practical applications, is meaningless when we consider the physics: one is comparing a material with the highest electronic thermal conductivity (copper) to the family of carbon materials with a low carrier density (diamond, HOPG, VDF, ...). Solid state physicists know that pure covalent materials have the highest lattice conductivities, which are often higher than the highest electronic conductivities. Also diamond and HOPG in-plane are known to be the best bulk thermal conductors. This high thermal conductivity might be understood qualitatively using a naïve mechanical picture: strong covalent bonding and light atoms favor the transmission of lattice vibrations.

Thermal Conductivity $Wm^{-1}K^{-1}$	Form of Carbon	Heat Treatment Temperature
> 3,000	Graphene	
> 3,000	Nanotubes	
2,000 – 2,500	Diamond	
~ 2,000	HOPG in-plane Vapor deposited fibers	> 3,000°C > 3,000°C
100 – 1,000	Pitch-derived fibers	> 3,000°C
450	Pure copper	
10	PAN-derived fibers	
< 10	Amorphous carbons	
0.1	Isotropic polymeric materials	

Fig. 3.13 Room temperature thermal conductivities of various carbons compared to copper and non oriented polymeric materials. All materials are pristine (undoped)

3.3.3.2 Electronic Thermal Conductivity

The electronic thermal conductivity is directly related to the electrical conductivity, σ, through the Wiedemann-Franz law [13, 71]:

$$\kappa_E = LT\sigma \tag{3.15}$$

In the temperature ranges where κ_E and κ_L depend on the same relaxation time, the Lorenz ratio, L, takes the value of the Lorenz number ($L = L_0 = 2.44 \times 10^{-8}\ V^2\,K^{-2}$). This applies for a degenerate free electron system which experiences elastic collisions with impurities and other static defects and above the Debye temperature when large angle intravalley electron-acoustic phonon interaction is dominant. In these situations, Eq. (3.15) allows computation of κ_E from the measured electrical resistivity.

κ_E is directly proportional to the electronic specific heat, C_E, to the Fermi velocity, v_F, which increases with the carrier density in 3D systems, and to the mean free path of the charge carriers, λ_E

$$\kappa_E = C_E v_F \lambda_E \tag{3.16}$$

At low temperature, where the electrical resistivity for metals is constant in the residual range, the electronic thermal conductivity, κ_E, of pure metals increases linearly with increasing temperature, then reaches a maximum as shown in Fig. 3.14, and the maximum is more pronounced for samples with less impurities and defects. For pure metal samples, κ_E decreases with increasing T, and then levels off at higher temperatures, where the electrical resistivity, which is due to large angle electron-phonon interactions, varies linearly with temperature. However, for samples with a high concentration of impurities or lattice defects, the linear increase may be directly followed by a temperature insensitive κ_E without the intermediate thermal conductivity peak [13, 71], as shown also in Fig. 3.14.

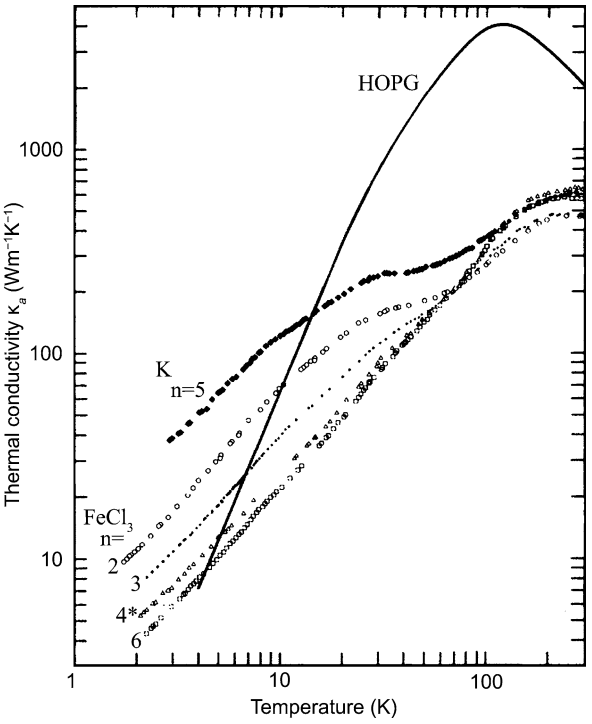

Fig. 3.14 Temperature variation of the in-plane thermal conductivity of GICs compared to that of pristine HOPG (*solid line*). Results are presented for pure stages: 2 (*open circles*), 3 (*dark circles*) and 6 (*open squares*), and a mixed 4* stage (*open triangles*) $FeCl_3$ acceptor GICs. Data for a stage-5 potassium donor intercalation compound are also presented (*dark squares*) (from [70])

3.3.3.3 Lattice Thermal Conductivity

The exceptionally large thermal conductivity observed in diamond and in HOPG in-plane at room temperature (Figs. 3.14 and 3.15) is due to the lattice. Naively, one may attribute this large κ to the small mass of the carbon atoms and the strong interatomic covalent forces which allow effective transmission of the vibrations and thus results in a relatively high lattice thermal conductivity. Any perturbation to the regular arrangement of carbon atoms in the lattice, such as defects or atomic vibrations, will give rise to scattering processes which decrease the thermal conductivity.

For a 3D solid, the lattice thermal conductivity κ_L is given by [13, 71]:

$$\kappa_L = \frac{1}{3}\sum_s \int_{\omega_0}^{\omega} c_s(\omega) v_s(\omega) \lambda_s(\omega) d\omega \tag{3.17}$$

where $c_s(\omega)d\omega$ is the contribution to the specific heat of phonons of polarization, s, and frequency, ω, in the range $\omega + d\omega$, $v_s(\omega)$ is the phonon velocity and $\lambda_s(\omega)$ is the phonon mean free path. The integral in (3.17) is taken from the lowest phonon frequency, ω_0, to the Debye cut off frequency, ω_D. The phonon mean free path $\lambda_s(\omega)$ is directly related to the phonon relaxation time, τ, through the relation $\lambda = v\tau$.

In the simplest form of (3.17), the Debye relation [13, 71]:

$$\kappa_L = \frac{1}{3} C v \lambda \tag{3.18}$$

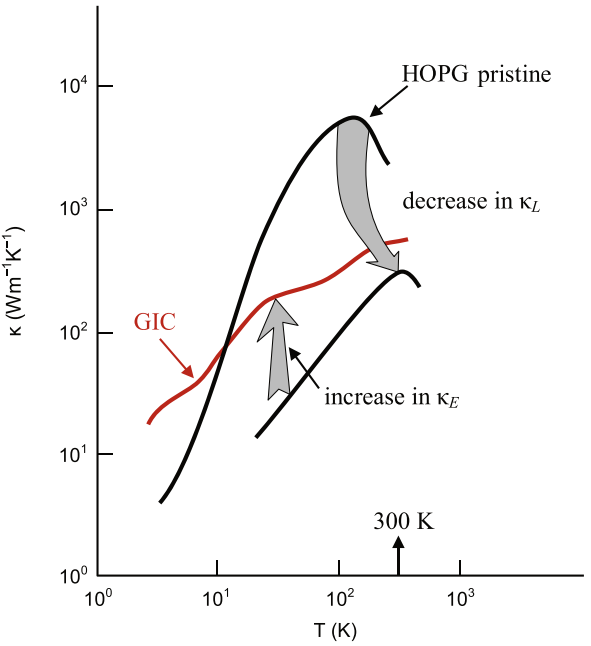

Fig. 3.15 Schematic representation of the effect of intercalation on the thermal conductivity of pristine graphites. Intercalation decreases the lattice thermal conductivity κ_L and increases the electronic thermal conductivity κ_E. The overall effect is a decrease of the thermal conductivity at high temperature and an increase at low temperature with respect to the pristine material (from [5])

can be used conveniently to discuss semi-quantitatively the experimental results for the thermal conductivity. In the dominant phonon mode approximation, we use an average phonon frequency, which is proportional to the absolute temperature ($\omega \sim k_B T$) and C in (3.18) is the lattice specific heat per unit volume and v is an average phonon velocity, which is approximated by the velocity of sound.

3.3.3.4 Graphene in the Bulk

At a given temperature, the thermal conductivity of carbons and graphites may vary by more than two orders of magnitude, according to their structural perfection [10]. HOPG and vapor deposited carbon fibers (VDF) heat treated at high temperatures are among the best bulk heat conductors around room temperature [72], exceeding 2,000 W m^{-1} K^{-1} (Fig. 3.13). The thermal conductivity above the liquid helium temperature range is entirely due to the phonons. In the lowest temperature range, the lattice thermal conductivity is mainly limited by phonon-boundary scattering and, as is the case for the electrical conductivity (cf. Sect. 3.2), the low temperature thermal conductivities are directly related to the in-plane coherence length, L_a. Since L_a varies according to the precursor and, more importantly, is highly sensitive to the heat treatment temperature (HTT), the higher is the HTT, the larger is the in-plane coherence length [10]. Furthermore, it was found that the phonon mean free path is almost equal to the in-plane coherence length [10] L_a. In fact the thermal conductivity behavior as a function of crystallite size, or in-plane coherence length,

is similar to that of the electrical conductivity illustrated in Fig. 3.1 and discussed in Sect. 3.1.

When boundary scattering is dominant, the phonon mean free path is independent of temperature. Since the velocity of sound is almost temperature insensitive, the temperature dependence of the thermal conductivity follows that of the specific heat. Thus, the larger is L_a, the higher is κ at a given temperature [9, 10]. For temperatures above that for the maximum in κ for GICs in Fig. 3.14, phonon scattering is largely due to intrinsic phonon-phonon umklapp processes, and the thermal conductivity should be the same for different well-ordered graphites.

Around the thermal conductivity maximum, scattering of phonons by point defects (small scale defects) becomes important. The position and the magnitude of the thermal conductivity maximum will thus depend on the competition between the various scattering processes (boundary, point defect, phonon). So, for different samples of the same material, the position and magnitude of the maximum depends on their specific point defect concentrations on L_a, since phonon-phonon interactions are assumed to be the same [9, 10] for different samples.

Intercalation dramatically modifies the thermal conductivity of pristine graphites [5, 70] (Figs. 3.14 and 3.15). Electronic conduction in GICs may contribute to heat transport well above the liquid helium temperature range, owing to the large increase in the charge carrier concentration in GICs due to charge transfer, especially at low temperatures where the lattice thermal conductivity of the pristine material decreases almost quadratically with temperature. Also, the fact that intercalation also introduces lattice defects leads to a decrease of the lattice thermal conductivity around the maximum. The overall effect is a decrease of the total thermal conductivity at high temperature and an increase at low temperature with respect to that of the pristine material [5, 70]. A schematic representation of the effect of intercalation on the thermal conductivity of pristine graphite is presented in Fig. 3.15.

Now let us consider the behavior of the graphene layers in a bulk graphene acceptor intercalation compound (GAC). First, if we consider pristine HOPG heat treated at high temperature, its in-plane room temperature thermal conductivity is around 2,000 $\mathrm{W\,m^{-1}\,K^{-1}}$ (Figs. 3.13 and 3.14), despite the fact that graphene planes are interacting in the bulk with their neighboring planes. In GACs the graphene planes interact with the intercalate planes for stage 1 and with intercalate planes and other graphene planes for higher stages. Second, the material which can be best compared to supported graphene is a GAC, since its graphene planes are sandwiched between two intercalate layers of different chemical compositions (Fig. 3.8). In GACs, heat is mainly transferred through the graphene layers at all temperatures, since the thermal conductivity of the intercalate layers was found to be negligibly small [73], except in a limited region at low temperature. In principle, GACs cannot be considered as a quasi-2D system for heat conduction, in contrast to the case of electrical conduction. Instead GACs are highly anisotropic thermal conductors, with anisotropy ratios κ_{in}/κ_{out} that are orders of magnitudes lower than for the electrical conductivity: GACs have an anisotropy ratio of around 500 for their thermal conductivity at room temperature, compared to 10^6 for their electrical conductivity σ_{in}/σ_{out}. However, when using the simplifying assumption that the contributions of the various

layers can be considered separately and added as conductors in parallel to give the total bulk conductivity, coherent results are obtained (as shown below), as for the case of the electrical conductivity. This assumption was validated by Klemens for pristine graphite on theoretical grounds [74].

Thus, intercalation of bulk graphites decreases the total thermal conductivity at high temperature and increases κ at low temperature with respect to that of the pristine material. Heat is mainly conducted by the graphene layers, though an extra contribution due to the intercalate phonons was obtained experimentally for a limited temperature range [73].

In GACs the highly conductive graphene layers are sandwiched between two electrically insulating and poorly thermally conducting layers. If we consider the case of a stage-2 $FeCl_3$-HOPG intercalation compound, a room temperature thermal conductivity of nearly 500 $W\,m^{-1}\,K^{-1}$ is observed for the bulk [70] (Fig. 3.14). This means that the thermal conductivity of the graphene layers in this compound should be much higher. Indeed, if, as was done for the case of the electrical conductivity (Fig. 3.8), we consider the various layers to be acting as conductors in parallel, we may express the measured thermal conductivity, κ, of a GIC of stage n in terms of that of graphene, κ_c, and of the intercalate, κ_i, as:

$$\kappa = \frac{d_i \kappa_i + n c_o \kappa_c}{I_c} \tag{3.19}$$

where

$$I_c = d_i + n c_o \tag{3.20}$$

is the c-axis repeat distance,[10] d_i, is the thickness of the $FeCl_3$ intercalate layer (0.606×10^{-9} m) and c_o is that of a carbon layer (0.335 nm). By neglecting the thermal conductivity of the intercalate layers with respect to that of the graphene, we may write:

$$\kappa = \frac{n c_o \kappa_c}{I_c}, \tag{3.21}$$

which gives a value for the thermal conductivity κ_c of the graphene sheet within the intercalation compound, which is roughly equal to 900 $Wm^{-1}\,K^{-1}$. The fact that in a typical GAC the graphene sheets have a thermal conductivity almost half that in the bulk pristine HOPG should be attributed to the phonon scattering length for large-scale defects, which is the boundary scattering length, λ_B. A previous study [70] has estimated the length λ_B for this GAC to be around 0.6 µm, while it is of the order of 1 to 15 µm for the bulk pristine HOPG host material. As was previously stated, these defects cannot be eliminated since they are inherent to the intercalation process. The great advantage of suspended graphene (SLG) is that it does not interact with other layers and can be obtained almost defect-free, thus providing direct information on the intrinsic properties of graphene. From the data reported in [70], an estimate was

[10]Note that I_c varies slightly with the stage of the compound, but the effect is too small to be taken into consideration in this context.

Table 3.1 Comparison of the variation of the thermal conductivity κ^* of the graphene layers as a function of the number of layers in and out of the bulk

Parameter	GAC Stage-2	GAC Stage-3	GAC Stage-6	HOPG	SLG	FLG-2	FLG-4
κ^*	470	480	560	2,000			
κ_{lattice}	340	400	480	2,000			
n	2	3	6		1	2	4
$I_c = d_i + nc_o$	1.28	1.61	2.62				
κ_c	895	769	729	2,000	5,000	2,800	1,300
λ_B	580	620	770				

κ^* total thermal conductivity measured on the bulk sample [70]

n = stage of the GIC or the number of graphene layers in FLG

I_c = c-axis repeat distance, in the intercalation compound

κ_c = thermal conductivity of graphene sheet in GIC

λ_B = mean free path for phonon-boundary scattering, which is equal to the in-plane coherence length L_a

The thermal conductivities are in units of $\text{Wm}^{-1}\,\text{K}^{-1}$ and I_c and λ_B are in units of 10^{-9} m

Data for the bulk material from is Issi, Heremans and Dresselhaus [70] while data for suspended graphene is from Ghosh et al. [66]

also made for the stage-3 and stage-6 compounds and the results are presented in Table 3.1. We have also included in Table 3.1 the data obtained on SLG and FLG-2 and FLG-4 for comparison [66]. As is the case for suspended graphene sheets [66], the thermal conductivity of a graphene sheet in the GAC decreases with increasing stage, i.e., with the number of graphene planes between the intercalate layers.

One should be cautious when making comparisons at a given temperature between samples of the same material with different defect structures. For HOPG at room temperature, we are, as regards the thermal conductivity, in the beginning of the high temperature range, i.e., a little above the temperature of the dielectric maximum, where the phonon-phonon umklapp processes start to dominate the thermal conductivity behavior. For $FeCl_3$ intercalation compounds, the dielectric maximum occurs at around 330 K and the thermal conductivity in this region is determined by the combined effects of various scattering processes, which are given here in order of decreasing importance: impurity, boundary and umklapp scattering processes. Note that the temperature of the maximum κ depends mainly on boundary scattering, while the magnitude of κ is mainly determined by point defect scattering (Fig. 3.15).

3.3.3.5 Graphene out of the Bulk (SLG and FLG)

Similar to bulk graphites and CNTs, the thermal conductivity of graphene is dominated by the lattice contribution κ_L. Micro-Raman spectroscopy-based techniques

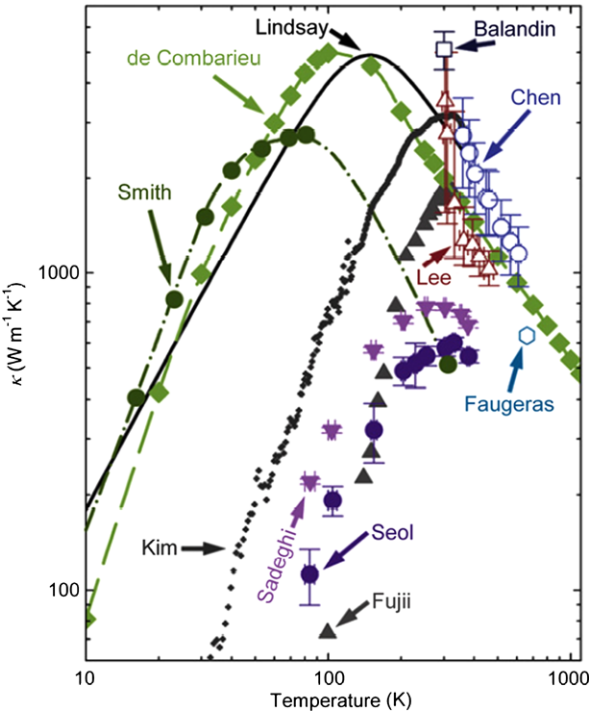

Fig. 3.16 Experimental thermal conductivity (κ) of SLG exfoliated from HOPG and suspended over a 2–5 μm trench reported by Balandin et al. [79], SLG exfoliated from natural graphite (NG) and suspended over a 44 μm diameter hole reported by Faugeras et al. [77], SLG grown by CVD and suspended over a 9.7 μm diameter hole reported by Chen et al. [78], SLG exfoliated from NG and suspended over a 6.6 μm diameter hole reported by Lee et al. [80], 9.5 μm long × 2.4 μm wide SLG exfoliated from NG and supported on SiO_2 reported by Seol et al. [88], and 12.4 μm long × 2.9 μm wide 8-layer graphene exfoliated from NG and supported on SiO_2 reported by Sadeghi and Shi [64]. Shown in comparison are the basal plane thermal conductivities of NG reported by Smith [89] and pyrolytic graphite reported by de Combarieu (*dash-dot* and *dashed lines* are visual guides to the eye) [76], a ∼14 nm outer diameter, 2.5 μm long suspended MWCNT synthesized by laser ablation reported by Kim et al. [81], a 16.1 nm outer diameter, 1.89 μm long suspended MWCNT synthesized by arc discharge reported by Fujii et al. [86], and the calculated κ for a 10 μm long suspended SLG by Lindsay for Seol et al. [88] (*solid line*). For Raman measurement results of graphene, the temperature is the hot side temperature measured by the Raman laser, instead of the average sample temperature used in other experimental and theoretical results. From: M.M. Sadeghi et al. [75]

and micro-resistance thermometry have been used to obtain the thermal conductivity of graphene, which was found to be in the range of 1500–5800 $Wm^{-1} K^{-1}$ for a suspended single layer graphene (SLG) (Fig. 3.16) and ∼600 $Wm^{-1} K^{-1}$ around room temperature for SLG supported by a SiO_2 substrate.

We present in Fig. 3.16 some values reported for the thermal conductivity of graphene obtained using optothermal techniques [75]. The values thus obtained are compared to the highest values reported for HOPG (de Combarieu [76] in Fig. 3.16).

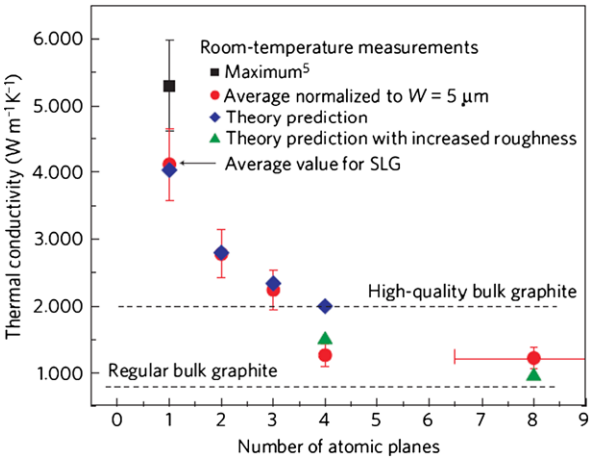

Fig. 3.17 Measured thermal conductivity as a function of the number of atomic planes in FLG. The *dashed straight lines* indicate the range of bulk graphite thermal conductivities. The *blue diamonds* were obtained from the first-principles theory of thermal conduction in FLG based on the actual phonon dispersion and accounting for all allowed three-phonon Umklapp scattering channels. The *green triangles* are Callaway–Klemens model calculations, which include extrinsic effects characteristic for thicker films [71]

It is worth noting that during the sample preparation of Faugeras et al. [77] and Chen et al. [78], the SLG was in contact with polymer resist residuals, which are difficult to remove and these residuals have been shown to strongly scatter phonons in suspended bi-layer graphene (BLG). In comparison, the graphene samples measured by Balandin et al. [79] and Lee et al. [80] were directly exfoliated onto the measurement device [75], and hence are expected to be relatively clean. However, one should be critical in comparing data because of the large experimental uncertainties associated with the experimental devices used and the large range of values reported for κ.

3.3.3.6 Graphene in and out the Bulk—Comparison

It is interesting to compare the behavior of the thermal conductivity of graphene in and out the bulk. In Table 3.1 we present the stage dependence of κ_{co}, the room temperature in-plane lattice thermal conductivity of the graphene layers in graphite-$FeCl_3$ intercalation compounds [70]. It may be seen that the thermal conductivity of the graphene layers in the bulk GAC decreases with increasing number of graphene planes between the intercalate layers. In Fig. 3.17, the measured thermal conductivity is presented as a function of the number of atomic planes in FLG [66]. Here also a decrease of the thermal conductivity is observed when the number of graphene planes increases. These observations are consistent with Klemens' theoretical predictions that the thermal conductivity of large enough single layer graphene sheets

Table 3.2 Experimental data for the room temperature thermal conductivity of carbon nanotubes CNTs

Sample	κ ($Wm^{-1}\,K^{-1}$)	Remarks	Reference
MNWT	>3,000	Individual, suspended	Kim et al. [81]
SWNT	3,400	Individual, suspended	Pop et al. [82]
SWNT	>1,750	Bundles	Hone et al. [83]
SWNT	>3,000	Individual, suspended	Yu et al. [84]
MWNT	300		Choi et al. [85]
	1,500–2,900	Individual	Fujii et al. [86]

should be higher than that of the basal planes of bulk graphite [67, 68]. The fact that in the case of FLG the thermal conductivities observed are much larger than in GACs should be attributed to the small in-plane coherence length and the presence of lattice defects in the graphene planes in GACs. Also, as stated above, the situation of graphene in GACS should be compared to that of supported graphene. Ghosh and co-workers [66] explain the evolution from two dimensions to bulk by the cross-plane coupling of the low-energy phonons and by the changes in the phonon Umklapp scattering with increasing layer number.

3.3.3.7 Carbon Nanotubes

Most of the reported room temperature values of the thermal conductivity of individual suspended carbon nanotubes (CNTs) range between 600–3,000 $Wm^{-1}\,K^{-1}$ for single and double-walled CNTs and between ~40–3,000 $Wm^{-1}\,K^{-1}$ for multiwalled CNTs. The large variations are generally ascribed to experimental uncertainties (heat losses and thermal contact resistances, for example), to CNT diameter determination uncertainties, and to differences in defect concentration arising from the different synthesis methods (see Table 3.2 and Refs. [81–86]). For multiwall carbon nanotubes (MWCNTs), the high temperature arc discharge and laser ablation methods yielded samples with the highest reported κ values. In Table 3.2, we present some published values for the thermal conductivity of CNTs, while in Fig. 3.18, a typical temperature dependence for the thermal conductivity of a carbon nanotube is shown [81]. Note that the general trend is the same as in bulk graphites and in graphenes (Figs. 3.14 and 3.16).

It was observed that the room temperature thermal conductivity of a CNT increases as its diameter decreases [86]. In Fig. 3.19 the room temperature thermal conductivity of individual multiwall carbon nanotubes of different diameters is presented [86]. The measured diameter-dependent thermal conductivity is ascribed to the interactions of phonons between multiwalled layers which affect the thermal conductivity. The thermal conductivity increases as the number of multiwalled layers decreases. A single-walled carbon nanotube is then expected to have the highest thermal conductivity, since the inter-tube phonon scattering effect is absent.

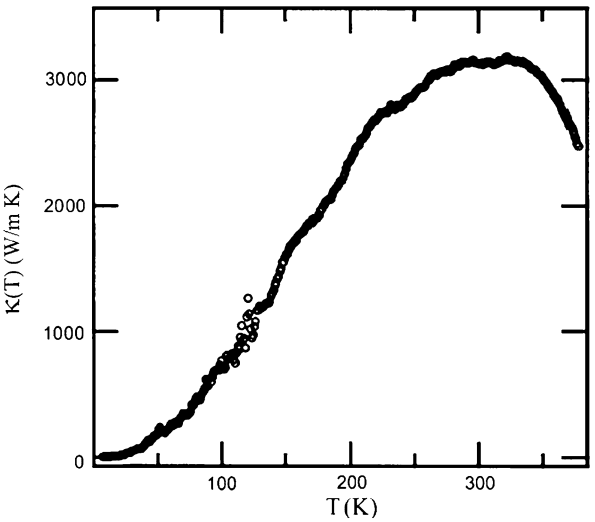

Fig. 3.18 Typical temperature dependence of the measured thermal conductivity of a nanotube [81]

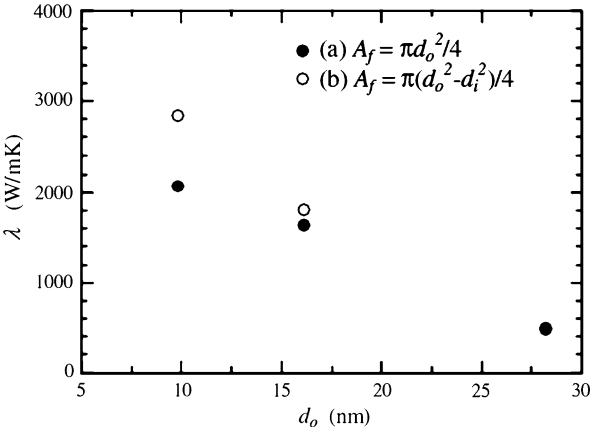

Fig. 3.19 Room temperature thermal conductivity of individual multiwall carbon nanotubes as a function of their diameter. Note that A_f stands for the carbon nanotube cross-sectional area, d_0 and d_i stand, respectively, for the outer tube diameter and for the inner-most diameter of the multi-walled tube structure [86]

Also, as is the case for the electrical conductivity, the thermal conductivity of nanotubes increases with increasing length [81, 87]. In the case of the thermal conductivity this could be ascribed to an addition of phonon modes, thus to an enhancement of the measured specific heat, and to an increase of the phonon mean free paths. Both effects lead to an increase in thermal conductivity (3.18). From theoretical works it appears that the present situation for MWCNTs is rather complex to analyze at this time.

3.3.4 Summary

After briefly introducing the mechanisms governing the thermal conductivity of solids, we have discussed above the main results obtained on bulk graphites and their intercalation compounds and we compare theoretical predictions to those recently measured on graphene (SLG) and FLG. We show that the qualitative behavior of graphene planes in and out of the bulk is the same, i.e., a decrease in the lattice thermal conductivity with increasing number of adjacent planes. However, the lattice thermal conductivity of graphene in bulk GACs is much lower than in SLG and FLG due to the limitation of the phonon mean free path by small- and large-scale lattice defects. This comparative study shows also that, though graphite is known to be the best bulk thermal conductor, there is little chance for further progress in bulk graphites, because of the limitations imposed by large-scale defects. By contrast, large area defect-free SLG and FLG still have large prospects for further increase of κ.

3.4 Inelastic Scattering of Light—Raman Scattering

3.4.1 A Brief Overview of Inelastic Scattering of Light

As stated earlier in the text, mostly due to the linear electronic dispersion relation observed in carbon structures, the inelastic scattering of light (well known as Raman scattering), has been shown to provide a particularly sensitive tool for understanding the electronic and vibrational properties of carbons and nanocarbons. Namely, resonant Raman scattering (RRS) is a fast, non-invasive and non-destructive experimental technique which, by means of first and second order scattering processes, allows us to study, for example, doping, disorder, thermal conductance, phonon self-energy renormalizations and phonon dispersions in nanocarbon systems. Indeed, phonons must be taken into account to properly explain many properties observed in carbon-based systems [90, 91]. More specifically, electron-phonon and phonon-phonon scattering mechanisms are fundamental to understanding relaxation processes governing the electronic and thermal properties [90, 91].

Briefly, the RRS process can be understood as follows: during a scattering event, (1) an electron is excited from the valence energy band to the conduction energy band by absorbing a photon, (2) the excited electron is scattered by emitting (or absorbing) phonons, and (3) the electron relaxes to the valence band by emitting a photon. We generally observe Raman spectra for the scattered photon (light), whose energy is smaller (called the Stokes process) by the phonon energy than that of the incident photon (note that if we were observing the scattered photon whose energy is larger by the phonon energy, we would be observing the called anti-Stokes process). By measuring the intensity of the Stokes scattered light as a function of frequency downshift (losing energy) of the scattered light, which is what is plotted in typical Raman spectra, we obtain an accurate measurement of the phonon frequencies of

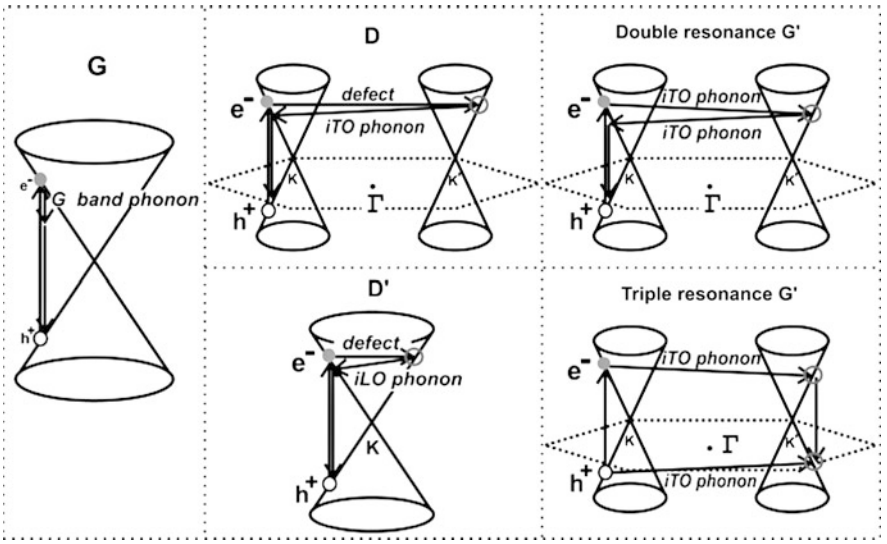

Fig. 3.20 (*Left*) First-order G-band process and (*Center*) one-phonon second-order DR process for the D-band (intervalley process) (*top*) and for the D′-band (intravalley process) (*bottom*) and (*Right*) two-phonon second-order resonance Raman spectral processes (*top*) for the double resonance G′ process, and (*bottom*) for the triple resonance G′-band process (TR) for monolayer graphene. For one-phonon, second-order transitions, one of the two scattering events is an elastic scattering event. Resonance points are shown as open circles near the K-point (*left*) and the K′-point (*right*) [91]

the material [90, 91]. It is important to note that every time the incident (scattered) light energy connects two real electronic states, the signal observed in the phonon spectra become very strong because of the resonance phenomenon that occurs in the presence of an external oscillating field.

As shown in Fig. 3.20, the order of a Raman scattering process will be defined by the number of phonons (and structural defects) involved. For example, if the scattering process involves just one phonon, the Raman process is of first order. However, if two phonons (or a combination of a phonon and a structural defect) are involved, the Raman process will be of second order. Both first order and second order processes will be of major importance to study carbon materials. Besides this, we can further classify the scattering process as an intravalley (AV) or an intervalley (EV) process. In the case of carbon materials, an AV scattering process occurs around the same high-symmetry K-point in the Brillouin zone, while in an EV scattering process, two inequivalent high symmetry K- and K′-points are involved (see Fig. 3.20).

Given this short introduction, we shall now understand how to interpret and extract information from the phonon spectra of carbon-based materials. Namely, there are two main features that are observable in almost all carbon based materials: the G-band (1583 cm^{-1}, which is a first order process (see Figs. 3.20 and 3.21) and the G′-band (or 2D-band) (2670 cm^{-1}), which is a second order process (see Figs. 3.20 and 3.21). When defects and impurities are present, a third defect-induced band,

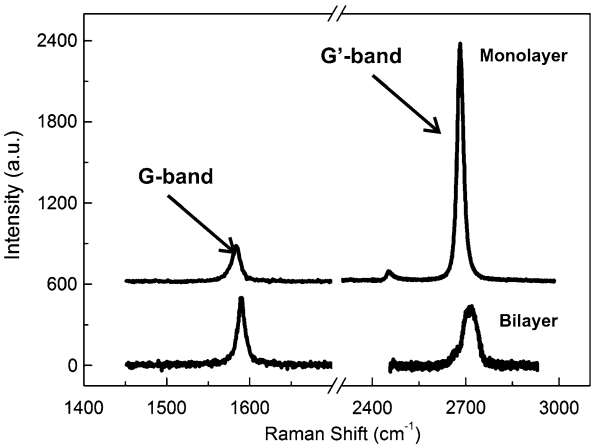

Fig. 3.21 (*Top*) the Raman spectrum showing the G- and G′ (or 2D)-bands. As experimentally observed, the G-band occurs around 1583 cm^{-1} while the G′-band occurs around 2670 cm^{-1}. (*Bottom*) the Raman spectrum showing the G- and G′-bands for Bi-layer graphene. The spectra were measured with a 532 nm laser line and the power density used was 1 $mW/\mu m^2$ [91, 98]

called the D-band, also appears. Like the G′-band, the D-band is also a second order process but the G′-band is symmetry allowed, but the D-band intensity requires symmetry-breaking phenomena. From now on, we will focus our discussion on these spectral features. In general, all of these features are somehow sensitive to dopants, stress, defects and impurities. However, each of them has been specifically used to fingerprint different phenomena, which will now be discussed further.

3.4.2 The G-Band Mode

The G-band mode [90, 91] is a first order Raman scattering process that comprises two degenerate optical phonon modes: the in-plane transverse optical mode (iTO) and the in-plane longitudinal optical mode (iLO). The peak frequency is observed from 1582 to 1585 cm^{-1} (for SLG, BLG, MLG and Graphite). In the case of carbon nanotubes, the iTO/iLO degeneracy is broken due to curvatures effects [91]. In carbon nanotubes the G-band has been extensively utilized to obtain information about the nanotube metallicity (metallic or semiconducting) as well as to obtain information about the nanotube diameter, since the nanotube diameter is inversely proportional to iTO G-band frequency for nanotubes (the reader should recall that the iTO mode will be vibrating along the nanotube circumference. As a consequence, if the circumference decreases, which increases the curvature of the tube, the iTO frequency will decrease).

However, it was with the rise of SLG graphene systems that the Raman G-band became strongly influential in providing evidence to show that we cannot describe graphene systems within the so-called adiabatic approximation [92–97] as well as to understand how this fact results in phonon self-energy corrections [92–97], which are very sensitive to the graphene density of electrons and holes. Namely, these phonon renormalizations occur any time we have an occupied (unoccupied) initial (final) electronic state, in the sense that an electron-hole pair can be created

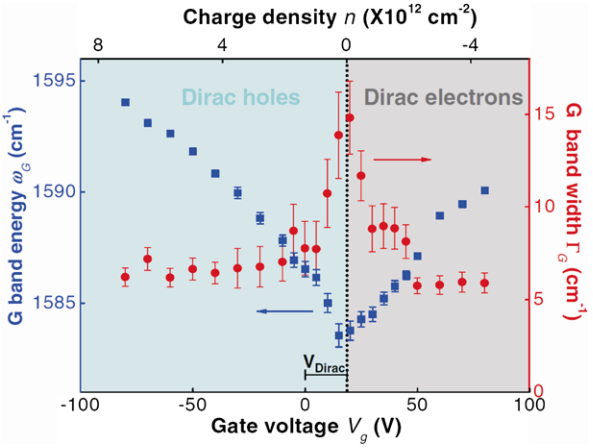

Fig. 3.22 G-band frequencies (*squares*) and G band linewidths (*circles*) extracted from the gate-modulated Raman experiments. The *vertical dotted line* is the approximate position of the charge-neutral Dirac point that is estimated from the symmetry of the data [97]

(annihilated) by a phonon absorption (emission) [92–97] and still conserve energy and momentum subject to symmetry selection rules. These renormalizations are extremely sensitive to the density of electrons and holes, and therefore, to the Fermi level energy E_F of the system. Strategies like doping graphene with foreign atoms (molecules) or the application of an electrostatic field through gate-modulated experiments were extensively applied [92–97]. Figure 3.22 shows the results of a gate-modulated Raman experiment [97]. As observed in this figure, the G-band frequency increases for both electrons and holes, while the spectral line width narrows with increasing $|E_F|$ [97].

Interestingly, the same results as in Fig. 3.22 are seen in Fig. 3.23 when doping graphene with Boron (p-type impurity) and Nitrogen (n-type impurity) atoms, as reported by Panchakarla et al. [99]. The impurities in this case are naturally introduced during the growth process and are, therefore, mainly substitutional. Basically these authors [99] report an asymmetric phonon renormalization of the G-band feature in which defects due to both n-type and p-type impurities result in a frequency upshift (note that the impurity concentration only changes the renormalization factor). Again, this hardening of the G-band is explained by means of the phonon self-energy in graphene within the non-adiabatic formalism, and its broadening is due to the absence or blockage of the decay channels of the phonons into forming electron–hole pairs [99]. However, the upshift rate shown in Fig. 3.23(b) is observed to be larger for p-doped samples in comparison to the n-doped monolayer graphene samples.

3.4.3 The G′-Band (or 2D) Mode

The G′-band (or 2D-band, which is a harmonic of the D-band) mode is a symmetry allowed intervalley (EV) second order Raman process accomplished by a combination of two iTO phonon modes around the K (K′)-point. The G′-band frequency

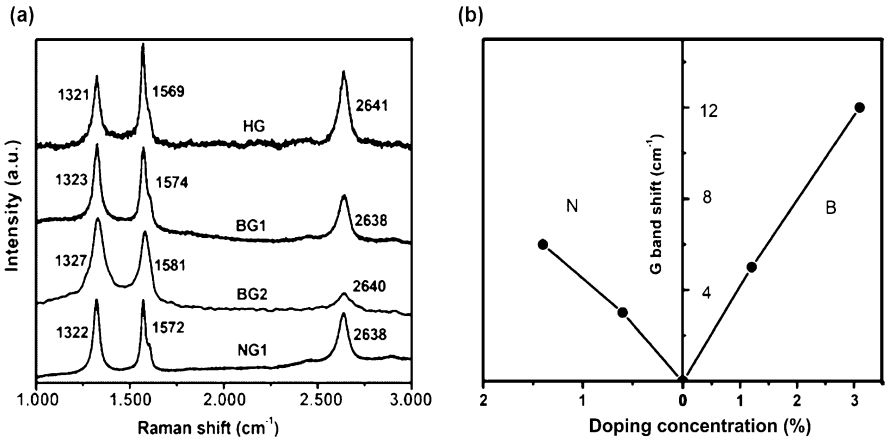

Fig. 3.23 (**a**) Raman spectra of undoped (HG), boron-doped (BG) and nitrogen-doped (NG) graphene samples. In (**a**) HG stands for undoped graphene, BG1 stands for 1.2 % boron doped graphene, BG2 stands for 3.1 % boron doped graphene and NG1 stands for 0.6 % nitrogen doped graphene. (**b**) G-band frequency shifts as a function of doping concentration caused by electron (N) doping (with pyridine) and hole (B) doping [99]

is laser energy (E_L) dependent so that the mode is known to be dispersive, showing a change in frequency with changing laser excitation energy E_L. In spite of the G′-band also being sensitive to both foreign dopants and electrostatic gating, the major usage of the G′-band spectrum has been to distinguish between the number of layers contained in a given graphene flake. This is possible because the G′-band is especially sensitive to the stacking order and to interlayer interactions in systems with 2 or more graphene layers [98]. As shown in Fig. 3.24, Raman scattering indeed provides a very straightforward approach to rapidly distinguish the different number layers in multi-layer graphene systems [90, 99]. It is worth commenting that recently it has been shown that the G′-band is also an efficient choice to decide whether a trilayer graphene is ABA-stacked (Bernal-stacking) or ABC-stacked (rhombohedral-stacking) [100] by observing the differences in the Raman G′ band frequency and lineshape.

3.4.4 The Disorder-Induced D-Band Mode

Carbon-based materials show a highly characteristic Raman feature called the D-band (the D denoting disorder-induced), which is a symmetry-breaking Raman peak that has no intensity in the absence of defects. Every time a given impurity breaks the translational symmetry of the carbon material's lattice, D-band intensity will appear in the Raman spectrum and its Raman scattering cross-section will be proportional to the defect concentration (see for example Fig. 3.23(a)). It is worth noting that not only can the D-band feature be used to understand defects in carbon materials, but

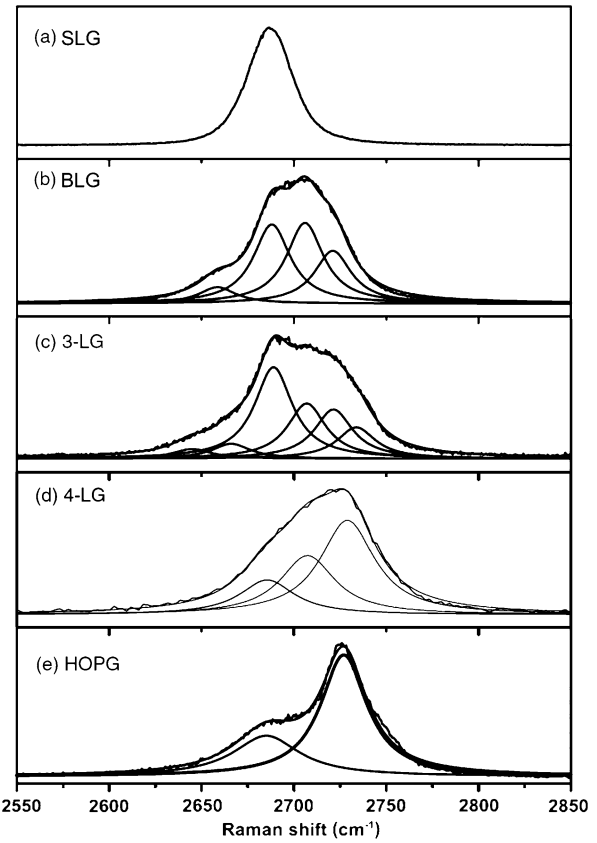

Fig. 3.24 The measured G′ (or 2D) Raman band with 2.41 eV laser energy for (**a**) monolayer graphene (1-LG), (**b**) bilayer graphene (BLG), (**c**) trilayer graphene (3-LG), (**d**) four layers graphene (4-LG), (**e**) HOPG and (**f**) turbostratic graphite. The splitting of the G′-band opens up in going from mono- to three-layer graphene and then closes up in going from 4-LG to HOPG [91, 100]

also the symmetry allowed G-band and G′ (2D) band in the Raman spectra provide valuable information about defects, especially when the impurity in question dopes the material by changing the bonding strength of the atomic species to the host carbon atoms [98].

Back in 1970, Tuinstra and Koenig [101] showed that the ratio between the D and G-band Raman intensities (I_D/I_G) is directly related to the crystallite size (L_a) of 3-D graphite. At that time, they explained their findings for only one excitation laser energy (E_L), namely, 514 nm (2.41 eV). More than 30 years later, in 2006, Cancado et al. [102] successfully extended the Tuinstra and Koenig findings to several E_L values and now the ratio I_D/I_G is more fully described by the equation:

$$\frac{I_D}{I_G} = L_a \frac{E_L^4}{560} \tag{3.22}$$

where L_a is given in nm, E_L is given in eV and the constant 560 is given in units of eV^4/nm. Although a general equation appeared through this scenario, a basic question still remained: whether the crystallite size L_a is a very special characterization parameter in graphite or would other types of symmetry-breaking features also follow a similar equation? The answer is, not exactly.

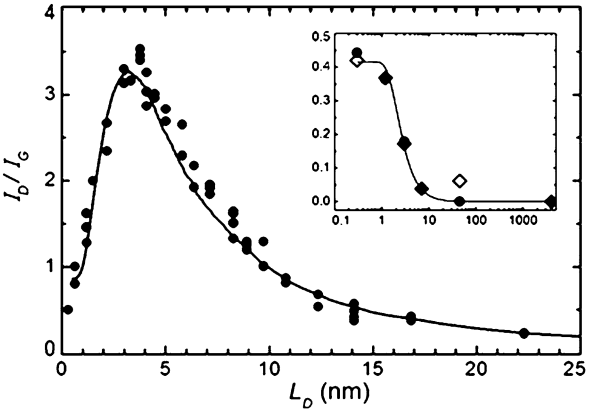

Fig. 3.25 The I_D/I_G data points from three different mono-layer graphene samples as a function of the average distance L_D between defects that are induced by the ion bombardment procedure. The *inset* shows the Raman intensity ratio I_D/I_G vs. L_D on a semilog scale for two graphite samples: (i) a ∼50-layer graphene sample found near one of the three mono-layer graphene samples (bullets); (ii) a bulk HOPG sample used for calibration (diamonds). The bulk HOPG values in the inset are scaled by $(I_D/I_G) \times 3.5$. The solid line is obtained from (3.23), where $C_A = (4.2 \pm 0.1)$, $C_S = (0.87 \pm 0.05)$, $r_A = (3.00 \pm 0.03)$ nm and $r_S = (1.00 \pm 0.04)$ nm [103]

In 2010, Lucchese et al. [103] used Raman scattering to study disorder in graphene caused by low energy (90 eV) Ar^+ ion bombardment. By varying the ion dose, these authors studied different densities of defects induced by the ion bombardment and were able to understand the evolution of the I_D/I_G ratio with ion dose (see Fig. 3.25). With this experiment, the authors provided a Raman spectroscopy-based method to quantify the density of defects in graphene, using HOPG (highly oriented pyrolytic graphite) for calibration. In Fig. 3.25 the density of defects due to different ion doses is probed by L_D, as given by (3.23), which denotes the average distance between defects. This study [103] revealed important information about the defect evolution by observing that I_D/I_G could be fitted by a phenomenological model for I_D/I_G vs. L_D [103]. The model considers that the impact of a single ion in the graphene sheet causes modifications on two length scales, here denoted by r_A and r_S (with $r_A > r_S$), which denote the radii of two circular areas measured from the incident ion impact point (the subscript A stands for "activated", whereas the subscript S stands for "structurally-defective"). Qualitatively speaking, only if the Raman scattering process occurs at distances smaller than $|r_A - r_S|$, will the corresponding "damaged" region contribute strongly to the D-band feature. Considering these assumptions in conjunction with statistical arguments, the I_D/I_G vs. L_D relation is given by [103]:

$$\frac{I_D}{I_G} = C_A \frac{r_A^2 - r_S^2}{r_A^2 - 2r_S^2}\left[e^{\left(\frac{-\pi r_S^2}{L_D^2}\right)} - e^{\left(\frac{-\pi (r_A^2 - r_S^2)}{L_D^2}\right)}\right] + C_S\left[1 - e^{\left(\frac{-\pi r_S^2}{L_D^2}\right)}\right] \qquad (3.23)$$

where C_A, C_S, r_A and r_S are adjustable parameters determined by experiment. The model is in conceptual agreement with a well-established amorphization trajectory

for graphitic materials [104]. Additionally, the results show that the broadly used Tuinstra and Koenig relation between I_D/I_G and L_a should be limited to the measurement of 3-D crystallite sizes. Recently, in 2011, Cancado et al. extended the proposed phenomenological model to be applicable to several laser lines [105].

3.4.5 Summary

In Sect. 3.4 a concise and tutorial discussion about inelastic scattering of light (Raman scattering) for the characterization of carbon materials was provided with particular emphasis to carbon nanomaterials, graphene, and carbon nanotubes. After introducing the basic concepts behind the Raman scattering phenomenon, a general discussion about the Raman G, G′ (or 2D), and D bands were made, in which for each of these features, a very focused discussion was given as regards the usage of these phonon modes to characterize electrons and phonon in carbon materials. Namely, the G-band is mostly used to gain insights about the phonon frequency and linewidth dependence on the Fermi level energy. The G′-band is mostly used to distinguish among the different number of layers and the stacking order in multi-layer graphene system [98]. Finally, the D-band is used to understand the effects caused by impurities and defects in nano carbon materials.

3.5 Conclusions

In this overview we mainly show how previous work on bulk carbons covering several decades has paved the way for finding some physical properties which were found later to be displayed in graphene out of the bulk. This mainly concerns the semiclassical and, more particularly, the quantum aspects of two-dimensional (2D) electronic transport and the behavior of phonons in low-dimensional covalently-bonded layered materials. Particular emphasis is placed on the obvious similarities and differences observed in the transport properties of SLG or FLG and those of stage-1 or higher stage graphite acceptor compounds (GACs). As regards electronic transport, we show that the same dispersion relations are applicable to SLG and stage-1 GACs as well as to double-layer graphene (DLG) and stage-2 GACs, respectively, and that since the beginning of the 1980s, the charge carriers in stage-1 GACs were considered as massless Dirac Fermions, as is the case for SLGs.

In pristine HOPG the mobilities are mainly limited by large-scale defect scattering and this effect is even more pronounced in GACs. The additional disorder introduced by intercalation is found to limit the scattering length of the charge carriers and to mask some of the effects which were recently observed in SLGs and FLGs. However, this disorder allows the observation of 2D weak localization effects in GACs. We observe too that the very high mobilities observed in graphene are by no means unique and that comparable values have been observed and reported in other semimetals and in 2D electron gases in semiconducting superlattices.

As regards phonon transport, we show that the qualitative behavior of graphene planes in and out of the bulk is the same, i.e., a decrease in the lattice thermal conductivity with increasing number of adjacent planes. However, the lattice thermal conductivity of graphene in bulk GACs is much lower than in SLG and FLG due to the limitation of the phonon mean free path by small- and large-scale lattice defects. These observations also clearly show the advantages of SLG and FLG over graphene in the bulk as regards their electron and phonon mean free paths. These are limited to around 10 micrometers for the highest quality HOPGs.

Finally, we briefly discussed the use of resonant Raman scattering (RRS) as a characterization tool, arguing that it is now recognized as a fast, non-invasive and non-destructive characterization technique which, by means of both first and second order scattering processes, allows us to study, for example, doping, disorder, phonon self-energy renormalizations and phonon dispersions in carbon systems. Such understanding was not available in the 1970s and 1980s, and the use of RRS at that time was much more limited. To understand phonons in solid-state materials (such as carbon-based ones) is very important since phonons must be taken into account to properly explain many properties observed in nanocarbon and other layered systems. Namely, electron-phonon and phonon-phonon scattering mechanisms are fundamental to understanding relaxation processes governing both the electronic and thermal properties of nanocarbons, as well as other related systems.

References

1. K.S. Novoselov et al., Science **306**, 666 (2004)
2. S. Mouras et al., Rev. Chim. Minér. **24**, 572 (1987)
3. A.W. Moore, A.R. Ubbelohde, D.A. Young, Proc. R. Soc. **280**, 153 (1964)
4. J. Blinowski, H.H. Nguyen, C. Rigaux, J.P. Vieren, R. LeToullec, G. Furdin, A. Hérold, J. Mélin, J. Phys. **41**, 47 (1980)
5. J.-P. Issi, in *Graphite Intercalation Compounds*, ed. by H. Zabel, S.A. Solin. Springer Series in Materials Science, vol. II (Springer, Berlin, 1992)
6. N. Daumas, A. Hérold, C.R. Séance Hebd, Acad. Sci. Paris C **268**, 373 (1969)
7. A.H. Castro Neto et al., Rev. Mod. Phys. **81**, 109 (2009)
8. A.K. Geim, Science **324**, 1530–1534 (2009)
9. J.-P. Issi, B. Nysten, Electrical and thermal transport properties in carbon fibers, in *Carbon Fibers*, ed. by J.-B. Donnet, S. Rebouillat, T.K. Wang, J.C.M. Peng (Marcel Dekker, New York, 1998)
10. B. Nysten, J.-P. Issi, R. Barton Jr., D.R. Boyington, J.G. Lavin, Phys. Rev. B **44**, 2142 (1991)
11. P.R. Wallace, Phys. Rev. **71**, 622 (1947)
12. H. Zabel, S.A. Solin, *Graphite Intercalation Compounds II*. Springer Series in Materials Science, vol. 18 (Springer, Berlin, 1992)
13. J.M. Ziman, *Electrons and Phonons* (Clarendon Press, Oxford, 1960)
14. B.T. Kelly, *Physics of Graphite* (Applied Science Publishers, London, 1981)
15. A.R. Ubbelohde, F.A. Lewis, *Graphite and Its Crystal Compounds* (Oxford University Press, Oxford, 1960)
16. S. Mrozowski, A. Chaberski, Phys. Rev. **104**, 74 (1956)
17. S. Mrozowski, Carbon **9**, 97 (1971)
18. A. Pacault, Carbon **12**, 1 (1974)

19. I.L. Spain, Electronic transport properties of graphite, carbons, and related materials, in *Chemistry and Physics of Carbon*, vol. 13, ed. by P.L. Walker Jr., P.A. Thrower (Marcel Dekker, New York, 1981), p. 119
20. P. Delhaes, A. Marchand, Carbon **3**, 115 (1965)
21. P. Delhaes, A. Marchand, Carbon **3**, 125 (1965)
22. P. Delhaes, *Carbon-Based Solids and Materials* (Wiley, Hoboken, 2011)
23. M.S. Dresselhaus, G. Dresselhaus, Adv. Phys. **30**, 139 (1981). Reprinted in 2002
24. A.K. Geim, K.S. Novoselov, Nat. Mater. **6**, 183–191 (2007)
25. N.M.R. Peres, J. Phys. Condens. Matter **21**, 323201 (2009)
26. D.R. Dreyer, R.S. Ruoff, C.W. Bielawski, Angew. Chem., Int. Ed. Engl. **49**, 9336 (2010)
27. M. Terrones et al., Nano Today **5**, 351 (2010)
28. A.A. Balandin, Nat. Mater. **10**, 569 (2011)
29. A.F. Young, P. Kim, Annu. Rev. Condens. Matter Phys. **2**, 101–120 (2011)
30. H.P. Boehm, Z. Naturforsch. **17b**, 150 (1962)
31. F.L. Vogel, G.M.T. Foley, C. Zeller, E.R. Falardeau, J. Gan, Mater. Sci. Eng. **31**, 261 (1977)
32. L. Piraux, J.-P. Issi, L. Salamanca-Riba, M.S. Dresselhaus, Synth. Met. **16**, 93 (1986)
33. J.-P. Issi, Transport in acceptor GICs: have our efforts been rewarded? Mater. Sci. Forum **91–93**, 471 (1992)
34. L. Piraux, J.-P. Issi, J.-P. Michenaud, E. McRae, J.-F. Marêché, Solid State Commun. **56**, 567 (1985)
35. J.L. Piraux, Mater. Res. **5**, 1285 (1990)
36. L. Langer, V. Bayot, E. Grivei, J.-P. Issi, J.P. Heremans, C.H. Olk, L. Stockman, C. Van Haesendonck, Y. Bruynseraede, Phys. Rev. Lett. **76**, 479 (1996)
37. E.H. Sondheimer, Proc. R. Soc. Lond. A **65**, 561 (1952)
38. J.-P. Issi, Electronic conduction, in *World of Carbon*, ed. by P. Delhaes (Gordon and Breach, London, 2001)
39. J.C. Slonczewski, P.R. Weiss, Phys. Rev. **109**, 272 (1958)
40. J.W. McClure, Phys. Rev. **108**, 612 (1957)
41. J.W. McClure, Phys. Rev. **119**, 606 (1960)
42. J. Blinowski, C.H.H. Rigaux, J. Phys. **41**, 667 (1980)
43. L.M. Malard et al., Phys. Rev. B **76**, 201401(R) (2007)
44. Z.Q. Li et al., Phys. Rev. Lett. **102**, 037403 (2009)
45. A.B. Kuzmenko et al., Phys. Rev. B **79**, 115441 (2009)
46. T.C. Chieu, M.S. Dresselhaus, M. Endo, Phys. Rev. B **26**, 5867 (1982)
47. L. Pietronero, S. Strassler, Synth. Met. **3**, 209 (1981)
48. X. Du, I. Skachko, A. Barker, E.Y. Andrei, Nat. Nanotechnol. **3**, 491 (2008)
49. M.S. Dresselhaus, J. Phys. Chem. Solids **32**, 3 (1971)
50. J.-P. Issi, Aust. J. Phys. **32**, 585 (1979)
51. R.N. Zitter, Phys. Rev. **127**, 1471 (1962)
52. R. Hartman, Phys. Rev. **181**, 1070 (1969)
53. J.-P. Michenaud, J.-P. Issi, J. Phys. C **5**, 3061 (1972)
54. S. Ilani, P.L. McEuen, Annu. Rev. Condens. Matter Phys. **1**, 1 (2010)
55. P.A. Lee, T.V. Ramakrishnan, Rev. Mod. Phys. **57**, 287 (1985)
56. G. Bergmann, Phys. Rep. **107**, 1 (1984)
57. V. Bayot, L. Piraux, J.-P. Michenaud, J.-P. Issi, Phys. Rev. B **40**, 3514 (1989)
58. B.L. Altshuler, A.G. Aronov, P.A. Lee, Phys. Rev. Lett. **44**, 1288 (1980)
59. H. Fukuyama, J. Phys. Soc. Jpn. **48**, 2169 (1980)
60. L. Piraux, V. Bayot, J.-P. Issi, M.S. Dresselhaus, M. Endo, T. Nakajima, Phys. Rev. B **41**, 4961 (1990)
61. M.S. Dresselhaus, M. Endo, J.-P. Issi, in *Chemistry, Physics and Applications of Fluorine-Carbon and Fluoride-Carbon Compounds*, ed. by T. Nakajima (Marcel Dekker, New York, 1995), p. 95
62. F. Withers, M. Dubois, A.K. Savchenko, Phys. Rev. B **82**, 073403 (2010)
63. X. Hong, S. Cheng, C. Herding, J. Zhu, Phys. Rev. B **83**, 085410 (2011)

64. S.-H. Cheng et al., Phys. Rev. B **81**, 205435 (2010)
65. K. Zou, J. Zhu, Phys. Rev. B **82**, 081407(R) (2010)
66. S. Ghosh et al., Nat. Mater. **9**, 555 (2010)
67. P.G. Klemens, J. Wide Bandgap Mater. **7**, 332 (2000)
68. P.G. Klemens, Graphite, graphene and carbon nanotubes, in *Proceedings of the 26th International Thermal Conductivity Conference and the 14th International Thermal Expansion Symposium*, ed. by R. Dinwiddie (2004). ISBN13: 978-1-932078-36-7
69. D.L. Nika, E.P. Pokatilov, A.S. Askerov, A.A. Balandin, Phys. Rev. B **79**, 155413 (2009)
70. J.-P. Issi, J. Heremans, M.S. Dresselhaus, Phys. Rev. B **27**, 1333 (1983)
71. R. Berman, *Thermal Conduction in Solids* (Clarendon Press, Oxford, 1976)
72. L. Piraux, B. Nysten, A. Haquenne, J.-P. Issi, M.S. Dresselhaus, M. Endo, Solid State Commun. **50**, 697 (1984)
73. B. Nysten, L. Piraux, J.-P. Issi, Synth. Met. **12**, 505 (1985)
74. P.G. Klemens, D.F. Pedraza, Carbon **32**, 735 (1994)
75. M.M. Sadeghi, M.T. Pettes, L. Shi, Thermal transport in graphene. Solid State Commun. **152**, 1321 (2012)
76. A. de Combarieu, Bull. Inst. Int. Froid. Annexe **2**, 63 (1965)
77. C. Faugeras, B. Faugeras, M. Orlita, M. Potemski, R.R. Nair, A.K. Geim, ACS Nano **4**, 1889 (2010)
78. S.S. Chen, A.L. Moore, W. Cai, J.W. Suk, J. An, C. Mishra, C. Amos, C.W. Magnuson, J. Kang, L. Shi, R.F. Ruoff, ACS Nano **5**, 321 (2011)
79. A.A. Balandin, S. Ghosh, W. Bao, I. Calizo, D. Teweldebrhan, F. Miao, C.N. Lau, Nano Lett. **8**, 902 (2008)
80. J.U. Lee, D. Yoon, H. Kim, S.W. Lee, H. Cheong, Phys. Rev. B **83**, 081419(R) (2011)
81. P. Kim, L. Shi, A. Majumdar, P.L. McEuen, Phys. Rev. Lett. **87**, 215502 (2001)
82. E. Pop, D. Mann, Q. Wang, K. Goodson, H. Dai, Nano Lett. **6**, 96 (2006)
83. J. Hone, M. Whitney, C. Piskoti, A. Zettl, Phys. Rev. B **59**, 2514(R) (1999)
84. C.H. Yu, L. Shi, Z. Yao, D.Y. Li, A. Majumdar, Nano Lett. **5**, 1842 (2005)
85. T.-Y. Choi, D. Poulikakos, J. Tharian, U. Sennhauser, Nano Lett. **6**, 1583 (2006)
86. M. Fujii, X. Zhang, H. Xie, H. Ago, K. Takahashi, T. Ikuta, H. Abe, T. Shimizu, Phys. Rev. Lett. **95**, 065502 (2005)
87. Z.L. Wang, D.W. Tang, X.B. Li, X.H. Zheng, W.G. Zhang, L.X. Zheng, Y.T. Zhu, A.Z. Jin, H.F. Yang, C.Z. Gu, Appl. Phys. Lett. **91**, 123119 (2007)
88. J.H. Seol, I. Jo, A.L. Moore, L. Lindsay, Z.H. Aitken, M.T. Pettes, X.S. Li, Z. Yao, R. Huang, D. Broido, N. Mingo, R.S. Ruoff, L. Shi, Science **328**, 213 (2010)
89. A.W. Smith, Phys. Rev. **95**, 1095 (1954)
90. M.S. Dresselhaus, G. Dresselhaus, R. Saito, A. Jorio, Phys. Rep. **409**, 45 (2005)
91. L.M. Malard, M.A. Pimenta, G. Dresselhaus, M.S. Dresselhaus, Phys. Rep. **473**, 51 (2009)
92. P.T. Araujo, D.L. Mafra, K. Sato, R. Saito, J. Kong, M.S. Dresselhaus, Phys. Rev. Lett. **109**, 046801 (2012)
93. D.L. Mafra, J. Kong, K. Sato, R. Saito, M.S. Dresselhau, P.T. Araujo, Phys. Rev. B **86**, 195434 (2012)
94. P.T. Araujo, D.L. Mafra, K. Sato, R. Saito, J. Kong, M.S. Dresselhaus, Sci. Rep. **2**, 1017 (2012)
95. M. Lazzeri, F. Mauri, Phys. Rev. Lett. **97**, 266407 (2006)
96. L.M. Malard, D.C. Elias, E.S. Alves, M.A. Pimenta, Phys. Rev. Lett. **101**, 257401 (2008)
97. J. Yan, E.A. Henriksen, P. Kim, A. Pinczuk, Phys. Rev. Lett. **101**, 136804 (2008)
98. A.C. Ferrari, J.C. Meyer, V. Scardaci, C. Casiraghi, M. Lazzeri, F. Mauri, S. Piscanec, D. Jiang, K.S. Novoselov, S. Roth, A.K. Geim, Phys. Rev. Lett. **97**, 187401 (2006)
99. L.S. Panchakarla, K.S. Subrahmanyam, S.K. Saha, A. Govindara, H.R. Krishnamurthy, U.V. Waghmare, C.N.R. Rao, Adv. Mater. **21**, 4726 (2009)
100. C.H. Lui, Z. Li, Z. Chen, P.V. Klimov, L.E. Brus, T.F. Heinz, Nano Lett. **11**, 164 (2011)
101. F. Tuinstra, J.L. Koenig, J. Phys. Chem. **53**, 1126 (1970)

102. L.G. Cancado, K. Takai, T. Enoki, M. Endo, Y.A. Kim, H. Mizusaki, A. Jorio, L.N. Coelho, R. Magalhaes-Paniago, M. Pimenta, Appl. Phys. Lett. **88**, 163106 (2006)
103. M.M. Lucchese, F. Stavale, E.H. Martins Ferreira, C. Vilani, M.V.O. Moutinho, R.B. Capaz, C.A. Achete, A. Jorio, Carbon **48**, 1592 (2010)
104. P.T. Araujo, M. Terrones, M.S. Dresselhaus, Mater. Today **15**, 98 (2012)
105. L.G. Cancado, A. Jorio, E.H. Martins Ferreira, F. Stavale, C.A. Achete, R.B. Capaz, M.V.O. Moutinho, A. Lombardo, T.S. Kulmala, A.C. Ferrari, Nano Lett. **11**, 3190 (2011)

Chapter 4
Optical Magneto-Spectroscopy of Graphene-Based Systems

C. Faugeras, M. Orlita, and M. Potemski

Abstract Recent results of magneto-absorption and Raman scattering studies of different graphene based systems are reviewed. The potential of these techniques to derive the band structure, scattering efficiency and effects of interactions is discussed in reference to studies of two representative allotropes of sp^2-bonded carbon: graphene and graphite.

4.1 Introduction

Graphene and its layered structures including graphite are usually classified as zero-bandgap semiconductors and/or semimetals [1, 2], and most naturally their properties are probed with electric conductivity measurements [3]. Indeed, our very first knowledge on graphite is that it is a strongly anisotropic (three dimensional) conductor [4] whereas the observation of the peculiar sequence of quantum Hall states (half-integer quantum Hall effect) is a fingerprint of the characteristic (two-dimensional) electronic states of graphene [5, 6]. What could be at first sight surprising is that optical spectroscopy has played and continues to play an important role in the research on graphene-based systems [7, 8]. Moreover, optical properties can also be decisive for a number of anticipated applications of graphitic layers, when, for example, they are used as saturable absorbers [9, 10], transparent conducting electrodes [11, 12] or plasmonic devices [13]. Notably, optical properties of graphene were a key ingredient to "see" the monolayer of carbon atoms deposited on Si/SiO_2 substrates through an optical microscope [14–18]—this was one of the unquestionable milestones in the development of the graphene oriented research. Optical spectroscopy of graphene based systems has developed today into a large area of research with many different directions. Raman scattering of phonons is one of the primary characterization tools of graphene materials [19–21] and also provides the relevant information on electron-phonon interaction in these materials [22–24]. Optical absorption is studied in a wide spectral range from far-infrared to

C. Faugeras · M. Orlita · M. Potemski (✉)
Laboratoire National des Champs Magnétiques Intenses, CNRS-UJF-UPS-INSA, 25, avenue des Martyrs, 38042 Grenoble, France
e-mail: marek.potemski@grenoble.cnrs.fr

H. Aoki, M.S. Dresselhaus (eds.), *Physics of Graphene*, NanoScience and Technology,
DOI 10.1007/978-3-319-02633-6_4,

the UV range. The experiments allow us to conclude about the characteristic doping (Drude-like free carrier absorption in the limit of low frequencies) and the specific band structure of the system studied (interband transitions in the infrared spectral range) [25]. More challenging are perhaps: the intriguing frequency independent (and given only by universal constants) optical absorption of graphene in a wide spectral range [26–28], the excitonic effects at high energies (related to van Hove singularities) [29–31] and possible modifications of the low frequency absorption response by electron-electron interactions (enhanced/suppressed Drude peak, plasmons) [32–35]. A large number of optical experiments are devoted to the studies of the dynamics of photo-excited carriers in graphene [36–45], which are closely related to possible application of graphene in optical devices. Interesting physics and also potential applications may follow the recent interest in the photo-conductivity response of graphene structures.

Optical spectroscopy appears to be a particularly forceful experimental tool to study electronic properties when it is combined with the application of magnetic fields. Primarily, this is because the application of a magnetic field significantly changes the character of the motion of a charge carrier (cyclotron motion) and/or induces a considerable modulation of the density of electronic states, including the appearance of discrete (and highly degenerate) Landau levels in the case of two-dimensional systems. When a magnetic field (B) is applied, the optical response becomes richer in resonances which notably can be tuned with the field strength. Very roughly speaking, the energies $E_n(B)$ of Landau levels (and in consequence the energies of cyclotron resonance and/or inter Landau level excitations) trace the dispersion relations $E(k)$ of the electronic states, following the approximate conjecture that $E_n(B) \propto E(k_n) = E(\frac{\sqrt{n}}{l_B})$, where n is an integer and $l_B = \sqrt{\frac{\hbar}{eB}}$ denotes the (characteristic) magnetic length. The Landau level spacing which, for example, scales as $B \cdot n$ is characteristic for parabolic bands whereas linear bands imply the $\sqrt{B \cdot n}$ scaling. Hence, Landau level spectroscopy provides, first of all, information about the band structure of the studied system. On the other hand, the analysis of the broadening of the magneto-resonances is often a relevant source of information about the efficiency of carrier scattering. The simple fact of observing the cyclotron resonance (at frequency ω_c and magnetic field B_0) already implies some estimate of the carrier scattering time (τ) and/or mobility (μ): $\omega_c \cdot \tau = \mu \cdot B_0 > 1$. Optical magneto spectroscopy is also a valuable tool to study the physics of interactions. This certainly concerns the electron-phonon interaction because of the convenient possibility to tune the electronic excitations (with the magnetic field) across the characteristic phonon energies. Furthermore, the magneto-optical response of an electronic system (in particular of a two-dimensional one) may also imply the effects of electron-electron interactions. One must however admit that those latter effects are most often hardly seen in the experiment. This can be understood when probing the electronic states with parabolic dispersion relations (optically active, zero momentum excitation are insensitive to electron-electron interactions) but remains surprising in the case of two-dimensional systems with linear bands.

As for the methods of optical magneto-spectroscopy, the typical magneto-absorption, essentially in the far-infrared and microwave spectral range, is the most

common technique applied to study graphene based materials. Pioneer magneto-absorption measurements provided a relevant input to understand the electronic properties of graphite already more than a half century ago [46, 47]. As shown in this paper, those measurements have been more recently applied to many other graphene based structures, providing valuable information on their band structure and on the scattering efficiency as well as some input to the physics of interactions in these systems. The methods of optical magneto-spectroscopy are complementary to other, for example, electric transport techniques widely applied to study graphene based materials. Optics appears to be obviously advantageous when structures cannot be contacted/gated or when they consist of multilayered material with different components (which can be spectrally resolved). So far, infrared magneto-spectroscopy studies have been mostly limited to simple absorption type measurements [7]. More information (particularly on the physics of the quantum Hall effect) can be deduced when investigating the response of graphene with Faraday rotation experiments [48], but only very first experiments towards this direction have been announced so far [49, 50]. A clear drawback of magneto-spectroscopy at long wavelengths is that it is hardly applied to small graphene flakes and that the polarization-resolved optics is also not very easy to handle in this spectral range. The methods of Raman scattering, in a visible optical range, becomes then advantageous. Notably, these are only very recent magneto-Raman scattering experiments [51, 52] which show the possibility to trace the electronic response (inter Landau level excitations) in graphene based structures [53, 54] using this technique. The results of these relatively new experiments are largely discussed here. High quality of the electronic system seems to be essential for tracing the electronic response in magneto-Raman scattering experiments but we believe this will be possible in case of many different graphene systems in the future.

The intention of this report is to present what can be learned from optical magneto-spectroscopy studies of graphene based materials. Our main focuses are two material systems: graphene (and/or graphene-like structures) and bulk graphite; and the results of two types of experiments: of the magneto-absorption at long wavelength (far-infrared and microwave range) and of the magneto-Raman scattering. Section 4.2 is devoted to graphene with the subsequent subsections focused on the aspects of the band structure, carrier scattering and the effects of interactions (essentially electron-phonon). Section 4.4, devoted to graphite, has a similar structure. Bilayer graphene is only briefly discussed (Sect. 4.3) since only few magneto-optical investigations of these system has been reported so far.

4.2 Magneto-Spectroscopy of Graphene

4.2.1 Classical Cyclotron Resonance of Dirac Fermions

Cyclotron motion of charge carriers and the related cyclotron resonance (absorption of light at the cyclotron frequency ω_c) is primarily a classical effect, probably the

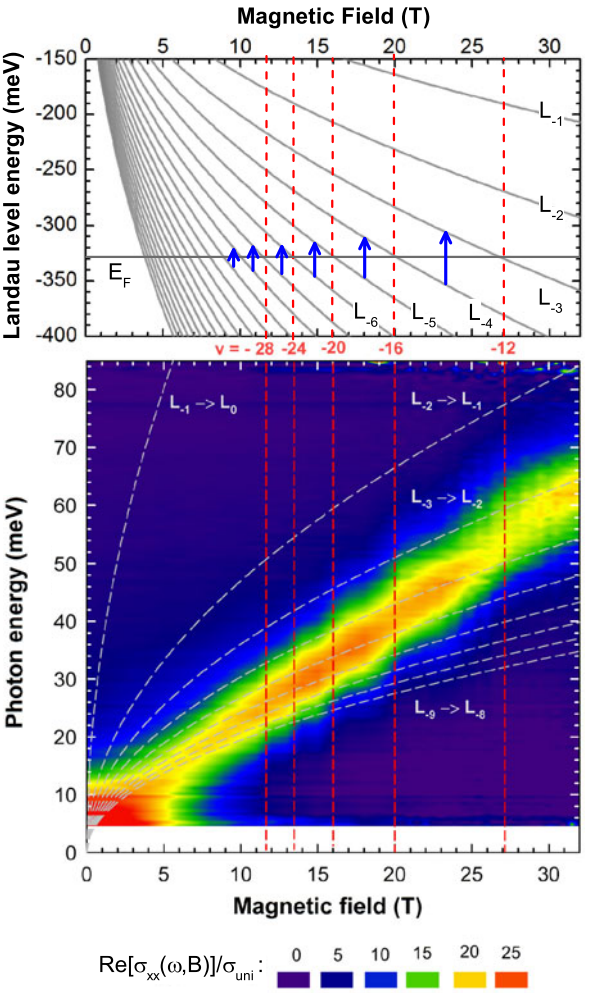

Fig. 4.1 *Upper panel*: Landau level fan chart with schematically-shown cyclotron resonance transitions in the quantum regime. *Lower panel*: A color plot of the real part of the experimentally determined longitudinal optical conductivity $\sigma_{xx}(\omega, B)$. The *dashed lines* correspond to transitions between adjacent (hole) Landau levels in graphene, $L_{-m} \rightarrow L_{-m+1}$. In both panels, a Fermi velocity $v_F = 0.99 \times 10^6$ m/s was considered to draw theoretical lines. Taken from Ref. [35]

most representative for magneto-optical spectroscopy studies. Importantly, the cyclotron motion is not only characteristic for a conventional charged (e) particle with mass m, which precesses with the frequency of $\omega_c = eB/m$, but also for massless Dirac fermions. The solution of the classical equation of motion for a charged particle with energy ε that depends linearly on momentum p ($\varepsilon = v_F p$), also results in the cyclotron motion but with a frequency $\omega_c = eB/(|\varepsilon|/v_F^2)$, in which one easily identifies the energy dependent mass $m = |\varepsilon|/v_F^2$. This latter expression, equivalent to the Einstein relation between mass and energy, invokes the relativistic-like character of electronic states in graphene. Perhaps surprisingly, the classical regime of the cyclotron resonance of graphene has been evidenced only recently [55]. This classical regime, characteristic of the linear in B cyclotron resonance (CR) absorption at low magnetic fields is illustrated in Fig. 4.1 with recent results obtained on

highly p-doped quasi-free standing epitaxial graphene on the silicon-terminated surface of silicon carbide. If the 2D translational symmetry of (highly-doped) graphene is broken either by the presence of specific disorder, or artificially, by lithographical patterning, effects of classical plasma dominate the optical response—CR is replaced by magneto-plasmon resonances [56, 57].

It is worth noticing that the classical CR absorption is accompanied by a Faraday-rotation effect, as demonstrated by Crassee et al. [49]. At higher fields, the quantum regime of CR is approached [35] and CR gains the characteristic $\sqrt{B}$ dependence, see Fig. 4.1. The related Faraday rotation is expected to be quantized in units of the fine structure constant [48], as indeed indicated in recent experiments [50]. Such a quantum regime of the magneto-optical response of graphene is described in the following section.

4.2.2 Magneto-Optical Response of Graphene: Quantum Regime

The specific electronic structure of graphene, namely the vanishing cyclotron mass in the vicinity of the Dirac point, implies a rather large spacing between Landau levels. A fully quantum-mechanical approach thus becomes necessary even in relatively low magnetic fields, if we deal with a weakly doped graphene specimen. In a quantum-mechanical picture, the application of the magnetic field B perpendicular to the graphene plane transforms the continuous electronic spectrum into discrete and highly degenerate Landau levels (LLs) [58]:

$$E_n = \mathrm{sign}(n) v_F \sqrt{2|e|\hbar B|n|} = \mathrm{sign}(n) E_1 \sqrt{|n|}, \quad n = 0, \pm 1, \pm 2 \ldots \tag{4.1}$$

which positions are defined by a single parameter, the Fermi velocity v_F ($E_1 = v_F\sqrt{2\hbar|e|B}$). The degeneracy of each Landau level is $\zeta(B) = g_v g_s |eB|/h$, where we take into account both spin g_s and valley g_v degeneracies. This LL spectrum consists of electron levels ($n > 0$), hole levels ($n < 0$) and a zeroth LL ($n = 0$) which is shared by both hole and electron types of carriers and which is responsible for the unusual sequence of the quantum Hall effect in graphene [5, 6]. We also immediately see that LLs in graphene are non-equidistant, they evolve as $\sqrt{B}$, see Fig. 4.2a, and both the spacing and the field dependence, can be understood as a consequence of the extreme non-parabolicity (in fact linearity) of the bands. The unusual $\sqrt{B}$-dependence of LLs is responsible for the surprising sensitivity of graphene electronic states to a magnetic field. Experimentally, well-defined LLs have been observed in this system down to 1 mT and almost up to the temperature of liquid nitrogen [59]. It might be realistic that Landau level quantization in pure graphene could also be observable in the magnetic field of the Earth ($B_{\mathrm{Earth}} \sim 10^{-5}$ T), which is unique for a condensed-matter system.

Interaction of light with graphene in a quantizing magnetic field has been explored extensively both theoretically and experimentally over the few past years [53, 59–73]. Graphene exhibits a relatively rich (multi-mode) magneto-optical response, where the energies of individual resonances correspond to the individual

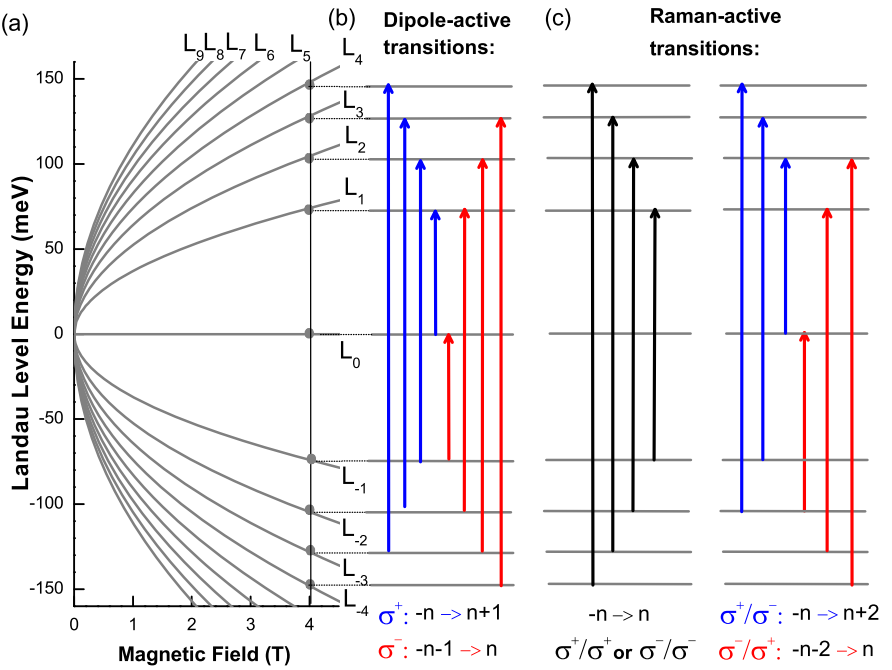

Fig. 4.2 (**a**) Characteristic $\sqrt{B}$-dependence of LLs in graphene shown for a few low-index levels. Dipole-allowed and Raman-active (Stokes branch) inter-LL transitions in undoped graphene are shown in parts (**b**) and (**c**), respectively

inter-LL transitions and scale as $\sqrt{B}$. This unique property of the Landau level spectrum is thus preserved in the magneto-optical response.

All dipole-allowed inter-LL transitions in graphene follow the selection rules $|n| \rightarrow |n| + 1$ and $|n| \rightarrow |n| - 1$, which are active in the σ^+ and σ^- polarizations of the incoming light [67, 69], respectively. These dipole-active transitions can be divided into three groups ($j \geq 1$): Inter-band resonances $L_{-j} \rightarrow L_{j+1}$ and $L_{-j-1} \rightarrow L_j$ at an energy $E_1(\sqrt{j+1} + \sqrt{j})$, intra-band resonances $L_j \rightarrow L_{j+1}$ and $L_{-j-1} \rightarrow L_{-j}$ at an energy $E_1(\sqrt{j+1} - \sqrt{j})$, and the mixed $L_{-1(0)} \rightarrow L_{0(1)}$ resonance, involving the $n = 0$ LL, which has an energy of E_1. Typical magneto-transmission data taken on quasi-neutral sheets of multilayer epitaxial graphene are shown in Fig. 4.3. The spectra are in this particular case dominated by the mixed mode $L_{-1(0)} \rightarrow L_{0(1)}$; nevertheless, a series of interband inter-LL resonances is also well resolved. Experimentally, this behaviour has been observed in multilayer epitaxial graphene with a characteristic rotational stacking of adjacent layers [62, 66, 67, 70, 71] and also in exfoliated graphene specimens [64, 68].

The intra-band transitions appear at low energies and are followed by inter-band resonances at higher energies. There is however no distinct separation in energy scale between these two types of transitions, which is in contrast to the case of conventional 2D systems based on gapped semiconductors, but somehow similar to the case of narrow-gap II/VI compound structures [74–77]. Nevertheless, in graphene,

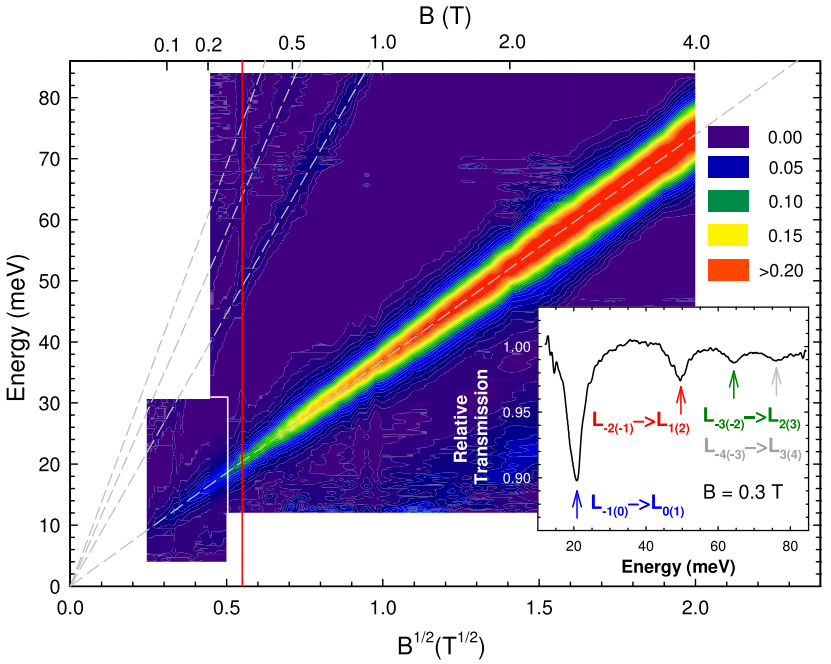

Fig. 4.3 Far infrared transmission $\mathcal{T}$ plotted as $-\ln\mathcal{T}$ as a function of the magnetic field at $T = 2.0$ K. The *dashed lines* denote the expected transitions for $v_F = 1.02 \times 10^6$ m s^{-1}. The *inset* shows the transmission spectrum at $B = 0.3$ T. Copyright (2008) by The American Physical Society

we deal with only one type of atomic orbital, and therefore both intra- and inter-band transitions follow similar selection rules: namely, the modulus of the LL index is changed by 1. This is again in contrast to the case of conventional 2D systems, made for instance from GaAs, for which the inter-band transitions conserve the LL index and their dipole moment is due to different s- and p-orbitals in the conduction and valence bands, respectively. Owing to the electron-hole symmetry of the graphene band structure, two different inter-band resonances, such as, for example $L_{-2} \rightarrow L_3$ and $L_{-3} \rightarrow L_2$ in Fig. 4.2b, may appear at the same energy. Such energy degenerated transitions are, however, active in opposite circular polarizations of light. At low temperatures one may expect at most two different intra-band transitions, but a series of inter-band transitions. The situation is even more complex at higher temperatures, when the thermal spreading of the Fermi distribution exceeds the separation between Landau levels. The intra-band absorption (CR) may then also reveal a multi-mode character, due to partial occupation of a few non-equidistant LLs curve depicts the thermal activation of $L_0 \rightarrow L_1$. Such a multi-mode intra-band absorption spectrum, with an envelop that corresponds, *nota bene*, to the classical cyclotron resonance, discussed at the beginning of this section, was recently observed in graphene (on the surface of bulk graphite) by Neugebauer et al. [59].

Inter-LL excitations visible in Raman scattering experiments follow different selection rules [53]. To indicate the different polarization configurations, we use the

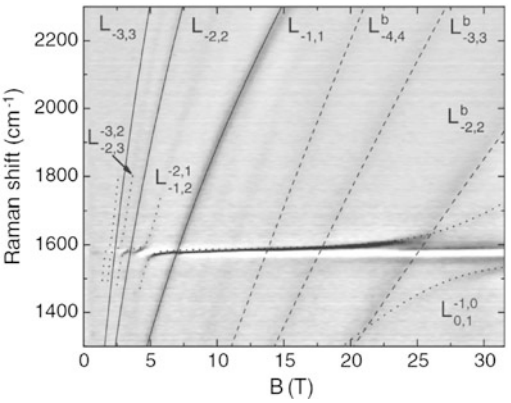

Fig. 4.4 Grey scale plot of the unpolarized scattered intensity as a function of the magnetic field measured on natural graphite specimens. The $B = 0$ spectrum has been subtracted from each spectra. Three different types of excitations are observed: *Solid* and *dotted lines* correspond to interband inter-LL excitations in decoupled graphene flakes on graphite. The latter are coupled with E_{2g} phonon line resulting in characteristic avoided crossing behavior. *Dashed lines* correspond to interband inter-LL excitations at the K point of bulk graphite. For details see Refs. [79] and [51]. Copyright (2011) by The American Physical Society

notation $\sigma_{Excitation}/\sigma_{Collection}$ where $\sigma_{Excitation}$ is the circular polarization of the excitation photon and $\sigma_{Collection}$ the one of the collected photon. The dominant contribution to the Stokes component of the Raman scattering spectrum is provided by transitions symmetric with respect to the $n = 0$ LL, $-n \rightarrow n$ with $n > 0$, see Fig. 4.2, that are visible in the so-called co-circular configuration, in which the in-coming and out-going photons keep the same circular polarization (σ^-/σ^- or σ^+/σ^+). These excitations have been detected in the Raman scattering spectra of graphene-like locations on the surface of bulk graphite and represent probably the first purely electronic excitation in graphene observed in Raman scattering experiments (see Fig. 4.4). It is worth noticing that more recently, a purely electronic Raman scattering signal has been also found in metallic carbon nanotubes [78]. The other (relatively weak) contribution, predicted to be active in the cross-circular polarization [53] (σ^+/σ^- and σ^+/σ^-) and following the selection rule $-n \rightarrow n + 2$ and $-n - 2 \rightarrow n$, respectively, see Fig. 4.2c, has not yet been observed experimentally.

4.2.3 Landau Level Fan Charts and Fermi Velocity

A clear illustration of the characteristic $\sqrt{|Bn|}$ scaling of Landau levels, in fact equivalent to the observation of linear dispersion relations of carriers, has been the first important feat of the Landau level spectroscopy of graphene systems [62]. Sadowski et al. [62] observed a practically perfectly $\sqrt{|Bn|}$-scaled Landau level fan chart in multilayer epitaxial graphene (MEG) structures and extracted the only scaling parameter—the Fermi velocity, $v_F = 1.03 \times 10^6$ m s^{-1}. Jiang et al. [64]

and subsequently Deacon et al. [68] found somehow higher values $v_F \approx 1.1 \times 10^6$ m s^{-1} for gated (exfoliated) graphene flakes on Si/SiO_2. We note that the Landau levels in MEG structures as well as in graphene flakes floating on the graphite surface have been also visualized using tunnelling spectroscopy in magnetic fields [80, 81]. The Fermi velocity found in these later STS experiments agrees well with the magneto-transmission data in the case of MEG structures [62, 71]. The STS experiments [80] on graphene flakes on graphite indicate a surprisingly low 0.79×10^6 m s^{-1} Fermi velocity in these systems in strike difference to the value of 1.00×10^6 m s^{-1}reported from microwave absorption measurements [59]. This contradiction might be due to a different renormalization of v_F seen by these two experimental probes, or perhaps due to a very local (and invasive) character of the STM tip.

4.2.4 Beyond Simple Band Models

Relatively small but noticeable deviations of the electronic bands from their ideal linearity, on the order of a few percent at large ± 0.5 eV distances from the Dirac point, have been found by a combination of far and near-infrared magneto-optical experiments performed on multi-layer epitaxial [70]. These deviations were revealed by a departure of the observed excitations from a simple $\sqrt{B}$-dependence, which increases with the photon energy of the probing light. No signs of the electron-hole asymmetry have been found in these experiments. On the other hand, traces of the electron-hole asymmetry have been reported by Deacon et al. [68] in exfoliated graphene placed on Si/SiO_2 substrate, who estimated the difference in the electron and hole Fermi velocities to be on the order of a few percent. Magneto-transmission experiments, if carried out on neutral graphene specimens, may also bring relevant information on a conceivable appearance of a gap at the Dirac point. Working in the limit of low magnetic fields, Orlita et al. have estimated a gap to be smaller than 1 meV in quasi-neutral MEG structures [71] and its maximum possible value of a fraction of 1 meV in graphene flakes on graphite substrates [59].

4.2.5 Scattering/Disorder

Cyclotron resonance measurements on graphene, in particular in the limit of low magnetic fields (and low frequencies), can be effectively used to estimate the scattering time and/or mobility of carriers. For instance, Orlita et al. [71] (working in fields down to 10 mT range) have shown (see Fig. 4.3) the possibility to achieve a room-temperature carrier mobility exceeding 250 000 cm^2/(V s) in multi-layer epitaxial graphene, which is a record value among all other known materials. Nevertheless, the dependence of the carrier mobility on the energy, i.e., on the distance from the Dirac point, was not determined. Recent line-shape analysis of interband inter-LL resonances in equivalent specimens allowed the authors to follow

the broadening of states as a function of energy. It was shown that the mobility is a parameter strongly dependent on energy (or carrier density) in the graphene system investigated [73]. This is in contrast with the behavior typical of exfoliated graphene specimens and points towards significantly different types of scattering mechanisms in quasi-neutral epitaxial graphene, most likely due to short-range scatterers [82]. Using also magneto-optical methods, a mobility of charged carriers exceeding 10^7 cm^2/(V s) up to the temperature of liquid nitrogen has been determined for high-quality graphene flakes on the surface of bulk graphite [59]. Even today, this observations sets a surprisingly high limit for the mobility of man made structures. For this particular, natural graphene system, the energy dependence of the scattering time and or mobility has not yet been clarified.

4.2.6 Electron-Electron Interaction

Since the discovery of graphene, the effects of electron-electron interaction were a subject of particular interest in this material. Nevertheless, a great majority of experimental results obtained on various graphene systems are fairly well understood within single electron models. This also concerns a number of magneto-transmission studies [59, 62, 70, 71]. Characteristically, they display a regular, defined by a single parameter v_F, series of transitions, which are thus very tempting to be assigned as those between single particle Landau levels. However, the excitations between highly degenerate Landau levels are known as nontrivial processes which involve the effect of electron-electron interaction. The corresponding electron-hole excitation is characterized by its wave vector (which is proportional to the electron-hole separation). The specific shapes of the dispersion relations for inter and intra Landau level excitations are central for the many-body physics of the integer [5, 6, 83] and fractional [84–86] quantum Hall effects, respectively. We know from this physics that, when considering a single parabolic band of a conventional two-dimensional electron gas (with equidistant Landau levels), the energies of optically active $k = 0$ inter-Landau level excitations correspond to those of single particle excitations. This can be viewed as a consequence of Kohn's (or Larmor's) theorem and can be seen as a result of the perfect cancellation of the Coulomb binding and exchange repulsion for the $k = 0$ electron-hole excitation. This reasoning does not hold for a 2D gas of Dirac electrons, for which the exchange term may even largely exceed the Coulomb binding, and in addition be different for different pairs of Landau levels. The apparent approximate validity of the Kohn's theorem in graphene is a surprising effect, and in our opinion calls for further clarifications of the theoretical background. The first theoretical works dealing with this problem have been already published [87–89]. We note, however, that there are small (within the line width) but noticeable deviations from a perfect single particle scaling of inter Landau level excitations that have been already reported in experiments on exfoliated graphene structures [64]. Recently, Henriksen et al. [72] have reported changes in the energy of the $L_{-1(0)} \rightarrow L_{0(1)}$ transition, which is especially pronounced at high magnetic fields, when tuning the Fermi energy in between $n = -1$

and $n = 1$ Landau levels. Both these observations [64, 72] are discussed in terms of electron-electron interactions but perhaps they also include some effects of disorder [90]. Notably, magneto-optics allows for probing the nature of quasi-neutral graphene in high magnetic fields (a possible appearance of a gap in the zero LL at a filling factor of zero), which became a subject of many theoretical considerations and experimental works, see, e.g., [91, 92]. Visualization of the strong Fermi velocity enhancement [93], observed recently near the Dirac point in free-standing neutral graphene by the magneto-transport technique, is another task for infrared magneto-spectroscopy. Magneto-optical experiments performed on graphene specimens with similar quality and carrier density (decoupled graphene flakes on graphite) [59] do not show this behavior, probably as a result of strong screening effects induced by the underlying substrate.

4.2.7 Effects of Electron-Phonon Interaction

The effective coupling of optical phonons (E_{2g}) to electronic excitations in graphene yields a particularly remarkable (resonant magneto-phonon) effect when the E_{2g} phonon response is investigated as a function of the magnetic field applied across the layer [94, 95]. Then, the E_{2g} phonon is expected to hybridize with the selected $L_{n\to m}$ inter Landau level excitations. In consequence, the ample magneto-oscillations in the phonon response (in disordered systems) [79] and/or a series of avoided crossing events (in cleaner systems) [51, 96] can be observed in Raman scattering experiments. So far, an increasing number of graphene-based systems such as quasi-neutral graphene-like systems: epitaxial graphene [79], doped exfoliated graphene [97] together with the circular dichroism associated with circularly polarized phonons and a non-zero Fermi energy, in quadrilayer graphene [98], bulk graphite [52] and graphene locations on graphite surface [51, 96, 99], have shown the clear magneto-phonon resonant effect. The amplitude of this effect depends on the electron-phonon coupling constant, on the oscillator strength of the inter LL excitation, which includes matrix elements and occupation factors of the initial and final state LLs and certainly on the quality of the electronic system investigated. As for today, the most pronounced magneto-phonon effect is observed for the high quality graphene locations on a graphite substrate. This is illustrated in Fig. 4.5 with the results of recent polarization resolved magneto-Raman scattering studies of such locations on a graphite substrate. As expected from theory [94, 95] the E_{2g} phonon, observed in the σ^+/σ^- (or σ^-/σ^+) configuration of the excitation/scattered light, hybridizes with the specific asymmetric $L_{n,m}$ excitations with $|n| - |m| = \pm 1$. The appropriate analysis of the hybrid modes yields the characteristic value of $\lambda = 4.4 \times 10^{-3}$ for the electron-phonon coupling in the system investigated. Surprisingly, however, experiments show that the E_{2g} phonon of graphene on graphite couples not only with asymmetric excitations but also with other inter Landau level excitations: $L_{-n,n}$ and $L_{0,2}$. These theoretically unexpected effects remain to be clarified and could possibly be related to the particular structure of

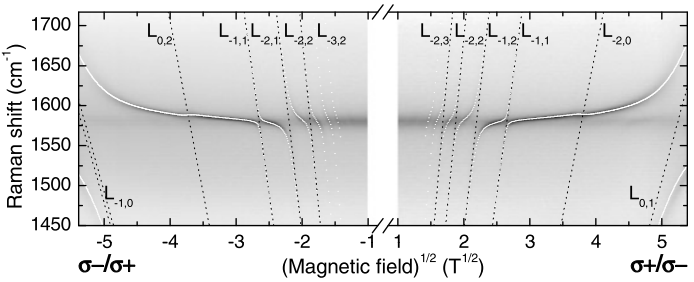

Fig. 4.5 (From Ref. [99]) Magneto-Raman scattering response: Intensity false color plot where *black* (*white*) corresponds to high (low) intensity. *Black dotted lines* are the energies of the inter-LL excitations that interact with the zone-center E_{2g}-phonon. *White lines* are the calculated hybrid electron-phonon mode energies including optical-like excitations, symmetric excitations and the $L_{0,2}$ excitation, with the parameters given on the right side. Copyright (2012) by The American Physical Society

graphene-like locations on graphite, as they were not observed in multilayer epitaxial graphene [79]. Another manifestation of electron-phonon interaction has been recently found in CR experiments on MEG structures, where a clear coupling of CR line with K point phonons has been demonstrated [100].

4.3 Magneto-Spectroscopy of Bilayer Graphene

Bernal-stacked (AB) bilayer graphene, with its nearly parabolic bands near the charge neutrality point, might provide us with a more conventional magneto-optical response as compared to graphene. Nevertheless, bilayer graphene with its zero-gap band structure and a chiral character of massive Dirac fermions carriers still exhibits a behavior that is distinctively different from other semiconducting materials.

The simplest quantum-mechanical approach to the Landau levels, originally used to interpret magneto-transport data on bilayer graphene [101], takes account of two-bands with a parabolic profile. It implies a spectrum of LLs that is linear in B [102], see Fig. 4.6a:

$$E_n = \pm\hbar\omega_c\sqrt{n(n-1)}, \quad n = 0, 1, 2, \ldots, \tag{4.2}$$

and in the limit of high n (practically even for $n > 2$), the LL spectrum (4.2) has the form $E_n \approx \pm\hbar\omega_c(n + 1/2)$, typical of conventional massive particles. The $n = 0$ and $n = 1$ levels becomes degenerate and thus form a zero-energy level with an eight-fold degeneracy and this results in a characteristic quantum Hall effect with the Berry phase of 2π [101, 102]. Dipole-allowed transitions in bilayer graphene, active in this simplest approach, follow the selection rule $|n| \rightarrow |n| \pm 1$ [69] seen in Fig. 4.6b. Raman-active modes fulfill a different set of selection rules, depending on the circular polarization of the incoming and outgoing light [54], as shown in Fig. 4.6c.

Two independent measurements have been performed up to now—on exfoliated flakes of graphene bilayer [103], and subsequently, on bilayer graphene that

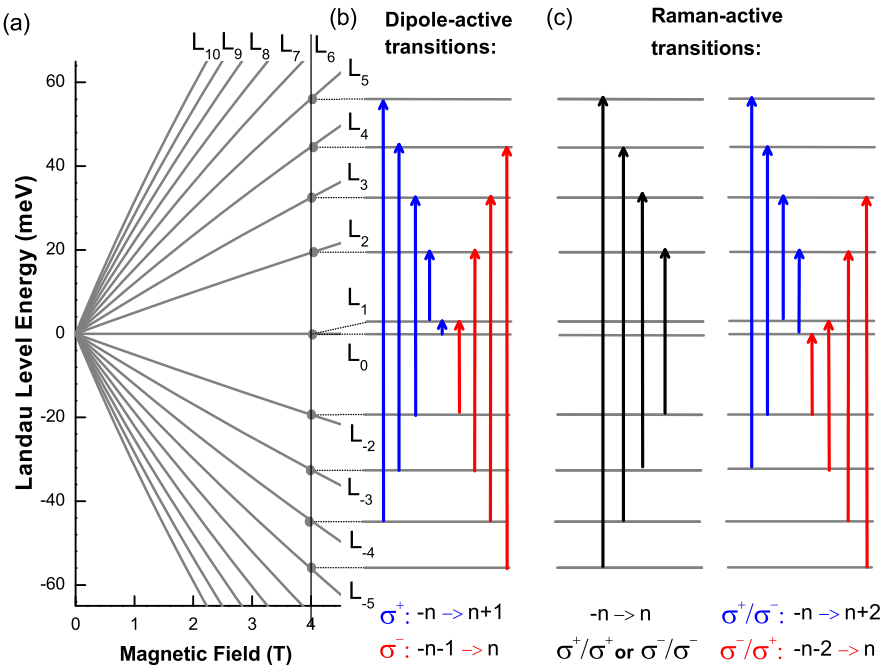

Fig. 4.6 Part (**a**): LLs in graphene bilayer, evolving nearly linearly with B at lower fields, but bending to sub-linear dependence at higher B and/or higher energies. Parts (**b**) and (**c**): Schematic plot of dipole-allowed and Raman-active inter-LL excitations in bilayer graphene

is present in a form of inclusions inside multilayer epitaxial graphene with the prevailing rotational stacking of adjacent layers [104]. The first study focuses on the intra-band response, i.e., on the cyclotron resonance of massive Dirac fermions (see Fig. 4.7a), and the second work deals with the interband inter-LL transitions (see Fig. 4.7b). In both cases, a clear departure of the optical response from a linear in B behavior has been reported, and therefore, the above theoretical model can provide a qualitative explanation only. A reasonable quantitative agreement is achieved if the LL spectrum is calculated within the four-band model. In the case of gated exfoliated flakes [72], the potential drop between layers induced by the back-gate has to be properly considered [105, 106].

Due to the lack of experimental data, a number of theoretical predictions for the magneto-optical response of bilayer graphene is still awaiting experimental verification [107–109]. These predictions involve, for instance, the appearance of the optically active transition within the zero-energy Landau level [109], corresponding to the splitting of $n = 0$ and $n = 1$ levels seen in Fig. 4.6a. Low-magnetic-field experiments in the microwave range should be a sensitive tool to study the Lifshitz transition in bilayer graphene. It is the trigonal warping, which at low energies transforms the nearly parabolic bands in bilayer graphene into four disconnected Dirac cones and changes thus significantly the topology of the band structure [69, 102, 110].

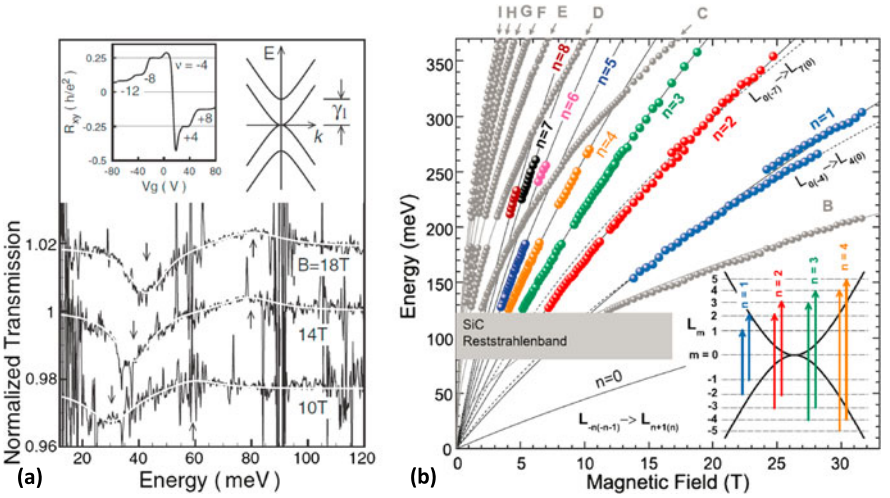

Fig. 4.7 Part (**a**): Cyclotron resonance absorption in exfoliated bilayer graphene. Taken from [103]. Copyright (2008) by The American Physical Society. Part (**b**): Fan chart of transitions observed in multi-layer epitaxial graphene. Transitions related to AB-stacked bilayer graphene inclusions are denoted by indices n and schematically depicted in the *inset*. Taken from Ref. [104]. Copyright (2011) by The American Physical Society

A new set of inter-Landau level excitations is also predicted to be active in Raman experiments [54]. Perhaps surprisingly, part of these predictions can be verified using another system, bulk graphite. As discussed in the next part, this material, namely at the K point of the band structure, shares the same single-particle Hamiltonian with bilayer graphene [111, 112].

4.4 Graphite

The renewed interest in the properties of bulk graphite is a direct consequence of the outbreak of current graphene physics. As a 3D crystal, graphite is a system characterized by a higher degree of complexity compared to graphene; nevertheless, both materials share many common properties. The appealing possibility of tracing the relativistic carriers not only in graphene monolayer and bilayer but also in bulk graphite resulted in a number of works which offer new pieces of information, new interpretations of old data, but unfortunately, often also rediscoveries of well-established prior knowledge [113].

4.4.1 Simplified Models for the Band Structure

As discussed in the preceding sections, optical spectroscopy combined with high magnetic fields can provide a unique insight into the band structure of graphene

based systems. Bulk graphite, graphene sheets in a Bernal type of stacking, is characterized by a 3D band structure defined on its 3D hexagonal Brillouin zone. A conventional description of the band structure of bulk graphite and its evolution with the magnetic field relies on the SWM model with seven $\gamma_0, \ldots, \gamma_5, \Delta$ tight binding parameters [114–116]. This model has been used to describe most of the data obtained from magneto-transport [4, 117–119], infrared magneto-reflectivity [47, 120–122], and magneto-transmission [112, 123, 124] experiments. It predicts the existence of massive electrons near the K point with a parabolic in-plane dispersion and of massless holes near the H point with a linear in-plane dispersion. Under an applied magnetic field, Landau bands are formed with a continuous dispersion along k_z, the wave vector measured in the units of the inverse inter-layer spacing, from equally spaced and linear in B Landau levels at the K point ($k_z = 0$) to non equally spaced and $\sqrt{B}$ evolving Landau levels at the H point [116] ($k_z = \pi/2$). Even though there is still no consensus concerning the precise values of the SWM parameters, mainly because of the different energy range probed in different experiments and because of the lack of polarization resolved measurements, the validity of the SWM model is generally accepted.

Instead of the full SWM model, it is often sufficient to use the effective two-parameter model [111, 125] (so-called "effective bilayer" model), which describes parabolic dispersion in the plane with the curvatures evolving along k_z. This model is obtained by (i) considering only the two first SWM parameters γ_0 and γ_1, the intra-layer and the inter-layer nearest-neighbor hopping integrals, respectively, and (ii) projecting the resulting k_z-dependent 4×4 Hamiltonian on the two low-energy bands. The Hamiltonian can be identified, at each value of k_z, to that of a graphene bilayer determined by the effective parameters γ_0 and $\gamma_1^* = 2\gamma_1 \cos k_z$. As a consequence, for $k_z = 0$ (corresponding to the K point), γ_1^* is twice enhanced with respect to γ_1 describing the real graphene bilayer. The Landau level fan chart with Landau level indices, together with dipole-allowed excitations and Raman scattering selection rules, is presented in Fig. 4.6. The electronic properties of the K point carriers in graphite are hence very similar to those of bilayer graphene.

The effective, two-parameter parabolic model has been proven to bring a fair frame to describe magneto-absorption experiments [112, 124]. It can be refined, as done in Ref. [124], by (i) introducing two different effective mass values describing positive and negative energy states, to reproduce electron-hole asymmetry, (ii) introducing a splitting of the lowest Landau level to reproduce the low energy Landau level structure of bilayer graphene and of bulk graphite. Figure 4.8a shows the results of such an analysis on magneto-absorption measurements performed on bulk graphite (from Ref. [124]). An excitation with a $\sqrt{B}$ evolution involving massless holes at the H point is observed (line A in Fig. 4.8a) together different linear in B excitations involving massive electrons at the K point. The effective two-parameter parabolic model describes most of the observed behaviors in the low magnetic field and low energy regime. Figure 4.8b shows that this model appears to be also efficient at higher values of magnetic field or of energy. It can also be used to describe few layer graphene specimens with band structures composed of superimposed graphene bilayer electronic dispersions with different values of k_z and hence of γ_1^* [111].

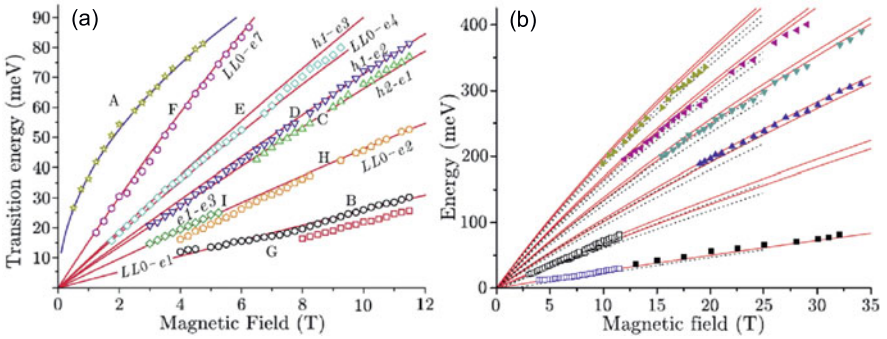

Fig. 4.8 Part (**a**): Transmission minima (*symbols*) as a function of the magnetic field. *Solid lines* are the results of the effective two-parameter model used in Ref. [124]. Part (**b**): High energy/magnetic field range with results after Ref. [112]. *Solid lines* are the same as in the *upper panel*. Adapted from Ref. [124]. Copyright (2009) by The American Physical Society

4.4.2 Full Slonczewski-Weiss-McClure Model

If polarization resolved measurements are complicated to achieve in the infrared range of energy, this problem can be overcome by using Raman scattering techniques, in the visible range of energy. Such experiments have recently been performed on bulk graphite [52]. Depending on the relative circular polarization of the excitation beam and of the scattered light, different types of electronic excitations can be selected: (i) $\Delta|n| = 0$ excitations in the co-circular polarization configurations (σ^-/σ^- and σ^+/σ^+) and (ii) $\Delta|n| = \pm 2$ and $\Delta|n| = \pm 1$ excitations in the crossed circular polarization configurations (σ^-/σ^+ and σ^+/σ^-). Strictly speaking, only $\Delta|n| = \pm 2$ excitations are expected to be Raman active, but $\Delta|n| = \pm 1$ excitations can also be observed in this polarization configuration thanks to trigonal warping. These experiments allowed us to make a direct estimation of the electron-hole asymmetry by selecting either an excitation from a level n^- to a level $(n+1)^+$ or from a level $(n+1)^-$ to n^+ for instance in the case of optical-like excitations. Figure 4.9a shows the evolution of the maxima of the scattered light as a function of the magnetic field for the two crossed circular polarization configuration together with the theoretical expectations in the frame of the full SWM model (solid and dashed lines). In contrast to the case of graphene where the main visible excitations in crossed circular polarization configuration are the $\Delta|n| = \pm 1$ excitations, the dominant contribution to the electronic Raman scattering spectrum of bulk graphite arises from $\Delta|n| = \pm 2$ electronic excitations.

Such an experiment also allowed us to probe the dispersion along k_z through the line shape of the electronic Raman scattering features, in particular those observed in both circular polarization configurations. As it is shown in Fig. 4.9b, the observed line shape is strongly asymmetric with a long tail on the high energy side of the feature. Theoretical calculations [126, 127] show that the scattered intensity, at a fixed value of the magnetic field, is directly proportional to the density of states

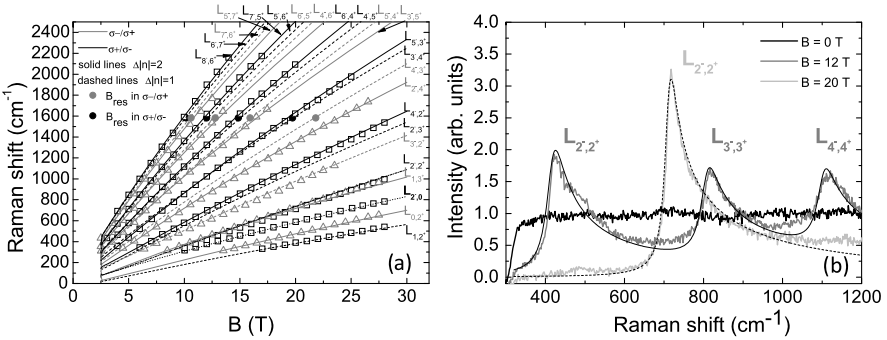

Fig. 4.9 Part (**a**): Evolution of the maxima of scattered light as a function of the magnetic field for both crossed circular polarization configurations (σ^-/σ^+ and σ^+/σ^-). *Solid* and *dashed lines* represent the expectations from the full SWM model. Part (**b**): Three Raman scattering spectra measured at $B = 0$, $B = 12$ T and $B = 20$ T in the co-circular polarization configuration (σ^-/σ^-). *Solid* and *dashed lines* are calculated line shapes. Adapted from Ref. [52]. Copyright (2011) by The American Physical Society

and one expects an energy independent response for a bilayer graphene characterized by a parabolic dispersion and a rather linear in energy response for graphene monolayer with linear dispersion. This is in striking contrast with the optical absorption which is energy independent in monolayer graphene [26] and which scales, at low energies, with the inverse of the energy for a bilayer graphene specimen [128]. Studying the K point carriers in bulk graphite with Raman scattering experiments confirms that there is a contribution of low energy electronic excitations to the Raman scattering spectrum of bulk graphite at $B = 0$, which is flat up to 1200 cm^{-1} in agreement with the expectation for a graphene bilayer, but that can be identified by applying a magnetic field. This energy independent response was also identified in unpolarized configuration [129]. Under an applied magnetic field, it then transforms into discrete features due to Landau quantization. The resulting line shape of the electronic feature observe through Raman scattering is determined mainly by the electronic dispersion around the K point and can be calculated quite accurately within the SWM model (solid and dashed lines in Fig. 4.9b). This set of experimental results can only be understood within the full SWM model taking into account the electron-hole asymmetry, the trigonal warping and the dispersion along k_z.

4.4.3 Band Structure Close to the Neutrality Point: Proximity to Lifshitz Transition

The low energy band structure of bilayer graphene and of bulk graphite, close to the charge neutrality point, is extremely sensitive to the effect of trigonal warping described by the γ_3 SWM parameter. In the case of bilayer graphene, recent magneto-transport experiments [110] performed on gated high mobility specimens, reveal that the low energy electronic dispersion is determined by interaction effects

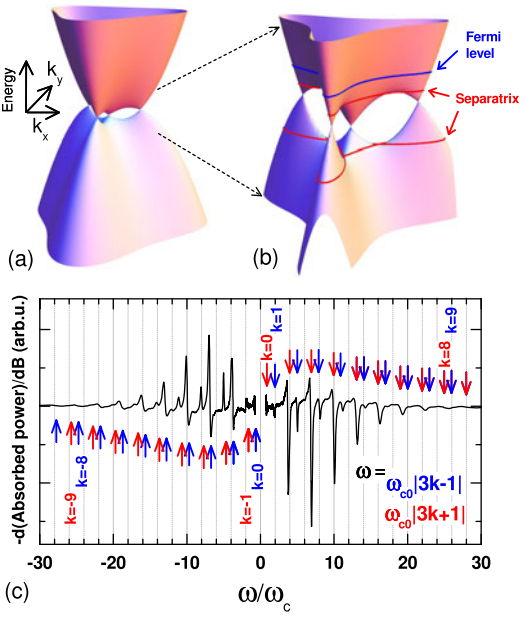

Fig. 4.10 Parts (**a**) and (**b**) Low energy in-plane band structure of bulk graphite close to the K point. *Solid red lines* show the two separatrices and the *blue solid line* shows the Fermi level. Part (**c**) Derivative of the magneto-absorption spectrum measured at a fixed microwave excitation energy of $\hbar\omega = 1.171$ meV as a function of ω/ω_c. Adapted from Ref. [130]. Copyright (2012) by The American Physical Society

which strongly modify the topology of the non trivial low energy Fermi surface. In case of ideal and noninteracting system, the electronic band structure evolves from a single electron (or hole) pocket at high energies to four distinct electron (or hole) Dirac cones when the Fermi energy is tuned to lower energies, below the topological transition named the Lifshitz transition. These magneto-transport measurements show that the low energy band structure is in fact composed of only two Dirac cones indicating a reduced symmetry caused either by the strain or, perhaps, pointing at a nematic electronic phase transition driven by a Coulomb interaction.

The band structure of bulk graphite is very similar to that of graphene bilayer, but the Fermi energy can hardly be tuned by gate effects. As a result, it is not nowadays possible to explore the situation where, as it was done for a graphene bilayer, the Fermi energy is below the separatrix. Bulk graphite is an electronic system with a Fermi energy slightly above the topological separatrices. Recent magneto-absorption experiments performed in the micro-wave range of energy (1 meV) reveal the rich physics associated with the topology of the low energy band structure close to the K point [130]. As is sketched in Fig. 4.10a and b, the band dispersion has six saddle points at two different energies ϵ_{e-sp} and ϵ_{h-sp}, which define two separatrices (iso-energetic lines separating regions with different topologies). When the Fermi energy ϵ_F crosses these separatrices, the topology of the Fermi surface changes from a single electron pocket around the K point to four disconnected cones for $\epsilon_F < \epsilon_{e\text{-}sp}$. These topological changes have a pronounced effect on the cyclotron frequency which vanishes at $\epsilon = \epsilon_{sp}$. Because ϵ_F in bulk graphite lies ~ 6 meV above ϵ_{sp}, the cyclotron resonance (CR) response measured at low energies is strongly affected. As is presented in Fig. 4.10c, which shows the derivative, with respect to magnetic field, of the magneto-absorption spectrum measured

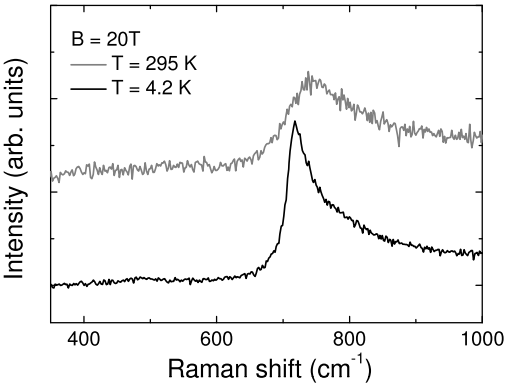

Fig. 4.11 Raman scattering spectra of the $L_{2^-,2^+}$ feature at $B = 20$ T and at $T = 4.2$ K and $T = 295$ K. Adapted from Ref. [52]. Copyright (2011) by The American Physical Society

at low temperature, this proximity results in (i) the appearance of a large number of CR harmonics (up to 20) (ii) an enhanced strength of $3k + 1$ harmonics as compared to $3k - 1$ harmonics and finally, (iii) a characteristic broadening of the observed resonances on the low energy side of the absorption peak. These are the magneto-optical signatures of the proximity to the Lifshitz transition in bulk graphite [130].

These results have been explained in the frame of a single particle model without taking interaction effects into account. Having the possibility to tune the Fermi energy across the separatrices in bulk graphite, for now, still remains a challenge.

4.4.4 Scattering Efficiency

In the case of optical excitations among discrete graphene-like Landau levels, the room temperature magneto-optical response is very similar to the one observed at low temperature, with no apparent shift nor broadening of the absorption lines [71]. This indicates that there is no relevant temperature activated scattering mechanism. The case of bulk graphite appears to be quite similar. As can be seen in Fig. 4.11, electronic Raman scattering features in a magnetic field, and in particular the $L_{2^-,2^+}$ feature, can be observed up to room temperature. The line shape of this feature is strongly affected by temperature with an overall blue shift and a smearing due to thermal population of the final state $n = 2^+$ Landau band. If the low energy onset of this feature is rather sharp at low temperature since all the $n = 2^+$ Landau band is empty down to the $k_z = 0$ states, the thermal population of this band leads to a Pauli blocking of the transitions starting from those involving the $k_z = 0$ final states. This effect quantitatively accounts for the shift and additional broadening of the $L_{2^-,2^+}$ spectrum at elevated temperatures. Thermal population effects appear to be the main source for the observed difference in the spectral response. This implies that other possible sources of spectral broadening have a negligible temperature dependence.

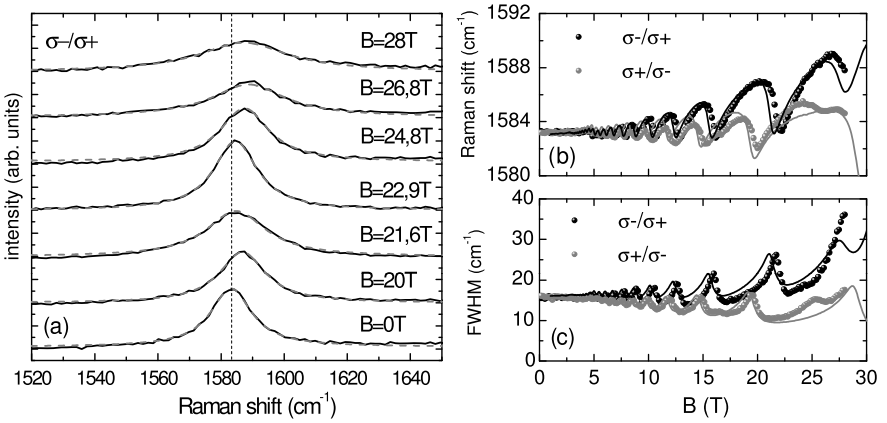

Fig. 4.12 Part (**a**) Raman scattering spectra in the E_{2g} phonon range of energy for different values of the magnetic field. Parts (**b**) and (**c**): Evolution of the Raman shift and of the FWHM of E_{2g} phonon feature as a function of the magnetic field in the two different crossed circular polarization configuration. *Solid lines* are the result of the calculation presented in Ref. [52]. Figures adapted from Ref. [52]. Copyright (2011) by The American Physical Society

4.4.5 Electron-Phonon Coupling

As in the case of graphene systems discussed in the preceding section, it is possible to tune the electron-phonon interaction to resonance in bulk graphite by applying high magnetic fields. Relevant electronic excitations for the electron-phonon coupling in bulk graphite are optical-like excitations ($\Delta k = 0$ at $B = 0$) which transform into inter Landau bands excitations with $\Delta|n| = \pm 1$ under an applied magnetic field. It is possible to tune these excitations in resonance with the E_{2g} optical phonon occurring around 1580 cm^{-1} by increasing the magnetic field. This leads to the magneto-phonon effect which manifests itself as pronounced oscillations of the phonon energy and line width, as it is shown in Fig. 4.12a. The Raman shift and the full width at half maximum (FWHM) extracted from the Lorentzian fitting of this line are presented in Fig. 4.12b and c. This effect in bulk graphite is significantly different that the one observed in the graphene monolayer. The fundamental difference between these two systems is the 3D nature of electronic states in bulk graphite and of the associated k_z dispersion. The magneto-phonon effect in bulk graphite involves Landau bands, in contrast to discrete Landau levels in graphene. The electronic dispersion close to the K point causes the oscillator strength of the optical-like excitations in this system to be spread over a significant range of energy (typically a few meV). As a result, the observed oscillations of the phonon energy and the line width are asymmetric and strongly damped, as shown in Fig. 4.12b and c. In graphene, a fully resonant coupling occurs between two discrete excitations while in bulk graphite, the 3D Landau bands that appear in magnetic field spread the interaction over a range of energy as wide as the observed electronic features. Although these oscillations are mainly due to K points excitations, they

also reflect the excitation spectrum of the H point carriers and their electron-hole asymmetry [52]. This results of the fact that the Fermi level at the H point lies below the charge neutrality point and the 0th Landau band at this particular point is completely empty. Hence, only the $L_{-1,0}$ has a finite oscillator strength and couples to the phonon while the oscillator strength of $L_{0,1}$ vanishes, creating the asymmetry observed in the two crossed circular polarization configurations, one component being blue shifted at high fields while the other component is red shifted. Modelling the magneto-phonon effect in bulk graphite allows us to extract the dimensionless electron-phonon coupling constant λ which, in this case, is 3.0×10^{-3}, approximately one third lower than the expected value. This difference probably arises from the approximation $\gamma_3 = 0$ made in the calculation which impacts the matrix elements and, *in fine*, the estimation of the coupling constant. To this end we note that in more recent, Raman scattering experiments with unpolarized light, the magneto-phonon resonance of bulk graphite could be traced in fields up to 45 T [131].

4.5 Conclusions

Concluding, the aim of our report has been to present the potential of optical magneto-spectroscopy methods to investigate the electronic properties of graphene based materials. Primarily, those methods provide the valuable information about the characteristic band structure of the system investigated. Furthermore, they also allow us to conclude on carrier scattering efficiency/mechanism and are the convenient techniques for studying the effects of electron-phonon coupling. Magneto-absorption in the far infrared range is naturally the most straightforward tool to studying the graphene and its derivatives, but this technique suffers an easy application to small size samples. A relevant step forward to applying magneto-optics to study the micron-size structure was the recent demonstration of the electronic response in magneto Raman scattering experiments. These experiments, as far performed only on graphite and on graphene locations on the graphite substrate, are certainly suitable to study all other high quality graphene structures. The fabrication of large size graphene structures (e.g., CVD growth) on one hand and a clear progress in increasing the quality (mobility) of well characterized individual graphene structures (e.g., graphene on boron nitride) on the other hand, will certainly open new possibilities for optical magneto-spectroscopy studies in a very near future. Those studies may in particular include the investigations of the effects of interactions (electron-phonon and electron-electron) in the regime of the quantum Hall effect. Other applications of optical magneto-spectroscopy might be relevant when searching for the graphene systems with an open energy gap, when studying the plasmonic structures and/or when searching for a light emission from graphene systems.

Acknowledgements The authors thank Denis Basko for stimulating discussions and acknowledge the support from the "Fondation Nanosciences" in Grenoble (DISPOGRAPH project) and the European Research Council (ERC-2012-AdG-320590-MOMB).

References

1. A.K. Geim, A.H. MacDonald, Graphene: exploring carbon flatland. Phys. Today **60**, 35–41 (2007)
2. A.K. Geim, K.S. Novoselov, The rise of graphene. Nat. Mater. **6**, 183 (2007)
3. K.S. Novoselov, A.K. Geim, S.V. Morozov, D. Jiang, M.I. Katsnelson, I.V. Grigorieva, S.V. Dubonos, A.A. Firsov, Electric field effect in atomically thin carbon films. Science **306**, 666 (2004)
4. J.A. Woollam, Spin splitting, Fermi energy changes, and anomalous g shifts in single-crystal and pyrolytic graphite. Phys. Rev. Lett. **25**, 810–813 (1970)
5. K.S. Novoselov, A.K. Geim, S.V. Morozov, D. Jiang, M.I. Katsnelson, I.V. Grigorieva, S.V. Dubonos, A.A. Firsov, Two-dimensional gas of massless Dirac fermions in graphene. Nature **438**, 197 (2005)
6. Y.B. Zhang, Y.W. Tan, H.L. Stormer, P. Kim, Experimental observation of the quantum Hall effect and Berrys phase in graphene. Nature **438**, 201 (2005)
7. M. Orlita, M. Potemski, Dirac electronic states in graphene systems: optical spectroscopy studies. Semicond. Sci. Technol. **25**, 063001 (2010)
8. F. Bonaccorso, Z. Sun, T. Hasan, A.C. Ferrari, Graphene photonics and optoelectronics. Nat. Photonics **4**, 611 (2010)
9. W.D. Tan, C.Y. Su, R.J. Knize, G.Q. Xie, L.J. Li, D.Y. Tang, Mode locking of ceramic Nd:yttrium aluminum garnet with graphene as a saturable absorber. Appl. Phys. Lett. **96**(3), 031106 (2010)
10. H. Zhang, D.Y. Tang, L.M. Zhao, Q.L. Bao, K.P. Loh, Large energy mode locking of an erbium-doped fiber laser with atomic layer graphene. Opt. Express **17**(20), 17630–17635 (2009)
11. X. Wang, L. Zhi, K. Mullen, Transparent, conductive graphene electrodes for dye-sensitized solar cells. Nano Lett. **8**(1), 323–327 (2008). PMID: 18069877
12. K.S. Kim, Y. Zhao, H. Jang, S.Y. Lee, J.M. Kim, K.S. Kim, J.-H. Ahn, P. Kim, J.-Y. Choi, B.H. Hong, Large-scale pattern growth of graphene films for stretchable transparent electrodes. Nature **457**, 706–710 (2009)
13. L. Ju, B. Geng, J. Horng, C. Girit, M. Martin, Z. Hao, H.A. Bechtel, X. Liang, A. Zettl, Y.R. Shen, F. Wang, Graphene plasmonics for tunable terahertz metamaterials. Nat. Nanotechnol. **6**, 630 (2011)
14. P. Blake, E.W. Hill, A.H. Castro Neto, K.S. Novoselov, D. Jiang, R. Yang, T.J. Booth, A.K. Geim, Making graphene visible. Appl. Phys. Lett. **91**, 063124 (2007)
15. D.S.L. Abergel, A. Russell, V.I. Fal'ko, Visibility of graphene flakes on a dielectric substrate. Appl. Phys. Lett. **91**, 063125 (2007)
16. S. Roddaro, P. Pingue, V. Piazza, V. Pellegrini, F. Beltram, The optical visibility of graphene: interference colors of ultrathin graphite on SiO_2. Nano Lett. **7**, 2707–2710 (2007)
17. C. Casiraghi, A. Hartschuh, E. Lidorikis, H. Qian, H. Harutyunyan, T. Gokus, K.S. Novoselov, A.C. Ferrari, Rayleigh imaging of graphene and graphene layers. Nano Lett. **7**, 2711–2717 (2007)
18. I. Jung, M. Pelton, R. Piner, D.A. Dikin, S. Stankovich, S. Watcharotone, M. Hausner, R.S. Ruoff, Simple approach for high-contrast optical imaging and characterization of graphene-based sheets. Nano Lett. **7**, 3569–3575 (2007)
19. A.C. Ferrari, J.C. Meyer, V. Scardaci, C. Casiraghi, M. Lazzeri, F. Mauri, S. Piscanec, D. Jiang, K.S. Novoselov, S. Roth, A.K. Geim, Raman spectrum of graphene and graphene layers. Phys. Rev. Lett. **97**, 187401 (2006)
20. D. Graf, F. Molitor, K. Ensslin, C. Stampfer, A. Jungen, C. Hierold, L. Wirtz, Spatially resolved Raman spectroscopy of single- and few-layer graphene. Nano Lett. **7**, 238–242 (2007)
21. C. Faugeras, A. Nerriere, M. Potemski, A. Mahmood, E. Dujardin, C. Berger, W.A. de Heer, Few-layer graphene on sic, pyrolitic graphite, and graphene: a Raman scattering study. Appl. Phys. Lett. **92**, 011914 (2008)

22. S. Pisana, M. Lazzeri, C. Casiraghi, K.S. Novoselov, A.K. Geim, A.C. Ferrari, F. Mauri, Breakdown of the adiabatic Born-Oppenheimer approximation in graphene. Nat. Mater. **6**, 198–201 (2007)
23. A.H. Castro Neto, F. Guinea, Electron-phonon coupling and Raman spectroscopy in graphene. Phys. Rev. B **75**, 045404 (2007)
24. J. Yan, Y. Zhang, P. Kim, A. Pinczuk, Electric field effect tuning of electron-phonon coupling in graphene. Phys. Rev. Lett. **98**, 166802 (2007)
25. T. Ando, Y. Zheng, H. Suzuura, Dynamical conductivity and zero-mode anomaly in honeycomb lattices. J. Phys. Soc. Jpn. **71**, 1318–1324 (2002)
26. R.R. Nair, P. Blake, A.N. Grigorenko, K.S. Novoselov, T.J. Booth, T. Stauber, N.M.R. Peres, A.K. Geim, Fine structure constant defines visual transparency of graphene. Science **320**, 1308 (2008)
27. K.F. Mak, M.Y. Sfeir, Y. Wu, C.H. Lui, J.A. Misewich, T.F. Heinz, Measurement of the optical conductivity of graphene. Phys. Rev. Lett. **101**, 196405 (2008)
28. A.B. Kuzmenko, E. van Heumen, F. Carbone, D. van der Marel, Universal optical conductance of graphite. Phys. Rev. Lett. **100**, 117401 (2008)
29. V.G. Kravets, A.N. Grigorenko, R.R. Nair, P. Blake, S. Anissimova, K.S. Novoselov, A.K. Geim, Spectroscopic ellipsometry of graphene and an exciton-shifted van Hove peak in absorption. Phys. Rev. B **81**, 155413 (2010)
30. K.F. Mak, J. Shan, T.F. Heinz, Seeing many-body effects in single- and few-layer graphene: observation of two-dimensional saddle-point excitons. Phys. Rev. Lett. **106**, 046401 (2011)
31. D.-H. Chae, T. Utikal, S. Weisenburger, H. Giessen, K.v. Klitzing, M. Lippitz, J. Smet, Excitonic Fano resonance in free-standing graphene. Nano Lett. **11**(3), 1379–1382 (2011)
32. S.H. Abedinpour, G. Vignale, A. Principi, M. Polini, W.-K. Tse, A.H. MacDonald, Drude weight, plasmon dispersion, and ac conductivity in doped graphene sheets. Phys. Rev. B **84**, 045429 (2011)
33. J. Horng, C.-F. Chen, B. Geng, C. Girit, Y. Zhang, Z. Hao, H.A. Bechtel, M. Martin, A. Zettl, M.F. Crommie, Y.R. Shen, F. Wang, Drude conductivity of Dirac fermions in graphene. Phys. Rev. B **83**, 165113 (2011)
34. H. Yan, F. Xia, W. Zhu, M. Freitag, C. Dimitrakopoulos, A.A. Bol, G. Tulevski, P. Avouris, Infrared spectroscopy of wafer-scale graphene. ACS Nano **5**(12), 9854–9860 (2011). doi:10.1021/nn203506n
35. M. Orlita, I. Crassee, C. Faugeras, A.B. Kuzmenko, F. Fromm, M. Ostler, T. Seyller, G. Martinez, M. Polini, M. Potemski, Classical to quantum crossover of the cyclotron resonance in graphene: a study of the strength of intraband absorption. New J. Phys. **14**(9), 095008 (2012)
36. J.M. Dawlaty, S. Shivaraman, M. Chandrashekhar, F. Rana, M.G. Spencer, Measurement of ultrafast carrier dynamics in epitaxial graphene. Appl. Phys. Lett. **92**, 042116 (2008)
37. P.A. George, J. Strait, J. Dawlaty, S. Shivaraman, M. Chandrashekhar, F. Rana, M.G. Spencer, Ultrafast optical-pump terahertz-probe spectroscopy of the carrier relaxation and recombination dynamics in epitaxial graphene. Nano Lett. **8**, 4248 (2008)
38. D. Sun, Z.-K. Wu, C. Divin, X. Li, C. Berger, W.A. de Heer, P.N. First, T.B. Norris, Ultrafast relaxation of excited Dirac fermions in epitaxial graphene using optical differential transmission spectroscopy. Phys. Rev. Lett. **101**, 157402 (2008)
39. H. Choi, F. Borondics, D.A. Siegel, S.Y. Zhou, M.C. Martin, A. Lanzara, R.A. Kaindl, Broadband electromagnetic response and ultrafast dynamics of few-layer epitaxial graphene. Appl. Phys. Lett. **94**(17), 172102 (2009)
40. P. Plochocka, P. Kossacki, A. Golnik, T. Kazimierczuk, C. Berger, W.A. de Heer, M. Potemski, Slowing hot-carrier relaxation in graphene using a magnetic field. Phys. Rev. B **80**, 245415 (2009)
41. T. Kampfrath, L. Perfetti, F. Schapper, C. Frischkorn, M. Wolf, Strongly coupled optical phonons in the ultrafast dynamics of the electronic energy and current relaxation in graphite. Phys. Rev. Lett. **95**(18), 187403 (2005)

42. M. Breusing, C. Ropers, T. Elsaesser, Ultrafast carrier dynamics in graphite. Phys. Rev. Lett. **102**, 086809 (2009)
43. R.W. Newson, J. Dean, B. Schmidt, H.M. van Driel, Ultrafast carrier kinetics in exfoliated graphene and thin graphite films. Opt. Express **17**, 2326–2333 (2009)
44. S. Winnerl, M. Orlita, P. Plochocka, P. Kossacki, M. Potemski, T. Winzer, E. Malic, A. Knorr, M. Sprinkle, C. Berger, W.A. de Heer, H. Schneider, M. Helm, Carrier relaxation in epitaxial graphene photoexcited near the Dirac point. Phys. Rev. Lett. **107**, 237401 (2011)
45. K.J. Tielrooij, J.C.W. Song, S.A. Jensen, A. Centeno, A. Pesquera, A. Zurutuza Elorza, M. Bonn, L.S. Levitov, F.H.L. Koppens, Photoexcitation cascade and multiple hot-carrier generation in graphene. Nat. Phys. **9**, 248 (2013)
46. J.K. Galt, W.A. Yager, H.W. Dail, Cyclotron resonance effects in graphite. Phys. Rev. **103**(5), 1586–1587 (1956)
47. P.R. Schroeder, M.S. Dresselhaus, A. Javan, Location of electron and hole carriers in graphite from laser magnetoreflection data. Phys. Rev. Lett. **20**, 1292 (1969)
48. T. Morimoto, Y. Hatsugai, H. Aoki, Optical Hall conductivity in ordinary and graphene quantum Hall systems. Phys. Rev. Lett. **103**, 116803 (2009)
49. I. Crassee, J. Levallois, A.L. Walter, M. Ostler, A. Bostwick, E. Rotenberg, T. Seyller, D. van der Marel, A.B. Kuzmenko, Giant Faraday rotation in single- and multilayer graphene. Nature Phys. **7**(1), 48–51 (2011)
50. R. Shimano, G. Yumoto, J.Y. Yoo, R. Matsunaga, S. Tanabe, H. Hibino, T. Morimoto, H. Aoki, Quantum Faraday and Kerr rotations in graphene. Nat. Commun. **4**, 1841 (2013)
51. C. Faugeras, M. Amado, P. Kossacki, M. Orlita, M. Kühne, A.A.L. Nicolet, Y.I. Latyshev, M. Potemski, Magneto-Raman scattering of graphene on graphite: electronic and phonon excitations. Phys. Rev. Lett. **107**, 036807 (2011)
52. P. Kossacki, C. Faugeras, M. Kuhne, M. Orlita, A.A.L. Nicolet, J.M. Schneider, D.M. Basko, Y.I. Latyshev, M. Potemski, Electronic excitations and electron-phonon coupling in bulk graphite through Raman scattering in high magnetic fields. Phys. Rev. B **84**, 235138 (2011)
53. O. Kashuba, V.I. Fal'ko, Signature of electronic excitations in the Raman spectrum of graphene. Phys. Rev. B **80**, 241404 (2009)
54. M. Mucha-Kruczyński, O. Kashuba, V.I. Fal'ko, Spectral features due to inter-Landau-level transitions in the Raman spectrum of bilayer graphene. Phys. Rev. B **82**, 045405 (2010)
55. A.M. Witowski, M. Orlita, R. Stępniewski, A. Wysmołek, J.M. Baranowski, W. Strupiński, C. Faugeras, G. Martinez, M. Potemski, Quasiclassical cyclotron resonance of Dirac fermions in highly doped graphene. Phys. Rev. B **82**, 165305 (2010)
56. I. Crassee, M. Orlita, M. Potemski, A.L. Walter, M. Ostler, T. Seyller, I. Gaponenko, J. Chen, A.B. Kuzmenko, Intrinsic terahertz plasmons and magnetoplasmons in large scale monolayer graphene. Nano Lett. **12**(5), 2470–2474 (2012)
57. H. Yan, Z. Li, X. Li, W. Zhu, P. Avouris, F. Xia, Infrared spectroscopy of tunable Dirac terahertz magneto-plasmons in graphene. Nano Lett. **12**(7), 3766–3771 (2012)
58. Y. Zheng, T. Ando, Hall conductivity of a two-dimensional graphite system. Phys. Rev. B **65**, 245420 (2002)
59. P. Neugebauer, M. Orlita, C. Faugeras, A.-L. Barra, M. Potemski, How perfect can graphene be? Phys. Rev. Lett. **103**, 136403 (2009)
60. N.M.R. Peres, F. Guinea, A.H. Castro Neto, Electronic properties of disordered two-dimensional carbon. Phys. Rev. B **73**(12), 125411 (2006)
61. V.P. Gusynin, S.G. Sharapov, Transport of Dirac quasiparticles in graphene: Hall and optical conductivities. Phys. Rev. B **73**, 245411 (2006)
62. M.L. Sadowski, G. Martinez, M. Potemski, C. Berger, W.A. de Heer, Landau level spectroscopy of ultrathin graphite layers. Phys. Rev. Lett. **97**, 266405 (2006)
63. V.P. Gusynin, S.G. Sharapov, J.P. Carbotte, Anomalous absorption line in the magneto-optical response of graphene. Phys. Rev. Lett. **98**, 157402 (2007)
64. Z. Jiang, E.A. Henriksen, L.C. Tung, Y.-J. Wang, M.E. Schwartz, M.Y. Han, P. Kim, H.L. Stormer, Infrared spectroscopy of Landau levels of graphene. Phys. Rev. Lett. **98**, 197403 (2007)

65. V.P. Gusynin, S.G. Sharapov, J.P. Carbotte, Magneto-optical conductivity in graphene. J. Phys. Condens. Matter **19**, 026222 (2007)
66. M.L. Sadowski, G. Martinez, M. Potemski, C. Berger, W.A. de Heer, Magnetospectroscopy of epitaxial few-layer graphene. Solid State Commun. **143**, 123 (2007)
67. M.L. Sadowski, G. Martinez, M. Potemski, C. Berger, W.A. de Heer, Magneto-spectroscopy of epitaxial graphene. Int. J. Mod. Phys. B **21**, 1145 (2007)
68. R.S. Deacon, K.-C. Chuang, R.J. Nicholas, K.S. Novoselov, A.K. Geim, Cyclotron resonance study of the electron and hole velocity in graphene monolayers. Phys. Rev. B **76**, 081406 (2007)
69. D.S.L. Abergel, V.I. Fal'ko, Optical and magneto-optical far-infrared properties of bilayer graphene. Phys. Rev. B **75**, 155430 (2007)
70. P. Plochocka, C. Faugeras, M. Orlita, M.L. Sadowski, G. Martinez, M. Potemski, M.O. Goerbig, J.-N. Fuchs, C. Berger, W.A. de Heer, High-energy limit of massless Dirac fermions in multilayer graphene using magneto-optical transmission spectroscopy. Phys. Rev. Lett. **100**, 087401 (2008)
71. M. Orlita, C. Faugeras, P. Plochocka, P. Neugebauer, G. Martinez, D.K. Maude, A.-L. Barra, M. Sprinkle, C. Berger, W.A. de Heer, M. Potemski, Approaching the Dirac point in high-mobility multilayer epitaxial graphene. Phys. Rev. Lett. **101**, 267601 (2008)
72. E.A. Henriksen, P. Cadden-Zimansky, Z. Jiang, Z.Q. Li, L.-C. Tung, M.E. Schwartz, M. Takita, Y.-J. Wang, P. Kim, H.L. Stormer, Interaction-induced shift of the cyclotron resonance of graphene using infrared spectroscopy. Phys. Rev. Lett. **104**, 067404 (2010)
73. M. Orlita, C. Faugeras, R. Grill, A. Wysmolek, W. Strupinski, C. Berger, W.A. de Heer, G. Martinez, M. Potemski, Carrier scattering from dynamical magnetoconductivity in quasineutral epitaxial graphene. Phys. Rev. Lett. **107**, 216603 (2011)
74. M. Schultz, U. Merkt, A. Sonntag, U. Rossler, Density dependent cyclotron and intersubband resonance in inverted CdTe/HgTe/CdTe quantum wells. J. Cryst. Growth **184–185**, 1180 (1998)
75. M. Schultz, U. Merkt, A. Sonntag, U. Rossler, R. Winkler, T. Colin, P. Helgesen, T. Skauli, S. Løvold, Crossing of conduction- and valence-subband Landau levels in an inverted HgTe/CdTe quantum well. Phys. Rev. B **57**, 14772 (1998)
76. M. Orlita, K. Masztalerz, C. Faugeras, M. Potemski, E.G. Novik, C. Brüne, H. Buhmann, L.W. Molenkamp, Fine structure of zero-mode Landau levels in HgTe/Hg_xCd_{1-x}Te quantum wells. Phys. Rev. B **83**, 115307 (2011)
77. M. Zholudev, F. Teppe, M. Orlita, C. Consejo, J. Torres, N. Dyakonova, M. Czapkiewicz, J. Wróbel, G. Grabecki, N. Mikhailov, S. Dvoretskii, A. Ikonnikov, K. Spirin, V. Aleshkin, V. Gavrilenko, W. Knap, Magnetospectroscopy of two-dimensional HgTe-based topological insulators around the critical thickness. Phys. Rev. B **86**, 205420 (2012)
78. H. Farhat, S. Berciaud, M. Kalbac, R. Saito, T.F. Heinz, M.S. Dresselhaus, J. Kong, Observation of electronic Raman scattering in metallic carbon nanotubes. Phys. Rev. Lett. **107**, 157401 (2011)
79. C. Faugeras, M. Amado, P. Kossacki, M. Orlita, M. Sprinkle, C. Berger, W.A. de Heer, M. Potemski, Tuning the electron-phonon coupling in multilayer graphene with magnetic fields. Phys. Rev. Lett. **103**, 186803 (2009)
80. G. Li, A. Luican, E.Y. Andrei, Scanning tunneling spectroscopy of graphene on graphite. Phys. Rev. Lett. **102**, 176804 (2009)
81. D.L. Miller, K.D. Kubista, G.M. Rutter, M. Ruan, W.A. de Heer, P.N. First, J.A. Stroscio, Observing the quantization of zero mass carriers in graphene. Science **324**, 924–927 (2009)
82. N.H. Shon, T. Ando, Quantum transport in two-dimensional graphite system. J. Phys. Soc. Jpn. **67**, 2421 (1998)
83. K.V. Klitzing, G. Dorda, M. Pepper, New method for high-accuracy determination of the fine-structure constant based on quantized Hall resistance. Phys. Rev. Lett. **45**, 494–497 (1980)
84. D.C. Tsui, H.L. Stormer, A.C. Gossard, Two-dimensional magnetotransport in the extreme quantum limit. Phys. Rev. Lett. **48**, 1559–1562 (1982)

85. X. Du, I. Skachko, F. Duerr, A. Luican, E.Y. Andrei, Fractional quantum Hall effect and insulating phase of Dirac electrons in graphene. Nature **462**, 192 (2009)
86. K.I. Bolotin, F. Ghahari, M.D. Shulman, H.L. Stormer, P. Kim, Observation of the fractional quantum Hall effect in graphene. Nature **462**, 196 (2009)
87. A. Iyengar, J. Wang, H.A. Fertig, L. Brey, Excitations from filled Landau levels in graphene. Phys. Rev. B **75**, 125430 (2007)
88. Y.A. Bychkov, G. Martinez, Magnetoplasmon excitations in graphene for filling factors $\nu \leq 6$. Phys. Rev. B **77**, 125417 (2008)
89. K. Asano, T. Ando, Approximate validity of Kohn's theorem in graphene. Work Presented at EP2DS-18 Conference, Japan, 2009
90. W. Zhu, Q.W. Shi, J.G. Hou, X.R. Wang, Comment on "interaction-induced shift of the cyclotron resonance of graphene using infrared spectroscopy". Phys. Rev. Lett. **105**, 159703 (2010)
91. M.I. Katsnelson, Graphene: carbon in two dimensions. Mater. Today **10**, 20–27 (2007)
92. A.J.M. Giesbers, U. Zeitler, M.I. Katsnelson, L.A. Ponomarenko, T.M. Mohiuddin, J.C. Maan, Quantum-Hall activation gaps in graphene. Phys. Rev. Lett. **99**, 206803 (2007)
93. D.C. Elias, R.V. Gorbachev, A.S. Mayorov, S.V. Morozov, A.A. Zhukov, P. Blake, L.A. Ponomarenko, I.V. Grigorieva, K.S. Novoselov, F. Guinea, A.K. Geim, Dirac cones reshaped by interaction effects in suspended graphene. Nat. Phys. **7**, 701 (2011)
94. T. Ando, Magnetic oscillation of optical phonon in graphene. J. Phys. Soc. Jpn. **76**, 024712 (2007)
95. M.O. Goerbig, J.-N. Fuchs, K. Kechedzhi, V.I. Fal'ko, Filling-factor-dependent magnetophonon resonance in graphene. Phys. Rev. Lett. **99**, 087402 (2007)
96. J. Yan, S. Goler, T.D. Rhone, M. Han, R. He, P. Kim, V. Pellegrini, A. Pinczuk, Observation of magnetophonon resonance of Dirac fermions in graphite. Phys. Rev. Lett. **105**, 227401 (2010)
97. P. Kossacki, C. Faugeras, M. Kuhne, M. Orlita, A. Mahmood, E. Dujardin, R.R. Nair, A.K. Geim, M. Potemski, Circular dichroism of magneto-phonon resonance in doped graphene. Phys. Rev. B **86**, 205431 (2012)
98. C. Faugeras, P. Kossacki, A.A.L. Nicolet, M. Orlita, M. Potemski, A. Mahmood, D.M. Basko, Probing the band structure of quadrilayer graphene with magneto-phonon resonance. New J. Phys. **14**, 095007 (2012)
99. M. Kühne, C. Faugeras, P. Kossacki, A.A.L. Nicolet, M. Orlita, Y.I. Latyshev, M. Potemski, Polarization-resolved magneto-Raman scattering of graphenelike domains on natural graphite. Phys. Rev. B **85**, 195406 (2012)
100. M. Orlita, L.Z. Tan, M. Potemski, M. Sprinkle, C. Berger, W.A. de Heer, S.G. Louie, G. Martinez, Resonant excitation of graphene k-phonon and intra-Landau-level excitons in magneto-optical spectroscopy. Phys. Rev. Lett. **108**, 247401 (2012)
101. K.S. Novoselov, E. McCann, S.V. Morozov, V.I. Fal'ko, K.I. Katsnelson, U. Zeitler, D. Jiang, F. Schedin, A.K. Geim, Unconventional quantum Hall effect and Berry's phase of 2π in bilayer graphene. Nat. Phys. **2**, 177–180 (2006)
102. E. McCann, V.I. Fal'ko, Landau-level degeneracy and quantum Hall effect in a graphite bilayer. Phys. Rev. Lett. **96**, 086805 (2006)
103. E.A. Henriksen, Z. Jiang, L.-C. Tung, M.E. Schwartz, M. Takita, Y.-J. Wang, P. Kim, H.L. Stormer, Cyclotron resonance in bilayer graphene. Phys. Rev. Lett. **100**, 087403 (2008)
104. M. Orlita, C. Faugeras, J. Borysiuk, J.M. Baranowski, W. Strupiński, M. Sprinkle, C. Berger, W.A. de Heer, D.M. Basko, G. Martinez, M. Potemski, Magneto-optics of bilayer inclusions in multilayered epitaxial graphene on the carbon face of sic. Phys. Rev. B **83**, 125302 (2011)
105. M. Mucha-Kruczynski, E. McCann, V.I. Fal'ko, The influence of interlayer asymmetry on the magnetospectroscopy of bilayer graphene. Solid State Commun. **149**, 1111–1116 (2009)
106. M. Mucha-Kruczynski, D.S.L. Abergel, E. McCann, V.I. Fal'ko, On spectral properties of bilayer graphene: the effect of an sic substrate and infrared magneto-spectroscopy. J. Phys. Condens. Matter **21**, 344206 (2009)

107. C. Töke, V.I. Falko, Intra-Landau-level magnetoexcitons and the transition between quantum Hall states in undoped bilayer graphene. Phys. Rev. B **83**, 115455 (2011)
108. V.E. Bisti, N.N. Kirova, Coulomb interaction and electron-hole asymmetry in cyclotron resonance of bilayer graphene in a high magnetic field. Phys. Rev. B **84**, 155434 (2011)
109. Y. Barlas, R. Côté, K. Nomura, A.H. MacDonald, Intra-Landau-level cyclotron resonance in bilayer graphene. Phys. Rev. Lett. **101**, 097601 (2008)
110. A.S. Mayorov, D.C. Elias, M. Mucha-Kruczynski, R.V. Gorbachev, T. Tudorovskiy, A. Zhukov, S.V. Morozov, M.I. Katsnelson, V.I. Falko, A.K. Geim, K.S. Novoselov, Interaction-driven spectrum reconstruction in bilayer graphene. Science **333**(6044), 860–863 (2011)
111. M. Koshino, T. Ando, Magneto-optical properties of multilayer graphene. Phys. Rev. B **77**, 115313 (2008)
112. M. Orlita, C. Faugeras, J.M. Schneider, G. Martinez, D.K. Maude, M. Potemski, Graphite from the viewpoint of Landau level spectroscopy: an effective graphene bilayer and monolayer. Phys. Rev. Lett. **102**, 166401 (2009)
113. N.B. Brandt, S.M. Chudinov, Y.G. Ponomarev, *Semimetals 1: Graphite and Its Compounds*. Modern Problems in Condensed Matter Sciences, vol. 20.1 (North-Holland, Amsterdam, 1988)
114. J.C. Slonczewski, P.R. Weiss, Band structure of graphite. Phys. Rev. **109**, 272 (1958)
115. J.W. McClure, Diamagnetism of graphite. Phys. Rev. **104**, 666–671 (1956)
116. K. Nakao, Landau level structure and magnetic breakthrough in graphite. J. Phys. Soc. Jpn. **40**, 761 (1976)
117. D.E. Soule, Magnetic field dependence of the Hall effect and magnetoresistance in graphite single crystals. Phys. Rev. **112**, 698–707 (1958)
118. D.E. Soule, J.W. McClure, L.B. Smith, Study of the Shubnikov-de Haas effect. Determination of the Fermi surfaces in graphite. Phys. Rev. **134**, 453–470 (1964)
119. J.M. Schneider, M. Orlita, M. Potemski, D.K. Maude, Consistent interpretation of the low-temperature magnetotransport in graphite using the Slonczewski-Weiss-McClure 3D band-structure calculations. Phys. Rev. Lett. **102**, 166403 (2009)
120. W.W. Toy, M.S. Dresselhaus, G. Dresselhaus, Minority carriers in graphite and the h-point magnetoreflection spectra. Phys. Rev. B **15**, 4077 (1977)
121. Z.Q. Li, S.-W. Tsai, W.J. Padilla, S.V. Dordevic, K.S. Burch, Y.J. Wang, D.N. Basov, Infrared probe of the anomalous magnetotransport of highly oriented pyrolytic graphite in the extreme quantum limit. Phys. Rev. B **74**, 195404 (2006)
122. J. Levallois, M. Tran, A.B. Kuzmenko, Decrypting the cyclotron effect in graphite using Kerr rotation spectroscopy. Solid State Commun. **152**(15), 1294–1300 (2012)
123. M. Orlita, C. Faugeras, G. Martinez, D.K. Maude, M.L. Sadowski, M. Potemski, Dirac fermions at the h point of graphite: magnetotransmission studies. Phys. Rev. Lett. **100**, 136403 (2008)
124. K.-C. Chuang, A.M.R. Baker, R.J. Nicholas, Magnetoabsorption study of Landau levels in graphite. Phys. Rev. B **80**, 161410 (2009)
125. B. Partoens, F.M. Peeters, Normal and Dirac fermions in graphene multilayers: tight-binding description of the electronic structure. Phys. Rev. B **75**, 193402 (2007)
126. O. Kashuba, V.I. Fal'ko, Signature of electronic excitations in the Raman spectrum of graphene. Phys. Rev. B **80**, 241404 (2009)
127. M. Mucha-Kruczynski, O. Kashuba, V.I. Fal'ko, Spectral features due to inter-Landau-level transitions in the Raman spectrum of bilayer graphene. Phys. Rev. B **82**, 045405 (2010)
128. E. McCann, D.S.L. Abergel, V.I. Falko, Electrons in bilayer graphene. Solid State Commun. **146**, 110 (2007)
129. A.F. García-Flores, H. Terashita, E. Granado, Y. Kopelevich, Landau levels in bulk graphite by Raman spectroscopy. Phys. Rev. B **79**, 113105 (2009)

130. M. Orlita, P. Neugebauer, C. Faugeras, A.-L. Barra, M. Potemski, F.M.D. Pellegrino, D.M. Basko, Cyclotron motion in the vicinity of a Lifshitz transition in graphite. Phys. Rev. Lett. **108**, 017602 (2012)
131. Y. Kim, Y. Ma, A. Imambekov, N.G. Kalugin, A. Lombardo, A.C. Ferrari, J. Kono, D. Smirnov, Magnetophonon resonance in graphite: high-field Raman measurements and electron-phonon coupling contributions. Phys. Rev. B **85**, 121403 (2012)

Chapter 5
Graphene Constrictions

S. Dröscher, F. Molitor, T. Ihn, and K. Ensslin

Abstract One of the goals for future electronic devices is to reduce their dimensions in order to improve their performance. Graphene is one of the potential materials systems for such applications due to its electronic properties and its impressive material stability. To date, narrow constrictions serve as a main component for nanoscale structures made out of graphene. This chapter aims to discuss electronic transport through graphene constrictions and will compare theoretical predictions with state of the art experimental findings.

5.1 Introduction

5.1.1 Graphene Electronics

Since its experimental discovery [1], graphene has been acclaimed for being a revolutionary material for electronic devices. Among the special properties, several meet the requirements of the present semiconductor technology. Graphene provides good accessibility for patterning and contacting, since all atoms are exposed at the surface. Lying only loosely on a substrate it has a remarkable stability even when shaped into nanoscale structures [2, 3]. Additionally, the semiconductor industry is thrilled by the sub-nanometer thickness of this mono-atomic layer. The channels of current silicon field effect transistors could be thinned by a factor of one hundred if being replaced by graphene [4]. Moreover, due to its unique band structure, charge carriers do not suffer from backscattering and exhibit room temperature mobilities ten times higher than in silicon.

Besides complementing standard technologies the realization of graphene quantum devices is of substantial interest to the field of quantum information processing. Graphene possibly satisfies the demand for long spin coherence times since the electron spin is expected to interact only weakly with its orbital motion due to the low atomic weight of its host material. As graphene predominantly

S. Dröscher · F. Molitor · T. Ihn · K. Ensslin (✉)
Solid State Physics Laboratory, ETH Zurich, 8093 Zurich, Switzerland
e-mail: ensslin@phys.ethz.ch

H. Aoki, M.S. Dresselhaus (eds.), *Physics of Graphene*, NanoScience and Technology,
DOI 10.1007/978-3-319-02633-6_5,

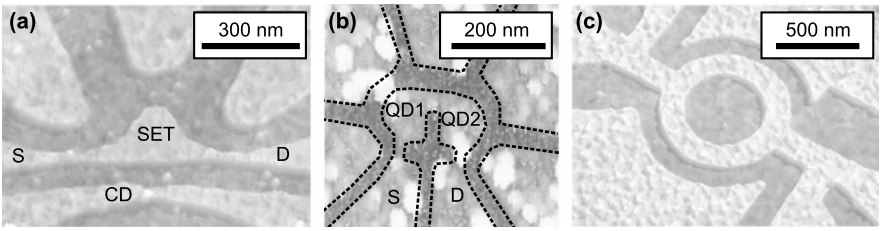

Fig. 5.1 Atomic force micrographs of different graphene nanostructures: (**a**) Single electron transistor (SET) with a nearby charge detector (CD) [5]. Source (S) and drain (D) are connected via narrow constrictions to the SET. Several in-plane side-gates are used to tune the states on the island and inside the constrictions. (**b**) Double quantum dot with in-plane gates [6]. The series connection of source (S), left quantum dot (QD1), right quantum dot (QD2) and drain (D) is implemented using narrow constrictions. In (**a**) and (**b**) constrictions are utilized as tunneling barriers. (**c**) Aharonov-Bohm ring for quantum interference measurements [7]. Here, constrictions are used as quasi one-dimensional transport channels

(98.9 %) consists of the ^{12}C isotope, which has zero nuclear spin, hyperfine coupling should be negligible as well. This property is promising for the realization of spin-based quantum bits as components of possible solid-state quantum computers.

5.1.2 Graphene Nanostructures

Like in semiconductor devices, the charge carrier density in a graphene sheet can be tuned by gate electrodes utilizing the field effect. However, the absence of a band gap does not allow for a complete depletion of charge carriers inside the system and hence precludes electrostatic confinement. Instead, a continuous transition between hole- and electron-like transport takes place close to the charge neutrality point. Theoretical considerations show, however, that cutting graphene into narrow ribbons along certain lattice directions can open a band gap depending on the lattice orientation at the formed edges. Although experimental studies of narrow ribbons could so far not achieve the requested perfection of the edges and accuracy of orientation, a suppression of electronic transport was observed. This so-called transport gap was adopted as a tunneling barrier in numerous different nano structures, where narrow constrictions are used to define the structures. Three exemplary devices are depicted in Fig. 5.1 including a single and a double quantum dot [Fig. 5.1(a) and (b)] and a quantum interference device [Fig. 5.1(c)]. A profound understanding of the transport mechanisms through the constrictions, which represent a basic building block for the aforementioned sophisticated nanostructures, is hence desirable to interpret observations and to enable control over their transport characteristics.

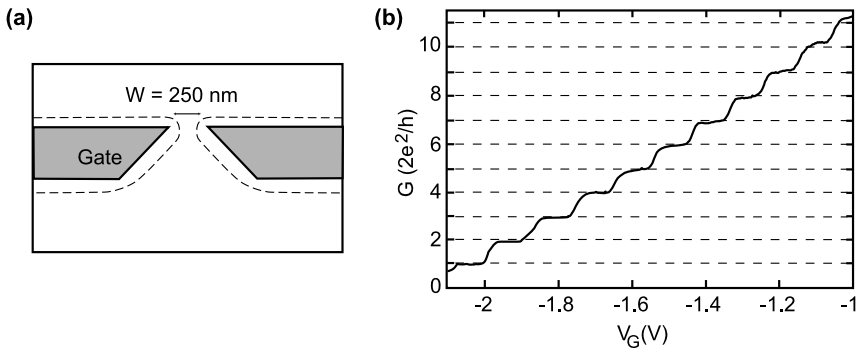

Fig. 5.2 (**a**) Schematic of a split-gate defined constriction in a semiconductor heterostructure as measured in Refs. [8] and [9]. The 2DEG is depleted underneath the gates and the region above the gates is connected only via a narrow opening with the lower part. (**b**) Conductance G as a function of gate voltage V_G for a quantum point contact of width $W = 250$ nm. Conductance is obtained from inversion of the measured resistance signal and the subtraction of a gate voltage independent background resistance. [Figure reprinted from Ref. [8]]

5.2 Constrictions in Conventional Semiconductors

Nanostructures have been studied in semiconductors for the last decades. Often, heterostructures that contain a two-dimensional electron gas (2DEG) buried underneath the surface are used as the starting material. In order to confine charge carriers to even lower dimensions, metal electrodes are placed on the surface. By applying a negative voltage to these so-called split-gates, the 2DEG below the gate area is depleted of charge carriers and hence electrically insulating.

As displayed in Fig. 5.2(a) a constriction is formed if only a small opening remains between two electrodes such that electrons have to pass this channel when crossing from one large reservoir to the other. Low-temperature transport measurements on such a gate geometry on top of a GaAs/AlGaAs heterostructure have been carried out in 1988 for the first time by two groups independently [8, 9]. The resistance recorded in these measurements was transformed into a conductance G which is shown in Fig. 5.2(b) as a function of the applied split-gate voltage V_G. Here, as an over-all tendency, the conductance increases in steps as the gate voltage is made less negative. The intuitive explanation for this effect is that the depleted area is reduced as V_G is tuned to more positive voltages and the channel in Fig. 5.2(a) gets effectively wider allowing more charge carriers to pass.

The more striking observation, however, is the appearance of conductance steps of equal height along the gate voltage axis. With each step the conductance increases by $\Delta G = 2e^2/h$ which equals twice the conductance quantum $G_0 = e^2/h$. The picture behind this experimental finding is that of discrete quantized states, called modes, propagating along the channel axis [10]. These are formed as a consequence of the lateral confinement normal to the direction of motion. Both the Fermi energies

in the reservoirs and the width of the constriction determine the number of occupied modes. If a small bias voltage V_{bias} is applied between the two reservoirs the current carried by the modes traveling to the left and to the right, respectively, differs and a net current flows. Each of the occupied quantum states contributes a net current of $I = (e^2/h)V_{bias}$, meaning one conductance quantum G_0. In zero magnetic field, electron spin degeneracy leads to a conductance contribution of $2e^2/h$ per mode as seen in Fig. 5.2(b).

The phenomenon discussed above is observed in experiment under the condition that the thermal energy $k_B T$ of charge carriers is smaller than the energy spacing between the transverse modes to resolve the discrete values of G. Additionally, the channel width and the length have to be much smaller than the mean free path (ballistic regime) of the electrons and the Fermi wavelength has to be comparable to the channel width. In semiconductor heterostructures these requirements are typically met with the present sample quality at $T \leq 4.2$ K (boiling point of helium). The device introduced in this section is usually referred to as a quantum point contact since its transport properties are a result of the quantum mechanical wave character of the charge carriers.

5.3 Conductance in Graphene Constrictions

The absence of a band gap in bulk graphene does not allow for the adaptation of the split-gate technique, which is commonly used in semiconductors, to graphene. In order to form a quasi one-dimensional transport channel in graphene, the material has to be cut into the desired geometry instead. In experiments, the propagation of electrons along the channel is very sensitive to edge disorder due to the absence of carrier depletion effects near the edges. A number of theoretical studies has been carried out considering different possible edge orientations and edge disorder in such ribbons which will be discussed in this section.

5.3.1 Nanoribbons with Ideal Edges

Like for bulk graphene, tight binding calculations were performed [11–14] to determine the band structure for both clean armchair termination and zigzag termination of the ribbon edges as sketched in Fig. 5.3(a) and (b). Fundamentally different characteristics were found depending on the edge type and the width of the ribbon. In Fig. 5.3(c)–(f) the energy bands of the four distinct cases are shown. Armchair nanoribbons result in either a gapped band structure [Fig. 5.3(c) and (e)] or a gapless metallic bandstructure [Fig. 5.3(d)] depending on the number of dimer lines N across the ribbon width. The latter is found only under the condition that $N = 3m - 1$, with m being an integer, and leads to a degenerate zero energy state at $k = 0$. The size of the direct bandgap ΔE_g in semiconducting armchair ribbons de-

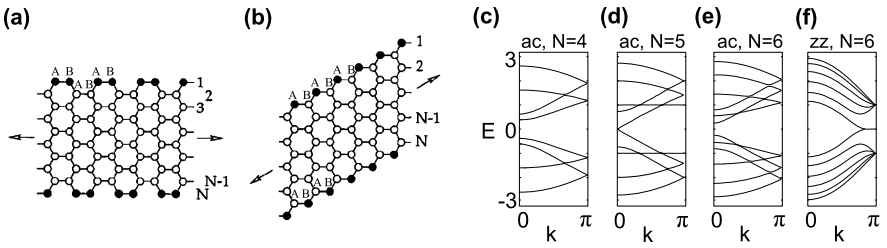

Fig. 5.3 Lattice structure of (**a**) an armchair nanoribbon with $N = 10$ and (**b**) a zigzag nanoribbon $N = 5$. Definition of dimer number N is indicated and the sublattice assignment is marked. (**c**)–(**f**) Tight binding calculations of nanoribbon subbands for (**c**) $N = 3m - 2$ armchair, (**d**) $N = 3m - 1$ armchair, (**e**) $N = 3m$ armchair and (**f**) zigzag with $N = 6$. [Figure reprinted from Ref. [12]]

creases with $1/W$ as the ribbon is made wider [14]. For zigzag nanoribbons the dispersion exhibits a degeneracy of the valence and conduction bands at $k = \pi$ [Fig. 5.3(f)]. As the wave vector is diminished towards the center of the Brillouin zone these two bands continue to lie close to the Fermi level within the wave vector interval $\pi \geq |k| \geq 2\pi/3$ and show almost no dispersion.

The fact that in the armchair case neighboring atoms at the edges belong to different sublattices, whereas all edge atoms belong to the same sublattice in the zigzag case, is responsible for the observed difference in the band structure. Armchair edges include both A- and B-type atoms and hence the wave function needs to vanish on both sublattices at the edges to fulfill the boundary conditions. A zigzag edge, on the other hand, consists of only one sublattice, e.g. A-type on the top edge of Fig. 5.3(b), allowing for a non-vanishing wave function on sublattice B. However, at the opposite side of the ribbon the wave function is required to be zero on the B sublattice. The two dispersionless states at finite k-values originate from this asymmetry between the sublattices and are as strongly localized electronic states at the edges of the zigzag ribbon.

In analogy to the one-dimensional wires formed in semiconductor heterostructures, a quantization of the transverse modes is present in perfect graphene nanoribbons as well. A fundamental variation of the phenomenology is however the symmetry of the quantized spectrum around the Fermi energy. According to the differing subband structures, the edge configuration results in characteristic quantization sequences for the three different cases [15–17]. For semiconducting armchair ribbons a quantization in steps of even multiples of G_0, namely 0, 2, 4, 6 ... $\times (e^2/h)$, is predicted. In the metallic case, the mode at zero energy is already two-fold degenerate and hence the conductance at zero energy is $2e^2/h$ and increases in steps of 2 G_0 as the energy is tuned away from the charge neutrality point. The ideal armchair edge leads to a lifting of the valley degeneracy and therefore only a factor of two for the spins is considered for the quantization [15–17]. For perfect zigzag edges in contrast, the valley degeneracy is expected to be maintained and a sequence of 2, 6, 10, 14 ... $\times (e^2/h)$ is obtained for the conductance.

5.3.2 Extension to Disordered Edges

So far, only nearest neighbor hopping was considered within a tight-binding band structure model, and any disorder was excluded from the discussion. Taking these effects into account, however, induces distinct changes to the results obtained above.

Armchair ribbons, which have a metallic band structure for certain widths in the ideal picture, are found to exhibit a bandgap of several 10 meV. This is obtained by the inclusion of next nearest neighbor hopping and a contraction of the bonds between the edge atoms by 3.5 % [18]. Similarly, a bandgap is opened in zigzag nanoribbons. Here, the reason is a magnetic ordering at the edges with opposite spin polarization on the two sublattices, which originates from on-site repulsion between the states at the Fermi level. This exchange potential difference on the two sublattices moves the previously flat bands that were lying close to the Fermi level, away from each other. Hence, a small but finite band gap is predicted for all nanoribbons with pure armchair [11, 14, 18–20] or zigzag [12, 13, 18] edge termination. For 20 nm wide ribbons band gap values 10 meV $\leq E_g \leq$ 70 meV should hence be achievable according to these calculations.

In order to resemble realistic devices more closely, ribbons consisting of both armchair and zigzag sections have been investigated [12]. Remarkably, the flat bands of the zigzag termination are extremely robust to the inclusion of armchair sites meaning that edge states are present even in ribbons having only few zigzag sites incorporated in the edges. While these electronic states are delocalized along the edge in pure zigzag ribbons, they get more and more localized as armchair fragments interrupt the zigzag termination.

As a consequence of disorder [at the edges] and the accompanying change in the density of states, the formation of subbands is getting less pronounced. Conductance quantization is therefore no longer expected to be observable.

All theoretical studies show a significant deviation of the electronic properties from the ideal case if the edges are assumed to be slightly imperfect. In to date realistic devices, however, disorder is expected to be present both at the edges and in the bulk of the graphene system. How this is affecting the transport properties is going to be the subject of the following sections.

5.4 Experimental Observations and Microscopic Pictures

5.4.1 Fabrication

In order to get close to the device dimensions investigated in theoretical studies, two-dimensional graphene sheets have to be patterned into narrow ribbons, which then act as transport channels for the charge carriers. The commonly applied method is a dry etching technique called reactive ion etching (RIE). After the standard mechanical exfoliation and subsequent identification of single layer graphene flakes by atomic force microscopy and Raman spectroscopy [21, 22], the chip is covered by

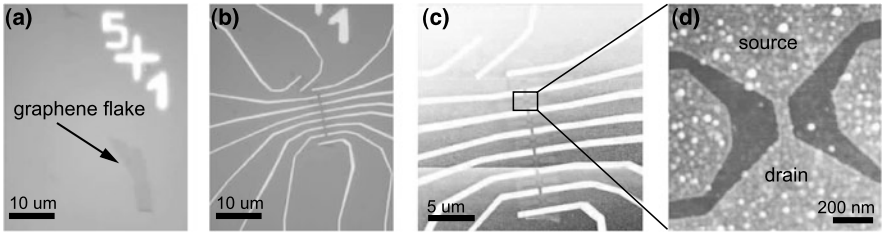

Fig. 5.4 Microscope images at different fabrication steps (**a**) Optical micrograph of a single layer flake on a SiO_2 substrate. (**b**) Graphene flake after fabrication of gold electrodes in an optical microscope. (**c**) Atomic force micrograph after etching process. A number of constrictions with varying aspect ratios is visible in between pairs of contacts. (**d**) Zoom into marked region of (**c**) showing one nanoribbon. Graphene remains in the *light grey areas* whereas in the *dark areas* the substrate is visible. The channel is formed between the source and drain reservoirs and has a width of 75 nm and length of 200 nm

a resist layer. Since the chains of this polymer dissociate when high-energy electrons impinge, electron beam lithography (EBL) can be used to modify the resist in certain areas. The short polymer chains are soluble in a developer and hence the irradiated areas are no longer covered by resist after this processing step. Next, metal is deposited by electron beam evaporation followed by a lift-off process. The created metallic fingers are needed as contacts for all electronic transport measurements discussed in this chapter. As a last step, a directed oxygen-argon plasma in the RIE chamber removes the graphene in the regions laid open in another EBL step. After removal of the remaining resist, the desired structure is left behind in the graphene sheet.

5.4.2 Dependence of Transport on the Charge Carrier Density

Graphene devices are conventionally fabricated on a Si substrate which is covered by a SiO_2 layer. Utilizing the field effect, the highly doped silicon serves as a global back-gate (BG), meaning that by changing the applied gate voltage, the charge carrier density in the graphene structure is tuned. Figure 5.5 shows a typical low-temperature ($T \approx 1.25$ K) gate voltage dependence of the conductance through a graphene nanoribbon with a width of 75 nm and a length of 200 nm. By sweeping the back-gate voltage V_{BG} from negative to positive values, the Fermi energy is tuned from the valence band through the charge neutrality point into the conduction band as is visualized by the sketched Dirac cones in Fig. 5.5. In these two regimes, transport can therefore be described as being hole-like and electron-like, respectively.

In contrast to transport data taken for bulk graphene, here, a region of strongly suppressed conductance is observed in the vicinity of the charge neutrality point around $V_{BG} = -2$ V. In this regime the measured conductance values drop considerably below e^2/h [dashed horizontal line in Fig. 5.5], indicating that the system is

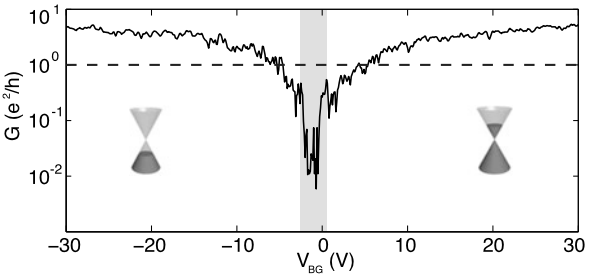

Fig. 5.5 Conductance G as a function of applied back-gate voltage V_{BG}. The data shown was measured for a constriction with length $L = 200$ nm and width $W = 75$ nm at a temperature of $T = 1.25$ K. A DC bias voltage $V_{bias} = 500$ µV was applied and the conductance was recorded using standard lock-in techniques at a frequency of 13 Hz and an AC bias modulation of $V_{mod} = 50$ µV. The *shaded region* indicates the range of the transport gap ΔV_{BG} and the dotted curve marks the value of the conductance quantum e^2/h. [Figure adapted from Ref. [23]]

strongly localized [24]. However, the formation of a band gap cannot explain this feature. The expected size of a band gap E_g for an ideal ribbon of the given dimensions is much smaller than the large change of Fermi energy ΔE_F necessary to overcome the region of conductance suppression ΔV_{BG} in this measurement. Since current flow is strongly inhibited throughout ΔV_{BG}, it is commonly called "transport gap" in the literature.

Additionally, the curve in Fig. 5.5 exhibits strong conductance fluctuations at low charge carrier densities and these fluctuations get smaller as the charge carrier density is increased. Similar features have been observed in measurements of narrow disordered channels in Si-inversion layers [25] where they were explained by hopping transport between strongly localized states caused by the structure of the underlying density of states.

A comparison of the gate voltage dependence for a channel formed in a two-dimensional electron gas plotted in Fig. 5.2(b) and the corresponding measurement of a graphene nanoribbon in Fig. 5.5 illustrates the absence of conductance quantization in the latter. This observation does not come as a surprise since as discussed here, the presence of disorder at the edges results in the disappearance of discrete plateaus in the conductance trace. Due to the top-down fabrication applied here, it is not possible to control the edge termination on the atomic scale as it would be necessary to observe the theoretical predictions of quantized conductance.

5.4.3 Dependence of Transport on the Applied Voltage Bias

It proves helpful to look into the transport characteristics around the charge neutrality point in more detail. A zoom into the transport gap is shown in Fig. 5.6(a) where a large number of conductance resonances show up as a function of back-gate voltage. In between these peaks the conductance is close to zero. A similar behavior

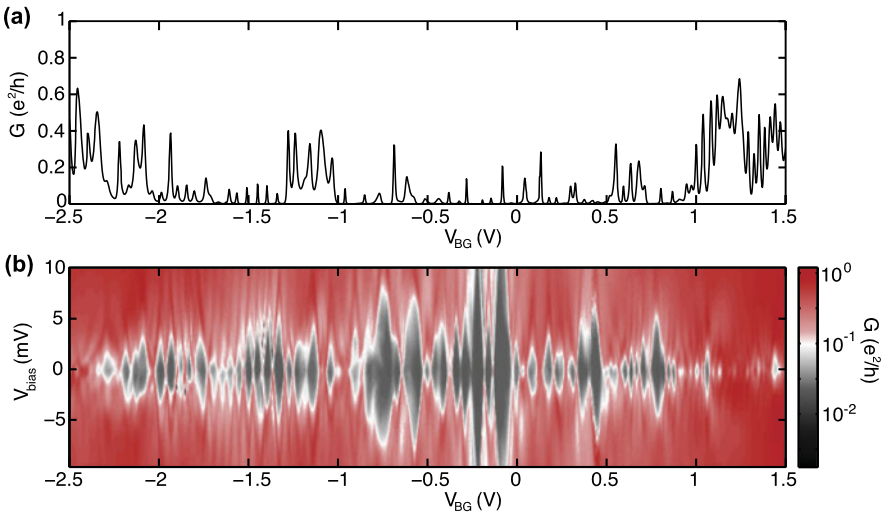

Fig. 5.6 (**a**) Close-up of the conductance spectrum as a function of back-gate voltage inside a transport gap [grey shaded region in Fig. 5.5] taken with an applied voltage bias $V_{bias} = 100$ μV. (**b**) Finite bias measurement of the same back-gate range as in (**a**) showing Coulomb blockade diamonds. Both measurements were obtained with the nanoribbon shown in Fig. 5.4 with $L = 200$ nm and $W = 75$ nm at a temperature of $T = 1.25$ K using lock-in techniques. [Figure adapted from Ref. [23]]

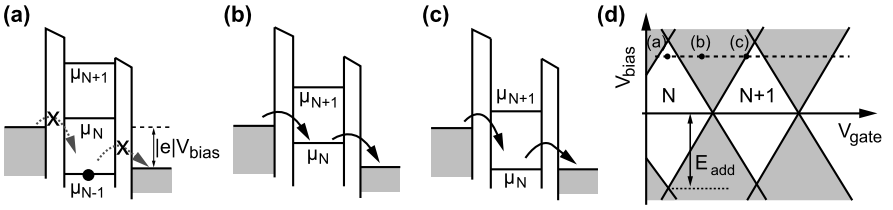

Fig. 5.7 (**a**)–(**c**) Energy diagram of a single electron transistor or single quantum dot. Tunneling barriers separate the island from the leads. The island contains discrete energy levels at electrochemical potential μ_N and μ_{N+1} that can be shifted to lower energies by increasing an applied gate voltage V_{gate} as done from (**a**) to (**c**). The electrochemical potentials of the source and drain reservoirs are offset by the bias voltage V_{bias}. (**d**) Charge stability diagram (V_{bias} vs. V_{gate}) showing regions of suppressed transport in *white*, and regions where transport is allowed in *grey*. [Figure adapted from Ref. [3]]

is known from systems in the Coulomb blockade regime as for example in a single electron transistor (SET) or a single quantum dot (QD) [26].

In such devices a chargeable island is coupled to a source and a drain contact via two tunneling barriers. Due to the size confinement of this island and the Coulomb interaction, the available addition energy levels take discrete values with spacing E_{add}. Figure 5.7(a)–(c) shows a sketch of the arrangement. Additionally, a finite bias can be applied across the structure inducing a difference in the electrochemi-

cal potentials of source and drain. If an energy level of the island lies within this window, as visualized in Fig. 5.7(a), transport is possible and a peak in the conductance is observed. If, on the other hand, no level is inside the bias window [see Fig. 5.7(b) and (c)], current flow is not allowed resulting in zero conductance—the Coulomb blockade. In order to tune the system into or out of the blockaded regime one can either shift the discrete energy levels by applying a gate voltage or change the size of the bias window. In a measurement where both applied bias and gate voltage are changed, diamond-like features of suppressed conductance are observable which are commonly referred to as Coulomb blockade diamonds. As indicated in Fig. 5.7(d), the size of these diamonds in the bias direction directly resembles the energy $E_{add} = |e|V_{bias}$ needed to add one more electron to the island. The addition energy E_{add} is composed of the charging energy $E_c = e^2/C$, where C is the capacitance of the island, and the single-particle level spacing Δ_s. For large islands, the contribution of Δ_s is negligible and hence $E_{add} \approx E_c$. Since the charging energy is related to the capacitance of the island, it is possible to extract information about the size of the SET.

Figure 5.6(b) depicts the result of finite-bias spectroscopy for the graphene nanoribbon introduced in this section. Strikingly, a large number of Coulomb diamonds is obtained similar to the ones expected for an SET. However, in contrast to the rhombi sketched in Fig. 5.7(d), which touch each other in discrete points along the gate-axis and are equal in size, in some regions the measured diamonds overlap each other and show a large variance of their extent in the bias direction. Such characteristics have been observed in devices consisting of several islands which all contribute to transport [27]. Due to the random gate dependence of charge carrier transfer through such a system as well as the randomly varying magnitude of the charging energy E_c, this phenomenology is called stochastic Coulomb blockade.

The described observations evoke the assumption that several localized islands form inside the narrow ribbon. For some back-gate voltage ranges, only one of these islands dominates charge transfer and the characteristics of transport through a single island is obtained [e.g. around -1.5 V in Fig. 5.6(b)]. In other voltage ranges multiple islands contribute to the measured conductance. It is important to notice that in the devices studied so far [23, 28–38], no self averaging is present, meaning that the number of localized sites is rather small. As a consequence the charging of individual islands is detectable in a finite-bias measurement by resolving individual Coulomb diamonds.

A rough estimate of the average size of the localized sites can be obtained from the charging energy extracted from the Coulomb diamonds utilizing a self capacitance model for a disc [26]. In the present device, the islands were found to extend across the total width of the ribbon and other devices yielded similar results [23, 28–38]. An arrangement of the islands in a quasi one-dimensional chain is hence likely and as a rule of thumb the number of puddles p can be approximated by the ratio between the length and width $p \approx L/W$.

5.4.4 Microscopic Pictures

Differing models have been put forward to explain the origin of the transport gap and the observed conductance resonances. Both assume a considerable influence of disorder at the edges and/or in the bulk. While the former originates from the etching process, which results in rough edges, the latter is induced by surface or trapped charges in the substrate or by organic residues left over from the fabrication and lying on top of the graphene sheet. Both types of disorder are hence inherent for the devices discussed here.

The picture of Anderson localization is generally used to describe the influence of disorder on electronic transport. In graphene nanoribbons non-perfect edge termination results in the formation of strongly localized low energy edge states as argued in Sect. 5.3.2, resulting in the suppression of current flow. The localization length is increased, however, as the absolute value of the Fermi energy is raised from zero [39]. When the localization length exceeds the system length, transport is no longer hindered and the transport gap ΔV_{BG} is overcome. In the language of Anderson localization, this transition is termed the "mobility edge". Additionally, the localized states lead to an enhanced density of states (DOS) around the charge neutrality point. Calculations have shown that correlated with the large local DOS at the boundaries there is a reduced DOS in the bulk of the nanoribbon [39, 40]. This may—for large edge defect concentration—span the complete ribbon width and induce a barrier for charge transport [40], leaving localized islands behind. The diameter of such an island is expected to be comparable to the ribbon width [41], in agreement with size estimates from Coulomb diamonds. Hence, the origin of the two identified energy scales ΔV_{BG} and E_c can be accounted for using the Anderson localization model.

A competing explanation involves the formation of localized islands as a consequence of bulk disorder combined with a small energy gap. Due to the disorder potential, a two-dimensional graphene sheet consists of electron-hole puddles [42] close to the charge neutrality point. In large area samples, charge carriers can be transferred from one puddle to another without energy expense via Klein tunneling. If a ribbon of only some nanometers width is considered, on the other hand, the confinement is predicted to open a small band gap [12–14, 18] and electron-electron interaction may additionally induce a Coulomb gap. The borders between adjacent puddles are hence no longer transparent but display real tunneling barriers. Much like in an SET, the particles have to pay a certain charging energy E_c to enter the puddle and Coulomb blockade is expected to occur in such a system. The size of the puddles depends on the spatial variation of the potential landscape. In this picture, the size of the transport gap ΔV_{BG} is given by the sum of the amplitude of the disorder potential and the size of the energy gap since transport is constricted as long as the Fermi level lies between the global minimum of the valence band and the global maximum of the conduction band.

Besides these two pictures, another model assumes transport in disordered graphene to happen along percolating paths of constant energy. In the presence of

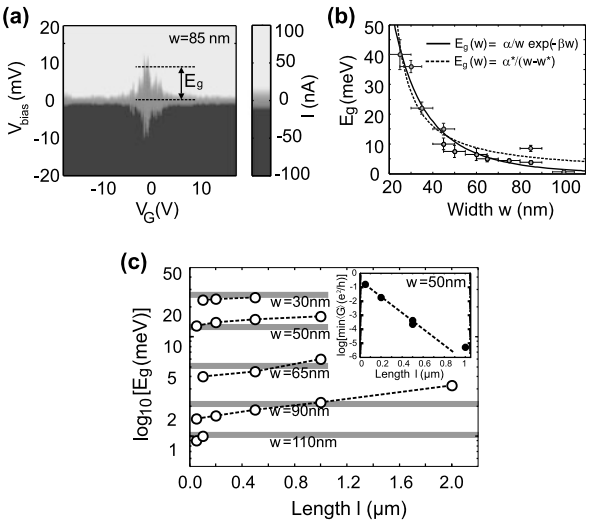

Fig. 5.8 (**a**) Finite-bias spectroscopy for a 85 nm wide and 500 nm long nanoribbon. A region of suppressed current is visible. The characteristic energy E_g was extracted from the size in the bias direction as indicated by the *dashed lines*. (**b**) E_g as a function of ribbon width W. Fits according to the equations indicated in the graph were carried out to compare the experimental data with theoretical predictions. (**c**) E_g as a function of ribbon length L for various different widths W between 30 and 110 nm. Indicated as *grey bars* are the expected values for the energy gap $E_g = \alpha / We^{-\beta W}$ according to Refs. [45] and [46]. The *inset* shows the minimum value of the running averaged conductivity as a function of ribbon length for a 50 nm wide device. [Figures reprinted from Refs. [44] and [38]]

an energy gap in nanoribbons, the system is expected to undergo a two-dimensional metal-insulator transition [43].

The so far presented experimental transport data can be understood in all these frameworks relatively well leaving the exact microscopic mechanisms behind transport a question yet to be answered. To shine further light on this open issue, more experiments have been carried out which will be the subject of discussion in Sect. 5.5.

5.4.5 Geometry Dependence

To get a better feeling for the meaning of the energy scales observed in transport spectroscopy, a large number of experiments were conducted on ribbons of varying geometries [28–30, 32, 34–38]. From these measurements, several empirical scaling laws could be extracted.

The first quantitative characterization of the transport gap was done by Han et al. [28]. By investigating the extent of the region of suppressed conductance ΔV_{BG} in the bias direction, they extracted a value for the size of the energy gap E_g. Figure 5.8(a) displays finite-bias measurements for a nanoribbon of width 85 nm

and the dashed lines indicate, how E_g is commonly extracted from such a conductance map. Data for twelve nanoribbons of varying dimensions was analyzed in Ref. [44] to find the width dependence of E_g. Plotting the determined values for E_g as a function of width W yields the graph shown in Fig. 5.8(b). This plot clearly shows the inverse proportionality between the two magnitudes. The data can be fitted well with the relation $E_g = \alpha/(W - W^*)$ with α being a scaling factor and W^* being the width of an inactive region at the edge of the ribbon. These two fitting parameters were found to take the values $\alpha = 0.38$ eV nm, in agreement with theoretical predictions [45], and $W^* = 16$ nm. Besides this empirical law, Sols et al. [45] explained the energy gap as a renormalized charging energy and derived the expression $E_g = (\alpha/W)e^{-\beta W}$, where α and β are free parameters. Fitting the data with this relation leads to values of $\alpha = 2$ eV nm and $\beta = 0.026$ nm^{-1}. Both models describe the data well within the experimental precision and quantify how the size of the transport gap can be tuned by the ribbon width over a remarkably wide range.

In contrast, studies investigating the size of the energy gap as a function of ribbon length L [38] obtain an almost constant E_g-value when the length of the constriction is changed [see Fig. 5.8(c)]. However, the minimum value of the averaged back-gate dependent conductance G_{min} exhibits a strong length dependence. With increasing L the conductance value drops exponentially as shown in the inset of Fig. 5.8(c). This finding is consistent with the microscopic picture of transport being dominated by tunneling processes between localized charged islands.

Surprisingly, even for very short constrictions ($L \leq 60$ nm) localization takes place [30, 38]. Charge stability maps taken on such devices look very similar to those of intentionally designed quantum dots. Inside the Coulomb diamonds a number of co-tunneling lines is visible, suggesting a rather strong coupling to the leads [38]. These systems might therefore be suitable to investigate the Kondo-effect in graphene and observe Fano-resonances. Additionally, the limit of short constrictions is very interesting for the fabrication of more sophisticated devices since the occurrence of localization allows for their use as tunneling barriers in graphene nanostructures.

5.5 Further Experiments for More Detailed Understanding

5.5.1 Temperature Dependence

The measurements covered in the previous sections indicated that a number of localized charge puddles form spontaneously in graphene nanoribbons around the charge neutrality point. However, the mechanism behind transport in those devices was not yet discussed. Studying the temperature dependence of the conductance reveals the activation processes for electronic transport inside the transport gap [23, 34, 36].

In Fig. 5.9(a) the conductance inside the transport gap is plotted for various temperatures between 1.25 K and 45 K [non-equal spacing in T]. The sharp conductance peak spectrum at the lowest temperatures gets washed out more and more as

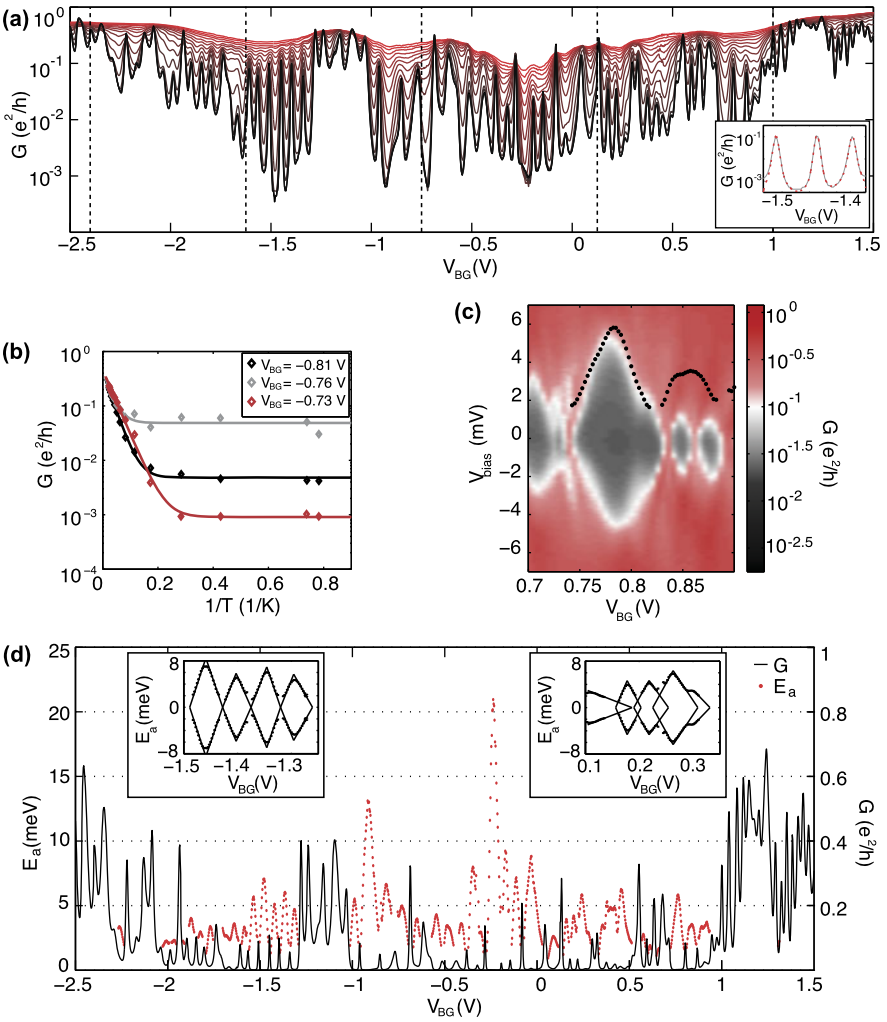

Fig. 5.9 (**a**) Conductance G as a function of back-gate voltage V_{BG} for temperatures 1.25 K $\leq T \leq$ 45 K (*black* to *red solid curves*). *Inset*: Three distinct conductance resonances reproduced by a convolution of the derivative of the Fermi function at $T = 1.25$ K and Lorentzian distributions of different widths. (**b**) Conductance G vs. temperature $1/T$ for three positions in back-gate voltage. *Discrete points* are the measured data and *solid lines* are the results of a fit to the Arrhenius-type law given in (5.1). (**c**) Extracted activation energy E_a superimposed onto a close-up of the finite-bias measurement in Fig. 5.6(b). (**d**) Back-gate dependence of the activation energy E_a (*red dotted line*) and the conductance (*black solid line*) inside the transport gap. *Insets*: Coulomb diamonds reconstructed from E_a for two characteristic regimes of the back-gate voltage. [Figure adapted from Ref. [23]]

the temperature is increased. This is due to a large increase of the conductance in the Coulomb blockaded regions in between resonances. For the conductance peaks, two distinct behaviors are observable. A number of peaks decrease in height as

the temperature is raised, whereas the majority exhibit an ever larger amplitude as T is raised and get broadened at the same time. Hence, a rather smooth conductance curve is obtained for the highest temperature approaching a conductance value of e^2/h.

For single quantum dots, the evolution of the peak shape was explained by the contributions of temperature, single-particle level spacing Δ_s and a coupling of the energy levels to the leads [47]. A $1/T$-dependence is expected for a strongly coupled ground state, as observed in Fig. 5.9(a) for peaks that are particularly sharp at the lowest temperatures. If, however, an excited state exhibits a stronger coupling to the leads than its ground state, a temperature increase will facilitate transport until, at $\Delta_s \lesssim k_B T$, both levels contribute to transport. The latter effect leads to the recorded amplitude increase and the broadening of conductance peaks in Fig. 5.9(a).

The thermal activation of G in the conductance valleys gives insight into the transport mechanisms. Figure 5.9(b) displays the conductance as a function of $1/T$ for three representative back-gate values, showing the different temperature dependences observed. In this Arrhenius-type plot, the curves show a branch with a linear slope for the higher temperatures [$T \gtrsim 3$ K] and a branch with almost constant value of G at lower T. The activation above the threshold temperature is linked to the energy needed to induce transport through the system. Empirically, the data can be fitted to

$$G(T) = G_0 \exp\left(-\frac{E_a}{k_B T}\right) + B \tag{5.1}$$

with the free parameters G_0 being a prefactor quantifying the high-T limit of G, E_a being the activation energy and B being a constant offset. The solid lines in Fig. 5.9(b) are the resulting fits and show that the data [diamond shaped markers in Fig. 5.9(b)] can be reproduced very well with this empirical law.

A physical motivation for (5.1) is found by reproducing the peak shape of the Coulomb blockade resonances considering both thermal and coupling broadening. The width of the peaks is resembled well by the derivative of the Fermi function at a given temperature. A large discrepancy is found, however, for the tails of the peak where the thermal broadening underestimates the conductance considerably. In order to obtain higher values for the conductance away from the resonances, the Fermi function is convoluted with a Lorentzian distribution function. With this additional contribution the coupling of the energy levels to the leads is taken into account. The tail of the Lorentzian, and hence the constant B in (5.1) can be interpreted as describing cotunneling processes in the system at the lowest temperatures.

To motivate (5.1), the low temperature limit of the Fermi distribution, $E_c = 2E_a \gg k_B T$, has to be considered, which reads

$$\begin{aligned} \frac{df(E)}{dE} &\propto G(T) \propto \cosh^{-2}\left(\frac{E_a}{2k_B T}\right) \\ \Rightarrow \quad G(T) &\propto \exp\left(-\frac{E_a}{k_B T}\right). \end{aligned} \tag{5.2}$$

Note that the maximum activation energy E_a for transport is half the charging energy E_c describing the spacing between two energy levels of a localized island. The

prefactor, G_0, specifies the conductance value at high temperatures where the exponential term in (5.2) approaches unity. It contains contributions from various transport mechanisms which cannot be quantified easily. Finally, cotunneling of charge carriers results in a constant background, B, which has to be added to (5.2). Hence, the application of (5.1) for fitting the experimental data is well motivated.

The three fitting parameters E_a, G_0 and B of (5.1) can be determined for each back-gate voltage to obtain their specific energy dependence. Meaningful values are attained for those back-gate values where G covers more than one order of magnitude as a function of T. In this section, the activation energy E_a will be discussed exclusively but further analysis can be found in Ref. [23].

Figure 5.9(d) shows the extracted energy spectrum $E_a(V_{BG})$ inside the transport gap. A number of peaks are observable in the E_a curve, which coincide with valleys in the conductance trace. Energies as high as 20 meV are necessary to activate transport in the device in Fig. 5.9(d). Away from the peak maxima, the activation energy decreases linearly towards the position of the adjacent conductance resonances.

This finding for the E_a dependence is very similar to the behavior of the Coulomb diamond edges in Fig. 5.6(b). To confirm this correlation, the two magnitudes are plotted on top of each other for a chosen back-gate position in Fig. 5.9(c). Indeed the shape of the large Coulomb blockade diamond is reproduced by the peak of the activation energy. Accordingly, these two energy scales have the same physical origin meaning that the activation energy corresponds to the Coulomb gap formed inside the nanoribbon.

To support this hypothesis further, a number of Coulomb blockade diamonds are reconstructed from the activation energy by reflecting the data at the gate voltage axis and inserting lines along the slopes of the energy peaks. As depicted in the insets of Fig. 5.9(d), two distinct characteristics are observable for certain back-gate voltage values. On the left hand side, the regions of suppressed conductance are separated from each other and exhibit similar size as is typical for a single quantum dot. The graph on the right hand side shows overlapping Coulomb blockade diamonds with varying edge slopes and different size in the bias direction, as yielded in a charge stability diagram for multiple quantum dots in series.

In summary, the interpretation of the finite-bias measurement presented in Sect. 5.4.3 and the analysis of the thermal activation measurements arrive at the same conclusions: Charge transport in graphene nanoribbons is dominated by mainly one or a few puddles arranged in series. Although details depend on the mesoscopic arrangements within the system, carrier transmission can be understood in a single-particle picture including Coulomb blockade.

5.5.2 Magnetic Field Dependence

Studying an electronic system in the presence of a perpendicular magnetic field allows for the detailed understanding of its properties since the spatial extent of the electron wave function is changed as an external B-field is tuned. In a semi-classical

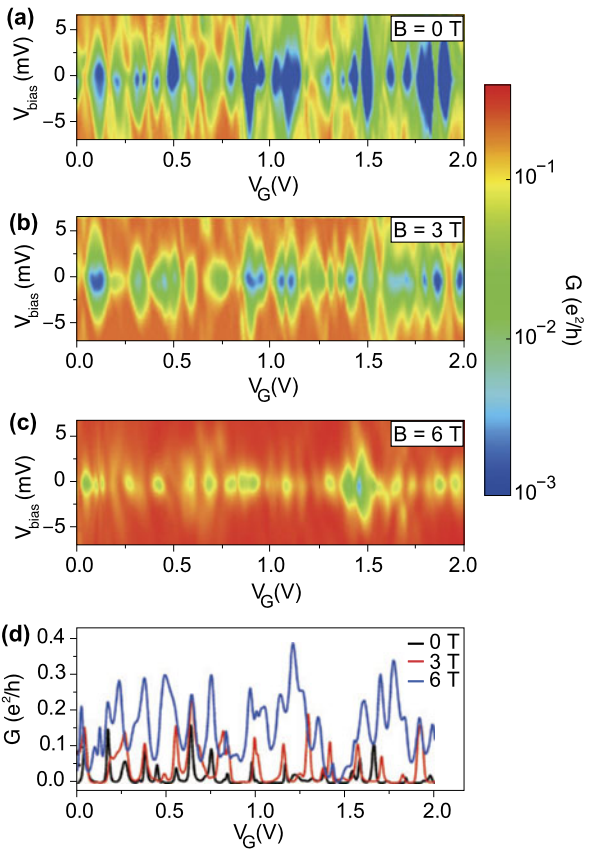

Fig. 5.10 (**a**)–(**c**) Differential conductance measurements as a function of source-drain bias and gate voltage at $B = 0$ T (**a**), 3 T (**b**) and 6 T (**c**) showing the evolution of the diamonds of suppressed conductance with increasing magnetic field. (**d**) Differential conductance G versus gate voltage at zero source-drain bias with an applied magnetic field of 0, 3 and 6 T. The device has a width of 37 nm and length of 200 nm and was measured at $T = 1.6$ K. [Figure reprinted from [37]]

picture, this is due to the propagation of charge carriers on cyclotron orbits of radius r_{cycl} as a Lorentz force acts on them. As a consequence, transport is mainly sensitive to potential fluctuations of certain length scales in the different regimes. Magneto transport in graphene nanoribbons was investigated to probe the effect of a magnetic field on the localized states inside the conduction channel [36, 37].

Figure 5.10(a)–(c) shows finite-bias measurements of a graphene nanoribbon of dimensions $W = 37$ nm and $L = 200$ nm at magnetic fields $B = 0$ T, 3 T and 6 T [37]. Coulomb blockade diamonds are visible indicating the formation of charged islands inside the ribbon. As the magnetic field is ramped up, the size of these regions of suppressed conductance shrinks considerably and the overall conductance is enhanced. This is best seen in Fig. 5.10(d) where cuts at zero source-drain bias are plotted for the three magnetic field values.

Smaller Coulomb diamonds indicate a decrease of the charging energy E_c and therefore an increase in island size. In agreement with these findings, temperature dependent measurements [23, 36] in finite magnetic fields indicated that the energy scales relevant for transport, namely ΔV_{BG} and E_a, are shrinking if a finite magnetic field is applied.

To explain these observations, we compare the dimensions of the nanoribbon with the magnetic length $l_B = (\hbar/eB)^{1/2}$. If the ribbon width W is much smaller than the cyclotron length $W \ll l_B$, the electron wave function extends across the whole width and hence transport is influenced by both edge and bulk disorder. This condition is fulfilled for low magnetic fields. As B gets larger the magnetic length falls below the system dimensions and the effect of both the quantum confinement and the edges becomes less relevant for transport [37].

A contrary effect of the applied magnetic field is that the localization of the wave function leads to a smaller wave function overlap and hence a smaller tunneling coupling between neighboring puddles. As a consequence, the conductance is reduced as the magnetic field is increased.

The two contributions are therefore expected to compete in nanoribbons. In the data presented here, the reduced backscattering is dominating causing an increase of the conductance. Following this observation, it is suggested [48–50], that the system eventually undergoes a semiconductor-metal transition at high magnetic fields. The data presented in Fig. 5.10 are in good agreement with this explanation and imply that the ribbon width is a good estimate for the size of the localized states.

However, as noted in Ref. [36], Landau level quantization should be observable at high magnetic fields where $W \gg l_B$. Under these conditions, edge channels are expected to be formed which each contribute to transport with (e^2/h). Measurements on wide channels [$W \gtrsim 100$ nm] have indeed shown indications of conductance quantization [51]. Conductance data of narrower ribbons, on the other hand, did not exhibit this feature. Possibly, scattering events between transport channels located at opposite edges, inhibit the transmission for narrow ribbons. As the edge channels are separated further for wider nanoribbons, scattering is less likely and Landau level formation may be recorded in conductance measurements.

Following the reasoning of Ref. [36], the enhanced conductance originates from the breaking of time reversal symmetry in a finite magnetic field [52, 53]. The magnetic flux through the area occupied by a localized state has to be comparable to a flux quantum h/e in order to break time reversal symmetry. Measurements of the B-field dependent conductance allow us to extract a size estimate for the localized sites. The obtained value is comparable to the ribbon width [36], and hence, magnetic field spectroscopy is providing yet more evidence for the spatial extent of the charged islands in graphene nanoribbons.

5.5.3 Side-Gate Influence

Changing the potential landscape locally helps to understand the spatial arrangement of localized islands inside the narrow channels. Transport studies on graphene nanoribbons with two nearby in-plane side-gates were carried out. While one of the side-gates (SG1) affected the drain-side of the ribbon preferentially, the other (SG2) acted more on the source-side. By tuning the side-gate voltage with respect to the back-gate voltage, the conductance resonances inside the transport gap are shifted

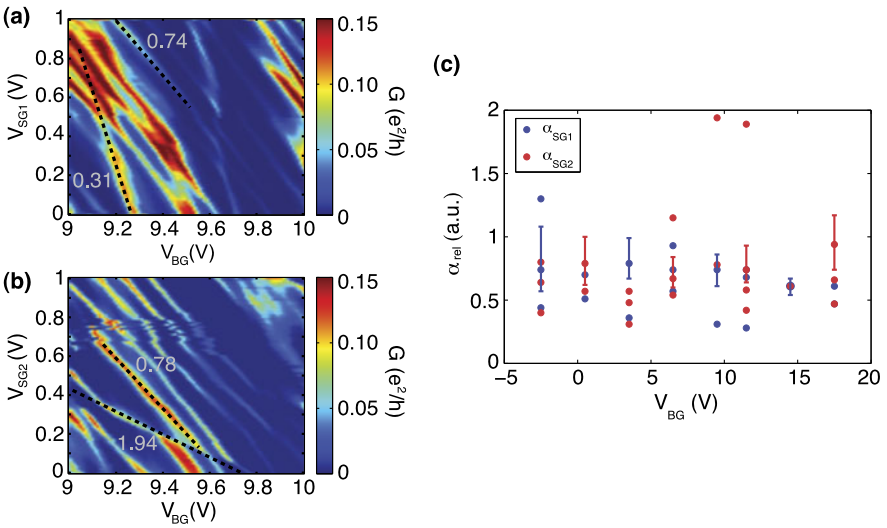

Fig. 5.11 Conductance G as a function of side-gate voltage V_{G1} in (**a**) and V_{G2} in (**b**) for the back-gate voltage 9 V $\leq V_{BG} \leq$ 10 V inside the transport gap. *Black lines* indicate the evolution of Coulomb blockade resonances and are labeled with the corresponding relative lever arms. (**c**) Relative lever arms α for different back-gate configurations inside the transport gap extracted from maps similar to (**a**) and (**b**). The exemplary error bars arise from the fitting imprecision

in energy according to the coupling of the side-gate to the respective localized state. Assuming that mainly the distance between the gate and the charged puddle determines the coupling, Coulomb blockade resonances evolving with similar slopes should originate from the same localized sites.

Representative gate-gate maps are shown in Fig. 5.11(a) and (b), where SG1 and SG2 were used, respectively, to tune the conductance resonances in the back-gate voltage range 9 V $\leq V_{BG} \leq$ 10 V. In each graph, two different slopes for the evolution of the Coulomb blockade resonances are distinguishable. This finding indicates that only two localized islands dominate the transmission through the nanoribbon in the investigated gate regime. The measured device has a length of $L = 200$ nm and a width of $W = 80$ nm. Applying the rule of thumb for the number of puddles $[p \approx L/W]$ in a ribbon of these dimensions, yields 2–3 localized islands and hence agrees well with the result of this measurement.

A relative lever arm α can be extracted from these slopes which characterizes the strength of the capacitive coupling of the side-gate with respect to the back-gate. The values determined from Fig. 5.11(a) and (b) are $\alpha_{SG1} \approx 0.74$ and 0.31 for SG1 and $\alpha_{SG2} \approx 0.78$ and 1.94 for SG2. A rough estimate for the position of the respective localized state is possible with these numbers. As the lever arm $\approx$0.75 appears in both plots, the corresponding puddle is likely sitting in between the two side-gates or in other words in the center of the ribbon. The other resonance is tuned only weakly by SG1 [$\alpha_{SG1} \approx 0.31$] but strongly by SG2 [$\alpha_{SG2} \approx 1.94$], which suggests that it is located much closer to SG2 than to SG1. Additionally, it couples better to

the side-gate than to the back-gate indicating that the back-gate influence is screened relative to the side-gate influence.

Measurements like those shown in Fig. 5.11(a) and (b) were performed for several back-gate ranges inside the transport gap and the corresponding lever arms were extracted [see Fig. 5.11(c)]. Generally, several slopes were recorded in all regimes, however never more than four different ones. Furthermore, the discussed anti-correlation of the relative lever arms originating from different side-gates is observed in most back-gate voltage ranges as well. For the analysis, several Coulomb resonances with similar slopes were fitted to extract the relative lever arms. Since the evolution of such resonances in the gate map is not perfectly linear, a dispersion around a mean value is obtained. This error is relatively large, as it can be seen from the exemplary error bars in Fig. 5.11(c). Nevertheless, the varying values for α inside the transport gap illustrate the modulation of the coupling of distinct states to the gates. This effect may be explained by puddles rearranging themselves inside the constriction. Along with the tuning of the back-gate voltage comes a change in the potential landscape and hence in the puddle size and position—some get larger and even merge with neighboring ones, others fall into smaller islands.

In conclusion, a small number of puddles along the nanoribbon influences the transmission. The exact number and arrangement of these islands is changed as a function of Fermi energy as reasoned from the lever arm modulation. Hence, the experiments on side-gated graphene nanoribbons support statements about the mesoscopic character of the system made earlier in this chapter.

5.5.4 Thermal Cycling

In the previous sections, transport properties were interpreted as the finger print of disorder in the graphene nanoribbons that were investigated. However, the microscopic origin of this disorder was not discussed based on experimental results so far. Two contributions—edge and bulk disorder—were identified in Sect. 5.4.4 but not further specified.

In order to shine light on the character of these influences, conductance spectra of a nanoribbon were measured at $T = 1.25$ K before and after warming the nanoribbon up to room temperature. The recorded data is shown in Fig. 5.12 where the conductance inside the transport gap is plotted as a function of applied back-gate voltage.

Both measurements exhibit the region of suppressed current in the gate voltage interval $-1.5\ \text{V} \leq V_{BG} \leq 1\ \text{V}$ and the conductance resonances show the same order of magnitude of suppression in this regime. Some Coulomb blockade resonances even fall on top of each other. As the gate voltage is moved away from the center of the gap, the conductance spectra differ more. In contrast, some main features like the small peak spacing at positive gate voltages and the larger spacing for negative V_{BG} are preserved.

These observations indicate that the potential landscape that is causing the conductance fluctuations at low temperatures undergoes a significant change at $\approx$300 K.

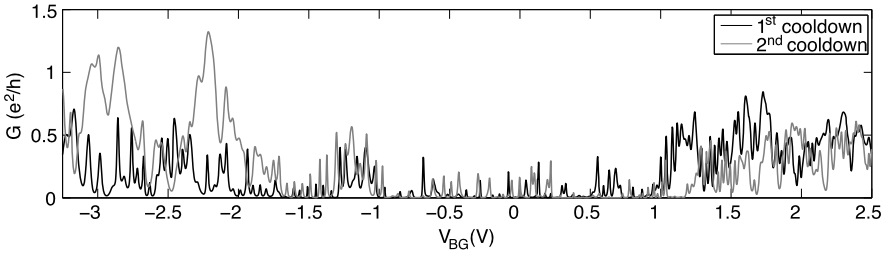

Fig. 5.12 Conductance G as a function of applied back-gate voltage V_{BG} before and after warming the sample to room temperature. The data shown was measured for a nanoribbon with length $L = 200$ nm and width $W = 75$ nm at a temperature of $T = 1.25$ K. A DC bias voltage $V_{bias} = 500\ \mu$V was applied and the conductance was recorded using standard lock-in techniques at a frequency of 13 Hz and an AC bias modulation of $V_{mod} = 50\ \mu$V

The thermal energy associated with room temperature is low compared to energies necessary to reconstruct the graphene lattice or break covalent bonds. Hence the disorder is not only caused by the disordered edge structure of the graphene lattice, nor is it only some bulk disorder due to lattice imperfections, rippling, or other structural properties. Imperfections that can be rearranged at room temperature, on the other hand, are charge traps in the SiO_2, adsorbates and debris on the surface, etc. The here discussed measurements therefore show that the environment [e.g. substrate, processing residues] has an important influence on the transport characteristics in graphene nanoribbons.

5.5.5 Tunneling Coupling in a Double Quantum Dot

In order to examine the role of constrictions as constituents of graphene nanostructures, we will discuss their effect on transport with the help of a double quantum dot (DQD) structure [6]. DQD systems are of great interest for quantum information processing and have been proposed for the implementation of solid-state spin qubits [54]. Graphene, due to its expected long spin coherence time, may be particularly well suited for such applications. An introduction to the basic electronic transport properties of such a structure can be found e.g. in Refs. [55] and [26].

The device is fabricated as described in Sect. 5.4.1 and consists of a source (S) and a drain (D) lead each coupled to an island (QD1 and QD2). As seen in the micrograph in Fig. 5.13, the series connection of these elements is realized by narrow constrictions. The fact that current flow in the constrictions is suppressed inside the transport gap is exploited here and these channels serve as tunneling barriers. If they are resistive enough, namely if $R > h/e^2$, the energies of charge states in the double quantum dot are governed by Coulomb repulsion and by the alignment of the electrochemical potentials in the source, drain and the two dots. Nearby gates allow for the control and manipulation of the electronic states in the individual dots. However,

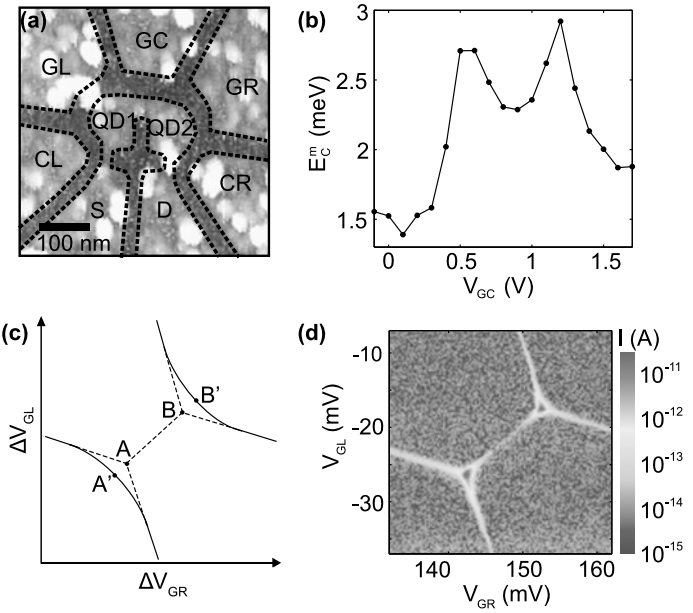

Fig. 5.13 (**a**) Atomic force micrograph of a graphene double quantum dot (same device as shown in Fig. 5.1(b)). The two quantum dots QD1 and QD2 are connected to source S and drain D via a narrow constriction. A number of in-plane side-gates can be used to tune the constrictions and the dots, respectively. (**b**) The capacitive coupling energy E_C^m as a function of center-gate voltage V_{GC} extracted from the splitting of the triple points in the charge stability diagram. (**c**) Schematic of a pair of triple point without (*dashed line*) and with tunneling coupling t (*solid line*). The kinks at the boundaries of hexagons are rounded as a result of the inter-dot doubling. (**d**) Measurement of charge stability diagram around a pair of triple points. Due to the low bias $V_{bias} = 15$ µV, no finite bias triangles are observed and the triple points can be examined separately. [Figure reprinted from [51]]

the interaction between the dots is fundamental for qubit operations. Therefore we will limit the discussion here to the constriction connecting the two quantum dots.

With the center-gate (GC), the coupling between the two dots can be tuned [6]. In a first step the capacitive coupling is determined from the splitting of triple points in the charge stability diagram at varying center-gate voltages V_{GC}. Since the center-gate voltage influences the electrostatics in the dots as well, the triple points shift in gate space. However, by applying compensation voltages to the other gates, care is taken to examine the same triple point for all gate configurations. The extracted coupling energy E_C^m as a function of V_{GC} is shown in Fig. 5.13(b). Clearly a non-monotonic behavior is observed in this voltage range and $E_C^m(V_{GC})$ doubles from $V_{GC} = 0.1$ V to $V_{GC} = 1.2$ V. This observation is different from comparable measurements of double quantum dots in conventional semiconductors where a monotonic tuning of the tunneling barrier is expected.

The implications of the previous sections in this chapter are, that graphene constrictions exhibit a strongly non-monotonic dependence of the conductance on the

applied gate voltage. As a consequence, transport is strongly modulated as a function of applied gate voltage. In the present device, the potential landscape inside the center constriction hence affects the capacitive coupling between the dots considerably.

Besides the capacitive contribution to the coupling, the barrier determines the tunneling coupling t in the system. A weak inter-dot coupling causes the two electron wave functions to be localized on either dot. Strong coupling on the other hand leads to delocalized quantum mechanical states that extend across the barrier and form a two-level system. Such a system can be thought of as an artificial molecule [55] since the wave functions of the two dots hybridize and form bonding and anti-bonding states. The effect of a finite tunneling coupling on the energy diagram is an anti-crossing at zero detuning of the energy levels in the two dots.

In experimental data, mixing of quantum states gets apparent again at triple points in the charge stability diagram. As a consequence of the energy level anti-crossing they get rounded as schematically drawn in Fig. 5.13(c). The shift of the triple points [from A to A′ and from B to B′ in Fig. 5.13(c)] due to the tunneling coupling t is expected to scale linearly with t.

A low-bias measurement [$V_{bias} = 15$ μV] of a pair of triple points in the graphene DQD is presented in Fig. 5.13(d) [46]. No rounding of the hexagon corners is evident in this graph and therefore an upper bound for the tunneling coupling can be given by $t \leq 20$ μV. The data was recorded at low temperatures of $T \approx 120$ mK and hence the thermal broadening of the conductance resonances is of the same order of magnitude as the tunneling coupling [$k_B T \approx 10$ μV]. On the other hand, the capacitive coupling energy E_C^m exceeds both energy scales by far. Numerical simulations based on the rate equation for a double quantum dot [46] were in good agreement with the experiment and yielded a value of $t = 14$ μV for the inter-dot tunneling coupling.

Two possible explanations were identified for the large discrepancy between the capacitive and the tunneling coupling. A narrow but high barrier would suppress the tunneling coupling and at the same time allow for a large capacitive coupling. This effect may originate from the potential fluctuation inside the constriction. The device geometry itself may however also cause a difference in energy scales. Here, the constriction is located at the upper edge of the structure where the probability amplitude of the wave function is expected to be small. An extension to the adjacent dot may therefore not be preferable, leading to small t. The capacitive coupling, on the other hand, stays unaffected. Similar observations of capacitive coupling dominating over tunneling coupling are made in GaAs double quantum dots as well. However, in many cases the ratio between these two contributions can be tuned monotonically [56] to achieve either single or double quantum dot behavior.

The experiment presented in this section illustrated the challenges involved with the application of graphene constrictions as tunneling barriers in nanostructures. The strongly non-monotonic transmission properties hamper the controlled tunability of these devices. However, the stability of the system over a large gate voltage range is remarkable [6] and—even though not monotonic—different coupling regimes can be achieved. In order to get a better control over the system, clean tunneling barriers

are required, however, and large effort need to be made to improve the transport properties of graphene constrictions.

5.6 Recent Advances and Outlook

All structures presented in the previous sections of this chapter were fabricated on a Si/SiO_2 substrate and carved into a graphene sheet by means of dry etching. The main conclusion of this chapter is, that the mesoscopic character of transport through graphene nanoribbons originates from disorder at both the edges and in the bulk. As discussed earlier, the environment like the substrate or adsorbates on the graphene surface are likely to have a large impact on the potential landscape. As a consequence of the strong disorder, the transmission tunability can be strongly non-monotonic due to conductance resonances in the constriction. Since narrow and short constrictions serve as tunneling barriers in nanoscale devices, the reduction of bulk disorder and well controlled edges are desirable. Several approaches have been realized recently to improve on these issues.

5.6.1 Bottom-Up Growth of Nanoribbons

High precision width and edge parameters are obtained by bottom-up growth of graphene nanoribbons following the reaction scheme shown in Fig. 5.14(a). Single molecules containing benzene rings [e.g. 10,10′-dibromo-9,9′-bianthryl] were used as precursor monomers for the fabrication of narrow ribbons [57]. Under well defined conditions these molecules are deposited onto either a gold or silver single crystalline substrate. At elevated temperatures of $T = 200$ °C, dehalogenation takes place and the generated radicals arrange themselves in linear polymer chains with interconnecting C–C bonds. A low-temperature, scanning tunneling micrograph of this intermediate step is depicted in Fig. 5.14(b) where the originally separated monomers are connected in series along the center benzene rings. Further annealing leads to a cyclodehydrogenation reaction, which removes the hydrogen termination atoms and allows covalent C–C bonds to be established between adjacent benzene rings.

The width of the resulting nanoribbons can be varied by the design of the precursor molecule and the type of edge termination—armchair or zigzag—is determined by the source chemical as well. The STM image in Fig. 5.14(c) demonstrates the extraordinary quality of this armchair ribbon with $N = 7$ dimers across the structure which resembles closely the nanoribbons discussed in Sect. 5.3.1. Potentially, nanoribbons with well defined band structures due to atomically precise edge termination and width can be achieved. However, measurements investigating the size of the band gap for these narrow channels either by optical or by elec-

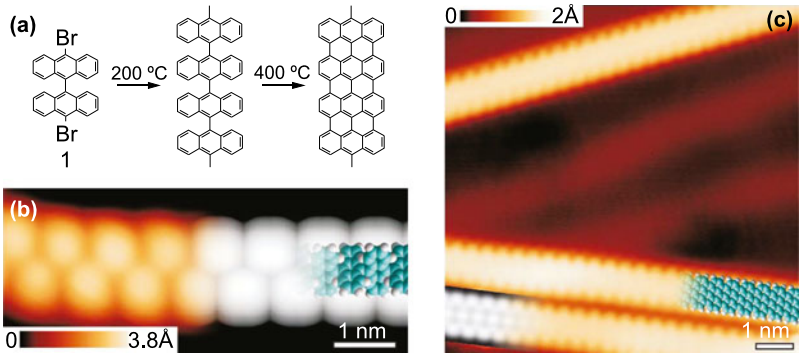

Fig. 5.14 (**a**) Reaction scheme from precursor **1** to straight $N = 7$ GNRs. (**b**) Scanning tunneling microscope (STM) image taken after surface-assisted C–C coupling at 200 °C but before the final cyclodehydrogenation step, showing a polyanthrylene chain (*left*, temperature $T = 5$ K, voltage $V = 1.9$ V, current $I = 0.08$ nA), and DFT-based simulation of the STM image (*right*) with partially overlaid model of the polymer (*blue*: carbon; *white*: hydrogen). (**c**) High-resolution STM image with partly overlaid molecular model (*blue*) of the ribbon ($T = 5$ K, $V = -0.1$ V, $I = 0.2$ nA). At the bottom left is a DFT-based STM simulation of the $N = 7$ ribbon shown as a greyscale image. [Figure reprinted from Ref. [57]]

tronic means remain to be carried out and to be compared to theoretical predictions.

5.6.2 *Quantized Conductance in Suspended Nanoribbons*

Since the SiO_2 substrate is believed to be a major source for the large disorder in graphene systems a possibility to improve the quality is to eliminate the substrate. Different methods have been established to obtain suspended graphene sheets. While the oxide is etched away in one approach [58, 59], a polymer spacer layer is patterned in the other [60]. In both methods the suspension is the last step of the fabrication applied to a contacted graphene flake. Directly before the measurements, a high current is sent through the structure. The high current density ($j \approx 1$ mA/μm) induces local Joule heating, which reaches temperatures larger than $T = 500$ °C, and removes organic residues from the surface and allows for reconstruction of the edges leading to high mobility devices. In Fig. 5.15(a) a scanning electron microscope image reveals the modification in the device induced by the high current.

Surprisingly, finite-bias spectroscopy at zero magnetic field [Fig. 5.15(b)] reveals a stair case-like pattern, with plateaus of constant conductance G along the zero bias axis [60]. The steps are located at even multiples of $G_0 = e^2/h$ as expected for a system in which the valley degeneracy is lifted [15–17]. Although strong statements about the exact edge structure cannot be made, the presence of conductance quantization in this system indicates ballistic transport and hence a remarkably high sample quality.

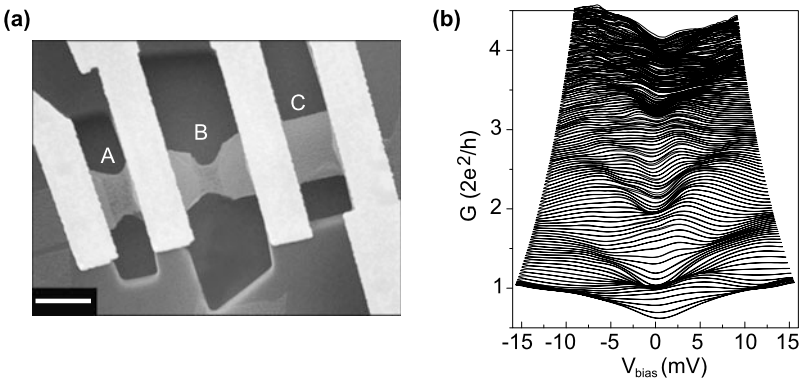

Fig. 5.15 (**a**) Scanning electron microscopy picture of a typical suspended high-mobility graphene device showing the formation of graphene constrictions after the current annealing step in vacuum at 4.2 K (regions A and B). The scale bar is 2 µm. No current annealing was applied to region C. (**b**) Finite-bias spectroscopy at $T = 4.2$ K. The differential conductance G versus DC-bias voltage V_{sd} at zero external magnetic field measured with an AC modulation of $V_{AC} = 150$ µV in the gate voltage interval of -6 V $< V_g < 0.8$ V. Each line in this plot corresponds to a DC bias measurement at a different gate voltage, from $V_G = -6$ V (*top*) to 0.8 V (*bottom*) in steps of 50 mV. For $V_{bias} = 0$ V we observe conductance quantization at 1, 2, 3 and $4 \times (2e^2/h)$. The energy spacing between the $n = 1$ and $n = 2$ subbands is approximately 8 meV, which is consistent with the energy spacing expected for a 240 nm wide constriction. [Figure reprinted from Ref. [60]]

5.6.3 Outlook

The results of these very recent studies give hope for graphene electronics since the influence of bulk and edge disorder is potentially negligible in these systems. However, both approaches come along with some drawbacks as well. The bottom-up ribbons are grown on a conductive substrate and need to be transferred to an insulator, and the suspended ribbons are extremely fragile [in addition they are very small so far, so processing, contacting etc is not trivial].

Substrate supported nanostructures are preferable due to their better stability. It was shown [61], that hexagonal boron nitride (BN) as a supporting material maintains high electronic quality of graphene sheets and is hence a promising substrate for devices. However, first studies indicate that the etched edges do influence transport in nanoribbons built on BN-substrate [62]. Conclusive investigations remain to be carried out.

Another alternative is the use of bilayer graphene instead of single layer graphene as has been shown recently [63]. Since a real band gap can be opened in this system as a perpendicular electric field is applied, electrostatic confinement like in GaAs devices is possible. The apparent advantage of this method would be the smooth confinement potential in contrast to the rough edges in devices fabricated until now.

In conclusion, a graphene nanostructure with low disorder and high tunability is most likely achieved by using a crystalline substrate, which matches the graphene lattice structure well (e.g. BN), and avoiding edge disorder induced in the patterning process.

References

1. K.S. Novoselov, A.K. Geim, S.V. Morozov, D. Jiang, Y. Zhang, S.V. Dubonos, I.V. Grigorieva, A.A. Firsov, Electric field effect in atomically thin carbon films. Science **306**(5696), 666–669 (2004)
2. X. Wang, Y. Ouyang, X. Li, H. Wang, J. Guo, H. Dai, Room-temperature all-semiconducting sub-10-nm graphene nanoribbon field-effect transistors. Phys. Rev. Lett. **100**(20), 206803 (2008)
3. T. Ihn, J. Güttinger, F. Molitor, S. Schnez, E. Schurtenberger, A. Jacobsen, S. Hellmüller, T. Frey, S. Dröscher, C. Stampfer, K. Ensslin, Graphene single-electron transistors. Mater. Today **13**, 44–50 (2010)
4. T. Ando, A.B. Fowler, F. Stern, Electronic properties of two-dimensional systems. Rev. Mod. Phys. **54**(2), 437 (1982)
5. J. Güttinger, C. Stampfer, S. Hellmuller, F. Molitor, T. Ihn, K. Ensslin, Charge detection in graphene quantum dots. Appl. Phys. Lett. **93**(21), 212102 (2008)
6. F. Molitor, S. Dröscher, J. Güttinger, A. Jacobsen, C. Stampfer, T. Ihn, K. Ensslin, Transport through graphene double dots. Appl. Phys. Lett. **94**(22), 222107 (2009)
7. M. Huefner, F. Molitor, A. Jacobsen, A. Pioda, C. Stampfer, K. Ensslin, T. Ihn, Investigation of the Aharonov-Bohm effect in a gated graphene ring. Phys. Status Solidi B **246**(11–12), 2756–2759 (2009)
8. B.J. van Wees, H. van Houten, C.W.J. Beenakker, J.G. Williamson, L.P. Kouwenhoven, D. van der Marel, C.T. Foxon, Quantized conductance of point contacts in a two-dimensional electron gas. Phys. Rev. Lett. **60**(9), 848–850 (1988)
9. D.A. Wharam, T.J. Thornton, R. Newbury, M. Pepper, H. Ahmed, J.E.F. Frost, D.G. Hasko, D.C. Peacock, D.A. Ritchie, G.A.C. Jones, One-dimensional transport and the quantisation of the ballistic resistance. J. Phys. C, Solid State Phys. **21**, 209–214 (1988)
10. H. van Houten, C. Beenakker, Quantum point contacts. Phys. Today **49**(7), 22–27 (1996)
11. M. Fujita, K. Wakabayashi, K. Nakada, K. Kusakabe, Peculiar localized state at zigzag graphite edge. J. Phys. Soc. Jpn. **65**, 1920 (1996)
12. K. Nakada, M. Fujita, G. Dresselhaus, M.S. Dresselhaus, Edge state in graphene ribbons: nanometer size effect and edge shape dependence. Phys. Rev. B **54**(24), 17954 (1996)
13. K. Wakabayashi, Electronic transport properties of nanographite ribbon junctions. Phys. Rev. B **64**(12), 125428 (2001)
14. C.T. White, J. Li, D. Gunlycke, J.W. Mintmire, Hidden one-electron interactions in carbon nanotubes revealed in graphene nanostrips. Nano Lett. **7**(3), 825–830 (2007)
15. N.M.R. Peres, A.H. Castro Neto, F. Guinea, Conductance quantization in mesoscopic graphene. Phys. Rev. B **73**(19), 195411 (2006)
16. L. Brey, H.A. Fertig, Electronic states of graphene nanoribbons studied with the Dirac equation. Phys. Rev. B **73**(23), 235411 (2006)
17. F. Muñoz-Rojas, D. Jacob, J. Fernández-Rossier, J.J. Palacios, Coherent transport in graphene nanoconstrictions. Phys. Rev. B **74**(19), 195417 (2006)
18. Y.-W. Son, M.L. Cohen, S.G. Louie, Energy gaps in graphene nanoribbons. Phys. Rev. Lett. **97**(21), 216803 (2006)
19. M.I.K.N.K. Kusakabe, K. Wakabayashi, M. Fujita, Magnetism of nanometer-scale graphite with edge or topological defects. Mol. Cryst. Liq. Cryst. **305**, 445–454 (1997)
20. S. Okada, A. Oshiyama, Magnetic ordering in hexagonally bonded sheets with first-row elements. Phys. Rev. Lett. **87**(14), 146803 (2001)
21. A.C. Ferrari, J.C. Meyer, V. Scardaci, C. Casiraghi, M. Lazzeri, F. Mauri, S. Piscanec, D. Jiang, K.S. Novoselov, S. Roth, A.K. Geim, Raman spectrum of graphene and graphene layers. Phys. Rev. Lett. **97**(18), 187401 (2006)
22. D. Graf, F. Molitor, K. Ensslin, C. Stampfer, A. Jungen, C. Hierold, L. Wirtz, Spatially resolved Raman spectroscopy of single- and few-layer graphene. Nano Lett. **7**(2), 238–242 (2007)

23. S. Dröscher, H. Knowles, Y. Meir, K. Ensslin, T. Ihn, Coulomb gap in graphene nanoribbons. Phys. Rev. B **84**(7), 073405 (2011)
24. D.J. Thouless, Electrons in disordered systems and the theory of localization. Phys. Rep. **13**(3), 93–142 (1974)
25. A.B. Fowler, A. Hartstein, R.A. Webb, Conductance in restricted-dimensionality accumulation layers. Phys. Rev. Lett. **48**(3), 196–199 (1982)
26. T. Ihn, *Semiconductor Nanostructures* (Oxford University Press, Oxford, 2010)
27. M. Kemerink, L.W. Molenkamp, Stochastic coulomb blockade in a double quantum dot. Appl. Phys. Lett. **65**(8), 1012–1014 (1994)
28. M.Y. Han, B. Ozyilmaz, Y. Zhang, P. Kim, Energy band-gap engineering of graphene nanoribbons. Phys. Rev. Lett. **98**(20), 206805 (2007)
29. Z. Chen, Y.-M. Lin, M.J. Rooks, P. Avouris, Graphene nano-ribbon electronics. Physica E **40**(2), 228–232 (2007)
30. K. Todd, H.-T. Chou, S. Amasha, D. Goldhaber-Gordon, Quantum dot behavior in graphene nanoconstrictions. Nano Lett. **9**(1), 416–421 (2009)
31. C. Stampfer, J. Güttinger, S. Hellmüller, F. Molitor, K. Ensslin, T. Ihn, Energy gaps in etched graphene nanoribbons. Phys. Rev. Lett. **102**(5), 056403 (2009)
32. F. Molitor, A. Jacobsen, C. Stampfer, J. Güttinger, T. Ihn, K. Ensslin, Transport gap in side-gated graphene constrictions. Phys. Rev. B **79**(7), 075426 (2009)
33. X. Liu, J.B. Oostinga, A.F. Morpurgo, L.M.K. Vandersypen, Electrostatic confinement of electrons in graphene nanoribbons. Phys. Rev. B **80**(12), 121407 (2009)
34. M.Y. Han, J.C. Brant, P. Kim, Electron transport in disordered graphene nanoribbons. Phys. Rev. Lett. **104**(5), 056801 (2010)
35. P. Gallagher, K. Todd, D. Goldhaber-Gordon, Disorder-induced gap behavior in graphene nanoribbons. Phys. Rev. B **81**(11), 115409 (2010)
36. J.B. Oostinga, B. Sacepe, M.F. Craciun, A.F. Morpurgo, Magneto-transport through graphene nano-ribbons. Phys. Rev. B **81**(19), 193408 (2010)
37. J. Bai, R. Cheng, F. Xiu, L. Liao, M. Wang, A. Shailos, K.L. Wang, Y. Huang, X. Duan, Very large magnetoresistance in graphene nanoribbons. Nat. Nanotechnol. **5**(9), 655–659 (2010)
38. B. Terres, J. Dauber, C. Volk, S. Trellenkamp, U. Wichmann, C. Stampfer, Disorder induced Coulomb gaps in graphene constrictions with different aspect ratios. Appl. Phys. Lett. **98**(3), 032109 (2011)
39. D. Querlioz, Y. Apertet, A. Valentin, K. Huet, A. Bournel, S. Galdin-Retailleau, P. Dollfus, Suppression of the orientation effects on bandgap in graphene nanoribbons in the presence of edge disorder. Appl. Phys. Lett. **92**(4), 042108 (2008)
40. M. Evaldsson, I.V. Zozoulenko, H. Xu, T. Heinzel, Edge-disorder-induced Anderson localization and conduction gap in graphene nanoribbons. Phys. Rev. B **78**(16), 161407 (2008)
41. I. Martin, Y.M. Blanter, Transport in disordered graphene nanoribbons. Phys. Rev. B **79**(23), 235132 (2009)
42. J. Martin, N. Akerman, G. Ulbricht, T. Lohmann, J.H. Smet, K. von Klitzing, A. Yacoby, Observation of electron-hole puddles in graphene using a scanning single-electron transistor. Nat. Phys. **4**(2), 144–148 (2008)
43. S. Adam, S. Cho, M.S. Fuhrer, S.D. Sarma, Density inhomogeneity driven percolation metal-insulator transition and dimensional crossover in graphene nanoribbons. Phys. Rev. Lett. **101**(4), 046404 (2008)
44. F. Molitor, C. Stampfer, J. Güttinger, A. Jacobsen, T. Ihn, K. Ensslin, Energy and transport gaps in etched graphene nanoribbons. Semicond. Sci. Technol. **25**(3), 034002 (2010)
45. F. Sols, F. Guinea, A.H.C. Neto, Coulomb blockade in graphene nanoribbons. Phys. Rev. Lett. **99**(16), 166803 (2007)
46. F. Molitor, H. Knowles, S. Dröscher, U. Gasser, T. Choi, P. Roulleau, J. Güttinger, A. Jacobsen, C. Stampfer, K. Ensslin, T. Ihn, Observation of excited states in a graphene double quantum dot. Europhys. Lett. **89**(6), 67005 (2010)
47. Y. Meir, N.S. Wingreen, P.A. Lee, Transport through a strongly interacting electron system: theory of periodic conductance oscillations. Phys. Rev. Lett. **66**(23), 3048–3051 (1991)

48. Y.C. Huang, C.P. Chang, M.F. Lin, Magnetic and quantum confinement effects on electronic and optical properties of graphene ribbons. Nanotechnology **18**(49), 495401 (2007)
49. J. Liu, A.R. Wright, C. Zhang, Z. Ma, Strong terahertz conductance of graphene nanoribbons under a magnetic field. Appl. Phys. Lett. **93**(4), 041106 (2008)
50. C. Ritter, S.S. Makler, A. Latgé, Energy-gap modulations of graphene ribbons under external fields: a theoretical study. Phys. Rev. B **77**(19), 195443 (2008)
51. F. Molitor, Electronic properties of graphene nanostructures, PhD thesis, ETH Zurich, 2010
52. B.I. Shklovskii, A.L. Efros, *Electronic Properties of Doped Semiconductors* (Springer, Heidelberg, 1984)
53. M.E. Gershenson, Y.B. Khavin, A.G. Mikhalchuk, H.M. Bozler, A.L. Bogdanov, Crossover from weak to strong localization in quasi-one-dimensional conductors. Phys. Rev. Lett. **79**(4), 725–728 (1997)
54. D. Loss, D.P. DiVincenzo, Quantum computation with quantum dots. Phys. Rev. A **57**(1), 120–126 (1998)
55. W.G. van der Wiel, S.D. Franceschi, J.M. Elzerman, T. Fujisawa, S. Tarucha, L.P. Kouwenhoven, Electron transport through double quantum dots. Rev. Mod. Phys. **75**, 1–22 (2002)
56. C. Livermore, C.H. Crouch, R.M. Westervelt, K.L. Campman, A.C. Gossard, The Coulomb blockade in coupled quantum dots. Science **274**(5291), 1332–1335 (1996)
57. J. Cai, P. Ruffieux, R. Jaafar, M. Bieri, T. Braun, S. Blankenburg, M. Muoth, A.P. Seitsonen, M. Saleh, X. Feng, K. Mullen, R. Fasel, Atomically precise bottom-up fabrication of graphene nanoribbons. Nature **466**(7305), 470–473 (2010)
58. K.I. Bolotin, F. Ghahari, M.D. Shulman, H.L. Stormer, P. Kim, Observation of the fractional quantum hall effect in graphene. Nature **462**(7270), 196–199 (2009)
59. X. Du, I. Skachko, F. Duerr, A. Luican, E.Y. Andrei, Fractional quantum hall effect and insulating phase of Dirac electrons in graphene. Nature **462**(7270), 192–195 (2009)
60. N. Tombros, A. Veligura, J. Junesch, M.H.D. Guimaraes, I.J. Vera-Marun, H.T. Jonkman, B.J. van Wees, Quantized conductance of a suspended graphene nanoconstriction. Nat. Phys. **7**(9), 697–700 (2011)
61. C.R. Dean, A.F. Young, I. Meric, C. Lee, L. Wang, S. Sorgenfrei, K. Watanabe, T. Taniguchi, P. Kim, K.L. Shepard, J. Hone, Boron nitride substrates for high-quality graphene electronics. Nat. Nanotechnol. **5**(10), 722–726 (2010)
62. D. Bischoff, T. Krähenmann, S. Dröscher, M.A. Gruner, C. Barraud, T. Ihn, K. Ensslin, Reactive-ion-etched graphene nanoribbons on a hexagonal boron nitride substrate. Appl. Phys. Lett. **101**(20), 203103 (2012)
63. S. Dröscher, C. Barraud, K. Watanabe, T. Taniguchi, T. Ihn, K. Ensslin, Electron flow in split-gated bilayer graphene. New J. Phys. **14**(10), 103007 (2012)

Part II
Theoretical

Chapter 6
Electronic Properties of Monolayer and Multilayer Graphene

Mikito Koshino and Tsuneya Ando

Abstract We present a theoretical review of the basic electronic properties of graphene and its multilayers in terms of the effective mass approximation. Using the low-energy effective Hamiltonian, we describe the electronic spectra, the transport properties, the optical absorption and the orbital magnetism, which are distinct from those of conventional systems.

6.1 Introduction

The physics of graphene and related materials has attracted broad interest since the experimental realizations of mono-crystalline graphene [1, 2]. Its unique band structure equivalent to a relativistic massless particle gives rise to unusual electronic properties quite different from those of conventional systems. In this chapter we present a short review of graphene's electronic properties from a theoretical point of view. The electronic structure of graphene is successfully described by the effective mass approximation. In the family of graphene related materials, the effective mass model was developed earlier for three dimensional graphite [3–5] and also for a single wall carbon nanotube [6] which is a rolled-up graphene. The effective Hamiltonian of graphene is shown to be equivalent to the Dirac Hamiltonian for a zero-mass particle, where the conduction band and valence band with linear dispersion touch at the so-called Dirac point [4, 7, 8]. This is a topologically singular point around which an electronic state acquires a geometrical phase factor called Berry's phase. The singularity at the Dirac point is responsible for the peculiar behavior in the transport properties, such as the minimum conductivity [9], the dynamical conductivity [10], and the localization effect [11, 12]. This singularity is also considered as the origin of the anomalous diamagnetic susceptibility [4, 13, 15–17], and the

M. Koshino (✉)
Department of Physics, Tohoku University, Sendai 980-8578, Japan
e-mail: koshino@cmpt.phys.tohoku.ac.jp

T. Ando
Department of Physics, Tokyo Institute of Technology, Tokyo 152-8551, Japan

H. Aoki, M.S. Dresselhaus (eds.), *Physics of Graphene*, NanoScience and Technology,
DOI 10.1007/978-3-319-02633-6_6,

half integer quantum Hall effect [18–20] through the formation of the zero-energy Landau level.

Multilayer systems containing few layers of graphene have also been fabricated [1, 21–24]. There the interlayer coupling drastically changes the band structure, giving characteristic features depending on the number of layers and the stacking manner [14, 25–27, 29–33]. Bilayer graphene contains a zero-gap band structure, but the dispersion around the band touching point is quadratic unlike monolayer graphene [25–28]. For multilayer graphenes with more than two layers, the electronic states can be understood in terms of a decomposition of Hamiltonian into subsystems that are effectively identical to monolayer or bilayer graphene [14, 35].

Here we theoretically describe the basic electronic properties in graphene using the effective-mass approximation. In Sect. 6.2, we introduce the effective mass Hamiltonian of monolayer graphene, and describe the electronic spectrum with and without a magnetic field. Based on this, we present the physical properties of monolayer graphene, including the orbital diamagnetism in Sect. 6.3, the transport properties in Sect. 6.4 and the optical properties in Sect. 6.5. We extend the arguments to bilayer graphene in Sect. 6.6, where we will see that several properties are significantly different from those of the monolayer. In Sect. 6.7, we present the effective Hamiltonian of a general N-layer graphene stack, and make arguments for the band decomposition into monolayer-like and bilayer-like subsystems.

6.2 Electronic Structure of Graphene

6.2.1 Effective Hamiltonian

Graphene is composed of a hexagonal network of carbon atoms, for which the atomic structure and the first Brillouin zone are shown in Fig. 6.1(a) and (b), respectively. A unit cell, including the two carbon atoms at A and B sites, is spanned by the primitive lattice vectors $\mathbf{a} = a(1, 0)$ and $\mathbf{b} = a(-1/2, \sqrt{3}/2)$, where $a \approx 0.246$ nm is the graphene lattice constant. Let us also define $\boldsymbol{\tau}_1 = a(0, 1/\sqrt{3})$, $\boldsymbol{\tau}_2 = a(-1/2, -1/2\sqrt{3})$, $\boldsymbol{\tau}_3 = a(1/2, -1/2\sqrt{3})$, which are the vectors from a B site to the nearest A sites. The reciprocal lattice vectors are given by $\mathbf{a}^* = (2\pi/a)(1, 1/\sqrt{3})$ and $\mathbf{b}^* = (2\pi/a)(0, 2/\sqrt{3})$. The Brillouin zone has two inequivalent corners called K and K′ points, defined by $\mathbf{K} = (2\pi/a)(1/3, 1/\sqrt{3})$ and $\mathbf{K}' = (2\pi/a)(0, 2/\sqrt{3})$, respectively.

The electronic structure of graphene in the low-energy region is described by the effective mass approximation in a similar manner to graphite [4–8]. In the following, we derive the effective Hamiltonian for low-energy graphene electrons, starting from the tight-binding model for the carbon π band. In the tight-binding model, the wavefunction is given by

$$\psi(\mathbf{r}) = \sum_{\mathbf{R}_A} \psi_A(\mathbf{R}_A)\phi(\mathbf{r} - \mathbf{R}_A) + \sum_{\mathbf{R}_B} \psi_B(\mathbf{R}_B)\phi(\mathbf{r} - \mathbf{R}_B), \tag{6.1}$$

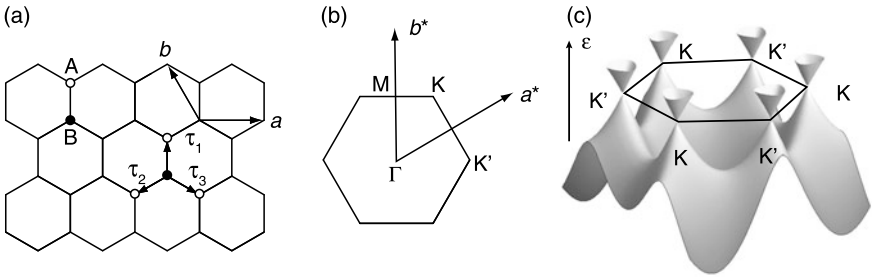

Fig. 6.1 (**a**) The lattice structure of a graphene sheet. The two primitive translation vectors are denoted by **a** and **b**. The three vectors directed from a B site to the nearest neighbor A sites are given by $\boldsymbol{\tau}_l$ ($l = 1, 2, 3$). (**b**) The first Brillouin zone. The vertices of the hexagon are called K and K′ points and reciprocal lattice vectors are denoted by $\mathbf{a}^*$ and $\mathbf{b}^*$. (**c**) The π-band structure of graphene in the nearest-neighbor tight-binding model. The upper band is cut for illustrative purposes

where $\phi(\mathbf{r})$ is the wavefunction of the p_z orbital of a carbon atom, which composes the π band, $\mathbf{R}_A = n_a\mathbf{a} + n_b\mathbf{b} + \boldsymbol{\tau}_1$, and $\mathbf{R}_B = n_a\mathbf{a} + n_b\mathbf{b}$ with n_a and n_b being integers. Let $-\gamma_0$ be the transfer integral (commonly denoted by t in the literature) between nearest-neighbor carbon atoms. The Hamiltonian is then given by

$$H = -\gamma_0 \sum_{\mathbf{R}_A} \sum_{l=1}^{3} |\mathbf{R}_A - \boldsymbol{\tau}_l\rangle\langle\mathbf{R}_A| + \text{h.c.}, \tag{6.2}$$

where $|\mathbf{R}\rangle$ represents $\phi(\mathbf{r} - \mathbf{R})$, i.e., the atomic state localized at site $\mathbf{R}$. The Schrödinger equation then becomes

$$\begin{aligned} \varepsilon\psi_A(\mathbf{R}_A) &= -\gamma_0 \sum_{l=1}^{3} \psi_B(\mathbf{R}_A - \boldsymbol{\tau}_l) \\ \varepsilon\psi_B(\mathbf{R}_B) &= -\gamma_0 \sum_{l=1}^{3} \psi_A(\mathbf{R}_B + \boldsymbol{\tau}_l), \end{aligned} \tag{6.3}$$

where the origin of energy is set to be the energy level of the carbon p_z orbital. When assuming the Bloch wavefunction, $\psi_A(\mathbf{R}_A) \propto e^{i\mathbf{k}\cdot\mathbf{r}} f_A(\mathbf{k})$, $\psi_B(\mathbf{R}_B) \propto e^{i\mathbf{k}\cdot\mathbf{r}} f_B(\mathbf{k})$, the Schrödinger equation becomes

$$\begin{pmatrix} 0 & h(\mathbf{k}) \\ h(\mathbf{k})^* & 0 \end{pmatrix} \begin{pmatrix} f_A(\mathbf{k}) \\ f_B(\mathbf{k}) \end{pmatrix} = \varepsilon \begin{pmatrix} f_A(\mathbf{k}) \\ f_B(\mathbf{k}) \end{pmatrix} \tag{6.4}$$

$$h(\mathbf{k}) = -\gamma_0 \sum_{l=1}^{3} \exp(i\mathbf{k}\cdot\boldsymbol{\tau}_l), \tag{6.5}$$

giving the eigenenergies

$$\varepsilon_{\pm} = \pm\sqrt{1 + 4\cos\frac{ak_x}{2}\cos\frac{\sqrt{3}ak_y}{2} + 4\cos^2\frac{ak_x}{2}}. \tag{6.6}$$

Here ε_+ and ε_- give the eigenenergies for the conduction and valence bands, respectively. There two bands touch each other at the K and K′ points where $\varepsilon_{\pm} = 0$. They are shown in Fig. 6.1(c). Since the π band is half-filled in graphene, the Fermi energy goes through the band touching point in Fig. 6.1(c), which is called Dirac point.

In the vicinity of K and K′, the energy dispersion approximates a linear form,

$$\varepsilon_{\pm} = \pm\hbar v|\mathbf{k}|, \tag{6.7}$$

where $\mathbf{k}$ is now a relative wave vector measured from K or K′, and v is the constant velocity defined by

$$v = \frac{\sqrt{3}}{2}\frac{a\gamma_0}{\hbar}. \tag{6.8}$$

With the parameter value $\gamma_0 \approx 3$ eV for graphite, we have $v \approx 10^6$ m/s, and this is compatible with the experimental estimations [1, 2].

Low-energy electronic states near $\varepsilon = 0$ are written in terms of the states near the K and K′ points. There the wave functions are expressed as a product of the Bloch factor associated with K or K′ and the envelope function which slowly varies compared to the atomic length scale a. Specifically, the wave amplitudes at A and B sites are written as

$$\begin{aligned}\psi_A(\mathbf{R}_A) &= e^{i\mathbf{K}\cdot\mathbf{R}_A}F_A^{\mathrm{K}}(\mathbf{R}_A) + e^{i\mathbf{K}'\cdot\mathbf{R}_A}F_A^{\mathrm{K}'}(\mathbf{R}_A)\\ \psi_B(\mathbf{R}_B) &= -\omega e^{i\mathbf{K}\cdot\mathbf{R}_B}F_B^{\mathrm{K}}(\mathbf{R}_B) + e^{i\mathbf{K}'\cdot\mathbf{R}_B}F_B^{\mathrm{K}'}(\mathbf{R}_B),\end{aligned} \tag{6.9}$$

respectively, where $F_A^{\mathrm{K}}, F_A^{\mathrm{K}'}, F_B^{\mathrm{K}}, F_B^{\mathrm{K}'}$ are the corresponding envelope functions, and the factor $\omega = \exp(2\pi i/3)$ is introduced to make the final equation simple. By putting the above expression into (6.3), and using the long wave approximation such as

$$F(\mathbf{r} + \boldsymbol{\tau}_l) \approx F(\mathbf{r}) + (\boldsymbol{\tau}_l \cdot \nabla)F(\mathbf{r}) \quad \left(F = F_A^{\mathrm{K}}, \text{etc.}\right), \tag{6.10}$$

we obtain

$$\mathcal{H}^{\mathrm{K}}\mathbf{F}^{\mathrm{K}} = \varepsilon\mathbf{F}^{\mathrm{K}}, \qquad \mathcal{H}^{\mathrm{K}'}\mathbf{F}^{\mathrm{K}'} = \varepsilon\mathbf{F}^{\mathrm{K}'}, \tag{6.11}$$

where

$$\mathcal{H}^{\mathrm{K}} = \begin{pmatrix} 0 & vp_- \\ vp_+ & 0 \end{pmatrix}, \qquad \mathcal{H}^{\mathrm{K}'} = \begin{pmatrix} 0 & vp_+ \\ vp_- & 0 \end{pmatrix}, \tag{6.12}$$

$$\mathbf{F}^{\mathrm{K}} = \begin{pmatrix} F_A^{\mathrm{K}}(\mathbf{r}) \\ F_B^{\mathrm{K}}(\mathbf{r}) \end{pmatrix}, \qquad \mathbf{F}^{\mathrm{K}'} = \begin{pmatrix} F_A^{\mathrm{K}'}(\mathbf{r}) \\ F_B^{\mathrm{K}'}(\mathbf{r}) \end{pmatrix}, \tag{6.13}$$

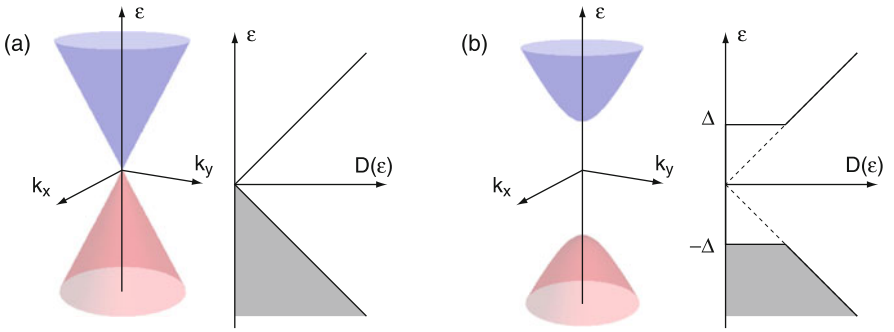

Fig. 6.2 The electronic band structures near the K and K′ points and the density of states in graphenes with a (**a**) zero gap and a (**b**) non-zero gap

$\mathbf{p} = (p_x, p_y) = -i\hbar\nabla$ and $p_\pm = p_x \pm i p_y$. The effective Hamiltonians $\mathcal{H}^{\mathrm{K}}$ and $\mathcal{H}^{\mathrm{K}'}$ give the identical eigenenergy

$$\varepsilon_s(\mathbf{p}) = svp \quad (s = \pm), \tag{6.14}$$

where $p = \sqrt{p_x^2 + p_y^2}$, in accordance with (6.7).

The density of electronic states is

$$D(\varepsilon) = \frac{g_s g_v |\varepsilon|}{2\pi\hbar^2 v^2}, \tag{6.15}$$

where $g_s = 2$ is the spin degeneracy and $g_v = 2$ is the valley degeneracy, i.e., the degrees of freedom for the K and K′ points. The energy bands and the density of states in the low energy region of graphene are plotted in Fig. 6.2(a). The electron or hole concentration at zero temperature is

$$n_s = \mathrm{sgn}(\varepsilon)\frac{g_s g_v \varepsilon^2}{4\pi\hbar^2 v^2}, \tag{6.16}$$

with

$$\mathrm{sgn}(x) = \begin{cases} +1 & (x > 0); \\ 0 & (x = 0); \\ -1 & (x < 0). \end{cases} \tag{6.17}$$

6.2.2 *Landau Levels*

Before considering quantum mechanics in detail, it is intuitive to consider the semi-classical motion of a graphene electron under a magnetic field. The equation of

motion for an electron in band s ($s = \pm$) is given by

$$\frac{d\mathbf{p}}{dt} = -\frac{e}{c}\mathbf{v}_s(\mathbf{p}) \times \mathbf{B}, \tag{6.18}$$

where $\mathbf{p} = (p_x, p_y)$ is the electron momentum, $\mathbf{B}$ is a uniform magnetic field perpendicular to the graphene layer, and

$$\mathbf{v}_s(\mathbf{p}) = \frac{\partial \varepsilon_s(\mathbf{p})}{\partial \mathbf{p}} = \frac{sv\mathbf{p}}{|\mathbf{p}|}. \tag{6.19}$$

Obviously the electron moves round on the equi-energy circle in p-space with the cyclotron frequency,

$$\omega_c(\varepsilon) = \frac{eBv^2}{c\varepsilon}, \tag{6.20}$$

which is inversely proportional to the energy ε, and c is the speed of light.

In quantum mechanics, the Hamiltonian in a magnetic field is obtained by replacing $\mathbf{p}$ with $\mathbf{p} + (e/c)\mathbf{A}$, where $\mathbf{A}$ is the vector potential giving the magnetic field $\mathbf{B} = \nabla \times \mathbf{A}$. Then $p_\pm$ in the Hamiltonian (6.12) is replaced with

$$\pi_\pm = \pi_x \pm i\pi_y, \qquad \boldsymbol{\pi} = \mathbf{p} + \frac{e}{c}\mathbf{A}. \tag{6.21}$$

The Landau level spectrum can be found using the relation $\pi_+ = (\sqrt{2}\hbar/l_B)a^\dagger$ and $\pi_- = (\sqrt{2}\hbar/l_B)a$. Here $l_B = \sqrt{c\hbar/(eB)}$ is magnetic length, and $a^\dagger$ and a are raising and lowering operators, respectively, which operate on the Landau-level wave function ϕ_n as $a\phi_n = \sqrt{n}\phi_{n-1}$ and $a^\dagger\phi_n = \sqrt{n+1}\phi_{n+1}$.

The eigenfunction of the Hamiltonian at the K point is written as $(c_1\phi_{n-1}, c_2\phi_n)$ with an integer $n \geq 0$. We define $\phi_n = 0$ for $n < 0$. The Hamiltonian matrix for (c_1, c_2) becomes

$$H^{\mathrm{K}} = \begin{pmatrix} 0 & \hbar\omega_B\sqrt{n} \\ \hbar\omega_B\sqrt{n} & 0 \end{pmatrix}, \tag{6.22}$$

where

$$\hbar\omega_B = \frac{\sqrt{2}\hbar v}{l_B}. \tag{6.23}$$

We obtain [4]

$$\varepsilon_n = \hbar\omega_B \,\mathrm{sgn}(n)\sqrt{|n|}, \quad n = 0, \pm 1, \pm 2, \ldots. \tag{6.24}$$

The Hamiltonian at the K′ point is obtained by exchanging $\pi_\pm$ and the energy spectrum at K′ becomes identical to K. Figure 6.3(a) shows the Landau level structure. Each Landau level is four-fold degenerate due to spin and valley degeneracies, when the spin-Zeeman splitting is neglected. The valley degeneracy is guaranteed by the spacial inversion symmetry with respect to the midpoint between A site and B site, because K and K′ are inverted by the space inversion [38].

Since the energy level is proportional to $\sqrt{n}$, the energy spacing between adjacent Landau levels is not constant but becomes narrower going further from the Dirac point. For large n, the energy spacing is written in terms of the classical cyclotron frequency as

$$\varepsilon_{n+1} - \varepsilon_n \sim \hbar\omega_c(\varepsilon_n). \tag{6.25}$$

The other frequency parameter ω_B defined in (6.23) represents the energy spacing between $n = 0$ and 1, and is regarded as the quantum limit of the classical cyclotron frequency $\omega_c(\varepsilon)$ in the limit $\varepsilon \to 0$.

The Hall conductivity σ_{xy} can be determined by counting the number of occupied levels above the charge neutral point. When the Fermi energy is between ε_n and ε_{n+1}, we have [18, 19]

$$\sigma_{xy} = -g_v g_s \frac{e^2}{h}\left(n + \frac{1}{2}\right), \tag{6.26}$$

giving a sequence of quantized Hall conductivity, $\pm 2, \pm 6, \pm 10, \ldots$ in units of $-e^2/h$. The factor $1/2$ in the bracket appears because the 0-th Landau level is half-filled when the system is charge neutral.

6.2.3 Band Gap in Graphene

In the presence of a potential asymmetry between A and B sites, the Hamiltonian becomes

$$\mathcal{H}^{\mathrm{K}} = \begin{pmatrix} \Delta & vp_- \\ vp_+ & -\Delta \end{pmatrix}. \tag{6.27}$$

The diagonal terms $\pm\Delta$ represent the potential at A and B sites opening an energy gap at the Dirac point, and the system is now equivalent to one with a massive Dirac electron. Although A and B are intrinsically symmetric in usual monolayer graphene, the asymmetry can arise in a sample placed on a certain substrate material, where the interaction between the graphene and the substrate lattice produces different potentials between A and B [36, 37]. We can safely assume $\Delta \geq 0$ without loss of generality. The energy band in $B = 0$ is then given by

$$\varepsilon_s(p) = s\sqrt{v^2p^2 + \Delta^2} \quad (s = \pm 1). \tag{6.28}$$

The density of states is correspondingly

$$D(\varepsilon) = \frac{g_v g_s |\varepsilon|}{2\pi\hbar^2 v^2}\theta\big(|\varepsilon| - \Delta\big), \tag{6.29}$$

where $\theta(t)$ is a step function, defined by

$$\theta(t) = \begin{cases} 1 & (t > 0); \\ 0 & (t < 0). \end{cases} \tag{6.30}$$

The energy bands and the density of states in the low energy region of gapped graphene are shown in Fig. 6.2(b).

In a magnetic field, the valley degeneracy of the Landau levels is generally broken by the asymmetric potential Δ, since it breaks the spacial inversion symmetry. The Hamiltonian in a magnetic field is again given by replacing $p_\pm$ with $\pi_\pm$ in (6.27). The eigenenergies then become [39]

$$\begin{aligned} \varepsilon_n^{\mathrm{K}} &= \mathrm{sgn}_-(n)\sqrt{(\hbar\omega_B)^2|n| + \Delta^2}, \\ \varepsilon_n^{\mathrm{K}'} &= \mathrm{sgn}_+(n)\sqrt{(\hbar\omega_B)^2|n| + \Delta^2} \end{aligned} \tag{6.31}$$

with $n = 0, \pm 1, \pm 2, \ldots$, and

$$\mathrm{sgn}_\pm(n) = \begin{cases} +1 & (n > 0); \\ \pm 1 & (n = 0); \\ -1 & (n < 0). \end{cases} \tag{6.32}$$

Figure 6.3(b) shows an example of a Landau level structure for $\Delta > 0$. The Landau levels for $n = 0$ go to the top of the valence band in K, and to the bottom of the conduction band in K′, while all other levels remain valley-degenerate. In the Hall conductivity, the phase of $\sigma_{xy} = 0$ newly appears in the gap region, due to the splitting of the $n = 0$ level.

Because the Hamiltonian of the gapped graphene is equivalent to a massive Dirac electron, the Landau level structure around the band edge should correspond to that of a conventional electron system. This is clearly illustrated by the effective Hamiltonian expanded in the vicinity of the band edge [39]. For the conduction band, the effective Hamiltonian for the A site near the band bottom ($\varepsilon = \Delta$) is written apart from the constant energy as

$$\mathcal{H} \approx \frac{v^2}{2\Delta}\pi_{-\xi}\pi_\xi = \hbar\omega_c\left(\hat{N} + \frac{1}{2}\right) + \frac{\xi}{2}\hbar\omega_c, \tag{6.33}$$

where $\hat{N} = a^\dagger a$, and $\xi = +, -$ are for K and K′, respectively. The index N (eigenvalue of $\hat{N}$) coincides with the number counted from the band bottom in each valley, and is generally different from n in the previous numbering scheme as shown in Fig. 6.3. Physically, N indicates the index of the Landau level wavefunction of the A site, which has the dominant amplitude over the B site in low energies.

The second term in (6.33) is responsible for the energy difference between the Landau levels of K and K′ belonging to the same N. This is written in the form of the pseudo-spin (valley) Zeeman term, $\xi\mu^* B$, where the different valleys K and K′ serve as pseudo-spin up ($\xi = +1$) and down ($\xi = -1$), respectively. The effective magnetic moment μ^* associated with the valley splitting is given by

$$\mu^* = \frac{1}{2}g^*\mu_B, \quad g^* = 2\frac{m}{m^*}, \; m^* = \frac{\Delta}{v^2}, \tag{6.34}$$

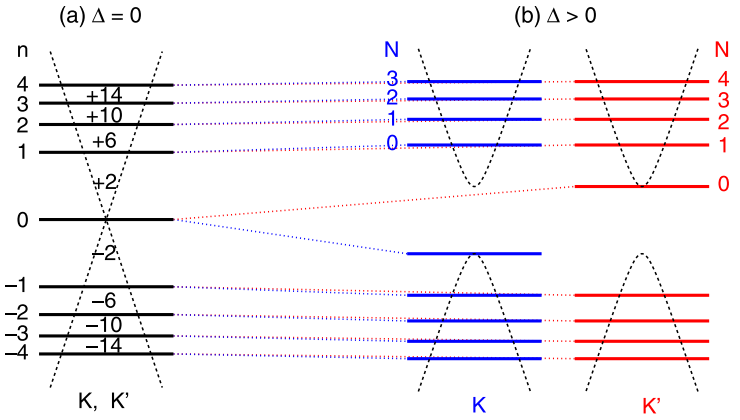

Fig. 6.3 Landau level structure in graphene with potential asymmetry (**a**) $\Delta = 0$ and (**b**) $\Delta > 0$. The *horizontal dotted lines* connecting levels indicate the correspondence of the levels in the limit of $\Delta \to 0$. In (**a**), numbers between the levels indicate the quantized Hall conductivity in units of $-e^2/h$

where $\mu_B = e\hbar/(2mc)$ is the Bohr magneton and m is the free electron mass. For instance, the effective g factor is estimated at $g^* \sim 60$ for $\Delta = 0.1$ eV. The origin of the valley-dependent magnetic moment is attributed to the orbital current circulation opposite between K and K′, which is inherent in the chiral nature of the Hamiltonian [58]. In the semiclassical picture, this is explained in terms of the self-rotation of the wave packet [59, 60].

6.3 Orbital Diamagnetism

6.3.1 The Susceptibility Singularity

In a condensed matter system, the orbital magnetism sensitively depends on the details of the band structure, and sometimes largely deviates from the conventional Landau diamagnetism. Particularly, narrow gap materials, such as graphite [4, 40, 41] or bismuth [42–44], exhibit a strong orbital diamagnetism which overcomes the spin paramagnetism. The orbital magnetism was also studied for related materials, such as graphite intercalation compounds [45–48], carbon nanotubes [49–53], few-layer graphenes [14, 54, 55], and organic compounds having a Dirac-like spectrum [56]. A graphene monolayer is an extreme case, in which the conduction and valence bands stick together, and accordingly the orbital susceptibility has a strong singularity at the Dirac point [4, 13, 15, 16, 39, 57], as we will see below.

The thermodynamical potential of graphene at temperature T and magnetic field B is written as

$$\Omega = -\frac{1}{\beta}\frac{g_v g_s}{2\pi l_B^2}\sum_{s=\pm}\sum_{n=0}^{\infty}\varphi\left[\varepsilon_s\left((\hbar\omega_B)^2 n\right)\right]\left(1-\frac{\delta_{n0}}{2}\right), \tag{6.35}$$

where $\beta = 1/k_B T$, $\varepsilon_s(x) = s\sqrt{x}$, $\varphi(\varepsilon) = \log[1+e^{-\beta(\varepsilon-\zeta)}]$ with ζ being the chemical potential. In a weak magnetic field, using the Euler-Maclaurin formula, the summation in n in (6.35) can be written as an integral in the continuous variable x and a residual term. In the lowest order in B, the latter becomes

$$\Delta\Omega = g_v g_s \frac{e^2 v^2 B^2}{12\pi}\int_{-\infty}^{\infty}\left(-\frac{\partial f(\varepsilon)}{\partial\varepsilon}\right)d\varepsilon, \tag{6.36}$$

where $f(\varepsilon)$ is the Fermi distribution function. The magnetization M and the magnetic susceptibility χ are defined by

$$M = -\left(\frac{\partial\Omega}{\partial B}\right)_\zeta, \quad \chi = \left.\frac{\partial M}{\partial B}\right|_{B=0} = -\left.\left(\frac{\partial^2\Omega}{\partial B^2}\right)_\zeta\right|_{B=0}. \tag{6.37}$$

Using (6.36) and (6.37), we obtain [4, 14, 45, 46]

$$\chi = -g_v g_s \frac{e^2 v^2}{6\pi c^2}\int_{-\infty}^{\infty}\left(-\frac{\partial f(\varepsilon)}{\partial\varepsilon}\right)d\varepsilon. \tag{6.38}$$

At zero temperature, the integral in (6.38) becomes a delta function in Fermi energy, yielding

$$\chi(\varepsilon_F) = -g_v g_s \frac{e^2 v^2}{6\pi c^2}\delta(\varepsilon_F). \tag{6.39}$$

This anomalous behavior can also be understood as the zero-mass limit of a gapped Dirac electron [39]. Using the Landau levels of (6.31), the susceptibility is calculated in a similar way as

$$\chi(\varepsilon_F) = -g_v g_s \frac{e^2 v^2}{6\pi c^2}\frac{1}{2\Delta}\theta\left(\Delta - |\varepsilon_F|\right), \tag{6.40}$$

which is non-zero only in the energy gap, $|\varepsilon| < \Delta$. In the limit of $\Delta \to 0$, $\chi(\varepsilon_F)$ goes to the delta function of (6.39). Figure 6.4(a) and (b) show the density of states and the susceptibility of gapped graphene, respectively. The magnetic susceptibility around the band edge corresponds to the conventional magnetism of an electron. The valley Zeeman energy argued in the previous section induces the Pauli paramagnetism as a real spin does, and the Landau quantization gives the Landau diamagnetism in the usual manner. Each component is written as

$$\chi_P(\varepsilon) = \left(\frac{g^*}{2}\right)^2 \mu_B^2 D(\varepsilon), \tag{6.41}$$

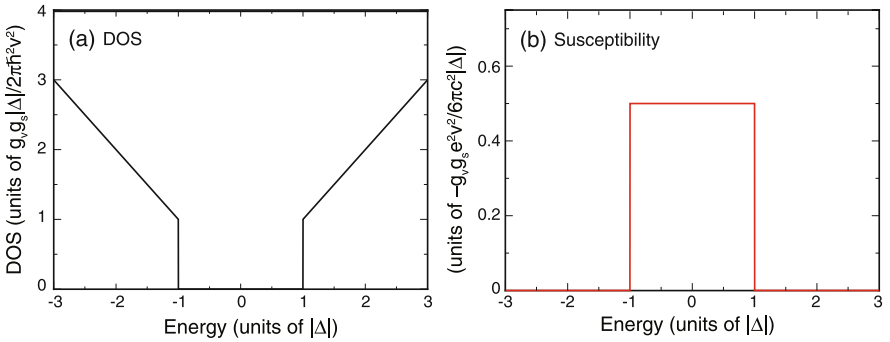

Fig. 6.4 (**a**) Density of states, and (**b**) susceptibility of monolayer graphene with the asymmetry gap Δ. In (**b**), the upward direction represents a negative (i.e., diamagnetic) susceptibility

$$\chi_L(\varepsilon) = -\frac{1}{3}\left(\frac{m}{m^*}\right)^2 \mu_B^2 D(\varepsilon), \tag{6.42}$$

with the density of states $D(\varepsilon) = g_v g_s m^*/(2\pi\hbar^2)\theta(\varepsilon)$. The total susceptibility $\chi_P + \chi_L$ actually agrees with the amount of the jump at the conduction band bottom in χ of (6.40). Because $g = 2m/m^*$ in the present case, we have $\chi_L = -\chi_P/3 \propto 1/m^*$ as for the free electron, giving the paramagnetic susceptibility in total. This gives a discrete jump of the total susceptibility toward the paramagnetic direction when the Fermi energy enters the conduction band.

6.3.2 *Response to a Non-uniform Magnetic Field*

The argument can be extended to spatially modulated magnetic fields. Monolayer graphene in a non-uniform magnetic field was studied in the context of the electron confinement [20, 61, 62], the peculiar band structures in superlattice [63, 64], transport [65], and the quantum Hall effect [66, 67]. Let us consider graphene placed under a magnetic field given by $B(\mathbf{r}) = B(\mathbf{q})\exp(i\mathbf{q}\cdot\mathbf{r}) + \text{c.c.}$, where 'c.c.' stands for complex conjugate. Within linear response, the induced magnetic moment can be written as

$$m(\mathbf{q}) = \chi(q)B(\mathbf{q}), \tag{6.43}$$

where $m(\mathbf{q})$ is the Fourier transform of the local magnetic moment perpendicular to the layer, $m(\mathbf{r})$, which is related to the local current density as $j_x = c\partial m/\partial y$, $j_y = -c\partial m/\partial x$.

For graphene at the zero temperature, the q-dependent susceptibility can be explicitly calculated as [57]

$$\chi(q;\varepsilon_F) = -\frac{g_v g_s e^2 v}{16\hbar c^2}\frac{1}{q}\theta(q-2k_F)\left[1+\frac{2}{\pi}\frac{2k_F}{q}\sqrt{1-\left(\frac{2k_F}{q}\right)^2}-\frac{2}{\pi}\sin^{-1}\frac{2k_F}{q}\right], \tag{6.44}$$

where $k_F = |\varepsilon_F|/(\hbar v)$ is the Fermi wave vector. Significantly, χ vanishes in the range $q < 2k_F$, i.e., no current is induced when the external field is smooth enough compared to the Fermi wavelength. As a function of ε_F at fixed q, χ is nonzero only in a finite region satisfying $|\varepsilon_F| < \hbar v q/2$, and its integral over ε_F becomes constant $-g_s g_v e^2 v^2/(6\pi^2 c^2)$. Thus, in the limit of $q \to 0$, χ goes to a delta function of (6.39).

The undoped graphene ($\varepsilon_F = 0$) has a special property in which the counter magnetic field induced by the response current copies the spatial distribution of the external magnetic field, regardless of its length scale [57]. At $\varepsilon_F = 0$, (6.44) becomes

$$\chi(q;0) = -\frac{g_v g_s e^2 v}{16\hbar c^2}\frac{1}{q}. \tag{6.45}$$

When undoped graphene is placed in a sinusoidal external field $B(\mathbf{r}) = B\cos qx$, the counter magnetic field induced by graphene is calculated with (6.45) as

$$B_{ind}(\mathbf{r}) = -\alpha_g B(\mathbf{r}), \quad \alpha_g = \frac{2\pi g_v g_s e^2 v}{16\hbar c^2} \approx 4\times 10^{-5}. \tag{6.46}$$

Because the ratio α_g is independent of q, (6.46) is actually valid for any external field $B(\mathbf{r})$, i.e., the magnetic field on the graphene is always reduced by the same factor $1-\alpha_g$. This property holds whenever $\chi(q)$ is proportional to $1/q$. The argument of the magnetic field screening can be extended to the three dimensional field distribution. When a certain magnetic object is placed above the undoped graphene ($z > 0$), the counter magnetic field in $z > 0$ is shown to be equivalent to the field induced by the mirror image of the original object reflected with respect to $z = 0$, and reduced by the factor α_g.

6.4 Transport Properties

Graphene exhibits peculiar transport properties due to its unusual band structure where the conduction and valence bands touch at the single energy. When the Fermi energy ε_F is much larger than the disorder level broadening, the system is not largely different from the conventional metal, and the conductivity is well described by the Boltzmann transport theory with a corresponding density of states and velocity. However, the approximation inevitably breaks down at the charge neutrality point ($\varepsilon_F = 0$), where it is highly nontrivial if the system is metallic or insulating, since the density of states vanishes whereas the band velocity is finite. To argue the transport behavior at the charge neutrality point, we need a refined approximation

that properly includes the finite level broadening. In this section, we first review the transport properties of graphene within the Boltzmann approach [68], and then introduce the self-consistent Born approximation to calculate the conductivity at $\varepsilon_F = 0$.

6.4.1 Boltzmann Conductivity

The conductivity tensor is written as

$$\sigma_{\mu\nu} = \int \left(-\frac{\partial f}{\partial \varepsilon}\right) \sigma_{\mu\nu}(\varepsilon) d\varepsilon \quad (\mu, \nu = x, y). \tag{6.47}$$

In the Boltzmann approach, the diagonal conductivity becomes

$$\sigma_{xx}(\varepsilon) = \frac{e^2 v^2}{2} D(\varepsilon) \frac{\tau_{tr}}{1 + \omega_c^2 \tau_{tr}^2}, \tag{6.48}$$

where τ_{tr} is the transport relaxation time defined as

$$\frac{1}{\tau_{tr}(\varepsilon_{s\mathbf{p}})} = \sum_{s'} \int \frac{d\mathbf{p}'}{(2\pi\hbar)^2} \langle |U_{s'\mathbf{p}',s\mathbf{p}}|^2 \rangle \delta\big[\varepsilon_s(\mathbf{p}) - \varepsilon_{s'}(\mathbf{p}')\big]\big[1 - \cos(\theta_{\mathbf{p}} - \theta_{\mathbf{p}'})\big], \tag{6.49}$$

where U represents impurity potential and $\langle \cdots \rangle$ denotes the average over impurity configurations. In $B = 0$, we have

$$\sigma_{xx}(\varepsilon) = \frac{e^2 v^2}{2} D(\varepsilon) \tau_{tr}, \tag{6.50}$$

which is identical to the conventional formula for metals.

The Hall conductivity then becomes

$$\sigma_{xy}(\varepsilon) = -\omega_c \tau_{tr} \sigma_{xx}(\varepsilon), \tag{6.51}$$

where ω_c is the cyclotron frequency defined in (6.20). In the case of a weak magnetic field $|\omega_c|\tau_{tr} \ll 1$, the Hall coefficient, defined by $R_H = -\sigma_{xy}/[B(\sigma_{xx}^2 + \sigma_{xy}^2)]$, becomes

$$R_H = -\frac{1}{n_s e c}, \tag{6.52}$$

at zero temperature. This is exactly the same as that in conventional semiconductors and metals.

For a model disorder potential, we consider a short-range scatterer where the length scale is much smaller than the Fermi wave length. This is modeled by

$$U(\mathbf{r}) = \sum_j u_j \delta(\mathbf{r} - \mathbf{r}_j), \tag{6.53}$$

where u_j is the strength of the scatterer and $\mathbf{r}_j$ its position. We also assume that the length scale of the scattering potential is longer than the atomic scale a, to neglect intervalley scattering between K and K′. The transport relaxation time in this model is written as [9]

$$\frac{1}{\tau_{tr}(\varepsilon)} = \frac{\pi}{\hbar} W|\varepsilon|. \tag{6.54}$$

Here W is a dimensionless parameter representing the strength of scatterers, defined as

$$W \equiv \frac{n_i u^2}{4\pi\hbar^2 v^2}, \tag{6.55}$$

where $u^2 = \langle u_j^2 \rangle$ and n_i is the concentration of scatterers per unit area. Equation (6.54) indicates that the ratio of the energy broadening $\hbar/\tau_{tr}(\varepsilon)$ to ε has the constant value πW. We should assume $W \ll 1$ except in very dirty graphene such that broadening is comparable to ε, i.e., the Dirac cone is completely smeared out by the disorder. In graphene, it should be noted that $\tau_{tr} = 2\tau$, where τ represents the usual scattering time corresponding to a single-particle lifetime. The factor two corresponds to the absence of backscattering [69, 70]. The diagonal conductivity at zero magnetic field then becomes

$$\sigma_{xx}(\varepsilon) = \frac{g_v g_s e^2}{2\pi^2\hbar} \frac{1}{2W}, \tag{6.56}$$

which is independent of the Fermi energy. The Hall conductivity in a weak magnetic field is

$$\sigma_{xy}(\varepsilon) = -\frac{g_v g_s e^3 B v^2}{4\pi^3 c} \frac{\mathrm{sgn}(\varepsilon)}{W^2\varepsilon^2}. \tag{6.57}$$

Experimentally, the conductivity increases almost linearly with n_s for sufficiently large n_s, showing that the effective scattering strength in actual graphene on a SiO_2 substrate varies considerably with n_s. The most plausible scatterers giving rise to such a strong n_s dependence are charged impurities [68, 71]. The short-range scatterers argued above approximately describe charged impurities, by assuming that $|u_j|$ effectively decreases when in proportion to k_F^{-1}, where k_F is the Fermi wave vector. This leads to $W \propto \varepsilon_F^{-2} \propto n_s^{-1}$, and consequently, the conductivity increases in proportion to the electron or hole concentration n_s, as if there is a constant mobility [68, 71]. However, this does not conclude that graphene is insulating at the charge neutral point ($n_s = 0$), since the present approach is no longer valid at zero Fermi energy. As we will see in the following section, the improved treatment predicts a finite conductivity, on the order of $e^2/\hbar$, at the Dirac point.

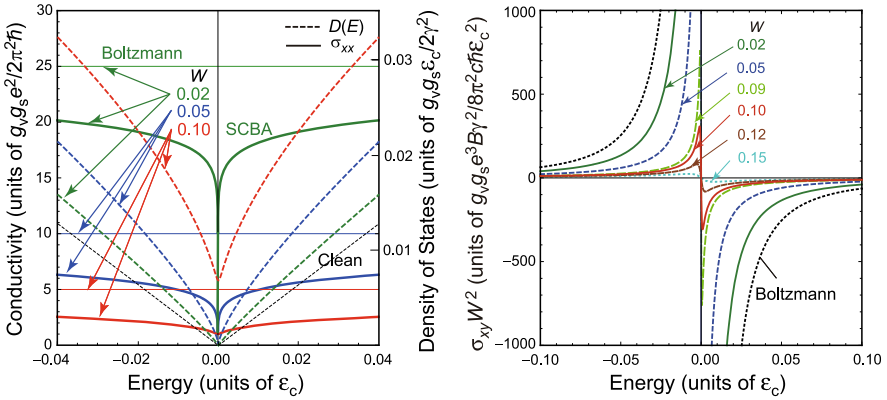

Fig. 6.5 (**a**) Some examples of the density of states (*dashed lines*) and the conductivity (*solid lines*) in the absence of a magnetic field, calculated in a self-consistent Born approximation (SCBA) for short-range scatterers. Thin *horizontal lines* are the Boltzmann conductivity [9]. (**b**) Some examples of calculated Hall conductivity as a function of the Fermi energy calculated in a self-consistent Born approximation for short-range scatterers [74]

6.4.2 Self-consistent Born Approximation

The self-consistent Born approximation is a technique which properly treats the finite level-broadening effect by estimating the selfenergy by Dyson's equation in a self-consistent manner. This was applied to describe the broadening of the degenerate Landau levels in a two-dimensional electron gas [72, 73], and also is useful in the present situation where the broadening energy can be larger than the Fermi energy [9]. Figure 6.5(a) shows some examples of the density of states and the conductivity in graphene calculated by the self-consistent Born approximation with short-range scatterers assumed. The density of states becomes nonzero at $\varepsilon_F = 0$ because of the level broadening and is also enhanced due to the level repulsion effect near $\varepsilon_F = 0$. Significantly, the electrical conductivity at $\varepsilon_F = 0$ is given by

$$\sigma_{min} = \frac{g_v g_s e^2}{2\pi^2 \hbar} \tag{6.58}$$

which is independent of the scattering strength. The resulting conductivity varies smoothly across $\varepsilon_F = 0$ but exhibits a sharp jump in the limit of weak scattering ($W \ll 1$) from the Boltzmann result in (6.56) for $\varepsilon_F \neq 0$ down to σ_{min} at $\varepsilon_F = 0$. The energy scale characterizing this singularity in the vicinity of $\varepsilon_F = 0$ turns out to be

$$\varepsilon_0 = 2W\varepsilon_c e^{-1/2W} \tag{6.59}$$

where ε_c is the cutoff energy roughly corresponding to a half of the π-band width (~ 9 eV). This becomes extremely small in clean graphene with $W \ll 1$.

Similar calculations in the self-consistent Born approximation were performed for the weak-field Hall conductivity [74]. Figure 6.5(b) shows some examples of

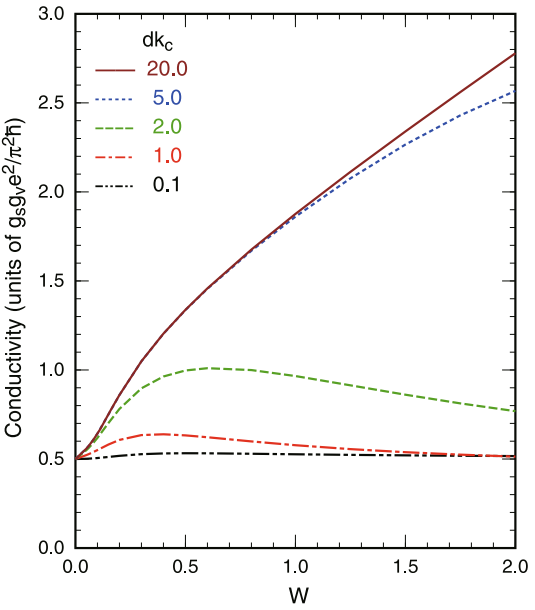

Fig. 6.6 Calculated minimum conductivity at the Dirac point versus W for scatterers with Gaussian potential [75]

the calculated σ_{xy}. The Hall conductivity behaves roughly as $-\varepsilon_F^{-1}$ outside of the region $|\varepsilon_F| > \varepsilon_0$, but is considerably reduced from the Boltzmann result. σ_{xy} varies almost linearly in the region $-\varepsilon_c < \varepsilon < \varepsilon_c$ and crosses zero at the Dirac point. The self-consistent Born approximation was also applied to the quantum Hall regime in which the spectrum is split into the Landau levels [9, 18].

Calculations can be extended to the case of scatterers with a long-range potential [75]. We consider, for example, scatterers with a Gaussian potential $U(r) = \sum_j (v_i/\pi d^2) \exp[-(\mathbf{r} - \mathbf{r}_j)^2/d^2]$ with the characteristic length scale d. The energy region affected strongly by the presence of scatterers is limited to $|\varepsilon| \lesssim \hbar v/d$ because scattering becomes ineffective for $k > d^{-1}$. Figure 6.6 shows the minimum conductivity at the Dirac point as a function of W, at several different d's. For very short-range case $k_c d < 1$, the conductivity is nearly independent of W, where $k_c = \varepsilon_c/(\hbar v)$ is the cutoff momentum. For $k_c d > 1$, on the other hand, the conductivity increases with W. States at the Dirac point have higher k components because of the strong forward scattering caused by long-range scatterers. These higher k states are weakly scattered in the backward direction and therefore tend to have a large contribution to the conductivity. Since the first experimental observation of a minimum conductivity [1], which is larger than the theoretical prediction [9], there have been various experimental [76–78] and theoretical works [79–86] to answer the question whether the minimum conductivity is really universal or not. The above discussion clearly shows that the conductivity at the Dirac point is not universal but depends on the degree of the disorder for scatterers with a long-range potential when the disorder is sufficiently large.

6.5 Optical Properties

The optical absorption is related to the dynamical conductivity of the system. Within the linear response, the dynamical conductivity is generally given by

$$\sigma_{xx}(\omega) = \frac{e^2\hbar}{iS}\sum_{\alpha,\beta}\frac{f(\varepsilon_\alpha) - f(\varepsilon_\beta)}{\varepsilon_\alpha - \varepsilon_\beta}\frac{|\langle\alpha|v_x|\beta\rangle|^2}{\varepsilon_\alpha - \varepsilon_\beta + \hbar\omega + i\delta}, \tag{6.60}$$

where S is the area of the system, $v_x = \partial\mathcal{H}/\partial p_x$ is the velocity operator, δ is the positive infinitesimal, $f(\varepsilon)$ is the Fermi distribution function, and $|\alpha\rangle$ and ε_α describe the eigenstate and the eigenenergy of the system. The optical absorption intensity is related to the real part of $\sigma_{xx}(\omega)$. The transmission of light incident perpendicular to a two-dimensional system T is given by [72]

$$T = \left|1 + \frac{2\pi}{c}\sigma_{xx}(\omega)\right|^{-2} \approx 1 - \frac{4\pi}{c}\,\mathrm{Re}\,\sigma_{xx}(\omega). \tag{6.61}$$

For graphene, $\sigma_{xx}(\omega)$ is written at zero temperature as [10]

$$\sigma_{xx}(\omega) = \frac{g_v g_s}{4}\frac{e^2}{4\hbar}\left[\frac{4}{\pi}\frac{i\varepsilon_F}{\hbar\omega + i\hbar/\tau(\varepsilon_F)} + 1 + \frac{i}{\pi}\ln\frac{\hbar\omega + i\hbar/\tau(\hbar\omega/2) - 2\varepsilon_F}{\hbar\omega + i\hbar/\tau(\hbar\omega/2) + 2\varepsilon_F}\right], \tag{6.62}$$

where the first term in the bracket represents the Drude (intra-band) part, and the second and third terms the inter-band part. We included the disorder effect by replacing δ with $\hbar/\tau(\varepsilon)$ where $\tau(\varepsilon)$ is the relaxation time at the energy ε. In the second term, we put $\tau(\hbar\omega/2)$, corresponding to the energy of the states giving a major contribution to the optical excitation.

When we assume that the disorder potential is dominated by the short-range scatterers, the relaxation time is given by (6.54), and the frequency dependence of the dynamical conductivity is scaled by $\hbar\omega/\varepsilon_F$. Figure 6.7(a) shows $\sigma_{xx}(\omega)$ as a function of $\hbar\omega/\varepsilon_F$ for several values of the disorder strength parameter W. The scaling of the dynamical conductivity as a function of $\hbar\omega/\varepsilon_F$ shows that $\sigma_{xx}(\omega)$ exhibits a singular behavior at the point $(\omega, \varepsilon_F) = (0, 0)$. In fact, when we set $\omega = 0$ with fixed nonzero ε_F, the static conductivity agrees with the Boltzmann result of (6.56). When we set $\varepsilon_F = 0$ first with nonzero ω, on the other hand, the limit $\omega \to 0$ becomes

$$\sigma_\infty = \frac{g_v g_s}{4}\frac{e^2}{\pi\hbar} \tag{6.63}$$

which is the universal interband conductivity. Therefore, the static conductivity, i.e., σ_{xx} in the limit of $\omega \to 0$ at each ε_F, has a singular jump at $\varepsilon_F = 0$. The calculation in the self-consistent Born approximation in the previous section shows that this anomaly manifests itself as a near singular dependence of σ_{xx} on ε_F even if level broadening effects are properly included, while the conductivity at $\varepsilon_F = 0$ becomes a different value of (6.58).

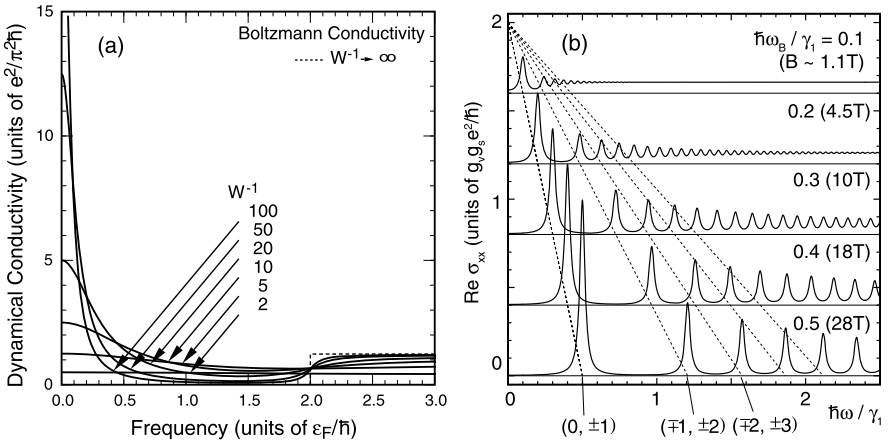

Fig. 6.7 (**a**) The dynamical conductivity $\mathrm{Re}\,\sigma_{xx}(\omega)$ calculated using the Boltzmann transport equation. The frequency is scaled by the Fermi energy [10]. (**b**) The interband part of the dynamical conductivity $\mathrm{Re}\,\sigma_{xx}(\omega)$ of graphene plotted against the frequency ω, calculated for different magnetic fields. *Dashed curves* indicate the transition energies between several Landau levels in the ideal limit [35]

The transmission of light incident perpendicular to a graphene sheet with $\varepsilon_F = 0$ is given by

$$T \approx 1 - \frac{4\pi}{c}\sigma_\infty = 1 - \frac{g_v g_s}{4}\frac{\pi e^2}{c\hbar} \tag{6.64}$$

showing that the absorption is given by $\pi\alpha \approx 0.023$ independent of the frequency or wavelength, with fine structure constant $\alpha \equiv e^2/(c\hbar) \approx 1/137$. This small absorption was experimentally observed [87–89].

The magneto-optical absorption is studied by calculating the dynamical conductivity for the Landau level structures. For graphene, the matrix element of the velocity operator v_x is non zero only between the Landau levels n and $n \pm 1$ with arbitrary combinations of $s = \pm$, and this gives the selection rule for the photo-excitation. Figure 6.7(b) shows the plots of the interband part of $\mathrm{Re}\,\sigma_{xx}(\omega)$ of graphene in several different magnetic fields [35]. Here we assume $\varepsilon_F = 0$, zero temperature, and a constant relaxation time for simplicity. Dotted lines represent the transition energies between several specific Landau levels as a continuous function of B. The peak positions of each panel correspond to the intersections of those and the bottom line of the panel. The peak position obviously shifts in proportion to $\sqrt{B}$ (i.e., $\propto \hbar\omega_B$). In the limit of vanishing magnetic field, the conductivity eventually becomes the constant value given by (6.63) [10].

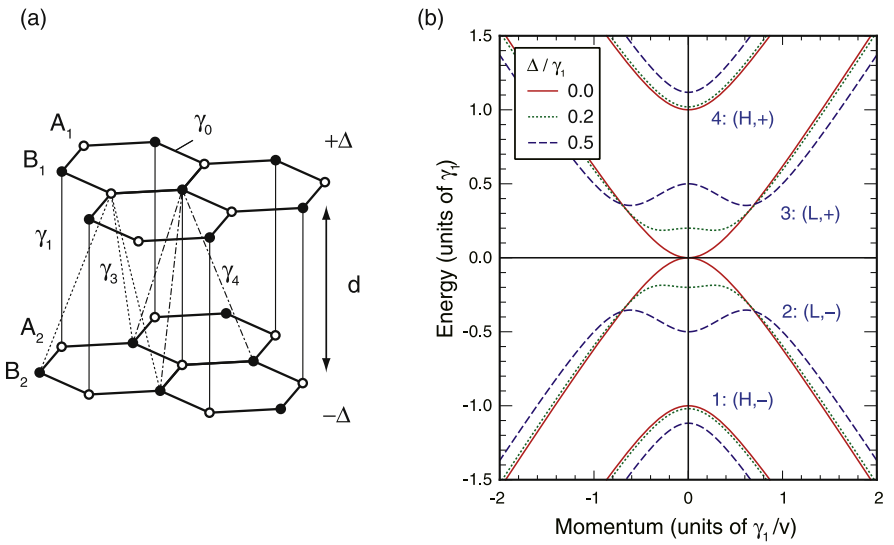

Fig. 6.8 (**a**) The lattice structure of AB-stacked bilayer graphene. (**b**) The energy dispersion of bilayer graphene with various values of interlayer potential asymmetry Δ

6.6 Bilayer Graphene

The most stable structure of bilayer graphene is known to be AB (Bernal) stacking as shown in Fig. 6.8(a) [1, 21–24, 28]. A unit cell includes A_1 and B_1 atoms on layer 1 and A_2 and B_2 on layer 2, and the layers are stacked with the interlayer spacing of $d_0 \approx 0.334$ nm, such that pairs of sites B_1 and A_2 lie directly above or below each other. We can also have different stacking structures depending on the experimental condition, such as AA stacked bilayer graphene where sites A_1 and A_2 lie directly above or below each other [90–92], and rotationally-stacked (turbostratic) bilayer graphene where two graphene layers are overlapped with a rotational misorientation [93–99].

Below we consider particularly the electronic properties of the most common AB stacked bilayer graphene. There the interlayer coupling drastically changes the linear band structure of monolayer, leaving a pair of quadratic energy bands touching at zero energy [25–27, 29–33]. Accordingly, the electronic properties of bilayer graphene become characteristic of this system as we will see in the following.

6.6.1 Electronic Structure

In order to write down an effective mass Hamiltonian, we adapt the Slonczewski-Weiss-McClure parameterization of the tight-binding couplings of bulk graphite [100]. The parameter γ_0 is the same as the intralayer nearest neighbor coupling

in monolayer graphene, and describes nearest-neighbor coupling between A_i and B_i within each layer. γ_1 describes the strong nearest-layer coupling between sites (B_1–A_2) that lie directly above or below each other, γ_3 describes nearest-layer coupling between sites $A1$–$B2$ and γ_4 is another nearest-layer coupling between A_1–A_2, and between B_1–B_2. There is an energy difference Δ' between the sites which have neighboring atoms right above or below, and the sites which do not. For typical values of bulk ABA graphite we quote [100] $\gamma_1 = 0.39$ eV, $\gamma_3 = 0.315$ eV, $\gamma_4 = 0.044$ eV, and $\Delta' = 0.047$ eV, while it should be mentioned that the improved band parameter values were reported in a recent experiment [101].

The Hamiltonian at the K point for the basis $(|A_1\rangle, |B_1\rangle, |A_2\rangle, |B_2\rangle)$ is given by [25]

$$\mathcal{H} = \begin{pmatrix} 0 & vp_- & -v_4 p_- & v_3 p_+ \\ vp_+ & \Delta' & \gamma_1 & -v_4 p_- \\ -v_4 p_+ & \gamma_1 & \Delta' & vp_- \\ v_3 p_- & -v_4 p_+ & vp_+ & 0 \end{pmatrix}, \tag{6.65}$$

where v and $p_\pm$ are the same as ones in (6.12) for monolayer graphene, and we defined

$$v_3 = \frac{\sqrt{3}}{2}\frac{a\gamma_3}{\hbar}, \qquad v_4 = \frac{\sqrt{3}}{2}\frac{a\gamma_4}{\hbar}. \tag{6.66}$$

The effective Hamiltonian for K′ can be obtained by exchanging p_+ and p_-, giving the equivalent spectrum in zero magnetic field.

The parameters v_3, v_4 and Δ' give relatively minor effects to the band structure as mentioned later. When we neglect them, the eigenenergies of (6.65) become [25, 26]

$$\varepsilon_{\mu,s}(\mathbf{p}) = s\left[\frac{\mu}{2}\gamma_1 + \sqrt{\frac{1}{2}\gamma_1^2 + v^2 p^2}\right]. \tag{6.67}$$

The branch $\mu = -$ gives a pair of conduction ($s = +$) and valence ($s = -$) bands touching at zero energy. The other branch $\mu = +$ is another pair repelled away by $\pm\gamma_1$. In the following we use the notation $\mu = H, L$ instead of $+, -$ and specify the four energy bands as $(\mu, s) = (L, \pm), (H, \pm)$. We will also use the notation the band indexes $1, 2, 3, 4$ for $(H, -), (L, -), (L, +), (H, +)$, respectively, in the ascending order in energy. In $\varepsilon \ll \gamma_1$, the lower subbands $(L, -)$ and $(L, +)$ are approximately expressed as a quadratic form,

$$\epsilon_{L,\pm}(\mathbf{p}) \approx \pm\frac{v^2 p^2}{\gamma_1} \equiv \frac{p^2}{2m^*}, \tag{6.68}$$

with the effective mass

$$m^* = \frac{\gamma_1}{2v^2}. \tag{6.69}$$

The energy band of (6.67) is shown in the curve of $\Delta = 0$ in Fig. 6.8(b), where Δ is the interlayer potential asymmetry that will be discussed later.

The Hamiltonian of (6.65) can be reduced to the low-energy expression with additional parameters retained. Using a basis (ψ_{A1}, ψ_{B2}), this is written as

$$\mathcal{H}^{(\mathrm{eff})} = -\frac{v^2}{\gamma_1}\begin{pmatrix} 0 & p_-^2 \\ p_+^2 & 0 \end{pmatrix} + v_3\begin{pmatrix} 0 & p_+ \\ p_- & 0 \end{pmatrix} + \frac{2vv_4p^2}{\gamma_1}\begin{pmatrix} 1 & 0 \\ 0 & 1 \end{pmatrix}. \tag{6.70}$$

The corresponding eigenenergies are

$$\epsilon_{L,\pm}(\mathbf{p}) \approx \pm\sqrt{\frac{v^4p^4}{\gamma_1^2} - 2\xi\frac{v_3v^2p^3}{\gamma_1}\cos 3\varphi + v_3^2p^2} + \frac{2vv_4p^2}{\gamma_1}, \tag{6.71}$$

where $\tan\varphi = p_y/p_x$. The parameter v_3 produces trigonal warping in a similar way to bulk graphite [100], where the energy band around each valley is stretched in three directions. In the low-energy region $|\varepsilon| < \varepsilon_{trig}$, we have the Lifshitz transition in which the equi-energetic line splits into four separate pockets, and the conduction band and valence band touch each other at four points inside the pockets [25, 27]. Here ε_{trig} is the characteristic energy defined as,

$$\varepsilon_{trig} = \frac{1}{4}\left(\frac{v_3}{v}\right)^2\gamma_1 \sim 1\ \mathrm{meV}. \tag{6.72}$$

The parameter v_4 gives the common quadratic term to both of the conduction and valence bands, and thus slightly breaks the electron hole asymmetry. The parameter Δ' appears in the second order of Δ'/γ_1 in (6.71), and is neglected here. This term influences mainly the $(H, \pm)$ branches by giving an energy shift of Δ' to these levels. In the following, we will neglect v_3, v_4 and Δ' unless otherwise stated.

6.6.2 Landau Levels

The Landau-level structure of the bilayer Hamiltonian (6.65) is derived in a similar way to monolayer graphene, by noting that $p_\pm$ are associated with the ascending/descending operators of the Landau levels [25, 26]. The eigenfunction can be written as

$$(c_1\phi_{n-1}, c_2\phi_n, c_3\phi_n, c_4\phi_{n+1}). \tag{6.73}$$

For $n \geq 1$, the Hamiltonian matrix for the vector (c_1, c_2, c_3, c_4) then becomes

$$\begin{pmatrix} 0 & \hbar\omega_B\sqrt{n} & 0 & 0 \\ \hbar\omega_B\sqrt{n} & 0 & \gamma_1 & 0 \\ 0 & \gamma_1 & 0 & \hbar\omega_B\sqrt{n+1} \\ 0 & 0 & \hbar\omega_B\sqrt{n+1} & 0 \end{pmatrix}, \tag{6.74}$$

which immediately gives four eigen values

$$\varepsilon_{\mu,s,n} = \frac{s}{\sqrt{2}}\Big[\gamma_1^2 + (2n+1)(\hbar\omega_B)^2 + \mu\sqrt{\gamma_1^4 + 2(2n+1)\gamma_1^2(\hbar\omega_B)^2 + (\hbar\omega_B)^4}\Big]^{1/2}. \tag{6.75}$$

For $n = 0$, the first component of the wave function (6.73) disappears and we have three levels,

$$\begin{aligned} \varepsilon_{L,0} &= 0, \\ \varepsilon_{H,s,0} &= s\sqrt{\gamma_1^2 + (\hbar\omega_B)^2}. \end{aligned} \tag{6.76}$$

For $n = -1$, only the last component survives in (6.73), leaving a single level

$$\varepsilon_{L,-1} = 0. \tag{6.77}$$

Each Landau level is degenerate in valley and spin. The zero-energy level is 8-fold degenerate due to the extra degeneracy of $\varepsilon_{L,0} = \varepsilon_{L,-1}$, while all others are four-fold degenerate as in monolayer graphene.

In low-energy region $\varepsilon \ll \gamma_1$, the Landau levels of the lower subband L approximate [25]

$$\varepsilon_{L,s,n} \approx s\frac{\hbar eB}{m^*}\sqrt{n(n+1)} \quad (n = 0, 1, 2, \ldots), \tag{6.78}$$

where the two lowest levels $\varepsilon_{L,0} = \varepsilon_{L,-1} = 0$ are included in $s = \pm$ at $n = 0$. Since the energy is proportional to B, the level spacing shrinks in the $B \to 0$ limit much faster than that in the monolayer, where the Landau levels behave as $\propto \sqrt{B}$. When the Fermi energy is between $\varepsilon_{L,s,n}$ and $\varepsilon_{L,s,n+1}$, the Hall conductivity becomes

$$\sigma_{xy} = -sg_v g_s \frac{e^2}{h}(n+1) \quad (s = \pm, n = 0, 1, 2, \ldots) \tag{6.79}$$

which gives the sequence of quantized Hall conductivity, $\pm 4, \pm 8, \pm 12, \ldots$ in units of $-e^2/h$. We notice that $\sigma_{xy}/(g_s g_v)$ is an integer in bilayer graphene, while it is a half-integer in monolayer graphene as we showed in (6.26). In experiments, this appears as a clear difference in the plateau structure of the Hall conductivity [1]. Figure 6.9(a) shows the bilayer's Landau level structure and the Hall conductivity in the low energy region for the gapless case.

6.6.3 Gapped Bilayer Graphene

In bilayer graphene, a potential asymmetry between the top and bottom layers gives rise to an energy gap at zero energy [25, 26, 29–31, 102–104]. The potential asymmetry is intrinsically zero, but is induced by applying an electric field perpendicular to the layers [21, 24, 105–107]. The interlayer potential difference is generally smaller than that given by the external electric field, because the graphene electron

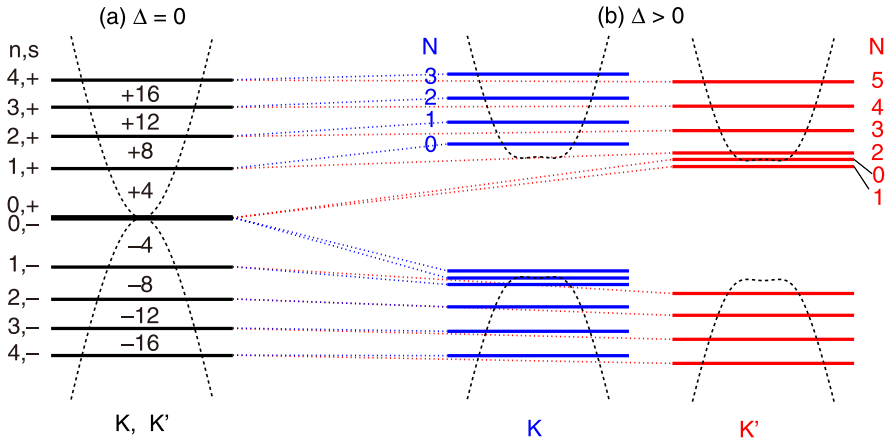

Fig. 6.9 Low-energy Landau level structure in bilayer graphene with interlayer potential asymmetry (**a**) $\Delta = 0$ and (**b**) $\Delta > 0$. The *horizontal dotted lines* connecting levels indicate the correspondence of the levels in the limit of $\Delta \to 0$. In (**a**), the numbers between the levels indicate the quantized Hall conductivity in units of $-e^2/h$. A corresponding diagram for monolayer graphene is shown in Fig. 6.3

induces an interlayer depolarization effect. The self-consistent calculation shows that the external field is decreased roughly by a factor of 2, in the weak field regime [102, 103]. In the experiment, an energy gap as large as 0.2 eV was actually observed in spectroscopic measurements [21, 106–108].

Let us assume an interlayer asymmetry between the on-site energy Δ for the atoms, $A1$ and $B1$, on the first layer and $-\Delta$ for the atoms, $A2$ and $B2$, on the second layer. The Hamiltonian matrix then becomes

$$\mathcal{H} = \begin{pmatrix} \Delta & vp_- & 0 & 0 \\ vp_+ & \Delta & \gamma_1 & 0 \\ 0 & \gamma_1 & -\Delta & vp_- \\ 0 & 0 & vp_+ & -\Delta \end{pmatrix}. \tag{6.80}$$

Figure 6.8(b) shows the energy bands with several values of Δ obtained by the diagonalization of (6.80). The low-energy Hamiltonian in a basis (ψ_{A1}, ψ_{B2}) becomes [25]

$$\mathcal{H}^{(\mathrm{eff})} = -\frac{v^2}{\gamma_1}\begin{pmatrix} 0 & p_-^2 \\ p_+^2 & 0 \end{pmatrix} + \Delta\left(1 - \frac{2v^2p^2}{\gamma_1^2}\right)\begin{pmatrix} 1 & 0 \\ 0 & -1 \end{pmatrix}. \tag{6.81}$$

When $\Delta \ll \gamma_1$, the dispersion in the region of $p \ll \gamma_1/v$ approximates [26, 58]

$$\epsilon \approx \pm\left(\Delta - 2\Delta\frac{v^2p^2}{\gamma_1^2} + \frac{1}{2\Delta}\frac{v^4p^4}{\gamma_1^2}\right) \equiv \pm\left(\Delta - \frac{p^2}{2m_0} + \frac{p^4}{4m_0p_0^2}\right), \tag{6.82}$$

where

$$m_0 = \frac{\gamma_1^2}{4v^2\Delta}, \qquad p_0 = \frac{\sqrt{2}\Delta}{v}. \tag{6.83}$$

Figure 6.10(a) shows the positive branch of (6.82). Due to coexistence of p^2 and p^4 terms, the energy bands have their extrema at off center momentum p_0 located at $\pm(\Delta - \varepsilon_0)$ with $\varepsilon_0 = 2\Delta^3/\gamma_1^2$, and the energy gap extends between these extrema.

In a magnetic field, the interlayer asymmetric potential Δ causes a valley splitting of the Landau levels that is similar to monolayer graphene, since it breaks the inversion symmetry [24, 25, 38]. Figure 6.9(b) illustrates an example of the Landau level structure in the presence of $\Delta > 0$. The two lowest levels of $(0, \pm)$, which used to be at the Dirac point when $\Delta = 0$, now move to the top of the valence band at point K, and to the bottom of the conduction band at point K′. Near the bottom of the conduction band, the Hamiltonian is reduced to [58]

$$\begin{aligned}\mathcal{H} &\approx \Delta - 2\Delta\frac{(v\pi_{-\xi})(v\pi_\xi)}{\gamma_1^2} + \frac{1}{2\Delta}\frac{(v\pi_{-\xi})^2(v\pi_\xi)^2}{\gamma_1^4} \\ &= \Delta + \frac{(\hbar\omega_0)^2}{4\varepsilon_0}\left[\left(\hat{N} + \frac{1}{2} + \xi\right)^2 - \frac{1}{4}\right] - \hbar\omega_0\left(\hat{N} + \frac{1}{2} + \frac{\xi}{2}\right),\end{aligned} \tag{6.84}$$

where $\xi = \pm$ are for K, K′, respectively, and $\omega_0 = eB/(m_0 c)$. The eigenvalue of $\hat{N}$ $(0, 1, 2, \ldots)$ is the Landau level index counted within the conduction band of each valley, and generally different from the previous numbering (s, n).

The energy difference between the Landau levels of K and K′ belonging to the same N can be written as a Zeeman-like form, $\pm\mu^* B$, to the lowest order in B. The effective magnetic moment μ^* is given by

$$\mu^*(p) = \frac{1}{2}g^*(p)\mu_B, \quad g^*(p) = \frac{2m}{m_0}\left(\frac{2p^2}{p_0^2} - 1\right), \tag{6.85}$$

which now depends on p. We can show that μ^* is induced by the intrinsic orbital current in a similar manner to monolayer graphene [58]. Figure 6.10(b) plots the Landau level energy of (6.84) as a function of magnetic field. A pair of dotted slopes represent the energy of the band minimum shifted by the valley Zeeman-like energy, i.e., $-\varepsilon_0 + \xi\mu^*(p_0)B$. In a small B-field, these dotted slopes actually serve as the envelope curves for Landau levels of $\xi = \pm$.

6.6.4 Orbital Diamagnetism

The delta-function susceptibility of monolayer graphene is strongly distorted by the interlayer coupling γ_1. For the Hamiltonian of the symmetric bilayer graphene, i.e.,

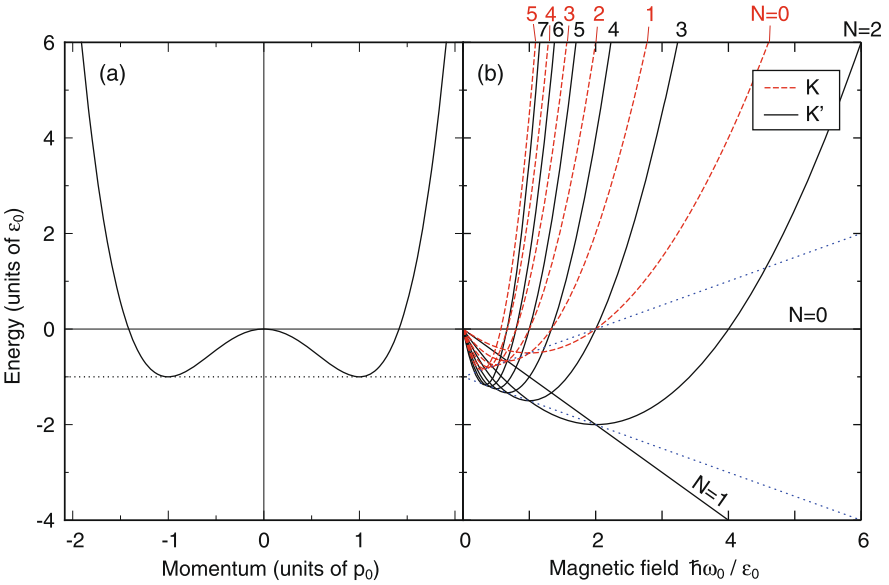

Fig. 6.10 (**a**) Low energy dispersion of gapped bilayer graphene given by (6.82). (**b**) Landau level spectrum of (6.84) with some small n's, as a function of magnetic field. Energy is measured from $\varepsilon = \Delta$. *Dashed* (*red*) and *solid* (*black*) *lines* represent K, K′, respectively. Numbers assigned to the curves indicate Landau level index n. A pair of dotted slopes (not energy levels) represent $-\varepsilon_0 \pm \mu^*(p_0)B$ [58]

(6.80) with $\Delta = 0$, the orbital susceptibility is calculated as [14, 46]

$$\chi(\varepsilon) = g_v g_s \frac{e^2 v^2}{4\pi c^2 \gamma_1} \theta\big(\gamma_1 - |\varepsilon|\big)\left(\log\frac{|\varepsilon|}{\gamma_1} + \frac{1}{3}\right). \tag{6.86}$$

In this case χ diverges logarithmically at $\varepsilon_F = 0$, becomes slightly paramagnetic near $|\varepsilon_F| = \gamma_1$, and vanishes for $|\varepsilon_F| > \gamma_1$ where the higher subband enters. The integration of χ in (6.86) over the Fermi energy becomes $-g_v g_s e^2 v^2/(3\pi c^2)$ independent of γ_1, which is exactly twice as large as that of the monolayer graphene, (6.39).

The susceptibility was also calculated in the presence of interlayer asymmetric potential [39]. Figure 6.11(a) and (b) show the density of states and the magnetic susceptibility, respectively, for bilayer graphene with $\Delta/\gamma_1 = 0$, 0.2, and 0.5. The figures are to be compared to the corresponding plots for monolayer graphene, in Fig. 6.4. The susceptibility diverges in the paramagnetic direction at the band edges $\varepsilon = \pm\varepsilon_0$, where the density of states also diverges. This huge paramagnetism can be interpreted as the Pauli paramagnetism induced by the valley pseudo-spin splitting discussed in the previous section, together with the diverging density of states [58]. The susceptibility always vanishes in the energy region where H bands contribute significantly.

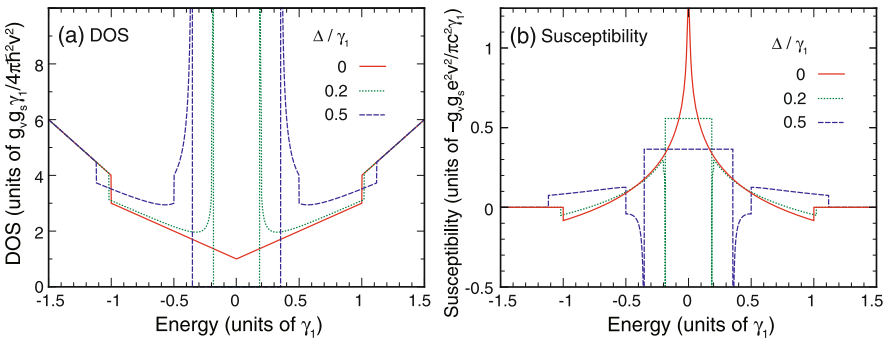

Fig. 6.11 (**a**) Density of states, and (**b**) susceptibility of bilayer graphenes with the asymmetry gap $\Delta/\gamma_1 = 0$, 0.2, and 0.5. In (**b**), the upward direction represents negative (i.e., diamagnetic) susceptibility [39]. A corresponding plot for monolayer graphene is Fig. 6.4

6.6.5 Transport Properties

The transport properties of bilayer graphene were theoretically studied in the literature [27, 109, 110]. In the following, we focus on the conductivity calculation in zero magnetic field using the self-consistent Born approximation [27, 34]. We consider the low-energy Hamiltonian (6.70) when the small electron-hole asymmetry depending on v_4 is neglected, and we assume the short-range scattering potential in (6.53). The electrical conductivity at zero temperature is then approximately written as

$$\sigma_{xx}(\varepsilon) \approx g_v g_s \frac{e^2}{\pi^2\hbar}\frac{1}{2}\left[1+\left(\frac{|\varepsilon_F|}{\Gamma}+\frac{\Gamma}{|\varepsilon_F|}\right)\arctan\frac{|\varepsilon_F|}{\Gamma}+\frac{4\pi\varepsilon_{trig}}{\Gamma}\right], \tag{6.87}$$

where Γ is the characteristic scale of energy broadening, defined by

$$\Gamma \equiv \frac{\pi}{2} n_{\rm i} u^2 \frac{m^*}{2\pi\hbar^2} = \frac{\pi}{2} W\gamma_1 \tag{6.88}$$

where u^2 is the square average of the scattering amplitude, $n_{\rm i}$ is the concentration of scatterers per unit area, and W is the parameter defined for monolayer graphene in (6.55). The term including ε_{trig} arises from the vertex correction due to the trigonal warping. At high energies $|\varepsilon| \gg \Gamma$, σ_{xx} approximates

$$\sigma_{xx}(\varepsilon) \approx g_v g_s \frac{e^2}{\pi^2\hbar}\frac{\pi}{4}\frac{|\varepsilon|}{\Gamma}, \tag{6.89}$$

which increases linearly with energy. The value $\sigma_{xx}(0)$ at zero energy is non-zero and becomes

$$\sigma_{xx}(0) = g_v g_s \frac{e^2}{\pi^2\hbar}\left(1+\frac{2\pi\varepsilon_{trig}}{\Gamma}\right). \tag{6.90}$$

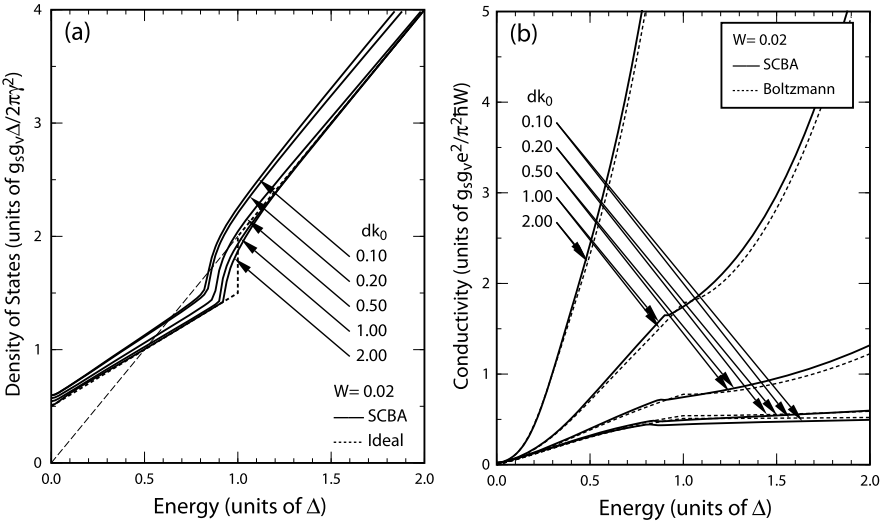

Fig. 6.12 (**a**) Calculated density of states and (**b**) electrical conductivity as a function of energy for scatterers with Gaussian potential with a range d and a dimensionless scattering strength $W = 0.02$. The *dotted line* in (**a**) represents the density of states of an ideal bilayer graphene and the thin dashed line represents twice that of monolayer graphene. The *dotted lines* in (**b**) show the Boltzmann conductivity [112]

In the strong disorder regime $\Gamma \gg 2\pi\varepsilon_{trig}$, the correction term in (6.90) arising from the trigonal warping vanishes and the conductivity approaches the universal value $g_v g_s e^2/(\pi^2\hbar)$ [27, 34, 109], which is twice as large as that in monolayer graphene in the same approximation. In transport measurements of suspended bilayer graphene [111], the minimum conductivity was estimated to be about 10^{-4} S, which is close to $g_v g_s e^2/(\pi^2\hbar)$.

The calculation was recently extended to include long-range scatterers [112]. Figure 6.12 shows the calculated (a) density of states and (b) conductivity as a function of energy for scatterers with a Gaussian potential with range d and for scattering strength $W = 0.1$. In Fig. 6.12(a) the dotted line represents the ideal density of states and the dashed line represents twice that in monolayer graphene and in (b) the dotted lines represent the Boltzmann electrical conductivity. The conductivity exhibits a kink-like structure when the energy crosses the bottom of the excited conduction band. Apart from the difference in the kink position, the overall behavior of the conductivity is very close to that of the Boltzmann result. It is also shown that the conductivity at zero energy is not universal but depends on the degree of the disorder for scatterers with long-range potential, similar to the result discussed above for monolayer graphene [75].

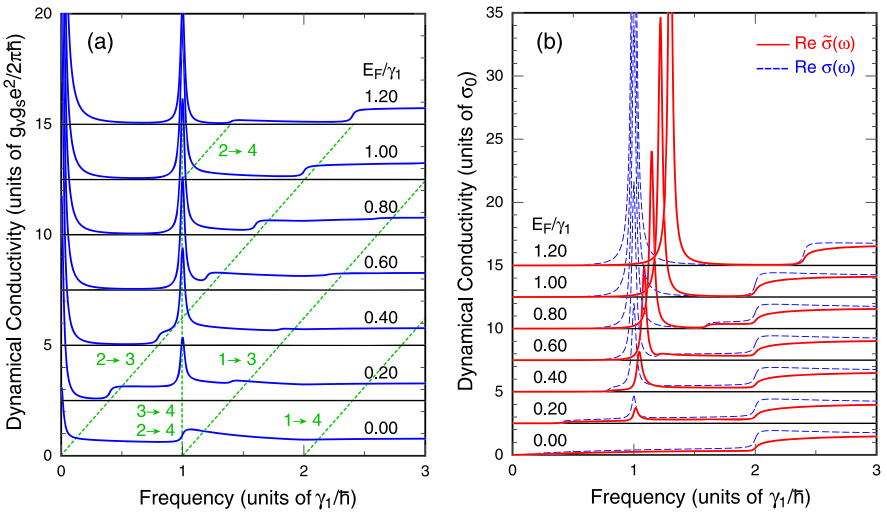

Fig. 6.13 Calculated dynamical conductivity for (**a**) parallel polarization (σ_{xx}) and (**b**) that for perpendicular polarization (σ_{zz}) in a symmetric bilayer graphene. The *dotted lines* in (**a**) denote the absorption edges of the interband transitions ($j \to j'$ means those from band j to band j'). The *dashed lines* in (**b**) represent $\sigma_{zz}(\omega)$ without a depolarization effect and the solid lines represent $\tilde{\sigma}_{zz}(\omega)$ with a depolarization effect [104]

6.6.6 Optical Properties

In bilayer graphene, optical absorption is possible in two different configurations, for light incident parallel and perpendicular to the layers. The optical absorption for perpendicularly incident light is described by the dynamical conductivity in a electric field parallel to the layers. For symmetric bilayer graphene, this is explicitly estimated as [113, 114]

$$\begin{aligned}\mathrm{Re}\,\sigma_{xx}(\omega) = \frac{g_v g_s}{16}\frac{e^2}{\hbar}\Bigg\{ & \frac{\hbar\omega+2\gamma_1}{\hbar\omega+\gamma_1}\theta\big(\hbar\omega-2|\varepsilon_F|\big) \\ & + \left(\frac{\gamma_1}{\hbar\omega}\right)^2\big[\theta(\hbar\omega-\gamma_1)+\theta\big(\hbar\omega-\gamma_1-2|\varepsilon_F|\big)\big] \\ & + \frac{\hbar\omega-2\gamma_1}{\hbar\omega-\gamma_1}\theta(\hbar\omega-2\gamma_1) \\ & + \gamma_1\log\left[\frac{2|\varepsilon_F|+\gamma_1}{\gamma_1}\right]\delta(\hbar\omega-\gamma_1)\Bigg\},\end{aligned} \tag{6.91}$$

where we assumed $|\varepsilon_F| < \gamma_1$. The first term represents the absorption from the band 2 to 3, the second term from 2 to 4, and from 1 to 3, the third term from 1 to 4, and the fourth term from 3 to 4, or from 1 to 2. Figure 6.13(a) shows some examples of the calculated dynamical conductivity $\mathrm{Re}\,\sigma_{xx}(\omega)$ with several values of the Fermi

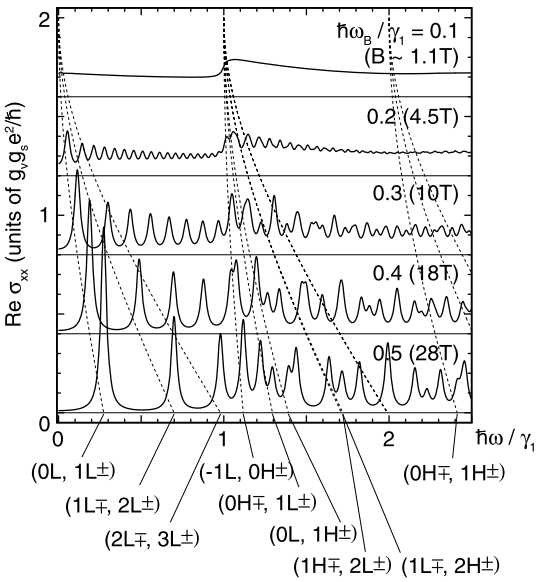

Fig. 6.14 Interband part of the dynamical conductivity σ_{xx} for bilayer graphene with Bernal stacking plotted against the frequency ω, calculated for different magnetic fields. *Dashed curves* indicate the transition energies between several Landau levels in the ideal limit [35]

energy [104]. The curve for $\varepsilon_F = 0$ has essentially no prominent structure except a step-like increase corresponding to transitions from 2 to 4. With increase in ε_F, a delta-function peak appears at $\hbar\omega = \gamma_1$, corresponding to allowed transitions 3 to 4.

In a magnetic field, the optical excitation by perpendicular incident light is only allowed between the Landau levels with n and $n \pm 1$ for arbitrary combinations of $\mu = H, L$ and $s = \pm$, since the matrix element of the velocity operator v_x vanishes otherwise. Figure 6.14 shows some plots of $\mathrm{Re}\,\sigma_{xx}(\omega)$ in magnetic fields at $\varepsilon_F = 0$ and zero temperature. Dotted lines penetrating panels represent the transition energies between several specific Landau levels as a continuous function of $\hbar\omega_B$. The every peak position behaves as a linear function of $B \propto \hbar\omega_B^2$ in weak fields but it switches over to $\sqrt{B}$-dependence as the corresponding energy is going out of the parabolic band region. In small magnetic fields, the peak structure is smeared out into the zero-field curve more easily in the bilayer than in the monolayer, because the Landau level spacing is narrower in bilayer due to the finite band mass.

For a perpendicular electric field (i.e., parallel incident light), the effective conductivity is calculated as follows [104]. We apply an external electric field $E_{ext}(\omega)e^{-i\omega t} + \text{c.c.}$ perpendicular to the layer. By including the screening effect by the depolarization of the graphene electrons, the total electric field becomes $E_{tot}(\omega)e^{-i\omega t} + \text{c.c.}$ where

$$E_{tot}(\omega) = \frac{E_{ext}(\omega)}{\varepsilon(\omega)},$$
$$\varepsilon(\omega) = 1 + \frac{4\pi i}{\omega\kappa d_0}\sigma_{zz}(\omega). \tag{6.92}$$

Here κ is the dielectric constant and d_0 is the interlayer spacing. σ_{zz} is the dynamical conductivity for a perpendicular electric field, which is calculated in a linear response theory as

$$\sigma_{zz}(\omega) = i\omega e^2 d_0^2 \frac{g_v g_s}{4} \frac{1}{L^2} \sum_{\alpha,\beta} \frac{[f(\varepsilon_\alpha) - f(\varepsilon_\beta)]|\hat{\tau}_{\alpha\beta}|^2}{\varepsilon_\alpha - \varepsilon_\beta + \hbar\omega + i\delta},$$

where α and β stand for a set of quantum numbers, δ is a phenomenological broadening energy, and $\hat{\tau}_{\alpha\beta}$ is a matrix with only diagonal terms,

$$\hat{\tau} = \begin{pmatrix} +1 & 0 & 0 & 0 \\ 0 & +1 & 0 & 0 \\ 0 & 0 & -1 & 0 \\ 0 & 0 & 0 & -1 \end{pmatrix}.$$

The power absorption per unit area is given by

$$P = \frac{1}{2} \mathrm{Re}\, \tilde{\sigma}_{zz}(\omega) \left| E_{ext}(\omega) \right|^2.$$

The typical magnitude of σ_{zz} becomes

$$\sigma_{zz}^0 = \frac{e^2}{\hbar} \frac{g_v g_s}{4} \frac{d_0^2}{2\pi\gamma^2} \Delta^2 \sim \frac{e^2}{\pi\hbar} \frac{g_v g_s}{4} \times 0.022,$$

where we have used $a = 2.46$ Å, $d_0 = 3.34$ Å, $\Delta \approx 0.4$ eV, and $\gamma_0 \approx 3$ eV in the last expression.

Figure 6.13(b) shows the calculated dynamical conductivity for perpendicular polarization, with several values of the Fermi energy. The dashed lines represent σ_{zz} without depolarization effect and the solid lines $\tilde{\sigma}_{zz}$ with depolarization effect. For perpendicular polarization, the sharp peak from the band 3 to 4 is shifted to the higher energy side due to the depolarization effect. When the Fermi level reaches the bottom of band 4 ($E_F/\gamma_1 = 1$), this shift is as large as 30 %.

6.7 Multilayer Graphenes

The electronic structure of Bernal graphene multilayers having three or more layers is more complicated, but we can show that the total Hamiltonian can be approximately decomposed into subsystems equivalent to monolayer or bilayer graphenes, regardless of the number of layers [14, 35]. Figure 6.15 illustrates the atomic structure of multilayer graphene arranged in the AB (Bernal) stacking. In N-layer graphene, a unit cell contains A_j and B_j atoms on the layer $j = 1, \ldots, N$. If the

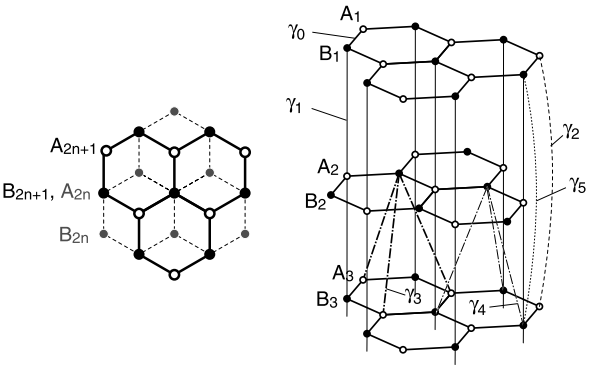

Fig. 6.15 Atomic structure of ABA-stacked multilayer graphene. Top view (*left*) and side view (*right*)

bases are sorted as $|A_1\rangle, |B_1\rangle; |A_2\rangle, |B_2\rangle; \ldots; |A_N\rangle, |B_N\rangle$, the Hamiltonian for multilayer graphene around the K point becomes [14, 26, 29, 30, 32, 33]

$$\mathcal{H} = \begin{pmatrix} H_0 & V & W & & & & \\ V^\dagger & H_0' & V^\dagger & W' & & & \\ W & V & H_0 & V & W & & \\ & W' & V^\dagger & H_0' & V^\dagger & W' & \\ & & \ddots & \ddots & \ddots & \ddots & \ddots \end{pmatrix}, \tag{6.93}$$

with

$$H_0 = \begin{pmatrix} 0 & vp_- \\ vp_+ & \Delta' \end{pmatrix}, \qquad H_0' = \begin{pmatrix} \Delta' & vp_- \\ vp_+ & 0 \end{pmatrix}, \tag{6.94}$$

$$V = \begin{pmatrix} -v_4 p_- & v_3 p_+ \\ \gamma_1 & -v_4 p_- \end{pmatrix}, \qquad W = \begin{pmatrix} \gamma_2/2 & 0 \\ 0 & \gamma_5/2 \end{pmatrix},$$
$$W' = \begin{pmatrix} \gamma_5/2 & 0 \\ 0 & \gamma_2/2 \end{pmatrix}. \tag{6.95}$$

The diagonal blocks H_0 and H_0' describe intralayer coupling, V nearest-neighbor interlayer coupling, and W next-nearest-neighbor interlayer coupling. In W, there are two similar band parameters γ_2 and γ_5, which couple vertically located atoms at distance of $2d$. They are generally different because γ_5 is for the atoms which are involved in the nearest interlayer coupling γ_1, while γ_2 is for those which are not. In graphite, they are estimated as $\gamma_2 = -0.02$ eV and $\gamma_5 = 0.04$ eV. Other parameters are already introduced for bilayer graphene. The effective Hamiltonian for K′ is obtained by exchanging p_+ and p_-.

In the following, we will rewrite the above Hamiltonian using a certain basis, and block-diagonalize it into monolayer-like and bilayer-like subcomponents [114, 115]. Let us define the functions:

$$f_m(j) = c_m \sqrt{\frac{2}{N+1}} \left[1 - (-1)^j\right] \sin \kappa_m j \tag{6.96}$$

$$g_m(j) = c_m \sqrt{\frac{2}{N+1}} \left[1 + (-1)^j\right] \sin \kappa_m j, \tag{6.97}$$

where

$$\kappa_m = \frac{\pi}{2} - \frac{m\pi}{2(N+1)}, \tag{6.98}$$

$$c_m = \begin{cases} 1/2 & (m = 0) \\ 1/\sqrt{2} & (m \neq 0). \end{cases} \tag{6.99}$$

Here $j = 1, 2, \ldots, N$ is the layer index, and m is the block index which ranges as

$$m = \begin{cases} 1, 3, 5, \ldots, N-1, & N = \text{even}, \\ 0, 2, 4, \ldots, N-1, & N = \text{odd}. \end{cases} \tag{6.100}$$

Obviously $f_m(j)$ is zero on even j layers, while $g_m(j)$ is zero on odd j layers. We construct the basis by assigning $f_m(j)$, $g_m(j)$ to each site as

$$\left|\phi_m^{(X,\text{odd})}\right\rangle = \sum_{j=1}^{N} f_m(j) |X_j\rangle, \qquad \left|\phi_m^{(X,\text{even})}\right\rangle = \sum_{j=1}^{N} g_m(j) |X_j\rangle, \tag{6.101}$$

where $X = A$ or B. A superscript such as (A, odd) indicates that the wave function has a non-zero amplitude only on $|A_j\rangle$ sites with odd j's.

We group the bases as $\mathbf{u}_m = \{|\phi_m^{(A,\text{odd})}\rangle, |\phi_m^{(B,\text{odd})}\rangle, |\phi_m^{(A,\text{even})}\rangle, |\phi_m^{(B,\text{even})}\rangle\}$. The Hamiltonian matrix between $\mathbf{u}_m$ and $\mathbf{u}_{m'}$ becomes

$$\mathcal{H}_{m'm} \equiv \mathbf{u}_{m'}^{\dagger} \mathcal{H} \mathbf{u}_m = \mathcal{U}(\lambda_m)\delta_{m'm} + \mathcal{W}(\alpha_{m'm}, \beta_{m'm}), \tag{6.102}$$

with

$$\mathcal{U}(\lambda) = \begin{pmatrix} 0 & vp_- & -\lambda v_4 p_- & \lambda v_3 p_+ \\ vp_+ & \Delta' & \lambda\gamma_1 & -\lambda v_4 p_- \\ -\lambda v_4 p_+ & \lambda\gamma_1 & \Delta' & vp_- \\ \lambda v_3 p_- & -\lambda v_4 p_+ & vp_+ & 0 \end{pmatrix}, \tag{6.103}$$

$$\mathcal{W}(\alpha, \beta) = \begin{pmatrix} \alpha\gamma_2 & 0 & 0 & 0 \\ 0 & \alpha\gamma_5 & 0 & 0 \\ 0 & 0 & \beta\gamma_5 & 0 \\ 0 & 0 & 0 & \beta\gamma_2 \end{pmatrix}, \tag{6.104}$$

where

$$\lambda_m = 2\cos\kappa_m, \tag{6.105}$$

$$\alpha_{m'm} = 2c_m c_{m'} \Big\{ \delta_{mm'}(1 + \delta_{m0}) \cos 2\kappa_m$$

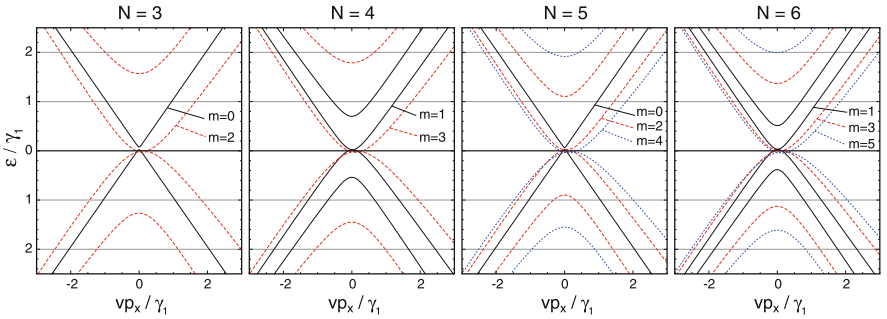

Fig. 6.16 Band structure of the multilayer graphene from $N = 3$ to 6. The energy bands belonging to different blocks labeled by m are shown in different styles

$$+\frac{\sin\kappa_m \sin\kappa_{m'}}{N+1}\left[2+(-1)^{\frac{m-m'}{2}}\left(1-(-1)^N\right)\right]\Bigg\}, \tag{6.106}$$

$$\beta_{m'm} = 2c_m c_{m'}\left\{\delta_{mm'}(1-\delta_{m0})\cos 2\kappa_m + \frac{\sin\kappa_m \sin\kappa_{m'}}{N+1}(-1)^{\frac{m-m'}{2}}\left(1+(-1)^N\right)\right\}.$$

$\mathcal{U}(\lambda_m)$, appearing in diagonal blocks $\mathcal{H}_{mm}$, is equivalent to the Hamiltonian of bilayer graphene with nearest-layer coupling parameters multiplied by λ_m. $\mathcal{W}$ in $\mathcal{H}_{mm}$ adds an on-site asymmetric potential to this effective bilayer system. For a pair of low-energy bands near zero energy, $\mathcal{W}$ effectively causes an overall energy shift of $(\alpha+\beta)\gamma_2/2$, and an energy gap of $\sim|(\alpha-\beta)\gamma_2|$ at the band touching point, as in asymmetric bilayer graphene.

The case of $m = 0$ is special in that $g_m(j)$ is identically zero, so that only two basis states $\{|\phi_0^{(A,\mathrm{odd})}\rangle, |\phi_0^{(B,\mathrm{odd})}\rangle\}$ survive in (6.101). The matrix for the $m = 0$ block for the two remaining bases is

$$\mathcal{H}_0 = \begin{pmatrix} 0 & vp_- \\ vp_+ & \Delta' \end{pmatrix} - \frac{N-1}{N+1}\begin{pmatrix} \gamma_2 & 0 \\ 0 & \gamma_5 \end{pmatrix}, \tag{6.107}$$

which, barring the diagonal terms, is equivalent to the Hamiltonian of monolayer graphene. Odd-layered graphene with $N = 2M+1$ is decomposed into one monolayer-type and M bilayer-type subsystems, while even-layered graphene with $N = 2M$ is decomposed into M bilayers but having no monolayer.

The subsystems with different m's are not exactly independent since they are mixed by off-diagonal matrix elements $\mathcal{H}_{mm'}(m \neq m')$, which contain only the next-nearest interlayer couplings, γ_2 and γ_5. The off-diagonal blocks are responsible for small band repulsion at crossing points between different m's, while the overall band structure is well described by only retaining the diagonal blocks [114]. Figure 6.16 plots the band structures from $N = 3$ to 6 with off-diagonal blocks neglected, showing the basic idea of how the decomposition works.

Figures 6.17(a) and (c) are the low-energy band structures of $N = 3$ and 4, respectively. In $N = 3$, the spectrum is composed of a monolayer-like band ($m = 0$,

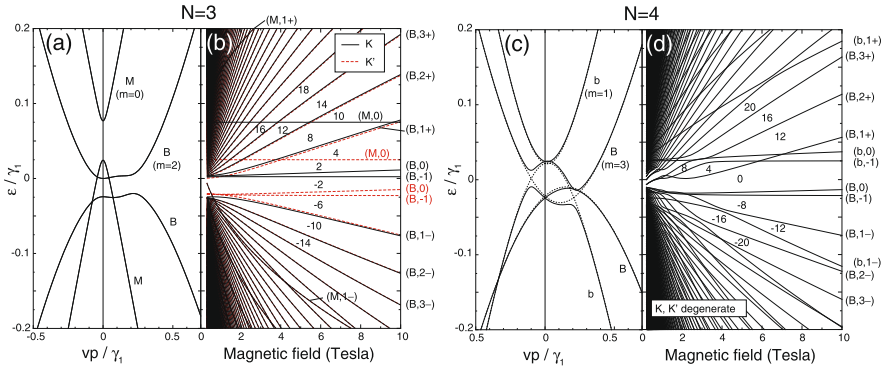

Fig. 6.17 (**a**) Low-energy band structure and (**b**) Landau levels as a function of magnetic field in ABA-trilayer graphene. (**c**), (**d**): Similar plots for ABA-fourlayer graphene. In (**b**) and (**d**), numbers represent the quantized Hall conductivity in units of $-e^2/h$ [38]

or M) and a bilayer-like band ($m = 2$, or B), while in $N = 4$ the spectrum includes the light-mass bilayer ($m = 1$, or b) and the heavy-mass bilayer band ($m = 3$, or B). In $N = 4$, the solid and dashed curves represent the band energies calculated with and without the off-diagonal matrix, where we actually see small anticrossing at the intersections (not shown in Fig. 6.16). In $N = 3$, there is no mixing between different blocks since the off-diagonal matrix vanishes due to a difference in the symmetry [114, 116]. For each subband, we see a relative shift of the band center as well as the energy gap at Dirac points, due to the diagonal potential containing terms such as γ_2, γ_5 and Δ', as argued above [114]. In the bulk limit $N \to \infty$, the quantity κ_m corresponds to the three-dimensional (3D) wave vector k_z, where the monolayer-type block $\kappa = \pi/2$ is related to the H-point in the 3D Brillouin zone, and $\kappa = 0$ is related to the K-point. The energy shift of the bilayer-like subband, $(\alpha + \beta)\gamma_2/2$, approximates $\gamma_2 \cos 2\kappa_m$ in the large N limit, and this is consistent with the semi-metallic property of graphite with the hole-doping near H-point and the electron-doping near K-point [100].

The Landau level spectrum is computed by replacing $p_\pm$ with $\pi_\pm$ in the Hamiltonian. Figures 6.17(b) and (d) show the energy levels for $N = 3$ and 4, respectively, as function of magnetic field [115]. In odd layered graphene of $N \geq 3$, generally, the Landau level splitting occurs because the spatial inversion symmetry is originally missing in the lattice structure. On the other hand, the monolayer and all even-layered graphenes are intrinsically spacial inversion symmetric, and that ensures the valley degeneracy of the Landau levels [38]. In the plot of Fig. 6.17(a), we actually observe the valley splitting in $N = 3$, while all the levels are completely valley-degenerate in $N = 4$ (Fig. 6.17(b)).

Using the decomposition of the Hamiltonian, the response function of the N-layered graphene can be written as a summation over each sub-Hamiltonian, as long as the external field is uniform in the z direction and does not mix different m's. For example, this decomposition can be used for the analysis of diamagnetic response of multi-layer graphenes [14]. In fact, in odd-layered graphenes, the monolayer-like

band gives a strong diamagnetic peak at $\varepsilon_F = 0$, while the bilayer-like bands present a broad logarithmic peak. With the increase of the layer number, the susceptibility is dominated by that of the bilayer-like bands. Thus, the large diamagnetic susceptibility of bulk graphite can be understood in terms of the logarithmic singularity of bilayer graphene. The optical absorption was also studied in this scheme [35], where each peak in the complicated absorption spectrum is identified as a particular excitation between Landau levels within the monolayer-like or bilayer-like subbands.

It should be noted that in graphene multilayer, there is another configuration called rhombohedral ($ABCABC\ldots$) stacking [117–119] which is distinct from Bernal ($ABAB\ldots$) stacking discussed above. A sequence such as $ABC\ldots$ represents the lattice point on every layer along a perpendicular axis, where A and B are inequivalent sublattices of hexagonal lattice, and C is the center of the hexagon. The Bernal phase is thermodynamically stable and common while it is known that some portion of natural graphite takes the rhombohedral form. A rhombohedral-stacked multilayer has a totally different spectrum from that of the Bernal case, including a pair of flat low-energy bands which disperse as p^N with momentum p and the number of layers N [26, 120–126]. More generally, graphitic structures are expected to take a Bernal-rhombohedral mixed form, and the electronic structure of such mixed multilayers was also studied theoretically [124, 127, 128]. The characteristic properties of multilayer graphene depending on the stacking structure were actually observed in several experiments [129–137].

6.8 Summary

We have theoretically studied the electronic properties of graphene and its multilayers. The motion of electrons in monolayer graphene is characterized by the massless Dirac spectrum, which gives rise to several unusual properties distinct from those of the conventional system. For multilayer graphenes, we considered particularly AB (Bernal) stacking structure which is most likely to appear. The low-energy band structure of bilayer graphene contains a conduction band and a valence band touching each other, but the dispersion is quadratic. The energy band of more than three layer graphene is decomposed into separate subbands which are effectively equivalent to either monolayer or bilayer graphene.

Using the low-energy effective Hamiltonian, we studied the electric transport properties, the optical absorption and the orbital magnetism. For the electric transport, we employed the self-consistent Born approximation to properly treat the finite level broadening. We found that, in both of monolayer and bilayer graphenes, the conductivity at the Dirac point becomes a finite value of the order of e^2/h in any disorder strength while the factor depends on the detail of the scattering potential. We also presented the Landau level spectrum in magnetic fields, and discussed the quantized Hall conductivity in details.

The optical absorption for perpendicular incident light in monolayer graphene is nearly constant except for the Drude peak at zero frequency, and this describes

nearly universal absorption ratio about 2.3 % observed in experiments. In bilayer graphene, the optical spectrum is characterized by absorption edges, which reflect the characteristics of the band structure. For bilayer graphene, we also considered the optical absorption for parallel incident light, which is described by σ_{zz}.

The orbital diamagnetism is generally strong in graphene related materials. In monolayer graphene, in particular, the magnetic susceptibility diverges at Dirac point, and this can be understood from the zero gap limit of gapped graphene in terms of valley pseudospin magnetic moment. The diamagnetic singularity at the Dirac point is relaxed by an asymmetry potential opening an energy gap, and also by interlayer coupling in a multilayer stack.

References

1. K.S. Novoselov, A.K. Geim, S.V. Morozov, D. Jiang, M.I. Katsnelson, I.V. Grigorieva, S.V. Dubonos, A.A. Firsov, Nature **438**, 197 (2005)
2. Y. Zhang, Y.-W. Tan, H.L. Stormer, P. Kim, Nature **438**, 201 (2005)
3. P.R. Wallace, Phys. Rev. **71**, 622 (1947)
4. J.W. McClure, Phys. Rev. **104**, 666 (1956)
5. J.C. Slonczewski, P.R. Weiss, Phys. Rev. **109**, 272 (1958)
6. T. Ando, J. Phys. Soc. Jpn. **74**, 777 (2005)
7. D.P. DiVincenzo, E.J. Mele, Phys. Rev. B **29**, 1685 (1984)
8. G.W. Semenoff, Phys. Rev. Lett. **53**, 2449 (1984)
9. N.H. Shon, T. Ando, J. Phys. Soc. Jpn. **67**, 2421 (1998)
10. T. Ando, Y. Zheng, H. Suzuura, J. Phys. Soc. Jpn. **71**, 1318 (2002)
11. H. Suzuura, T. Ando, Phys. Rev. Lett. **89**, 266603 (2002)
12. E. McCann, K. Kechedzhi, V.I. Falko, H. Suzuura, T. Ando, B.L. Altshuler, Phys. Rev. Lett. **97**, 146805 (2006)
13. M. Koshino, T. Ando, Phys. Rev. B **75**, 235333 (2007)
14. M. Koshino, T. Ando, Phys. Rev. B **76**, 085425 (2007)
15. H. Fukuyama, J. Phys. Soc. Jpn. **76**, 043711 (2007)
16. M. Nakamura, Phys. Rev. B **76**, 113301 (2007)
17. A. Ghosal, P. Goswami, S. Chakravarty, Phys. Rev. B **75**, 115123 (2007)
18. Y. Zheng, T. Ando, Phys. Rev. B **65**, 245420 (2002)
19. V.P. Gusynin, S.G. Sharapov, Phys. Rev. Lett. **95**, 146801 (2005)
20. N.M.R. Peres, F. Guinea, A.H. Castro Neto, Phys. Rev. B **73**, 125411 (2006)
21. T. Ohta, A. Bostwick, T. Seyller, K. Horn, E. Rotenberg, Science **313**, 951 (2006)
22. K.S. Novoselov, E. McCann, S.V. Morozov, V.I. Falko, M.I. Katsnelson, U. Zeitler, D. Jiang, F. Schedin, A.K. Geim, Nat. Phys. **2**, 177 (2006)
23. T. Ohta, A. Bostwick, J.L. McChesney, T. Seyller, K. Horn, E. Rotenberg, Phys. Rev. Lett. **98**, 206802 (2007)
24. E.V. Castro, K.S. Novoselov, S.V. Morozov, N.M.R. Peres, J.M.B. Lopes dos Santos, J. Nilsson, F. Guinea, A.K. Geim, A.H. Castro Neto, Phys. Rev. Lett. **99**, 216802 (2007)
25. E. McCann, V.I. Falko, Phys. Rev. Lett. **96**, 086805 (2006)
26. F. Guinea, A.H. Castro Neto, N.M.R. Peres, Phys. Rev. B **73**, 245426 (2006)
27. M. Koshino, T. Ando, Phys. Rev. B **73**, 245403 (2006)
28. E. McCann, M. Koshino, Rep. Prog. Phys. **76**, 056503 (2013)
29. C.L. Lu, C.P. Chang, Y.C. Huang, J.M. Lu, C.C. Hwang, M.F. Lin, J. Phys. Condens. Matter **18**, 5849 (2006)
30. C.L. Lu, C.P. Chang, Y.C. Huang, R.B. Chen, M.L. Lin, Phys. Rev. B **73**, 144427 (2006)

31. J. Nilsson, A.H. Castro Neto, N.M.R. Peres, F. Guinea, Phys. Rev. B **73**, 214418 (2006)
32. B. Partoens, F.M. Peeters, Phys. Rev. B **74**, 075404 (2006)
33. B. Partoens, F.M. Peeters, Phys. Rev. B **75**, 193402 (2007)
34. M. Koshino, T. Ando, AIP Conf. Proc. **893**, 621 (2007)
35. M. Koshino, T. Ando, Phys. Rev. B **77**, 115313 (2008)
36. S.Y. Zhou, G.-H. Gweon, A.V. Fedorov, P.N. First, W.A. de Heer, D.-H. Lee, F. Guinea, A.H. Castro Neto, A. Lanzara, Nat. Mater. **6**, 770 (2007)
37. S.Y. Zhou, D.A. Siegel, A.V. Fedorov, F.E. Gabaly, A.K. Schmid, A.H. Castro Neto, D.-H. Lee, A. Lanzara, Nat. Mater. **7**, 259 (2008)
38. M. Koshino, E. McCann, Phys. Rev. B **81**, 115315 (2010)
39. M. Koshino, T. Ando, Phys. Rev. B **81**, 195431 (2010)
40. J.W. McClure, Phys. Rev. **119**, 606 (1960)
41. M.P. Sharma, L.G. Johnson, J.W. McClure, Phys. Rev. B **9**, 2467 (1974)
42. P.A. Wolff, J. Phys. Chem. Solids **25**, 1057 (1964)
43. H. Fukuyama, R. Kubo, J. Phys. Soc. Jpn. **27**, 604 (1969)
44. H. Fukuyama, R. Kubo, J. Phys. Soc. Jpn. **28**, 570 (1970)
45. S.A. Safran, F.J. DiSalvo, Phys. Rev. B **20**, 4889 (1979)
46. S.A. Safran, Phys. Rev. **30**, 421 (1984)
47. J. Blinowski, C. Rigaux, J. Phys. (Paris) **45**, 545 (1984)
48. R. Saito, H. Kamimura, Phys. Rev. B **33**, 7218 (1986)
49. H. Ajiki, T. Ando, J. Phys. Soc. Jpn. **62**, 1255 (1993)
50. H. Ajiki, T. Ando, J. Phys. Soc. Jpn. **62**, 2470 (1993)
51. H. Ajiki, T. Ando, J. Phys. Soc. Jpn. **63**, 4267 (1994) (Erratum)
52. H. Ajiki, T. Ando, J. Phys. Soc. Jpn. **64**, 4382 (1995)
53. M. Yamamoto, M. Koshino, T. Ando, J. Phys. Soc. Jpn. **77**, 084705 (2008)
54. M. Nakamura, L. Hirasawa, Phys. Rev. B **77**, 045429 (2008)
55. A.H. Castro Neto, F. Guinea, N.M. Peres, K.S. Novoselov, A.K. Geim, Rev. Mod. Phys. **81**, 109 (2009)
56. A. Kobayashi, Y. Suzumura, H. Fukuyama, J. Phys. Soc. Jpn. **77**, 064718 (2008)
57. M. Koshino, Y. Arimura, T. Ando, Phys. Rev. Lett. **102**, 177203 (2009)
58. M. Koshino, Phys. Rev. B **84**, 125427 (2011)
59. M.-C. Chang, Q. Niu, Phys. Rev. B **53**, 7010 (1996)
60. D. Xiao, W. Yao, Q. Niu, Phys. Rev. Lett. **99**, 236809 (2007)
61. A. De Martino, L. DellAnna, R. Egger, Phys. Rev. Lett. **98**, 066802 (2007)
62. M.R. Masir, P. Vasilopoulos, A. Matulis, F.M. Peeters, Phys. Rev. B **77**, 235443 (2008)
63. C.-H. Park, L. Yang, Y.-W. Son, M.L. Cohen, S.G. Louie, Phys. Rev. Lett. **101**, 126804 (2008)
64. C.-H. Park, Y.-W. Son, L. Yang, M.L. Cohen, S.G. Louie, Nano Lett. **8**, 2920 (2008)
65. Y.-X. Li, J. Phys. Condens. Matter **22**, 015302 (2010)
66. J.S. Park, K. Sasaki, R. Saito, W. Izumida, M. Kalbac, H. Farhat, G. Dresselhaus, M.S. Dresselhaus, Phys. Rev. B **80**, 081402 (2009)
67. I. Snyman, Phys. Rev. B **80**, 054303 (2009)
68. T. Ando, J. Phys. Soc. Jpn. **75**, 074716 (2006)
69. T. Ando, T. Nakanishi, J. Phys. Soc. Jpn. **67**, 1704 (1998)
70. T. Ando, T. Nakanishi, R. Saito, J. Phys. Soc. Jpn. **67**, 2857 (1998)
71. K. Nomura, A.H. MacDonald, Phys. Rev. Lett. **96**, 256602 (2006)
72. T. Ando, J. Phys. Soc. Jpn. **38**, 989 (1975)
73. T. Ando, Y. Uemura, J. Phys. Soc. Jpn. **36**, 959 (1974)
74. T. Fukuzawa, M. Koshino, T. Ando, J. Phys. Soc. Jpn. **78**, 094714 (2009)
75. M. Noro, M. Koshino, T. Ando, J. Phys. Soc. Jpn. **79**, 094713 (2010)
76. A.K. Geim, K.S. Novoselov, Nat. Mater. **6**, 183 (2007)
77. Y.-W. Tan, Y. Zhang, H.L. Stormer, P. Kim, Eur. Phys. J. Spec. Top. **148**, 15 (2007)
78. K.I. Bolotin, K.J. Sikes, Z. Jiang, G. Fundenberg, J. Hone, P. Kim, H.L. Stormer, Solid State Commun. **146**, 351 (2008)

79. H. Kumazaki, D.S. Hirashima, J. Phys. Soc. Jpn. **75**, 053707 (2006)
80. I.L. Aleiner, K.B. Efetov, Phys. Rev. Lett. **97**, 236801 (2006)
81. K. Ziegler, Phys. Rev. Lett. **97**, 266802 (2006)
82. K. Nomura, A.H. MacDonald, Phys. Rev. Lett. **98**, 076602 (2007)
83. J.H. Bardarson, J. Tworzydo, P.W. Brouwer, C.W.J. Beenakker, Phys. Rev. Lett. **99**, 106801 (2007)
84. S. Adam, E.H. Hwang, V.M. Galitski, S. Das Sarma, Proc. Natl. Acad. Sci. USA **104**, 18392 (2007)
85. K. Ziegler, Phys. Rev. B **78**, 125401 (2008)
86. S. Adam, E.H. Hwang, E. Rossi, S. Das Sarma, Solid State Commun. **149**, 1072 (2009)
87. R.R. Nair, P. Blake, A.N. Grigorenko, K.S. Novoselov, T.J. Booth, T. Stauber, N.M.R. Peres, A.K. Geim, Science **320**, 1308 (2008)
88. Z.Q. Li, E.A. Henriksen, Z. Jiang, Z. Hao, M.C. Martin, P. Kim, H.L. Stormer, D.N. Basov, Nat. Phys. **4**, 532 (2008)
89. K.F. Mak, M.Y. Sfeir, Y. Wu, C.H. Lui, J.A. Misewich, T.F. Heinz, Phys. Rev. Lett. **101**, 196405 (2008)
90. J.-K. Lee, S.-C. Lee, J.-P. Ahn, S.-C. Kim, J.I.B. Wilson, P. John, J. Chem. Phys. **129**, 234709 (2008)
91. Z. Liu, K. Suenaga, P.J.F. Harris, S. Iijima, Phys. Rev. Lett. **102**, 015501 (2009)
92. J.H. Ho, C.L. Lu, C.C. Hwang, C.P. Chang, M.F. Lin, Phys. Rev. B **74**, 085406 (2006)
93. J. Hass, R. Feng, J.E. Millan-Otoya, X. Li, M. Sprinkle, P.N. First, W.A. de Heer, E.H. Conrad, C. Berger, Phys. Rev. B **75**, 214109 (2007)
94. J. Hass, F. Varchon, J.E. Millán-Otoya, M. Sprinkle, N. Sharma, W.A. de Heer, C. Berger, P.N. First, L. Magaud, E.H. Conrad, Phys. Rev. Lett. **100**, 125504 (2008)
95. G. Li, A. Luican, J. Dos Santos, A. Neto, A. Reina, J. Kong, E. Andrei, Nat. Phys. **6**, 109 (2009)
96. J.M.B. Lopes dos Santos, N.M.R. Peres, A.H. Castro Neto, Phys. Rev. Lett. **99**, 256802 (2007)
97. S. Shallcross, S. Sharma, O.A. Pankratov, Phys. Rev. Lett. **101**, 056803 (2008)
98. P. Moon, M. Koshino, Phys. Rev. B **85**, 195458 (2012)
99. P. Moon, M. Koshino, Phys. Rev. B **87**, 205404 (2013)
100. M.S. Dresselhaus, G. Dresselhaus, Adv. Phys. **51**, 1 (2002)
101. L.M. Malard, M.A. Pimentada, G. Dresselhaus, M.S. Dresselhaus, Phys. Rep. **473**, 51 (2009)
102. E. McCann, Phys. Rev. B **74**, 161403 (2006)
103. T. Ando, M. Koshino, J. Phys. Soc. Jpn. **78**, 034709 (2009)
104. T. Ando, M. Koshino, J. Phys. Soc. Jpn. **78**, 104716 (2009)
105. J.B. Oostinga, H.B. Heersche, X.-L. Liu, A.F. Morpurgo, L.M.K. Vandersypen, Nat. Mater. **7**, 151 (2008)
106. Y.-B. Zhang, T.-T. Tang, C. Girit, Z. Hao, M.C. Martin, A. Zettl, M.F. Crommie, Y.R. Shen, F. Wang, Nature **459**, 820 (2009)
107. K.F. Mak, C.H. Lui, J. Shan, T.F. Heinz, Phys. Rev. Lett. **102**, 256405 (2009)
108. A.B. Kuzmenko, E. van Heumen, D. van der Marel, P. Lerch, P. Blake, K.S. Novoselov, A.K. Geim, Phys. Rev. B **79**, 115441 (2009)
109. J. Cserti, Phys. Rev. B **75**, 033405 (2007)
110. J. Cserti, A. Csordas, G. David, Phys. Rev. Lett. **99**, 066802 (2007)
111. B.E. Feldman, J. Martin, A. Yacoby, Nat. Phys. **5**, 889 (2009)
112. T. Ando, J. Phys. Soc. Jpn. **80**, 014707 (2011)
113. D.S.L. Abergel, V.I. Falko, Phys. Rev. B **75**, 155430 (2007)
114. M. Koshino, T. Ando, Solid State Commun. **149**, 1123 (2009)
115. M. Koshino, E. McCann, Phys. Rev. B **83**, 165443 (2011)
116. M. Koshino, E. McCann, Phys. Rev. B **79**, 125443 (2009)
117. H. Lipson, A.R. Stokes, Proc. R. Soc. Lond. A **181**, 101 (1942)
118. R.R. Haering, Can. J. Phys. **36**, 352 (1958)
119. J.W. McClure, Carbon **7**, 425 (1969)

120. S. Latil, L. Henrard, Phys. Rev. Lett. **97**, 036803 (2006)
121. M. Aoki, H. Amawashi, Solid State Commun. **142**, 123 (2007)
122. C.L. Lu, C.P. Chang, Y.C. Huang, J.H. Ho, C.C. Hwang, M.F. Lin, J. Phys. Soc. Jpn. **76**, 024701 (2007)
123. J.L. Mañes, F. Guinea, M.A.H. Vozmediano, Phys. Rev. B **75**, 155424 (2007)
124. H. Min, A.H. MacDonald, Phys. Rev. B **77**, 155416 (2008)
125. M. Koshino, E. McCann, Phys. Rev. B **80**, 165409 (2009)
126. M. Koshino, Phys. Rev. B **81**, 125304 (2010)
127. D.P. Arovas, F. Guinea, Phys. Rev. B **78**, 245416 (2008)
128. M. Koshino, E. McCann, Phys. Rev. B **87**, 045420 (2013)
129. M.F. Craciun, S. Russo, M. Yamamoto, J.B. Oostinga, A.F. Morpurgo, S. Tarucha, Nat. Nanotechnol. **4**, 383 (2009)
130. C.H. Lui, Z. Li, Z. Chen, P.V. Klimov, L.E. Brus, T.F. Heinz, Nano Lett. **11**, 164 (2011)
131. A. Kumar, W. Escoffier, J.M. Poumirol, C. Faugeras, D.P. Arovas, M.M. Fogler, F. Guinea, S. Roche, M. Goiran, B. Raquet, Phys. Rev. Lett. **107**, 126806 (2011)
132. W. Bao, L. Jing, J. Velasco Jr., Y. Lee, G. Liu, D. Tran, B. Standley, M. Aykol, S.B. Cronin, D. Smirnov, M. Koshino, E. McCann, M. Bockrath, C.N. Lau, Nat. Phys. **7**, 948 (2011)
133. L. Zhang, Y. Zhang, J. Camacho, M. Khodas, I. Zaliznyak, Nat. Phys. **7**, 953 (2011)
134. T. Taychatanapat, K. Watanabe, T. Taniguchi, P. Jarillo-Herrero, Nat. Phys. **7**, 621 (2011)
135. T. Khodkov, F. Withers, D.C. Hudson, M.F. Craciun, S. Russo, Appl. Phys. Lett. **100**, 013114 (2012)
136. E.A. Henriksen, D. Nandi, J.P. Eisenstein, Phys. Rev. X **2**, 011004 (2012)
137. J. Ping, M.S. Fuhrer, Nano Lett. **12**, 4635 (2012)

Chapter 7
Graphene: Topological Properties, Chiral Symmetry and Their Manipulation

Yasuhiro Hatsugai and Hideo Aoki

Abstract This chapter looks at graphene from the viewpoint of underlying chiral symmetry and topological properties. This reveals why a seemingly simple honeycomb lattice can harbour such a rich physics, which includes doubled Dirac cones at K and K′ points in the Brillouin zone, anomalously sharp Landau level and quantum Hall effect at the Dirac point in magnetic fields even with ripples, and a host of other peculiar features of graphene. After giving a self-contained description of these notions, we then describe how topological and chiral properties also dictate that there is a close link between bulk and edge states. We also emphasise that the notion of chiral and topological properties are so universal (and robust) that we can also examine various extensions to electron-hole asymmetric cones, tilted cones, cone + flat-band system, bilayer graphene, and many-body graphene. As a novel way of manipulating the system, we also describe a Floquet topological state for graphene in nonequilibrium.

7.1 Chiral Symmetry as a Generic Symmetry in Graphene

In the physics of graphene [1–3], which has been now developed into one of the most active areas in condensed-matter physics, there are several unique features that make graphene stand out. Above all, topological properties and the chiral symmetry in graphene are fundamental in graphene physics. Namely, graphene is not just a zero-gap semiconductor that has "massless Dirac particles" (or Weyl neutrino in the field-theoretic language), but the system is topological, where positions and gap-opening of Dirac cones dominate the physics, and the chiral symmetry is behind various physical properties.

Y. Hatsugai
Institute of Physics, University of Tsukuba, Tsukuba, Ibaraki 305-8571, Japan
e-mail: hatsugai.yasuhiro.ge@u.tsukuba.ac.jp

H. Aoki (✉)
Department of Physics, University of Tokyo, Hongo, Tokyo 113-0033, Japan
e-mail: aoki@phys.s.u-tokyo.ac.jp

H. Aoki, M.S. Dresselhaus (eds.), *Physics of Graphene*, NanoScience and Technology,
DOI 10.1007/978-3-319-02633-6_7,

In other words, a key question about graphene to start with is: what makes the seemingly simple honeycomb lattice accommodate such a rich physics? Topological and chiral properties inherent in graphene are just the reason. Indeed, a most remarkable hallmark of graphene is the quantum Hall effect that is peculiar to graphene [1, 2, 4, 5], as described in the chapter by Kim and coauthors in this volume, and this reflects both these properties. So the purpose of the present chapter is to explore the topological and chiral properties. In doing so we also address the question of why the Dirac cones appear at two places (K and K′ points) in the Brillouin zone, which is in fact related to Nielsen-Ninomiya theorem, a theorem in the field theory [6–9].

Graphene physics all started when Wallace back in 1947 [10] noticed, theoretically, that graphene's band structure contains a pair of massless Dirac dispersion (or "Dirac cones") with a $\mathbf{k}\cdot\mathbf{p}$ method in the effective-mass formalism. The Dirac cone is nowadays observed experimentally with ARPES (angle-resolved photo emission spectroscopy) [11]. Then McClure, as early as in 1956, showed that graphene in magnetic fields has a peculiar Landau's quantisation [12].

Is the appearance of a Dirac cone surprising? If we have a gap closing in a two-dimensional (2D) system, that should be in general accidental, since a degeneracy is required for a three-component quantity (which we shall call $\mathbf{R}$ in later sections) according to, mathematically, the von Neumann-Wigner theorem, while there are only two tunable parameters (two components of the 2D wave number) [13, 14]. By contrast, the emergence of the doubled Dirac cones at the K and K′ points in the first Brillouin zone is dictated by the honeycomb crystal structure (and its group theory) [15]. In a more general framework, however, one may consider the doubled Dirac cones arise due to a symmetry called the chiral symmetry, where the exotic name came from the four-dimensional lattice gauge theory. Many characteristic features of graphene are those of the chiral-symmetric lattice fermions [16–18]. Topology is another main, and chirality-related, ingredient in graphene, as we shall show in the chapter. Namely, the Dirac cones themselves, specifically their robustness, have a topological origin, and are responsible for many of the anomalous properties of graphene. An example is the existence of a Landau level at zero-energy (i.e., right at the Dirac point), is "protected" by the index theorem, which is a topological theorem. Another example is the existence of edge states, which are inherent in topological systems.

Most simply, the chiral symmetry has to do with the honeycomb lattice being a non-Bravais but bipartite lattice, that is, the lattice points are decomposed into two (• and ○) sublattices (Fig. 7.1). The hopping matrix elements in the honeycomb lattice connect neighbouring • − ○ sites. From this comes the chiral symmetry, readily stated in terms of the tight-binding model, but the notion is applicable to wider cases as we shall see. Edge states are ubiquitous in topological systems, since there is a universal theorem stating that edge states have to exist if the bulk is a topological system, but massless Dirac fermions exhibit this in a specific manner [19, 20]. An analogous phenomenon appears in superconductors with d-wave pairing [20]. Also, the physics of graphene is now being extended to cold-atom systems in optical lattices, where the topological and chiral properties are now intensively explored,

where a vast controllability of system parameters in optical lattice systems greatly extends the horizon [21–23].

In this chapter we also discuss whether and how the chiral symmetry is affected in various situations modified from the ideal honeycomb lattice. In real graphene, the chiral symmetry does not rigorously hold. For instance, even within a tight-binding model the electron hopping should comprise not only nearest-neighbour ones but also second-neighbour ones etc, although the chiral-symmetry-breaking parameters are relatively small in magnitude in the standard tight-binding parameters for graphene [24, 25]. There are various other manipulations of Dirac cones. We can for instance discuss the situation when the two Dirac cones are shifted in energy. In some organic metals, we encounter tilted Dirac cones [26]. The question is how the chiral symmetry is modified in these situations. Another essential question is a real system should also have disorders, and will the chiral symmetry be always washed out when we introduce disorder? We shall show, first, we can still extend the definition of the chiral symmetry, where the extended symmetry in fact governs the anomalous properties associated with the Dirac cones [27, 34–36]. We then show that a disorder lets the zero-energy Landau level remain anomalously sharp (delta-function like in fact), as long as the disorder respects the chiral symmetry [27]. Thus the chiral symmetry is quite useful for discussion of the low-energy physics of graphene in various situations, including multi-layer graphene [37]. In this sense, we can say that the chiral symmetry, most typically manifests itself in graphene, is rather an "generic symmetry" applicable to diverse condensed-matter systems, which even encompass cold-atom systems [23].

We further ask ourselves: (i) while usually static properties are studied for the phenomena arising from the Dirac cones, do we have interesting ac responses (i.e., optical properties) for graphene, (ii) while usually properties in equilibrium are examined, do we have novel phenomena when graphene is put *out of equilibrium*. (iii) can the chiral symmetry a useful one for many-body physics. Yes to all the questions, and we shall show, first, ac (optical) Hall conductivity exhibits an interesting plateau structures, second, we can indeed manipulate the topological property by e.g., shining a circularly polarised light to graphene, which will produce a dc Hall current. This is remarkable as a non-equilibrium realization of "anomalous quantum Hall effect", which is defined as a quantum Hall effect in zero magnetic field. Third, we shall briefly describe how the chiral symmetry can be applied to many-body systems. All in all the purpose of the present chapter is to show how graphene harbours general and rich physics.

7.2 Chiral Symmetry, Dirac Cones and Fermion Doubling

7.2.1 Chiral Symmetry for Lattice Systems

Let us start with a tight-binding model of graphene. Mind you: many of the properties of graphene, including the chiral symmetry, are general enough, which are

not restricted to the tight-binding model but come from a honeycomb transnational symmetry. However, a tight-binding description is clear for heuristic purposes. In graphene, the chemical bonds responsible for the honeycomb crystal are formed from carbon orbitals (called σ orbitals) that stretch along the graphene plane, while the conduction band arise from the carbon p_z orbital (called π orbitals), so that we can focus on the single orbital on each site. The honeycomb lattice is not a Bravais lattice, but contains two atoms in a unit cell. If we denote the two non-equivalent sites as $\circ$ and $\bullet$, the Hamiltonian is given as

$$\mathcal{H} = -t \sum_{ij} c_i^\dagger c_j + \text{h.c.} = \mathbf{c}^\dagger \mathbf{H} \mathbf{c},$$

where (i, j) are nearest-neighbour sites (with π orbitals of carbon atoms) on the honeycomb lattice with the hopping, t ($\simeq$2.8 eV in graphene). On the right-hand side we have recasted the Hamiltonian into a matrix form spanned by the atomic sites as

$$\mathbf{c} = \begin{bmatrix} c_\bullet \\ c_\circ \end{bmatrix}, \quad c_\bullet = \begin{pmatrix} c_{\bullet 1} \\ \vdots \\ c_{\bullet N_\bullet} \end{pmatrix}, \; c_\circ = \begin{pmatrix} c_{\circ 1} \\ \vdots \\ c_{\circ N_\circ} \end{pmatrix},$$

$$\mathbf{H} \equiv \begin{bmatrix} \mathbf{O} & \mathbf{D} \\ \mathbf{D}^\dagger & \mathbf{O} \end{bmatrix},$$

where we have divided the honeycomb lattice, which is bipartite, into two sublattices, $\bullet$ and $\circ$. Since each nearest-neighbour transfer connects neighbouring $\bullet$ and $\circ$ sites, the Hamiltonian in this representation is block-offdiagonal. The off-diagonal block is denoted as $\mathbf{D}$, an $N_\bullet \times N_\circ$ matrix, where $N_\bullet (N_\circ)$ is the total number of $\bullet(\circ)$ sites. We have $N_\bullet = N_\circ$ unless we consider edges (we come to this point later).

This implies the Hamiltonian changes its sign if we perform a transformation,

$$c_{i\bullet} \to +c_{i\bullet}$$
$$c_{i\circ} \to -c_{i\circ}.$$

We can put this in a form,

$$\{\mathbf{H}, \mathbf{\Gamma}\} \equiv \mathbf{H}\mathbf{\Gamma} + \mathbf{\Gamma}\mathbf{H} = \mathbf{O}, \quad \mathbf{\Gamma} = \begin{bmatrix} \mathbf{I}_{N_\bullet} & \mathbf{O} \\ \mathbf{O} & -\mathbf{I}_{N_\circ} \end{bmatrix},$$

where $\mathbf{I}$ is a unit matrix. The property that the Hamiltonian anticommutes with an operator $\mathbf{\Gamma}$ (called a chiral operator) defines the *chiral symmetry*.

If a Hamiltonian has a chiral symmetry, then from the Schrödinger equation $\mathbf{H}\psi_E = E\psi_E$, we can see that any eigenstate, ψ_E, with an eigenenergy E should have a "chiral partner", $\psi_{-E} = \Gamma\psi_E$ with an eigenenergy $-E$. In terms of the matrix form, the Schrödinger equation reads

$$\begin{bmatrix} \mathbf{O} & \mathbf{D} \\ \mathbf{D}^\dagger & \mathbf{O} \end{bmatrix} \begin{bmatrix} \psi_\bullet \\ \psi_\circ \end{bmatrix} = E \begin{bmatrix} \psi_\bullet \\ \psi_\circ \end{bmatrix},$$

with $\psi_E = \left[\begin{smallmatrix}\psi_\bullet \\ \psi_\circ\end{smallmatrix}\right]$. The chiral partner then becomes

$$\psi_{-E} = \mathbf{\Gamma}\psi_E = \begin{bmatrix} \mathbf{I}_{N_\bullet} & \mathbf{O} \\ \mathbf{O} & -\mathbf{I}_{N_\circ} \end{bmatrix} \begin{bmatrix} \psi_\bullet \\ \psi_\circ \end{bmatrix} = \begin{bmatrix} \psi_\bullet \\ -\psi_\circ \end{bmatrix}$$

with an inverted sign for the $\circ$ component, which indeed has an eigenenergy $-E$ as

$$\begin{bmatrix} \mathbf{O} & \mathbf{D} \\ \mathbf{D}^\dagger & \mathbf{O} \end{bmatrix} \begin{bmatrix} \psi_\bullet \\ -\psi_\circ \end{bmatrix} = (-E) \begin{bmatrix} \psi_\bullet \\ -\psi_\circ \end{bmatrix}.$$

Thus the chiral operation amounts to, as far as the tight-binding picture is concerned, a sign reversal for one of the two sublattice components. The two components, $\psi_\bullet$ and $\psi_\circ$, are related, for nonzero energy states, as

$$\psi_\bullet = \frac{1}{E}\mathbf{D}\psi_\circ, \quad \psi_\circ = \frac{1}{E}\mathbf{D}^\dagger\psi_\bullet.$$

The chiral symmetry tells us that the zero-energy states are special: Such a state, having its chiral partner at the same energy, can be made an eigenstate of the chiral operator if we take linear combinations, that is, for any zero-energy eigenstate $\psi_{E=0}$, we construct eigenstates of the chiral operator $\mathbf{\Gamma}$ as

$$\begin{aligned} \mathbf{\Gamma}\psi_\pm &= \pm\psi_\pm, \\ \psi_\pm &= \mathbf{P}_\pm\psi_{E=0} \end{aligned}$$

with

$$\mathbf{P}_\pm = (\mathbf{1} \pm \mathbf{\Gamma})/2,$$

a projection onto the eigenstates of the chiral operator $\mathbf{\Gamma}$ (with $(\mathbf{P}_\pm)^2 = \mathbf{P}_\pm$). From the factor $(\mathbf{1} \pm \mathbf{\Gamma})$, ψ_+ has finite amplitudes only on $\bullet$ sites, while ψ_- on $\circ$ sites in a lattice model.

When we apply a uniform magnetic field normal to graphene, the states coalesce into graphene Landau levels. Since this also occurs at $E = 0$ (with the Landau index $n = 0$), for which the states are exactly degenerate in the presence of the chiral symmetry as we shall see, one can take the one-particle states of the $n = 0$ Landau level as the eigenstates of the chiral operator $\mathit{\Gamma}$. This is important for discussing not only one-body problems but also many-body physics of graphene [37–39]. Another situation where the chiral symmetry plays an important role is its relevance to edge states that appear along sample boundaries. It has long been known that edge states ("Fujita states") [40] appear along zigzag edges, where the states are in fact eigenstates of the chiral operator [37–39, 41], as we shall discuss later.

In momentum space, the Hamiltonian is written as

$$\mathcal{H} = \mathbf{c}(\mathbf{k})^\dagger \mathbf{H}(\mathbf{k})\mathbf{c}(\mathbf{k}), \quad \mathbf{c}(\mathbf{k}) = \begin{bmatrix} c_\bullet(\mathbf{k}) \\ c_\circ(\mathbf{k}) \end{bmatrix}$$

where $c_{\bullet\circ}(\mathbf{k}) = (1/N)\sum_i e^{i\mathbf{k}\cdot\mathbf{x}_i} c_{i\bullet\circ}$ is a Bloch representation, and

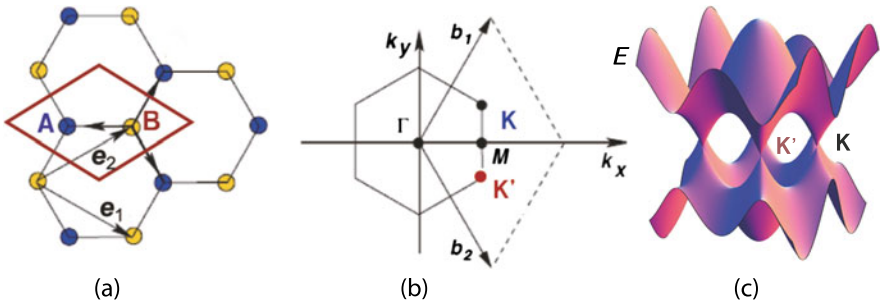

Fig. 7.1 (**a**) Unit cell of graphene in real space, with primitive vectors $\hat{\mathbf{e}}_i$ indicated. (**b**) Brillouin zone in reciprocal space, with primitive vectors $\hat{\mathbf{b}}_i$ indicated. (**c**) Energy dispersion (in an extended zone)

$$\mathbf{H}(\mathbf{k}) = \begin{bmatrix} 0 & D(\mathbf{k}) \\ D^*(\mathbf{k}) & 0 \end{bmatrix}, \tag{7.1}$$

$$D(\mathbf{k}) = t\left(1 + e^{-ik_1} + e^{-ik_2}\right), \tag{7.2}$$

where k_1, k_2 are respectively wavenumbers along the primitive directions (Fig. 7.1, centre panel). In this representation we have the chiral symmetry, $\{\mathbf{H}, \boldsymbol{\gamma}\} = 0$, with $\boldsymbol{\gamma} = \sigma_z$, the z component of Pauli matrix. Since the eigenequation becomes $|D(\mathbf{k})|^2 = E^2$, the energy dispersion is given by $\pm|D(\mathbf{k})|$ (Fig. 7.1, right panel).

7.2.2 *Fermion Doubling for Chiral Symmetric Lattice Fermions*

While graphene is often described as a realisation of massless Dirac particles, graphene harbours even more interesting physics that is related to the honeycomb lattice. Namely, if a fermion system on a lattice, for which we have to work in a reciprocal space, there is an interesting phenomenon called the "fermion doubling" when the lattice possesses the chiral symmetry.

In more general terms of the band theory in the solid state physics, the task is to find the chiral operator $\boldsymbol{\gamma}$, with $\{\mathbf{H}, \boldsymbol{\gamma}\} = 0, \boldsymbol{\gamma}^\dagger = \boldsymbol{\gamma}$, and $\boldsymbol{\gamma}^2 = 1$, for a general two-band system (i.e., valence and conduction bands), so we depart for the moment from the honeycomb lattice. A two-band system has a 2×2 matrix Hamiltonian in k space, which is actually the situation considered by Berry [13], who discussed the behaviour of wavefunctions around a (generally accidental) degeneracy (level crossing) point. The Hamiltonian can then be expanded by Pauli matrices $\boldsymbol{\sigma} = (\sigma_1, \sigma_2, \sigma_3)$ as

$$\mathbf{H}(\mathbf{k}) = \mathbf{R}(\mathbf{k}) \cdot \boldsymbol{\sigma} = \begin{bmatrix} R_3 & R_1 - iR_2 \\ R_1 + iR_2 & -R_3 \end{bmatrix}, \quad R_1, R_2, R_3 \in \mathbb{R}$$

where $\mathbf{R} = {}^t(R_1, R_2, R_3)$, is a three-dimensional real vector with $R_1(\mathbf{k}) = \mathrm{Re}\, D(\mathbf{k})$ and $R_2(\mathbf{k}) = -\mathrm{Im}\, D(\mathbf{k})$. In (7.1) $R_3 = 0$, but R_3 can generally be finite, and we

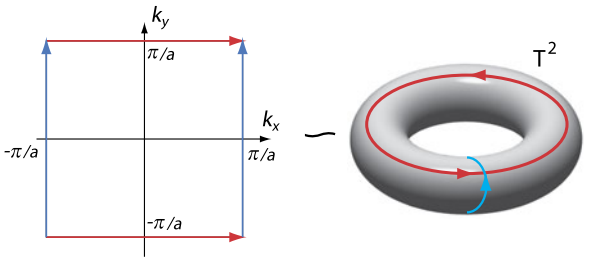

Fig. 7.2 Two-dimensional Brillouin zone (*left panel*), which is topologically a torus (*right*)

have taken the origin of energy in such a way that $\mathbf{H}$ is traceless. Then the secular equation becomes $E^2 = R^2$ with $R \equiv |\mathbf{R}|$, so that the valence and conduction bands correspond respectively to $E(\mathbf{k}) = \pm R(\mathbf{k})$. Now, in a 2D system as is the case with graphene, the wavenumber $\mathbf{k}$ lives on a 2D plane (Fig. 7.2), while the Hamiltonian is defined by $\mathbf{R}(\mathbf{k})$ which is a 3D vector. Since the degree of freedom for $\mathbf{R}(\mathbf{k})$ is greater than the number of variables, the energy gap can close only accidentally in general (i.e., when there is no chiral symmetry) [13].

How about the chiral-symmetric case? The chiral operator in the present representation should also be a 2×2 matrix, so that it should point to a general direction $(\mathbf{n}_\gamma)$ in the Pauli-matrix space as

$$\boldsymbol{\gamma} = \mathbf{n}_\gamma \cdot \boldsymbol{\sigma}.$$

The condition for the chiral symmetry, $\{\mathbf{H}, \boldsymbol{\gamma}\} = 2\mathbf{R} \cdot \mathbf{n}_\gamma = 0$,[1] then reads

$$\mathbf{R}(\mathbf{k}) \perp \mathbf{n}_\gamma,$$

i.e., a geometrical condition that the vector $\mathbf{R}(\mathbf{k})$ be always normal to a constant vector. Case of graphene corresponds to $\mathbf{n}_\gamma \perp z$ with $\gamma = \sigma_z$. In this case, the role of gamma matrices, $\gamma_0, \gamma_1, \gamma_5$, in the $(3+1)$-dimensional field theory is played by $\sigma_x, \sigma_y, \sigma_z$ in $(2+1)$-dimensions, hence the nomenclature "chiral operator".

Thus the degree of freedom in $\mathbf{R}(\mathbf{k})$ is reduced to two in the chiral-symmetric case. Figure 7.3 schematically shows how $\mathbf{R}(\mathbf{k})$, generally a three-dimensional object, is flattened in the presence of chiral symmetry, and Dirac points appear whenever the flattened object intersects zero points of $\mathbf{R}$. This simple fact already implies a topological stability of the Dirac cones [8, 9, 14]. The topological stability means that the degeneracy is stable against finite (as opposed to infinitesimal) modifications, up to a certain extent.

Let us elaborate this. If we denote the momentum as $\mathbf{k}_0$ at which a zero point occurs $(\mathbf{R}(\mathbf{k}_0) = \mathbf{0})$, we can expand the Hamiltonian, as a $\mathbf{k} \cdot \mathbf{p}$ scheme, around this momentum, where the leading term should be linear in $\delta\mathbf{k} = \mathbf{k} - \mathbf{k}_0$ (unless the leading term is quadratic for a specific reason), so that we end up with an effective Hamiltonian,

$$\mathbf{H} \approx \mathbf{h} \equiv (\mathbf{X} \cdot \boldsymbol{\sigma})\delta k_x + (\mathbf{Y} \cdot \boldsymbol{\sigma})\delta k_y,$$
$$\mathbf{X} = \partial_{k_x}\mathbf{R},\ \mathbf{Y} = \partial_{k_y}\mathbf{R},$$

[1] We have made use of $(\mathbf{A} \cdot \boldsymbol{\sigma})(\mathbf{B} \cdot \boldsymbol{\sigma}) = \mathbf{A} \cdot \mathbf{B} + i(\mathbf{A} \times \mathbf{B}) \cdot \boldsymbol{\sigma}$.

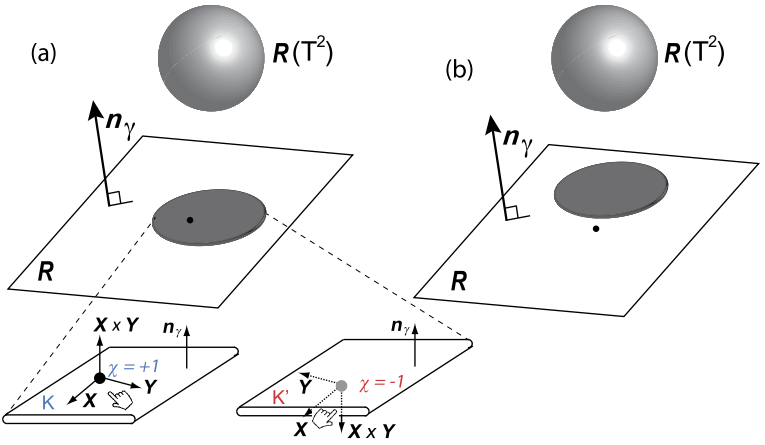

Fig. 7.3 Topological stability of Dirac cones: Three-dimensional "balloons" at the top schematically represent the general image of $\mathbf{R}(\mathbf{k})$ when $\mathbf{k}$ moves over the first Brillouin zone (a torus T^2; previous figure). Flattened balloons below represent the chiral-symmetric case, where the objects reside on a plane normal to $\mathbf{n}_\gamma$. (**a**) is the case in which a zero point (origin) of $\mathbf{R}(\mathbf{k})$ (*dot*) is within the flattened object and Dirac cones appear in pairs, or (**b**) outside the object. *Inset* below (**a**) shows doubled Dirac cones with chirality $+1$ (at K; *left panel*) and -1 (at K′; *right*), here represented in $\mathbf{R}$ space

which is a massless Dirac Hamiltonian. Since $\mathbf{X}$ and $\mathbf{Y}$ are both perpendicular to $\mathbf{n}_\gamma$ as we have seen, the three vectors $(\mathbf{X}, \mathbf{Y}, \mathbf{n}_\gamma)$ can be either right-handed (which we call the chirality $\chi = +1$) or left-handed ($\chi = -1$). Namely,

$$\mathbf{n}_\gamma = \chi \mathbf{X} \times \mathbf{Y}/(c\hbar)^2,$$

Here $c = |\mathbf{X} \times \mathbf{Y}|^{1/2}/\hbar$ plays the role of the "speed of light" (velocity of a massless Dirac particle), which corresponds to $\sqrt{3}at/2$ in the tight-binding model, and is numerically $\sim 10^6$ m s^{-1}, some $1/300$ times the velocity of light, for graphene.

The energy dispersion is obtained by calculating $\mathbf{h}^2$ as

$$\mathbf{h}^2 = (c\hbar)^2 (\delta k_x, \delta k_y)\, \Xi \begin{bmatrix} \delta k_x \\ \delta k_y \end{bmatrix},$$

$$\Xi = \frac{1}{(c\hbar)^2} \begin{bmatrix} \mathbf{X}\cdot\mathbf{X} & \mathbf{X}\cdot\mathbf{Y} \\ \mathbf{Y}\cdot\mathbf{X} & \mathbf{Y}\cdot\mathbf{Y} \end{bmatrix},$$

where Ξ, a real symmetric matrix with $\det \Xi = 1$, can be diagonalised by an orthogonal matrix $\mathbf{V}$ as

$$\Xi = \mathbf{V}^\dagger \mathrm{diag}\,(\xi_1, \xi_2)\mathbf{V},$$

where $\xi_1, \xi_2 > 0$ with $\xi_1 \xi_2 = 1$. We have then

$$E = \pm c\bar{p},$$
$$\bar{p} = \hbar\sqrt{\xi_1 k_1^2 + \xi_2 k_2^2}, \quad \begin{bmatrix} k_1 \\ k_2 \end{bmatrix} = \mathbf{V}\begin{bmatrix} \delta k_x \\ \delta k_y \end{bmatrix},$$

an (in general elliptic) Dirac cone.

Although we have so far restricted ourselves to the vicinity around K and K′ points in the Brillouin zone, we can extend the argument on the chiral symmetry for the whole Brillouin zone, which will put a global constraint on the Dirac cones. Since the two-dimensional Brillouin zone with its periodic boundaries is topologically a two-torus T^2 (Fig. 7.2), Berry's parameterization of the Hamiltonian means that the map, $\mathbf{k} \to \mathbf{R}(\mathbf{k})$, when $\mathbf{k}$ moves over the first Brillouin zone generates an image $\mathbf{R}(T^2)$ as a compact, oriented surface (a "balloon") in three dimensional space of $\mathbf{R}$ (Fig. 7.3). We have seen that the chiral symmetry requires that the balloon be flattened. The zero-energy point corresponds to the case where the origin ($\mathbf{R} = \mathbf{0}$) intersects the flattened balloon. Then it is graphically obvious that the Dirac cones always appear in pairs, where each pair comprises opposite chiralities (i.e., left- and right-handed) (Fig. 7.3). This is (two-dimensional analogue of) the fermion doubling and Nielsen-Ninomiya theorem usually discussed for $(3+1)$ dimensions. Existence of the doubled Dirac cones at K and K′ points in graphene with the opposite chiralities,

$$\chi(\mathrm{K}) + \chi\left(\mathrm{K}'\right) = 0,$$

is a simplest realization of this.

In the case of graphene (i.e., a honeycomb lattice) the fermion doubling can be attributed to the crystal symmetry, where the Dirac points correspond to, in a space-group argument, the existence of two-dimensional representations at K and K′ [15]. We can also show that only the honeycomb symmetry of the periodic potential of the crystal is required for the Dirac cones to arise, so that the Dirac cones appear not only in the tight-binding model but more generally. Hsu and Reichl [42] have shown this approximately for a honeycomb array of atomic potentials with a plane-wave expansion for the band calculation. Later, the presence of Dirac cones was analytically shown with renormalisation of the potential strength and a regularisation of the potential [43]. These works also indicate that the second-neighbour hopping integral is small, $\sim$0.1 eV.

7.2.3 *When and How Dirac Cones Appear?—Generalised Chiral Symmetry*

We have seen that if the Hamiltonian has a chiral symmetry, then (an even number of) Dirac cones have to exist as far as the Hamiltonian contains zero point in the sense of Fig. 7.3. Now we can pose an "inverse problem". Namely, if a Hamiltonian has gap-closing point(s), does this imply the Hamiltonian has a chiral symmetry? This question is nontrivial, since the zero gap alone may not guarantee the existence

of chiral symmetry. We have seen that the low-energy effective Hamiltonian around a gap-closing point is expressed in general by a 2×2 matrix expanded by the Pauli matrices. The gap closing point itself where the two bands become degenerate has a co-dimension of 3 [13]. This implies that, in two spatial dimensions, the degeneracy only occurs accidentally *unless* some constraint, such as the chiral symmetry, exists.

So let us here consider the gap closing when the chiral symmetry is absent. Around the gap closing point the Hamiltonian is expanded as

$$H = \big[\big(\sigma_0 X^0 + \boldsymbol{\sigma}\cdot\mathbf{X}\big)\delta k_x + \big(\sigma_0 Y^0 + \boldsymbol{\sigma}\cdot\mathbf{Y}\big)\delta k_y\big].$$

Here we have included a terms proportional to σ_0, a unit matrix, which is required when we discuss non-chiral-symmetric case. When this term exists, the energy dispersion is affected when the term has a momentum dependence, and the Dirac cones become tilted (Fig. 7.4(b)).

We can show, however, that even in this case we can define a "generalised chiral symmetry". Namely, if we define a generalised chiral operator,

$$\begin{aligned}
\gamma &= \mathbf{n}\cdot\boldsymbol{\sigma},\\
\mathbf{n} &= (\mathbf{X}\times\mathbf{Y} + i\boldsymbol{\eta})/(c\hbar)^2,\\
\boldsymbol{\eta} &= X^0\mathbf{Y} - \mathbf{X}Y^0,\\
c^2 &= \sqrt{|\mathbf{X}\times\mathbf{Y}|^2 - |\boldsymbol{\eta}|^2},
\end{aligned}$$

then we can show that the Hamiltonian satisfies

$$H\gamma + \gamma^\dagger H = 0.$$

While the matrix γ is now non-hermitian ($\gamma^\dagger \neq \gamma$), we still have $\gamma^2 = \sigma_0$, which implies that the eigenvalues of γ are again ± 1. An interesting observation is that the generalised chiral operator is definable only when the tilting is not too large ($|\boldsymbol{\eta}| \leq |\mathbf{X}\times\mathbf{Y}|$) [35, 44], which is a condition that the Hamiltonian as a differential operator be elliptic (as opposed to hyperbolic). The latter is exactly the condition for the *index theorem* to hold, so that we can say there really is a well-defined mathematical relation between the Dirac cone physics and the index theorem. The tilted Dirac cones are related to the physics of some organic metal, as discussed in terms of the chiral symmetry by Kawarabayashi et al. [35, 36].

The chiral symmetry can also be discussed (a) when there is a second-neighbour hopping in the honeycomb lattice, which degrades the electron-hole symmetry, with a dispersion displayed in Fig. 7.4(a) [34]. There are various other modified forms of Dirac cones: (b) Tilted cones discussed above. (c) A single cone with a flat band inserted occurs in a model proposed by Lieb [45], and in a class of graphene systems with antidot arrays (periodically perforated graphene, or, in today's language, graphene nanomesh), originally considered by Shima and Aoki [46]. This can be regarded as a Dirac cone with the (spin-1 realisation of) SU(2) symmetry [22]. (d) Two parabolic dispersions touching at the apices appear in bilayer graphene. In this case the chiral symmetry is preserved but the dispersion is no longer cones, but still the anomalously sharp zero-energy Landau level is theoretically predicted [47].

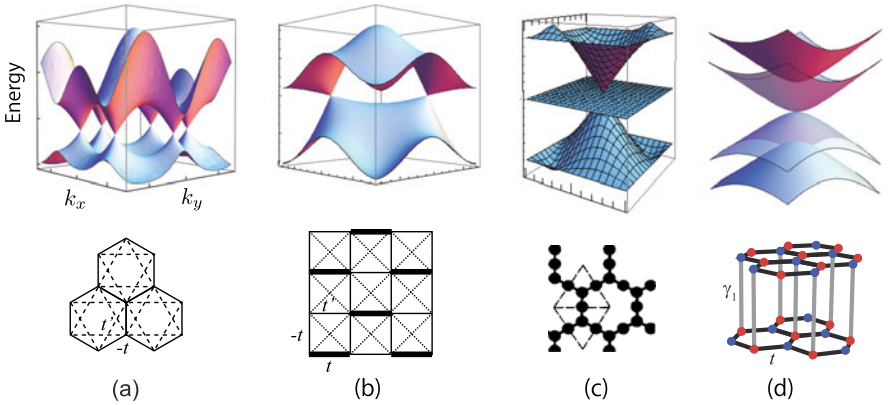

Fig. 7.4 Various modified forms of Dirac cones: (**a**) Electron-hole asymmetric cones with second-neighbour transfers [34], (**b**) tilted cones [35], (**c**) a single cone with a flat band inserted [22, 46], and (**d**) two parabolic dispersions touching at the apices in bilayer graphene [47]. *Bottom insets* depict the corresponding lattice structures

7.3 Hall Conductivity of Dirac Fermions in Magnetic Fields

7.3.1 Landau Level of the Dirac Fermions

Graphene quantum Hall effect is one of the most remarkable phenomena inherent in graphene. So let us first consider the electronic structure of Dirac fermions when a uniform magnetic field $\mathbf{B}$ is applied perpendicular to graphene. We can then put $\hbar\delta\mathbf{k} \to \boldsymbol{\pi} \equiv \mathbf{p} - e\mathbf{A}$, where $\mathbf{p} = -i\hbar\nabla$ and $\mathrm{rot}\,\mathbf{A} = \mathbf{B} = (0, 0, B)$. The Hamiltonian becomes

$$\mathbf{h}(B) = \hbar^{-1}\big[(\mathbf{X}\cdot\boldsymbol{\sigma})\pi_x + (\mathbf{Y}\cdot\boldsymbol{\sigma})\pi_y\big],$$

where $\boldsymbol{\pi}$ has a commutation relation,

$$[\pi_x, \pi_y] = i\hbar e(\partial_x A_y - \partial_y A_x) = i\hbar eB.$$

Here we assume $e < 0$, $B < 0$ (with $eB > 0$) without loss of generality.

It is a straightforward exercise to treat the Landau levels for Dirac particles, but here we opt for a general expression in terms of the above Hamiltonian. Then, by again taking the squared Hamiltonian, we have

$$\begin{aligned}
\mathbf{h}^2 &= \hbar^{-2}\big\{\big[\mathbf{X}^2\pi_x^2 + \mathbf{Y}^2\pi_y^2 + \mathbf{X}\cdot\mathbf{Y}(\pi_x\pi_y + \pi_y\pi_x)\big]\sigma_0 + i(\mathbf{X}\times\mathbf{Y})\cdot\boldsymbol{\sigma}[\pi_x, \pi_y]\big\} \\
&= c^2\left[(\pi_x, \pi_y)\boldsymbol{\Xi}\begin{bmatrix}\pi_x \\ \pi_y\end{bmatrix}\sigma_0 + i\chi\boldsymbol{\gamma}[\pi_x, \pi_y]\right] \\
&= c^2\big[\big(\xi_1\Pi_1^2 + \xi_2\Pi_2^2\big)\sigma_0 + i\chi\boldsymbol{\gamma}[\Pi_1, \Pi_2]\big] \\
&= \frac{1}{2m}\boldsymbol{\Pi}'^2\sigma_0 - \chi\frac{1}{2}\hbar\omega_c\gamma.
\end{aligned}$$

Here we have defined

$$\mathbf{\Pi} = (\Pi_1, \Pi_2) = \mathbf{V}\boldsymbol{\pi}, \qquad \Pi_i' = \xi_i^{1/2}\Pi_i (i = 1, 2), \qquad \left[\Pi_1', \Pi_2'\right] = i\hbar eB,$$

in terms of the orthogonal matrix $\mathbf{V}$ introduced in the previous section. We have also defined a mass by $\frac{1}{2m} \equiv c^2$ and the cyclotron frequency $\omega_c \equiv eB/m = 2c^2 eB$. The first term on the right-hand side of the last line is the standard Hamiltonian for two-dimensional electrons in a uniform magnetic field, so that its eigenvalues are $(n' + 1/2)\hbar\omega_c$ with n': integer. The second term ($\propto \chi\gamma$) is either $+1$ or -1 according as the eigenvalue of γ has the same sign as χ or not, and we end up with the final Landau level structure,

$$\mathbf{h}^2 \mathbf{\Psi}_{\pm}^{n'} = \hbar\omega_c \left(n' + \frac{1}{2} \mp \chi \frac{1}{2} \right) \mathbf{\Psi}_{\pm}^{n'},$$
$$\mathbf{\Psi}_{\pm}^{n'} = \phi_{n'} \boldsymbol{\phi}_{\pm},$$

where n' is the Landau index, $\phi_{n'}$ the Landau wavefunction, while $\boldsymbol{\phi}_{\pm}$ is the eigenstate of γ with $\boldsymbol{\gamma}\boldsymbol{\phi}_{\pm} = \pm\boldsymbol{\phi}_{\pm}$. For the original $\mathbf{h}$ we have the Landau levels of the Dirac fermions given as

$$\epsilon_{n\pm} = \pm c\sqrt{2\hbar eB|n|}, \quad n = 0, \pm 1, \pm 2, \ldots \tag{7.3}$$

with $n = n' + (1 \mp \chi)/2$.

This is the graphene Landau spectrum, which is special in two respects: (i) the levels have absolute magnitudes proportional to $\sqrt{nB}$ (as opposed to $\propto (n + 1/2)B$ in usual 2DEG), and (ii) we have a zero-energy Landau level (for $n = 0$) right at the Dirac point ($E = 0$). The zero Landau level is special in that its eigenstates can be made eigenstates of the chiral operator $\boldsymbol{\gamma}$ with the eigenvalue χ, since we have to take the minus sign in the factor $(1 \mp \chi)$ appearing above. By putting

$$\mathbf{h}^2 = c^2 \mathbf{P}_{\chi}^{\dagger} \mathbf{P}_{\chi},$$

where $\mathbf{P}_{\chi} = \Pi_1' \boldsymbol{\sigma}_0 + i\chi\boldsymbol{\gamma}\Pi_2'$ with $[\mathbf{P}_{\chi}, \mathbf{P}_{\chi}^{\dagger}] = \chi\gamma\hbar eB$, we can in fact rewrite the condition for zero-energy states with chirality χ as $\mathbf{h}^2 \mathbf{\Psi}_{\chi}^0 = c^2 \mathbf{P}_{\chi}^{\dagger} \mathbf{P}_{\chi} \mathbf{\Psi}_{\chi}^0 = 0$, which implies $(\mathbf{P}_{\chi} \mathbf{\Psi}_{\chi}^0)^{\dagger} \mathbf{P}_{\chi} \mathbf{\Psi}_{\chi}^0 = \|\mathbf{P}_{\chi} \mathbf{\Psi}_{\chi}^0\|^2 = 0$, namely

$$\mathbf{P}_{\chi} \mathbf{\Psi}_{\chi}^0 = 0.$$

7.3.2 *Stability of the $n = 0$ Landau Level*

Real samples are always disordered, and usual Landau levels in two-dimensional electron gases are broadened accordingly. Now, an amazing property of graphene is its zero Landau level remains sharp even in the presence of disorder under a certain condition, which turns out to be just the chiral symmetry. For a heuristic purpose, let us show this for the case of spatially inhomogeneous magnetic fields (i.e., random gauge fields) following an argument due to Aharonov and Casher [16, 36], or

more generically in terms of the index theorem. Namely, the zero-energy condition $\mathbf{P}_\chi \mathbf{\Psi}^0_\chi = 0$ can be satisfied for an inhomogeneous $B(\mathbf{r})$. Let us here summarise the Aharonov-Casher argument with a slight extension. Introducing a scalar function ϕ, we can express the vector potential as

$$(A_1, A_2) = (-\xi_2 \partial_2 \phi,\ \xi_1 \partial_1 \phi).$$

Then the secular equation for the zero mode becomes

$$0 = \mathbf{P}_\chi \mathbf{\Psi}^0_\chi = -i\hbar \left(\partial'_1 + i \frac{2\pi}{\phi_0} \partial'_2 \phi + i \partial'_2 + \frac{2\pi}{\phi_0} \partial'_1 \phi \right) \mathbf{\Psi}^0_\chi$$

with $\phi_0 = e/h$ the flux quantum, and $\partial'_i = \xi_i^{1/2} \partial_i$. If we put

$$\mathbf{\Psi}^0_\chi = e^{-2\pi \frac{\phi}{\phi_0}} f,$$

the function f satisfies $(\partial'_1 + i\partial'_2) f = \partial_{\bar{z}} f = 0$ ($z \equiv x'_1 + i x'_2$). Namely, f is an entire function of z on the whole complex plane $z \in \mathbb{C}$, that is, polynomials. The function ϕ needs to satisfy the equation, $B = \partial_1 A_2 - \partial_2 A_1 = (\xi_1 \partial_1^2 + \xi_2 \partial_2^2)\phi$. When the magnetic field is nonzero only in a finite region, we have an asymptotic behaviour,[2]

$$\phi \overset{r \to \infty}{\longrightarrow} \frac{\Phi}{2\pi} \log \left(\frac{r}{r_0} \right),$$

where $\Phi = \int d\tilde{x}_1 d\tilde{x}_2 B$ is the total flux. This implies an asymptotic behaviour,

$$\psi \overset{r \to \infty}{\longrightarrow} f(z) \left(\frac{r}{r_0} \right)^{-\frac{\Phi}{\phi_0}},$$

namely, the degeneracy of the zero modes is precisely Φ/ϕ_0. Since this exhausts the total number of states in a Landau level, the zero-energy Landau level exactly has a delta-function density of states. This holds even when B has a spatial dependence, and concludes that the zero energy Landau level remains intact against spatial randomness in magnetic field as far as the chiral symmetry exists.

As for graphene, an intrinsic randomness comes from ripples, i.e., random corrugations of the honeycomb lattice plane. Ripples can be modeled by a randomness in the hopping in the tight-binding model. Now, random bonds preserve the chiral symmetry: We have seen that in real space we can decompose the honeycomb lattice into two sub-lattices $\circ$ and $\bullet$, for which the chiral operator acts as $\gamma c_i \gamma^{-1} = \pm c_i$ with $+(-)$ for $i \in \circ(\bullet)$. Obviously, the random hopping preserves the symmetry, while a potential disorder does not. A ripple (spatial corrugation) is represented by a spatially correlated randomness in the hopping [48, 49]. The robustness of the sharp zero-energy Landau level, and the associated sharp QHE step, is confirmed numerically with a random hopping model of the graphene [27] as shown in Fig. 7.5. We can also extend the Aharonov-Casher argument to $n = 0$ Landau level for ripples [27].

[2] This can be shown from $\phi(x'_1, x'_2) = \int d\tilde{x}'_1 d\tilde{x}'_2 G(\tilde{x}_1 - \tilde{x}'_1, \tilde{x}_2 - \tilde{x}'_2) B(\tilde{x}'_1, \tilde{x}'_2)$, where $G(\tilde{x}_1, \tilde{x}_2) = \frac{1}{2\pi} \log \frac{r}{r_0}$, $r^2 = \tilde{x}_1^2 + \tilde{x}_2^2$, and the quantities with tilde are scaled by (ξ_1, ξ_2).

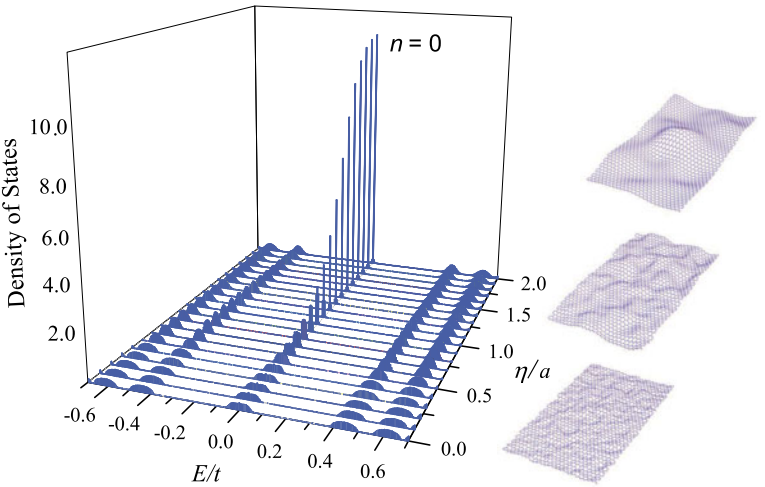

Fig. 7.5 Density of states of graphene in a magnetic field for a spatially correlated random-bond model for various values of the correlation length η of the randomness with the magnitude of the disorder fixed. *Insets on the right* schematically depict an increased spatial scale of the ripple [27]

7.3.3 Massless vs Massive Dirac Fermions

We have emphasised that the massless nature is essential for the $n = 0$ Landau level in the Dirac QHE. Then a natural question is how the massive case would cross over to the massless case. For this heuristic purpose let us break the chiral symmetry to consider a Dirac fermion having a mass m, for which the Hamiltonian, in zero magnetic field, is

$$\mathbf{h}_m = (\mathbf{X}\cdot\boldsymbol{\sigma})k_x + (\mathbf{Y}\cdot\boldsymbol{\sigma})k_y + mc^2\gamma.$$

The mass enters into a term proportional to the chiral operator $\gamma = \hat{\mathbf{e}}_{\mathbf{X}\times\mathbf{Y}}\cdot\boldsymbol{\sigma}$, which is usually $\gamma = \sigma_z$. In this case the dispersion (in zero magnetic field) is hyperbolic, $\pm c\sqrt{p^2 + m^2c^2}$, since $\mathbf{h}_m^2 = c^2p^2 + m^2c^4$. Such a massive case is not entirely artificial, since monolayer graphene has been reported to become massive when deposited on substrates such as BN [28–30] or Ru [31]. Incidentally, manipulation of the massive case is also interesting, as in the impurity states [32] or graphene quantum dot with charged vacuum [33].

Now, if we put $\mathbf{h}_m = \mathbf{R}\cdot\boldsymbol{\sigma}$ as before, then the eigenenergies are $\pm|\mathbf{R}|$ with $\mathbf{R}(k_x, k_y)$ again defining a plane in three-dimensional space as

$$\mathbf{R} = \mathbf{X}k_x + \mathbf{Y}k_y + m\chi c^2\mathbf{n}_\gamma.$$

The difference from the massless case is the point $\mathbf{R} = 0$ is now away from the plane spanned by $\mathbf{X}$ and $\mathbf{Y}$, since the mass term is proportional to $\mathbf{n}_\gamma \perp \mathbf{X}, \mathbf{Y}$. Since the Dirac particle has both of negative-energy (hole) and positive-energy (electron) branches in its dispersion, with the hole branch being occupied ("Dirac sea"), the

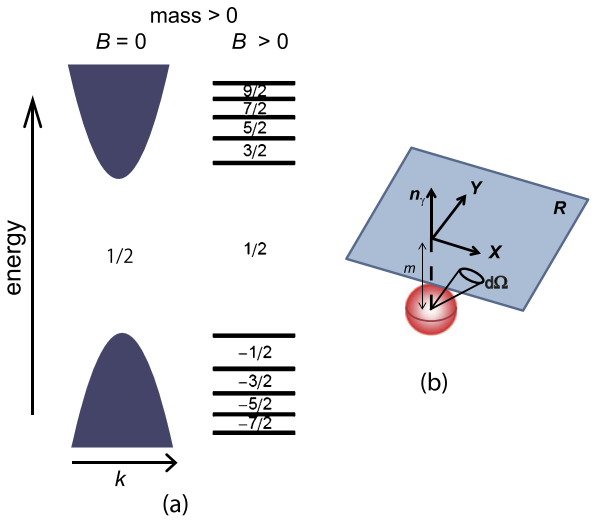

Fig. 7.6 (**a**) For valence and conduction bands with a mass > 0, energy spectrum in zero magnetic field (*left panel*) and the Landau levels in a finite field (*right*) are schematically shown, with the Chern number for each energy gap indicated. (**b**) How $\mathbf{R}(k_x, k_y)$ in Fig. 7.3 looks like in a massive case with a finite m

projection P onto the hole branch is expressed in terms of the normalised eigenstate ψ that has $(\hat{\mathbf{R}} \cdot \boldsymbol{\sigma})\psi = -\psi$ with $\hat{\mathbf{R}} \equiv \mathbf{R}/R$ as [14]

$$P = \psi\psi^\dagger = \frac{1}{2}(1 - \hat{\mathbf{R}} \cdot \boldsymbol{\sigma}).$$

Let us evaluate the Chern number with the general gauge-invariant formula, $C = (2\pi i)^{-1} \int \mathrm{Tr}\, \mathbf{P} d\mathbf{P}^2$ (see (7.4) below), which in the present case reads

$$dP = -\frac{1}{2} d\hat{\mathbf{R}} \cdot \boldsymbol{\sigma},$$

$$dP^2 = \frac{i}{4}(d\hat{\mathbf{R}} \times d\hat{\mathbf{R}}) \cdot \boldsymbol{\sigma},$$

$$\mathrm{Tr}\, P dP^2 = -\frac{i}{4} \hat{\mathbf{R}} \cdot (d\hat{\mathbf{R}} \times d\hat{\mathbf{R}}),$$

$$C = -\frac{1}{8\pi} \int \hat{\mathbf{R}} \cdot (d\hat{\mathbf{R}} \times d\hat{\mathbf{R}}) = -\mathrm{sgn}(m\chi) \int \frac{d\Omega}{4\pi} = -\frac{1}{2}\mathrm{sgn}(m\chi),$$

where $d\Omega$ is the solid-angle element (see Fig. 7.6(b)). The last equality follows from the fact that the total solid angle is half the full solid angle when the origin of $\mathbf{R}$ is off-plane for a nonzero mass. This is a graphical way for understanding the half-integer Chern numbers, well-known in the field theory.

Now, we can apply a magnetic field. The Hall conductivity of a gapped two-dimensional system is given by a topological invariant, which is the first Chern number, C, as shown by Thouless et al. [50, 51]. From the above procedure we can deduce the Chern number for Landau levels of Dirac fermions in a magnetic field by adiabatically turning on the magnetic field as depicted in Fig. 7.6(a). We can then remember that the effect of the mass term is to shift the zero-energy Landau level by $mc^2\chi$ (i.e., upwards or downwards according as the chirality $\chi = 1$ or -1),

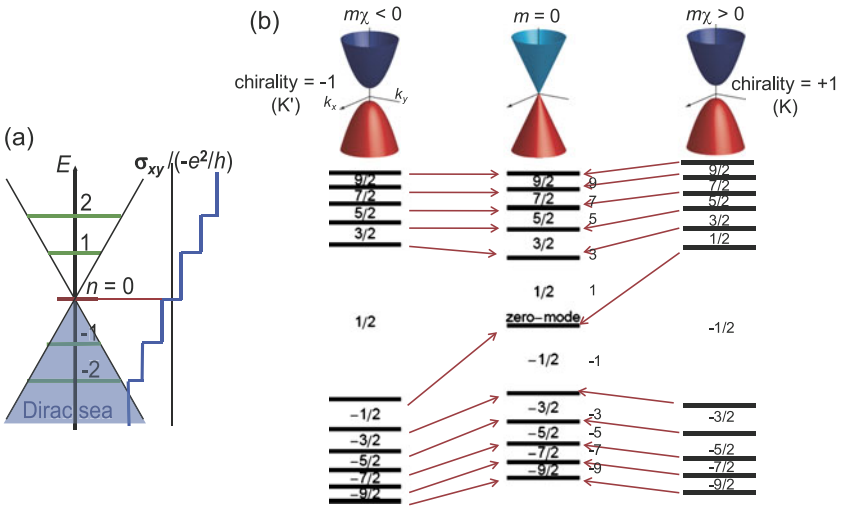

Fig. 7.7 (**a**) Schematic Landau levels and the quantised Hall conductivity σ_{xy}. (**b**) The way in which the Landau levels of a massive Dirac fermion with chirality -1 (*left column*) or $+1$ (*right*) cross over to those for the massless Dirac cones. The numbers represent the Chern numbers (with $\pm 1, \pm 3, \ldots$ indicating the sum of K and K$'$ contributions). Top insets depict the dispersion

with the states being eigenstates of $\boldsymbol{\gamma}$ having eigenvalue χ (see Fig. 7.7). Since the Chern number cannot change in an adiabatic process unless the gap closes, the Chern number in the mass gap remains, for magnetic field $B = 0 \to$ finite, to be $-1/2$ for $\chi = +1$ (or, more precisely, for $m\chi > 0$). In other words, the Landau level (LL) that becomes the zero-mode ($n = 0$) LL in the massless limit ($m \to 0$) is adiabatically connected to the LL just above the bottom of the positive-energy branch in the massive case. Conversely, for $m\chi < 0$, the Chern number for the mass gap is $+1/2$. The LL that becomes the zero-mode ($n = 0$) LL in the massless limit resides just below the top of the negative-energy branch. These are for single Dirac fermions, while in graphene with the honeycomb lattice, the total Chern number is the sum of the contributions from K point (with $m\chi > 0$) and from K$'$ point (with $m\chi < 0$), so that we end up with the graphene QHE with $\sigma_{xy} = 2n + 1$ ($n = 0, \pm 1, \ldots$) (in units of $-e^2/h$, with the spin degeneracy dropped) as in Fig. 7.7. There, each Landau level carries the Chern number of two.

7.3.4 Chern Number for Many-Particle Configurations

In the case of graphene, we are interested in the graphene QHE with $\sigma_{xy} = -(2n + 1)(e^2/h)$ (Fig. 7.7) in terms of the topological number. To be precise, a special care is needed here, since we are specifically interested in the region around the Dirac (charge-neutrality) point, where we have filled negative-energy states ("Dirac sea"). So if we want to question the Chern numbers in this region, we have to deal with

many-particle (i.e., filled Dirac sea) configurations. According to the Niu-Thouless-Wu formula [52], the Chern number formulation can be extended to many-particle configurations as

$$\sigma_{xy} = \frac{e^2}{h}\frac{1}{q}C,$$

where we have included a possibility that the ground state has a (topological) degeneracy of q with a many-body multiplet $(|\Psi_1\rangle, \ldots, |\Psi_q\rangle)$. The Chern number C, in the differential geometry, is an integral of Berry's connection $\mathbf{A}$ over a two-dimensional (oriented) surface S as [53–55]

$$\begin{aligned}
C &= \frac{1}{2\pi i}\int_S \mathrm{Tr}\,\mathbf{F} = \frac{1}{2\pi i}\int_S \mathrm{Tr}\,d\mathbf{A},\\
\mathbf{F} &= d\mathbf{A} + \mathbf{A}^2,\\
\mathbf{A} &= \mathbf{\Psi}^\dagger d\mathbf{\Psi} = \begin{pmatrix} \langle\Psi_1|d\Psi_1\rangle & \cdots & \langle\Psi_1|d\Psi_q\rangle \\ \vdots & \ddots & \vdots \\ \langle\Psi_q|d\Psi_1\rangle & \cdots & \langle\Psi_1|d\Psi_q\rangle \end{pmatrix},\\
\mathbf{\Psi} &= \big(|\Psi_1\rangle, \ldots, |\Psi_q\rangle\big),
\end{aligned}$$

where the differential is parametrised as $d = d\phi^x \frac{\partial}{\partial\phi^x} + d\phi^y \frac{\partial}{\partial\phi^y}$, and $d\phi^x d\phi^y = -d\phi^y d\phi^x$. Here, each of the many-particle configuration $\mathbf{\Psi}$ is a low-energy orthonormalized ($\mathbf{\Psi}^\dagger\mathbf{\Psi} = \mathbf{1}$) state of the many-body Hamiltonian H for a parameter $(\phi_x, \phi_y) \in S$ that specifies twisted boundary conditions along x and y,

$$\begin{aligned}
\big|\Psi(x + L_x, y)\big\rangle &= e^{i\phi_x}\big|\Psi(x, y)\big\rangle,\\
\big|\Psi(x, y + L_y)\big\rangle &= e^{i\phi_y}\big|\Psi(x, y)\big\rangle.
\end{aligned}$$

Since the twisted boundary condition for $\phi_\mu = 2\pi$ $(\mu = x, y)$ is equivalent to the periodic boundary condition, the parameter space, S, is a two-dimensional torus T^2. This guarantees that the Chern number is a topological invariant (integers).

In a degenerate case, $q > 1$, a gap is required between the lowest q states and the above ones for this formula to be applicable, but in general the low-energy q states may have level crossings against the twist in the boundary condition. We can still treat the situation with a unitary (gauge) transformation $\mathbf{g} \in U(q)$ for the multiplet as

$$\begin{aligned}
\mathbf{\Psi} &= \mathbf{\Psi}_\mathbf{g}\mathbf{g},\\
\mathbf{A} &= \mathbf{g}^{-1}\mathbf{A}_\mathbf{g}\mathbf{g} + \mathbf{g}^{-1}d\mathbf{g} \quad \big(\mathbf{A}_\mathbf{g} \equiv \mathbf{\Psi}_\mathbf{g}^\dagger d\mathbf{\Psi}_\mathbf{g}\big),\\
\mathbf{F} &= \mathbf{g}^{-1}\mathbf{F}_\mathbf{g}\mathbf{g} \quad \big(\mathbf{F}_\mathbf{g} \equiv d\mathbf{A}_\mathbf{g} + \mathbf{A}_\mathbf{g}^2\big).
\end{aligned}$$

The Chern number is then safely defined even in the presence of level crossings among the q states in a gauge-invariant manner as [14, 56, 57]

$$C_\mathbf{g} = \frac{1}{2\pi i}\int \mathrm{Tr}\,\mathbf{F}_\mathbf{g} = C.$$

Although the Chern number itself is gauge invariant, Berry's connection $\mathbf{A}$ is not. One may have a manifestly gauge-invariant expression for the Chern number using the gauge-invariant projection, $\mathbf{P} = \mathbf{\Psi}\mathbf{\Psi}^\dagger = \mathbf{\Psi}_g\mathbf{\Psi}_g^\dagger$, to the multiplet $\mathbf{\Psi}$, which is given [14] as

$$
\begin{aligned}
d\mathbf{P} &= d\mathbf{\Psi}\mathbf{\Psi}^\dagger + \mathbf{\Psi}d\mathbf{\Psi}^\dagger, \\
(d\mathbf{P})^2 &= -d\mathbf{\Psi}d\mathbf{\Psi}^\dagger\mathbf{\Psi}\mathbf{\Psi}^\dagger + d\mathbf{\Psi}d\mathbf{\Psi}^\dagger + \mathbf{\Psi}d\mathbf{\Psi}^\dagger d\mathbf{\Psi}\mathbf{\Psi}^\dagger - \mathbf{\Psi}\mathbf{\Psi}^\dagger d\mathbf{\Psi}d\mathbf{\Psi}^\dagger, \\
\mathbf{P}(d\mathbf{P})^2\mathbf{P} &= \mathbf{\Psi}\big[d\mathbf{\Psi}^\dagger d\mathbf{\Psi} + \big(\mathbf{\Psi}^\dagger d\mathbf{\Psi}\big)^2\big]\mathbf{\Psi}^\dagger = \mathbf{\Psi}\mathbf{F}\mathbf{\Psi}^\dagger.
\end{aligned}
$$

Now we have the manifestly gauge-invariant expression for the first Chern number as [14, 56]

$$
C = \frac{1}{2\pi i}\int \mathrm{Tr}\,\mathbf{P}d\mathbf{P}^2. \tag{7.4}
$$

Having established the general formula, let us apply it to graphene in the absence of electron-electron interactions. The ground state is non-degenerate for an integer Landau level filling, and the many-particle ground state $|\Psi\rangle$ is given by filling the single-particle states below the Fermi energy, $\psi_1, \ldots, \psi_M$, as

$$
|\psi\rangle = \prod_{\ell=1}^{M}\big(\mathbf{c}^\dagger\psi_\ell\big)|0\rangle = \big(\mathbf{c}^\dagger\psi_1\big)\cdots\big(\mathbf{c}^\dagger\psi_M\big)|0\rangle, \quad \mathbf{c}^\dagger = \big(c_1^\dagger, \ldots, c_N^\dagger\big)
$$

where $c_i^\dagger$ is the creation operator of a fermion, M the total number of occupied states, and N the total number of sites. Then the Berry's connection for the many-electron state $|\Psi\rangle$ is given as [18]

$$
\begin{aligned}
A &= \langle\Psi|d\Psi\rangle = \mathrm{Tr}\,\mathbf{a}, \\
\mathbf{a} &= \boldsymbol{\psi}^\dagger d\boldsymbol{\psi}, \\
\boldsymbol{\psi} &= (\psi_1, \ldots, \psi_M).
\end{aligned}
$$

By applying the above procedure we have

$$
\begin{aligned}
F &= dA + A^2 = dA = \mathrm{Tr}\,d\mathbf{a}, \\
C &= \frac{1}{2\pi i}\int d\,\mathrm{Tr}\,\mathbf{a}.
\end{aligned}
$$

In the case where the one-particle states have no level crossings, the expression simply reduces to the sum of the Chern numbers in the TKNN formula [50] as

$$
C = \sum_{j=1}^{M} c_j, \quad c_j = \frac{1}{2\pi i}\int da_j,\ a_j = \psi_j^\dagger d\psi_j.
$$

7.3.5 Quantum Hall Effect in Graphene

Now we are ready to discuss the quantum Hall effect (QHE) around the Dirac (charge-neutrality) point, with a filled Dirac sea. We can do so by combining the method described above with some technique originally developed for lattice gauge theories [58], and the computed Hall conductivity for graphene is as displayed in Fig. 7.8(b), third column for the Chern numbers against Fermi energy [8]. Dirac-like behaviour [59, 60],

$$\sigma_{xy} = -(2n+1)\frac{e^2}{h}, \tag{7.5}$$

(with the spin degeneracy of two suppressed here) is clearly shown in a region around the Dirac point. We can immediately notice an intriguing point here: if we look at the band dispersion of graphene on the whole Brillouin zone (Fig. 7.1, right panel), the Dirac cone with the k-linear dispersion occurs only in the vicinity of K and K′ points. So what would be the fate of the graphene QHE when we shift E_F away from the charge-neutrality point? The figure shows a clear answer to this question: the Dirac-like QHE persists *all the way up to* the van Hove singularities, which can be identified as the energies at which saddle points occur in the dispersion. Beyond each of these energies, the usual QHE with $\sigma_{xy} = -N\frac{e^2}{h}$ (N: usual Landau index) takes over, but this is accompanied by a *huge jump* with a sign change in the Hall conductivity. The anomaly at the van-Hove singularities is topological in that it is a boundary between different sequences of topological quantum numbers.

It is also possible to calculate these topological quantum numbers algebraically in terms of the TKNN formula [8]. We can perform this by noting that the honeycomb lattice can be continuously deformed into the usual square lattice or into the π-flux lattice by introducing a diagonal (third-neighbour) transfer in the former. Then we can use the adiabatic continuity for the topological numbers in the TKNN Diophantine equation to derive those in the honeycomb lattice from those in the square lattice, as depicted in Fig. 7.8. The calculation can also be extended to the realistic multi-band electronic structure (that involves carbon's σ bands) [61].

Now, an interesting point is that the factor of two coming from the doubled Dirac cones at K and K′ inherently appears in the graphene QHE, so that the half integers we talked about in terms of the field theory is actually hidden in the Hall conductivity. We can then pose a question: is it impossible to resolve the half-integer components? As far as lattice models are concerned we cannot go around the TKNN formula, so the quantum Hall number is always integer, but we can go around the Nielsen-Ninomiya theorem to resolve the fermion doubling by considering a lattice model in a wider (i.e., chiral-symmetry breaking) class. Watanabe et al. considered a lattice model in which the relative energy between the two Dirac points is systematically shifted (Fig. 7.9(b)) [21, 22]. With an explicit calculation of the Chern number, we can confirm that each Dirac cone does indeed contribute to the Hall conductivity as the half odd integer series $(\ldots, -3/2, -1/2, 1/2, 3/2, \ldots)$ when the Fermi energy traverses the (shifted sets of) Landau levels. The model has a complex

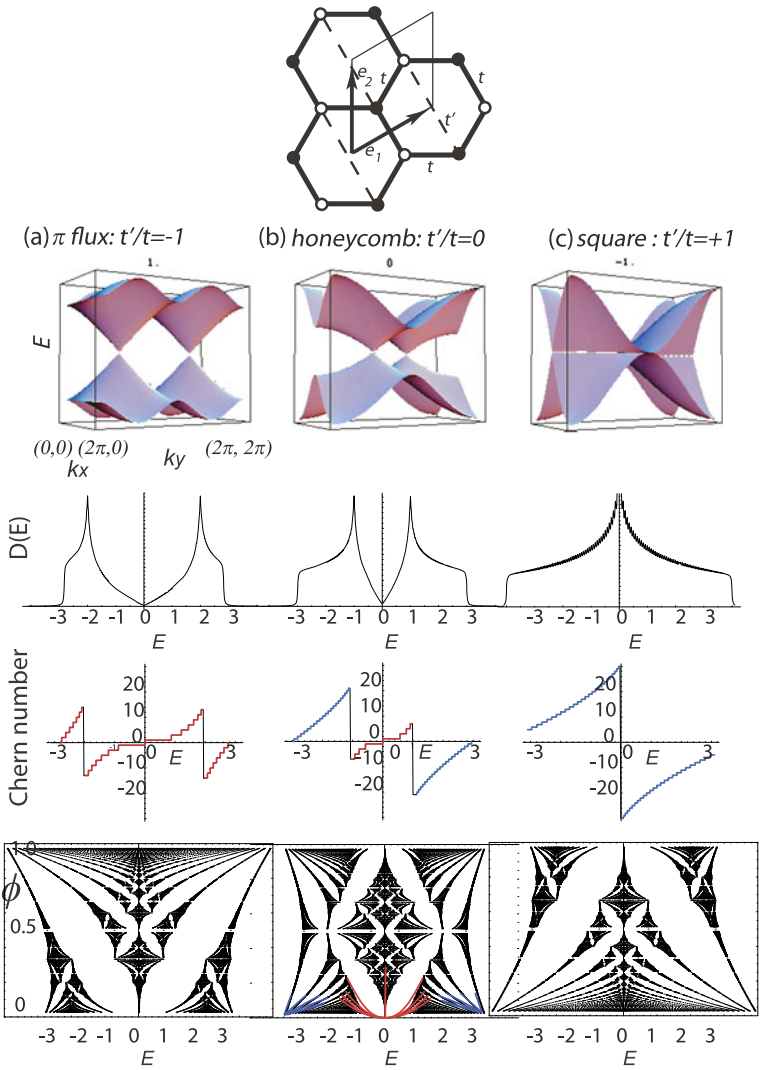

Fig. 7.8 For a honeycomb lattice (*top inset*) with an extra transfer t' (*dashed lines*), energy dispersion (*first column*), density of states (*second*), Chern number (*third*) with red lines indicating the graphene QHE, and Hofstadter's diagram, i.e., energy spectrum against the magnetic flux ϕ (*fourth*) are shown for (**a**) $t'/t = -1$ (π-flux lattice), (**b**) $t'/t = 0$ (honeycomb), and (**c**) $t'/t = 1$ (*square*) [8]. For the honeycomb Hofstadter's diagram, the Dirac-like Landau fan ($\propto \sqrt{B}$) and the 2DEG-like ones ($\propto B$) are indicated

transfer, and reminds us of Haldane's model for the "anomalous quantum Hall effect" in which a complex-transfer model accommodates Landau levels despite the total magnetic flux being zero [62] (Fig. 7.9(a)). In this model, two Dirac cones are made massive one by one, while the model in [21, 22] has two, massless cones

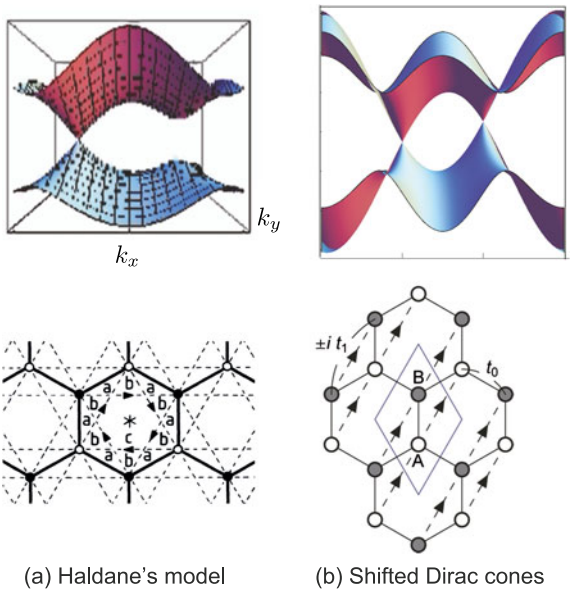

Fig. 7.9 Energy dispersion (*top column*) and the lattice model (*bottom*) for (**a**) Haldane's model for the anomalous quantum Hall effect [62], and (**b**) shifted Dirac cones [21, 22]

shifted in energy. The model, with a complex transfer, may seem unrealistic, but this can be realised in cold atoms on an optical lattice, where non-Abelian gauge structure can be experimentally realisable from an intra-atomic degree of freedom with a fine-tuning of parameters [23, 63]. This is related to a field theory in which a two-component (two hyperfine components in the case of cold atoms) fermion systems can accommodate non-Abelian gauge fields as shown by Wilczek and Zee in 1984 [53].

7.4 Bulk-Edge Correspondence for the Chiral-Symmetric Dirac Fermions

7.4.1 Boundary Physics of Graphene

Usually, effects of edges are negligible for bulk systems, since edge (or surface) states only cover a spatial dimension smaller by one than that in the bulk. However, it often happens, both in condensed-matter physics and in field theories, that the bulk properties are intimately related with the "boundary states" when the system is finite. A remarkable example is the "topological states" in which the bulk state in fact dictates the way in which the edge states appear. So let us look at the physics for graphene, where the meaning of the "topological states" will be clarified.

A typical example of the topological states is the one that historically appeared for the first time, namely the quantum Hall system. In the quantum Hall effect (QHE) [5], the quantisation of the Hall conductivity as a bulk property is connected

to the edge Hall conductivity, as first recognised by Laughlin and subsequently by various authors [19, 64–66]. When the bulk has an energy gap (the Landau gap in the case of a QHE system), which is not related to any order parameters, the gap closes around edges. We can then question how the gapless edge modes affect the properties of the system. As discussed in Sect. 7.2, the Hall conductivity in the bulk has a topological meaning of the first Chern number. We can also show that the edge transport has its topological meaning. So the question is how these two topological numbers are related. From a topological argument we can show that the two are in fact identical, which is called the "bulk-edge correspondence" [19]. In this sense, the bulk Hall conductivity and the edge Hall conductivity are one and the same. Experimentally, for the usual two-dimensional electron gas in semiconductor heterostructures, experimental results indicate that the Hall current flows both in the bulk and along the edges [5].

Thus the QHE can be explained either as a bulk phenomenon or an edge phenomenon. Mathematically, one can recognise the edge topological number as a winding number (the number of times a zero point winds around the origin on the complex energy surface [66]), which can be shown to be the same as the Chern number for the bulk, despite the completely different expressions [19]. The bulk-edge correspondence is now widely accepted, and applied for various physical systems. They include gapped quantum spins [67–69], cold atoms [70], photonic crystals [71–73], and quantum spin Hall states [74, 75]. There, we can regard a gapped bulk as a vacuum, while edge states as a kind of particles.

In the case of graphene, the bulk-edge correspondence plays a two-fold role. On one hand, graphene has a peculiar quantum Hall topological numbers distinct from those in the usual 2DEGs, and we can interpret this in terms of the bulk-edge correspondence for Dirac fermions [8, 40]. While this appears already on the level of effective Dirac field (around K or K′ point), the second aspect concerns the (honeycomb) lattice structure—the edge states only appear, reflecting the honeycomb lattice structure, along zigzag edges (while absent along armchair edges) in zero magnetic field as first recognized by Fujita and coworkers [40]. The latter point has an interesting analogy in superconductors [17, 20].

7.4.2 Types of Edges and Zero-Energy Edge States

In the tight-binding model described in Sect. 7.2, the appearance of zero-energy edge states are very simply understood. In a sample with edges, we can have $N_\bullet \neq N_\circ$, say, $N_\bullet > N_\circ$. Then the nonzero, off-diagonal matrix $\mathbf{D}$ in Sect. 7.2.1 is not a square matrix, and from a simple linear algebra we can show that there are as many as $N_\bullet - N_\circ$ exact zero-energy states. The situation $N_\bullet > N_\circ$ occurs for zigzag edges, where an edge is terminated by $\bullet$ (while an armchair edge has equal numbers of $\bullet$s and $\circ$s, as displayed in Fig. 7.10. Whereas a Dirac field theory can capture the low-energy physics for each of K and K′ points in the Brillouin zone, we have thus to go back to the honeycomb lattice model if we want to address the problem of boundary

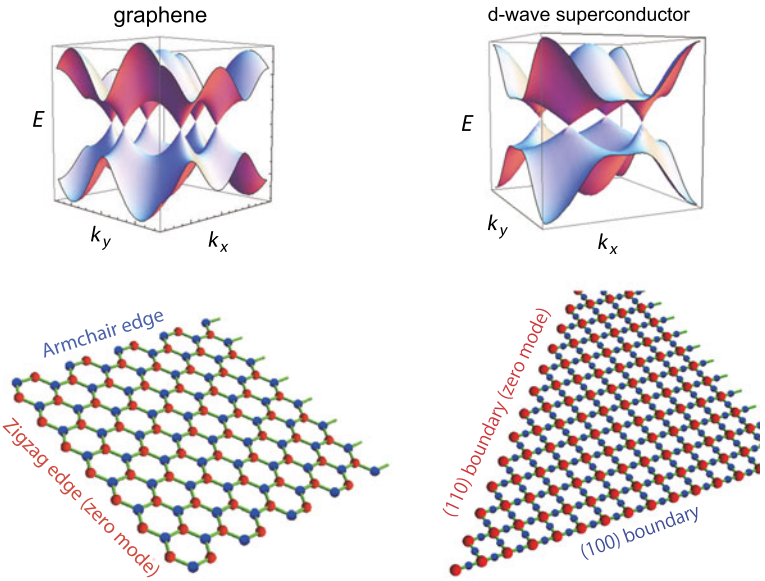

Fig. 7.10 *Left*: Dispersion (*top panel*) and two kinds of edges (*bottom*) for graphene. Atoms on the Klein edge are not shown. *Right*: Dispersion of the Bogoliubov quasiparticle and two kinds of edges for a two-dimensional d-wave superconductor, represented here as a CuO_2 plane (after [78])

states. One-body energy dispersion for these edges are shown in Fig. 7.11 [40]. One can immediately notice an edge mode that has a flat dispersion at $E = 0$ for the zigzag edge, as discovered by Fujita and coworkers [40]. The wavefunction on the flat band is localised along the zigzag boundary and decays exponentially into the bulk. The edge states are in fact governed by the chiral symmetry of graphene, and indeed provides an example of the bulk-edge correspondence in the presence of chiral symmetry as elaborated below. While this is a one-body picture, appearance of such edge states has been confirmed in the local density approximation [76]. Experimentally, edge states have long been observed with STM [77] (Fig. 7.11).

7.4.3 Edge States and Chiral Symmetry

Thus a crucial question is whether the appearance of the edge states localised along zigzag boundaries is an accident or not. This is answered by the bulk-edge correspondence for chiral-symmetric Dirac fermions, where (Z_2) Berry phase (sometimes called Zak phase) is responsible for a topological reason [17, 20]. To facilitate discussion let us take a cylindrical geometry with a periodic boundary condition along y. Now the Hamiltonian without boundary in two dimensions are expressed as

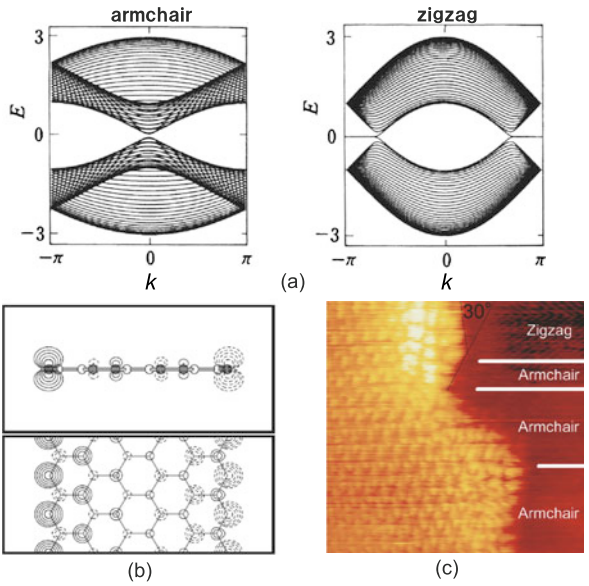

Fig. 7.11 (**a**) One-particle energy dispersion along the edge for graphene with zigzag or armchair edge [40]. (**b**) Charge density in the density functional theory for graphene [76]. (**c**) An STM image of charge densities near edges [77]

$$H^{2D} = \sum_{k_x,k_y} H_Z(k_x,k_y) \quad \text{or} \quad \sum_{k_x,k_y} H_A(k_x,k_y).$$

Here $H_Z(H_A)$ are Hamiltonians where we take a unit cell in such a way that zigzag (armchair) boundaries appear when the boundary condition along one of the primitive vectors is open. We call this direction y. We also recall that the honeycomb system has the chiral symmetry ($\{H,\gamma\}=0$).

As for the bulk, we can consider the one-dimensional energy bands against k_y parametrised by k_x. By filling the negative energy state, one has a unique many-particle configuration. Note that the two-dimensional energy gap closes at K and K′ points, so that the one-dimensional dispersion as a function of k_y is gapped except at the two gap closing momenta. Let us write this many-particle configuration with negative-energy states filled as $|k_x,k_y\rangle_{Z,A}$ with $H_{Z,A}(k_x,k_y)|k_x,k_y\rangle_{Z,A} = E(k_x,k_y)|k_x,k_y\rangle_{Z,A}$, and define the Berry (Zak) phase,

$$-i\gamma^{1D}_{Z,A}(k_y) = \int_0^{2\pi} dk_x \, {}_{Z,A}\langle k_x,k_y|\frac{\partial}{\partial k_x}|k_x,k_y\rangle_{Z,A}\Big|_{k_y:\text{fixed}}.$$

According to a generic argument for the Berry phase of chiral symmetric systems [18], the Berry phase is shown to take only two values, 0 or π (mod 2π), if the one-dimensional system is gapped against k_y. This is the Z_2 Berry phase.

Then using an adiabatic continuity and the locality of the chiral symmetry, one has a sufficient condition for the appearance of the zero-mode edge states in terms of the Z_2 Berry phase as [17, 20]

Table 7.1 Correspondence between graphene and two-dimensional d-wave superconductors [20, 81, 82]

Physical observables	Graphene	2D d-wave superconductors
Massless Dirac dispersion	Band dispersion	Dispersion of Bogoliubov quasiparticle
Chiral symmetry	Bipartite honeycomb lattice	Time-reversal invariance
Zero-mode boundary states	Fujita states along zigzag edges	Andreev bound states along (1, 1) edges
Local chiral-symmetry breaking	Spin alignment along zigzag edges	Broken time-reversal symmetry along (1, 1) boundaries

$$\gamma_{Z,A}^{1D} = \begin{cases} \pi & \text{zero-mode edge states must exist,} \\ 0 & \text{not necessarily.} \end{cases}$$

Namely, the Berry phase of π is a sufficient condition for the zero-mode edge states to exist, so the above property is consistent with the presence (absence) of zero-mode edge states along zigzag (armchair) boundaries, since they have $\pi(0)$ phase. This is the bulk-edge correspondence of the chiral symmetric Dirac fermions.

We have an interesting analogy of this in the excitation modes of Bogoliubov quasiparticle excitations in the two-dimensional d-wave superconductors, which belongs to the same universality class in the present context. This comes from the fact that the Bogoliubov-de Gennes equation describing the excitation mode in a d-wave superconductor has the same form as the Dirac equation we have described for graphene. In the former system with tetragonal symmetry there are four Dirac cones (Fig. 7.10). The bulk-edge correspondence translates into the Andreev bound states of the d-wave superconductor in the edge along the $(1, 1)$ crystallographic direction, and the chiral symmetry translates into the time-reversal symmetry (i.e., the superconducting order parameter be real), which is broken in this boundary state. As is known theoretically [78, 79] and experimentally [80], the existence and nature of Andreev bound states is dictated by the boundary, which is thus understood by the Z_2 Berry phases of the Bogoliubov states [17, 20]. The parallelism between graphene and d-wave superconductors is summarised in Table 7.1 and Fig. 7.10.

This attests the universality of the bulk-edge correspondence for Dirac dispersion. We can further argue the following. The chiral symmetry on a lattice system implies the existence of zero-mode flat bands for some type of boundaries. When we regard the boundary states as one-dimensional systems, it is natural to expect some instability to set in. Such a boundary Peierls instability has indeed physical implications as an appearance of the local spin alignment in graphene [76, 81, 82], or local vortex generation supplemented by a local breaking of the time-reversal symmetry in d-wave superconductors [83, 84] (see Table 7.1).

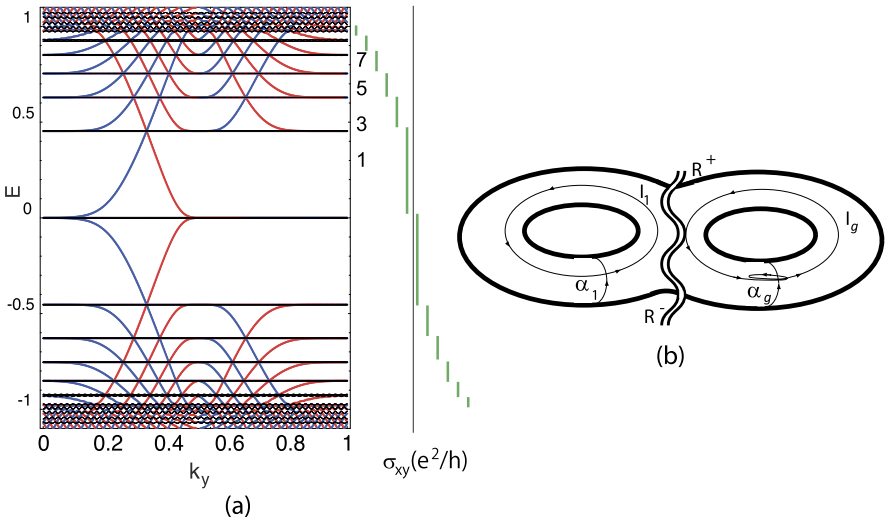

Fig. 7.12 (**a**) Energy spectrum against the wavenumber normal to the edges for a graphene QHE system with zigzag edges [8]. *Left* (*right*) edge modes are shown as *blue* (*red*) *lines*. The quantised values of the bulk Hall conductance in units of e^2/h are shown by numbers and *green bars on the right*. Here the magnetic flux per hexagon is $(1/51)\phi_0$. (**b**) A Riemann surface for the complex energy for the Bloch function (see text). Its genus coincides with the number of energy gaps [8, 66]

7.4.4 Quantum Hall Edge States of Graphene

While the above is for zero magnetic field, we can examine graphene in the quantum Hall regime for both of the bulk and edge states along the chiral/topological argument. Namely, one can extend the theory for the square lattice [66] to graphene [8]. When the Fermi energy is in the j-th energy gap from below, the Hall conductivity, σ_{xy}^{edge}, of the system with zigzag boundaries is analytically determined by the behaviour of the edge states in the Laughlin argument. It is explicitly expressed by the topological number I_j as [8, 19, 66]

$$\sigma_{xy}^{edge} = -\frac{e^2}{h} I_j .$$

Although we do not go into detail, the topological flavour is the following: The edge-state wavefunction for each cylindrical momentum k_y is given by an analytic continuation of the Bloch wavefunction of the one-dimensional system. For this continuation, it is necessary to consider a complex energy surface, which turns out to have a genus $g = q - 1$ Riemann surface, Σ_g, for a magnetic flux per hexagon of p/q in units of Φ_0. When the momentum k_y is scanned from 0 to 2π, the zeros of the edge-state wavefunctions move around the perforations (Fig. 7.12(b)) of Σ_g, which are gap regions. Since 0 and 2π are equivalent, the locus forms a loop, and the winding number of the loop is I_j which gives the Hall conductivity when the

Fermi energy is in a gap. We can further show that the winding numbers assigned to the gaps and the Chern number, C_j, assigned to the jth band are directly related as

$$C_j = I_j - I_{j-1}.$$

For a many-electron configuration, we have $\sigma_{xy}^{bulk} = -\frac{e^2}{h}\sum_{\ell}^{j} C_\ell$, so that we end up with

$$\sigma_{xy}^{bulk} = \sigma_{xy}^{edge}.$$

This is the analytical derivation for the bulk-edge correspondence for graphene [8].

7.4.5 $n = 0$ *Landau Level and the Zero Modes*

In the conventional quantum Hall system, the local charge density is depleted from the boundaries due to the boundary potential [65], which results in locally-raised Landau levels with gapless edge modes traversing adjacent Landau levels and intersecting the Fermi energy. A similar situation occurs in graphene for armchair boundaries [85] (see Fig. 7.13(b)). For zigzag edges, on the other hand, the situation is quite different. While the Fujita state localised along a zigzag edge and its flat band are considered for zero magnetic field, we can show that quite different, but still zero-energy, states appear even in strong magnetic fields. Since the bulk has the $n = 0$ Landau level just at the zero energy in a magnetic field, the zero-mode edge states are embedded in the Landau level. We can show that an effect of this appears as an *enhancement* (as opposed to depletion) of the local charge density on one of the sublattices along the zigzag boundary [69, 85] (see Fig. 7.13(a)). The edge states, being resonant, are hybridised with the bulk Landau states, with the edge-state amplitude decaying exponentially into the bulk with a decay length of the order of the magnetic length. Hence Arikawa et al. called this a "topological compensation" [85]. This contrasts with the zero magnetic field case, where the Fujita state decays into the bulk with a power law. These states may be closely related with experimental results on scanning tunnelling spectroscopy in graphene [86].

7.5 Optical Hall Effect in Graphene

So far we have described the (static) Hall conductivity. Among various fascinations in graphene, optical properties are particularly interesting, as described in the chapter by Potemski and coauthors in this volume. So we can raise a question: does graphene exhibit interesting optical properties in the quantum Hall regime? The question is realistic, since recent experimental advances in spectroscopy in the THz regime are making optical measurements feasible for QHE systems with the relevant energy scale (cyclotron energy) being THz in magnetic fields of a few tesla.

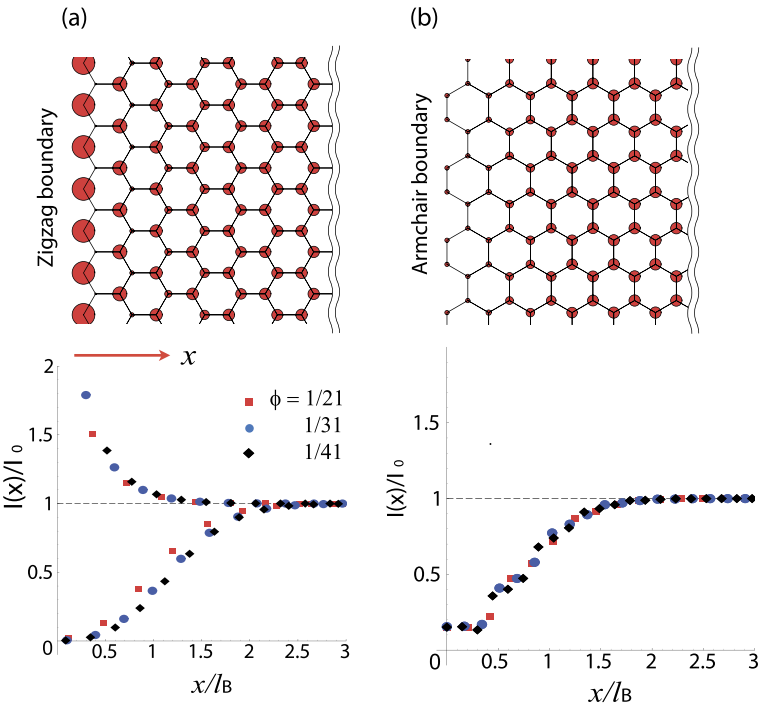

Fig. 7.13 (**a**) *Top*: Local density of states at $E = 0$ (here represented by the size of a *circle* at each atom) around a zigzag boundary where the $n = 0$ Landau level and the zero-modes for the edge states coexist [69, 85]. *Bottom*: The charge density against the distance from the boundary, x, normalized by the magnetic length, ℓ_B, for various values of the magnetic flux per hexagon, ϕ. (**b**) Similar plot for an armchair boundary

For instance, we can examine a possibility of a Landau-level laser under strong pumping [87].

The optical *Hall* conductivity $\sigma_{xy}(\omega)$, on the other hand, is especially interesting. Morimoto et al. have looked into this problem theoretically [88], and predicted that (i) in the usual two-dimensional electron gas (2DEG) formed in the semiconductor heterostructures, the plateau structure is retained, up to significant degree of disorder, even in the ac (THz) regime, although the heights of the plateaus are no longer quantised in the ac regime. The unexpected robustness is attributed to an effect of localisation, where the existence of extended states and mobility gaps ensures the step structures in the ac Hall conductivity. (ii) For graphene, the plateau structure in the optical Hall conductivity is again predicted, where the structure reflects the graphene Landau levels. (iii) The optical Hall conductivity should be detected through Faraday rotation measurements (Fig. 7.14(b)) as a step structure in Faraday rotation angle. Its magnitude is estimated to be of the order of the fine-structure constant α ($\sim$10 mrad), which is within the experimental feasibility. If one utilizes a free-standing graphene, for which α has been seen as transparency [89], the rotation angle is exactly the fine structure constant.

The optical Hall conductivity can be generally calculated with the Kubo formula,

$$\sigma_{xy}(\omega) = \frac{i\hbar e^2}{L^2} \sum_{\epsilon_a < \varepsilon_F} \sum_{\epsilon_b \geq \varepsilon_F} \frac{1}{\epsilon_b - \epsilon_a} \left(\frac{j_x^{ab} j_y^{ba}}{\epsilon_b - \epsilon_a - \hbar\omega} - \frac{j_y^{ab} j_x^{ba}}{\epsilon_b - \epsilon_a + \hbar\omega} \right), \quad (7.6)$$

which is the extension of the static Hall conductivity [90] to the ac response. Here ϵ_a is the eigenenergy, j_x^{ab} the current matrix elements, ε_F the Fermi energy and L the sample size. The difference in graphene from the usual 2DEG is that the eigenstates are those of the Dirac Hamiltonian, Landau levels are graphene Landau levels ($\mathrm{sgn}(n)\sqrt{n}\hbar\omega_c$ with $\omega_c = v_F\sqrt{2eB/\hbar}$), and accordingly the selection rule for the current matrix elements is $|n| - |n'| = \pm 1$ (as opposed to $|n - n'| = 1$ in 2DEG).

The theoretical result in Fig. 7.14(a) numerically obtained with exact diagonalisation (to incorporate the localisation effect) shows that, while there is a series of cyclotron resonances between graphene Landau levels, a flat (plateau) structure is clearly seen in the optical Hall conductivity. Robustness of the plateaus can be discussed in terms of Anderson localisation, more precisely in terms of the dynamical scaling argument for the ac response [91].

The optical Hall conductivity can be detected as the Faraday rotation angle Θ_H which is directly connected to the optical Hall conductivity via

$$\Theta_H \simeq \frac{1}{(n_0 + n_s)c\varepsilon_0} \sigma_{xy}(\omega), \quad (7.7)$$

where $n_0(n_s)$ is the refractive index of air (substrate). Hence the plateau structure in $\sigma_{xy}(\omega)$ should be observed as steps in Faraday rotation, where the step size is estimated for the QHE regime by putting $\sigma_{xy} \sim e^2/h$, i.e., $\Theta_H \sim [2/(n_0 + n_s)]\alpha \sim 7$ mrad, where $\alpha = e^2/(4\pi\varepsilon_0\hbar c)$ is the fine-structure constant. Experimental detection of the plateau structure was first done for a 2DEG system [92]. Then the structure was observed in graphene as shown in Fig. 7.14(c) [93]. Thus the message is that, although the Hall conductivity is no longer a topological invariant in the ac regime, we still have its remnant in the ac response.

7.6 Nonequilibrium Control of Topological Property

So far we have concentrated on equilibrium (or linear-response) properties of graphene and their manipulations. Now, an entirely different and novel avenue exists in nonequilibrium situations. Let us briefly describe this, which is now called "Floquet topological states". It was Oka and Aoki who first pointed out that illuminating an intense circularly polarised light to the two-dimensional (2D) Dirac system (honeycomb model for graphene) can change and control topological properties of its quantum states [94]. Then, a dc Hall conduction is shown to emerge in zero magnetic field (Fig. 7.15(a)). Namely, the graphene QHE, which is a topological phenomena associated with Chern quantum number, can be generated as a nonequilibrium state. Emergence of the "photovoltaic (or light-induced) quantum Hall effect" indeed comes from the laser that dynamically opens a topological gap

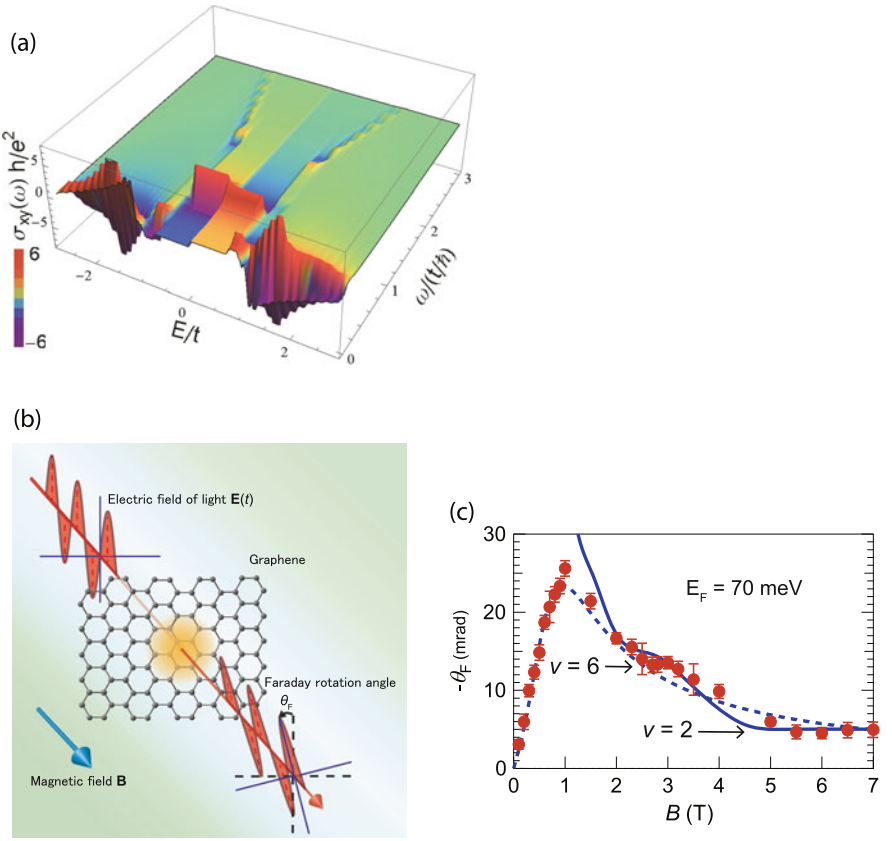

Fig. 7.14 (**a**) Optical Hall conductivity $\sigma_{xy}(\varepsilon_F, \omega)$ plotted against Fermi energy ε_F and frequency ω calculated for the honeycomb tight-binding model with random hopping $\sqrt{\langle \delta t^2 \rangle} = 0.1t$ which respects the chiral symmetry [34, 88]. (**b**) Schematic magneto-optical Faraday rotation in graphene. (**c**) Experimental result for magnetic field dependence of the Faraday rotation at the photon energy of 4 meV (1 THz) [93]. *Dashed curve* is calculated by the Drude model, while *solid curve* is the theoretical calculation obtained from the Kubo formula with the exact diagonalisation method

(as opposed to the usual band gap) at the Dirac points in the Floquet spectrum. Below, we briefly sketch how this phenomenon physically arises.

In an intense ac field such as laser, we need a framework that can deal with strong ac modulations. Floquet's formalism is just that, which is applicable to time-periodic fields so that the formalism is a temporal analogue of Bloch's formalism for spatially periodic potentials. For the time-dependent Schrödinger equation (with $\hbar = 1$), $i\frac{d}{dt}\Psi(t) = H(t)\Psi(t)$, where the Hamiltonian $H(t)$ is assumed to be periodic in time with period $\mathcal{T}$, $H(t + \mathcal{T}) = H(t)$, Floquet's theorem states that there exists a solution of the form $\Phi_\alpha(t) = e^{-i\varepsilon_\alpha t}u_\alpha(t)$, where $u_\alpha(t) = u_\alpha(t + \mathcal{T})$ is a periodic function of t, and the real number ε_α is called the Floquet quasienergy. To

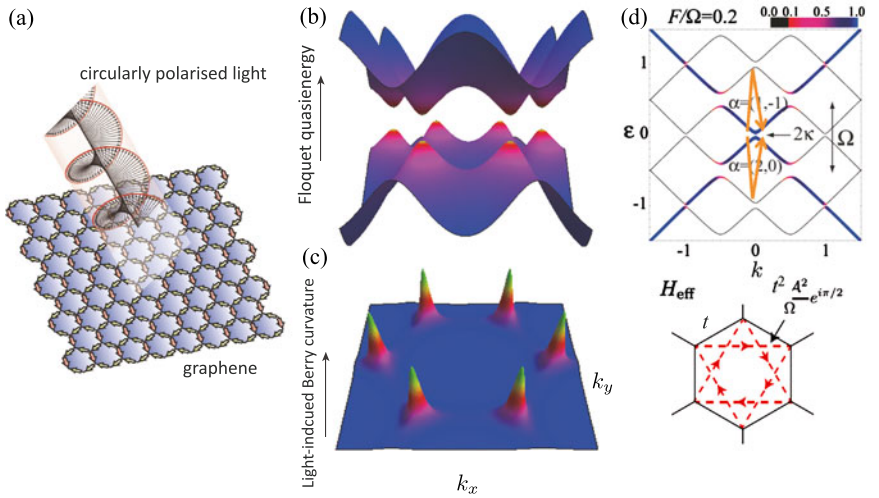

Fig. 7.15 (**a**) Graphene in a circularly polarised laser, and emergence of the photoinduced quantum Hall effect in zero magnetic field is schematically shown. (**b**) Its Floquet quasi-energy spectrum, in which a gap opens dynamically at K and K′ points. (**c**) Associated light-induced Chern density. (**d**) *Top*: Floquet quasi-energy (*black curves*) plotted against k_x with $k_y = 0$ for $F/\Omega = 0.2$. The colour coding represents the weight of the $m = 0$ component. Arrows represent the leading second-order processes. *Bottom*: An effective model from the second-order processes, which is equivalent to Haldane's model (Fig. 7.9). (After [94, 95])

determine ε_α, we can Fourier expand as $u_\alpha(t) = \sum_n e^{-in\Omega t} u_\alpha^n$ (with $\Omega = 2\pi/\mathcal{T}$), where u_α^n is called the nth Floquet mode, for which the Schrödinger equation reads

$$\sum_n (H_{mn} - n\Omega\delta_{mn}) u_\alpha^n = \varepsilon_\alpha u_\alpha^m,$$

where

$$H_{mn} \equiv \frac{1}{\mathcal{T}} \int_0^{\mathcal{T}} dt\, e^{i(m-n)\Omega t} H(t)$$

is the Floquet Hamiltonian. Thus the quasienergies $\{\varepsilon_\alpha\}$ are the eigenvalues of the infinite dimensional Floquet matrix $H_{mn} - n\Omega\delta_{mn}$, where each element corresponds to the probability amplitude of m photon absorption and n photon emission. Thus the problem is cast into a time-independent one, but the price to pay is now we have a matrix equation spanned by the Floquet modes (or photon-dressed states). Namely, if ε_α is an eigenvalue, $\varepsilon_\alpha + n\Omega$ (n: an integer) is another eigenvalue, so that we have an infinite ladder of energies with spacing Ω.

Now, if we apply this formalism to a tight-binding honeycomb lattice in a circularly polarised light, the Floquet spectrum consists of a ladder of graphene dispersion, and specifically a ladder of Dirac cones around K and K′ points as depicted in Fig. 7.15(d). Since the set of Floquet modes exhibit avoided level crossing due to the off-diagonal elements of H_{mn}, a gap dynamically opens at each crossing,

specifically at the Dirac points (Fig. 7.15(b)) [94]. Floquet's quasi-energy can be expressed as

$$\varepsilon_\alpha = \langle\langle \Phi_\alpha | H(t) | \Phi_\alpha \rangle\rangle + \Omega \gamma_\alpha^{AA}/2\pi,$$

with Φ_α the Floquet state and double brackets the inner product averaged over the time period. Here the first term is the dynamical phase while $\gamma_\alpha^{AA} = \mathcal{T} \langle\langle \Psi_\alpha | i\partial_t | \Psi_\alpha \rangle\rangle$ represents the Aharonov-Anandan phase (non-adiabatic generalisation of Berry's phase) [96]. Physically, a circularly polarised light as represented by a vector potential $\mathbf{A}_{ac}(t) = (F/\Omega)(\cos\Omega t, \sin\Omega t)$ makes each crystal-momentum to follow a motion $\mathbf{k} - \mathbf{A}(t)$. Around a Dirac cone, this gives rise to a nonzero Aharonov-Anandan phase,

$$\gamma_\alpha^{AA} = \pm\pi \left\{ \left[4\left(F/\Omega^2\right)^2 + 1 \right]^{-1/2} - 1 \right\},$$

where $\pm$ refers to $\alpha = (\text{hole}, m = -1)$ and (electron, 0) with hole/electron indicating the negative/positive energy branch. In the adiabatic limit ($\Omega \to 0$) this reduces to Berry's phase of $\pm\pi$. It is this geometric effect that opens the gap at the Dirac points in the Floquet spectrum. The size of the nonequilibrium topological gap is [94]

$$\kappa = \frac{1}{2}\left[\sqrt{4(F/\Omega)^2 + \Omega^2} - \Omega \right] \sim v_F^2 a^2 e^2 \left(F^2/\Omega^3\right),$$

where v_F is graphene's Fermi velocity, and a the lattice constant, so that the required field strength scales as $F \propto \Omega^{3/2}$. This gap opens only when circularly (or elliptically) polarised light is applied which breaks the time reversal symmetry.

The topological quantum number (quantum Hall number) can be computed in terms of a Floquet extension of the Kubo formula for single-particle states as

$$\sigma_{xy}(\mathbf{A}_{ac}) = i \int \frac{d\mathbf{k}}{(2\pi)^2} \sum_{\alpha,\, \beta \neq \alpha} \frac{[f_\beta(\mathbf{k}) - f_\alpha(\mathbf{k})]}{\varepsilon_\beta(\mathbf{k}) - \varepsilon_\alpha(\mathbf{k})} \frac{\langle\langle \Phi_\alpha(\mathbf{k}) | J_y | \Phi_\beta(\mathbf{k}) \rangle\rangle \langle\langle \Phi_\beta(\mathbf{k}) | J_x | \Phi_\alpha(\mathbf{k}) \rangle\rangle}{\varepsilon_\beta(\mathbf{k}) - \varepsilon_\alpha(\mathbf{k}) + i0},$$

where $\mathbf{J}$ is the current operator, which results in a dc Hall current in a strongly ac-driven system. Important differences in the nonequilibrium situation are: ε_α is the Floquet quasi-energy, f_α is a nonequilibrium distribution function, and the matrix elements are computed from the Floquet states Φ. Note that the sum is taken over the whole Floquet spectrum with a series of Floquet sidebands (i.e., one-photon dressed states, two-photon dressed states, ...). We can cast the formula into a Floquet extension of the conventional Thouless-Kohmoto-Nightingale-den Nijs (TKNN) formula [50], which reads [94]

$$\sigma_{xy}(\mathbf{A}_{ac}) = e^2 \int \frac{d\mathbf{k}}{(2\pi)^2} \sum_\alpha f_\alpha(\mathbf{k}) \left[\nabla_{\mathbf{k}} \times \mathcal{A}_\alpha(\mathbf{k}) \right]_z,$$

where the gauge field,

$$\mathcal{A}_\alpha(\mathbf{A}_{ac}; \mathbf{k}) = -i \langle\!\langle \Phi_\alpha(\mathbf{k}) | \nabla_{\mathbf{k}} | \Phi_\alpha(\mathbf{k}) \rangle\!\rangle,$$

is defined in terms of the Floquet states and its rotation, $\mathcal{B}_\alpha(\mathbf{A}_{ac};\mathbf{k}) = \nabla_{\mathbf{k}} \times \mathcal{A}_\alpha(\mathbf{k})$, gives the photo-induced Berry's curvature (i.e., Chern density). Figure 7.15(c) depicts the photo-induced curvature, and we can see that peaks do appear around the Dirac points. This contrasts with a trivial gap (e.g., from the level offset between A and B lattice sites), where the curvature would have opposite signs between the K and K′ points, leading to a zero net effect.

The light-induced quantum Hall effect described here is intimately related to Haldane's model of the "quantum Hall effect without Landau levels" [62], which is sometimes called the quantum anomalous Hall effect in zero magnetic field. Haldane proposed a honeycomb lattice model, where a complex second-neighbor hopping term is added (Fig. 7.9(a)). This term opens a gap at the Dirac points, and the Hall coefficient takes a quantized value, despite the model having zero total magnetic flux. Now, after the proposal for graphene of the light-induced quantum Hall effect [94], Kitagawa et al. have noticed that, if we take the leading contribution (second-order process between the original and a photon-dressed states) in the Floquet formalism in graphene, the Haldane model is dynamically realized as a Floquet model (Fig. 7.15(d)) [95].

The idea for the Floquet topological state is so general that the effect should occur in various systems besides graphene, such as the surface Dirac states of topological insulators [95, 112], or bilayer graphene [97] or quantum wells [98]. While the phenomenon has features common to topological insulators and superconductors [99, 100], this is a purely nonequilibrium, nonlinear effect, as evident from the topological gap $\propto F^2/\Omega^3$, where F is the laser field intensity and Ω the frequency. A classification for the topological Floquet states, even going beyond two spatial dimensions, was put forward [101].

Experimentally, graphene illuminated by circularly polarised THz lasers has recently begins to be studied, and a light-induced Hall effect was observed as an associated edge current [102, 103]. Although a theory predicts that the Hall effect should be quantised in the scaling limit [104], the experiments at the moment show a classical Hall effect, i.e., the Hall current is not quantised. Several factors such as disorder, electron-phonon and electron-electron interactions may cause this discrepancy.

7.7 Chiral Symmetry for Interacting Electrons

Up to this point we have concentrated on the one-body problem. While many-body effects in graphene is a most interesting problem when we consider the electron-electron interaction, this is out of the scope of the present chapter. However, let us explain here that the chiral symmetry can play important roles even in many-body physics. As in the one-body problem, we can focus on the $n = 0$ Landau level around the charge-neutrality point. Then we can pose a question: can many-body interaction exert interesting effects right at the Dirac point? Soon after the observation of the graphene quantum Hall effect, experiments have indeed discovered new conductivity plateaus, most notably at the Landau level filling $\nu = 0$, for strong enough

magnetic fields [105, 106]. The new plateaus have attracted considerable theoretical attention [107]. Specifically, unusual behaviours at $\nu = 0$ distinct from other fillings are observed, including an insulating behaviour with exponentially diverging longitudinal resistivity suggestive of a Mott transition at half filling [108]. More recent experiments based on high quality samples revealed a spin-unpolarised aspect of the $\nu = 0$ state [109].

Now, the chiral symmetry discussed in this chapter in one-body physics should also be important for many-body problems in the $n = 0$ Landau level. This is because we can characterise many-body states by the chiralities of filled zero modes. Indeed, for a spin-split $n = 0$ Landau level, we can show that the ground state is a chiral condensate, i.e., a many-body state in which electrons occupy the eigenstates of the chiral operator, where the state has a finite excitation energy with a topological two-fold degeneracy [37–39]. The total Chern number for the chiral condensate turns out to be zero, where the contribution from the Dirac sea (negative-energy states) cancels the zero-mode Chern number, but a topological nature of the state appears as edge states, which is an example of the bulk-edge correspondence in topological systems [19]. This line of approach can be extended to spin-unpolarised states of the $\nu = 0$ Landau level by extending the picture of the chiral condensate to accommodate the spin degree of freedom. Hamamoto et al. have suggested that the many-body ground state is a doubly-degenerate *spin-resolved chiral condensate*, in which all the zero-energy states with up spin are condensed into chirality $+$, while down spins to chirality $-$ [38, 39]. The charge gap in this situation turns out to grow linearly with the magnetic field, in qualitative agreement with the experiments [109, 110].

To describe the many-body problem for $n = 0$, it is useful to consider a projected Hamiltonian, $\tilde{H} = P(H_{kin} + H_U + H_J)P^{-1}$, with P denoting the projection onto the $n = 0$ Landau level. The kinetic part is given by a tight-binding Hamiltonian,

$$H_{kin} = -t \sum_{\langle ij \rangle} \sum_{\sigma=\uparrow\downarrow} e^{i\theta_{ij}} c^{\dagger}_{i\sigma} c_{j\sigma} + \text{h.c.},$$

where σ denotes spin and θ_{ij} the usual Peierls phase. To derive the effective Hamiltonian in the $n = 0$ Landau level in a many-body case, we can first diagonalise the kinetic term. Due to the chiral symmetry, $\{H_{kin}, \gamma\} = 0$ with γ being the chiral operator, a one-body state ψ_ε at energy ε is related to its chiral partner as $\psi_{-\varepsilon} = \gamma\psi_\varepsilon$. Thus a special situation arises at $n = 0$, where particle- and hole-states are degenerate. We denote the number of zero modes as $2M$, with M being an integer determined by the magnetic field. By reconfiguring these zero modes, one obtains a chiral basis,

$$\psi = (\psi_{1+}, \ldots, \psi_{M_+ +}, \psi_{1-}, \ldots, \psi_{M_- -}),$$

where $\{\psi_{k\pm}\}$ with $k = 1, \ldots, M_\pm$ are eigenstates of the chiral operator satisfying $\gamma\psi_{k\pm} = \pm\psi_{k\pm}$. $M_\pm$ is the degeneracy of the zero modes with chirality $\pm$, hence $M_+ + M_- = 2M$. While the kinetic energy is quenched in the $n = 0$ Landau level, the information on the kinetic part is encoded in the properties of the chiral zero modes. A simplest example is the fact that chirality designates the sublattice on

which a zero mode resides, i.e., $\psi_{k+(-)}$ has nonzero amplitudes only on A(B) sublattice.

In terms of the chiral basis, the projection onto the $n = 0$ Landau level is defined by a mapping $c^\dagger_{i\sigma} \mapsto \tilde{c}^\dagger_{i\sigma} \equiv (c^\dagger_\sigma \psi \psi^\dagger)_i$, with a row vector $c^\dagger_\sigma = (c^\dagger_{1\sigma}, \ldots, c^\dagger_{2N\sigma})$ and a projection matrix $\psi\psi^\dagger$. Note that $\tilde{c}^\dagger_{i\sigma}$ no longer obeys the canonical anticommutation relations, since the chiral basis is not complete. Alternatively, we can introduce creation operators of the zero modes, $d^\dagger_{k\sigma\pm} \equiv c^\dagger_\sigma \psi_{k\pm}$, which satisfy the anticommutation relations,

$$\left\{d_{k\sigma\chi}, d^\dagger_{l\sigma'\varepsilon}\right\} = \delta_{kl}\delta_{\sigma\sigma'}\delta_{\chi\varepsilon}, \qquad \{d_{k\sigma\chi}, d_{l\sigma'\varepsilon}\} = \left\{d^\dagger_{k\sigma\chi}, d^\dagger_{l\sigma'\varepsilon}\right\} = 0. \tag{7.8}$$

With these fermions we can rewrite the interaction Hamiltonian.

Although we do not go into detail [37–39], let us mention that, when a many-body state is constructed by occupying the chiral zero modes, the *total chirality* is conserved, since the projected interaction Hamiltonian $\tilde{H}$ commutes with an operator,

$$\mathcal{G} = \sum_{\sigma=\uparrow\downarrow} \left(\sum_{k=1}^{M_+} d^\dagger_{k\sigma+} d_{k\sigma+} - \sum_{k=1}^{M_-} d^\dagger_{k\sigma-} d_{k\sigma-} \right). \tag{7.9}$$

This enables us to diagonalise $\tilde{H}$ separately in a subspace for each sector in the total chirality. For instance, we can consider a (doubly-degenerate) chiral condensate,

$$|G_\pm\rangle = \prod_{k=1}^{M_\pm} d^\dagger_{k\uparrow\pm} \prod_{l=1}^{M_\mp} d^\dagger_{l\downarrow\mp} |D_<\rangle, \tag{7.10}$$

where $|D_<\rangle$ denotes the Dirac sea of the negative-energy states. In the above equation, the zero modes with up-spin form a chiral condensate with chirality $+$, while those with down-spin a chiral condensate with chirality $-$, or vice versa. If we restrict ourselves to the case of $M_+ = M_-$, which holds when the two sublattices contain the same number of sites, the ground state falls upon the sector of total chirality $\chi_{tot} \equiv \langle \mathcal{G} \rangle = 0$, in sharp contrast to the spinless case, where the ground state is a chiral condensate with fully polarised chirality. The many-body physics, especially for the $n = 0$ Landau level, will open a new avenue in the physics of graphene.

7.8 Concluding Remarks

We have overviewed the chiral symmetry and topological aspects in graphene physics. From this standpoint, stability of massless Dirac cones at K and K′ points and the $n = 0$ Landau level are discussed. We have also described the graphene quantum Hall effect, along with the bulk-edge correspondence for graphene from the topological point of view. We have also touched upon the optical Hall effect and nonequilibrium Hall effect in graphene. The chiral symmetry further suggests importance of possible many-body physics as the chiral condensate, etc.

We have interdisciplinary spinoffs of graphene physics in d-wave superconductors, cold atoms on optical lattices, optical graphene, Floquet topological systems, and so on, so that we can expect an interesting outlook for various directions and systems. A Dirac cone appears even in an iron-based superconductor, with an implication on the spin Hall effect [111].

Acknowledgements We wish to thank illuminating discussions with Andre Geim and Tsuneya Ando. We also appreciate discussions with Toshiaki Enoki and Yshai Avishai. The present chapter contains descriptions of authors' work in collaboration with Takahiro Fukui, Toru Kawarabayashi, Takahiro Morimoto, Takashi Oka, Haruki Watanabe, Mitsuhiro Arikawa, Shinsei Ryu and Yuji Hamamoto. These works were supported in part by Grants-in-Aid for Scientific Research, Nos. 23340112, 23654128, 24840047 and 23540460 from JSPS. The computation in this work has been done in part with the facilities of the Supercomputer Center, Institute for Solid State Physics, University of Tokyo.

References

1. K.S. Novoselov et al., Nature **438**, 197 (2005)
2. A.K. Geim, K.S. Novoselof, Nat. Mater. **6**, 183 (2007)
3. A.H. Castro Neto et al., Rev. Mod. Phys. **81**, 109 (2009)
4. Y. Zhang, Y.-W. Tan, H.L. Stormer, P. Kim, Nature **438**, 197 (2005)
5. H. Aoki, in *Comprehensive Semiconductor Science & Technology*, ed. by P. Bhattacharya, R. Fornari, H. Kamimura (Elsevier, Amsterdam, 2011), pp. 175–209
6. H.B. Nielsen, M. Ninomiya, Nucl. Phys. B **185**, 20 (1981)
7. M. Creutz, J. High Energy Phys. **17**, 0804 (2008)
8. Y. Hatsugai, T. Fukui, H. Aoki, Phys. Rev. B **74**, 205414 (2006)
9. Y. Hatsugai, T. Fukui, H. Aoki, Eur. Phys. J. Spec. Top. **148**, 133 (2007)
10. P.R. Wallace, Phys. Rev. **71**, 622 (1947)
11. A. Bostwick et al., Nat. Phys. **3**, 36 (2007)
12. J.W. McClure, Phys. Rev. **104**, 666 (1956)
13. M.V. Berry, Proc. R. Soc. A **392**, 45 (1984)
14. Y. Hatsugai, New J. Phys. **12**, 065004 (2010)
15. W.H. Lomer, Proc. R. Soc. Lond. **330**, A227 (1955)
16. Y. Aharonov, A. Casher, Phys. Rev. A **19**, 2461 (1979)
17. Y. Hatsugai, Solid State Commun. **149**, 1061 (2009)
18. Y. Hatsugai, J. Phys. Soc. Jpn. **75**, 123601 (2006)
19. Y. Hatsugai, Phys. Rev. Lett. **71**, 3697 (1993)
20. S. Ryu, Y. Hatsugai, Phys. Rev. Lett. **89**, 077002 (2002)
21. H. Watanabe, Y. Hatsugai, H. Aoki, Phys. Rev. B **82**, 241403(R) (2010)
22. H. Watanabe, Y. Hatsugai, H. Aoki, J. Phys. Conf. Ser. **334**, 012044 (2011)
23. F. Mei, S.-L. Zhu, Z.-L. Feng, A.-M. Zhang, X.H. Oh, Phys. Rev. A **84**, 023622 (2011)
24. J.C. Slonczewsky, P.R. Weiss, Phys. Rev. **109**, 272 (1958)
25. M. Dresselhaus, G. Dresselhaus, Adv. Phys. **30**, 139 (1981)
26. S. Katayama, A. Kobayashi, Y. Suzumura, J. Phys. Soc. Jpn. **75**, 054705 (2006)
27. T. Kawarabayashi, Y. Hatsugai, H. Aoki, Phys. Rev. Lett. **103**, 156804 (2009)
28. G. Giovannetti, P.A. Khomyakov, G. Brocks, P.J. Kelly, J. van den Brink, Phys. Rev. B **76**, 073103 (2007)
29. L. Ci, L. Song, C. Jin, D. Jariwala, D. Wu, Y. Li, A. Srivastava, Z.F. Wang, K. Storr, L. Balicas, F. Liu, P.M. Ajayan, Nat. Mater. **9**, 430 (2010)
30. C. Yelgel, G.P. Srivastava, Appl. Surf. Sci. **258**, 8342 (2012)

31. C. Enderlein, Y.S. Kim, A. Bostwick, E. Rotenberg, K. Horn, New J. Phys. **12**, 033014 (2010)
32. V.M. Pereira, V.N. Kotov, A.H. Castro Neto, Phys. Rev. B **78**, 085101 (2008)
33. P.A. Maksym, H. Aoki, Phys. Rev. B **88**, 081406(R) (2013)
34. T. Kawarabayashi, T. Morimoto, Y. Hatsugai, H. Aoki, Phys. Rev. B **82**, 195426 (2010)
35. T. Kawarabayashi, Y. Hatsugai, H. Aoki, Phys. Rev. B **83**, 153414 (2011)
36. Y. Hatsugai, T. Kawarabayashi, H. Aoki, in preparation; see also Y. Hatsugai, J. Phys., Conf. Ser. **334**, 012004 (2011)
37. Y. Hatsugai, T. Morimoto, T. Kawarabayashi, H. Aoki, New J. Phys. **15**, 035023 (2013)
38. Y. Hamamoto, Y. Hatsugai, H. Aoki, Phys. Rev. B **86**, 205424 (2012)
39. Y. Hamamoto, T. Kawarabayashi, H. Aoki, Y. Hatsugai, Phys. Rev. B **88**, 195141 (2013)
40. M. Fujita, K. Wakabayashi, K. Nakada, K. Kusakabe, J. Phys. Soc. Jpn. **65**, 1920 (1996)
41. B. Sutherland, Phys. Rev. B **34**, 5208 (1986)
42. H. Hsu, L.E. Reichl, Phys. Rev. B **72**, 155413 (2005)
43. T. Nakajima, H. Aoki, Physica E **40**, 1354 (2008)
44. M.O. Goerbig, J.-N. Fuchs, G. Montambaux, F. Piéchon, Phys. Rev. B **78**, 045415 (2008)
45. E.H. Lieb, Phys. Rev. Lett. **62**, 1201 (1989)
46. N. Shima, H. Aoki, Phys. Rev. Lett. **71**, 4389 (1993)
47. T. Kawarabayashi, Y. Hatsugai, H. Aoki, Phys. Rev. B **85**, 165410 (2012)
48. J.C. Meyer, A.K. Geim, M.I. Katsnelson, K.S. Novoselov, T.J. Booth, S. Roth, Nature **446**, 60 (2007)
49. A. Fasolino, J.H. Los, M.I. Katsnelson, Nat. Mater. **6**, 858 (2007)
50. D.J. Thouless, M. Kohmoto, P. Nightingale, M. den Nijs, Phys. Rev. Lett. **49**, 405 (1982)
51. Y. Hatsugai, J. Phys. C **9**, 2507 (1997)
52. Q. Niu, D.J. Thouless, Y.S. Wu, Phys. Rev. B **31**, 3372 (1985)
53. F. Wilczek, A. Zee, Phys. Rev. Lett. **52**, 2111 (1984)
54. Y. Hatsugai, J. Phys. Soc. Jpn. **73**, 2604 (2004)
55. Y. Hatsugai, J. Phys. Soc. Jpn. **74**, 1374 (2005)
56. J.E. Avron, R. Seiler, B. Simon, Phys. Rev. Lett. **51**, 51 (1983)
57. J.E. Avron, R. Seiler, Phys. Rev. Lett. **54**, 259 (1985)
58. T. Fukui, Y. Hatsugai, H. Suzuki, J. Phys. Soc. Jpn. **74**, 1674 (2005)
59. Y. Zheng, T. Ando, Phys. Rev. B **65**, 245420 (2002)
60. V.P. Gusynin, S.G. Sharapov, Phys. Rev. Lett. **95**, 146801 (2005)
61. M. Arai, Y. Hatsugai, Phys. Rev. B **79**, 075429 (2009)
62. F.D.M. Haldane, Phys. Rev. Lett. **61**, 2015 (1988)
63. N. Goldman et al., Phys. Rev. Lett. **103**, 035301 (2009)
64. R.B. Laughlin, Phys. Rev. B **23**, 5632 (1981)
65. B.I. Halperin, Phys. Rev. B **25**, 2185 (1982)
66. Y. Hatsugai, Phys. Rev. B **48**, 11851 (1993)
67. T. Kennedy, J. Phys. Condens. Matter **2**, 5737 (1990)
68. M. Arikawa, S. Tanaya, I. Maruyama, Y. Hatsugai, Phys. Rev. B **79**, 205107 (2009)
69. M. Arikawa, Y. Hatsugai, H. Aoki, J. Phys. Conf. Ser. **150**, 022003 (2009)
70. V.W. Scarola, S. Das Sarma, Phys. Rev. Lett. **98**, 210403 (2007)
71. Z. Wang, Y.D. Chong, J.D. Joannopoulos, M. Soljacic, Phys. Rev. Lett. **100**, 013905 (2008)
72. Z. Wang, Y.D. Chong, J.D. Joannopoulos, M. Soljacic, Nature **461**, 772 (2009)
73. F.D.M. Haldane, S. Raghu, Phys. Rev. Lett. **100**, 013904 (2008)
74. C.L. Kane, E.J. Mele, Phys. Rev. Lett. **95**, 146802 (2005)
75. B.A. Bernevig, T.L. Hughes, S.-C. Zhang, Science **314**, 1757 (2006)
76. S. Okada, A. Oshiyama, Phys. Rev. Lett. **87**, 146803 (2001)
77. Y. Kobayashi et al., Phys. Rev. B **71**, 193406 (2005)
78. C. Hu, Phys. Rev. Lett. **72**, 1526 (1994)
79. Y. Tanaka, S. Kashiwaya, Phys. Rev. Lett. **74**, 3451 (1995)
80. M. Aprili, E. Badica, L.H. Greene, Phys. Rev. Lett. **83**, 4630 (1999)
81. S. Ryu, Y. Hatsugai, Physica C **388–389**, 90 (2003)

82. S. Ryu, Y. Hatsugai, Physica E **22**, 779 (2003)
83. M. Matsumoto, H. Shiba, J. Phys. Soc. Jpn. **64**, 3384 (1995)
84. M. Sigrist, D.B. Bailey, R.B. Laughlin, Phys. Rev. Lett. **74**, 3249 (1995)
85. M. Arikawa, Y. Hatsugai, H. Aoki, Phys. Rev. B **78**, 205401 (2008)
86. D.L. Miller et al., Science **324**, 924 (2009)
87. T. Morimoto, Y. Hatsugai, H. Aoki, Phys. Rev. B **78**, 073406 (2008)
88. T. Morimoto, Y. Hatsugai, H. Aoki, Phys. Rev. Lett. **103**, 116803 (2009)
89. R. Nair et al., Science **320**, 1308 (2008)
90. H. Aoki, T. Ando, Solid State Commun. **38**, 1079 (1981)
91. T. Morimoto, Y. Avishai, H. Aoki, Phys. Rev. B **82**, 081404(R) (2010)
92. Y. Ikebe, T. Morimoto, R. Masutomi, T. Okamoto, H. Aoki, R. Shimano, Phys. Rev. Lett. **104**, 256802 (2010)
93. R. Shimano, G. Yumoto, J.Y. Yoo, R. Matsunaga, S. Tanabe, H. Hibino, T. Morimoto, H. Aoki, Nat. Commun. **4**, 1841 (2013)
94. T. Oka, H. Aoki, Phys. Rev. B **79**, 081406 (2009); see also Phys. Rev. B **79**, 169901(E) (2009)
95. T. Kitagawa, T. Oka, A. Brataas, L. Fu, E. Demler, Phys. Rev. B **84**, 235108 (2011)
96. Y. Aharonov, J. Anandan, Phys. Rev. Lett. **58**, 1593 (1987)
97. T. Oka, H. Aoki, J. Phys. Conf. Ser. **334**, 012060 (2011)
98. N.H. Lindner, G. Refael, V. Galitski, Nat. Phys. **7**, 490 (2011)
99. X.-L. Qi, S.-C. Zhang, Rev. Mod. Phys. **83**, 1057 (2011)
100. M.Z. Hasan, C.L. Kane, Rev. Mod. Phys. **82**, 3045 (2010)
101. T. Kitagawa, E. Berg, M. Rudner, E. Demler, Phys. Rev. B **82**, 235114 (2010)
102. J. Karch et al., Phys. Rev. Lett. **105**, 227402 (2010)
103. J. Karch et al., Phys. Rev. Lett. **107**, 276601 (2011)
104. Z. Gu, H.A. Fertig, D.P. Arovas, A. Auerbach, Phys. Rev. Lett. **107**, 216601 (2011)
105. Y. Zhang et al., Phys. Rev. Lett. **96**, 136806 (2006)
106. Z. Jiang et al., Phys. Rev. Lett. **99**, 106802 (2007)
107. K. Nomura, A.H. MacDonald, Phys. Rev. Lett. **96**, 256602 (2006)
108. J.G. Checkelsky et al., Phys. Rev. Lett. **100**, 206801 (2008)
109. Y. Zhao et al., Phys. Rev. Lett. **108**, 106804 (2012)
110. A.F. Young et al., Nat. Phys. **8**, 550 (2012)
111. S. Pandey, H. Kontani, D. Hirashima, R. Arita, H. Aoki, Phys. Rev. B **86**, 060507 (2012)
112. Y.H. Wang, H. Steinberg, P. Jarillo-Herrero, N. Gedik, Science **342**, 453 (2013)

Chapter 8
Aspects of the Fractional Quantum Hall Effect in Graphene

Tapash Chakraborty and Vadim Apalkov

Abstract We present a brief overview of the nature of the fractional quantum Hall effect (FQHE) in monolayer and bilayer graphene. After a short introduction on the effect and the pseudopotential description of interacting electrons in the quantum Hall regime, we discuss in detail the magnetic field effects on electrons in monolayer graphene. We also briefly discuss the experimental signatures of the effect reported in the literature. In bilayer graphene, the effect manifests itself in a very different manner and we discuss in detail the various novel effects one expects there due to electron-electron interactions. The nature of the collective excitations of Dirac fermions in trilayer graphene is also briefly discussed. Existence of some exotic states in bilayer graphene, such as the Pfaffian state is also highlighted. Finally, we have touched upon the properties of the FQHE states of Dirac fermions on the surface of a topological insulator.

8.1 A Brief History of the Fractional Quantum Hall Effect

The quantum Hall effects (QHEs), both the integral [1, 2] and fractional [3, 4] QHEs are undoubtedly two of the most spectacular discoveries of the past century that have enormously enriched the field of condensed matter physics. Similarly, the theoretical explanation of the fractional QHE (FQHE) by Laughlin [5, 6] was a brilliant contribution to the annals of many-body physics. The experimental observation of the QHEs is summarized in Fig. 8.1. A two-dimensional electron gas in ultra-pure semiconductor materials, subjected to a high magnetic field and very low temperatures, i.e., in the extreme quantum limit, exhibits nearly vanishing longitudinal conductivity, $\sigma_{xx} \to 0$ and formation of steps in the Hall conductance

$$\sigma_{xy} = \nu \frac{e^2}{h},$$

T. Chakraborty (✉)
Department of Physics and Astronomy, University of Manitoba, Winnipeg, Canada R3T 2N2
e-mail: Tapash.Chakraborty@umanitoba.ca

V. Apalkov
Department of Physics and Astronomy, Georgia State University, Atlanta, GA 30303, USA

H. Aoki, M.S. Dresselhaus (eds.), *Physics of Graphene*, NanoScience and Technology,
DOI 10.1007/978-3-319-02633-6_8,

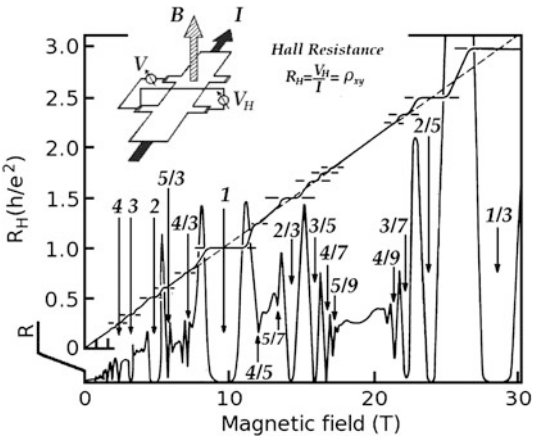

Fig. 8.1 Fractional (and integer) filling factors where the QHE is observed (adopted from [7])

for special values of the quantum number ν. The *filling factor* ν is a simple integer for the IQHE, and a rational fraction $\nu = \frac{p}{q}$, with q being an *odd* integer, for the FQHE.

In an ideal (non-interacting and disorder free) two-dimensional (2D) electron gas, an external magnetic field applied perpendicular to the electron plane influences the orbital motion of the electron and the energy spectrum is quantized into highly degenerate *Landau levels* with energies

$$\mathcal{E} = \left(n + \frac{1}{2}\right)\hbar\omega_c,$$

where $\omega_c = eB/m^*$ is the cyclotron energy ($\sim$10 meV for a magnetic field of $B =$ 10 Tesla). The number of states per unit area is $N_\Phi = eB/h = 1/2\pi\ell_0^2$, where $\ell_0 = (\hbar/eB)^{\frac{1}{2}}$ is the magnetic length. In units of the flux quantum, $\Phi_0 = h/e$, $N_\Phi = B/\Phi_0$. Therefore in an area $\mathcal{A}$, $N_\Phi = \Phi/\Phi_0$, the number of flux quanta threading through that area, which is the Landau level degeneracy in area $\mathcal{A}$. The Landau level filling factor is then

$$\nu = N_e/N_\Phi = 2\pi\ell_0^2 n_e,$$

where N_e is the number of electrons and n_e is the electron density in the system.

For an integer filling factor, $\nu = j$, the lowest j Landau levels are completely filled. The next electron that is added to the system must then go to the next energy level which requires a jump across the energy gap $\hbar\omega_c$. At very low temperatures where the thermal energy is much lower than the cyclotron energy, the presence of a gap guarantees a dissipationless flow of current as indicated by the vanishing longitudinal conductivity. The FQHE occurs when the magnetic field is so strong that electrons partially fill only the lowest Landau level (LLL). In this case, for noninteracting electrons the ground state is macroscopically degenerate. It is the Coulomb interaction between the electrons that lifts the degeneracy and opens a gap [7, 8]. The origin of the FQHE cannot therefore be understood based on the behavior of

individual electrons in a magnetic field. It is the behavior of the collective ensemble wherein lies the clue, i.e., in the language of Laughlin [6, 9], it is an *emergent* phenomenon. In the words of Störmer, electrons in this state conduct "*an elaborate, mutual, quantum-mechanical dance*" [4]. The nature of that state is discussed below.

8.1.1 A Novel Many-Body Incompressible State

The problem we face in describing the origin of the FQHE[1] can be clearly stated. We have at our disposal, N_e two-dimensional electrons moving on a plane perpendicular to a magnetic field B. The field is so strong that the energy separation between adjacent Landau levels and the spin Zeeman energy are far greater than the characteristic energy scale of the electron-electron (Coulomb) interactions. Mixing of Landau levels can then be safely neglected. In that case, our job at hand is to evaluate the energy spectrum and the wave functions of the system in the lowest Landau level. We also need to determine the nature and origin of the excitation gap. It is seemingly an intractable many-body problem with no small parameter present.

In 1983, just a year after the report of the discovery of the FQHE, Laughlin proposed, based on an inspired guess, the celebrated trial wave function for the many-electron state in the LLL [5]

$$\Psi_q(z_1 \cdots z_{N_e}) = \prod_{i<j}(z_i - z_j)^q \exp\left(-\sum_i |z_i|^2/4\right) \tag{8.1}$$

where $z \equiv x + iy$ is the (complex) electron position and q is an odd integer thus satisfying the antisymmetry requirement. By counting the maximal power of each z_i one can easily verify that the wave function given above corresponds to $\nu = \frac{1}{q}$ when $N_e \to \infty$ [7]. An important property of this wave function is that, it vanishes as the q-th power when one electron approaches the other [7]. This property minimizes the Coulomb interaction energy and hence the ground state energy. The wave function describes a uniform density charge-neutral liquid state in which the electrons condense [7].

Laughlin then explained why the $\nu = \frac{1}{3}$ state is so special. The many-electron system at this filling factor is in fact, *incompressible*, and there exists an energy gap. The energy gap implies that there is a positive discontinuity in the chemical potential at this filling factor [11], which means a vanishing compressibility. The chemical potential jump has indeed been measured experimentally for the FQHE states [12]. Starting with the $\nu = \frac{1}{q}$ state if we increase or decrease the number of states by one, elementary excitations containing *fractional charge*, $e^* = \mp\frac{e}{q}$ are created [7]. These 'quasiparticles' also obey fractional statistics [13].

[1] In this brief introduction to the FQHE, we limit ourselves only to the description of the filling factor $\nu = \frac{1}{q}$. Interested readers could consult other sources for a more detailed account [7, 8, 10].

Laughlin's theory for the FQHE is like good poetry in physics, rich in profound ideas that has inspired researchers for decades and even from many other subfields of physics [14]. Its novel concepts on correlated quantum fluids were certainly unconventional in the field where it was applied, viz. the semiconductors. In explaining a truly remarkable macroscopic quantum phenomenon, Lauglin opened a floodgate of novel ideas with a flow that is yet to subside. Description of all those ideas is however, far beyond the scope of this brief introduction.

8.1.2 Pseudopotential Description of Interacting Electrons

In the FQHE regime where the magnetic field is so strong that the spacing between the Landau levels are (in the absence of any disorder) much larger than e.g., the thermal energy, and all the degree of freedom are confined to a single Landau level. In that situation, the Hamiltonian of the system is simply the projected interparticle interaction. Haldane was the first to point out [15] that the interaction energy of a pair of particles with the same Landau indices can be written as

$$\mathcal{H}_{ij} = \sum_{m=0}^{\infty} V_m \mathcal{P}_{ij}^m,$$

where $\mathcal{P}_{ij}^m$ projects the pair of particles i, j onto the relative angular momentum m. Antisymmetry of the electron wave function dictates that m is an odd integer. The parameters V_m are the so-called Haldane pseudopotentials, which are defined as the energy of two electrons with the relative angular momentum m. They are determined by the structure of the wave functions of the corresponding Landau level and for the n-th Landau level can be found from the following expression [15]

$$V_m^{(n)} = \int_0^{\infty} \frac{dq}{2\pi} q V(q) \big[F_n(q)\big]^2 L_m\big(q^2\big) e^{-q^2}, \tag{8.2}$$

where $L_m(x)$ are the Laguerre polynomials, $V(q) = 2\pi e^2/(\kappa q \ell_0)$ is the Coulomb interaction in the momentum space, κ is the background dielectric constant, and $F_n(q)$ is the form factor of the n-th Landau level. The form factor is completely determined by the n-th Landau level wave functions. For conventional semiconductor systems, the form factors have the following form

$$F_n(q) = L_n\big(q^2/2\big). \tag{8.3}$$

Therefore, any translationally and rotationally invariant two-body interaction, projected to a single Landau level can be described completely by a set of pseudopotentials.

For the repulsive Coulomb potential, the pseudopotentials decrease with increasing value of m [15]. In this context, it is interesting to note that the Laughlin state at $\nu = \frac{1}{q}$, with q being an odd integer, is quite unique. It has the property

$$\mathcal{P}_{ij}^m \Psi_L = 0, \quad \text{for } m < q.$$

The $\nu = \frac{1}{q}$ Laughlin state is a zero-energy eigenstate with only $V_m (m < q)$ being non-zero. As the mean squared distance between the electrons is proportional to q [7], the model potential is of short range. However, Haldane pointed out [16] that, when one varies the pseudopotentials between a hard-core model with only non-zero V_1 and the true Coulomb system, the overlap between the true ground state (in finite-size systems) and the Laughlin state is extremely good. This explains why the Laughlin state captures the essential physics of the FQHE state by being close to the exact ground state. It was also noted by Haldane that the pair interaction potential $\mathcal{H}_{ij}$ after projection into the subspace of fixed Landau index is discrete [15]. This is the central feature of the physics underlying the incompressible many-electron states that gives rise to the FQHE [8, 15].

8.1.3 Composite Fermions and the Fermion-Chern-Simons Theory

In addition to the primary filling factors, $\nu = \frac{1}{q}$ (with q as an odd integer), which correspond to the Laughlin states, the FQHE was also observed in many other higher-order fractional fillings of the Landau levels, such as $\nu = \frac{2}{5}, \frac{3}{7}, \frac{4}{9}$, and so on [3, 7]. Some of those filling factors, such as $\nu = \frac{2}{3}$, can be explained by the particle-hole symmetry [7], while the presence of other filling factors can be described within the composite fermion approach [17–19] and the Chern-Simons theory [20, 21]. The hierarchy of the FQHE states based on the composite fermion picture is constructed in the following way [17–19]. If the many-electron system is placed in a magnetic field B^* such that the filling factor of the system is $\nu^* = n_0 \Phi_0 / B^*$, where n_0 is the electron density, then by multiplying the corresponding multi-particle wave function, Ψ^* by a symmetric factor

$$F_p(z_1, \ldots, z_N) = \prod_{j<k} (z_j - z_k)^{2p} \tag{8.4}$$

where p is a positive integer, we construct the wave function, $\Psi = F_p \Psi^*$ corresponding to a new filling factor ν. To find the relation between ν^* and ν we notice that the factor F_p introduces an additional effective magnetic field, $\Delta B = 2pn_0\Phi_0$ in the system. In fact, if we consider a particle travelling in a large orbit covering an area $\mathcal{A}$ and encloses $n_0\mathcal{A}$ other particles, then due to the additional factor F_p that particle acquires an extra phase factor $2p2\pi n_0\mathcal{A} = 2\pi(\Delta B\mathcal{A}/\Phi_0)$. Therefore, the additional factor, F_p in the many-particle wave function can be thought of as an extra magnetic field, ΔB. Then the relation between the magnetic field B^*, corresponding to the filling factor ν^* and the new magnetic field B becomes

$$B = B^* + \Delta B = B^* + 2pn_0\Phi_0 = B^*\big(1 + 2p\nu^*\big). \tag{8.5}$$

Therefore, the filling factor corresponding to the wave function Ψ, i.e., for n_0 particles in a magnetic field B, is

$$\nu = \frac{\nu^*}{2p\nu^* + 1}. \tag{8.6}$$

Multiplying the many-particle wave function by the complex conjugated factor F_p^*, we can construct the wave function corresponding to the filling factor $\frac{\nu^*}{2p\nu^*-1}$. The factor F_p thus introduces $2p$ magnetic flux quanta attached to each electron, thereby creating a composite fermion. On average, such magnetic fluxes produce an effective magnetic field, ΔB. If we start with completely filled Landau levels with integer filling factor n, then multiplication by the factor F_p, i.e., attaching the magnetic flux quanta to the electrons produces the fractional filling factors of the form

$$\nu = \frac{n}{2pn \pm 1}. \tag{8.7}$$

As an example, for $n = 2$, $p = 1$ we obtain $\nu = \frac{2}{5}$. Therefore, the integer filling factor of the composite fermions, i.e., electrons with even number of flux quanta, corresponds to fractional filling factor of real electrons. Since the ground state of the composite fermion system is incompressible, we can assume that the ground state of actual electrons with fractional filling is also incompressible. Numerical comparison of composite fermion wave functions and the exact wave functions evaluated in finite-size systems shows that the composite fermion approach indeed provides a good description of the FQHE ground states at general filling factors. The composite fermion description of FQHE states is closely related to the Chern-Simons theory of the quantum Hall systems [20, 21]. Within the Chern-Simons theory, a gauge Chern-Simons magnetic field is introduced through an unitary transformation. Such a gauge field introduces an even number of magnetic flux quanta attached to the electrons. Within the mean-field approximation, the Chern-Simons magnetic field is replaced by an uniform average magnetic field, which reproduces the same effective filling factors as in the composite fermion approach. In the Chern-Simons approach, one can go beyond the mean-field approximation and calculate low-energy excitation properties of the quantum systems. One of the applications of the Chern-Simons theory is the description of the $\nu = \frac{1}{2}$ quantum state. In this case an external magnetic field exactly cancels the mean Chern-Simons field and the composite fermions experience no average magnetic field. Therefore the $\nu = 1/2$ quantum system in this picture is equivalent to an electron system in the absence of an external magnetic field. Experimental indications of such a situation, e.g., the existence of a Fermi surface [22] at this filling factor provides ample support for this theoretical picture.

8.2 The Advent of Graphene

Just when everyone thought the glory days of the QHEs are perhaps over, along came graphene [23–25]. It is a single sheet of carbon atoms arranged in a honeycomb (hexagonal) lattice, often described as a molecular chicken wire where one carbon atom sits at each 120° corner. This material is perhaps the most interesting two-dimensional system possible, with unique electronic properties that are entirely different (and unexpected) from those of conventional two-dimensional systems [26]. The electronic band structure of graphene was theoretically studied as far

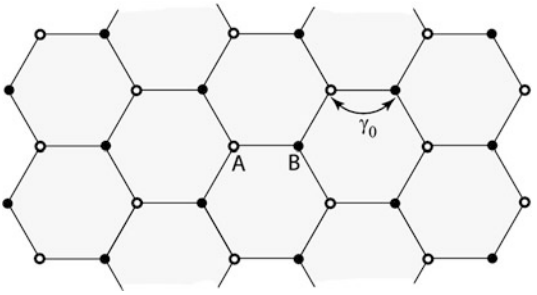

Fig. 8.2 The honeycomb lattice structure of graphene with two sublattices A and B. Within the nearest neighbor tight-binding approximation the atoms of sublattice A are coupled to atoms of sublattice B through the hopping integral γ_0

back as 1947 [27]. Electrons and holes in graphene are described as 'massless Dirac fermions' because of their linear energy dispersion near the Fermi surface [28]. Graphene is a bipartite lattice made up of two interpenetrating triangular sublattices that provides a new degree of freedom for the electronic state, the pseudospin. Transport properties of graphene exhibit many novel features, most notably (in our context), the room temperature QHE [29]. Bilayer graphene has also proven to be rich with unique properties, e.g., the gate tunable band gap. Here the energy dispersion corresponds to that of massive chiral fermions. A detailed account of all these can be found in a review article by the present authors [30].

Since its isolation in 2004 [25], graphene has maintained a dominant presence in the community. By August 2011, there were more than 11,000 publications with the word 'graphene' in their titles. With the continued plethora of articles, most notably, the superabundance of review articles [25, 28, 30–48] about various properties of graphene makes it abundantly clear that our fascination with this system is far from being over, and one expects more surprising discoveries in the coming years.

8.2.1 Massless Dirac Fermions

The two-dimensional lattice of graphene has the honeycomb structure, consisting of two inequivalent sublattices of carbon atoms, say A and B (Fig. 8.2). The nearest-neighbor tight-binding description of graphene results in a band structure with the Fermi level located at two inequivalent points, $\mathrm{K} = (2\pi/a)(\frac{1}{3}, \frac{1}{\sqrt{3}})$ and $\mathrm{K}' = (2\pi/a)(\frac{2}{3}, 0)$, of the first Brillouin zone. Here $a = 0.246$ nm is the lattice constant. The tight-binding approximation is valid over a wide range of energy. Within the effective mass approximation which addresses the low-energy properties, these points correspond to two valleys, K and K′. In each valley the low-energy electron dynamics near the Fermi energy is described by the following Hamiltonian [28]

$$\mathcal{H}_\xi = \xi v_F \begin{pmatrix} 0 & p_- \\ p_+ & 0 \end{pmatrix}, \tag{8.8}$$

where $p_- = p_x - ip_y$, $p_+ = p_x + ip_y$, and $\mathbf{p}$ is the two-dimensional momentum of an electron. Here $v_F \approx 10^6$ m/s is the Fermi velocity, which can be related to

the hopping integral, γ_0, between the nearest neighbor sites, $v_F = \sqrt{3}\gamma_0 a/2\hbar$. The index ξ is 1 and -1 for valleys K and K′, respectively. Without the spin-orbit interaction [49–51], each level determined by the Hamiltonian (8.8) has a two-fold spin degeneracy. The wave functions corresponding to the Hamiltonian (8.8) have two components belonging to sublattices A and B, and can be expressed as $(\psi_A, \psi_B)^T$ for valley K and $(\psi_B, \psi_A)^T$ for valley K′, where ψ_A and ψ_B are wave functions of sublattices A and B, respectively. The superscript T indicates the transpose of a vector.

The single-electron states obtained from the Hamiltonian (8.8) has a linear dispersion relation given by

$$\varepsilon(p) = \pm v_F p, \tag{8.9}$$

which is the dispersion relation of Dirac "relativistic" massless particles. In addition to spin degeneracy, each energy level has a two-fold valley degeneracy. The smooth impurity potentials or electron-electron interactions introduce coupling of different valleys. However, due to the large momentum separation of the valley states this coupling is weak and can be safely ignored.

8.2.2 Landau Levels in Graphene

In the tight-binding model the magnetic field is introduced through the Peierls substitution which introduces a magnetic field dependence of the hopping integrals. Within this approach the Landau levels with low, intermediate and very high indices can be obtained. Formation of the incompressible liquids in graphene due to electron-electron interactions is expected to occur at low Landau level indices. To study those Landau levels the effective mass approximation described by the Hamiltonian (8.8) is fully adequate. The magnetic field is introduced in the Hamiltonian (8.8) by replacing the electron momentum $\mathbf{p}$ with the generalized momentum $\boldsymbol{\pi} = \mathbf{p} + e\mathbf{A}/c$ where $\mathbf{A}$ is the vector potential. Then the Hamiltonian of an electron in a perpendicular magnetic field in valley ξ takes the form

$$\mathcal{H}_\xi = \xi v_F \begin{pmatrix} 0 & \pi_- \\ \pi_+ & 0 \end{pmatrix}. \tag{8.10}$$

The eigenfunctions of the Hamiltonian (8.10) can be expressed in terms of the conventional Landau wave functions, $\phi_{n,m}$ [52], for a particle obeying the parabolic dispersion relation with the Landau index n and intra-Landau index m, which depends on the choice of the gauge. For example, in the Landau gauge, $A_x = 0$ and $A_y = Bx$, the index m is the y-component of the momentum, while in the symmetric gauge, $\mathbf{A} = \frac{1}{2}\mathbf{B} \times \mathbf{r}$, the index m is the z-component of electron angular momentum. For these wave functions, $\phi_{n,m}$, the operators π_+ and π_- are the raising and lowering operators, respectively. This means that they increase or decrease the Landau level index, n:

$$v_F \pi_+ \phi_{n,m} = -i\hbar\omega_B \sqrt{n+1}\,\phi_{n+1,m},$$
$$v_F \pi_- \phi_{n,m} = i\hbar\omega_B \sqrt{n}\,\phi_{n-1,m},$$

where $\omega_B = \sqrt{2}v_F/\ell_0$, and ℓ_0 is the magnetic length defined in Sect. 1. The Landau eigenfunctions of the Hamiltonian (8.10) can then be written in the form

$$\Psi_{n,m} = \begin{pmatrix} i^{n-1}\chi_1 \phi_{n-1,m} \\ i^n \chi_2 \phi_{n,m} \end{pmatrix}, \tag{8.11}$$

where the coefficients χ_1 and χ_2 satisfy the following eigenvalue matrix equations

$$\varepsilon \chi_1 = -\xi\hbar\omega_B \chi_2 \tag{8.12}$$
$$\varepsilon \chi_2 = -\xi\hbar\omega_B \chi_1. \tag{8.13}$$

The resulting discrete Landau energy spectrum has both negative (valence band) and positive (conduction band) values, which are described by introducing integer values for the Landau index $n = 0, \pm 1, \pm 2, \ldots$, which also include the negative values of n. In terms of n, the Landau energy spectrum of electrons in graphene takes the form

$$\varepsilon_n = \hbar\omega_B \,\mathrm{sgn}(n)\sqrt{|n|}, \tag{8.14}$$

where

$$\mathrm{sgn}(n) = \begin{cases} 0 & (n = 0) \\ 1 & (n > 0) \\ -1 & (n < 0). \end{cases} \tag{8.15}$$

Each energy level (8.14) has a two-fold valley degeneracy. The wave functions corresponding to the Landau levels (8.14) can be obtained from (8.12)–(8.13) in the following form

$$\Psi^{\mathrm{K}}_{n,m} = \begin{pmatrix} \psi_A \\ \psi_B \end{pmatrix} = C_n \begin{pmatrix} \mathrm{sgn}(n) i^{|n|-1} \phi_{|n|-1,m} \\ i^{|n|} \phi_{|n|,m} \end{pmatrix}, \tag{8.16}$$

for valley K ($\xi = 1$) and

$$\Psi^{\mathrm{K}'}_{n,m} = \begin{pmatrix} \psi_B \\ \psi_A \end{pmatrix} = C_n \begin{pmatrix} \mathrm{sgn}(n) i^{|n|-1} \phi_{|n|-1,m} \\ i^{|n|} \phi_{|n|,m} \end{pmatrix}, \tag{8.17}$$

for valley K′ ($\xi = -1$). Here $C_n = 1$ for $n = 0$ and $C_n = 1/\sqrt{2}$ for $n \neq 0$.

The Landau levels in graphene have a square-root dependence on both the magnetic field and the Landau level index. For $v_F \sim 10^6$ m/s, the Landau level energy spectrum takes the form, $\varepsilon_n \approx 36\sqrt{B[\mathrm{Tesla}]}\sqrt{n}$ (meV). This behavior is clearly different from that in conventional (henceforth called *non-relativistic* to distinguish it from the graphene system) semiconductor 2D system with a parabolic dispersion relation, for which the energy spectrum has a linear dependence on both the magnetic field and the Landau level index. As an example, for the GaAs system the Landau energy spectrum is $\varepsilon_n^{\mathrm{GaAs}} = \hbar\omega_c(n + \frac{1}{2}) \approx 1.7B[\mathrm{Tesla}](n + \frac{1}{2})$ (meV). The Landau level spectra for graphene and for the GaAs systems are shown in Fig. 8.3, which illustrates their different behaviors.

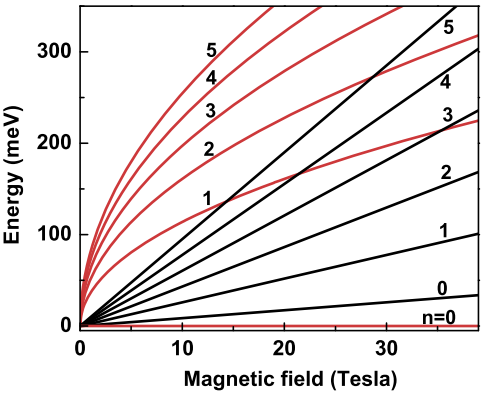

Fig. 8.3 The Landau levels as a function of the perpendicular magnetic field for graphene (*red solid lines*) and a GaAs system (*black solid lines*). Numbers next to the lines are Landau level indices. In the case of graphene, only the Landau levels with positive energy, corresponding to the conduction band, are shown

It is noteworthy that the $n = 0$ Landau level in graphene has zero energy at all values of the magnetic field. It is populated equally by electrons and holes. The wave functions at this Landau level are identical to those of $n = 0$ non-relativistic Landau level [see (8.16)–(8.17)]. Therefore the interaction properties and the FQHE of the $n = 0$ Landau level in graphene are the same as for the non-relativistic $n = 0$ Landau level. The wave functions in higher Landau levels ($|n| \geq 1$) are mixtures of non-relativistic Landau wave functions belonging to different Landau level indices. Therefore the interaction effects in these Landau levels should be very different from those of the non-relativistic systems. The nature of the Landau levels, in particular the lowest level, can be effectively studied by measuring the quantum Hall activation gaps in graphene. Measurements of the inter-Landau level activation gap in graphene [53] revealed that the lowest LL is very sharp in contrast to the broadened higher LLs, and the measured gap between the zeroth and the first Landau level approaches the bare Landau-level splitting for high magnetic fields.

8.2.3 Pseudopotentials in Graphene

As mentioned earlier, the interaction properties of electrons within a single Landau level are completely determined by the Haldane pseudopotentials (8.2). With the known wave functions (8.16)–(8.17), the form factors in (8.2), can be readily evaluated. For the n-th graphene Landau level,[2] they are given by the following expressions [see (8.3)] [54, 55]

$$F_0(q) = L_0\left(q^2/2\right) \tag{8.18}$$

$$F_n(q) = \frac{1}{2}\left[L_n\left(q^2/2\right) + L_{n-1}\left(q^2/2\right)\right]. \tag{8.19}$$

[2] If not otherwise stated, in what follows, we consider the positive values of n.

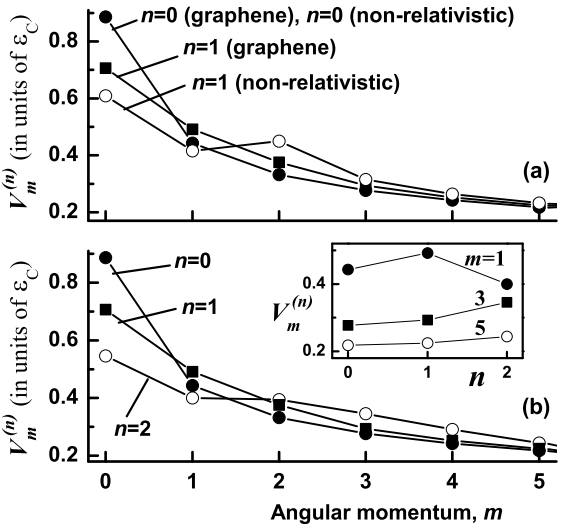

Fig. 8.4 The Haldane pseudopotentials shown as a function of the relative angular momentum for non-relativistic and graphene systems at $n = 0, 1$ Landau levels (**a**) and for graphene at $n = 0, 1$ and 2 Landau levels (**b**). The *inset* in panel (**b**) shows the dependence of the pseudopotentials on the Landau level index n for graphene. The energy is evaluated in units of ε_C

With these form factors the pseudopotentials for graphene are then calculated from (8.2). The pseudopotentials are given in units of the Coulomb energy, $\varepsilon_C = e^2/\kappa\ell_0$, where κ is the background dielectric constant of the system.

To compare the interaction properties of graphene and the conventional non-relativistic systems, we present in Fig. 8.4 the pseudopotentials calculated from (8.2) for graphene and for the non-relativistic system. Since the FQHE can be realized only in the low-index Landau levels, in Fig. 8.4 the results are shown only for small values of n ($n \leq 2$). As it was mentioned above, for $n = 0$ graphene and a non-relativistic system have the same pseudopotentials [Fig. 8.4(a)]. In a higher Landau level index there is an important difference in the behavior of the pseudopotentials in these two systems. More specifically, for $n = 1$, the graphene system shows a stronger electron-electron repulsion, i.e., a larger pseudopotential, at small relative angular momentum, $m < 2$, and a weaker repulsion at a large angular momentum, $m \geq 2$, compared to that for a non-relativistic system [Fig. 8.4(a)]. Based on the general properties of the Laughlin incompressible state, we can conclude that the stronger repulsion at small values of the angular momentum implies a more stable FQHE state.

In Fig. 8.4(b), the pseudopotentials of graphene are shown for different Landau levels. Due to the antisymmetry of the electronic wave functions, only the pseudopotentials with odd relative angular momenta contribute to the spin-polarized FQHE states. Hence only the pseudopotentials with $m = 1, 3, 5, \ldots$ determine the spin-polarized, and in the case of graphene, the valley-polarized properties of the system. For these values of m the pseudopotentials in the $n = 1$ Landau level show an interesting behavior: while for $m = 3$ and 5 the pseudopotential, $V_m^{(n)}$, monotonically increases with n, and for $m = 1$, the pseudopotential $V_1^{(n)}$ has a maximum at $n = 1$ [see inset in Fig. 8.4(b)]. Therefore the electrons with relative angular momentum $m = 1$ show the strongest repulsion in the $n = 1$ Landau level. This is different from

Table 8.1 Characteristics of Haldane pseudopotentials for graphene and for conventional electron systems

	$V_1^{(n)}/V_3^{(n)}$	$V_3^{(n)}/V_5^{(n)}$
$n=0$ (graphene)	1.60	1.26
$n=0$ (non-relativistic)	1.60	1.26
$n=1$ (graphene)	1.68	1.33
$n=1$ (non-relativistic)	1.32	1.36

the behavior of a non-relativistic system, where the strongest repulsion is in the lowest $n=0$ Landau level.

The stability of the incompressible FQHE state, i.e., the magnitude of the FQHE gap, depends on how fast the pseudopotentials decay with increasing relative angular momentum. For spin and valley polarized electron systems this decay is determined by the ratios $V_1^{(n)}/V_3^{(n)}$ and $V_3^{(n)}/V_5^{(n)}$. The larger the ratios, the more stable is the FQHE. In Table 8.1, the values of the ratios are shown for graphene and for non-relativistic systems in the two lowest Landau levels with $n=0$ and 1. These values clearly indicate that $V_1^{(n)}/V_3^{(n)}$ has the largest value for graphene in the $n=1$ Landau level which suggests that the gaps of the FQHE states should have the largest value in graphene in the $n=1$ Landau level.

8.2.4 Nature of the Incompressible States in Graphene

Each Landau level in graphene is four-fold degenerate due to two-fold valley and two-fold spin degeneracies. The spin degeneracy is partially lifted due to the Zeeman splitting, which is $\Delta_Z = g\mu_B B \approx 1.5B$ [Tesla] (K) $\approx 0.13B$ [Tesla] (meV), where $g \approx 2.2$. The symmetry-breaking terms should be compared with the typical energy of the inter-electron interactions within a single Landau level, which is the Coulomb energy, $\varepsilon_C = e^2/\kappa\ell_0$. The Coulomb energy determines the magnitude of the Haldane pseudopotentials and in graphene it is $\varepsilon_C \approx (54/\kappa)\sqrt{B\,[\text{Tesla}]}$ (meV). For $\kappa \approx 4$ the Coulomb energy becomes $\varepsilon_C \approx 14\sqrt{B\,[\text{Tesla}]}$ (meV). Due to the small value of the dielectric constant, the Coulomb energy in graphene is a few times larger than the corresponding energy in a non-relativistic system, where the dielectric constant is about $\kappa \sim 13$. Although the Coulomb interaction in graphene is strong, it is still less than the inter-Landau level spacing. For example, the energy separation between the $n=0$ and $n=1$ Landau levels in graphene is $36\sqrt{B[\text{Tesla}]}$ (meV) (see Sect. 8.2.2). The Coulomb interaction also introduces the valley-symmetry breaking terms [55, 56], which are algebraically small in a/ℓ_0. For typical values of the magnetic field, the Zeeman energy in graphene is almost two orders of magnitude smaller than the Coulomb energy, $\Delta_Z/\varepsilon_C \approx 0.01\sqrt{B\,[\text{Tesla}]}$, and within a good approximation, a single Landau level in graphene can be considered as the four-fold degenerate level. Electrons within a single Landau level therefore have the SU(4) symmetry with weak symmetry breaking terms due to the Zeeman splitting and the valley asymmetry terms in the interaction Hamiltonian.

The properties of the FQHE are determined by the nature of the ground states, e.g., valley or spin polarization of the ground states, and the value of the FQHE gap, which characterizes the stability of the FQHE with respect to the temperature and the disorder. Theoretically, the FQHE states are generally studied by numerical diagonalization of the Hamiltonian matrix for finite-size electron systems in either the planar (torus) or the spherical geometry [7]. In the spherical geometry [16, 57–59] the magnetic field is introduced in terms of the integer number $2S$ of magnetic flux quanta through the sphere in units of the flux quantum. Then the radius of the sphere R is defined as $R = \sqrt{S}\ell_0$. The single-electron states are characterized by the angular momentum S, and its z component, S_z. The number of available states in a sphere is $(2S + 1)$. These states correspond to a single Landau level in the planar geometry. Then for a given number of electrons N_e the parameter S determines the filling factor of the Landau level. In the thermodynamic limit, the filling factor is $\nu = N_e/(2S + 1)$, but the exact relation between the FQHE filling factor and the number of electrons depends on the type of the FQHE state. In the spherical geometry, the many-particle states are described by the total angular momentum L and its z component, while the energy depends only on L. For the many-electron system only the lowest eigenvalues and eigenvectors of the interaction Hamiltonian matrix are calculated [58]. These eigenstates determine the nature of the ground state of the system and its neutral collective excitation gap. By varying the magnetic field flux through the system the charged excitations can be also studied.

The valley and spin polarizations of the ground states at the major FQHE filling factors, $\frac{1}{3}$, $\frac{2}{3}$, and $\frac{2}{5}$, were studied numerically for $n = 0$ and $n = 1$ Landau levels [60–62]. It was found that in the $n = 0$ Landau level the $\nu = \frac{1}{3}$ ground state is valley and spin polarized, but the $\nu = \frac{2}{3}$ and $\nu = \frac{2}{5}$ ground states are valley unpolarized [56, 60, 61]. This behavior is similar to the non-relativistic 2D system with zero Zeeman splitting, i.e., with the SU(2) symmetry. For the $n = 1$ level the graphene system however shows a different behavior. In this case, the ground states at $\nu = \frac{1}{3}$, $\frac{2}{3}$, and $\frac{2}{5}$ are all valley polarized [61]. It was also shown that for the graphene system in the $n = 0$ Landau level with filling factor $\nu = 2 + \frac{1}{3}$, the $\frac{1}{3}$ state is valley polarized even at a small Zeeman splitting [62].

The gaps of the FQHE states, i.e., the stability of the incompressible states, are determined by the Haldane pseudopotentials. From the general analysis of the pseudopotentials in different Landau levels we can conclude that the FQHE is more stable in the $n = 1$ Landau level in graphene. Therefore the largest FQHE gap is expected in the $n = 1$ Landau level. This property is illustrated in Fig. 8.5, where the energy spectra of the valley and spin polarized electron system at filling factors $\frac{1}{3}$ and $\frac{1}{5}$ are shown. In the spherical geometry, the filling factors $\nu = 1/q$ (q is an odd integer) are realized at $S = (q/2)(N_e - 1)$. The ground state of the $1/q$ FQHE is well described by the Laughlin function [5, 7].

The energy spectra of the $\nu = \frac{1}{3}$ FQHE system is shown in Fig. 8.5(a) for $N_e = 8$ electrons at the $n = 0$ and $n = 1$ Landau levels. The energy spectra in the $n = 0$ Landau level for graphene and the non-relativistic 2D system are exactly the same with the same value of the excitation gap. For a non-relativistic system this is the largest excitation gap of the $\nu = \frac{1}{3}$ FQHE state. That is not the case with graphene

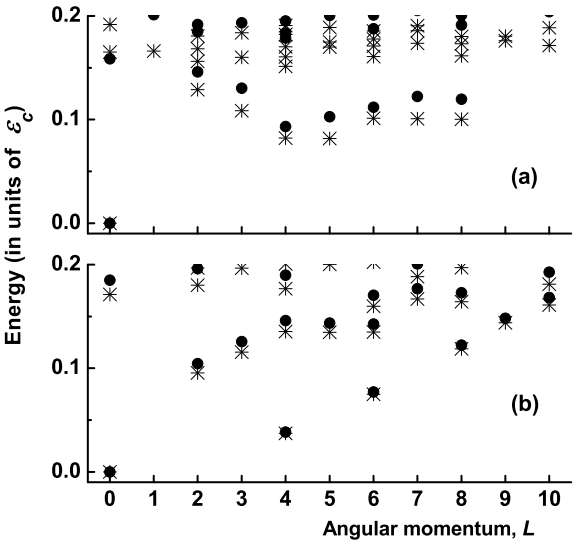

Fig. 8.5 (**a**) The energy spectra of an eight-electron $\nu = \frac{1}{3}$-FQHE system shown for different Landau levels: $n = 0$ (*stars*) and $n = 1$ (*filled circles*). The flux quanta are $2S = 21$. (**b**) Energy spectra of the six-electron $\nu = \frac{1}{5}$-FQHE system is shown for different Landau levels: $n = 0$ (*stars*) and $n = 1$ (*filled circles*). The flux quanta here are $2S = 25$

where the FQHE gap has the largest value in the $n = 1$ Landau level [Fig. 8.5(a)]. For smaller filling factors, i.e., at $\nu = \frac{1}{5}$, the pseudopotentials with larger values of the relative angular momentum determine the properties of the system. As a result, the difference between the FQHE states in the $n = 0$ and $n = 1$ Landau levels becomes less pronounced, which is illustrated in Fig. 8.5(b) for $N_e = 6$ electrons and at the filling factor $\nu = \frac{1}{5}$. This tendency is completely different from that of the non-relativistic systems where the FQHE is strongly suppressed in the $n = 1$ Landau level. A similar conclusion about the unique interaction properties of the $n = 1$ Landau level in graphene was reported in Ref. [60], where the properties of the FQHE states in graphene and GaAs systems were compared. In the $n = 0$ Landau level the graphene system becomes similar to the GaAs system, while in the $n = 1$ Landau level, only the graphene system exhibits stable FQHE states.

The spectra shown in Fig. 8.5 correspond to the polarized neutral excitations of the electron system and illustrate the relative strength of the electron-electron interactions at different Landau levels in graphene. Due to the valley degeneracy of the Landau levels in graphene, valley unpolarized excitations, which are of the type of valley skyrmions, can have lower energies than those for polarized excitations. Numerical analysis indicates that the lower-energy charged excitations at major filling factors, $\nu = \frac{1}{3}$, $\frac{2}{3}$, and $\frac{2}{5}$, are unpolarized valley skyrmions [61].

For the SU(4) symmetric graphene electron system, i.e., at small Zeeman splitting, new types of FQHE states at filling factors $\nu = q/(2pq \pm 1)$ with $q \geq 3$ were also proposed [63] in the $n = 0$ and $n = 1$ Landau levels. These states are expected in graphene because of the interplay between the spin and valley degrees of freedom.

From the discussions above, it is quite clear that the electron-electron interactions in graphene are more pronounced in the $n = 1$ Landau level, which should result in more stable FQHE states with large excitation gaps in the $n = 1$ Landau level. This

is opposite to what we observe in a non-relativistic 2D system, where the strongest interactions are realized in the $n = 0$ Landau level.

8.2.5 Experimental Observations of the Incompressible States

As explained in earlier chapters, experimental demonstration of the quantum Hall plateaus at filling factors $\nu = 4(q + \frac{1}{2})$ [64, 65] quite convincingly confirmed the Dirac nature of electron dynamics in graphene that was purely non-interacting and devoid of any effects due to interactions among the electrons. Interestingly, any collective behavior due to electron-electron interactions, akin to the FQHE was found to be very difficult to observe. This is notwithstanding the strong unscreened Coulomb forces that were supposed to exist between the charge carriers. Taking the cue from earlier studies of the FQHE in a conventional two-dimensional electron gas (2DEG), it was clear that experimental observation of these states crucially depends on significantly high-quality samples where the Coulomb energy scale far exceeds that of the impurity-induced random potential fluctuations. Such a significant improvement in sample quality was indeed achieved in suspended graphene (SG) samples, where the substrate-induced perturbations were entirely eliminated [66, 67]. Observation of the quintessential $\frac{1}{3}$-FQHE in suspended graphene was first reported by two groups [68–70]. Observation of a few other fractions followed soon after.

It has been correctly pointed out by Skachko et al. [71] (also elaborated in the previous subsection) that the FQHE in graphene can be expected to deviate from that in conventional 2DEG in several important ways. First of all, electrons in graphene are dynamically more two dimensional than in semiconductor quantum wells, where the well widths range from 10–30 nm. This implies that the interaction at short distances in graphene is much stronger than in conventional quantum wells. Secondly, electron-electron interactions in SG are enhanced even further due to the absence of substrate screening ($\kappa \sim 1$) as compared to, e.g., in GaAs, where $\kappa \sim 13$. This enhanced interaction in graphene leads to a larger gap [54], and therefore the FQHE state persists at much higher temperatures. Finally, due to the four-fold spin and valley degeneracy, the situation in graphene resembles more like what would be realized in a double quantum well system, rather than a single quantum well. However, unlike in a GaAs system, the intra- and inter-well interactions in graphene are almost identical. This suggests the existence of new FQHE states which are absent in conventional systems [60, 72].

Experimental results of Andrei et al. [68, 69, 71] for quantum Hall plateaus at $\nu = \frac{1}{3}$ in monolayer SG are shown in Fig. 8.6(a) for various values of the applied magnetic field. These authors noted that the plateau at the $\frac{1}{3}$ filling factor was very robust—it appeared at $\sim$2 Tesla at low temperatures ($\sim$1 K) and persisted up to 20 K at $B = 12$ Tesla. The robustness of the FQHE states can be further assessed by studying the excitation gap [7]. The temperature dependence of the diagonal resistivity ρ_{xx} (or diagonal conductivity σ_{xx}, since $\sigma_{xx} \sim \rho_{xx}/\rho_{xy}^2$ near the ρ_{xx} minima) is interpreted as the activation energies in the FQHE [73–75]. These energies are

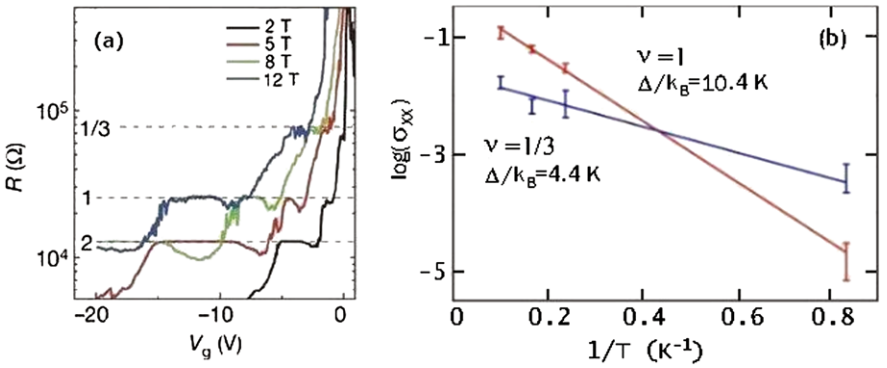

Fig. 8.6 The results of Andrei et al. [68, 69, 71]: (**a**) Gate voltage dependence of resistance for a suspended graphene sample shown at different magnetic fields and at temperature 1.2 K. The plateaus at $\nu = 1$, 2, and $\frac{1}{3}$ are clearly visible. (**b**) The activation gap at $\nu = 1$ and $\nu = \frac{1}{3}$, obtained from the temperature dependence of the diagonal conductivity

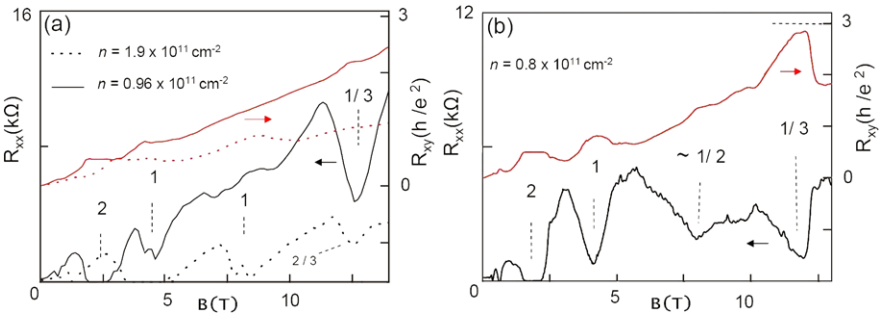

Fig. 8.7 Results of Kim et al. [70, 77]: The Hall resistance and the diagonal resistance as a function of the magnetic field for two samples in four-terminal measurements

attributed to the energy gaps of the incompressible state at $\nu = \frac{1}{3}$ that separate the many-body ground state from the excited states. Measurements of activation gaps at integer filling factors have been already reported for monolayer [53] and bilayer [76] graphene.

The activation gap at $\nu = \frac{1}{3}$ in monolayer SG, as reported by Andrei et al. [69], is shown in Fig. 8.6(b). They obtained a value of $\Delta/k_B = 4.4$ K at 12 Tesla, where k_B is the Boltzmann constant. The corresponding value at $\nu = 1$ was $\Delta/k_B = 10.4$ K. These values are much higher than those in conventional semiconductor structures. For example, in high mobility GaAs heterostructures, the $\nu = \frac{1}{3}$ activation gap is ~ 2 K at 12 Tesla. The larger gap clearly signifies the robust nature of the $\frac{1}{3}$-FQHE state in graphene.

The fractional QHE on ultraclean suspended graphene devices was also reported by Kim et al. in two-terminal [70], and in multi-terminal [77] magnetotransport measurements (Fig. 8.7). They also observed a remarkable stability of the corre-

lated state in graphene, as compared to that in a conventional 2DEG, due to the enhanced electron-electron interaction. The energy gap was measured via thermal activation, and they reported the gap to be ~ 20 K at 14 Tesla. The hierarchy of FQHE states observed experimentally [78] in high-mobility graphene samples at $n = 0$ Landau level confirms the existence of strong inter-electron interaction in graphene. For $n = 0$, this interaction results in a spontaneous breaking of the SU(4) symmetry (two spin and two valley degrees of freedom) at the FQHE filling factors. The results in Ref. [78] also suggest a strong interaction between the composite fermions within the composite fermion description of the FQHE. Therefore in the composite fermion description of the FQHE in graphene the interaction between the composite fermions should be taken into account. The large $\nu = \frac{1}{3}$-FQHE gap in the $n = 1$ Landau level observed in Ref. [78] supports the theoretical conclusion about strong electron-electron interaction in the $n = 1$ Landau level in graphene. Details about the measurements by these leading experimental groups can also be found elsewhere in this book. Finally, magnetotransport measurements on suspended bilayer and trilayer graphene systems have also been reported [79]. In bilayer systems, a small plateau at $\nu = \frac{1}{3}$ was observed. The $\frac{1}{3}$-FQH state was not observed in trilayer graphene. More experiments on bilayer graphene would certainly help resolving many of the novel effects found theoretically and discussed below.

8.3 Bilayer Graphene

Bilayer graphene consists of two coupled monolayers of graphene [80]. Depending on the orientation of the monolayers, there are two main stacking arrangements of graphene bilayer: (i) AA stacking and (ii) Bernal (AB) stacking. These two possibilities are shown schematically in Fig. 8.8. Only the nearest neighbor inter-layer coupling, characterized by the inter-layer hopping integral, γ_1, is introduced. A typical value of inter-layer hopping integral is $\gamma_1 \approx 400$ meV. Unlike in monolayer graphene, the low energy excitations in bilayer graphene are massive with a parabolic dispersion. The band structure is gapless. The dispersion can be probed by measuring the activation gaps between the neighboring Landau levels [76].

The Hamiltonian of a bilayer graphene in a perpendicular magnetic field is described by a 4×4 matrix, which, within the basis of Hamiltonian (8.10) can be expressed as

$$\mathcal{H}_{\xi}^{(AA)} = \xi \begin{pmatrix} 0 & v_F\pi_- & \xi\gamma_1 & 0 \\ v_F\pi_+ & 0 & 0 & \xi\gamma_1 \\ \xi\gamma_1 & 0 & 0 & v_F\pi_- \\ 0 & \xi\gamma_1 & v_F\pi_+ & 0 \end{pmatrix}, \tag{8.20}$$

for the AA stacking and

$$\mathcal{H}_{\xi}^{(AB)} = \xi \begin{pmatrix} 0 & v_F\pi_- & 0 & 0 \\ v_F\pi_+ & 0 & \xi\gamma_1 & 0 \\ 0 & \xi\gamma_1 & 0 & v_F\pi_- \\ 0 & 0 & v_F\pi_+ & 0 \end{pmatrix}, \tag{8.21}$$

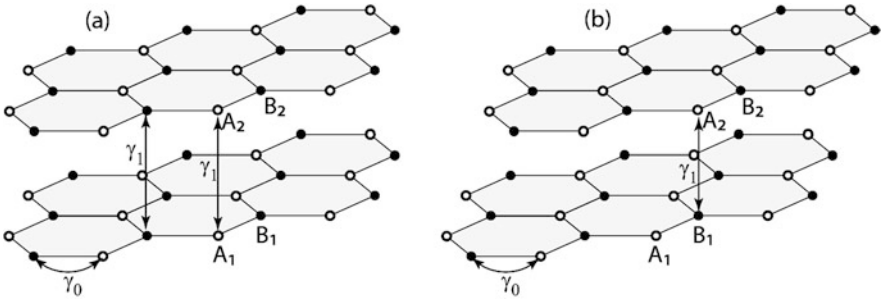

Fig. 8.8 Schematic illustration of two different stacking of bilayer graphene, consisting of two coupled monolayers of graphene: (**a**) AA stacking; (**b**) Bernal (AB) stacking. Each graphene layer consists of two inequivalent sites A and B. The intra-layer and intra-layer hopping integrals are shown by γ_0 and γ_1, respectively

for the Bernal stacking. The Hamiltonians (8.20)–(8.21) are expressed in the basis $(\psi_{A_1}, \psi_{B_1}, \psi_{A_2}, \psi_{B_2})^T$ for the K valley ($\xi = 1$) and $(\psi_{B_2}, \psi_{A_2}, \psi_{B_1}, \psi_{A_1})^T$ for the K′ valley ($\xi = -1$), where the superscript 'T' indicates the transpose of a vector. Here A_1, B_1 and A_2, B_2 correspond to sublattices of monolayers 1 and 2, respectively.

8.3.1 Magnetic Field Effects

In an external magnetic field each monolayer has discrete sets of Landau levels, which are coupled in bilayer graphene. For the AA and AB stackings the coupling of Landau levels have different structures. For the AA stacking the coupling occurs between the same Landau levels, i.e., with the same Landau index n, of two monolayers, resulting in a splitting of the initially degenerate Landau levels of two monolayers. The wave functions of bilayer graphene with AA stacking have the following form

$$\Psi_{n,m}^{(bi,AA)} = \begin{pmatrix} \Psi_{n,m}^{(mono)} \\ \pm\Psi_{n,m}^{(mono)} \end{pmatrix} \sim \begin{pmatrix} \phi_{|n|-1,m} \\ \phi_{|n|,m} \\ \phi_{|n|-1,m} \\ \phi_{|n|,m} \end{pmatrix}, \tag{8.22}$$

which shows that the wave functions of bilayer graphene with AA stacking are a mixture of $|n|$-th and $(|n|-1)$-th non-relativistic Landau wave functions [81]. The Haldane pseudopotentials of bilayer Landau levels are completely identical to the corresponding pseudopotentials of the monolayer graphene. Therefore the FQHE in such a bilayer does not bring in any new features.

A different situation occurs for the Bernal stacking, which introduces coupling between different Landau levels of the two layers. The structure of the wave functions of such a bilayer graphene is as follows

$$\Psi_{n,m}^{(bi,AB)} \sim \begin{pmatrix} \phi_{|n|-1,m} \\ \phi_{|n|,m} \\ \phi_{|n|,m} \\ \phi_{|n|+1,m} \end{pmatrix}. \tag{8.23}$$

In this case the wave functions of bilayer graphene correspond to mixtures of the non-relativistic Landau wave functions with indices $n-1$, n, and $n+1$. Such a mixture can modify the interaction within a single Landau level of bilayer graphene and can influence the properties of the FQHE in this system. In what follows, we consider only the bilayer graphene with Bernal stacking.

8.3.2 Biased Bilayer Graphene

In addition to the inter-layer coupling, there are few other parameters, which can control the interaction properties of bilayer graphene. These parameters are inter-layer bias voltage, U, which can be varied for a given system [82, 83], and the intra-layer asymmetry, Δ, in the bottom layer, which is in contact with a substrate. Such an asymmetry depends on the substrate and results in different on-site energies for sublattices A_1 and B_1. With these additional terms the Hamiltonian of bilayer graphene with Bernal stacking (for valley $\xi = \pm 1$) takes the form [84]

$$\mathcal{H}_{\xi}^{(AB)} = \xi \begin{pmatrix} \frac{U}{2} + \frac{\Delta}{4}(1+\xi) & v_F\pi_- & 0 & 0 \\ v_F\pi_+ & \frac{U}{2} - \frac{\Delta}{4}(1+\xi) & \xi\gamma_1 & 0 \\ 0 & \xi\gamma_1 & -\frac{U}{2} + \frac{\Delta}{4}(1-\xi) & v_F\pi_- \\ 0 & 0 & v_F\pi_+ & -\frac{U}{2} - \frac{\Delta}{4}(1-\xi) \end{pmatrix}. \tag{8.24}$$

The eigenfunctions of Hamiltonian (8.24) have the following form [see (8.23)]

$$\Psi_{n,m}^{(bi)} = \begin{pmatrix} \xi C_1 \phi_{|n|-1,m} \\ iC_2\phi_{|n|,m} \\ iC_3\phi_{|n|,m} \\ \xi C_4 \phi_{|n|+1,m} \end{pmatrix}, \tag{8.25}$$

where the coefficients, C_1, C_2, C_3, and C_4, can be found from the following linear system of equations

$$\varepsilon C_1 = \left[\xi u + \delta(1+\xi)\right] C_1 - \sqrt{n} C_2 \tag{8.26}$$

$$\varepsilon C_2 = \left[\xi u - \delta(1+\xi)\right] C_2 - \sqrt{n} C_1 + \tilde{\gamma}_1 C_3 \tag{8.27}$$

$$\varepsilon C_3 = \left[-\xi u - \delta(1-\xi)\right] C_3 + \sqrt{n+1} C_4 + \tilde{\gamma}_1 C_2 \tag{8.28}$$

$$\varepsilon C_4 = \left[-\xi u + \delta(1-\xi)\right] C_4 + \sqrt{n+1} C_3, \tag{8.29}$$

where all energies are expressed in units of the Coulomb energy, $\varepsilon_B = \hbar v_F/\ell_0$, ε is the energy of the Landau level, $\delta = \Delta/(4\varepsilon_B)$, $u = U/(2\varepsilon_B)$, and $\tilde{\gamma}_1 = \gamma_1/\varepsilon_B$.

Then the eigenvalue equation which determines the Landau energy spectrum of bilayer graphene is given by [85]

$$\begin{aligned}&\left[(\varepsilon+\xi u)^2-\delta^2(1-\xi)^2-2n\right]\left[(\varepsilon-\xi u)^2-\delta^2(1+\xi)^2-2(n+1)\right]\\&\quad=\tilde{\gamma}_1^2\left[(\varepsilon-\delta)^2-(u+\delta)^2\right].\end{aligned}\tag{8.30}$$

For each value of $n \geq 0$ there are four solutions of the eigenvalue equation (8.30), corresponding to four Landau levels in a bilayer graphene for a given valley, $\xi = \pm 1$. For convenience, let us introduce the following labelling scheme for these Landau levels. The four Landau levels correspond to two valence levels which usually have negative energies, and two conduction levels, which have positive energies. Then the four Landau levels of bilayer graphene for a given value of n ($n \geq 0$) and a given valley, ξ, can be labelled as $n_i^{(\xi)}$, where $i = -2, -1, 1, 2$ is the label of the Landau level in the ascending order of energy. Here negative and positive values of i correspond to valence and conduction levels, respectively. For zero bias voltage, $U = 0$, and zero intra-layer asymmetry, $\Delta = 0$, these four Landau levels are

$$\varepsilon = \pm\sqrt{2n+1+\frac{\tilde{\gamma}_1^2}{2} \pm \frac{1}{2}\sqrt{\left(2+\tilde{\gamma}_1^2\right)^2+8n\tilde{\gamma}_1^2}}.\tag{8.31}$$

In this case each Landau level has two-fold valley degeneracy, i.e., no dependence on the index ξ in (8.31). For finite values of U and Δ, the valley degeneracy is lifted. For zero intra-layer asymmetry, $\Delta = 0$, the Landau energy spectra of two valleys are not independent. They are related through the equation $\varepsilon(n_i^{(\xi)}) = -\varepsilon(n_{-i}^{(-\xi)})$, where $\varepsilon(n_i^{(\xi)})$ is the energy of the Landau level $n_i^{(\xi)}$.

The coefficients C_1, C_2, C_3, and C_4, determined from the solution of the eigenvalue equation (8.30) and the system of equations (8.26)–(8.29), are expressed as

$$C_1 = f\left[\frac{2\tilde{\gamma}_1 n}{[\varepsilon+\xi u-\delta(1-\xi)][(\varepsilon+\xi u)^2-\delta^2(1-\xi)^2-2n]}\right]^{\frac{1}{2}}$$

$$C_2 = f\left[\frac{\tilde{\gamma}_1[\varepsilon-\xi u-\delta(1+\xi)]}{[(\varepsilon-\xi u)^2-\delta^2(1+\xi)^2-2(n+1)]}\right]^{\frac{1}{2}}$$

$$C_3 = f\left[\frac{\tilde{\gamma}_1[\varepsilon+\xi u-\delta(1-\xi)]}{[(\varepsilon+\xi u)^2-\delta^2(1-\xi)^2-2n]}\right]^{\frac{1}{2}}$$

$$C_4 = f\left[\frac{2\tilde{\gamma}_1(n+1)}{[\varepsilon-\xi u-\delta(1+\xi)][(\varepsilon-\xi u)^2-\delta^2(1+\xi)^2-2(n+1)]}\right]^{\frac{1}{2}}.$$

Here the constant f is determined from the normalization condition, $|C_1|^2+|C_2|^2+|C_3|^2+|C_4|^2 = 1$.

Since the FQHE is expected to be observable only in the Landau levels with low values i of the index, n, we consider below the sets of Landau levels of bilayer graphene with $n = 0$ and $n = 1$ only. The wave functions of these Landau levels

are mixtures of the conventional non-relativistic Landau functions with indices 0, 1, and 2.

There are two special Landau levels of bilayer graphene which have unique properties. For $n = 0$ there is a solution of (8.30) with energy $\varepsilon = -u$ for the K valley ($\xi = 1$) and $\varepsilon = u + 2\delta$ for the K′ valley ($\xi = -1$). The corresponding wave function has the form

$$\Psi^{(bi)}_{0_1,m} = \begin{pmatrix} \phi_{0,m} \\ 0 \\ 0 \\ 0 \end{pmatrix}. \tag{8.32}$$

This Landau level of bilayer graphene does not have any admixture of other Landau levels and has exactly the same properties as the 0-th conventional non-relativistic Landau level. At zero u and δ this Landau level has exactly zero energy.

For small values of u and δ there is another solution of (8.30) with $n = 0$ and almost zero energy, $\varepsilon \approx 0$. The corresponding Landau level has the following wave functions

$$\Psi^{(bi)}_{0_{-1},m} = \frac{1}{\sqrt{\tilde{\gamma}_1^2 + 2}} \begin{pmatrix} \tilde{\gamma}_1 \phi_{1,m} \\ 0 \\ \sqrt{2}\phi_{0,m} \\ 0 \end{pmatrix} = \frac{1}{\sqrt{\gamma_1^2 + 2\varepsilon_B^2}} \begin{pmatrix} \gamma_1 \phi_{1,m} \\ 0 \\ \sqrt{2}\varepsilon_B \phi_{0,m} \\ 0 \end{pmatrix}. \tag{8.33}$$

The properties of this Landau level depends on the strength of the magnetic field. In a small magnetic field, $\varepsilon_B \ll \gamma_1$, the wave function becomes $(\psi_{1,m}, 0, 0, 0)^T$ and the Landau level becomes identical to the $n = 1$ non-relativistic Landau level. For a large magnetic field $\varepsilon_B \gg \gamma_1$, the Landau level wave function becomes $(0, 0, \psi_{0,m}, 0)^T$ and the bilayer Landau level has the same properties as for the $n = 0$ non-relativistic Landau level.

8.3.3 Pseudopotentials in Bilayer Graphene

Once the wave functions (8.25) of the bilayer Landau level are evaluated, the form factor in the Haldane pseudopotentials (8.2) can be obtained from

$$F_n(q) = |C_1|^2 L_{n-1}\left(q^2/2\right) + \left(|C_2|^2 + |C_3|^2\right) L_n\left(q^2/2\right) + |C_4|^2 L_{n+1}\left(q^2/2\right). \tag{8.34}$$

In fact, the shape of the form factor tells us about the interaction effects within the bilayer Landau levels. For the Landau level 0_1, defined by (8.32), the form factor is $F_{0_1} = L_0(q^2/2)$, which is exactly the same as the form factor in (8.3) of the non-relativistic system in the $n = 0$ Landau level. Therefore the interaction effect in this Landau level is the same as in the $n = 0$ non-relativistic Landau level.

The bilayer Landau level 0_{-1}, defined by (8.33), exhibits an interesting behavior of bilayer graphene with increasing magnetic fields. The form factor corresponding to that Landau level (8.33) is given by

$$F_{0_{-1}}(q) = \left[\frac{\gamma_1^2}{\gamma_1^2 + 2\varepsilon_B^2}\right] L_1\left(q^2/2\right) + \left[\frac{2\varepsilon_B^2}{\gamma_1^2 + 2\varepsilon_B^2}\right] L_0\left(q^2/2\right). \tag{8.35}$$

With increasing magnetic field, i.e., increasing ε_B, the bilayer Landau level 0_{-1} becomes identical to (i) the $n = 1$ non-relativistic Landau level with the form factor $L_1(q^2/2)$ for a small magnetic field, $\varepsilon_B \ll \gamma_1$; (ii) the $n = 1$ Landau level of monolayer graphene with the form factor $\frac{1}{2}[L_0(q^2/2) + L_1(q^2/2)]$ for $\varepsilon_B = \gamma_1/\sqrt{2}$; and, (iii) the $n = 0$ non-relativistic Landau level with the form factor $L_0(q^2/2)$ for a large magnetic field, $\varepsilon_B \gg \gamma_1$. For typical values of γ_1, only the first regime will be accessible experimentally. For example, for $\gamma_1 = 400$ meV the condition $\varepsilon_B = \gamma_1/\sqrt{2}$ is only achieved for a magnetic field of $B = 120$ Tesla.

8.3.4 Novel Effects from Electron-Electron Interactions

Once the pseudopotentials are known, the FQHE states in a graphene bilayer can be studied using very accurate numerical techniques. Compared to monolayer graphene, bilayer graphene has additional parameters by which we can control the electron-electron interaction strength. As we recall, in monolayer graphene the interaction strength depends only on the Landau level index. In bilayer graphene the inter-electron interaction strength depends also on the magnetic field, the bias voltage U, and the intra-layer asymmetry Δ. By varying these parameters, the stability, i.e., the excitation gap of the FQHE states can therefore be controlled [86].

Stable FQHE states in bilayer graphene are expected in the $n = 0$ and $n = 1$ bilayer Landau level sets. These sets are the mixtures of $n = 0$, $n = 1$, and $n = 2$ non-relativistic Landau level wave functions. The mixture depends on the values of the parameters of the system. With a non-zero bias voltage and intra-layer asymmetry, the valley degeneracy of the Landau levels of bilayer graphene is lifted, resulting in different properties of Landau levels for different valleys.

The stability of the FQHE state is characterized by the value of the corresponding FQHE gap. For the primary filling fractions of the FQHE, i.e., $\nu = \frac{1}{3}$, $\frac{1}{5}$, $\frac{2}{5}$ etc., the bilayer system shows a similar behavior. Therefore, in what follows, only the results for the $\nu = \frac{1}{3}$ FQHE state are shown. The general behavior of the FQHE gap for different parameters of the bilayer system is illustrated in Figs. 8.9, 8.10 and 8.11. For each value of n, $n = 0$ and $n = 1$, there are four Landau levels in each valley. Within this set of bilayer Landau levels, there is one special Landau level which has an unique property. This Landau level has the label $0_1^{(+)}$ with the wave function given by (8.32), which is just the $n = 0$ non-relativistic Landau wave function for *all parameters* of bilayer graphene. Therefore, the interaction properties within this Landau level are identical to the interaction properties of the $n = 0$ non-relativistic

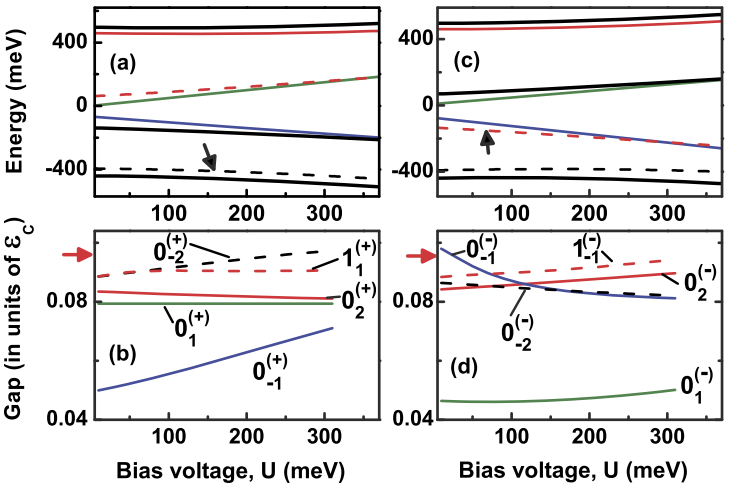

Fig. 8.9 Landau levels of bilayer graphene [panels (**a**) and (**c**)] are shown as a function of the bias voltage, U, i.e., the difference between the on-site energies in the two layers. Panels (**b**) and (**d**): the Coulomb gaps of $\frac{1}{3}$-FQHE in corresponding Landau levels. The numbers next to the lines are the labels of the Landau levels. The same types of lines [in panels (**a**) and (**b**) and panels (**c**) and (**d**)] correspond to the same Landau levels. Panels (**a**) and (**b**) correspond to valley K, while panels (**c**) and (**d**) correspond to valley K′. The system is characterized by $\Delta = 150$ meV, $\gamma_1 = 400$ meV, and a magnetic field $B = 15$ Tesla. The *arrows* in panels (**a**) and (**c**) show the Landau level with the strongest $\frac{1}{3}$-FQHE. The *arrows* in panels (**b**) and (**d**) indicate the gap of $\frac{1}{3}$-FQHE in the $n = 1$ Landau level of monolayer graphene

Landau level and correspondingly the $n = 0$ Landau level of monolayer graphene. The gap of the FQHE at this Landau level does not depend on the parameters of the system and is the same as that of the $n = 0$ monolayer graphene. This property is shown in Figs. 8.9–8.11 as a function of bias voltage, asymmetry parameter Δ, and the magnetic field, where it is shown that the FQHE gap of the Landau level $0^{(+)}_1$ does not depend on the parameters of bilayer graphene.

From Figs. 8.9–8.11 it is quite clear that in each valley the bilayer graphene has four Landau levels with a strong $\frac{1}{3}$-FQHE for all values of the parameters of the system. These levels have the following labels: $0^{(+)}_{-2}$, $0^{(+)}_1$, $0^{(+)}_2$, $1^{(+)}_1$ (valley K) and $0^{(-)}_{-2}$, $0^{(-)}_{-1}$, $0^{(-)}_2$, $1^{(-)}_{-1}$ (valley K′). Therefore for a given valley there are three Landau levels with $n = 0$ and one Landau level with $n = 1$, which all show a stable FQHE. The gaps of the corresponding FQHE states are usually between the gaps of $n = 0$ and $n = 1$ $\nu = \frac{1}{3}$-FQHE state in monolayer graphene. The value of the gap of the $\frac{1}{3}$-FQHE state in the $n = 1$ Landau level of monolayer graphene is shown by red arrows in Figs. 8.9–8.11. In the Landau level $0^{(+)}_{-2}$, for a large asymmetry (see Fig. 8.10), the FQHE state becomes more stable than the corresponding state in monolayer graphene.

The Landau level with the label $0^{(+)}_{-1}$ shows a strong dependence of the interaction properties on the parameters of the system. Namely, with increasing bias voltage or

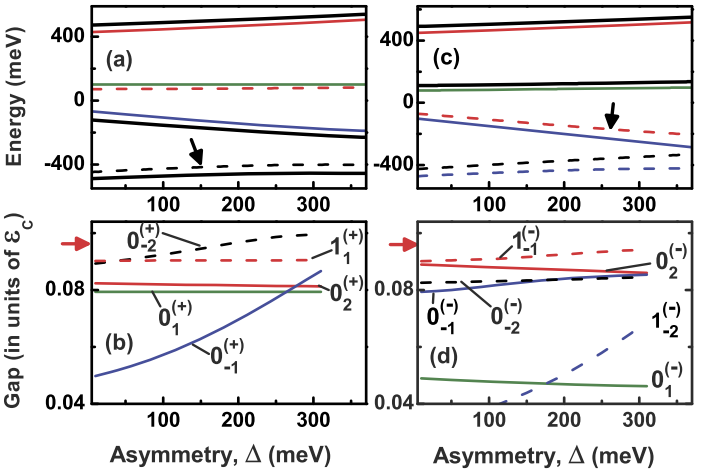

Fig. 8.10 Landau levels of bilayer graphene [panels (**a**) and (**c**)] are shown as a function of the intra-layer asymmetry, Δ. Panels (**b**) and (**b**): the Coulomb gaps of $\frac{1}{3}$-FQHE in corresponding Landau levels. The numbers next to the lines are the labels of the Landau levels. The same types of lines [in panels (**a**) and (**b**) and panels (**c**) and (**d**)] correspond to the same Landau levels. Panels (**a**) and (**b**) correspond to valley K, while panels (**c**) and (**d**) correspond to valley K$'$. The system is characterized by $U = 200$ meV, $\gamma_1 = 400$ meV, and a magnetic field $B = 15$ Tesla. The *arrows* in panels (**a**) and (**c**) show the Landau level with the strongest $\frac{1}{3}$-FQHE. The *arrows* in panels (**b**) and (**d**) indicate the gap of $\frac{1}{3}$-FQHE in the $n = 1$ Landau level of monolayer graphene

intra-layer asymmetry, the gap of the FQHE state and correspondingly its stability strongly increases. At a fixed filling factor of bilayer graphene, this type of behavior can result in the unique experimental observation of a transition from a non-FQHE state at small values of the bias voltage (for example) to a FQHE state at large bias voltages.

The solid black lines in Figs. 8.9–8.11 correspond to the Landau levels without a stable FQHE state. It should be noted that there is also no clear boundary between the Landau levels with and without the FQHE, i.e., between two Landau levels with the FQHE there is a Landau level without FQHE (see Fig. 8.9). This property can be observed experimentally if the FQHE is studied as a function of the filling factor of bilayer graphene while the other parameters of the system are fixed. That means, if one varies the filling factor of bilayer graphene and studies the $\frac{1}{3}$-state at each Landau level then one should be able to observe transitions from the FQHE to no-FQHE state and back to the FQHE state. We should emphasize that this unique phenomenon has never been observed before in conventional two-dimensional systems.

The results illustrated in Fig. 8.9–8.11 are typical for the large inter-layer hopping integral, $\gamma_1 \approx 400$ meV. At smaller values of γ_1, bilayer graphene shows additional features due to anticrossing of the Landau levels as a function of the parameters of the system, i.e., the bias voltage. Such an anticrossing results in a transition of the type, FQHE—no FQHE—FQHE *within the same Landau level* [86]. This be-

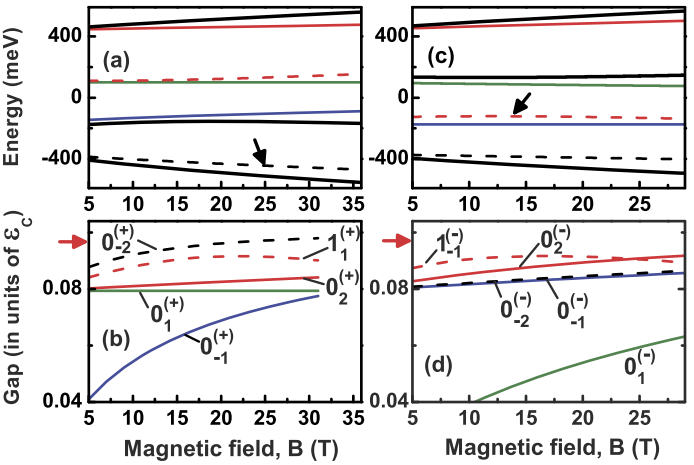

Fig. 8.11 Landau levels of bilayer graphene [panels (**a**) and (**c**)] are shown as a function of the magnetic field. Panels (**b**) and (**b**): the Coulomb gaps of the $\frac{1}{3}$-FQHE in corresponding Landau levels. The numbers next to the lines are the labels of the Landau levels. The same types of lines [in panels (**a**) and (**b**) and panels (**c**) and (**d**)] correspond to the same Landau levels. Panels (**a**) and (**b**) correspond to the valley K, while panels (**c**) and (**d**) correspond to the valley K′. The system is characterized by $\Delta = 150$ meV, $U = 200$ meV, and $\gamma_1 = 400$ meV. The *arrows* in panels (**a**) and (**c**) show the Landau level with the strongest $\frac{1}{3}$-FQHE. The *arrows* in panels (**b**) and (**d**) indicate the gap of the $\frac{1}{3}$-FQHE state in the $n = 1$ Landau level of monolayer graphene

havior is illustrated in Fig. 8.12 for three different values of the inter-layer hopping integral. The actual values of the inter-layer hopping integral depend on the experimental realization of bilayer graphene and is about 400 meV. The anticrossing and the coupling of different Landau levels is more pronounced at small values of γ_1. The anticrossing should be experimentally observable if the filling factor of bilayer graphene is kept fixed and the bias voltage is varied.

For a small inter-layer tunnelling integral and a small bias voltage, some Landau levels in bilayer graphene show strong non-monotonic behavior of the FQHE gap with well-pronounced maxima. This property is illustrated in Fig. 8.13, where the FQHE gap is shown as a function of the inter-layer coupling, γ_1, for two values of the bias voltage, U. The inter-layer coupling can be varied experimentally, for example, by applying a tilted magnetic field, where the parallel component of the magnetic field influences the inter-layer coupling [81]. For small bias voltage, the Landau level $0_1^{(-)}$ has the wave function of the form of (8.33). With variation of the intra-layer tunnelling integral, the wave function (8.33) transforms from the $n = 0$ non-relativistic Landau wave function for small γ_1 to the $n = 1$ monolayer graphene Landau function for $\gamma_1 = 2^{\frac{1}{2}}\hbar v_F/\ell_0$ and finally to the $n = 1$ non-relativistic Landau level function for large γ_1. Therefore the FQHE gap of bilayer graphene in the $0_1^{(-)}$ Landau level is equal to the FQHE gap of the $n = 0$ non-relativistic Landau level for small γ_1 and to the FQHE gap of the $n = 1$ monolayer graphene Landau level for $\gamma_1 = 2^{\frac{1}{2}}\hbar v_F/\ell_0$. This property is illustrated in Fig. 8.13(a), where a strong

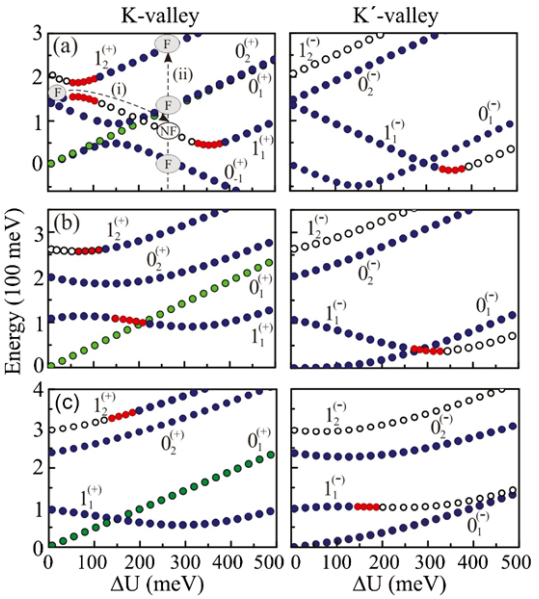

Fig. 8.12 A few lowest Landau levels of the conduction band as a function of the bias potential, U, for different values of inter-layer coupling: (**a**) $\gamma_1 = 30$ meV (**b**) $\gamma_1 = 150$ meV and (**c**) $\gamma_1 = 300$ meV and a magnetic field of 15 Tesla. The intra-layer asymmetry Δ is zero. The *numbers next to the curves* denote the corresponding Landau levels. *Left* and *right columns* correspond to the K and K′ valleys, respectively. The Landau levels where the FQHE can be observed are drawn as *blue* and *green filled dots*. The *green dots* correspond to the Landau levels where the FQHE states are identical to that of a monolayer of graphene or a non-relativistic conventional system. The *red dots* represent Landau levels with weak FQHE. The *open dots* correspond to Landau levels where the FQHE is absent. In (**a**), the *dashed lines* labeled by (i) illustrates the transition between FQHE (symbol 'F') and no FQHE (symbol 'NF') states under a constant gate voltage and variable bias potential [86]

non-monotonic behavior of the FQHE gap of the $0_1^{(-)}$ Landau level is shown. The maximum of the FQHE gap at $\gamma_1 \approx 2^{\frac{1}{2}} \hbar v_F/\ell_0$ corresponds to the FQHE gap at $n = 1$ monolayer graphene Landau level.

The above analysis clearly indicates that the interaction properties of biased bilayer graphene depend both on the magnetic field and on the parameters of the system, such as the bias voltage, intra-layer asymmetry, and the inter-layer hopping integral. In each valley there are a few Landau levels which display a strong FQHE, the gap of which depends on the parameters of the bilayer. This dependence can be observed experimentally as transitions between the FQHE and no-FQHE states within the same Landau level when the parameters of the system, e.g., the bias voltage, are changed. Although the FQHE gaps can be controlled by the parameters of the bilayer system, the gaps usually do not exceed the corresponding FQHE gaps in monolayer graphene.

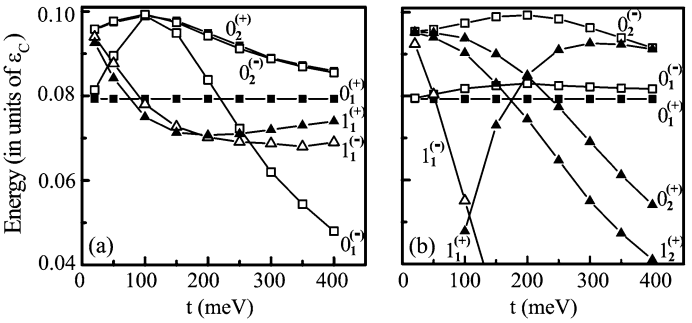

Fig. 8.13 The FQHE gaps shown for different Landau levels. The *labels next to the lines* denote the corresponding Landau levels. (**a**) $U = 10$ meV, and (**b**) $U = 300$ meV. All systems are fully spin polarized and the magnetic field is 15 Tesla. The intra-layer asymmetry Δ is zero [86]

8.3.5 Interacting Electrons in Rotated Bilayer Graphene

Epitaxial graphene [87], which is thermally grown on the C face of the SiC substrate, as well as graphene grown by chemical vapor deposition (CVD) [88], are multilayer films and yet, quite surprisingly display behavior similar to that of a single layer graphene [89]. These systems are known to have a high degree of rotational misalignments [90]. Theoretical studies of turbostratic bilayer graphene [91–94] have indicated that in this case the interlayer coupling is suppressed and the systems can be roughly considered as two decoupled layers of graphene, as confirmed by scanning tunneling spectroscopy together with Landau level spectroscopy measurements [95]. At the same time due to the modulated nature [93] of the interlayer transfer integral, these systems show quite rich low-energy physics, which strongly depends on the nature of the commensurate stacking faults [94]. In this section, we will deal with the question: how does the electron-electron interaction manifest itself in a rotated bilayer graphene?

In a misoriented bilayer graphene, one graphene layer is rotated relative to the other layer by an angle θ. We assume that the axis of rotation passes through the atoms of A-sublattices in the two layers (Fig. 8.14). In general, the axis can pass through any point of the bilayer. There is a special type of rotation, called commensurate rotation, which is determined by the condition that the atoms of the two layers are coincident not only at the axis of rotation but also at some other points. The angles corresponding to the commensurate stacking fault are determined from: $\cos\theta = (3q^2 - p^2)/(3q^2 + p^2)$, where $q > p > 0$ are integers [93].

There are two types of commensurate rotations that are distinguished by their symmetry, even or odd, with respect to the sublattice exchange [94]. For the even commensurate stacking fault both A and B sublattice sites of the two layers are coincident at some point, while for the odd stacking fault only A sublattice sites of the two layers are coincident both at the axis of rotation and at some other points. The regular stacking orientations, AA or Bernal, are realized at the following angles: AA-stacking—at angle $\theta = 0$, which corresponds to the even stacking orientation, and Bernal stacking—at angle $\theta = 60°$, which is the odd orientation.

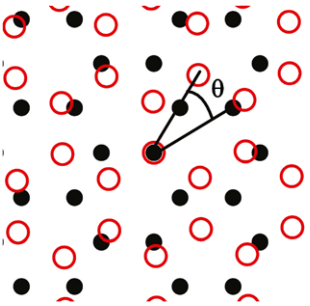

Fig. 8.14 Misoriented graphene bilayer with angle of rotation θ, shown schematically in real space. The axis of rotation passes through atoms of A-sublattice in the two layers. The *black solid dots* and the *red open dots* are the atomic positions in two different layers

The even and odd stacking faults can also be described in terms of the properties of the reciprocal lattices of the two layers [94]. The reciprocal lattice of a graphene layer consist of K and K′ sets of points: $\mathbf{K}+\mathbf{G}_{m,k}$, $\mathbf{K}'+\mathbf{G}_{m,k}$, where $\mathbf{G}_{m,k} = m\mathbf{G}_1 + k\mathbf{G}_2$, m and k are integers, $\mathbf{G}_1 = 2\pi/a(1, \frac{1}{\sqrt{3}})$ and $\mathbf{G}_2 = 2\pi/a(0, \frac{2}{\sqrt{3}})$ are primitive reciprocal lattice vectors, and $\mathbf{K} = 2\pi/a(\frac{1}{3}, \frac{1}{\sqrt{3}})$, $\mathbf{K}' = 2\pi/a(\frac{2}{3}, 0)$. These two sets of points correspond to the two valleys of graphene. Then in terms of the reciprocal lattices, a rotation by an angle θ in real space corresponds to a rotation by an angle θ in reciprocal space about the origin, i.e, (0,0). For an even commensurate stacking fault, the K points of the reciprocal lattices of the two layers are then coincident [94], i.e., $\mathbf{K} + \mathbf{G}_{m,k} = \mathbf{K}(\theta) + \mathbf{G}_{m',k'}(\theta)$, while for the odd stacking fault the K and K′ points are coincident, i.e., $\mathbf{K} + \mathbf{G}_{m,k} = \mathbf{K}'(\theta) + \mathbf{G}_{m',k'}(\theta)$ [94]. Here k, m, k', and m' are integer numbers.

Due to the periodic modulation of rotated bilayer graphene at the commensurate angles, the effective interlayer coupling, γ_{eff}, is determined by the Fourier transform of the interlayer potential function at the wave vector $\mathbf{K} + \mathbf{G}_{m,k}$. Then the effective low-energy Hamiltonians of the rotated bilayer at the commensurate condition are given by [94]

$$\mathcal{H}_{even} = \begin{pmatrix} 0 & v_F\pi_- & \gamma_\theta e^{i\phi/2} & 0 \\ v_F\pi_+ & 0 & 0 & \gamma_\theta e^{-i\phi/2} \\ \gamma_\theta^+ e^{i\phi/2} & 0 & 0 & v_F\pi_- \\ 0 & \gamma_\theta^+ e^{i\phi/2} & v_F\pi_+ & 0 \end{pmatrix}, \tag{8.36}$$

$$\mathcal{H}_{odd} = \begin{pmatrix} 0 & v_F\pi_- & 0 & 0 \\ v_F\pi_+ & 0 & \gamma_\theta & 0 \\ 0 & \gamma_\theta^+ & 0 & v_F\pi_- \\ 0 & 0 & v_F\pi_+ & 0 \end{pmatrix}. \tag{8.37}$$

The Hamiltonians (8.36) and (8.37) are generalization of the Hamiltonians (8.20) and (8.21) of regular bilayer graphene. Here $\gamma_\theta = \gamma_{eff} e^{i\theta}$ and the phase angle ϕ is determined by the interlayer potential.

For the odd rotated bilayer and for all rotation angles, the Hamiltonian (8.37) is completely identical to the Hamiltonian (8.21) of bilayer graphene with Bernal stacking. The only difference is the magnitude of the interlayer coupling. While for Bernal stacking the interlayer coupling γ_1 is around 400 meV, the coupling

in the rotated bilayer is an order of magnitude smaller, $\gamma_\theta \sim 10$ meV. Therefore, for the effects of the electron-electron interaction and the properties of FQHE, the odd-rotated bilayer behaves similar to bilayer graphene with Bernal stacking and the results of the previous section are applicable to the odd-rotated bilayer.

For the even rotated bilayer the Hamiltonian is similar to the Hamiltonian of bilayer graphene with AA stacking and the interaction properties of the even rotated bilayer become completely identical to the bilayer graphene with AA stacking. The additional phases in the Hamiltonian (8.36) affect the phases of the wave function components, which can be visible in magneto-optics experiments [96], but the pseudopotentials do not depend on these phases and correspondingly on the interlayer coupling. The pseudopotentials for the even rotated bilayer are identical to those of individual graphene layers. Therefore, as far as the FQHE is concerned, the even rotated bilayer can be considered as two decoupled graphene layers for any twist angle.

8.4 Fractional Quantum Hall Effect in Trilayer Graphene

A trilayer graphene consisting of three coupled graphene layers, has a very unique electronic energy spectrum. Within the nearest-neighbor inter-layer coupling approximation, the energy spectrum of trilayer graphene with Bernal stacking consists effectively of decoupled single-layer graphene and the bilayer graphene energy spectra. Therefore the trilayer graphene system allows us to study experimentally both the massless and massive energy spectra within a single system. In a strong perpendicular magnetic field the Landau energy spectrum of trilayer graphene becomes the combination of Landau levels of single-layer and bilayer graphene. This combination exhibits many crossings of the Landau levels as a function of the magnetic field. At the crossing points the Landau levels are highly degenerate. The degeneracy is lifted when the higher-order inter-layer coupling terms are taken into account, resulting in rich properties of quantum Hall effect in trilayer graphene [97, 98].

Novel features of the FQHE should be also expected in trilayer graphene [99]. In what follows, we explore the properties of FQHE in trilayer graphene within the nearest-neighbor inter-layer coupling approximation. The trilayer graphene can be in two main stacking arrangements: the ABA (Bernal) stacking and the ABC stacking, which are schematically shown in Fig. 8.15.

Within the nearest neighbour inter-layer coupling approximation, the Hamiltonian of trilayer graphene is characterized by two parameters alone: the intra-layer, γ_0, and inter-layer, γ_1, tunnelling integrals. In a perpendicular magnetic field the Hamiltonian of trilayer graphene for a single valley, e.g. valley K, takes the form [97, 100]

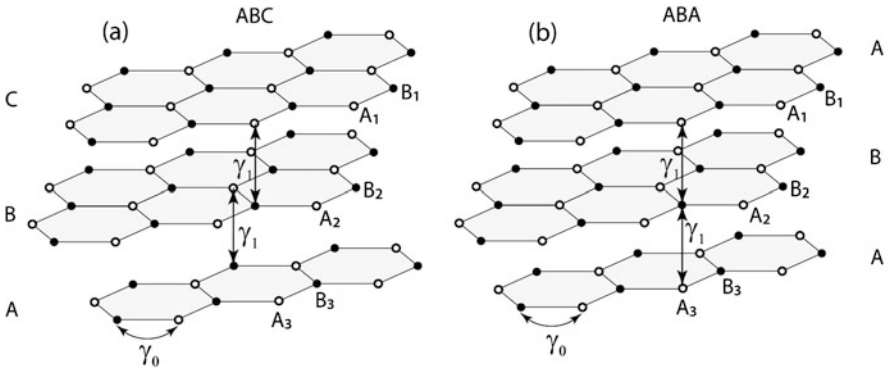

Fig. 8.15 Schematic illustration of two different stacking arrangements of trilayer graphene, consisting of three coupled monolayers of graphene: (**a**) ABC stacking; (**b**) ABA stacking. Each graphene layer consists of two inequivalent sites A and B. The intra-layer and inter-layer hopping integrals are shown by γ_0 and γ_1, respectively

$$\mathcal{H}^{(ABA)} = \begin{pmatrix} 0 & v_F\pi_- & 0 & 0 & 0 & 0 \\ v_F\pi_+ & 0 & \gamma_1 & 0 & 0 & 0 \\ 0 & \gamma_1 & 0 & v_F\pi_- & 0 & \gamma_1 \\ 0 & 0 & v_F\pi_+ & 0 & 0 & 0 \\ 0 & 0 & 0 & 0 & 0 & v_F\pi_- \\ 0 & 0 & \gamma_1 & 0 & v_F\pi_+ & 0 \end{pmatrix}, \tag{8.38}$$

for the ABA stacking and

$$\mathcal{H}^{(ABC)} = \begin{pmatrix} 0 & v_F\pi_- & 0 & 0 & 0 & 0 \\ v_F\pi_+ & 0 & \gamma_1 & 0 & 0 & 0 \\ 0 & \gamma_1 & 0 & v_F\pi_- & 0 & 0 \\ 0 & 0 & v_F\pi_+ & 0 & \gamma_1 & 0 \\ 0 & 0 & 0 & \gamma_1 & 0 & v_F\pi_- \\ 0 & 0 & 0 & 0 & v_F\pi_+ & 0 \end{pmatrix}, \tag{8.39}$$

for the ABC stacking. The Landau levels of trilayer graphene can be obtained from the Hamiltonian matrix (8.38) (or (8.39)). The corresponding wave functions are parametrized by the integer n and can be expressed through the non-relativistic Landau level wave functions as

$$\Psi^{(ABA)} = \begin{pmatrix} C_1\phi_{n-1,m} \\ C_2\phi_{n,m} \\ C_3\phi_{n,m} \\ C_4\phi_{n+1,m} \\ C_5\phi_{n-1,m} \\ C_6\phi_{n,m} \end{pmatrix}, \tag{8.40}$$

for the ABA stacking and

$$\Psi^{(ABC)} = \begin{pmatrix} C_1\phi_{n-1,m} \\ C_2\phi_{n,m} \\ C_3\phi_{n,m} \\ C_4\phi_{n+1,m} \\ C_5\phi_{n+1,m} \\ C_6\phi_{n+2,m} \end{pmatrix}, \tag{8.41}$$

for the ABC stacking. Therefore the Landau wave functions of trilayer graphene are the combinations of n, $n-1$, and $n+1$ non-relativistic Landau functions for the ABA stacking, and n, $n-1$, $n+1$, and $n+2$ non-relativistic Landau functions for the ABC stacking. With the known wave functions, the corresponding form factors of the Haldane pseudopotential can be evaluated from the following expressions

$$\begin{aligned} F_n^{ABA}(q) = {} & \left(|C_1|^2 + |C_5|^2\right) L_{n-1}\left(q^2/2\right) \\ & + \left(|C_2|^2 + |C_3|^2 + |C_6|^2\right) L_n\left(q^2/2\right) + |C_4|^2 L_{n+1}\left(q^2/2\right), \end{aligned} \tag{8.42}$$

for the ABA stacking and

$$\begin{aligned} F_n^{ABC}(q) = {} & |C_1|^2 L_{n-1}\left(q^2/2\right) + \left(|C_2|^2 + |C_3|^2\right) L_n\left(q^2/2\right) \\ & + \left(|C_4|^2 + |C_5|^2\right) L_{n+1}\left(q^2/2\right) + |C_6|^2 L_{n+2}\left(q^2/2\right), \end{aligned} \tag{8.43}$$

for the ABC stacking.

The Landau energy spectrum found from the Hamiltonian matrices (8.38) and (8.39) have the following properties:

ABA Stacking The ABA stacking has the unique property that it is completely identical to the combination of the single graphene layer and the bilayer graphene systems. This property follows directly from the Hamiltonian (8.38). Therefore the Landau levels of trilayer graphene consist of the Landau levels of single layer graphene and the Landau levels of bilayer graphene. Within the nearest neighbour inter-layer coupling approximation, considered in the Hamiltonian (8.38) these Landau levels are decoupled. Hence the FQHE in this system should be identical to the FQHE in a single layer graphene and in bilayer graphene.

ABC Stacking For each $n \geq 0$ there are six Landau energy levels with energies [100]

$$\varepsilon_n^{(1)} = \pm\sqrt{2\sqrt{\eta}\cos\left(\frac{\eta}{3}\right) - \frac{\delta_1}{3}} \tag{8.44}$$

$$\varepsilon_n^{(2)} = \pm\sqrt{2\sqrt{\eta}\cos\left(\frac{\eta+4\pi}{3}\right) - \frac{\delta_1}{3}} \tag{8.45}$$

$$\varepsilon_n^{(3)} = \pm\sqrt{2\sqrt{\eta}\cos\left(\frac{\eta+2\pi}{3}\right) - \frac{\delta_1}{3}} \tag{8.46}$$

where

$$\cos\eta = \frac{-\frac{\delta_1^3}{27} + \frac{\gamma_1\gamma_2}{6} - \frac{\gamma_3}{2}}{(\frac{\delta_1^2}{9} - \frac{\delta_2}{3})^{3/2}} \tag{8.47}$$

and

$$\delta_1 = -2\gamma_1^2 - 3(1+n)\varepsilon_B^2 \tag{8.48}$$

$$\delta_2 = \gamma_1^4 + 2(1+n)\gamma_1^2\varepsilon_B^2 + \left(2+6n+3n^2\right)\varepsilon_B^4 \tag{8.49}$$

$$\delta_3 = -n(n+1)(n+2)\varepsilon_B^6. \tag{8.50}$$

At $n = -1$, there are three Landau levels. One Landau level has zero energy, $\varepsilon = 0$, with the wave function $\Psi^{(ABC)} \propto (0, 0, 0, -\varepsilon_B\phi_{0,m}, 0, \gamma_1\phi_{1,m})$. The other two levels have the energies $\varepsilon = \pm\sqrt{\varepsilon_B^2 + \gamma_1^2}$ with the wave functions $\Psi^{(ABC)} \propto (0, 0, 0, \gamma_1\phi_{0,m}, \varepsilon\phi_{0,m}, \varepsilon_B\phi_{1,m})$.

At $n = -2$ there is only one Landau level with energy $\varepsilon = 0$ and the wave function $\Psi^{(ABC)} \propto (0, 0, 0, 0, 0, \phi_{0,m})$. This Landau level is completely identical to the $n = 0$ non-relativistic Landau level. Therefore, the FQHE at this Landau level should have exactly the same strength as for the $n = 0$ non-relativistic Landau level.

With the known wave functions of the Landau levels of trilayer graphene, we evaluate the form factors and the corresponding pseudopotentials. With these pseudopotentials we then analyse the properties of the FQHE in trilayer graphene. In Fig. 8.16, the lowest Landau levels of trilayer graphene are shown, where the red and blue lines correspond to the Landau levels with a strong FQHE. The strength of the FQHE is characterized by the excitation gap, which are shown in Fig. 8.16 for the filling factor $\nu = \frac{1}{3}$.

For the ABA stacking, the trilayer graphene can be considered as the decoupled system of single layer and bilayer graphene. The blue and red lines correspond to the Landau levels with a strong FQHE of single layer graphene and bilayer graphene, respectively. The strongest FQHE with a gap of $0.09\varepsilon_C$ is observed in the $n = 1$ single graphene layer [see Fig. 8.16(a)]. At the zero energy, the Landau levels of bilayer graphene and the single-layer graphene are degenerate, having the FQHE of the same strength.

For the ABC stacking (see Fig. 8.16), the trilayer graphene cannot be divided into more simple systems. Similar to the ABA stacking there is one Landau level with the strongest FQHE (the gap is $0.09\varepsilon_C$), the gap of which is close to the FQHE gap of the $n = 1$ single layer graphene. The Landau level with zero energy is identical to the $n = 0$ Landau level of the single-layer graphene and the $n = 0$ non-relativistic Landau level. With a few Landau levels showing the strong FQHE, the strength of the FQHE for the ABC stacking does not exceed the strength of the FQHE in a single-layer graphene.

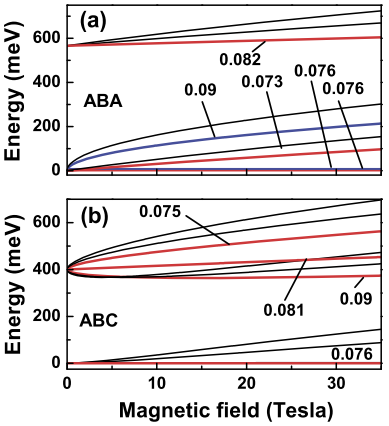

Fig. 8.16 The lowest Landau energy spectra of trilayer graphene shown as the function of the magnetic field for (**a**) ABA and (**b**) ABC stacking. The *red* and *blue lines* correspond to the Landau levels with strong FQHE. The numbers next to the lines are the values of the $\nu = \frac{1}{3}$ FQHE gap (in units of $\varepsilon_C = e^2/\kappa\ell_0$) at the corresponding Landau level. In panel (**a**) the *blue* and *red lines* corresponds to the Landau levels of the single layer and bilayer graphene, respectively

8.5 Some Unique Properties of Interacting Dirac Fermions

In this section, we discuss some of the exotic properties of interacting Dirac fermions. These include the pfaffians in graphene and the FQHE in a topological insulator.

8.5.1 The Pfaffians in Condensed Matter

The vast majority of fractional quantum Hall states observed in the experiments occur at rational filling fractions $\nu = p/q$, with q being an *odd* integer [3, 7]. Further, there have never been any experimental indications that the FQHE would occur at $\nu = \frac{1}{2}$. One also expects that the states in the $(n+1)$-th lowest Landau level (LLL) should be similar to that at the LLL for $\nu = \frac{1}{2}$, because the lower n Landau levels are then completely filled. The discovery of FQHE in a traditional 2DEG at $\nu = \frac{5}{2}$ in 1987 [101, 102] was therefore a total surprise, for which a proper explanation of the nature of the state has remained elusive ever since [103]. The state was found to be quite robust with a sizeable excitation gap ($\Delta \sim 0.6$ K) and a well-defined plateau. The Laughlin wave function (8.1) is not suitable for this state because at $\nu = \frac{1}{2}$, the appropriate state represents a system of bosons. In order to explain the origin of the corresponding incompressible state, it has been proposed that the ground state of $\nu = \frac{5}{2}$ is described by a Pfaffian [104–107] (or anti-Pfaffian [108, 109]) function. Within this description, the elementary charged excitations have a charge $e^* = e/4$ and obey 'non-abelian' statistics [110, 111]. These unique charged excitations have been recently observed experimentally [112, 113]. Interesting properties

of these quasiparticles, which carry the signatures of Majorana fermions [114–116], have initiated a lot of theoretical interest in the Pfaffian description of the even-denominator FQHE.

The filling factor $\nu = \frac{5}{2} = 2 + \frac{1}{2}$ corresponds to a completely occupied $n = 0$ Landau level with two components of spin and half-filling of the $n = 1$ Landau level. Therefore the Pfaffian state, which is proposed as the incompressible state of $\nu = \frac{5}{2}$, is the ground state of the half-filled $n = 1$ Landau level. It is obtained by operating the Pfaffian factor on the Laughlin state (8.1) at $\nu = \frac{1}{2}$:

$$\Psi_{Pf} = \mathrm{Pf}\left(\frac{1}{z_i - z_j}\right)\prod_{i<j}(z_i - z_j)^2 \exp\left(-\sum_i \frac{z_i^2}{4\ell_0^2}\right), \tag{8.51}$$

where the positions of the electrons are, as usual, described in terms of complex variable $z = x - iy$ and the Pfaffian factor is defined for any $N \times N$ anisymmetric matrix M_{ij} as [104–107]

$$\mathrm{Pf}\, M_{ij} = \frac{1}{2^{N/2}(N/2)!}\sum_{\sigma\in S_N} \mathrm{sgn}\,\sigma \prod_{l=1}^{N/2} M_{\sigma(2l-1)\sigma(2l)}. \tag{8.52}$$

Here S_N is the group of permutations of N objects. The Pfaffian factor therefore provides the necessary antisymmetry to the Laughlin state at $\nu = \frac{1}{2}$.

The Pfaffian state is realized at half occupation of the Landau level, i.e., at a filling factor $\nu = \frac{1}{2}$ in a given Landau level, and only for special interaction potentials. The Pfaffian is the exact ground state with zero energy of the electron system at half filling for a special *three-particle* interaction which is non-zero only if all three particles are in close proximity to each other [106, 107]. In spherical geometry with flux quanta $2S$, it means that the three-particle interaction potential is non-zero only if the total angular momentum of the three particles is $3S - 3$, which is described by the following interaction Hamiltonian

$$\mathcal{H}_{int} = \frac{e^2}{\kappa\ell_0}\sum_{i<j<k} P_{ijk}(3S - 3), \tag{8.53}$$

where $P_{ijk}(L)$ is the three-particle projection operator onto the state with total angular momentum L. For realistic two-particle interactions the $\nu = \frac{1}{2}$ Pfaffian state is not an exact eigenstate. By varying the two-particle interaction function, i.e., the Haldane pseudopotentials, a close proximity of the ground state to the Pfaffian state with an overlap of 99 % can be achieved.

It was shown in Ref. [117] that for traditional non-relativistic systems the Pfaffian (Moore-Read) states can be adiabatically connected to the $\nu = \frac{1}{2}$ Coulomb ground state in the $n = 1$ Landau level by varying the interaction potential from a three-body interaction (8.53) to the Coulomb two-body interaction. However, there is no such connection for the $\nu = \frac{1}{2}$ Coulomb ground state in the $n = 0$ Landau level. The adiabatic connection means that by varying the interaction potential, the system is always kept in the incompressible state with a finite collective excitation gap. This

result illustrates that for the Coulomb interactions, the $\nu = \frac{1}{2}$ state in the $n = 1$ non-relativistic Landau level is in the same topological phase as the Pfaffian state, but the system in the $n = 0$ Landau level does not show any connection to the Pfaffian phase. For the pure Coulomb interaction the overlap of the ground state of the $\nu = \frac{1}{2}$ system in the $n = 1$ Landau level with the Pfaffian function is about 80 %. This overlap can be increased by varying the electron-electron potential strength, for example, by increasing the thickness of the two-dimensional layer [118].

The Pfaffian states are usually studied numerically in the spherical geometry [106, 107, 119]. For a system of N electrons the size of the sphere for which the Pfaffian ground state is realized, is determined by the condition $2S = 2N - 3$, which corresponds to the filling factor $\nu = \frac{1}{2}$ in the thermodynamic limit. For such a system and for the interaction potential of the form of (8.53), the Pfaffian state is an exact ground state with zero energy and finite excitation gap. For the two-particle interaction the interaction potential is characterized by Haldane pseudopotentials (8.2). The proximity of the actual $\nu = \frac{1}{2}$ ground state to the Pfaffian state is most sensitive to the lowest pseudopotentials, V_1, V_3, and V_5.

8.5.2 The Pfaffians in Graphene

The interaction potentials in monolayer and bilayer graphene are different from those of the non-relativistic 2D systems. This can modify the properties of the $\nu = \frac{1}{2}$ state and its proximity to the Pfaffian state in graphene. The numerical analysis in a spherical geometry of a finite-size monolayer graphene system with up to 14 electrons shows that an incompressible $\nu = \frac{1}{2}$ Pfaffian state is unlikely to be found in monolayer graphene [120]. The overlap of the ground state of the $\nu = \frac{1}{2}$ system with the Pfaffian function is less than 0.5 for all Landau levels of the monolayer graphene. The corresponding collective excitation gap is also small.

Interestingly, a very different situation occurs in bilayer graphene. The stability of the $\nu = \frac{1}{2}$ Pfaffian state in bilayer graphene can be greatly enhanced as compared to the non-relativistic system. Here the stability of the incompressible state is determined by the value of the collective excitation gap, which is correlated to the overlap of the ground state and the Pfaffian state. In bilayer graphene there is one 'special' Landau level (for each valley), which is described by (8.33) and has the label $0_{-1}^{(+)}$ in valley K (or $0_{1}^{(-)}$ in valley K′). Numerical studies [120] in a spherical geometry show that only in this special Landau level the overlap of the ground state with the Pfaffian state and the excitation gap is large. In all other bilayer Landau levels the overlap of the $\nu = \frac{1}{2}$ ground state with the Pfaffian state is found to be small (< 0.6) and those states cannot be described by the Pfaffian.

At the zero bias voltage this special Landau level has zero energy and is degenerate with the level given by (8.32). In addition to this accidental degeneracy, each level has a two-fold valley degeneracy, which makes the zero-energy state four-fold degenerate. At a finite bias voltage this degeneracy is completely lifted and the special Landau level of bilayer graphene can be isolated. In Fig. 8.17, several bilayer

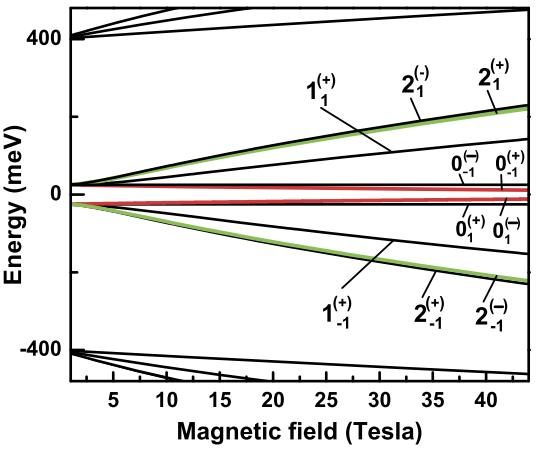

Fig. 8.17 Few LLLs of a bilayer graphene, shown for $U = 50$ meV, $\Delta = 0$, and $t = 400$ meV. The *two solid red lines* belonging to different valleys show the 'special' Landau levels where the $\nu = \frac{1}{2}$ Pfaffian state can be observed. The *two solid green lines* show the Landau levels, which at small magnetic field, $B \to 0$, become identical to the $n = 1$ Landau level of the non-relativistic 2D system

Landau levels are shown at a small bias voltage ($U = 50$ meV) and zero intra-valley asymmetry ($\Delta = 0$). The special Landau levels, $0_{-1}^{(+)}$ and $0_1^{(-)}$, corresponding to two different valleys, are shown by red lines. The interaction potentials and the many-particle properties of these two levels are identical.

From the expression (8.35) for the form factor, F_n, of the Landau level $0_{-1}^{(+)}$ (or $0_1^{(-)}$) we can obtain the following general property: At a small magnetic field, $\gamma_1 \ll \epsilon_B$, the form factor is identical to the form factor of the non-relativistic $n = 1$ Landau level. Therefore in this limit we should expect that the $\nu = \frac{1}{2}$ state is described by the Pfaffian and it is in the same topological phase as the Pfaffian state. By increasing the magnetic field we can change the relation between γ_1 and ϵ_B, which changes the interaction properties of the system and the properties of the $\nu = \frac{1}{2}$ state. Finally, at a very large magnetic field, $\gamma_1 \ll \epsilon_B$, the form factor becomes identical to that of the $n = 0$ non-relativistic system, for which there are no $\nu = \frac{1}{2}$ Pfaffian states. At an intermediate magnetic field there are two possibilities: (i) the excitation gap of the $\nu = \frac{1}{2}$ state and the overlap with the Pfaffian state decrease monotonically with the magnetic field and finally disappear or (ii) the system shows a non-monotonic dependence with the maximum stability, i.e., the maximum gap, at the intermediate magnetic field. Our numerical results show that for bilayer graphene the second situation is indeed realized (see Fig. 8.18 and the discussion below).

In Fig. 8.18, the parameters of the $\nu = \frac{1}{2}$ state are illustrated at the intermediate magnetic field. Here the overlap of the ground state with the Pfaffian state and the corresponding excitation gap are shown. These results clearly indicate that with increasing magnetic field the properties of the system change non-monotonically and for $\gamma_1 = 400$ meV the overlap with the Pfaffian state reaches its maximum at a magnetic field of ~ 10 Tesla. The corresponding excitation gap also reaches its maximum at this point. In dimensionless units the maximum is achieved at $\gamma_1/\epsilon_B \approx 4.89$. Therefore, for smaller values of γ_1 the maximum is achieved at smaller magnetic fields, which is shown in Fig. 8.18 for $\gamma_1 = 300$ meV. The overlap with the Pfaffian state at the maximum point is ≈ 0.92, which is a major improvement over the

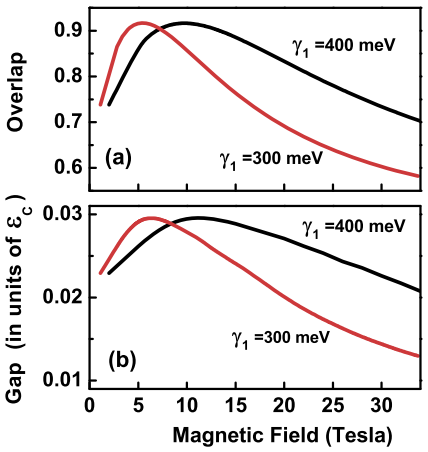

Fig. 8.18 (**a**) Overlap of the exact many-particle ground state with the Pfaffian function. (**b**) Collective excitation gap of the $\nu = \frac{1}{2}$ state. The results are for $N = 14$, $2S = 25$, and $U = 0$, $\Delta = 0$. The *black* and *red lines* correspond to $\gamma_1 = 400$ meV and 300 meV, respectively. The results are shown for of the $\nu = \frac{1}{2}$ system at 'special' Landau levels marked by red lines in Fig. 8.17

non-relativistic system (~ 0.75, which is the value at zero magnetic field limit in Fig. 8.18).

Within this picture the magnetic field should be considered as the parameter which adiabatically changes the interaction Hamiltonian from the $n = 1$ non-relativistic system to the bilayer system at the special Landau level, $0^{(+)}_{-1}$. These changes are adiabatic since the gap remains non-zero and large. Therefore, we conclude that the $\nu = \frac{1}{2}$ state at the special bilayer Landau level is in the same topological phase as the $\nu = \frac{1}{2}$ state in the $n = 1$ non-relativistic Landau level and correspondingly as the Pfaffian state. At the same time the overlap with the Pfaffian state and the excitation gap is larger in bilayer graphene (at $B \sim 10$ Tesla) than in the non-relativistic system. Therefore, bilayer graphene provides the more stable Pfaffian state.

At a large magnetic field the bilayer system, at the special Landau level, $0^{(+)}_{-1}$, becomes close to the $n = 0$ non-relativistic Landau level, the overlap with the Pfaffian state becomes small, the excitation gap becomes small, and the $\nu = \frac{1}{2}$ state finally becomes compressible. This dependence on the magnetic field opens up interesting possibilities to investigate the stability and appearance and disappearance of the $\nu = \frac{1}{2}$ Pfaffian state in a single Landau level of bilayer graphene. Although the Pfaffian state becomes unstable only at large magnetic fields, this property strongly depends on the value of the hopping integral. At smaller hopping integrals the magnetic field range of stability of the Pfaffian state shrinks. For example, at $t = 300$ meV the Pfaffian state is expected to be unstable at $B \sim 40$ Tesla (note the suppression of the FQHE gap with increasing magnetic field in Fig. 8.18). The dependence of the properties of the $\nu = \frac{1}{2}$ state on the bias voltage is weak within the broad range of U [120].

In bilayer graphene there is another set of Landau levels, which are shown by green lines in Fig. 8.17 and are labelled as $2^{(+)}_{1}$ for valley K and $2^{(-)}_{-1}$ for valley K′. These Landau levels have the following property. At a finite bias voltage and a small magnetic field, the corresponding Landau level wave functions are described

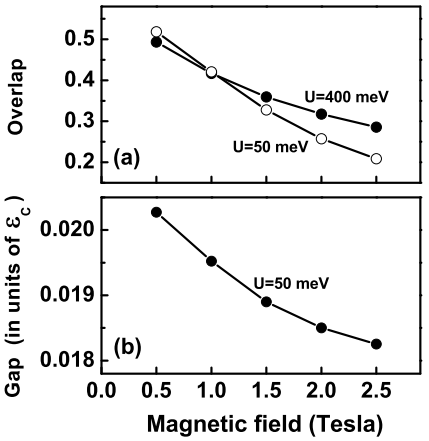

Fig. 8.19 (**a**) Overlap of the exact many-particle ground state with the Pfaffian function. (**b**) Collective excitation gap of the $\nu = \frac{1}{2}$ state. The results are for $N = 14$, $2S = 25$, and $\gamma_1 = 0$, $\Delta = 0$, and two values of $U = 50$ meV and 400 meV. The results are shown for the $\nu = \frac{1}{2}$ system at the Landau levels $2_1^{(+)}(2_{-1}^{(-)})$ marked by green lines in Fig. 8.17

by the $n = 1$ non-relativistic Landau wave functions, $(0, \phi_{1,m}, 0, 0)$. Therefore in this limit the interaction potentials become identical to the interaction potentials of the non-relativistic system in the $n = 1$ Landau level. Then the $\nu = \frac{1}{2}$ Pfaffian state should be realized in the bilayer Landau level $2_1^{(+)}$ $(2_{-1}^{(-)})$ for small values of the magnetic field. With increasing magnetic field the interaction potentials are modified which should influence the properties of the $\nu = \frac{1}{2}$ state. In Fig. 8.19, we present the magnetic field dependence of the parameters of the $\nu = \frac{1}{2}$ state in the Landau level $2_1^{(+)}$ $(2_{-1}^{(-)})$. Evidently, in this case with an increasing magnetic field the overlap with the Pfaffian state and the excitation gap are strongly suppressed. Therefore in this bilayer Landau level the $\nu = \frac{1}{2}$ Pfaffian state cannot be realized.

The stability of the $\nu = \frac{1}{2}$ ground state and its proximity to the Pfaffian state can also be analyzed in terms of the general dependence of the Haldane pseudopotentials, V_m, on the relative angular momentum, m. The $\nu = \frac{1}{2}$ Pfaffian state is most sensitive to the following parameters of the pseudopotential: V_1/V_5 and V_3/V_5 [117]. These parameters depend on the strength of the magnetic field. By varying the magnetic field, we introduce an adiabatic transition of the pseudopotentials from one set to another. Such a transition can be shown as a line in the (V_1/V_5)–(V_3/V_5) plane (see Fig. 8.20). That line connects the initial point at $B = 0$ to the final point, corresponding to a large magnetic field, $B = \infty$. In Fig. 8.20, three regions which were identified in Ref. [117] are shown: (i) region of large overlap of the $\nu = \frac{1}{2}$ ground state with the Pfaffian function and the largest excitation gap and correspondingly the most stable $\nu = \frac{1}{2}$ Pfaffian state. (ii) That region is surrounded by the region of less stable Pfaffian state. (iii) The region of compressible states, i.e., with zero excitation gap.

The red line in Fig. 8.20 (a) corresponds to the special bilayer Landau level $0_{-1}^{(+)}$ $(0_1^{(-)})$ (Fig. 8.17). In this Landau level the $\nu = \frac{1}{2}$ bilayer graphene system at the initial and final points are identical to the non-relativistic 2D systems in the first $(n = 1)$ and zero $(n = 0)$ Landau levels, respectively. For the intermediate magnetic

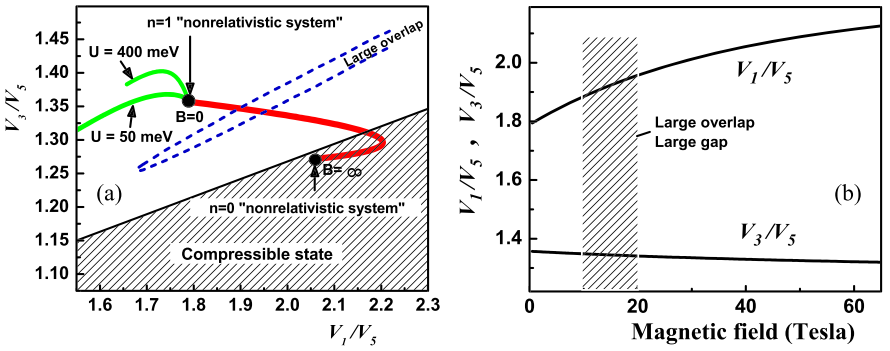

Fig. 8.20 (**a**) The trajectory of the inter-electron interaction pseudopotential with varying magnetic field, shown by a *solid red line* in the plane (V_1/V_5)–(V_3/V_5) for the 'special' bilayer Landau levels $0_1^{(-)}$ and $0_{-1}^{(+)}$. The corresponding Landau levels are marked by a red line in Fig. 8.17. The *green lines* depict the trajectory of the interaction potential corresponding to the Landau levels $2_{-1}^{(-)}$ and $2_1^{(+)}$, marked by green lines in Fig. 8.17. The initial point of the trajectory (at $B = 0$) corresponds to the non-relativistic system in the $n = 1$ Landau level, while the final point (at $B = \infty$) corresponds to the non-relativistic system in the $n = 0$ Landau level. The *shaded region* illustrates the compressible $\nu = \frac{1}{2}$ state, while the *blank region* corresponds to the incompressible $\nu = \frac{1}{2}$ state (Ref. [117]). The crossing of the boundary between the compressible and incompressible states occurs at $B \sim 100$ Tesla for the hopping integral $\gamma_1 = 400$ meV. The *blue dashed line* shows the region of large overlap with the Pfaffian state (Ref. [117]). (**b**) Ratios of the pseudopotentials at two values of the angular momentum are shown as a function of the magnetic field for two 'special' Landau levels $0_1^{(-)}$ and $0_{-1}^{(+)}$. The *dashed region* corresponds to a large overlap of the ground state with the Pfaffian function and also a large excitation gap

field the line goes through the region of most stable Pfaffian state. Therefore with an increasing magnetic field, the $\nu = \frac{1}{2}$ bilayer graphene system in the special Landau level transforms from a $\nu = \frac{5}{2}$ non-relativistic state (at small values of B) to a more stable incompressible state with a large overlap and a large gap, and finally to a compressible state (at a large magnetic field). This behavior is consistent with the result shown in Fig. 8.18, where the large excitation gap is realized at a finite magnetic field. For the hopping integral $t = 400$ meV, the transition from the incompressible to a compressible $\nu = \frac{1}{2}$ state occurs at $B \sim 100$ Tesla. In Fig. 8.20(b) the dependences of both parameters (V_1/V_5) and (V_3/V_5) on the magnetic field are shown for the bilayer Landau level $0_{-1}^{(+)}$. These dependences correspond to the red line in Fig. 8.20(a). The dashed region shows the region of the stable $\nu = \frac{1}{2}$ ground state with a large excitation gap and a large overlap with the Pfaffian state. This region is realized at a finite magnetic field, $B \sim 10$ Tesla, which is consistent with the results of Fig. 8.18.

The green lines in Fig. 8.20 correspond to the Landau level $2_1^{(+)}$ $(2_{-1}^{(-)})$ (Fig. 8.17). The results clearly show that with increasing magnetic field and for all values of U and Δ, the $\nu = \frac{1}{2}$ system becomes less stable by having a smaller excitation gap, which support the results shown in Fig. 8.19.

Therefore, the incompressible $\nu = \frac{1}{2}$ Pfaffian state can actually be found in a bilayer graphene in one of the Landau levels. The properties of this state strongly depend on the magnetic field strength. With increasing magnetic field the graphene system at this special Landau level shows a transition from the incompressible to a compressible state with increasing magnetic field. At a finite magnetic field the Pfaffian state in bilayer graphene becomes more stable with the larger excitation gap than its counterpart in non-relativistic 2D electron systems.

8.5.3 *Interacting Dirac Fermions on the Surface of a Topological Insulator*

The relativistic dispersion relation, observed in monolayer graphene, is also realized in special insulators with topologically protected surface states [121, 122]. Those states in topological insulators are gapless with a linear (relativistic) dispersion relation similar to the energy spectra of graphene. Therefore the properties of the surface states of topological insulators are expected to be similar to the properties of graphene. Experimentally the topological insulator has been realized in $Bi_{1-x}Sb_x$ and Bi_2Se_3 materials, containing a *single Dirac cone* on the surface [123, 124].

In an external magnetic field the properties of surface Landau levels of a topological insulator are similar to those of Landau levels in graphene [125, 126]. Although the low-energy dynamics of the surface states is similar to graphene, there is however, an important difference between these two systems. While the electronic states of graphene are strictly two-dimensional and are localized within a single graphene plane, the surface states in a topological insulator have a finite width in the growth direction. The finite width of the surface states in topological insulators modifies the electron-electron interaction potential which in turn, modifies the properties of the FQHE states. In traditional (non-relativistic) electron systems, an increase in the width of the 2D layer causes a reduction of the FQHE gaps and hence a reduction of the stability of the corresponding incompressible states. Therefore, we should expect that the FQHE gaps in a topological insulator would be smaller than those in graphene.

To analyze the properties of the FQHE in the surface states of a topological insulator (TI), we start with the low-energy effective Hamiltonian introduced in Ref. [127, 128]. The Hamiltonian has the matrix form of size 4×4 and is given by

$$\mathcal{H}_{TI} = \begin{pmatrix} \epsilon(\mathbf{p}) + M(\mathbf{p}) & (A_1/\hbar)p_z & 0 & (A_2/\hbar)p_- \\ (A_1/\hbar)p_z & \epsilon(\mathbf{p}) - M(\mathbf{p}) & (A_2/\hbar)p_- & 0 \\ 0 & (A_2/\hbar)p_+ & \epsilon(\mathbf{p}) + M(\mathbf{p}) & -(A_1/\hbar)p_z \\ (A_2/\hbar)p_+ & 0 & -(A_1/\hbar)p_z & \epsilon(\mathbf{p}) - M(\mathbf{p}) \end{pmatrix}, \quad (8.54)$$

where $\epsilon(\mathbf{p}) = C_1 + (D_1/\hbar^2)p_z^2 + (D_2/\hbar^2)(p_x^2 + p_y^2)$, $M(\mathbf{p}) = M_0 - (B_1/\hbar)p_z^2 - (B_2/\hbar^2)(p_x^2 + p_y^2)$. Here for the Bi_2Se_3 topological insulator the material constants are $A_1 = 2.2$ eV Å, $A_2 = 4.1$ eV Å, $B_1 = 10$ eV Å^2, $B_2 = 56.6$ eV Å^2,

$C_1 = -0.0068$ eV, $D_1 = 1.3$ eV Å^2, $D_2 = 19.6$ eV Å^2, and $M_0 = 0.28$ eV. The topological insulator film has a finite thickness of L_z, where the axis z is a trigonal axis of Bi_2Se_3 with three-fold rotational symmetry. We assume that the two surfaces of the film are at $z = 0$ and $z = L_z$. The four-component wave functions corresponding to the Hamiltonian (8.54) determine the amplitudes of the wave functions at the positions of Bi and Se atoms: $(Bi_\uparrow, Se_\uparrow, Bi_\downarrow, Se_\downarrow)$, where the arrows indicate the electron spin directions.

The external magnetic field is introduced along the z-direction which results in Landau quantization of the electron motion in the x–y plane. The corresponding Landau levels, which include both the surface and bulk Landau levels, can be found from the Hamiltonian matrix by replacing the x and y components of the momentum by the generalized momentum [129] and introducing the Zeeman energy, $\Delta_z = \frac{1}{2} g_s \mu_B B$. Here $g_s \approx 8$ is the effective g-factor of surface states [128, 130] and μ_B is the Bohr magneton. The Landau levels are characterized by an integer index n with the corresponding wave functions

$$\Psi_n^{(TI)} = \begin{pmatrix} \chi_n^{(1)}(z)\phi_{|n|-1,m} \\ \chi_n^{(2)}(z)\phi_{|n|-1,m} \\ i\chi_n^{(3)}(z)\phi_{|n|,m} \\ i\chi_n^{(4)}(z)\phi_{|n|,m} \end{pmatrix}, \tag{8.55}$$

for $n > 0$ and

$$\Psi_n^{(TI)} = \begin{pmatrix} 0 \\ 0 \\ i\chi_n^{(3)}(z)\phi_{|n|,m} \\ i\chi_n^{(4)}(z)\phi_{|n|,m} \end{pmatrix}, \tag{8.56}$$

for $n = 0$. The functions $\chi_n^{(i)}(z)$ satisfy the following eigenvalue equations

$$\begin{aligned} \varepsilon\chi_n^{(1)}(z) &= (\epsilon_{z,n} + M_{z,n} + \Delta_z)\chi_n^{(1)}(z) \\ &\quad + iA_1\frac{d\chi_n^{(2)}(z)}{dz} - \frac{\sqrt{2(n+1)}}{\ell_0}A_2\chi_n^{(4)}(z) \qquad (8.57) \\ \varepsilon\chi_n^{(2)}(z) &= (\epsilon_{z,n} - M_{z,n} + \Delta_z)\chi_n^{(2)}(z) \\ &\quad + iA_1\frac{d\chi_n^{(1)}(z)}{dz} - \frac{\sqrt{2(n+1)}}{\ell_0}A_2\chi_n^{(3)}(z) \qquad (8.58) \\ \varepsilon\chi_n^{(3)}(z) &= (\epsilon_{z,n+1} + M_{z,n+1} - \Delta_z)\chi_n^{(3)}(z) \\ &\quad - iA_1\frac{d\chi_n^{(4)}(z)}{dz} - \frac{\sqrt{2(n+1)}}{\ell_0}A_2\chi_n^{(2)} \qquad (8.59) \\ \varepsilon\chi_n^{(4)}(z) &= (\epsilon_{z,n+1} - M_{z,n+1} - \Delta_z)\chi_n^{(4)}(z) \\ &\quad - iA_1\frac{d\chi_n^{(3)}(z)}{dz} - \frac{\sqrt{2(n+1)}}{\ell_0}A_2\chi_n^{(1)}, \qquad (8.60) \end{aligned}$$

where $\epsilon_{z,n} = C_1 + D_2\frac{2n+1}{\ell_0^2} - D_1\frac{d^2}{dz^2}$ and $M_{z,n} = M_0 - B_2\frac{2n+1}{\ell_0^2} - B_1\frac{d^2}{dz^2}$. The solution of the system of equations (8.57)–(8.60) determines the Landau level energy spectra and the corresponding wave functions. We are interested only in the surface

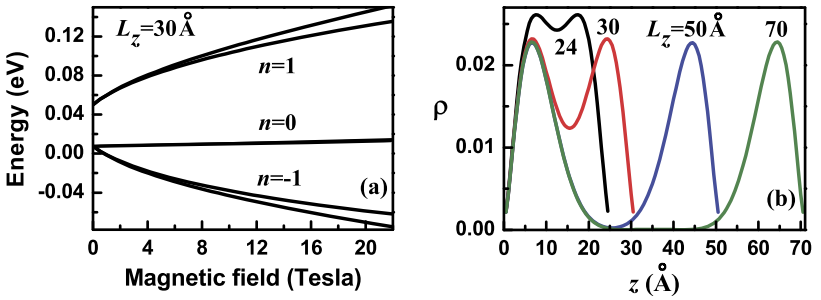

Fig. 8.21 (**a**) The lowest surface Landau levels of a TI film are shown at a film thickness of $L_z = 30$ Å. For each n there are two LLs of the TI film, belonging to the two surfaces of the film. (**b**) The electron density along the z axis for one of the $n = 1$ Landau levels and for different values of the thickness, L_z, of the Bi_2Se_3 film. The *numbers next to the lines are* the values of L_z. The magnetic field is at 15 Tesla

Landau levels. These Landau levels are separated from the bulk Landau levels by finite energy gaps and the wave functions of the surface Landau levels are localized near the surface of the topological insulator. We assume that the wave functions χ_n satisfy open boundary conditions (zero values) at the two surfaces of the TI film, which correspond to a suspended TI film. The substrate can be taken into account by modification of the boundary conditions.

For a topological insulator film there are two surfaces which results in two sets of surface Landau levels. For thick films the separation between the Landau levels of the two surfaces is large and the levels with the same n are degenerate. The wave functions of the surface Landau levels have a finite width and therefore for small thicknesses of the films, the wave functions of the two surfaces of the Bi_2Se_3 film overlap. This results in inter-Landau level coupling which lifts the degeneracy of the Landau levels of the two surfaces. In Fig. 8.21(a) the lowest energy surface Landau levels with indices $n = 0$ and $n = 1$ are shown for a Bi_2Se_3 topological insulator film of thickness $L_z = 30$ Å. For each n there are two Landau levels of the two surfaces of the film. The degeneracy of the Landau levels is lifted due to the finite film thickness and the finite inter-Landau level coupling. This coupling is more pronounced at a small film thickness due to the larger overlap of the corresponding wave functions [Fig. 8.21(b)] where results for four film thicknesses are shown. For small L_z, the wave functions of the two surface states have a large overlap and a large value within the whole topological insulator film, which results in a strong inter-Landau level coupling. For large L_z, the surface Landau levels are localized at the two surfaces of the film, resulting in a weak inter-Landau level coupling. The strong inter-Landau level coupling lifts the degeneracy of the surface Landau levels and changes the corresponding wave functions. The most important effect is how this coupling affects the contributions of the n and $n - 1$ non-relativistic Landau functions, $\phi_{|n|,m}$ and $\phi_{|n|-1,m}$ (see (8.55)), to the Landau wave functions of the surface states. For the $n = 0$ surface Landau level this is not important since only $n = 0$ non-relativistic Landau functions enter in the expression (8.56), while for the

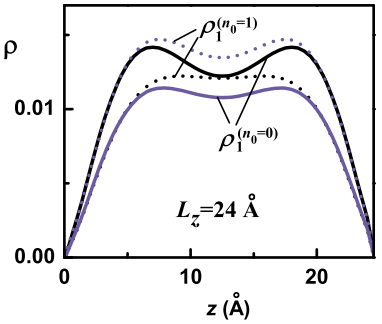

Fig. 8.22 The electron densities $\rho_1^{(n=1)}(z)$ and $\rho_1^{(n=0)}(z)$ of two $n=1$ Landau levels for film thickness of $L_z = 24$ Å. The *black* (*solid* and *dotted*) *lines* and *blue* (*solid* and *dotted*) *lines* correspond to two $n=1$ Landau levels. The densities $\rho_1^{(n=1)}(z)$ and $\rho_1^{(n=0)}(z)$ show the occupations of the $n=1$ and $n=0$ non-relativistic Landau level functions, respectively

$n=1$ surface state both the $n=1$ and $(n-1)=0$ non-relativistic Landau functions determine the properties of the topological insulator state. To show the effect of the inter-Landau level coupling on the wave functions we present in Fig. 8.21 the electron densities

$$\rho_1^{(n_0=1)}(z) = \left|\chi_{n=1}^{(3)}(z)\right|^2 + \left|\chi_{n=1}^{(4)}(z)\right|^2, \tag{8.61}$$

$$\rho_1^{(n_0=0)}(z) = \left|\chi_{n=1}^{(1)}(z)\right|^2 + \left|\chi_{n=1}^{(2)}(z)\right|^2, \tag{8.62}$$

which determine the contribution of the $n_0=1$ and $n_0=0$ non-relativistic Landau functions to the corresponding surface Landau levels. The results are shown in Fig. 8.21(b) for two $n=1$ surface Landau levels, which are coupled due to inter-Landau level coupling. Figure 8.22 shows clearly that one of the $n=1$ surface Landau levels has a larger contribution from the $n_0=0$ non-relativistic Landau function, $\phi_{n_0=0,m}$, while the other $n=1$ surface Landau level has a large contribution from the $n_0=1$ non-relativistic Landau function, $\phi_{n_0=1,m}$.

With the known wave functions of the surface Landau levels (8.55)–(8.56), the Haldane pseudopotentials, (8.2), can be readily evaluated from the following expression

$$V_m^{(n=0)} = \int_0^\infty \frac{dq}{2\pi} q V(q) F_{1,1}(q) L_n^2\left(\frac{q^2}{2}\right) L_m\left(q^2\right) e^{-q^2}, \tag{8.63}$$

for $n=0$, and

$$\begin{aligned} V_m^{(n)} = \int_0^\infty \frac{dq}{2\pi} q V(q) \frac{1}{4}\Bigg[& F_{1,1}(q) L_n^2\left(\frac{q^2}{2}\right) \\ & + 2F_{1,2}(q) L_n\left(\frac{q^2}{2}\right) L_{n-1}\left(\frac{q^2}{2}\right) \\ & + F_{2,2}(q) L_{n-1}^2\left(\frac{q^2}{2}\right)\Bigg] L_m\left(q^2\right) e^{-q^2}, \end{aligned} \tag{8.64}$$

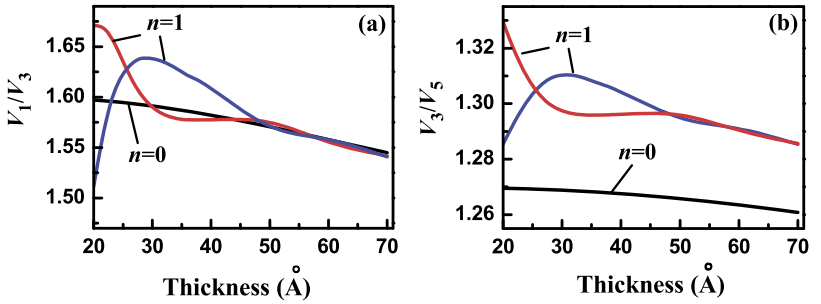

Fig. 8.23 The ratios of pseudopotentials, (V_1/V_3) (panel (**a**)) and (V_3/V_5) (panel (**b**)), for the surface Landau levels of a Bi_2Se_3 topological insulator at two odd relative angular momenta shown as a function of the thickness of the topological insulator film. The ratios are shown for the $n = 0$ and two $n = 1$ surface Landau levels of the topological insulator

for $n > 0$. Here the form factors $F_{i,j}(q)$ are evaluated from,

$$F_{1,1}(q) = \int dz_1 dz_2 \rho_n^{(n_0=n)}(z_1)\rho_n^{(n_0=n)}(z_2)e^{-|z_1-z_2|q},$$
$$F_{1,2}(q) = \int dz_1 dz_2 \rho_n^{(n_0=n)}(z_1)\rho_n^{(n_0=n-1)}(z_2)e^{-|z_1-z_2|q},$$
$$F_{2,2}(q) = \int dz_1 dz_2 \rho_n^{(n_0=n-1)}(z_1)\rho_n^{(n_0=n-1)}(z_2)e^{-|z_1-z_2|q},$$

where $\rho_n^{(n_0=n)}(z) = |\chi_n^{(3)}(z)|^2 + |\chi_n^{(4)}(z)|^2$ and $\rho_n^{(n_0=n-1)}(z) = |\chi_n^{(1)}(z)|^2 + |\chi_n^{(2)}(z)|^2$ determine the occupation of $n_0 = n$-th and $n_0 = n - 1$-th non-relativistic LLs for the topological insulator surface Landau level with index n.

The mixture of surface Landau levels has a strong effect on the pseudopotentials, which is visible only at a small thickness of the film and for $n = 1$ Landau levels [see (8.63) and (8.64)]. The stability of the incompressible states (i.e., the gaps of the FQHE states) depends on how fast the pseudopotentials decreases with increasing relative angular momentum, m. In Fig. 8.23, the ratios of the two nearest odd pseudopotentials, (V_1/V_3) and (V_3/V_5), are shown as the function of the thickness of the film for the $n = 0$ and $n = 1$ surface Landau levels. For the $n = 0$ Landau level the ratios of the pseudopotentials monotonically decrease with the thickness, L_z. This monotonic dependence shows that the $n = 0$ surface Landau level does not depend on the mixture of two surface states and the reduction is due to the increase of the width of the surface wave functions in the z-direction [Fig. 8.21(b)]. For two $n = 1$ surface Landau levels there is a different dependence on the L_z. For a small thickness the inter-Landau level coupling is large, which results in a strong nonmonotonic dependence of the pseudopotential ratios on L_z. For one of the $n = 1$ Landau levels the pseudopotential ratios have a well pronounced maximum. For a large thickness of the topological insulator film, the inter-Landau level coupling is weak and the pseudopotentials monotonically decrease with L_z, which is similar to that of the $n = 0$ Landau level and is due to the increase of the width of the surface wave functions in the z-direction. For a large thickness of the topological insulator film, the ratio of the first two pseudopotentials, V_3/V_1, becomes the same for all

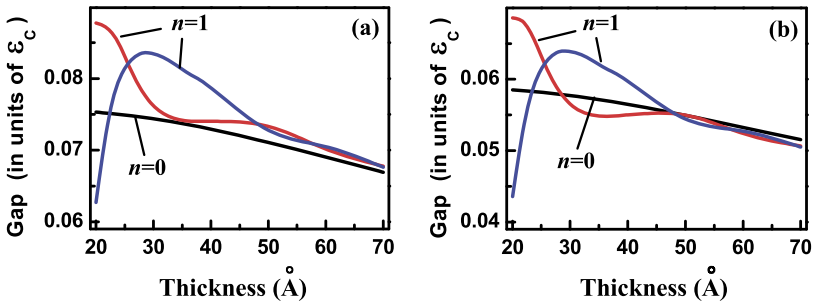

Fig. 8.24 (**a**) The $\nu = \frac{1}{3}$ FQHE gap shown for different Landau levels of a topological insulator film as a function of the film thickness. The FQHE gaps were evaluated numerically for a finite-size system of $N = 9$ electrons and flux quanta $2S = 24$. (**b**) The $\nu = \frac{2}{5}$ FQHE gap is shown for different Landau levels of the topological insulator film as a function of the film thickness. The FQHE gaps were evaluated numerically for a finite-size system of $N = 10$ electrons and the flux quanta $2S = 21$. The magnetic field is 15 Tesla and the energy is shown in units of the Coulomb energy, $\varepsilon_C = e^2/\kappa\ell_0$

Landau levels. This fact suggests that for large L_z ($L_z > 50$ Å) the FQHE gaps are almost the same in the $n = 0$ and $n = 1$ Landau levels.

With the known pseudopotentials the energy spectra of the $\nu = \frac{1}{3}$ and $\nu = \frac{2}{5}$ FQHE systems are evaluated numerically in the spherical geometry. The corresponding energy gaps are shown in Fig. 8.24(a) and (b), as a function of film thickness [131]. The L_z dependence of the energy gaps is very similar to the L_z dependence of the ratio of the pseudopotentials of the energy gaps at the corresponding LLs (see Fig. 8.23). For a small thickness, the non-monotonic dependence for the $n = 1$ Landau levels is due to the inter-Landau mixture, while for a large thickness, the FQHE gaps monotonically decrease with the thickness due to the increase of the width in the z-direction of the surface wave functions. The FQHE gaps in the $n = 1$ and $n = 0$ Landau levels become almost the same for large thicknesses of the film.

Experimentally it would be easier to study the dependence of the FQHE gaps on the parameters of the system for a given thickness of the film by varying the strength of the external magnetic field. In Fig. 8.25, we show the dependence of the $\nu = \frac{1}{3}$ FQHE gap on the magnetic field for two different films with a small thickness, $L_z = 25$ Å, and a large thickness, $L_z = 50$ Å. The results presented in Figs. 8.24 and 8.25 are shown for actual values of the film thicknesses and the magnetic field. Within the inter-Landau level mixture, the properties of the TI film are determined by a dimensionless parameter which is the dimensionless thickness of the film, expressed in units of the magnetic length. Therefore with increasing magnetic field the magnetic length decreases, and the dimensionless thickness increases. Then without any inter-Landau mixture we would expect a monotonic decrease of the excitation gaps with magnetic field due to the increase of the dimensionless width of the surface wave functions. For the small thickness of 25 Å, which is about two quintuple layers of Bi_2Se_3 [Fig. 8.25(a)], the inter-Landau coupling is strong. As a result the FQHE gap at one of the $n = 1$ Landau levels increases monotonically with magnetic field, while the other $n = 1$ Landau level displays a monotonic decrease of the gap

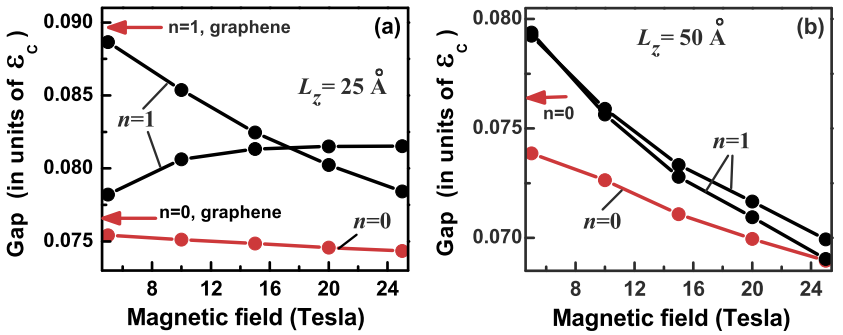

Fig. 8.25 The $\nu = \frac{1}{3}$ FQHE gap as a function of the magnetic field shown for different Landau levels of a topological insulator film: two $n = 1$ LLs (*black lines*) and one $n = 0$ LL (*red line*). The thickness of the film is (**a**) $L_z = 25$ Å and (**b**) $L_z = 50$ Å. The *red arrows* show the FQHE gaps in the $n = 0$ and $n = 1$ Landau levels of graphene. The FQHE gaps were evaluated numerically for a finite-size system of $N = 9$ electrons and flux quanta $2S = 24$. The energy is shown in units of the Coulomb energy, $\varepsilon_C = e^2/\kappa\ell_0$

with magnetic field, B. An experimental observation of the monotonic increase of the FQHE gaps with magnetic field would be a direct manifestation of the strong inter-Landau level coupling.

For a large film thickness of 50 Å, i.e., five quintuple layers of Bi_2Te_3 [Fig. 8.25(b)], the inter-Landau level coupling is weak and we see a monotonic decrease of the FQHE gaps with magnetic field for all Landau levels. This is due to the increase of the dimensionless width of the surface Landau level wave functions. For the $n = 0$ Landau levels, which are not affected by the Landau level coupling, a monotonic decrease with magnetic field, B, is visible for both small and large thicknesses of the film. The results shown in Fig. 8.25 also illustrate the fact that the FQHE gaps in a topological insulator are less than the maximum FQHE gap that is expected in graphene in the $n = 1$ Landau level.

The FQHE can indeed be observed on the surface Landau levels of a topological insulator. The strength of the FQHE, which is characterized by the value of the excitation gap, has non-trivial dependence on the thickness of the film. For a small thickness of the topological insulator film, the inter-Landau level coupling and the mixture of the Landau levels are strong, which results in a non-monotonic dependence, with a well-pronounced maximum of the FQHE gaps on the thickness of the film, in the $n = 1$ Landau levels. For a large thickness of the film, when the inter-Landau level coupling is small, the FQHE gaps monotonically decrease with the thickness, which is due to an increase of the width of the surface Landau levels. The effect of the inter-Landau level coupling on the $n = 0$ surface states is very weak. As a result, for the $n = 0$ Landau levels the FQHE gaps monotonically decrease with the thickness for all values of L_z. In general, for a finite thickness of the topological insulator films, the FQHE gaps are the largest in the $n = 1$ Landau levels, which is similar to the case of a monolayer graphene. At a large enough thickness of the film, $L_z > 50$ Å, the gaps of FQHE states in the $n = 0$ and $n = 1$ Landau levels become comparable (Fig. 8.24). Experimental observation of these theoretical predictions,

just as in the case of graphene [54, 69, 77] would be an important advancement in our understanding of this unique state of matter. The possibility of a controllable growth of the Bi_2Se_3 nanofilm in a wide range of one quintuple layer (10 Å) to 15 quintuple layer (150 Å) has been demonstrated in [132]. This indeed opens up the interesting possibility to study the FQHE in Bi_2Se_3 films of different thicknesses.

8.6 Conclusions

We have briefly reviewed the rich physics exhibited by interacting electrons in monolayer and bilayer graphene in the quantum Hall effect regime. The behavior of massless Dirac fermions in monolayer graphene and massive chiral fermions in bilayer graphene are distinctly different from the electron dynamics in traditional two-dimensional electron systems. In bilayer graphene, we described in detail about possible transitions from the fractional quantum Hall state to a compressible state and back to the FQHE state in the same Landau level by simply tuning the band gap at a given electron density. Similarly, we suggest the possibility of a FQHE—no-FQHE—FQHE transition within a Landau level of bilayer graphene. These controllable driven transitions are unique to bilayer graphene and do not exist in conventional 2D electron systems. Experimental observation of these will provide a rare glimpse into the properties of incompressible and compressible states in bilayer graphene. Incompressible states in trilayer graphene are also briefly discussed. Novel states, such as the incompressible Pfaffian state at $\nu = \frac{5}{2}$ are expected to be present in bilayer graphene. Finally, we present a brief description of the properties of FQHE states of Dirac fermions on the surface of a topological insulator.

Acknowledgements This work has been supported by the Canada Research Chairs program of the Government of Canada. We would like to thank Peter Maksym for carefully reading the manuscript and offering valuable comments to improve the article.

References

1. K. von Klitzing, G. Dorda, M. Pepper, Phys. Rev. Lett. **45**, 494 (1980)
2. K. von Klitzing, Rev. Mod. Phys. **58**, 519 (1986)
3. H.L. Störmer, Physica B **177**, 401 (1992)
4. H.L. Störmer, Rev. Mod. Phys. **71**, 875 (1999)
5. R.B. Laughlin, Phys. Rev. Lett. **50**, 1395 (1983)
6. R.B. Laughlin, Rev. Mod. Phys. **71**, 863 (1999)
7. T. Chakraborty, P. Pietiläinen, *The Quantum Hall Effects*, 2nd edn. (Springer, New York, 1995)
8. S.M. Girvin, in *The Quantum Hall Effects: Poincarè Seminar 2004*, ed. by B. Ducot, B. Duplantier, V. Pasquier, E. Rivasseau (Birkhäuser, Basel, 2005), p. 133
9. R.B. Laughlin, *A Different Universe* (Basic Books, New York, 2005)
10. S. Das Sarma, A. Pinczuk (eds.), *Perspectives in Quantum Hall Effects* (Wiley, New York, 1997)
11. B.I. Halperin, Helv. Phys. Acta **56**, 75 (1983)

12. V.S. Khrapai, A.A. Shashkin, M.G. Trokina, V.T. Dolgopolov, V. Pellegrini, F. Beltram, G. Biasiol, L. Sorba, Phys. Rev. Lett. **100**, 196805 (2008)
13. B.I. Halperin, Phys. Rev. Lett. **52**, 1583 (1984)
14. T. Chakraborty, K. von Klitzing, Phys. Can. **67**(3), 161 (2011). arXiv:1102.5250
15. F.D.M. Haldane, in *The Quantum Hall Effect*, ed. by R.E. Prange, S.M. Girvin (Springer, New York, 1987), p. 303
16. F.D.M. Haldane, E.H. Rezayi, Phys. Rev. Lett. **54**, 237 (1985)
17. J.K. Jain, Phys. Rev. Lett. **63**, 199 (1989)
18. J.K. Jain, Phys. Rev. B **40**, 8079 (1989)
19. O. Heinonen (ed.), *Composite Fermions* (World Scientific, Singapore, 1998)
20. B.I. Halperin, in *Perspectives in Quantum Hall Effects*, ed. by S. Das Sarma, A. Pinczuk (Wiley, New York, 1997)
21. B.I. Halperin, Physica E **20**, 71 (2003)
22. R.L. Willett, Adv. Phys. **46**, 447 (1997)
23. K.S. Novoselov, Rev. Mod. Phys. **83**, 837 (2011)
24. A.K. Geim, Rev. Mod. Phys. **83**, 851 (2011)
25. A.K. Geim, K.S. Novoselov, Nat. Mater. **6**, 183 (2007)
26. T. Ando, A.B. Fowler, F. Stern, Rev. Mod. Phys. **54**, 437 (1982)
27. P.R. Wallace, Phys. Rev. **71**, 622 (1947)
28. T. Ando, Physica E **40**, 213 (2007)
29. K.S. Novoselov, Z. Jiang, Y. Zhang, S.V. Morozov, H.L. Stormer, U. Zeitler, J.C. Maan, G.S. Boebinger, P. Kim, A.K. Geim, Science **315**, 1379 (2007)
30. D.S.L. Abergel, V. Apalkov, J. Berashevich, K. Ziegler, T. Chakraborty, Adv. Phys. **59**, 261 (2010)
31. C. Beenakker, Rev. Mod. Phys. **80**, 1337 (2008)
32. V.P. Gusynin, V.A. Miransky, S.G. Sharapov, I.A. Shovkovy, Low Temp. Phys. **34**, 778 (2008)
33. V.P. Gusynin, S.G. Sharapov, J.P. Carbotte, Int. J. Mod. Phys. B **21**, 4611 (2007)
34. A.H. Castro Neto, F. Guinea, N.M.R. Peres, K.S. Novoselov, A.K. Geim, Rev. Mod. Phys. **81**, 109 (2009)
35. N.M.R. Peres, J. Phys. Condens. Matter **21**, 323201 (2009)
36. L.M. Malard, M.A. Pimenta, G. Dresselhaus, M.S. Dresselhaus, Phys. Rep. **473**, 51 (2009)
37. A.K. Geim, Science **324**, 1530 (2009)
38. N.J.M. Horing, Philos. Trans. R. Soc. Lond. A **368**, 5525 (2010)
39. Y.H. Wu, T. Yu, Z.X. Shen, J. Appl. Phys. **108**, 071301 (2010)
40. M. Orlita, M. Potemski, Semicond. Sci. Technol. **25**, 063001 (2010)
41. C. Soldano, A. Mahmood, E. Dujardin, Carbon **48**, 2127 (2010)
42. W. Choi, I. Lahiri, R. Seelaboyina, Y.S. Kang, Crit. Rev. Solid State Mater. Sci. **35**, 52 (2010)
43. C.N.R. Rao, A.K. Sood, R. Voggu, K.S. Subrahmanyam, J. Phys. Chem. Lett. **1**, 572 (2010)
44. Y. Zhu, S. Murali, W. Cai, X. Li, J.W. Suk, J.R. Potts, R.S. Ruoff, Adv. Mater. **22**, 3906 (2010)
45. M.J. Allen, V.C. Tung, R.B. Kaner, Chem. Rev. **110**, 132 (2010)
46. N.M.R. Peres, Rev. Mod. Phys. **82**, 2673 (2010)
47. S. Das Sarma, S. Adam, E.H. Hwang, E. Rossi, Rev. Mod. Phys. **83**, 407 (2011)
48. A.V. Rozhkov, G. Giavaras, Y.P. Bliokh, V. Freilikher, F. Nori, Phys. Rep. **503**, 77 (2011)
49. C.L. Kane, E.J. Mele, Phys. Rev. Lett. **95**, 226801 (2005)
50. X.F. Wang, T. Chakraborty, Phys. Rev. B **75**, 033408 (2007)
51. N.A. Sinitsyn et al., Phys. Rev. Lett. **97**, 106804 (2006)
52. L.D. Landau, E.M. Lifshitz, *Quantum Mechanics, Non-relativistic Theory*, 3rd edn. (Pergamon Press, New York, 1977)
53. A.J.M. Giesbers, U. Zeitler, M.I. Katsnelson, L.A. Ponomarenko, T.M. Mohiuddin, J.C. Maan, Phys. Rev. Lett. **99**, 206803 (2007)
54. V.M. Apalkov, T. Chakraborty, Phys. Rev. Lett. **97**, 126801 (2006)
55. M.O. Goerbig, R. Moessner, B. Ducot, Phys. Rev. B **74**, 161407(R) (2006)

56. V. Apalkov, X.F. Wang, T. Chakraborty, Int. J. Mod. Phys. B **21**, 1165 (2007)
57. F.D.M. Haldane, Phys. Rev. Lett. **51**, 605 (1983)
58. G. Fano, F. Ortolani, E. Colombo, Phys. Rev. B **34**, 2670 (1986)
59. M. Greiter, Phys. Rev. B **83**, 115129 (2011)
60. C. Toke, P.E. Lammert, V.H. Crespi, J.K. Jain, Phys. Rev. B **74**, 235417 (2006)
61. N. Shibata, K. Nomura, J. Phys. Soc. Jpn. **78**, 104708 (2009)
62. Z. Papic, M.O. Goerbig, N. Regnault, Phys. Rev. Lett. **105**, 176802 (2010)
63. C. Toke, J.K. Jain, Phys. Rev. B **75**, 245440 (2007)
64. K.S. Novoselov, A.K. Geim, S.V. Morozov, D. Jiang, M.I. Katsnelson, I.V. Grigorieva, S.V. Dubonos, A.A. Firsov, Nature **438**, 197 (2005)
65. Y. Zhang, Y.-W. Tan, H.L. Stormer, P. Kim, Nature **438**, 201 (2005)
66. K.I. Bolotin, K.J. Sikes, Z. Jiang, G. Fudenberg, J. Hone, P. Kim, H.L. Störmer, Solid State Commun. **146**, 351 (2008)
67. X. Du, I. Skachko, A. Barker, E. Andrei, Nat. Nanotechnol. **3**, 491 (2008)
68. X. Du, I. Skachko, F. Duerr, A. Luican, E.Y. Andrei, Nature **462**, 192 (2009)
69. D.A. Abanin, I. Skachko, X. Du, E.Y. Andrei, L.S. Levitov, Phys. Rev. B **81**, 115410 (2010)
70. K.I. Bolotin, F. Ghahari, M.D. Shulman, H.L. Störmer, P. Kim, Nature **462**, 196 (2009)
71. I. Skachko, X. Du, F. Duerr, A. Luican, D.A. Abanin, L.S. Levitov, E.Y. Andrei, Philos. Trans. R. Soc. Lond. A **368**, 5403 (2010)
72. H. Wang, D.N. Sheng, L. Sheng, F.D.M. Haldane, Phys. Rev. Lett. **100**, 116802 (2008)
73. G.S. Boebinger, A.M. Chang, H.L. Störmer, D.C. Tsui, Phys. Rev. Lett. **55**, 1606 (1985)
74. G. Ebert, K. von Klitzing, J.C. Maan, G. Remenyi, C. Probst, G. Weimann, W. Schlapp, J. Phys. C, Solid State Phys. **17**, L775 (1984)
75. D.C. Tsui, H.L. Störmer, J.C.M. Hwang, J.S. Brooks, M.J. Naughton, Phys. Rev. B **28**, 2274(R) (1983)
76. E.V. Kurganova, A.J.M. Giesbers, R.V. Gorbachev, A.K. Geim, K.S. Novoselov, J.C. Maan, U. Zeitler, Solid State Commun. **150**, 2209 (2010)
77. F. Ghahari, Y. Zhao, P. Cadden-Zimansky, K. Bolotin, P. Kim, Phys. Rev. Lett. **106**, 046801 (2011)
78. C.R. Dean, A.F. Young, P. Cadden-Zimansky, L. Wang, R. Hen, K. Watanabe, T. Taniguchi, P. Kim, J. Hone, K.L. Shepard, Nat. Phys. **7**, 693 (2011)
79. W. Bao, Z. Zhao, G. Liu, P. Kratz, L. Jing, J. Velasco Jr., D. Smirnov, C.N. Lau, Phys. Rev. Lett. **105**, 246601 (2010)
80. E. McCann, V.I. Fal'ko, Phys. Rev. Lett. **96**, 086805 (2006)
81. T. Chakraborty, V.M. Apalkov, Solid State Commun. (2013)
82. E. McCann, Phys. Rev. B **74**, 161403 (2006)
83. E.V. Castro, K.S. Novoselov, S.V. Morozov, N.M.R. Peres, J.M.B. Lopes dos santos, J. Nilsson, F. Guinea, A.K. Geim, A.H. Castro Neto, Phys. Rev. Lett. **99**, 216802 (2007)
84. M. Mucha-Kruczynski, D.S.L. Abergel, E. McCann, V.I. Fal'ko, J. Phys. Condens. Matter **21**, 344206 (2009)
85. J.M. Pereira Jr., F.M. Peeters, P. Vasilopoulos, Phys. Rev. B **76**, 115419 (2007)
86. V.M. Apalkov, T. Chakraborty, Phys. Rev. Lett. **105**, 036801 (2010)
87. C. Berger, J. Veuillen, L. Magaud, P. Mallet, V. Olevano, M. Orlita, P. Plochoka, C. Faugeras, G. Martinez, M. Potemski, C. Naud, L.P. Levy, D. Mayou, Int. J. Nanotechnol. **7**, 383 (2010)
88. A. Reina, X. Jia, J. Ho, D. Nezich, H. Son, V. Bulovic, M.S. Dresselhaus, J. Kong, Nano Lett. **9**, 30 (2009)
89. D.L. Miller, K.D. Kubista, G.M. Rutter, M. Ruan, W.A. de Heer, P.N. First, J.A. Stroscio, Science **324**, 924 (2009)
90. J. Hass, F. Varchon, J.E. Millan-Otoya, M. Sprinkle, N. Sharma, W.A. de Heer, C. Berger, P.N. First, L. Magaud, E.H. Conrad, Phys. Rev. Lett. **100**, 125504 (2008)
91. S. Latil, L. Henrard, Phys. Rev. Lett. **97**, 036803 (2006)
92. S. Shallcross, S. Sharma, O.A. Pankratov, Phys. Rev. Lett. **101**, 056803 (2008)
93. J.M.B. Lopes dos Santos, N.M.R. Peres, A.H. Castro Neto, Phys. Rev. Lett. **99**, 256802 (2007)

94. E.J. Mele, Phys. Rev. B **81**, 161405 (2010)
95. A. Luican, G. Li, A. Reina, J. Kong, R.R. Nair, K.S. Novoselov, A.K. Geim, E.Y. Andrei, Phys. Rev. Lett. **106**, 126802 (2011)
96. V.M. Apalkov, T. Chakraborty, Phys. Rev. B **84**, 033408 (2011)
97. T. Taychatanapat, K. Watanabe, T. Tanigushi, P. Jarillo-Herrero, Nat. Phys. **7**, 621 (2011)
98. A. Kumar, W. Escoffier, J.M. Poumirol, C. Faugeras, D.P. Arovas, M.M. Fogler, F. Guinea, S. Roche, M. Goiran, B. Raquet, Phys. Rev. Lett. **107**, 126806 (2011)
99. V.M. Apalkov, T. Chakraborty, Phys. Rev. B **86**, 035401 (2012)
100. S. Yuan, R. Roldan, M.I. Katsnelson, Phys. Rev. B **84**, 125455 (2011)
101. J.P. Eisenstein, in *Perspectives in Quantum Hall Effects*, ed. by S. Das Sarma, A. Pinczuk (Wiley-Interscience, New York, 1996), p. 37
102. R. Willett, J.P. Eisenstein, H.L. Störmer, D.C. Tsui, A.C. Gossard, J.E. English, Phys. Rev. Lett. **59**, 1776 (1987)
103. C. Zhang, T. Knuuttila, Y. Dai, R.R. Du, L.N. Pfeiffer, K.W. West, Phys. Rev. Lett. **104**, 166801 (2010)
104. N. Read, Physica B **298**, 121 (2001)
105. G. Moore, N. Read, Nucl. Phys. B **360**, 362 (1991)
106. M. Greiter, X.-G. Wen, F. Wilczek, Phys. Rev. Lett. **66**, 3205 (1991)
107. M. Greiter, X.-G. Wen, F. Wilczek, Nucl. Phys. B **374**, 567 (1992)
108. M. Levin, B.I. Halperin, B. Rosenow, Phys. Rev. Lett. **99**, 236806 (2007)
109. S.S. Lee, S. Ryu, C. Nayak, M.P.A. Fisher, Phys. Rev. Lett. **99**, 236807 (2007)
110. A. Stern, B.I. Halperin, Phys. Rev. Lett. **96**, 016802 (2006)
111. A. Stern, Ann. Phys. **323**, 204 (2008)
112. M. Dolev, M. Heiblum, V. Umansky, A. Stern, D. Mahalu, Nature **452**, 829 (2008)
113. V. Venkatchalam, A. Yacoby, L. Pfeiffer, K. West, Nature **469**, 185 (2011)
114. N. Read, D. Green, Phys. Rev. B **61**, 10267 (2000)
115. D.A. Ivanov, Phys. Rev. Lett. **86**, 268 (2001)
116. R.F. Service, Science **332**, 193 (2011)
117. M. Storni, R.H. Morf, S. Das Sarma, Phys. Rev. Lett. **104**, 076803 (2010)
118. M.R. Peterson, Th. Jolicoeur, S. Das Sarma, Phys. Rev. Lett. **101**, 016807 (2008)
119. N. Read, E. Rezayi, Phys. Rev. B **54**, 16864 (1996)
120. V. Apalkov, T. Chakraborty, Phys. Rev. Lett. **107**, 186803 (2011)
121. M.Z. Hasan, C.L. Kane, Rev. Mod. Phys. **82**, 3045 (2010)
122. X.-L. Qi, S.-C. Zhang, Phys. Today **63**, 33 (2010)
123. D. Hsieh, D. Qian, L. Wray, Y. Xia, Y.S. Hor, R.J. Cava, M.Z. Hasan, Nature (London) **452**, 970 (2008)
124. Y. Xia, D. Qian, D. Hsieh, L. Wray, A. Pal, H. Lin, A. Bansil, D. Grauer, Y.S. Hor, R.J. Cava, M.Z. Hasan, Nat. Phys. **5**, 398 (2009)
125. T. Hanaguri, K. Igarashi, M. Kawamura, H. Takagi, T. Sasagawa, Phys. Rev. B 081305(R) (2010)
126. P. Cheng, C. Song, T. Zhang, Y. Zhang, Y. Wang, J.-F. Jia, J. Wang, Y. Wang, B.-F. Zu, X. Chen, X. Ma, K. He, L. Wang, Z. Fang, X. Xie, X.-L. Qi, C.-X. Liu, S.-C. Zhang, Q.-K. Xue, Phys. Rev. Lett. **105**, 076801 (2010)
127. H. Zhang, C.-X. Liu, X.-L. Qi, X. Dai, Z. Fang, S.-C. Zhang, Nat. Phys. **5**, 438 (2009)
128. C.-X. Liu, X.-L. Qi, H.J. Zhang, X. Dai, Z. Fang, S.-C. Zhang, Phys. Rev. B **82**, 045122 (2010)
129. Z. Yang, J.H. Han, Phys. Rev. B **83**, 045415 (2011)
130. Z. Wang, Z.-G. Fu, S.-X. Wang, P. Zhang, Phys. Rev. B **82**, 085429 (2010)
131. V. Apalkov, T. Chakraborty, Phys. Rev. Lett. **107**, 186801 (2011)
132. G. Zhang, H. Qin, J. Teng, J. Guo, Q. Guo, X. Dai, Z. Fang, K. Wu, Appl. Phys. Lett. **95**, 053114 (2009)

Chapter 9
Symmetry Breaking in Graphene's Quantum Hall Regime: The Competition Between Interactions and Disorder

Yafis Barlas, A.H. MacDonald, and Kentaro Nomura

Abstract Graphene is a two-dimensional carbon material with a honeycomb lattice and Dirac-like low-energy excitations. When Zeeman interaction is neglected its Landau levels are four-fold degenerate, explaining the $4e^2/h$ separation between quantized Hall conductivity values seen in recent experiments. In this chapter we derive a criterion for the occurrence of interaction-driven quantum Hall effects near intermediate integer values of e^2/h due to charge gaps in broken symmetry states in monolayer and bilayer graphene systems.

9.1 Introduction

Phase transitions characterized by spontaneous symmetry breaking are of broad interest in modern physics, playing a central role in high energy physics, condensed matter physics, and statistical physics. Spontaneous symmetry breaking is common because the particle-interaction energy is almost invariably minimized by breaking Hamiltonian symmetries. The simplest example of this tendency is crystallization, in which atomic nuclei avoid each other's proximity by breaking translational symmetry. Similarly, because of Fermi statistics systems, in which many interacting particles carry a spin degree of freedom, can usually reduce their energy by aligning spin orientations. Broken symmetry phases support soft Goldstone collective modes and nontrivial topological order parameter textures, such as kinks, vortices, and hedgehog textures [1], that depend on the original and residual symmetries and also on the number of spatial dimensions.

Y. Barlas
Department of Physics and Astronomy, University of California at Riverside, Riverside, CA 92521, USA

A.H. MacDonald
Department of Physics, University of Texas at Austin, Austin, TX 78712, USA

K. Nomura (✉)
Institute for Materials Research, Tohoku University, Sendai 980-8577, Japan
e-mail: nomura@imr.tohoku.ac.jp

H. Aoki, M.S. Dresselhaus (eds.), *Physics of Graphene*, NanoScience and Technology,
DOI 10.1007/978-3-319-02633-6_9,

Quantum Hall systems [2] exhibit many states in which spin symmetry is spontaneously broken. In a strong magnetic field kinetic energy is quenched when a single Landau level (LL) or a set of degenerate Landau levels is partially occupied. Under these circumstances electron-electron interaction plays the essential role and broken symmetry states are extremely common. The circumstance in which the filling factor is an integer has especially robust order that is especially easy to describe because Hartree-Fock mean-field-theory provides an excellent starting point for its description. Because Zeeman coupling is often weak compared to Coulomb coupling, for example in GaAs, the Hamiltonian for an electron in a magnetic field can have an approximate SU(2) symmetry in spin space. This symmetry is broken at odd integer filling factors $\nu = N_e/N_\phi$, where N_e is the number of electrons and N_ϕ is the degeneracy of a single Landau level. This phenomenon is referred to as quantum Hall ferromagnetism. Interactions lead to spontaneous electron spin polarization due to the presence of a large exchange enhanced spin gap which induces quasiparticle gaps and hence interaction driven integer quantum Hall (QH) effects. The neutral and charged excitations of these spin-polarized ground states are spin waves and topological spin textures called Skyrmions [2].

Another example of a multicomponent quantum Hall system is realized in double-quantum well structures where the *which-layer* degree of freedom (pseudospin) doubles the LL degeneracy. Because intra- and interlayer Coulomb interactions are different, double-layer systems no longer exhibit SU(2) symmetry but rather U(1) symmetry associated with the conservation of the charge difference between the two layers (assuming there is no interlayer tunneling). The ground state for sufficiently small layer spacing at odd fillings can be viewed as an easy-plane pseudospin ferromagnet in which the layer pseudospin orders spontaneously in the $\hat{x}$–$\hat{y}$-plane. At odd integer fillings, this state also supports a dissipationless counterflow (excitonic) supercurrent with transport properties different from either superfluids or superconductors [3]. Charged vortex excitations associated with the U(1) broken symmetry are *half-Skyrmion* like objects called merons.

Graphene is a recently discovered purely two-dimensional carbon material with a honeycomb lattice structure [6]. One of the most interesting aspects of graphene is that its low-energy excitations are accurately described as two-dimensional massless Dirac fermions. Many of the unusual properties of Dirac fermions show up in graphene, in particular an unusual sequence of integer quantum Hall plateaus. In graphene, besides the realspin degree of freedom, there are two equivalent points in the first Brillouin zone with linear energy dispersion and hence four-fold degenerate Dirac bands. In bilayer graphene, along, with the four-fold spin$\times$valley degeneracy, there is an additional doubling of the $N = 0$ Landau level which is half-filled in an electrically neutral graphene sheet. The additional degeneracy occurs because two LL's that have the same orbital character as the $n = 0$ and $n = 1$ LLs in an ordinary non-relativistic electron gas appear at the charge neutrality (Dirac) point. When this additional degeneracy is accounted for, the $N = 0$ Landau level is eightfold degenerate. In a strong magnetic field, the Coulomb interaction leads to broken symmetries within the approximately degenerate Landau levels that produce gaps for charged excitations (and hence quantum Hall effects) and lead to new physical

phenomena. The microscopic physics which controls the appearance and determines the character of these interaction-induced quantum Hall states is the subject of this chapter.

This chapter is organized as follows. In Sect. 9.2 we introduce the physics of single particle states of Dirac Hamiltonian in the presence of a magnetic field and/or disorder. Section 9.3 directs the reader to quantum Hall ferromagnetism to describe symmetry breaking of realspin and pseudospin (valley-spin). A competition between the interaction and disorder is described. In Sect. 9.4 we discuss neutral graphene (the $\nu = 0$ case) in which, depending on broken symmetries, several types of ground states and associated transport properties are considered. Section 9.5 covers symmetry breaking in bilayer graphene which has additional degeneracy leading to quantum Hall ferromagnetism in the Landau index at zero energy. In Sect. 9.6 the notion of quantum Hall ferromagnetism is generalized to the case of fractional fillings. Finally in Sect. 9.7 we present a summary of the issues of quantum Hall effects in graphene. Due to space limitation we are not able to review the subject fully in this chapter. We therefore direct readers to two other recent reviews [4, 5] that emphasize different aspects of this topic.

9.2 The Quantum Hall Effect of Massless Dirac Fermions

9.2.1 Landau Levels and Quantized Hall Conductivities

The single-particle $k \cdot p$ Hamiltonian which describes the low energy properties of graphene is the two-dimensional Dirac Hamiltonian [6]:

$$\begin{aligned}\mathcal{H} &= v_F(p_x + eA_x)\sigma_x + v(p_y + eA_y)\tau_z\sigma_y \\ &= \begin{pmatrix} \mathcal{H}_K & 0 \\ 0 & \mathcal{H}_{K'} \end{pmatrix},\end{aligned} \tag{9.1}$$

where $\mathcal{H}_K = v_F\boldsymbol{\sigma} \cdot [-i\hbar\nabla + e\mathbf{A}]$, $\mathcal{H}_{K'}$ is the transpose of $\mathcal{H}_K$, v_F is the Fermi velocity at the Dirac point, and the Pauli matrices $\boldsymbol{\sigma}$ and $\boldsymbol{\tau}$ act on the sublattice and valley degrees of freedom, respectively. In a finite magnetic field $\mathbf{B} = \nabla \times \mathbf{A} = (0, 0, B)$, the spectrum of $\mathcal{H}_K$ consists of LLs with degeneracy $4N_\phi = 4SB/\Phi_0$ ($\Phi_0 = hc/e$ is the electron magnetic flux quantum and S is the area of the system) and eigenvalues [6]

$$E_n = \mathrm{sgn}(N)\hbar\omega_0\sqrt{|N|} \tag{9.2}$$

with N being an integer. The factor of $4 = 2 \times 2$ in the Landau level degeneracy accounts for both spin and valley degeneracy. The energy and length scales are set by $\omega_0 = \sqrt{2}v_F/\ell_B$ and $\ell_B = \sqrt{\hbar/eB}$. The filling fraction $\nu > 0$ is the ratio of the number of carriers to N_ϕ with the number of carriers calculated as the difference between the number of electrons in the system and the number of carriers in a neutral system with filled valence bands and empty conduction bands.

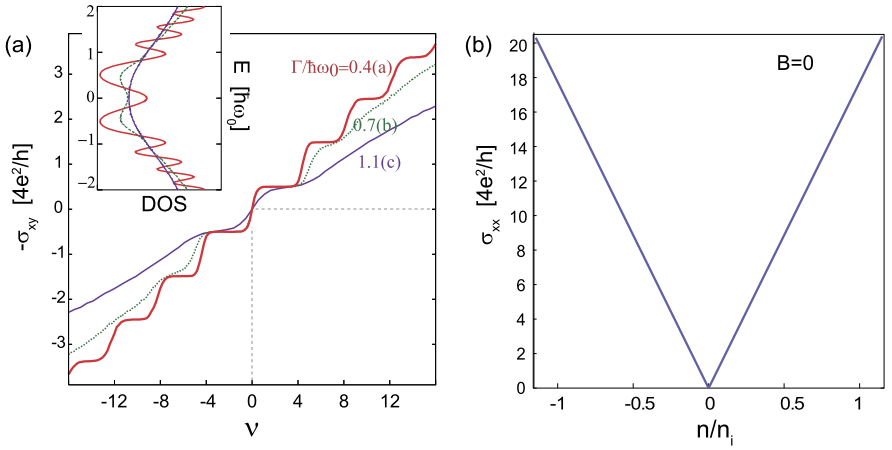

Fig. 9.1 (**a**) Hall conductivity of Dirac fermions in graphene calculated using the Kubo formula as a function of the filling factor ν for several disorder induced Landau level widths Γ. *Inset*: Density of states in the presence of disorder (after Ref. [13]). (**b**) Boltzmann theory results for zero magnetic field longitudinal conductivity as a function of n/n_i in the presence of screening (see text), where n is the carrier density and n_i is the density of charged impurities

In graphene the quantization rule for integer quantum Hall effect conductivity plateaus is [6–12]

$$\sigma_{xy} = \left(N + \frac{1}{2}\right)\frac{4e^2}{h}. \tag{9.3}$$

This quantization rule can be crudely understood as follows, starting from the relativistic Dirac equation Landau level (LL) structure. For a neutral graphene layer, the Fermi level is located at the center of the $N = 0$ Landau level and $\sigma_{xy} = 0$ because electron and hole currents cancel. As is well known from the integer quantum Hall literature, the zero-temperature Hall conductivity suddenly jumps between plateaus when a single Landau level, or a set of essentially degenerate Landau levels, is approximately half-filled. For the $N = 0$ Landau level of graphene, the Hall conductivity has to jump by $4e^2/h$ from the $\sigma_{xy} = -2e^2/h$ plateau to the $\sigma_{xy} = 2e^2/h$ plateau.

The quantum Hall effect is observable in practice only when disorder is sufficiently weak, i.e. when the Landau level spacing is larger than the impurity-induced Landau level widths. As the density of impurities increases, the quantization of the Hall conductivity becomes weaker at accessible experimental temperatures. The typical behavior is shown in Fig. 9.1(a) for different Landau level width, where the Hall conductivity was calculated numerically using the Kubo formula [13]. In the following we discuss the impurity effects seen in typical graphene samples.

9.2.2 Zero-Field Mobility and Charged Impurities

The starting point for discussions of impurity effects in graphene samples is Boltzmann transport theory at zero magnetic field. When applied to the four-fold degenerate Bloch bands of graphene it leads to [14]

$$\sigma_{xx}^{B=0} = \frac{e^2 \tau v_F^2 \mathcal{D}(E_F)}{2} = \frac{e^2}{h} \frac{2E_F \tau}{\hbar} \tag{9.4}$$

where τ^{-1} is the scattering rate, and $\mathcal{D}(E_F)$ is the density of states at the Fermi level E_F. When Boltzmann transport theory is evaluated using a golden-rule expression for the collision integral, graphene's carrier scattering rate is given by

$$\frac{1}{\tau} = \frac{n_i k_F}{2\pi \hbar^2 v} \int_0^{2\pi} d\theta \left| U_{dis}(q) \right|^2 (1 - \cos\theta) \frac{(1 + \cos\theta)}{2} \tag{9.5}$$

where θ is the scattering angle, k_F is the Fermi wavevector, $U_{dis}(q)$ is the scattering potentials, n_i is the density of impurities and $q = 2k_F \sin(\theta/2)$ is the scattering wavevector on the circular two-dimensional Fermi surface. This expression assumes that the scattering potential varies slowly on the lattice constant scale so that scattering events conserve valley indices and the scattering potential is independent of the sublattice pseudospin. The last θ-dependent factor in (9.5) is non-standard and is due to the wavevector dependence of the relative phase of graphene Bloch band wavefunctions on the two sites within its honeycomb lattice unit cell. The factor of k_F in (9.5) reflects the density dependence of the density-of-final states for elastic scattering of Fermi surface quasiparticles. For short-range scatterers ($U(q)$ independent of q) the integral in (9.5) is independent of k_F. Since $\mathcal{D}(E_F)$ is proportional to k_F for two-dimensional Dirac bands, (9.4) implies a conductivity that is independent of k_F and therefore independent of carrier density $n \propto k_F^2$. Indeed theoretical studies of the conductivity of graphene [15] predict that the conductivity has a weak carrier density dependence, remaining finite as $k_F \to 0$. Experiment, on the other hand, finds that in graphene the mobility $\mu = \sigma_{xx}/ne$, not the conductivity, is nearly constant except at very low-densities and that it has values $\sim 10^4$ cm^2 V^{-1} s^{-1} in samples that are sufficiently high quality to exhibit the integer quantum Hall effect. Evidently, quasiparticle scattering amplitudes are enhanced at lower densities in such a way as to convert the k_F^{+1} dependence of the scattering rate in (9.5) to a k_F^{-1} dependence. One plausible explanation for this behavior is that Dirac band quasiparticle scattering is dominated by the Coulomb scattering potential $V_C(q)$ from charged impurities near the graphene plane. For two-dimensional graphene $U_{dis}(q) = V_C(q) = 2\pi e^2/q$. Inserting this expression in (9.4) and (9.5) one obtains that

$$\sigma_{xx} = \frac{e^2}{h} \frac{n}{n_i} \frac{2}{\pi \alpha_g^2} \tag{9.6}$$

where $\alpha_g = \frac{e^2}{\epsilon\hbar v} \sim 1-3$ is the effective *fine structure constant* used to characterize the ratio of the Coulomb interaction and the band energy scales in graphene. In (9.6) n_i should be thought of as the density of Coulomb scatterers that are located in the substrate within a Fermi wavelength of the graphene plane. The influence of more remote scatterers is suppressed by the factor $\exp(-qd)$ that appears in the two-dimensional Fourier transform of the Coulomb interaction. From (9.4) and (9.6), one finds that the mobility

$$\mu \equiv \frac{\sigma_{xx}}{ne} \simeq \frac{1}{\alpha_g^2} \frac{155}{n_i[10^{12}\ \mathrm{cm}^{-2}]} \left[\mathrm{cm}^2/(\mathrm{V\,s})\right] \tag{9.7}$$

In systems with Coulomb electron-electron or electron-impurity interactions, screening normally plays an essential role, changing long-range interactions into short-range ones. In a static approximation, the screened disorder potential in graphene is

$$U_{sc}(q) = \frac{2\pi e^2}{q + 2\pi e^2 \Pi(q)} \tag{9.8}$$

where $\Pi(q)$ is the polarization function of the graphene Dirac bands. Screening does not change the density dependence of the conductivity in graphene because $\Pi(q)$ also scales like k_F. The influence of screening on the mobility can be estimated by making a Tomas-Fermi approximation, replacing $\Pi(q)$ by $\Pi(q = 0) = \mathcal{D}(E_F)$. When the coupling constant α_g is much larger than 1 $U_{sc}(q) \simeq (\hbar v\pi)/(2k_F)$ and

$$\sigma_{xx} = \frac{e^2}{h} \frac{n}{n_i} \frac{32}{\pi} \tag{9.9}$$

yielding a value for the mobility that is

$$\mu \simeq \frac{2500}{n_i[10^{12}\ \mathrm{cm}^{-2}]} \left[\mathrm{cm}^2/(\mathrm{V\,s})\right], \tag{9.10}$$

$16\alpha_g^2$ times larger than the unscreened value [14]. We note that α_g cancels in (9.9), which makes it easier to estimate the mobility because its effective value can be influenced by non-universal substrate dielectric screening. Corrections to (9.9) become important for $\alpha_g < 1$ [16]. One can use these expressions to extract a value for the density of scatterers n_i from measured mobilities. Figure 9.1(b) shows the transverse conductivity at $\alpha_g = 1$ computed by the Boltzmann theory [14, 16].

9.2.3 *Self-consistent Treatment of Screened Impurities in a Magnetic Field*

Although the perturbative Born approximation is often quite successful in the absence of a magnetic field in estimating band state lifetimes and transport properties,

it fails from the outset at $B \neq 0$. The problem is the Landau level degeneracy, which makes the density-of-states that appears in the golden rule diverge. This problem can be partially solved by using a self-consistent Born approximation [17], in which the finite lifetime of final states is accounted for in the scattering rate determination. The self-consistent Born approximation is also useful in accounting qualitatively for the finite density-of-states at the carrier-neutrality (Dirac) point in the absence of a magnetic field. When the self-consistent Born approximation is applied to the Landau levels, with mixing between Landau levels neglected and a static approximation used for screening, the width of each LL Γ is determined by the equation [17]

$$\frac{\Gamma^2}{4} = n_s \int \frac{d^2q}{(2\pi)^2} \left| \frac{2\pi e^2}{q + 2\pi e^2 \Pi(q)} \right|^2 \exp\left(-q^2\ell_B^2/2\right)\left[F(q)\right]^2. \tag{9.11}$$

The integral over scattering processes yields an expression for Γ^2 rather than Γ because the density of final states is strongly influenced by disorder, varying as Γ^{-1}. Note that the polarization function $\Pi(q)$ is finite for $q \to 0$ even for $N = 0$ because of the enhanced density-of-states at the carrier neutrality point in a magnetic field. Since Γ^2 diverges if we neglect screening, its role is essential.

We now need to specify the Landau level form factor $F(q)$. Taking the Coulomb interaction to be diagonal in the honeycomb lattice site index it follows that the form factor

$$F(q) \equiv 1 \tag{9.12}$$

for $N = 0$, and that

$$F(q) = \frac{1}{2}\left[L_{|N|}\left(q^2\ell_B^2/2\right) + L_{|N|-1}\left(q^2\ell_B^2/2\right)\right] \tag{9.13}$$

for $N \neq 0$ [14, 18–20]. If the magnetic field is strong enough to neglect coupling between different Landau levels the normal state static polarization function $\Pi(q)$ is given approximately by

$$\Pi(q) \approx \frac{4\exp(-q^2\ell_B^2/2)}{2\pi\ell_B^2} \frac{2}{\pi\Gamma} \sqrt{1 - \left(\frac{\mu_0}{\Gamma}\right)^2}. \tag{9.14}$$

The factor of 4 in (9.14) is due to the spin×valley degeneracy and the factor $\exp(-q^2\ell_B^2/2)$ accounts for the orbital character of Landau level wavefunctions. Since the polarization function is larger (the screening is stronger) when the Landau level width Γ is smaller, (9.11) must be solved self-consistently.

9.3 Spontaneous Breaking of Spin and Valley Symmetry

9.3.1 Exchange Interactions

The relevant energy scales for graphene in a magnetic field are

- The separation between $n = 0$ and $n = \pm 1$ LLs; $\hbar\omega_0 \equiv \sqrt{2}\hbar v_F/\ell_B \simeq 400\sqrt{B[T]}[K]$,
- Zeeman coupling; $\Delta_z \equiv g\mu_B|\mathbf{B}| \simeq 1.3 \times (B[T])[K]$, and
- The Coulomb energy; $e^2/\epsilon\ell_B \simeq 100\sqrt{B[T]}[K]$.

When the weak Zeeman coupling term is neglected, the Landau levels of graphene are four-fold degenerate. This degeneracy is directly responsible for the size of the steps in the Hall conductivity in the quantization rule (9.3). Although the Coulomb interaction is spin and valley degenerate in a continuum model, it can split Landau levels by breaking symmetries. Experimental studies of the quantum Hall effect have demonstrated that gaps appear at essentially all integer filling factors because of Coulomb interactions, and in particular at $\nu = 0, \pm 1, \pm 4$ [21, 22], only because electron-electron interactions play an essential role [14, 18–24]. Recent experiments observed further plateaus at $\nu = \pm 3$ in suspended graphene [25, 26].

There have been a number of theoretical investigations of possible broken symmetry ground states and there are two leading theoretical scenarios for the origin of the additional gaps and associated quantum Hall effects. Electron-electron interaction can lead to charge-density-wave (CDW) or spin-density-wave (SDW) order at the carrier neutrality point [27–35]. In these states the A sublattice and B sublattice spin-densities occupancies for a particular spin orientation are unequal, with the unbalance being spin-independent in the CDW case and opposite for opposite spin in the SDW case. These broken symmetry states have a mass term, i.e. a term proportional to sublattice pseudospin operator σ_z added to their quasiparticle Dirac equation due to interactions between quasiparticles and the condensate. If it is assumed [27–30] that this is the only type of broken symmetry that can occur, and Zeeman splitting is neglected, then the only filling factor at which an additional interaction induced quantum Hall effect will occur is $\nu = 0$. The second scenario is often referred to as quantum Hall ferromagnetism (QHF) [2], and has usually been discussed in a framework which assumes that Landau level mixing is negligible. In this scenario [14, 18–20, 36], when a group of essentially degenerate Landau levels is filled, energy gaps are likely at all intermediate integer filling factors because the system can open a gap and lower its energy by ordering the additional degrees of freedom associated with the degeneracy—spin, valley, or layer for example—which can always be viewed as pseudospins.

Although these scenarios are not entirely orthogonal, they do lead to different predictions, particularly for the occurrence of gaps in $N \neq 0$ LLs. From a microscopic point of view, quantum Hall ferromagnetism is often well described by a Hartree-Fock mean-field theory. Coulombic exchange interactions favor the spontaneous polarization of the real and/or valley spins at integer filling factors to the maximum degree permitted by the Pauli exclusion principle. The many body ground state wavefunction in the Hartree-Fock approximation is

$$\left|\Psi^{\nu_n}\right\rangle = \prod_{\alpha=1}^{\nu_N} \prod_{m=1}^{N_\phi} c^\dagger_{m,\alpha}|0\rangle, \tag{9.15}$$

where α is four component spin-pseudospin index, ν_N (=1, 2, or 3) is the filling factor measured from the bottom of the nth Landau level, and m labels all the orbital states within a Landau level.

An elementary calculation in Hartree-Fock theory yields the following expression for the size of the energy gaps induced by Coulomb interactions:

$$E_{exc} = \int \frac{d^2q}{(2\pi)^2} \frac{2\pi e^2}{\epsilon|\boldsymbol{q}| + 2\pi e^2 \Pi(\boldsymbol{q})} \big[F_n(q)\big]^2 \exp\big(-|\boldsymbol{q}|^2 \ell_B^2/2\big) \tag{9.16}$$

In the absence of screening $\Pi(\boldsymbol{q}) = 0$,

$$E_{exc} = \sqrt{\pi/2}\big(e^2/\epsilon\ell_B\big) \simeq 120\sqrt{B\ [\mathrm{T}]}\ [\mathrm{K}] \tag{9.17}$$

in the $N = 0$ LL, and $E_{ex} = \frac{11}{16}\sqrt{\pi/2}(e^2/\epsilon\ell_B)$ for the $N = 1$ LL.

9.3.2 Phase Diagram: Disorder vs Exchange

Real materials always have disorder that lift their Landau level degeneracies with a finite width Γ. The possibility of reducing the electron-electron interaction energy by breaking pseudospin symmetries competes with the possibility of reducing the disorder potential interaction energy by maximizing the electron density in the regions of the sample with the most attractive disorder potentials. We now discuss a criterion for the occurrence of interaction-driven quantum Hall effects [14] in disordered samples. In a weak magnetic field, the Coulomb interaction scale which grows with field strength is weak and has a minor role. The four (nearly) degenerate Landau levels are then equally occupied as indicated schematically in Fig. 9.2(a). The disordered state is unstable in a strong magnetic field only when the exchange energy is more important than the disorder potential. This symmetry breaking transition occurs at a critical magnetic field B^* which is in the range where the LL width and the exchange interaction are similar in size, as known as the Stoner criterion. In Ref. [14], the LL width and the exchange energy were computed self-consistently in order to construct a phase diagram. Given a disorder potential model, the spontaneous symmetry breaking point can be related to the zero-field mobility of graphene by applying the Stoner-like criterion that follows from mean-field theory, as illustrated in Fig. 9.2(b). The mobility is conveniently measured experimentally. The origin of the weaker tendency toward ordered states in the $N = 1$ Landau level is the difference in form factor $F(q)$ which weakens exchange interactions. This trend is expected to persist to higher N.

These theoretical estimates are uncertain because they depend on mean-field-theory considerations and because they depend on a particular model of disorder which may not apply to all samples. Since the dominant disorder source, whatever it is, yields a dependence of conductivity on density that is similar to the Coulomb disorder model, it seems reasonable that the phase boundary estimate expressed

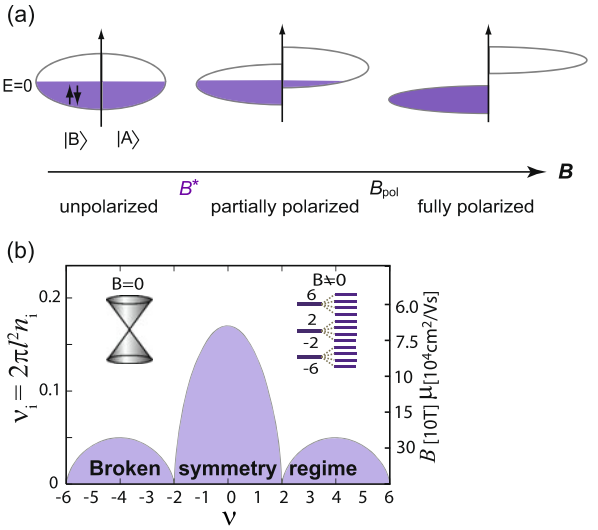

Fig. 9.2 (**a**) Splitting of a disorder broadened Landau band when the exchange interaction strength exceeds the Landau level's disorder broadening. At $B = B^*$ the two Landau bands start to split via spontaneous sublattice symmetry breaking. When Landau level mixing is neglected sublattice symmetry breaking is equivalent to valley symmetry breaking. At $B \geq B_{pol}$, the sublattice pseudospins are fully polarized. Above B_{pol} the density of states at the Fermi level vanishes and the exchange energy E_{ex} is unscreened in the static screening approximation. (**b**) Phase Diagram for $SU(4)$ quantum Hall ferromagnetism in the $N = 0$ and $N = 1$ Landau levels of graphene. For disorder due to charged scatterers, the ordered region can be characterized by a maximum value of ν_i, the ratio of the density of Coulomb scatterers to the density of a full Landau level. ν_i is inversely proportional to the product of the sample mobility at $B = 0$ and the external field strength. Order near integer filling factors requires the minimum values for this product indicated on the *right-hand vertical axis*

as a mobility-field product may be approximately universal. Although the Stoner criterion in the presence of disorder can be applied at all filling factors and provides a reasonable assessment of the crossover between interaction dominated and disorder dominated physics, we caution that the simple quantum Hall ferromagnetic states occur only at integer values of the total filling factor. We expect the emergence of interaction-driven gaps at intermediate integer filling factors to be the first signal that sample quality is adequate to see interaction-dominated physics. For very weak disorder the physics of the fractional quantum Hall effect will become relevant at non-integer filling factors.

Here we can compare the theoretical result in Fig. 9.2 with the first experiment [21] to report quantum Hall ferromagnetism in graphene. The mobility of the sample used in [21] is $\mu = 5 \times 10^4$ [cm^2/(V s)]. Figure 9.2 indicates that for this mobility and $\nu = \pm 1$ the symmetry breaks at 17 T, in good agreement with experiment [21]. The appearance of quantum Hall plateaus observed at $\nu = \pm 4$, in the middle of the four-fold degenerate $N = \pm 1$ Landau levels at around 30 T is also in reasonable agreement with Fig. 9.2 which predicts a critical field 40 T. The $\nu = \pm 3$ states were

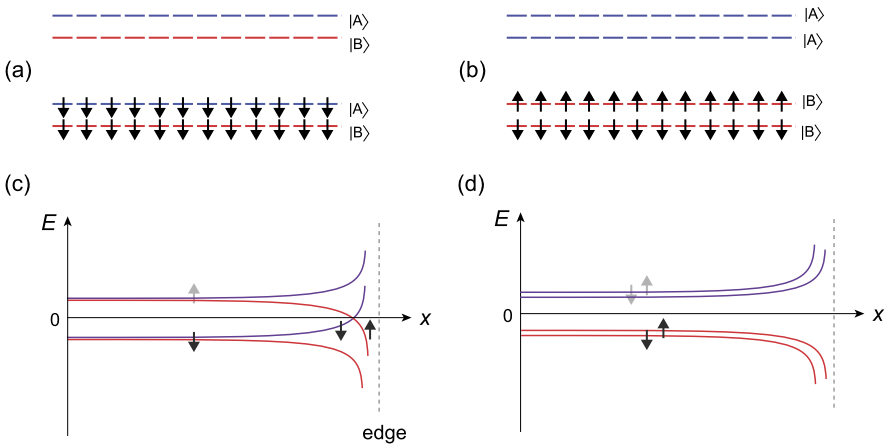

Fig. 9.3 (**a**) Realspin polarized $\nu = 0$ graphene quantum Hall state in which both A and B sublattices (pseudospins) are occupied. (**b**) Charge density wave state in which the pseudospin is polarized by occupying only the B sublattice. The spin-density wave is similar except that the sense of pseudospin polarization is opposite for opposite spins. (**c**) Energy spectrum for state (**a**). (**d**) Same for state (**b**) [24]

observed in a suspended graphene sample with $\mu \sim 2 \times 10^5$ [cm^2/(V s)] [25, 26] that is also reasonably consistent with above results.

9.4 Field-Induced Insulator at $\nu = 0$

9.4.1 Field-Induced Dissipative States and Insulating States

We have so far neglected the Zeeman energy and other symmetry breaking perturbations, because they are much weaker than the competing disorder and interaction energy scales and will have little influence on whether or not quantum Hall ferromagnetism occurs. When quantum Hall ferromagnetism does occur, however, the symmetry breaking interactions will play a larger role, since the long-range part of Coulomb interaction is independent of spin and valley pseudospin degrees of freedom. Taking account of Zeeman splitting at $\nu = 0$, it follows that the continuum model ground state at $\nu = 0$ should be one with majority spin $N = 0$ states occupied and minority spin $N = 0$ states empty, i.e. a state with $\nu = 1$ for majority spins and $\nu = -1$ for minority spins. This spin-polarized state is expected to support counter propagating edge states, whereas the charge and spin density wave states both have partial filling factors equal to zero and no edge states. This distinction is illustrated in Fig. 9.3. It was argued, on the basis of early data, that the transport properties of graphene at $\nu = 0$ are described by the spin filtered edge state model which gives

rise to a metallic conductance [23]

$$G = \frac{2e^2}{h}. \tag{9.18}$$

As pointed out in Ref. [35], intervalley exchange, which is readily captured in lattice models, favors the spin-density-wave state over charge-density-wave and spin-polarized states. Determining the character of the ground state on the basis of theoretical considerations alone is therefore challenging.

Reference [24] reports observation of the metallic dissipative transport expected from the spin filtered edge state picture, and concluded on this basis that the ground state is spin polarized. Later experiments, however, with higher quality samples and stronger magnetic fields revealed a rapid growth of the longitudinal resistance R_{xx} as a critical field B_c is approached [21, 25, 37–39].

The resistance can be fit by the Kosterlitz-Thouless (KT) form [37, 38]

$$R_{xx} \sim e^{a/\sqrt{B-B_c}} \tag{9.19}$$

over three decades of resistance. The KT transition is a phase transition known to occur in the two-dimensional XY model at which vortex-antivortex pairs change between bound and unbound. Interestingly the critical field B_c tends to be lower as the quality of samples increases. For $B < B_c$ the resistance saturates at low temperature at a value much larger than the quantum of resistance. For $B > B_c$, on the other hand, the strongly insulating behavior observed suggests that other scenarios might be at play.

9.4.2 Possible Broken Symmetries at $\nu = 0$

The diverging resistance observed experimentally in Refs. [37, 38] is difficult to account for in the realspin polarization scenario, since these states always support counter-propagating spin-filtered edge states that give rise to a metallic conductance of $2e^2/h$ [23, 24]. An attempt has been made to understand the observed insulating behavior by invoking spin-flipping backscattering due to magnetic impurities to localize the counter propagating edge states [40]. However, this scenario does not explain the experimental finding that there is a correlation between the critical field B_c and the sample quality. In the CDW scenario [27–30] it is difficult to explain the KT type resistance divergence, and the high-resistance metallic state below the critical field [37, 38].

The KT transition occurs in two-dimensional systems described by an XY model, which describes the breaking of $U(1)$ symmetry [41]. The ordered phase is destroyed at the KT transition by unbinding of pairs of topological excitations (e.g. vortices). Motivated by the KT behavior and the highly resistive metallic state, an alternative scenario has been proposed [43]: the degeneracy splitting at $\nu = 0$ is due to a spontaneous ordering of the pseudospin on the T_x–T_y plane (XY pseudospin

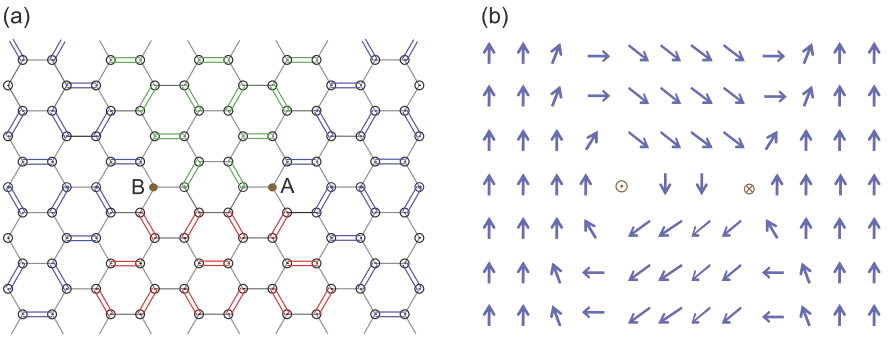

Fig. 9.4 (**a**) The Kekule bond-density wave order with two defects marked by a *filled circle*. *Red*, *Green*, and *Blue* indicate possible Kekule patterns. The defects at A and B are charged since they support a midgap electron state. (**b**) The U(1) phase $\phi = \tan^{-1}(T_y/T_x)$ corresponding to the bond order pattern (**a**)

ferromagnet). This involves a spontaneously generated hybridization between the $N = 0$ LLs associated with B (K) and A (K'), and is represented by the ground state wavefunction

$$|\Psi\rangle = \prod_{m,s=\uparrow\downarrow} \frac{1}{\sqrt{2}}\left[c^{\dagger}_{Kms} + e^{i\phi}c^{\dagger}_{K'ms}\right]|0\rangle, \tag{9.20}$$

where $c^{\dagger}_{\tau ms}$ is the creation operator for an electron in the m-th $N = 0$ LL orbital at valley $\tau = K, K'$ with realspin $s = \uparrow, \downarrow$. By specifying the value of ϕ this state breaks the $U(1)$ symmetry. This type of order also breaks the lattice translation symmetry due to the mixing of B and A, and represents a bond-density-wave (BDW) of some kind (Kekule order) [see Fig. 9.4(a)] [31–34, 42]. The phase ϕ of this hybridization matrix element is the U(1) phase angle which represents a direction in the T_x–T_y plane, $\mathbf{T} = (\cos\phi, \sin\phi, 0)$, and is associated with the sliding degrees of freedom of the density-wave. The low-energy charged excitations are vortices and antivortices [Fig. 9.4(b)] and depend on phase angle ϕ. Their binding-unbinding transition can be driven either by magnetic fields or by disorder.

We now describe in greater detail the parts of the Hamiltonian which break the SU(4) symmetry. The full Hamiltonian has the structure

$$H_{SB} = \int d^2r\left[-\frac{1}{2}\Delta_z S_z - U_0|\mathbf{S}|^2 - U_z T_z^2 - U_{\perp}\left(T_x^2 + T_y^2\right)\right]. \tag{9.21}$$

Here $\mathbf{S}$ is the realspin operator. The first term in H_{SB} represents the Zeeman energy where $\Delta_z \equiv g\mu_B B \simeq 1.3 \times (B[\mathrm{T}])[\mathrm{K}]$. The short-range part of the Coulomb interaction is SU(4) symmetric, and instead has a pseudospin dependence specified by U_z and $U_{\perp}$. These parameters be estimated from the on-site and the nearest neighbor interactions, and are smaller than E_C^{ex} by a factor $\sim a/\ell_B$ [18, 19], where a is the lattice constant. While U_0 favors realspin polarization, U_z, on the other hand, favors the CDW phase ($T_z \neq 0$) [18, 19, 36].

Table 9.1 SU(4) symmetry breaking terms, with the pattern of symmetry breaking and the energy scales [43]. This model does not account for electrostatic energies that favor charge density-wave states over spin density wave states [35]

	Residual symmetry [(spin) × (valley)]	Energy scale
Δ_z	No × SU(2)	1.3[K] × B[T] [22]
U_0	SU(2) × SU(2)	1.0[K] × B[T] [19]
U_z	SU(2) × $\mathbb{Z}_2$ (CDW)	0.5[K] × B[T] [19]
$U_\perp$	SU(2) × U(1) (Kekule)	2.0[K] × B[T] [31–33]

Furthermore, the $U_\perp$ term can arise from the electron-phonon interactions, for example from the in-plane optical mode at the K point [31–33, 42–44]. Out-of-plane lattice distortions are studied in Ref. [30], and are shown to contribute to U_z, but the effect is much weaker than that associated with the in-plane modes in graphene. The SU(4) breaking terms are summarized in Table 9.1.

Since the SU(4) symmetric part of the Coulomb interaction is much stronger than the symmetry breaking parts H_{SB}, it is the former that sets the basic energy scale for the SU(4) symmetry breaking. The symmetry breaking terms simply select the way the SU(4) symmetry is broken: they determine the nature of the ordered phase. Since $U_0, U_z, U_\perp$ in Table 9.1 all have similar energy scales, it is difficult to predict a priori which order occurs. However, these considerations at least suggest that the U(1) broken inter-valley coherent state given by (9.20) is a reasonable candidate for lifting the degeneracy of the $N = 0$ LLs.

9.4.3 Field-Induced Transition and Divergence of Resistance

When $B \gg B_c$ and when the energy scales associated with the temperature is sufficiently lower than the Coulomb exchange energy but still finite, the U(1) phase fluctuations are described by the following classical energy functional [2, 41]

$$E_{XY} = \frac{\rho_s}{2} \int d^2x (\nabla \phi)^2. \tag{9.22}$$

Elementary excitations are vortices and antivortices as illustrated in Fig. 9.4. The unbinding of the vortex-antivortex pairs triggers the KT transition from the pseudo spin XY quasi-long-range ordered phase to the disorder phase at B_c.

Vortices and anti-vortices are charged [2, 43, 44] and they can contribute to electrical transport. The reason why they carry a charge can be understood, in the lattice point of view, as follows from Fig. 9.4(a): A defect in the Kekule order can be visualized as a A or B sublattice a site that is not dimerized with neighbors, and hence supports a midgap state (zero energy mode). The presence (absence) of an electron on such site makes the Kekule vortex or antivortex positively (negatively) charged. The pseudospin is pointing along $T_z = +1$ (-1) at the vortex core while

along $T_z = -1$ $(+1)$ at the antivortex core. In the continuum model, the charge and currents generated by vortex excitations are given by [2]

$$\delta\rho(\mathbf{x}) = \frac{T_z}{4\pi}\nabla \times \nabla\phi. \tag{9.23}$$

Thus, in the presence of an impurity potential $V_{imp}(\mathbf{x})$, the energy cost is given by

$$\begin{aligned} E_{imp} &= \int d^2x\, V_{imp}(\mathbf{x})\delta\rho(\mathbf{x}) \\ &= -\int d^2x \rho_s \mathbf{a}(\mathbf{x}) \cdot \nabla\phi(\mathbf{x}) \end{aligned} \tag{9.24}$$

where we have introduced the random vector potential, $\mathbf{a}(\mathbf{x}) = \frac{1}{4\pi\rho_s}\hat{z} \times \nabla V_{imp}(\mathbf{x})$. Thus, as claimed above, the charge impurities amount to a position dependent phase shift,

$$E_{randomXY} = \frac{\rho_s}{2}\int d^2x \big[\nabla\phi - \mathbf{a}(\mathbf{x})\big]^2. \tag{9.25}$$

Equation (9.25) describes the KT transition induced by randomness [41].

In the KT disordered phase ($B^* < B < B_c$), the vortices are unbound, and their diffusion gives rise to a conductivity given by $\sigma \propto n_{vtx}\mu_{vtx}$ where n_{vtx} is the density of vortices and μ_{vtx} their mobility. This vortex conducting mechanism is a two-dimensional analog of the soliton conduction mediated by charged defects (domain walls) in polyacetylene [45]. In the KT disordered phase $n_{vtx} \sim 1/\xi^2$ where ξ is the KT correlation length [41]. Since $\xi \propto e^{a/\sqrt{B_c - B}}$, this gives rise to the KT-divergent resistivity. This argument closely follows the one used by Halperin and Nelson in analyzing the behavior of the electrical conductivity of a thin film superconductor above its KT transition [46]. Indeed, our situation is dual to theirs. In Ref. [46] the Cooper pair (charge) current exerts the Magnus force on the vortices and, through the finite vortex mobility, induces a vortex current perpendicular to it. Since the vortex current causes an transverse electric field (hence a voltage drop) through the Josephson relation, this gives rise to a finite electrical resistivity. In our case the vortex is charged, and it is the external electric field that induced the vortex (charge) current. Thus our electric field plays the role of charge (Cooper pair) current in Ref. [46], while our charge (vortex) current plays the role of electric field in Ref. [46]. As the result, the electrical conductivity in Ref. [46] should be translated into an electric resistivity ρ in our case; the finding of $\sigma \sim \xi^2$ in Ref. [46] implies $\rho \sim \xi^2$ in our situation.

A self-consistent Hartree-Fock study [43] concluded that symmetry breaking occurs at

$$B^* \simeq \frac{100}{\mu[10^3\ \mathrm{cm}^2/(\mathrm{V\,s})]}\ [\mathrm{T}] \tag{9.26}$$

as a function of sample mobility μ and the critical field is given by

$$B_c \simeq \frac{400}{\mu[10^3\ \mathrm{cm}^2/(\mathrm{V\,s})]}\ [\mathrm{T}]. \tag{9.27}$$

This is reasonably consistent with experiments with high mobility samples on SiO_2 where $\mu \sim 2\text{–}3 \times 10^4$ $[\mathrm{cm}^2/(\mathrm{V\,s})]$ and $B_c \simeq 10\text{–}20$ [T] [37, 38]. Moreover a suspended graphene sample which has a mobility 10 times larger than that of samples on SiO_2 indicates $B_c \sim 2$ [T] [25] that is also consistent with above estimation. Further experimental work will be necessary to determine unequivocally that this is the correct microscopic picture of the field-induced insulator.

The spontaneous inter-valley coherence discussed above is very similar to the inter-layer coherence in the double-layer $\nu = 1$ QH effect [2, 3]. However, there are several important differences: (i) The parameter of d/ℓ_B (d is the interlayer separation and ℓ_B is the magnetic length) in the double-layer QH system is replaced by a/ℓ_B where a is the lattice spacing. For the current system $a/\ell_B \ll 1$, a regime which has not been achieved in the double layer system. (ii) The inter-valley coherent state in graphene is a spin singlet rather than being spin polarized. (From this point of view, the $\nu = 1$ bilayer QH system is similar to the $\nu = \pm 1$ QH effect in graphene rather than to $\nu = 0$.) Although the supercurrent cannot be directly measured in the inter-valley coherent state in graphene, the two facts identified above may make it easier to observe Kosterlitz-Thouless physics.

9.5 Quantum Hall Ferromagnetism in Bilayer Graphene

9.5.1 Bilayer Graphene

The $N \neq 0$ Landau levels of bilayer graphene have the same spin$\times$valley four-fold degeneracy as single layer graphene and can be described by an approximate SU(4) invariant Hamiltonian. The ground states corresponding to the interaction induced plateaus are then captured by the variational wavefunctions in (9.15). Generally the physics associated with these states should be similar to that of the higher Landau levels in single layer graphene, with the same number of collective modes and the presence of Skyrmions. However there will be some important quantitative differences related to bilayer graphene's orbital structure. This is because the spatial structure of the electron-electron interactions is modified due to the chiral nature of bilayer graphene's charge carriers. The most interesting aspects of bilayer graphene are associated with the interaction driven states that form between the $\nu = -4$ and $\nu = 4$ QH plateaus [47], many of which do not have a counterpart in either graphene or other semiconducting QH systems.

In this section we focus on the rich quantum Hall ferromagnetism within the eight-fold degenerate bilayer graphene $N = 0$ Landau level [48]. The $N = 0$ Landau level manifold in bilayer graphene has an extra pseudospin corresponding to

the $N = 0$ and $N = 1$ orbital degree of freedom, referred to below as the Landau level degree of freedom. The ordering and fluctuations of this pseudospin degree of freedom is unique to bilayer graphene and leads to unusual collective modes [47], anomalous exciton condensation [49], and spiral ordering [50]. It is this new aspect associated with the physics of bilayer graphene that will be the focus of the rest of this section.

Bilayer graphene's Landau-level octet was immediately apparent in the earliest [51] bilayer quantum Hall experiments because of the $8e^2/h$ Hall conductivity jump between well formed plateaus centered on the Landau-level filling factors $\nu = -4$ and $\nu = 4$. When external magnetic fields are strong enough or disorder is weak enough, interactions drive quantum Hall effects at the octet's seven intermediate integer filling factors [52, 53]. The unusual character of some of these broken symmetry states was anticipated by theory. For example, in Ref. [47] it was predicted that these quantum- Hall ferromagnets (QHFs) will exhibit unusual intra-Landau-level cyclotron modes at odd filling factors, and that the collective mode excitations at these filling factors are nearly gapless, even though there is no continuous symmetry breaking.

When trigonal warping and Zeeman coupling are neglected, the low energy properties of Bernal stacked unbalanced bilayer graphene are described by the band Hamiltonian [48]

$$\mathcal{H} = \frac{1}{2m}\begin{pmatrix} 0 & \pi^{\dagger 2} \\ \pi^2 & 0 \end{pmatrix} + \lambda\Delta_V\left[\frac{1}{2}\begin{pmatrix} 1 & 0 \\ 0 & 1 \end{pmatrix} - \frac{v^2}{\gamma_1^2}\begin{pmatrix} \pi^\dagger\pi & 0 \\ 0 & -\pi\pi^\dagger \end{pmatrix}\right], \tag{9.28}$$

where the influence of an external potential difference Δ_V between the layers is captured by the last two terms. In (9.28), $\boldsymbol{\pi} = \mathbf{p} + (e/c)\mathbf{A}$ is the kinetic momentum and $\pi = \pi_x + i\pi_y$, the 2×2 matrices act on the pseudospin degree of freedom associated with the two low energy sites (the top and bottom layer sites without a near neighbor in the opposite layer), v is the single-layer Dirac velocity, $\gamma_1 \sim 0.4$ eV is the interlayer hopping amplitude, and the effective mass $m = \gamma_1/2v^2 \simeq 0.054m_e$. $\mathcal{H}$ describes both K ($\lambda = 1$) and K' ($\lambda = -1$) valleys provided that we choose the pseudospin representation $(A, \tilde{B})$ for K and $(\tilde{A}, B)$ for K'.

In bilayer graphene the $n = 0$ and $n = 1$ orbital Landau levels are members of the same octet. This peculiarity is behind most of the physics explored in the following. Neutral bilayer graphene's Landau-level octet is the direct product of three $S = 1/2$ doublets: realspin and which-layer pseudospins (as in a normal bilayer), and the Landau-level pseudospins for the $n = 0$, 1 orbitals and their degrees of freedom which is responsible for new physics.

9.5.2 Octet Hund's Rules

The octet Hartree-Fock Hamiltonian was studied in Ref. [47] and the result for a balanced bilayer ($\Delta_V = 0$) is summarized in Fig. 9.5. The large gaps ($\sim (\pi/8)^{1/2}$

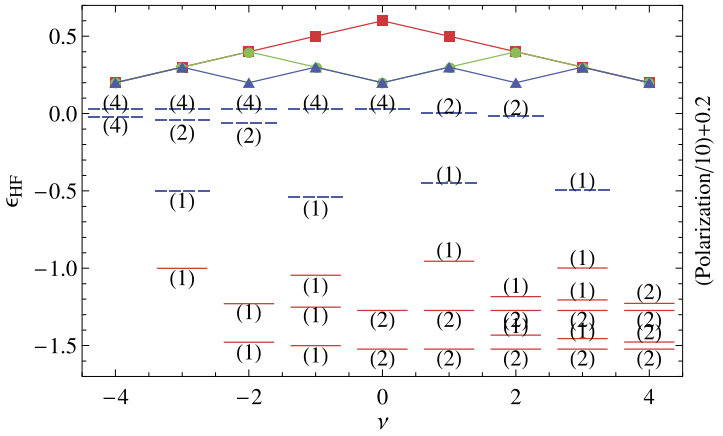

Fig. 9.5 Filling factor dependence of the integer filling factor Hartree-Fock theory occupied state (spectrum of the bilayer graphene octet at $\Delta_V = 0$). Energies of occupied (*solid red lines*) and unoccupied (*dashed blue lines*) states are in units of $\sqrt{\pi/2}e^2/\epsilon\ell_B$

in $e^2/\varepsilon\ell_B$ units) separating occupied and empty states, at the odd integer filling factors of primary interest, partially justify the use of mean-field theory. The octet filling, proceeding in integer increments starting from filling factor $\nu = -4$, follows a Hund's rule behavior: we first maximize spin-polarization, then maximize layer-polarization to the greatest extent possible, then maximize Landau-level polarization to the extent allowed by the first two rules. For balanced bilayers, the layer symmetric states (S) are filled before the layer antisymmetric states (AS), so that the layer-pseudospin polarization is achieved by forming an interlayer coherent state, instead of a state with more electrons in one layer than the other. The first four states to be filled are (S, $n = 0, \uparrow$), (S, $n = 1, \uparrow$), (AS, $n = 0, \uparrow$) and (AS, $n = 1, \uparrow$) in this order. This sequence is then repeated for the next four states with down ($\downarrow$) spin. Because the layer separation is small compared to the magnetic length in bilayer graphene, the continuum model interaction Hamiltonian is nearly SU(4) invariant. The priority of spin over layer in the Hund's rules is therefore mainly reflective of the Zeeman energy. As in the single-layer case it is possible that at weak fields, the inter-valley (and therefore interlayer) exchange process could alter this order of priority in lead, for example, to density wave states rather than spin-polarized states, at $\nu = 0$.

The Hund's rules imply that the Landau-level pseudospin is polarized at all odd integer filling factors between $\nu = -4$ and $\nu = 4$. The physics of this new type of pseudospin polarization is the main qualitative physics that is unique to the bilayer case. An important distinction between layer and Landau-level polarization is that the former is associated with spontaneous inter-layer phase coherence whenever a Landau level occupies both layers simultaneously, whereas the latter polarization is controlled by the Landau-level dependence of the microscopic Hamiltonian.

Octet quantum Hall ferromagnets have an interesting and intricate dependence on the external potential Δ_V. Because the two-layers are close together, a small value of Δ_V is sufficient to change the character of the layer polarization from the

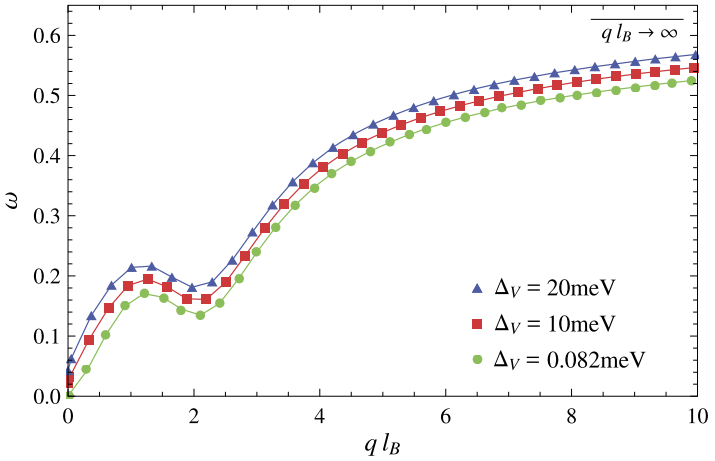

Fig. 9.6 Collective mode ω_q of the Landau-level pseudospin polarized state in units of interaction strength $e^2/\epsilon\ell_B = 11.2\sqrt{B[\mathrm{T}]}$ meV plotted as a function of $q\ell_B$ at different values of the external potential difference Δ_V at a magnetic field of 20 T. The *black* (*solid*) *line* indicates the $q\ell_B \to \infty$ asymptote for $\Delta_B = 0$

XY spontaneous-coherence form, to an Ising polarization form in which one layer is occupied before the other. We find that for Δ_V larger than a critical value Δ_V^*, the layer filling proceeds by filling the top layer first (for $\nu = -3$, $\Delta_V^* = 0.082(0.31)$ meV at $B = 20(50)$ [T]). As we explain later, this filling sequence has qualitative consequences for the odd-integer filling factor LL pseudospin polarized states.

9.5.3 Collective Modes of Landau Level Pseudospins

We now focus on the LL pseudospin fluctuations of a state with odd-integer filling factor, freezing the spin and layer degrees of freedom. Fluctuating LL spinors are linear combinations of $n = 0$ orbitals (even with respect to their cyclotron orbit center) and $n = 1$ orbitals (odd with respect to orbit center), and therefore carry an electric dipole proportional to the in-plane component of their pseudospin. Because dipole-dipole interactions are long-range, they play a dominant role in the quantum Hall ferromagnet (QHF) long-wavelength effective action [54]. We find that the effective action $S[\mathbf{m}]$ is given by

$$S[\mathbf{m}] = \int dt \left[\int d^2q \boldsymbol{\mathcal{A}} \cdot \partial_t \mathbf{m} - E[\mathbf{m}] \right], \tag{9.29}$$

where the first term is the Berry-phase contribution [54, 55] which appears in the path-integral formalism for spins. For small fluctuations away from $m_z = 1$ (full

$n = 0$ polarization), the energy is given by

$$E[\mathbf{m}] = \frac{e^2}{\varepsilon \ell_B} \int d^2q \left[\frac{1}{2|q|} (\mathbf{q} \cdot \mathbf{m})^2 + \frac{\tilde{\Delta}_{LL}}{2} \left(m_x^2 + m_y^2 \right) \right], \tag{9.30}$$

where $\tilde{\Delta}_{LL} = \Delta_{LL}/(e^2/\epsilon \ell_B)$, and Δ_{LL} is the single particle induced splitting between the $n = 0$ and $n = 1$ LL orbitals and m_x, m_y denote the in-plane magnetization. The mass term $\tilde{\Delta}_{LL}$ in (9.30) is due to the single-particle splitting between $n = 0$ and $n = 1$ levels and the interaction term is due to electric-dipole interactions. The absence of interaction contributions to the mass terms is a surprise, since the interaction is Landau-level pseudospin dependent. We address this point below. Because of the in-plane electric dipoles associated with LL pseudospinors, the long-wavelength pseudo-spinwave collective mode dispersion is not analytic:

$$\lim_{q \to 0} \hbar\omega \sim \left(\Delta_{LL}^2 + \Delta_{LL} e^2 (q \ell_B)/\epsilon \right)^{1/2}, \tag{9.31}$$

which for $\Delta_{LL} \to 0$ is proportional to $q^{3/2}$ when exchange interactions are included in the energy functional. The in-plane dipoles are also responsible for an unusual intra-Landau-level cyclotron resonance signal.

The energy dispersion of the collective modes of the LL polarized state is plotted vs $q\ell_B$ in Fig. 9.6. This collective mode has a roton minimum at $q\ell_B \approx 2.3$ and approaches the Hartree-Fock theory band splitting for $q \to \infty$ as expected. Surprisingly there is no interaction contribution to the gap at $q = 0$. This absence of the gap can be understood by examining the dependence of the uniform state interaction energy on global rotations in LL pseudospin space:

$$\frac{2\mathcal{E}[z]}{N_\phi} = -\frac{e^2}{\varepsilon \ell_B} \sqrt{\frac{\pi}{2}} \left[|z_0|^4 + \frac{3}{4} |z_1|^4 + 2|z_0|^2 |z_1|^2 \right], \tag{9.32}$$

where $z_0(z_1)$ are the coherent state amplitudes corresponding to the $n = 0, 1$ LL-pseudospin. The factor in square brackets above is $1 - |z_1|^4/4$, and is independent of z_1 to quadratic order. This is expected as Kohn's theorem within the projected lowest Landau level leads to a gapless mode due to a vanishing contribution from electron-electron interactions. Hence this intra-Landau level mode would acquire a gap in the presence of a single particle induced Landau level-splitting. It was proposed in Ref. [47] that this mode could be observed in the cyclotron resonance signal by applying an external potential difference between the layers.

9.5.4 *Instabilities, Ordering and Topological Excitations of LL-Pseudospins*

Notice that because $\Delta_{LL} < 0$ for $\nu = -1, 3$ the absence of interaction contributions to the gap implies that the fully LL-pseudospin-polarized state is unstable. The pres-

ence of the Landau level-pseudospin also has important consequences on the properties of the exciton condensates at the odd fillings $\nu = -3, 1$. The superfluid density vanishes at these filling factors leading to a finite-temperature fluctuation-induced first order isotropic-smectic phase transition when the layer densities are not balanced. This vanishing superfluid stiffness leads to a quadratic rather than expected linear [54] phonon collective mode. The transition to the smectic state is a consequence of the negative Landau level-pseudospin gap in one of the valleys along with the zero superfluid stiffness; combined, this leads to a long-wavelength instability of the Brazovskii-type [56, 57].

At other odd filling factors $\nu = -1, 3$, due to a negative Landau level-gap [48], the single particle Landau level splitting competes with the interaction induced Landau level exchange splitting which prefers $n = 0$ Landau level polarization. This leads to a sequence of transitions from (i) an inter-layer coherent state, and (ii) a mixed state with inter-orbital and inter-layer coherence to (iii) an inter-orbital coherence state spiral Landau level-pseudospin ordering [50]. The spiral state is due to the presence of Dzyaloshinskii-Moriya terms which occur as the application of the electric potential breaks inversion symmetry of the QH ferromagnet at the filling factors $\nu = -1, 3$. The presence of orbital coherence leads to a finite density of in-plane electric dipoles [58] which can be manipulated by in-plane electric fields.

Another interesting aspect associated with the broken symmetry $N = 0$ octet states in bilayer graphene is the possibility of new and interesting topological excitations not expected in monolayer graphene and semiconducting 2DEGs. It has been proposed that charge-$2e$ Skyrmions are the low energy charged excitation near the filling factors $\nu = -2, 2$ [59]. As expected these charge-$2e$ Skyrmions have textures in both $n = 0$ and $n = 1$ Landau level orbitals. Interlayer charge-$2e$ meron and Skyrmions crystals with checkerboard patterns for balanced and unbalanced layers have subsequently been identified in numerical calculations [60]. These charge-$2e$ objects also condense in a rich variety of crystal states at odd filling factors where these pseudoskyrmions are associated with the Landau level-orbital degree of freedom. The orbital Skyrmions exhibit an unusual vorticity and charge relationship exhibiting textures of in-plane electric dipoles and can be seen as an analogue of spin Skyrmions which carry a magnetic textures. These texture would couple to an in-plane electric field and the modulation of the electronic density in the crystalline phases should be experimentally accessible through a scanning tunneling microscope measurement of their local density of states [59, 60].

9.5.5 $\nu = 0$ QH Plateaus in Bilayer Graphene

Just like for monolayer graphene, the $\nu = 0$ state in bilayer graphene has drawn special attention. In the quantum Hall regime the ordering seems to indicate either spin or valley polarization, or both [52, 53]. The interest in the $\nu = 0$ QH state of bilayer graphene is different from that in graphene though, as the parabolic dispersion of bilayer graphene makes it susceptible to interaction-induced symmetry breaking even

at zero magnetic field [61–65]. Incompressibilities for suspended bilayer graphene were seen to survive even in the $B \to 0$ limit [66, 67], where it was concluded that the incompressibility at the charge neutrality point was consistent with either spontaneously broken time-reversal symmetry or spontaneously broken rotational symmetry. The broken time reversal symmetry leads to an anomalous quantum Hall state where electrons in one layer occupy valley **K** whereas electrons in the other layer occupy valley $\mathbf{K}'$ [63]. This state supports topologically protected edge modes and would exhibit a finite conductance. However, the time-reversal symmetric state is predicted to exhibit nematic order where the parabolic dispersion is expected to split into two Dirac cones. This would result in a lowering of the density of states at the charge neutrality point [64, 65].

Some authors [61, 62, 68] have concluded that the $B = 0$ broken symmetry states have spin and valley dependent sublattice polarization. If this is true, the states are associated with interesting momentum space Berry curvature [69], anomalous Hall, and orbital magnetism effects. Among the states in this class with no overall layer polarization, are [70] SDW states, usually called LAF states (layer antiferromagnet) in the bilayer case, QSH (quantum spin Hall) and QAH [68] (quantum anomalous Hall states). These three states have quantized Hall conductances with the values 0, 0, and $\pm 4e^2/h$ for the LAF, QSH, and QAH states, respectively. In each case the gaps associated with order evolve smoothly into quantum Hall gaps with filling factors $\nu = 0, 0, 4$, respectively. In a magnetic field the QAH state evolves into a bilayer state that is similar to the non-interacting $\nu = 4$ state. The QSH state evolves in field into a spin-polarized state with a total filling factor $\nu = 0$ but a filling factor difference of 4 between the majority and minority spins. The LAF state evolves into a state which appears at $\nu = 0$ and has no spin-polarization. Given these properties, studies of the quantum Hall effect at weak magnetic fields can shed light on the character of the $B = 0$ broken symmetry states. For example if the QAH state is the $B = 0$ ground state [68], the $\nu = 4$ quantum Hall effect should persist to $B = 0$, whereas if the LAF state where the ground state, it is the $\nu = 0$ quantum Hall state that would persist. Current experiments do not yet provide consistent results on these points, presumably because of small differences in the disorder potential. The possibility of observing quite different transport properties on quite similar samples suggests that the various potential ordered states of bilayers compete with each other closely.

9.6 Quantum Hall Ferromagnetism at Fractional Fillings

The quantum Hall ferromagnetism at integer filling discussed above can be generalized to the case of fractional fillings [71]. Now we introduce the effective filling factor ν_N for the Nth LL defined by

$$\nu_N = \nu - 4(N - 1/2), \tag{9.33}$$

measured from the bottom of nth Landau level. For simplicity we focus on the two-component systems by assuming that the realspin is fully polarized by the Zeeman

splitting. (As we discussed in Sect. 9.4, we need to be careful at this point for the $N = 0$ LL.) The trial wave function at the $\nu_N = 1/m$ state is written by [2, 18, 20, 72–75]

$$\Psi = \prod_{i<j}(z_i - z_j)^m \prod_{i<j}(w_i - w_j)^m \prod_{i,j}(z_i - w_j)^m, \tag{9.34}$$

where $z_i = x_i + iy_i$ is the position of ith electron on the B sublattice, and w_i is that on the A sublattice. The charged excitations from the ground state are described by Skyrmions [20]. The excitation energies Δ are estimated by the numerical diagonalization and the density matrix renormalization group method. The activation energies at $\nu_N = 1/3$ obtained in finite systems are extrapolated to the thermodynamic limit; $\Delta = 0.03$ $[e^2/\epsilon\ell_B]$ for the $N = 0$ LL, and $\Delta = 0.05$ $[e^2/\epsilon\ell_B]$ for the $N = 1$ LL. Interestingly the gap in the $N = 1$ LL is larger than that in the $N = 0$. This gap enhancement originates from the unique properties of the effective Coulombic interaction projected onto the $N = 1$ LL. Judging by the relative size of the charge gaps at integer and fractional filling factors, we estimate that the first fractional filling factors will require mobilities approximately five times larger than those required to realize quantum Hall ferromagnetism. Under an available magnetic field $\lesssim 50$[T], estimated mobility above which fractional states could be measured is $\mu \sim 2 \times 10^5$ [cm^2/(V s)] [14, 74, 75].

Recently the fractional quantum Hall states have been observed in suspended graphene and also in graphene on boron nitride substrates. The mobilities of these samples are reported as high as $\sim 10^5$ [cm^2/(V s)] [25, 26, 76, 77]. Since the Zeeman interaction and other interactions which explicitly break $SU(4)$ symmetry are much smaller in energy than the long-range part of the Coulomb interaction, one has to consider the problem in four-component systems [20, 78]. Indeed a recent experiment indicates that the hierarchy structure in graphene reflects the spin and valley degeneracy [77]. The SU(4) nature of these Landau levels will open up a new frontier for the fractional quantum Hall effect that is likely to yield some surprises.

9.7 Concluding Remarks

Because of their Landau-level degeneracy, two-dimensional electron systems subjected to a perpendicular magnetic field are always in the limit of strong correlations. In general to unravel the mysteries of these strongly correlated electron systems, an understanding of the internal degrees of freedom, such as spin and pseudospin, is essential. Graphene has realspin and (valley) pseudospins which gives rise to the rich physics of spontaneous symmetry breaking. The Coulomb exchange interaction which is SU(4) invariant if lattice effects are neglected favors the spontaneous polarization of SU(4) pseudospins. The polarization could occur in the realspin or valley pseudospin degrees of freedom, or some combination of both. Small SU(4) symmetry breaking terms, like Zeeman splitting, can play an essential role in determining the character of the ground state. Because it lifts Landau level degeneracy,

disorder which is always present to some degree in practice, can also play an essential role in determining the character of the ground state. In many cases explicit symmetry breaking terms in the Hamiltonian can have similar magnitudes to the disorder potential and compete closely. Lattice effects can be subtle and difficult to estimate and this often makes it difficult to predict the ground state order. At $\nu = 0$, for example, disorder competes with the Coulomb exchange interaction and a phase transition can occur between a disorder dominated normal phase and an interaction dominated ordered phase as the magnetic field changes magnitude. In this review, we have discussed some possible scenarios to explain the field induced transition observed at $\nu = 0$. Further experimental work will be necessary to determine the correct physical picture associated with these phenomena. Measurements at tilted magnetic fields, and careful studies of the dependence of the gap on field magnitude may give important hints.

Bilayer graphene has additional ingredients for the manifestation of various broken symmetry states. One important and enriching ingredient is the presence of an experimentally controllable external field, the potential difference between the two layers, which can be tuned between large and small values with external gates. In addition, the $N = 0$ Landau level supports a Landau level orbital degree of freedom along with the four-fold degeneracy already present due to spin and valley degeneracy. Speaking loosely, the Landau level degree of freedom appears because quantum states corresponding to cyclotron orbits with different radius, which would have different energies in an ordinary two-dimensional electron gas, are degenerate. Subtle interplays between layer and orbital Landau level pseudospin degrees of freedom lead to novel collective excitations with unusual dispersion relations and are also expected to lead to new types of skyrmion excitations. Experiments have confirmed the role of such interactions in bilayer graphene, as additional integer quantum Hall plateaus due to interaction-induced gaps within the eight-fold degenerate zero-energy Landau level have been observed by several groups. When the Landau level orbital degree of freedom is active (for example at odd integer filling factors in bilayer graphene), Landau level orbital ordering reveals exotic QH states, which in the pseudospin language are analogs of spiral and helical ferromagnets. Because the quantum Hall effects at odd integer filling factors are least strong and more easily altered by disorder, they have not yet been studied extensively. However as sample quality gets better, these plateaus will become more robust and transport experiments in separately contacted bilayers, along with optical measurements are likely to yield many surprises.

Fractional quantum Hall states in both monolayer and bilayer graphene have been studied theoretically and experimentally. The SU(4) nature of these Landau levels will open up a new frontier for the fractional quantum Hall effect that is likely to yield some surprises. The FQH states observed so far in the $N = 0$ Landau level are most likely multicomponent generalizations of the Laughlin states that are prominent in ordinary two-dimensional electron gases. The gaps at these filling factors are most likely determined by spontaneous broken symmetries; hence understanding of the internal degrees of freedom such as spin and pseudospin, is essential. The competition between incompressible states and disorder is certainly influenced by

the difference in Landau level degeneracy, and this could be important in explaining the fractions which have been observed to date. We anticipate increasing interest in studies of the physics of symmetry breaking in graphene and especially, bilayer graphene's quantum Hall regime.

Acknowledgements The work discussed here is the results of an active and ongoing collaboration with our colleagues R. Cote, D.-H. Lee, S. Ryu, N. Shibata and K. Yang. It is pleasure to acknowledge numerous useful conversations with J. Checkelsky, C.-Y. Hou, P. Kim, C. Mudry, A. Young, and Y. Zhang.

References

1. S. Coleman, *Aspects of Symmetry* (Cambridge University Press, Cambridge, 1988)
2. S.M. Girvin, A.H. MacDonald, in *Perspectives in Quantum Hall Effects*, ed. by S. Das Sarma, A. Pinczuk (Wiley, New York, 1997)
3. J.P. Eisenstein, A.H. MacDonald, Nature **432**, 691 (2004) and references therein
4. M.O. Goerbig, Rev. Mod. Phys. **83**, 1193 (2011)
5. Y. Barlas, K. Yang, A.H. MacDonald, Nanotechnology **23**, 052001 (2012)
6. A.H. Castro Neto, F. Guinea, N.M.R. Peres, K.S. Novoselov, A.K. Geim, Rev. Mod. Phys. **81**, 109 (2009)
7. S. Deser, R. Jackiw, S. Templeton, Ann. Phys. **140**, 372 (1982)
8. A.W.W. Ludwig et al., Phys. Rev. B **50**, 7526 (1994)
9. Y. Zheng, T. Ando, Phys. Rev. B **65**, 245420 (2002)
10. V.P. Gusynin, S.G. Sharapov, Phys. Rev. Lett. **95**, 146801 (2005)
11. K.S. Novoselov, A.K. Geim, S.V. Morozov, D. Jiang, M.I. Katsnelson, I.V. Grigorieva, S.V. Dubonos, A.A. Firsov, Nature **438**, 197 (2005)
12. Y. Zhang, Y.-W. Tan, H.L. Stormer, P. Kim, Nature **438**, 201 (2005)
13. K. Nomura, S. Ryu, M. Koshino, C. Mudry, A. Furusaki, Phys. Rev. Lett. **100**, 246806 (2008)
14. K. Nomura, A.H. MacDonald, Phys. Rev. Lett. **96**, 256602 (2006)
15. N.H. Shon, T. Ando, J. Phys. Soc. Jpn. **67**, 2421 (1998)
16. K. Nomura, A.H. MacDonald, Phys. Rev. Lett. **98**, 076602 (2007)
17. T. Ando, Y. Uemura, J. Phys. Soc. Jpn. **37**, 1044 (1968)
18. M.O. Goerbig, R. Moessner, B. Doucot, Phys. Rev. B **74**, 161407(R) (2006)
19. J. Alicea, M.P.A. Fisher, Phys. Rev. B **74**, 075422 (2006)
20. K. Yang, S. Das Sarma, A.H. MacDonald, Phys. Rev. B **74**, 075423 (2006)
21. Y. Zhang, Z. Jiang, J.P. Small, M.S. Purewal, Y.-W. Tan, M. Fazlollahi, J.D. Chudow, J.A. Jaszczak, H.L. Stormer, P. Kim, Phys. Rev. Lett. **96**, 136806 (2006)
22. Z. Jiang et al., Phys. Rev. Lett. **99**, 106802 (2007)
23. D.A. Abanin, P.A. Lee, L.S. Levitov, Phys. Rev. Lett. **96**, 176803 (2006)
24. D.A. Abanin, K.S. Novoselov, U. Zeitler, P.A. Lee, A.K. Geim, L.S. Levitov, Phys. Rev. Lett. **98**, 196806 (2007)
25. X. Du, I. Skachko, F. Duerr, A. Luican, E.Y. Andrei, Nature **462**, 192 (2009)
26. K.I. Bolotin, F. Ghahari, M.D. Shulman, H.L. Stormer, P. Kim, Nature **462**, 196 (2009)
27. D.V. Khveshchenko, Phys. Rev. Lett. **87**, 206401 (2001)
28. V.P. Gusynin, V.A. Miransky, S.G. Sharapov, I.A. Shovkovy, Phys. Rev. B **74**, 195429 (2006)
29. I.F. Herbut, Phys. Rev. B **75**, 165411 (2007)
30. J.N. Fuchs, P. Lederer, Phys. Rev. Lett. **98**, 016803 (2007)
31. N.A. Viet, H. Ajiki, T. Ando, J. Phys. Soc. Jpn. **63**, 3036 (1994)
32. H. Ajiki, T. Ando, J. Phys. Soc. Jpn. **64**, 260 (1995)
33. H. Ajiki, T. Ando, J. Phys. Soc. Jpn. **65**, 2976 (1996)

34. Y. Hatsugai, T. Fukui, H. Aoki, Physica E **40**, 1530 (2008)
35. J. Jung, A.H. MacDonald, Phys. Rev. B **80**, 235417 (2009)
36. L. Sheng, D.N. Sheng, F.D.M. Haldane, L. Balents, Phys. Rev. Lett. **99**, 196802 (2007)
37. J.G. Checkelsky, L. Li, N.P. Ong, Phys. Rev. Lett. **100**, 206801 (2008)
38. J.G. Checkelsky, L. Li, N.P. Ong, Phys. Rev. B **79**, 115434 (2009)
39. L. Zhang, Y. Zhang, M. Khodas, T. Valla, I.A. Zaliznyak, Phys. Rev. Lett. **105**, 046804 (2010)
40. E. Shimshoni, H.A. Fertig, G.V. Pai, Phys. Rev. Lett. **102**, 206408 (2009)
41. D. Nelson, in *Phase Transitions and Critical Phenomena*, vol. 7, ed. by C. Domb, J.L. Lebowitz (Academic Press, London, 1983)
42. A. Sedeki, L.G. Caron, C. Bourbonnais, Phys. Rev. B **62**, 6975 (2000)
43. K. Nomura, S. Ryu, D.-H. Lee, Phys. Rev. Lett. **103**, 216801 (2009)
44. C.-Y. Hou, C. Chamon, C. Mudry, Phys. Rev. B **81**, 075427 (2010)
45. A.J. Heeger, S. Kivelson, J.R. Schrieffer, W.-P. Su, Rev. Mod. Phys. **60**, 781 (1988)
46. B.I. Halperin, D.R. Nelson, J. Low Temp. Phys. **36**, 599 (1979)
47. Y. Barlas, R. Cote, K. Nomura, A.H. MacDonald, Phys. Rev. Lett. **101**, 097601 (2008)
48. E. McCann, V.I. Falko, Phys. Rev. Lett. **96**, 086805 (2006)
49. Y. Barlas, R. Cote, J. Lambert, A.H. MacDonald, Phys. Rev. Lett. **104**, 096802 (2010)
50. R. Cote, J. Lambert, Y. Barlas, A.H. MacDonald, Phys. Rev. B **82**, 035445 (2010)
51. K.S. Novoselov, E. McCann, S.V. Morozov, V.I. Fal'ko, M.I. Katsnelson, U. Zeitler, D. Jiang, F. Schedin, A.K. Geim, Nat. Phys. **2**, 177 (2006)
52. B.E. Feldman, J. Martin, A. Yacoby, Nat. Phys. **5**, 889 (2010)
53. Y. Zhao, P. Cadden-Zimansky, Z. Jiang, P. Kim, Phys. Rev. Lett. **104**, 066801 (2010)
54. K. Moon, H. Mori, K. Yang, S.M. Girvin, A.H. MacDonald, L. Zheng, D. Yoshioka, S.-C. Zhang, Phys. Rev. B **51**, 5138 (1995)
55. A. Auerbach, *Interacting Electrons and Quantum Magnetism* (Springer, New York, 1994)
56. S.A. Brazovskii, Sov. Phys. JETP **41**, 85 (1975)
57. P.C. Hohenberg, J.B. Swift, Phys. Rev. E **52**, 1828 (1995)
58. K. Shizuya, Phys. Rev. B **79**, 165402 (2009)
59. D.A. Abanin, S.A. Parameswaran, S.L. Sondhi, Phys. Rev. Lett. **103**, 076802 (2009)
60. R. Cote, W. Luo, B. Petrov, Y. Barlas, A.H. MacDonald, Phys. Rev. B **82**, 245307 (2010)
61. H. Min, G. Borghi, M. Polini, A.H. MacDonald, Phys. Rev. B **77**, 041407 (2008)
62. F. Zhang, H. Min, M. Polini, A.H. MacDonald, Phys. Rev. B **81**, 041402 (2010)
63. R. Nandkishore, L. Levitov, Phys. Rev. Lett. **104**, 156803 (2010)
64. O. Vafek, K. Yang, Phys. Rev. B **81**, 041401 (2010)
65. Y. Lemonik, I.L. Aleiner, C. Toke, V.I. Falko, Phys. Rev. B **82**, 201408 (2010)
66. R.T. Weitz, M.T. Allen, B.E. Feldman, J. Martin, A. Yacoby, Science **330**, 812 (2010)
67. J. Velasco Jr., L. Jing, W. Bao, Y. Lee, P. Kratz, V. Aji, M. Bockrath, C.N. Lau, C. Varma, R. Stillwell, D. Smirnov, F. Zhang, J. Jung, A.H. MacDonald, Nat. Nanotechnol. **7**, 156 (2012)
68. R. Nandkishore, L. Levitov, Phys. Rev. B **82**, 115124 (2010)
69. W.-K. Tse, Z. Qiao, Y. Yao, A.H. MacDonald, Q. Niu, Phys. Rev. B **83**, 155447 (2010)
70. F. Zhang, J. Jung, G.A. Fiete, Q. Niu, A.H. MacDonald, Phys. Rev. Lett. **106**, 156801 (2011)
71. T. Chakraborty, P. Pietilainen, *The Quantum Hall Effects*, 2nd edn. (Springer, Berlin, 1995)
72. V.M. Apalkov, T. Chakraborty, Phys. Rev. Lett. **97**, 126801 (2006)
73. C. Toke, P.E. Lammert, V.H. Crespi, J.K. Jain, Phys. Rev. B **74**, 235417 (2006)
74. N. Shibata, K. Nomura, Phys. Rev. B **77**, 235426 (2008)
75. N. Shibata, K. Nomura, J. Phys. Soc. Jpn. **78**, 104708 (2009)
76. F. Ghahari, Y. Zhao, P. Cadden-Zimansky, K. Bolotin, P. Kim, Phys. Rev. Lett. **106**, 046801 (2011)
77. C.R. Dean, A.F. Young, P. Cadden-Zimansky, L. Wang, H. Ren, K. Watanabe, T. Taniguchi, P. Kim, J. Hone, K.L. Shepard, Nat. Phys. **7**, 693 (2011)
78. M.O. Goerbig, N. Regnault, Phys. Rev. B **75**, 241405 (2007)

Chapter 10
Weak Localization and Spin-Orbit Coupling in Monolayer and Bilayer Graphene

Edward McCann and Vladimir I. Fal'ko

Abstract The effective Hamiltonian of low-energy electrons in monolayer and bilayer graphene is described, taking into account static disorder and spin-orbit coupling. We review different regimes of weak localization in these materials that arise from an interplay between lattice, valley, and spin degrees of freedom and the relative strength of different types of symmetry-breaking scattering. At very low temperature, weak localization may be sensitive to the presence and nature of spin-orbit coupling, and we derive formulae for the corresponding low-field magnetoresistance. If Bychkov-Rashba spin-orbit coupling is present, it tends to induce weak anti-localization in both monolayers and bilayers—as in semiconductors and metals—but, if intrinsic spin-orbit coupling prevails, it results in a suppression of weak localization.

10.1 Introduction

In conventional metals and semiconductors, anti-localization is usually indicative of the presence of strong spin-orbit (SO) coupling [1]. In graphene, two types of SO coupling have been suggested. The first, introduced by Kane and Mele [2–11] in the context of the quantum spin Hall insulator, is a full invariant of the system while the second is a Bychkov-Rashba term [2–4, 12, 13] requiring broken inversion symmetry of the graphene plane. While the latter tends to induce anti-localization, as in conventional systems [1, 14–16], the former tends to suppress weak localization, mimicking saturation of the dephasing time.

In this chapter, the tight-binding model of electrons in monolayer and bilayer graphene is described, and we show how the low-energy Hamiltonians support chiral quasiparticles with corresponding Berry's phase π and 2π, respectively. We review the model of disorder in them and the calculation of the weak localization correction to conductivity [17–22], explaining how the interplay of disorder with lattice and valley degrees of freedom is characterized by the magnetoresistance signature at low magnetic field. Then, SO coupling is taken into account through the

E. McCann · V.I. Fal'ko (✉)
Department of Physics, Lancaster University, Lancaster LA1 4YB, UK
e-mail: v.falko@lancaster.ac.uk

H. Aoki, M.S. Dresselhaus (eds.), *Physics of Graphene*, NanoScience and Technology,
DOI 10.1007/978-3-319-02633-6_10,

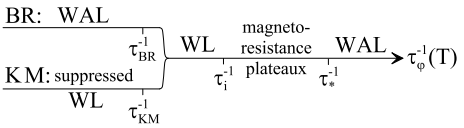

Fig. 10.1 Regimes of weak localization (WL) and weak anti-localization (WAL) behavior in monolayer and bilayer graphene as determined by the magnitude of the inelastic dephasing rate τ_φ^{-1} relative to characteristic relaxation rates describing intravalley symmetry-breaking τ_*^{-1} and intervalley scattering τ_i^{-1}. The *left side* shows the expected behavior when the dephasing rate is smaller than scattering rates related to either Bychkov-Rashba (BR) or Kane-Mele (KM) spin-orbit coupling

influence of the intrinsic Kane-Mele and the Bychkov-Rashba terms on the weak localization correction in monolayers and bilayers, and we derive formulae for the corresponding low-field magnetoresistance.

Figure 10.1 summarizes the nature of weak localization [1, 17] in monolayer graphene. Different regimes of weak localization (WL) and weak anti-localization (WAL) behavior are determined by the magnitude of the inelastic dephasing rate τ_φ^{-1} relative to characteristic relaxation rates describing intravalley symmetry-breaking τ_*^{-1} and intervalley scattering τ_i^{-1} [18–30]. At very low temperature, when the dephasing rate is smaller than scattering rates related to either Bychkov-Rashba (BR) or Kane-Mele (KM) spin-orbit coupling, then weak anti-localization or suppressed weak localization is expected, respectively [14–16].

10.2 The Low-Energy Hamiltonian of Monolayer Graphene

10.2.1 Massless Dirac-Like Quasiparticles in Monolayer Graphene

The crystal structure of monolayer graphene, Fig. 10.2(a), consists of an hexagonal Bravais lattice with a basis of two atoms, labeled A and B, per unit cell. The primitive lattice vectors are $\mathbf{a}_1 = (a/2, \sqrt{3}a/2)$ and $\mathbf{a}_2 = (a/2, -\sqrt{3}a/2)$ where a is the lattice constant, $|\mathbf{a}_1| = |\mathbf{a}_2| = a$. The reciprocal lattice is an hexagonal Bravais lattice, Fig. 10.2(b), with primitive lattice vectors $\mathbf{b}_1 = (2\pi/a, 2\pi/\sqrt{3}a)$ and $\mathbf{b}_2 = (2\pi/a, -2\pi/\sqrt{3}a)$, and the first Brillouin zone is a hexagon [the shaded hexagon in Fig. 10.2(b)]. The Fermi level lies near two inequivalent corners of the Brillouin zone, known as K points or valleys and labeled $\mathbf{K}_+$ and $\mathbf{K}_-$ in Fig. 10.2(b), with wave vectors $\mathbf{K}_\xi = \xi(4\pi/(3a), 0)$ where $\xi = \pm 1$ is a valley index.

In graphene, the electronic orbitals are sp^2 hybridized [31], meaning that the $2s$ orbital and two of the $2p$-orbitals, $2p_x$ and $2p_y$, mix, resulting in σ bonds between each atom and its three nearest neighbors [shown as solid lines in Fig. 10.2(a)]. The remaining orbital, $2p_z$, lies perpendicular to the graphene plane and forms π orbitals when combined with $2p_z$ orbitals on adjacent atoms. A tight-binding model, taking into account one $2p_z$ orbital per atom, provides an accurate description of states in the vicinity of the Fermi level [31].

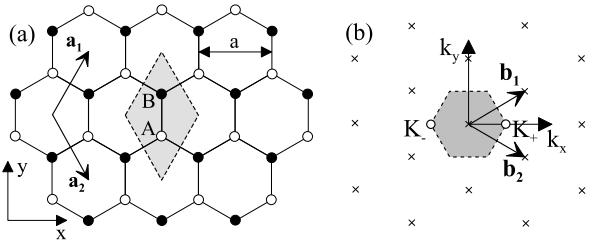

Fig. 10.2 (**a**) The crystal structure of monolayer graphene, consisting of an hexagonal Bravais lattice with a basis of two atoms, labeled A and B, per unit cell. Primitive lattice vectors $\mathbf{a}_1$ and $\mathbf{a}_2$ are of length equal to the lattice constant a, the *shaded rhombus* shows a conventional unit cell. (**b**) The reciprocal lattice (*crosses*) is an hexagonal Bravais lattice with primitive vectors $\mathbf{b}_1$ and $\mathbf{b}_2$. The *shaded hexagon* shows the first Brillouin zone, points K_+ and K_- are non-equivalent points at the corner of the Brillouin zone, known as K points

The tight-binding model includes two atomic orbitals per unit cell, ϕ_A and ϕ_B. Assuming translational invariance, the model is based upon two Bloch functions, one each for the A and B sublattices:

$$\Phi_j(\mathbf{k},\mathbf{r}) = \frac{1}{\sqrt{N}} \sum_{i=1}^{N} e^{i\mathbf{k}\cdot\mathbf{R}_{j,i}} \phi_j(\mathbf{r}-\mathbf{R}_{j,i}), \tag{10.1}$$

where $j = A$ or B, the sum with respect to index $i = 1 \ldots N$ counts N different unit cells, and $\mathbf{R}_{j,i}$ denotes the position of the jth orbital in the ith unit cell. The electronic wave function $\Psi_l(\mathbf{k},\mathbf{r})$ is written as a linear superposition of the Bloch functions, $\Psi_l(\mathbf{k},\mathbf{r}) = \sum_{j=1}^{n} c_{lj}(\mathbf{k})\Phi_j(\mathbf{k},\mathbf{r})$, where c_{lj} are coefficients. The tight-binding model, described in detail in the book by Saito, Dresselhaus, and Dresselhaus [31], leads to an energy eigenvalue equation $H\psi_l = \epsilon_l \psi_l$, $l = 1, 2$, where the Hamiltonian, H, is a transfer integral matrix with matrix elements given by $H_{ij} = \langle \Phi_i | \mathcal{H} | \Phi_j \rangle$, and $\psi_l = (c_{lA}, c_{lB})^T$ is a column vector.

The form of the matrix elements $H_{ij} = \langle \Phi_i | \mathcal{H} | \Phi_j \rangle$ may be determined using the Bloch functions (10.1). As the A and B atoms are chemically identical, the diagonal elements are assumed to be equal, and they may be set to zero without loss of generality $H_{AA} = H_{BB} = 0$. The off-diagonal element, $H_{AB} = \langle \Phi_A | \mathcal{H} | \Phi_B \rangle$, describes hopping between adjacent atoms. Assuming a dominant contribution from nearest neighbors, $H_{AB} = H^*_{BA} = -\gamma_0 f(\mathbf{k})$ where parameter $\gamma_0 = -\langle \phi_A(\mathbf{r}-\mathbf{R}_{A,i}) | \mathcal{H} | \phi_B(\mathbf{r}-\mathbf{R}_{B,l}) \rangle$ characterizes the strength of coupling between adjacent atoms, leading to

$$\hat{H}_1^{(0)} = -\gamma_0 \begin{pmatrix} 0 & f(\mathbf{k}) \\ f^*(\mathbf{k}) & 0 \end{pmatrix}. \tag{10.2}$$

Here, function $f(\mathbf{k}) = \sum_{l=1}^{3} \exp(i\mathbf{k}.\boldsymbol{\delta}_l)$, where the position vector of atom B_l relative to the A_i atom is denoted $\boldsymbol{\delta}_l = \mathbf{R}_{B,l} - \mathbf{R}_{A,i}$, takes into account phase factors accumulated in hopping from an atom to its three nearest-neighbors. For

three B atoms surrounding one A atom, Fig. 10.2(a), the displacement vectors are $\boldsymbol{\delta}_1 = (0, a/\sqrt{3})$, $\boldsymbol{\delta}_2 = (a/2, -a/2\sqrt{3})$, $\boldsymbol{\delta}_3 = (-a/2, -a/2\sqrt{3})$, giving $f(\mathbf{k}) = \exp(ik_y a/\sqrt{3}) + 2\exp(-ik_y a/2\sqrt{3})\cos(k_x a/2)$.

At the two inequivalent corners of the Brillouin zone, known as valleys and labeled $\mathbf{K}_{+/-}$ in Fig. 10.2(b), the wave vectors are $\mathbf{K}_\xi = \xi(4\pi/(3a), 0)$ where $\xi = \pm 1$. At these points, $f(\mathbf{K}_\xi) = 0$. We introduce a small momentum $\mathbf{p}$ measured from the center of the $\mathbf{K}_\xi$ point, $\mathbf{p} = \hbar\mathbf{k} - \hbar\mathbf{K}_\xi$, so that $f(\mathbf{k}) \approx -\sqrt{3}a(\xi p_x - ip_y)/2\hbar + a^2(\xi p_x + ip_y)^2/8\hbar^2$ an expansion that is valid near to the valley $\mathbf{K}_\xi$, i.e. for $pa/\hbar \ll 1$, where $p = |\mathbf{p}| = (p_x^2 + p_y^2)^{1/2}$. Then, the Hamiltonian in the vicinity of each valley may be written [32] as

$$\hat{H}_1^{(0)} \approx v \begin{pmatrix} 0 & \xi p_x - ip_y \\ \xi p_x + ip_y & 0 \end{pmatrix} - \mu \begin{pmatrix} 0 & (\xi p_x + ip_y)^2 \\ (\xi p_x - ip_y)^2 & 0 \end{pmatrix}, \quad (10.3)$$

where the velocity is $v = \sqrt{3}a\gamma_0/(2\hbar)$ and parameter $\mu = \gamma_0 a^2/(8\hbar^2)$.

The first term in (10.3) describes massless Dirac-like chiral quasiparticles with linear dispersion $\epsilon = \pm vp$ and a pseudospin degree of freedom related to the relative amplitude of the electronic wave function on the A and B sublattices, as determined by the components of the column vector $\psi_l = (c_{lA}, c_{lB})^T$. The second term in (10.3) is quadratic in momentum and describes a weak 'trigonal warping' of the Fermi circle in the vicinity of the valley center [32], introducing a perturbation of the chiral nature of the quasiparticles that tends to increase with distance away from the center of the valley.

The matrix (10.3) is explicitly written in the A/B sublattice space, but, in the following, we will describe the valley and spin structure, too. For this, we consider a space of eight-component Bloch functions $[\Phi_{\mathbf{K}_+,A,\uparrow}, \Phi_{\mathbf{K}_+,B,\uparrow}, \Phi_{\mathbf{K}_-,B,\uparrow}, \Phi_{\mathbf{K}_-,A,\uparrow}, \Phi_{\mathbf{K}_+,A,\downarrow}, \Phi_{\mathbf{K}_+,B,\downarrow}, \Phi_{\mathbf{K}_-,B,\downarrow}, \Phi_{\mathbf{K}_-,A,\downarrow}]$ consisting of two valleys $\mathbf{K}_+/\mathbf{K}_-$, two sublattices A/B, and two spin components $\uparrow/\downarrow$. Then, the Hamiltonian is written using direct products of Pauli matrices $\Pi_{x,y,z}$, $\Pi_0 \equiv \hat{1}$ acting in the $\mathbf{K}_\pm$ valley space, $\sigma_{x,y,z}$, $\sigma_0 \equiv \hat{1}$ acting in the A/B sublattice space, and $S_{x,y,z}$, $S_0 \equiv \hat{1}$ acting in the $\uparrow/\downarrow$ spin space:

$$\hat{H}_1^{(0)} \approx v\Pi_z S_0 \boldsymbol{\sigma} \cdot \mathbf{p} - \mu\Pi_0 S_0 \left[\sigma_x\left(p_x^2 - p_y^2\right) - 2\sigma_y p_x p_y\right], \quad (10.4)$$

the presence of S_0 indicating that this Hamiltonian is spin degenerate.

10.2.2 Model of Disorder in Monolayer Graphene

In order to develop a general model of static disorder in graphene, we identify terms in the electronic Hamiltonian that satisfy symmetry requirements at the K points [20, 21, 33]. Our analysis includes time reversal $t \to -t$ and, for this, the sublattice and valley matrices σ_i, Π_j are not ideal because some of them are $t \to -t$ symmetric, others are $t \to -t$ asymmetric.

Table 10.1 Irreducible representations and characters of the planar group C''_{6v} [33]. Representations A_1, A_2, B_1, B_2, E_1, E_2 are part of the point group of two-dimensional graphene C_{6v} including classes labeled by operations E, C_6, C_3, C_2, σ_d, σ_v, representations E'_1, E'_2, G' incorporate primitive translations, denoted t, with classes labeled t, tC_3, $t\sigma_d$. The last column gives the bases (in terms of Σ and Λ matrices) for irreducible subspaces in the space of 4×4 matrices

Irr. Rep.	E	C_6	C_3	C_2	σ_d	σ_v	t	tC_3	$t\sigma_d$	Σ_a, Λ_l
A_1	1	1	1	1	1	1	1	1	1	$\hat{I}$
A_2	1	1	1	1	−1	−1	1	1	−1	Σ_z
B_1	1	−1	1	−1	1	−1	1	1	1	Λ_z
B_2	1	−1	1	−1	−1	1	1	1	−1	$\Sigma_z\Lambda_z$
E_1	2	1	−1	−2	0	0	2	−1	0	$\begin{pmatrix}\Sigma_x\\ \Sigma_y\end{pmatrix}$
E_2	2	−1	−1	2	0	0	2	−1	0	$\begin{pmatrix}\Lambda_z\Sigma_x\\ \Lambda_z\Sigma_y\end{pmatrix}$
E'_1	2	0	2	0	2	0	−1	−1	−1	$\begin{pmatrix}\Lambda_x\Sigma_z\\ \Lambda_y\Sigma_z\end{pmatrix}$
E'_2	2	0	2	0	−2	0	−1	−1	1	$\begin{pmatrix}\Lambda_x\\ \Lambda_y\end{pmatrix}$
G'	4	0	−2	0	0	0	−2	1	0	$\begin{pmatrix}\Lambda_x\Sigma_x\\ \Lambda_x\Sigma_y\\ \Lambda_y\Sigma_x\\ \Lambda_y\Sigma_y\end{pmatrix}$

Instead of σ_i, Π_j, we use two sets of 4×4 Hermitian matrices [20, 21] describing sublattice 'isospin' $\vec{\Sigma} = (\Sigma_x, \Sigma_y, \Sigma_z)$ with $[\Sigma_{s_1}, \Sigma_{s_2}] = 2i\varepsilon^{s_1 s_2 s_3}\Sigma_{s_3}$, and valley 'pseudospin' $\vec{\Lambda} = (\Lambda_x, \Lambda_y, \Lambda_z)$ with $[\Lambda_{l_1}, \Lambda_{l_2}] = 2i\varepsilon^{l_1 l_2 l_3}\Lambda_{l_3}$, defined as

$$\Sigma_x = \Pi_z \otimes \sigma_x, \qquad \Sigma_y = \Pi_z \otimes \sigma_y, \qquad \Sigma_z = \Pi_0 \otimes \sigma_z, \tag{10.5}$$

$$\Lambda_x = \Pi_x \otimes \sigma_z, \qquad \Lambda_y = \Pi_y \otimes \sigma_z, \qquad \Lambda_z = \Pi_z \otimes \sigma_0. \tag{10.6}$$

These matrices have the advantage, as compared to σ_i, Π_j, that the operators $\boldsymbol{\Sigma}$ and $\boldsymbol{\Lambda}$ change sign upon time inversion. Hence *all* pairs $\Sigma_a\Lambda_l$ are $t \to -t$ invariant and can, thus, be used as a basis for a phenomenological description of nonmagnetic static disorder [20, 21].

Terms Σ_a and Λ_l, $t \to -t$ asymmetric, and products $\Sigma_a\Lambda_l$, $t \to -t$ invariant, form irreducible representations of the point group of graphene, as shown in Table 10.1. In fact, as shown by Basko [33], for a description of two valleys, it is appropriate to consider the planar group C''_{6v} which incorporates primitive translations (denoted t in Table 10.1) into the point group C_{6v} of graphene. Hence, intervalley matrices Λ_x, Λ_y appear in the irreducible representations E'_1, E'_2, G' that incorporate the primitive translations.

Using matrices Σ_a, Λ_l, the Hamiltonian in weakly-disordered monolayer graphene [20, 21] may be written as

$$\hat{H}_1 = v\boldsymbol{\Sigma}\cdot\mathbf{p} + \hat{h}_{1w} + \hat{U}, \tag{10.7}$$

$$\hat{h}_{1w} = -\mu\Lambda_z\left[\Sigma_x\left(p_x^2 - p_y^2\right) - 2\Sigma_y p_x p_y\right], \tag{10.8}$$

$$\hat{U} = \hat{\mathrm{I}}u(\mathbf{r}) + \sum_{a,l=x,y,z} \Sigma_a \Lambda_l u_{a,l}(\mathbf{r}), \tag{10.9}$$

where we included the clean Hamiltonian (10.3, 10.4). The term $\hat{U}$ incorporates the possible nonmagnetic static disorder terms where the diagonal part $\hat{\mathrm{I}}u(\mathbf{r})$ describes the influence of remote charges that don't break the valley or sublattice symmetry. Intravalley terms include $u_{z,z}(\mathbf{r})$ describing different on-site energies of the A/B sublattices, and $u_{x,z}(\mathbf{r})$, $u_{y,z}(\mathbf{r})$ accounting for fluctuations of A/B hopping. The remaining terms, $u_{a,x}(\mathbf{r})$ and $u_{a,y}(\mathbf{r})$ for $a = x, y, z$, generate intervalley scattering.

10.2.3 Spin-Orbit Coupling in Monolayer Graphene

For electrons in graphene in the vicinity of the K points, two different spin-orbit terms have been considered. The first is an intrinsic term $\hat{h}_{KM} = \alpha_{KM} \Pi_0 \sigma_z S_z$, a full invariant of the transformations of the point group, as discussed by Kane and Mele [2] in the context of the quantum spin Hall insulator. The second term is a Bychkov-Rashba term [2–4, 12, 13] that requires the breaking of mirror symmetry in the graphene plane, $\hat{h}_{BR} = \alpha_{BR} \Pi_z (\sigma_x S_y - \sigma_y S_x)$. Using the Σ_a, Λ_l matrices, the spin-orbit terms may be written as

$$\hat{h}_{KM} = \alpha_{KM} \Sigma_z S_z, \tag{10.10}$$

$$\hat{h}_{BR} = \alpha_{BR} (\Sigma_x S_y - \Sigma_y S_x). \tag{10.11}$$

10.3 Weak Localization vs Antilocalization in Monolayer Graphene

To describe the influence of spin-orbit coupling on weak localization in graphene, we generalize previous calculations [20, 21] that neglected spin-orbit coupling, and refer the reader there for further details. We assume that the Dirac-like Hamiltonian $v\boldsymbol{\Sigma} \cdot \mathbf{p}$ dominates the electronic behavior and that diagonal disorder, $\hat{\mathrm{I}}u(\mathbf{r})$ in (10.9), determines the elastic scattering rate, $\tau^{-1} \approx \tau_0^{-1} = \pi \gamma u^2/\hbar$, where $\gamma = p_F/(2\pi\hbar^2 v)$ is the density of states per spin, per valley. Using the standard diagrammatic technique for disordered systems [1, 17] at $p_F v\tau \gg \hbar$, the disorder-averaged single-particle Green's function in graphene [18, 20, 21] may be written as

$$G^{R/A}(\mathbf{p}, \epsilon) = \frac{\epsilon_{R/A} + v\boldsymbol{\Sigma} \cdot \mathbf{p}}{\epsilon_{R/A}^2 - v^2 p^2}, \quad \epsilon_{R/A} = \epsilon \pm \frac{i\hbar}{2\tau_0}. \tag{10.12}$$

The current operator corresponding to the Dirac-like Hamiltonian is momentum independent, $\hat{\mathbf{v}} = v\boldsymbol{\Sigma}$. This means that the current vertex $\tilde{v}_j$, $j = x, y$, entering the

Drude conductivity is renormalized by vertex corrections $\tilde{\mathbf{v}} = 2\hat{\mathbf{v}} = 2v\boldsymbol{\Sigma}$. Then, the Drude conductivity

$$\sigma = \frac{e^2}{\pi\hbar}\int \frac{d^2p}{(2\pi)^2}\mathrm{Tr}\left\{\tilde{v}_j G^{R/A}(\mathbf{p},\epsilon)\hat{v}_j G^{R/A}(\mathbf{p},\epsilon)\right\}, \tag{10.13}$$

is equal to $\sigma = 4e^2\gamma D$ where the diffusion coefficient is $D = v^2\tau_{tr}/2$ and the transport time is twice the scattering time, $\tau_{tr} = 2\tau_0$ [18].

The weak localization correction is written in terms of disorder-averaged two-particle correlation functions known as Cooperon propagators [1, 17] that are singlets and triplets in the spin, sublattice and valley spaces. Thus, there are sixty four Cooperons to take into account. However, for diagonal disorder $\hat{\mathrm{I}}u(\mathbf{r})$, the sublattice isospin-triplet modes all acquire relaxation gaps of the order of τ_0^{-1} and they may be neglected [20, 21]. However, sublattice isospin-singlet modes remain gapless. Thus, in the following, we consider only sublattice isospin-singlet Cooperons C_s^l where index l refers to pseudospin (related to matrices Λ describing valley degrees of freedom), and s refers to spin (related to matrices S).

Taking only the gapless isospin-singlet modes into account, the weak localization correction to the conductivity may be written in terms of a summation with respect to sixteen Cooperons consisting of combinations of spin and pseudospin singlet and triplets:

$$\delta\sigma = \frac{e^2 D}{\pi\hbar}\int \frac{d^2q}{(2\pi)^2}\sum_{s,l=0,x,y,z} c_s c_l C_s^l. \tag{10.14}$$

Here, the factors $c_0 = 1$, $c_x = c_y = c_z = -1$ take into account the fact that singlet and triplet Cooperons (of both spin and pseudospin) appear with opposite signs.

In the Hamiltonian (10.7), we take into account symmetry-breaking perturbations $\hat{h}_{1w}$ (10.8), $\hat{h}_{KM}$ (10.10), and $\hat{h}_{BR}$ (10.11), as well as the symmetry-breaking disorder terms $u_{a,l}(\mathbf{r})$ (10.9). They contribute relaxation gaps Γ_s^l to the otherwise gapless Cooperons C_s^l, although, owing to time-reversal symmetry, mode C_0^0 remains gapless. In the presence of a finite inelastic decoherence rate τ_φ^{-1} and external magnetic field $\mathbf{B} = \mathrm{rot}\,\mathbf{A}$, each Cooperon [1, 17] is given by

$$\left[D\left(i\nabla + \frac{2e\mathbf{A}}{c\hbar}\right)^2 + \Gamma_s^l + \tau_\varphi^{-1} - i\omega\right]C_s^l(\mathbf{r},\mathbf{r}') = \delta(\mathbf{r}-\mathbf{r}'). \tag{10.15}$$

Then, the zero-field temperature-dependent correction, $\delta\rho(0)$, to the graphene sheet resistance, where $\delta\rho(0)/\rho^2 \equiv -\delta\sigma$, may be written as

$$\delta\rho(0) = -\frac{e^2\rho^2}{2\pi h}\sum_{s,l=0,x,y,z} c_s c_l \ln\left(\frac{\tau^{-1}}{\tau_\varphi^{-1} + \Gamma_s^l}\right). \tag{10.16}$$

The magnetoresistance, $\Delta\rho(B) = \rho(B) - \rho(0)$, is given by

$$\Delta\rho(B) = \frac{e^2\rho^2}{2\pi h} \sum_{s,l=0,x,y,z} c_s c_l F\left(\frac{B}{B_\varphi + B_s^l}\right), \tag{10.17}$$

where

$$F(z) = \ln z + \psi\left(\frac{1}{2} + \frac{1}{z}\right), \tag{10.18}$$

$$B_\varphi = \frac{\hbar c}{4De}\tau_\varphi^{-1}, \qquad B_s^l = \frac{\hbar c}{4De}\Gamma_{0;s}^l, \tag{10.19}$$

and ψ is the digamma function.

We assume that different types of disorder, (10.9), are uncorrelated, $\langle u_{a,l}(\mathbf{r}) u_{a',l'}(\mathbf{r}')\rangle = u_{a,l}^2 \delta_{aa'}\delta_{ll'}\delta(\mathbf{r}-\mathbf{r}')$, resulting in scattering rates $\tau_{a,l}^{-1} = \pi\gamma u_{a,l}^2/\hbar$. Assuming isotropy of disorder in the x–y plane, we write $\tau_{a,x}^{-1} = \tau_{a,y}^{-1} = \tau_{a,\perp}^{-1}$, $\tau_{x,l}^{-1} = \tau_{y,l}^{-1} = \tau_{\perp,l}^{-1}$ and, following Ref. [20], combine them into the intravalley scattering rate τ_z^{-1} and the intervalley scattering rate τ_i^{-1}:

$$\tau_z^{-1} = 4\tau_{\perp,z}^{-1} + 2\tau_{z,z}^{-1}, \qquad \tau_i^{-1} = 4\tau_{\perp,\perp}^{-1} + 2\tau_{z,\perp}^{-1}. \tag{10.20}$$

The trigonal warping term $\hat{h}_{1w}$ in the Hamiltonian (10.7) produces relaxation of the intravalley Cooperons, C_s^x and C_s^y, as characterized by the rate [20]

$$\tau_w^{-1} = 2\tau_0\left(\epsilon^2\mu/\hbar v^2\right)^2, \tag{10.21}$$

although, as the trigonal warping has an opposite effect in the two valleys, this relaxation does not affect the intervalley modes, C_s^0 and C_s^z.

Neglecting the spin-orbit terms, $\hat{h}_{KM}$ and $\hat{h}_{BR}$, (10.10, 10.11), the total relaxation rate of the intravalley Cooperons is written as $\tau_*^{-1} = \tau_w^{-1} + \tau_z^{-1} + \tau_i^{-1}$ [20],

$$\Gamma_s^0 = 0, \qquad \Gamma_s^x = \Gamma_s^y = \tau_*^{-1}, \qquad \Gamma_s^z = 2\tau_i^{-1},$$

with resulting zero-field temperature-dependent correction to the sheet resistance [20] written as

$$\delta\rho(0) = \frac{e^2\rho^2}{\pi h}\left[\ln\left(\frac{\tau^{-1}}{\tau_\varphi^{-1}}\right) - 2\ln\left(\frac{\tau^{-1}}{\tau_\varphi^{-1} + \tau_*^{-1}}\right) - \ln\left(\frac{\tau^{-1}}{\tau_\varphi^{-1} + 2\tau_i^{-1}}\right)\right], \tag{10.22}$$

and magnetoresistance given by

$$\Delta\rho(B) = -\frac{e^2\rho^2}{\pi h}\left[F\left(\frac{B}{B_\varphi}\right) - 2F\left(\frac{B}{B_\varphi + B_*}\right) - F\left(\frac{B}{B_\varphi + 2B_i}\right)\right]. \tag{10.23}$$

The spin-orbit terms $\hat{h}_{KM}$ and $\hat{h}_{BR}$, (10.10, 10.11), give rise to relaxation rates τ_{KM}^{-1} and τ_{BR}^{-1}, respectively, with different parameter dependences:

$$\tau_{KM}^{-1} = \tau_0^{-1}\left(\frac{\alpha_{KM}}{\epsilon_F}\right)^2, \qquad \tau_{BR}^{-1} = \frac{2\tau_0\alpha_{BR}^2}{\hbar^2}. \tag{10.24}$$

The Bychkov-Rashba term $\hat{h}_{BR}$, (10.11), behaves in a similar way to the Bychkov-Rashba spin-orbit interaction in other materials, producing spin relaxation through the D'yakonov-Perel mechanism [34] with a corresponding relaxation rate τ_{BR}^{-1} which is inversely proportional to the elastic scattering rate τ_0^{-1} [34, 35]. The intrinsic term $\hat{h}_{KM}$, (10.10), however, causes relaxation through the Elliott-Yafet mechanism [36, 37], and the corresponding relaxation rate τ_{KM}^{-1} is proportional to the elastic scattering rate τ_0^{-1}. The spin-orbit terms contribute to the relaxation rates of the Cooperons C_s^l as

$$\Gamma_0^l = 0; \qquad \Gamma_x^l = \Gamma_y^l = \tau_{BR}^{-1} + \tau_{KM}^{-1}; \qquad \Gamma_z^l = 2\tau_{BR}^{-1}. \tag{10.25}$$

Combined with the spin-independent symmetry breaking terms in the Hamiltonian (10.9), they give:

$$\begin{aligned}
\Gamma_0^0 &= 0,\\
\Gamma_0^x = \Gamma_0^y &= \tau_*^{-1},\\
\Gamma_0^z &= 2\tau_i^{-1},\\
\Gamma_x^0 = \Gamma_y^0 &= \tau_{BR}^{-1} + \tau_{KM}^{-1},\\
\Gamma_x^x = \Gamma_x^y = \Gamma_y^x = \Gamma_y^y &= \tau_*^{-1} + \tau_{BR}^{-1} + \tau_{KM}^{-1},\\
\Gamma_x^z = \Gamma_y^z &= 2\tau_i^{-1} + \tau_{BR}^{-1} + \tau_{KM}^{-1},\\
\Gamma_z^0 &= 2\tau_{BR}^{-1},\\
\Gamma_z^x = \Gamma_z^y &= \tau_*^{-1} + 2\tau_{BR}^{-1},\\
\Gamma_z^z &= 2\tau_i^{-1} + 2\tau_{BR}^{-1}.
\end{aligned}$$

Used in conjunction with (10.16, 10.17), these results determine the weak localization correction to the zero-field resistance and the magnetoresistance, respectively.

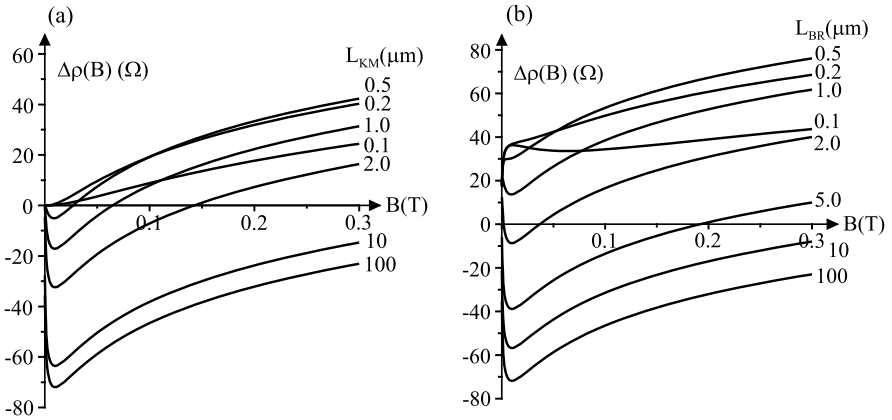

Fig. 10.3 (**a**) Low-field magnetoresistance of monolayer graphene for different strengths of the intrinsic spin-orbit coupling (10.10), neglecting the Bychkov-Rashba term (10.11). Values of the spin-orbit relaxation length L_{KM} are shown on the right hand side. (**b**) Low-field magnetoresistance for different strengths of the Bychkov-Rashba spin-orbit coupling (10.11), neglecting the intrinsic term (10.10). Values of the Bychkov-Rashba relaxation length L_{BR} are shown on the right hand side. Other parameter values are $\rho = 1000\ \Omega$, $L_\varphi = 10$ μm, $L_i = 500$ nm, $L_* = 200$ nm, and plots were made using (10.26)

Explicitly, the latter is given by

$$\begin{aligned}\Delta\rho(B) = \frac{e^2\rho^2}{2\pi h}\Bigg[& F\left(\frac{B}{B_\varphi}\right) - 2F\left(\frac{B}{B_\varphi + B_*}\right) \\ & - F\left(\frac{B}{B_\varphi + 2B_i}\right) - 2F\left(\frac{B}{B_\varphi + B_{BR} + B_{KM}}\right) \\ & + 4F\left(\frac{B}{B_\varphi + B_* + B_{BR} + B_{KM}}\right) \\ & + 2F\left(\frac{B}{B_\varphi + 2B_i + B_{BR} + B_{KM}}\right) \\ & - F\left(\frac{B}{B_\varphi + 2B_{BR}}\right) + 2F\left(\frac{B}{B_\varphi + B_* + 2B_{BR}}\right) \\ & + F\left(\frac{B}{B_\varphi + 2B_i + 2B_{BR}}\right)\Bigg],\end{aligned} \tag{10.26}$$

where $B_{\varphi,i,*,BR,KM} = (\hbar c/4De)\tau^{-1}_{\varphi,i,*,BR,KM}$.

The low-field magnetoresistance, (10.26), for different strengths of the intrinsic spin-orbit coupling (10.10), neglecting the Bychkov-Rashba term (10.11), is plotted in Fig. 10.3(a). Relaxation length scales are related to relaxation times as $L_{\varphi,i,*,BR,KM} = (D\tau_{\varphi,i,*,BR,KM})^{1/2}$. When the spin-orbit coupling is negligible (e.g. the curve for $L_{KM} = 100$ μm), graphene displays negative magnetoresistance

indicating weak localization, but note that the up-turn in the curve at larger magnetic field B occurs because the chirality of quasiparticles in monolayer graphene tends towards anti-localization [25]. The intrinsic term $\hat{h}_{KM}$, (10.10), tends to suppress weak localization [14, 15]. Taking it into account, but neglecting the Rashba term $\hat{h}_{BR}$, (10.11), then the Hamiltonian, (10.7), splits into separate spin 'up' and 'down' components. Although time-reversal symmetry of graphene is not broken by spin-orbit coupling, the Hamiltonian of each spin component breaks an effective time-reversal symmetry. The contributions of the $s = 0$ and $s = z$ Cooperon components (C_0^l and C_z^l) cancel exactly. Then, the influence of the intrinsic spin-orbit term may be absorbed into a modified definition of the inelastic dephasing rate as $\tau_\varphi^{-1} \Rightarrow \tau_\varphi^{-1} + \tau_{KM}^{-1}$ in the formulae obtained by neglecting spin-orbit coupling, such as (10.22, 10.23). When the combined effective dephasing rate $\tau_\varphi^{-1} + \tau_{KM}^{-1}$ is relatively large, as compared to the symmetry-breaking rates $\tau_{\rm i}^{-1}$ and τ_*^{-1}, then the weak anti-localization of chiral quasiparticles is observable, Fig. 10.3(a).

The low-field magnetoresistance, (10.26), for different strengths of the Bychkov-Rashba spin-orbit coupling (10.11), neglecting the intrinsic term (10.10), is plotted in Fig. 10.3(b). The Bychkov-Rashba term $\hat{h}_{BR}$, (10.11), tends to drive weak localization towards weak anti-localization [14–16], as in conventional materials [1]. Taken with the Dirac-like Hamiltonian $v\boldsymbol{\Sigma}\cdot\mathbf{p}$, the Bychkov-Rashba terms forces the electronic spin to lie in the graphene plane and perpendicular to the electronic momentum $\mathbf{p}$. Propagation of electrons around a closed trajectory is then accompanied by an additional phase change related to spin rotation, resulting in anti-localization behavior.

10.4 The Low-Energy Hamiltonian of Bilayer Graphene

10.4.1 Massive Chiral Quasiparticles in Bilayer Graphene

Bilayer graphene [38–40] consists of two coupled monolayers, with inequivalent atomic sites $A1$, $B1$ on the lower layer, $A2$, $B2$ on the upper layer, Fig. 10.4. In Bernal (A-B) stacked bilayer graphene, half of these atomic sites, $B1$ and $A2$, say, have a counterpart on the other layer that lies directly above or below it, whereas the other sites, $A1$ and $B2$, have no such partners.

We generalise the tight-binding Hamiltonian of monolayer graphene, (10.2), to write an effective Hamiltonian [39, 41–44] for bilayer graphene taking into account one $2p_z$ orbital on each site $A1$, $B2$, $A2$, $B1$:

$$\hat{H}_2^{(0)} = \begin{pmatrix} 0 & \gamma_3 f^*(\mathbf{k}) & 0 & -\gamma_0 f(\mathbf{k}) \\ \gamma_3 f(\mathbf{k}) & 0 & -\gamma_0 f^*(\mathbf{k}) & 0 \\ 0 & -\gamma_0 f(\mathbf{k}) & 0 & \gamma_1 \\ -\gamma_0 f^*(\mathbf{k}) & 0 & \gamma_1 & 0 \end{pmatrix},$$

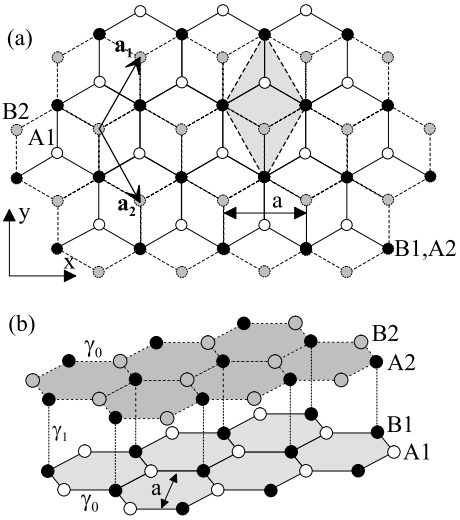

Fig. 10.4 (**a**) Plan view of the crystal structure of bilayer graphene, consisting of two coupled monolayers with two atoms per unit cell on the lower layer, labeled $A1$ (*white circles*) and $B1$ (*black circles*), and two atoms per unit cell on the upper layer, labeled $A2$ (*black circles*) and $B2$ (*grey circles*). Atomic sites $B1$ and $A2$ (*black circles*) lie directly below and above each other. Primitive lattice vectors $\mathbf{a}_1$ and $\mathbf{a}_2$ are of length equal to the lattice constant a, the shaded rhombus shows a conventional unit cell. (**b**) Side view, showing intralayer coupling γ_0 and interlayer coupling γ_1 between $B1$ and $A2$ sites

where parameter γ_0 describes nearest-neighbor intralayer hopping, as in the monolayer, (10.2). Interlayer coupling between orbitals on sites $B1$ and $A2$ that lie directly above or below each other is described by parameter γ_1, whereas parameter γ_3 describes skew interlayer coupling between orbitals on the other sites, $A1$ and $B2$.

Interlayer coupling γ_1 between the $B1$ and $A2$ sites has a significant influence on the electronic band structure at low energy: p_z orbitals on the $B1$ and $A2$ sites form 'dimer' states that result in two bands that are split away from zero energy, whereas p_z orbitals on the $A1$ and $B2$ sites form two bands with an approximately parabolic dispersion in the vicinity of the Fermi level. The two low-energy bands may be described by an effective Hamiltonian describing two components consisting of orbitals on the $B2$ and $A1$ sites. It is obtained by eliminating the contribution of the split bands, described by the $B1$ and $A2$ components, using a Schrieffer-Wolff transformation [45]. Then, the two low-energy bands [39] may be described by an effective Hamiltonian:

$$\hat{H}_2^{(0)} \approx \hat{h}_2 + \hat{h}_{2w}, \tag{10.27}$$

$$\hat{h}_2 = -\frac{1}{2m}\Pi_0 S_0\left[\sigma_x\left(p_x^2 - p_y^2\right) - 2\sigma_y p_x p_y\right], \tag{10.28}$$

$$\hat{h}_{2w} = v_3 \Pi_z S_0 \boldsymbol{\sigma} \cdot \mathbf{p}. \tag{10.29}$$

This Hamiltonian operates in a space of eight-component Bloch functions $\Phi = [\phi_{\mathbf{K}_+,B2,\uparrow}, \phi_{\mathbf{K}_+,A1,\uparrow}, \phi_{\mathbf{K}_-,A1,\uparrow}, \phi_{\mathbf{K}_-,B2,\uparrow}, \phi_{\mathbf{K}_+,B2,\downarrow}, \phi_{\mathbf{K}_+,A1,\downarrow}, \phi_{\mathbf{K}_-,A1,\downarrow}, \phi_{\mathbf{K}_-,B2,\downarrow}]$ consisting of two valleys $\mathbf{K}_+/\mathbf{K}_-$, two lattice sites $B2/A1$, and two spin components $\uparrow/\downarrow$. As for the monolayer, the bilayer Hamiltonian is written using direct products of Pauli matrices $\Pi_{x,y,z}, \Pi_0 \equiv \hat{1}$ acting in the $\mathbf{K}_\pm$ valley space, $\sigma_{x,y,z}, \sigma_0 \equiv \hat{1}$ acting in the $B2/A1$ sublattice space, and $S_{x,y,z}, S_0 \equiv \hat{1}$ acting in the $\uparrow/\downarrow$ spin space.

The first term in the Hamiltonian (10.28) describes massive chiral quasiparticles with quadratic dispersion $\epsilon \approx \pm p^2/2m$, $p = |\mathbf{p}|$, and chirality associated with Berry's phase 2π [39]. The mass, $m = \gamma_1/2v^2$, is related to the $B1$-$A2$ interlayer coupling, γ_1, and the monolayer Fermi velocity v. The second term, $\hat{h}_{2w}$, is linear in momentum and describes trigonal warping [32, 39]. The effective velocity $v_3 = (\sqrt{3}/2)a\gamma_3/\hbar$ is related to the skew interlayer coupling γ_3 between p_z orbitals on atomic sites $A1$ and $B2$.

10.4.2 Model of Disorder in Bilayer Graphene

We employ Σ_i, Λ_i matrices, (10.5, 10.6), to describe bilayer graphene at low energy, in the space of two lattice sites $B2/A1$ and two valleys $\mathbf{K}_+/\mathbf{K}_-$. As in monolayer graphene, all matrices $\mathbf{\Sigma}$ and $\mathbf{\Lambda}$ change sign upon time inversion so that pairs $\Sigma_a\Lambda_l$ are $t \to -t$ invariant and can be used as a basis for a phenomenological description of nonmagnetic static disorder. Then, the Hamiltonian for nonmagnetic disorder in bilayer graphene may be written as in the monolayer equation (10.9).

10.4.3 Spin-Orbit Coupling in Bilayer Graphene

For the two low-energy bands, in the vicinity of the valley center, the form of SO coupling in bilayer graphene is analogous to that in monolayer graphene, with two distinct terms. The first is the intrinsic SO coupling $\hat{h}_{KM} = \alpha_{KM}\Pi_0\sigma_z S_z$ [2, 8–11] and the second is a Bychkov-Rashba term $\hat{h}_{BR} = \alpha_{BR}\Pi_z(\sigma_x S_y - \sigma_y S_x)$ [2–4, 8, 12, 13]. Using the matrices Σ_i, Λ_i, (10.5, 10.6) to describe $B2$-$A1$ sublattice 'isospin' and K_+, K_- valley 'pseudospin', the Hamiltonian in weakly-disordered bilayer graphene at low energy may be written as

$$\hat{H}_2 = \hat{h}_2 + \hat{h}_{2w} + \hat{h}_{KM} + \hat{h}_{BR} + \hat{U}, \tag{10.30}$$

$$\hat{h}_2 = -\frac{1}{2m}\Lambda_z\left[\Sigma_x\left(p_x^2 - p_y^2\right) - 2\Sigma_y p_x p_y\right], \tag{10.31}$$

$$\hat{h}_{2w} = v_3\mathbf{\Sigma}\cdot\mathbf{p}, \tag{10.32}$$

where $\hat{U}$, $\hat{h}_{KM}$, and $\hat{h}_{BR}$ have the same form as in monolayer graphene, (10.9, 10.10, 10.11), with different parameter values.

10.5 Weak Localization in Bilayer Graphene

We assume that the chiral term in the Hamiltonian [for bilayer, the term $\hat{h}_2$, (10.31)] controls the electronic behavior and that diagonal disorder, $\hat{I}u(\mathbf{r})$ in (10.9), dominates the elastic scattering rate, $\tau^{-1} \approx \tau_0^{-1} = \pi\gamma u^2/\hbar$, where $\gamma = m/(2\pi\hbar^2)$ is the density of states per spin, per valley. Using the standard diagrammatic technique for disordered systems [1, 17] at $p_F v\tau \gg \hbar$, the disorder-averaged single-particle Green's function in bilayer graphene [21, 22] may be written as

$$G^{R/A}(\mathbf{p},\epsilon) = \frac{\epsilon_{R/A} - (\Lambda_z/2m)[\Sigma_x(p_x^2 - p_y^2) - 2\Sigma_y p_x p_y]}{\epsilon_{R/A}^2 - (p^2/2m)^2},$$

where $\epsilon_{R/A} = \epsilon \pm i\hbar/(2\tau_0)$.

A marked difference from the monolayer is that the current operator corresponding to the chiral Hamiltonian [the term $\hat{h}_2$, (10.31)] is momentum dependent [21, 46],

$$\hat{\mathbf{v}} = -\frac{\Lambda_z}{m}\big[(\Sigma_x p_x - \Sigma_y p_y)\hat{\boldsymbol{\imath}} - (\Sigma_y p_x + \Sigma_x p_y)\hat{\boldsymbol{\jmath}}\big].$$

This means that the current vertex entering the Drude conductivity is not renormalized by vertex corrections, so that the Drude conductivity is equal to $\sigma = 4e^2\gamma D$ where the diffusion coefficient is $D = v_F^2\tau_0/2$ and the transport time is equal to the scattering time τ_0. The Fermi velocity $v_F = p_F/m$ is also momentum dependent, unlike the Fermi velocity v in monolayer graphene.

The weak localization correction is written in terms of Cooperon propagators $C^l_{a;s}$ where index a refers to isospin (related to matrices Σ describing sublattice degrees of freedom), l refers to pseudospin (related to matrices Λ describing valley degrees of freedom), and s refers to spin (related to matrices S). For diagonal disorder $\hat{I}u(\mathbf{r})$, the gapless modes are either combined intervalley and lattice isospin-singlets $C^0_{0;s}$ and $C^z_{0;s}$ or they are combined intravalley and lattice isospin-triplets $C^x_{z;s}$ and $C^y_{z;s}$ [21, 22]. The remaining modes have relaxation gaps: $C^l_{x;s}$ and $C^l_{y;s}$ for all valley indices $l = 0, x, y, z$ have relaxation gaps $\Gamma^l_{x;s} = \Gamma^l_{y;s} = \frac{1}{2}\tau_0^{-1}$ and modes $C^x_{0;s}$, $C^y_{0;s}$, $C^0_{z;s}$ and $C^z_{z;s}$ have gaps equal to τ_0^{-1}.

Taking only the gapless modes into account, the weak localization correction to the conductivity of bilayer graphene may be written in terms of a summation with respect to sixteen Cooperons:

$$\delta\sigma = \frac{e^2 D}{\pi\hbar}\int \frac{d^2q}{(2\pi)^2}\sum_s c_s\big[C^0_{0;s} + C^x_{z;s} + C^y_{z;s} - C^z_{0;s}\big].$$

Here, the factors $c_0 = 1$, $c_x = c_y = c_z = -1$ take into account the fact that spin singlet and triplet Cooperons appear with opposite signs.

We take into account the symmetry-breaking perturbations $\hat{h}_{2w}$, $\hat{h}_{KM}$, and $\hat{h}_{BR}$ in the Hamiltonian (10.30), as well as the symmetry-breaking disorder terms $u_{a,l}(\mathbf{r})$.

They contribute relaxation gaps $\Gamma^l_{a;s}$ to the otherwise gapless Cooperons $C^l_{a;s}$, although, owing to time-reversal symmetry, mode $C^0_{0;0}$ remains gapless. In the presence of finite inelastic decoherence rate τ_φ^{-1} and external magnetic field $\mathbf{B} = \mathrm{rot}\,\mathbf{A}$, each Cooperon has the same form as in a monolayer, (10.15), and it gives an analogous contribution to the weak localization correction to the conductivity. The zero field temperature-dependent correction to the bilayer graphene sheet resistance may be written as

$$\delta\rho(0) = -\frac{e^2\rho^2}{2\pi h}\sum_s c_s\left[\ln\left(\frac{\tau^{-1}}{\tau_\varphi^{-1}+\Gamma^0_{0;s}}\right)+\ln\left(\frac{\tau^{-1}}{\tau_\varphi^{-1}+\Gamma^x_{z;s}}\right)\right.$$
$$\left.+\ln\left(\frac{\tau^{-1}}{\tau_\varphi^{-1}+\Gamma^y_{z;s}}\right)-\ln\left(\frac{\tau^{-1}}{\tau_\varphi^{-1}+\Gamma^z_{0;s}}\right)\right], \tag{10.33}$$

and the magnetoresistance is given by

$$\Delta\rho(B) = \frac{e^2\rho^2}{2\pi h}\sum_s c_s\left[F\left(\frac{B}{B_\varphi+B^0_{0;s}}\right)+F\left(\frac{B}{B_\varphi+B^x_{z;s}}\right)\right.$$
$$\left.+F\left(\frac{B}{B_\varphi+B^y_{z;s}}\right)-F\left(\frac{B}{B_\varphi+B^z_{0;s}}\right)\right], \tag{10.34}$$

where

$$F(z) = \ln z + \psi\left(\frac{1}{2}+\frac{1}{z}\right), \tag{10.35}$$

$$B_\varphi = \frac{\hbar c}{4De}\tau_\varphi^{-1}, \qquad B^l_{0;s} = \frac{\hbar c}{4De}\Gamma^l_{0;s}, \tag{10.36}$$

and ψ is the digamma function.

We assume that different types of disorder are uncorrelated, $\langle u_{a,l}(\mathbf{r})u_{a',l'}(\mathbf{r}')\rangle = u^2_{a,l}\delta_{aa'}\delta_{ll'}\delta(\mathbf{r}-\mathbf{r}')$, resulting in scattering rates $\tau^{-1}_{a,l} = \pi\gamma u^2_{a,l}/\hbar$. Assuming isotropy of disorder in the x-y plane, we write $\tau^{-1}_{a,x} = \tau^{-1}_{a,y} = \tau^{-1}_{a,\perp}$, $\tau^{-1}_{x,l} = \tau^{-1}_{y,l} = \tau^{-1}_{\perp,l}$ and, following Refs. [20–22], combine them into the intravalley scattering rate τ_z^{-1} and the intervalley scattering rate τ_i^{-1}:

$$\tau_z^{-1} = 2\tau^{-1}_{z,z}, \qquad \tau_i^{-1} = 4\tau^{-1}_{\perp,\perp} + 2\tau^{-1}_{z,\perp}. \tag{10.37}$$

The trigonal warping term $\hat{h}_{2w}$ in the Hamiltonian (10.30) produces relaxation of the intravalley Cooperons, $C^x_{0;s}$ and $C^y_{0;s}$, as characterized [22] by the rate

$$\tau_w^{-1} = 2\tau_0(v_3 p_F/\hbar)^2, \tag{10.38}$$

although, as the trigonal warping has an opposite effect in the two valleys, this relaxation does not affect the intervalley modes, $C^0_{0;s}$ and $C^z_{0;s}$.

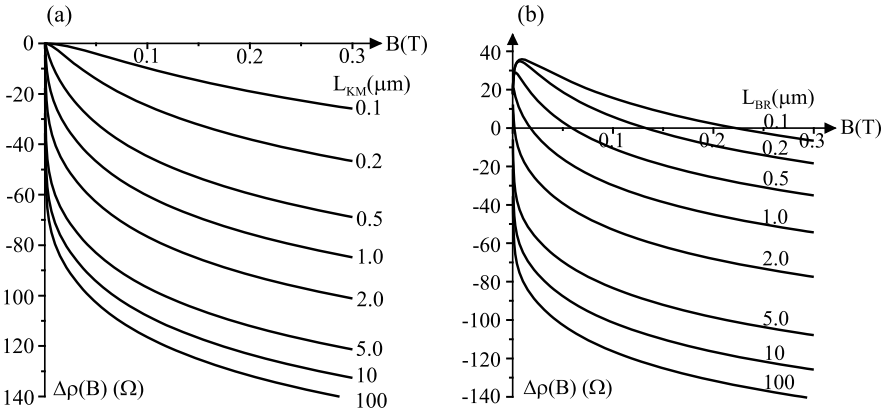

Fig. 10.5 (**a**) Low-field magnetoresistance of bilayer graphene for different strengths of the intrinsic spin-orbit coupling $\hat{h}_{KM}$, neglecting the Rashba term $\hat{h}_{BR}$. Values of the spin-orbit relaxation length L_{KM} are shown on the right hand side. (**b**) Low-field magnetoresistance for different strengths of the Bychkov-Rashba spin-orbit coupling $\hat{h}_{BR}$, neglecting the intrinsic term $\hat{h}_{KM}$. Values of the Bychkov-Rashba relaxation length L_{BR} are shown on the right hand side. Other parameter values are $\rho = 1000\ \Omega$, $L_\varphi = 10$ μm, $L_i = 500$ nm, $L_* = 200$ nm, and plots were made using (10.40)

In the absence of the spin-orbit terms, $\hat{h}_{KM}$ and $\hat{h}_{BR}$ in (10.30), the total relaxation rate of the intravalley Cooperons is written as $\tau_*^{-1} = \tau_w^{-1} + \tau_z^{-1} + \tau_i^{-1}$ [22],

$$\Gamma^0_{0;s} = 0, \qquad \Gamma^x_{z;s} = \Gamma^y_{z;s} = \tau_*^{-1}, \qquad \Gamma^z_{0;s} = 2\tau_i^{-1},$$

and the magnetoresistance [22] is given by

$$\Delta\rho(B) = -\frac{e^2\rho^2}{\pi h}\left[F\left(\frac{B}{B_\varphi}\right) + 2F\left(\frac{B}{B_\varphi + B_*}\right) - F\left(\frac{B}{B_\varphi + 2B_i}\right)\right]. \tag{10.39}$$

In the absence of intervalley scattering, intravalley symmetry-breaking as parameterized by τ_*^{-1} suppresses the weak localization effect but the presence of intervalley scattering τ_i^{-1} tends to restore it. This prediction is consistent with experimental observations [47, 48].

The spin-orbit terms $\hat{h}_{KM}$ and $\hat{h}_{BR}$ give rise to relaxation rates τ_{KM}^{-1} and τ_{BR}^{-1}, respectively, of the same form as in monolayer graphene, (10.24). In the presence of the spin-orbit terms, the relaxation of the bilayer Cooperons $C^l_{0;s}$ can be described by the following combination of rates:

$$\Gamma^0_{0;0} = 0,$$
$$\Gamma^x_{z;0} = \Gamma^y_{z;0} = \tau_*^{-1} + 2\tau_{BR}^{-1},$$

$$
\begin{aligned}
\Gamma^{z}_{0;0} &= 2\tau_i^{-1}, \\
\Gamma^{0}_{0;x} = \Gamma^{0}_{0;y} &= \tau_{BR}^{-1} + \tau_{KM}^{-1}, \\
\Gamma^{x}_{z;x} = \Gamma^{y}_{z;x} = \Gamma^{x}_{z;y} = \Gamma^{y}_{z;y} &= \tau_*^{-1} + \tau_{BR}^{-1} + \tau_{KM}^{-1}, \\
\Gamma^{z}_{0;x} = \Gamma^{z}_{0;y} &= 2\tau_i^{-1} + \tau_{BR}^{-1} + \tau_{KM}^{-1}, \\
\Gamma^{0}_{0;z} &= 2\tau_{BR}^{-1}, \\
\Gamma^{x}_{z;z} = \Gamma^{y}_{z;z} &= \tau_*^{-1}, \\
\Gamma^{z}_{0;z} &= 2\tau_i^{-1} + 2\tau_{BR}^{-1}.
\end{aligned}
$$

These results, combined with (10.33, 10.34), determine the weak localization correction to the zero-field resistance and the magnetoresistance, respectively. Explicitly, the latter is given by

$$
\begin{aligned}
\Delta\rho(B) = \frac{e^2\rho^2}{2\pi h}\Bigg[& F\left(\frac{B}{B_\varphi}\right) + 2F\left(\frac{B}{B_\varphi + B_* + 2B_{BR}}\right) \\
& - F\left(\frac{B}{B_\varphi + 2B_i}\right) - 2F\left(\frac{B}{B_\varphi + B_{BR} + B_{KM}}\right) \\
& - 4F\left(\frac{B}{B_\varphi + B_* + B_{BR} + B_{KM}}\right) \\
& + 2F\left(\frac{B}{B_\varphi + 2B_i + B_{BR} + B_{KM}}\right) \\
& - F\left(\frac{B}{B_\varphi + 2B_{BR}}\right) - 2F\left(\frac{B}{B_\varphi + B_*}\right) \\
& + F\left(\frac{B}{B_\varphi + 2B_i + 2B_{BR}}\right)\Bigg].
\end{aligned}
\tag{10.40}
$$

The low-field magnetoresistance, (10.40), for different strengths of the intrinsic spin-orbit coupling $\hat{h}_{KM}$, neglecting the Bychkov-Rashba term $\hat{h}_{BR}$, is plotted in Fig. 10.5(a). The intrinsic term $\hat{h}_{KM}$ tends to suppress weak localization. As in the monolayer, when the Bychkov-Rashba term $\hat{h}_{BR}$ is neglected, the influence of the intrinsic spin-orbit term may be absorbed into a modified definition of the inelastic dephasing rate as $\tau_\varphi^{-1} \Rightarrow \tau_\varphi^{-1} + \tau_{KM}^{-1}$ in the formulae obtained by neglecting spin-orbit coupling, such as (10.39). Unlike monolayer graphene, however, chiral quasiparticles produce weak localization in bilayers, and no crossover to weak antilocalization is visible, Fig. 10.5(a), even when the combined effective dephasing rate $\tau_\varphi^{-1} + \tau_{KM}^{-1}$ is relatively large.

The low-field magnetoresistance, (10.40), for different strengths of the Bychkov-Rashba spin-orbit coupling $\hat{h}_{BR}$, neglecting the intrinsic term $\hat{h}_{KM}$, is plotted in Fig. 10.5(b). The Bychkov-Rashba term $\hat{h}_{BR}$ tends to drive weak localization

towards weak anti-localization as in conventional materials [1] and monolayer graphene.

10.6 Summary and Conclusions

The weak localization correction to the classical conductivity arises from the interference of electrons that travel along long diffusive paths and, thus, it is a sensitive probe of symmetry breaking and scattering [14–27, 29, 30]. Regimes of weak localization (WL) and weak anti-localization (WAL) behavior, arising from the interplay between lattice, valley and spin degrees of freedom in graphene, are summarized in Fig. 10.1 for monolayer and bilayer. In the absence of symmetry breaking, $\tau_\varphi \ll \tau_*, \tau_i$, the chirality of electrons in monolayer and bilayer graphene would be manifest as WAL and WL behavior, respectively. However, in typical graphene samples, sources of symmetry breaking including trigonal warping, random-bond disorder (due to bending of a graphene sheet) and dislocation/antidislocation pairs will tend to suppress weak localization (in the regime $\tau_* \ll \tau_\varphi \ll \tau_i$), so that weak localization can only be observed in the presence of strong inter-valley scattering, $\tau_i \ll \tau_\varphi$.

At very low temperature, weak localization in graphene may be sensitive to the presence and nature of spin-orbit coupling, resulting in weak anti-localization—as in semiconductors and metals [1]—in both monolayers and bilayers if the spin-orbit coupling is of the Bychkov-Rashba (BR) type, $\tau_{BR} \ll \tau_\varphi$. This would be distinguishable from the presence of intrinsic spin-orbit coupling, which would lead to suppressed weak localization once $\tau_{KM} \ll \tau_\varphi$.

Acknowledgements This project has been funded by JST-EPSRC Japan-UK Cooperative Programme Grant EP/H025804/1, EU STREP ConceptGraphene, and the Royal Society.

References

1. S. Hikami, A.I. Larkin, Y. Nagaoka, Prog. Theor. Phys. **63**, 707 (1980)
2. C.L. Kane, E.J. Mele, Phys. Rev. Lett. **95**, 226801 (2005)
3. H. Min, J.E. Hill, N.A. Sinitsyn, B.R. Sahu, L. Kleinman, A.H. MacDonald, Phys. Rev. B **74**, 165310 (2006)
4. D. Huertas-Hernando, F. Guinea, A. Brataas, Phys. Rev. B **74**, 155426 (2006)
5. Y. Yao, F. Ye, X.-L. Qi, S.-C. Zhang, Z. Fang, Phys. Rev. B **75**, 041401(R) (2007)
6. J.C. Boettger, S.B. Trickey, Phys. Rev. B **75**, 121402(R) (2007)
7. M. Gmitra, S. Konschuh, C. Ertler, C. Ambrosch-Draxl, J. Fabian, Phys. Rev. B **80**, 235431 (2009)
8. R. van Gelderen, C. Morais Smith, Phys. Rev. B **81**, 125435 (2010)
9. F. Guinea, New J. Phys. **12**, 083063 (2010)
10. H.-W. Liu, X.C. Xie, Q.-f. Sun, arXiv:1004.0881
11. E. McCann, M. Koshino, Phys. Rev. B **81**, 241409(R) (2010)
12. Y.A. Bychkov, E.I. Rashba, J. Phys. C **17**, 6039 (1984)
13. E.I. Rashba, Phys. Rev. B **79**, 161409 (2009)

14. K.-I. Imura, Y. Kuramoto, K. Nomura, Phys. Rev. B **80**, 085119 (2009)
15. K.-I. Imura, Y. Kuramoto, K. Nomura, Europhys. Lett. **89**, 17009 (2010)
16. E. McCann, V.I. Fal'ko, Phys. Rev. Lett. **108**, 166606 (2012)
17. B.L. Altshuler, D. Khmelnitski, A.I. Larkin, P.A. Lee, Phys. Rev. B **22**, 5142 (1980)
18. H. Suzuura, T. Ando, Phys. Rev. Lett. **89**, 266603 (2002)
19. A.F. Morpurgo, F. Guinea, Phys. Rev. Lett. **97**, 196804 (2006)
20. E. McCann, K. Kechedzhi, V.I. Fal'ko, H. Suzuura, T. Ando, B.L. Altshuler, Phys. Rev. Lett. **97**, 146805 (2006)
21. K. Kechedzhi, E. McCann, V.I. Fal'ko, H. Suzuura, T. Ando, B.L. Altshuler, Eur. Phys. J. Spec. Top. **148**, 39 (2007)
22. K. Kechedzhi, V.I. Fal'ko, E. McCann, B.L. Altshuler, Phys. Rev. Lett. **98**, 176806 (2007)
23. S.V. Morozov, K.S. Novoselov, M.I. Katsnelson, F. Schedin, L.A. Ponomarenko, D. Jiang, A.K. Geim, Phys. Rev. Lett. **97**, 016801 (2006)
24. H.B. Heersche, P. Jarillo-Herrero, J.B. Oostinga, L.M.K. Vandersypen, A.F. Morpurgo, Nature **446**, 56 (2007)
25. X. Wu, X. Li, Z. Song, C. Berger, W.A. de Heer, Phys. Rev. Lett. **98**, 136801 (2007)
26. F.V. Tikhonenko, D.W. Horsell, R.V. Gorbachev, A.K. Savchenko, Phys. Rev. Lett. **100**, 056802 (2008)
27. D.-K. Ki, D. Jeong, J.-H. Choi, H.-J. Lee, K.-S. Park, Phys. Rev. B **78**, 125409 (2008)
28. F.V. Tikhonenko, A.A. Kozikov, A.K. Savchenko, R.V. Gorbachev, Phys. Rev. Lett. **103**, 226801 (2009)
29. A.A. Kozikov, D.W. Horsell, E. McCann, V.I. Fal'ko, Phys. Rev. B **86**, 045436 (2012)
30. S. Lara-Avila, A. Tzalenchuk, S. Kubatkin, R. Yakimova, T.J.B.M. Janssen, K. Cedergren, T. Bergsten, V. Fal'ko, Phys. Rev. Lett. **107**, 166602 (2011)
31. R. Saito, M.S. Dresselhaus, G. Dresselhaus, *Physical Properties of Carbon Nanotubes* (Imperial College Press, London, 1998)
32. T. Ando, T. Nakanishi, R. Saito, J. Phys. Soc. Jpn. **67**, 2857 (1998)
33. D.M. Basko, Phys. Rev. B **78**, 125418 (2008)
34. M.I. D'yakonov, V.I. Perel, Sov. Phys. JETP **33**, 1053 (1971)
35. D. Huertas-Hernando, F. Guinea, A. Brataas, Eur. Phys. J. Spec. Top. **148**, 177 (2007)
36. R.J. Elliott, Phys. Rev. **96**, 266 (1954)
37. Y. Yafet, in *Solid State Physics*, vol. 14, ed. by F. Seitz, D. Turnbull (Academic, New York, 1963)
38. K.S. Novoselov, E. McCann, S.V. Morozov, V.I. Fal'ko, M.I. Katsnelson, U. Zeitler, D. Jiang, F. Schedin, A.K. Geim, Nat. Phys. **2**, 177 (2006)
39. E. McCann, V.I. Fal'ko, Phys. Rev. Lett. **96**, 086805 (2006)
40. T. Ohta, A. Bostwick, T. Seyller, K. Horn, E. Rotenberg, Science **313**, 951 (2006)
41. F. Guinea, A.H. Castro Neto, N.M.R. Peres, Phys. Rev. B **73**, 245426 (2006)
42. B. Partoens, F.M. Peeters, Phys. Rev. B **74**, 075404 (2006)
43. M. Mucha-Kruczyński, O. Tsyplyatyev, A. Grishin, E. McCann, V.I. Fal'ko, A. Bostwick, E. Rotenberg, Phys. Rev. B **77**, 195403 (2008)
44. J. Nilsson, A.H. Castro Neto, F. Guinea, N.M.R. Peres, Phys. Rev. B **78**, 045405 (2008)
45. J.R. Schrieffer, P.A. Wolff, Phys. Rev. **149**, 491 (1966)
46. M. Koshino, T. Ando, Phys. Rev. B **73**, 245403 (2006)
47. R.V. Gorbachev, F.V. Tikhonenko, A.S. Mayorov, D.W. Horsell, A.K. Savchenko, Phys. Rev. Lett. **98**, 176805 (2007)
48. Z.-M. Liao, B.-H. Han, H.-C. Wu, D.-P. Yu, Appl. Phys. Lett. **97**, 163110 (2010)

Index

H. Aoki, M.S. Dresselhaus (eds.), *Physics of Graphene*, NanoScience and Technology,
DOI 10.1007/978-3-319-02633-6,